Université de Liège
Département d'Aérospatiale et Mécanique

von Karman Institute for Fluid Dynamics
Turbomachinery and Propulsion Department

Aerodynamics of a High-Speed Low-Pressure Turbine Cascade with Unsteady Wakes and Purge Flow

Gustavo Lopes

Thesis presented in order to obtain the degree of
Doctor of Philosophy in Engineering Sciences
Université de Liège
August 2024

Université de Liège
Département d'Aérospatiale et Mécanique

von Karman Institute for Fluid Dynamics
Turbomachinery and Propulsion Department

Supervisor(s):
Prof. Sergio Lavagnoli (von Karman Institute for Fluid Dynamics, Belgium)
Prof. Koen Hillewaert (Université de Liège, Belgium)

Doctoral Committee:
Prof. Loïc Salles, President of the jury (Warsaw University of Technology, Poland)
Prof. Koen Hillewaert, Promoter and Secretary of the jury (University of Liège, Belgium)
Prof. Sergio Lavagnoli, Supervisor (Université catholique de Louvain, Belgium)
Prof. Thomas Andrianne (University of Liège, Belgium)
Prof. John Coull (University of Oxford, United Kingdom)
Prof. Davide Lengani (University of Genoa, Italy)
Prof. Slawomir Kubacki (Warsaw University of Technology, Poland)

Cover art: The SPLEEN C1 cascade: Phase-resolved measurements at Plane 02 and 03, and secondary flow signature at Plane 06.

von Karman Institute for Fluid Dynamics
Turbomachinery and Propulsion Department

Waterloosesteenweg 72, 1640 Sint-Genesius-Rode
Phone: +32 359 96 11, https://www.vki.ac.be

D/2024/0238/781, T. Magin, Editor-in-Chief
Published by the von Karman Institute for Fluid Dynamics with permission.

ISBN 978-2-87516-212-0

Summary

An experimental investigation on the aerodynamics of a high-speed low-pressure turbine was performed at engine-relevant Mach and Reynolds numbers. Measurements were performed in a transonic low-Reynolds linear cascade. Rotating bars were used to recreate the incoming wakes characterized by engine-representative wake velocity triangles. A secondary air system connected to a cavity slot injects purge flows upstream of the cascade.

Time-averaged measurements of the midspan inlet and outlet flowfield and blade loading were performed to characterize the inlet boundary conditions and cascade performance. The blade aerodynamics were compared against numerical simulations to highlight the challenges of the latter in capturing the correct physics of high-speed low-pressure turbines. Surface-mounted hot-films and fast-response pressure sensors were used to comprehensively characterize the blade boundary layer and transition mechanisms. Classical transition features were observed for all cases up to Mach numbers at which passage shocks occur. For the highest Mach number investigated, the separation was impacted by the shock impingement on the SS for the steady inlet flow cases. In the time-resolved frame of reference, the separated wake-induced transition mechanism was characterized by Kelvin-Helmholtz instabilities. An exception occurred for the case described by a shock in the passage.

The cascade inlet boundary layer was also characterized with time-averaged and time-resolved instrumentation. The secondary flows were found to be weakened with increasing Mach number. Upon the introduction of unsteady wakes in the flow domain, the secondary flows were found to be modulated. The periodic thinning of the inlet boundary layer partially suppressed the passage vortex during one wake cycle. Similar findings were found for cases characterized by purge flow injection. The secondary flows were strengthened and displaced away from the endwall with an increasing purge massflow ratio. The classical secondary flow structures were still observed with the purge: passage vortex, trailing shed vorticity, and corner vortex. The structures were found to be modulated by the wake passing. Opposite from the case without purge, the passage vortex is always identifiable during each wake-passing cycle. The passage vortex suffered the most considerable degree of fluctuations due to the wake. The endwall flow is largely uncorrelated to the unsteady wake.

The experimental data was used to challenge state-of-the-art loss models. Classical empirical loss models failed to predict the profile loss correctly. A physics-based loss correlation that models the boundary layer development along the blade surfaces revealed that further calibration is required to widen its application to the current blade geometry. Classical secondary loss correlations also struggled to capture the loss. Physics-based loss correlation satisfactorily predicted the secondary loss for the investigated flow conditions without unsteady wakes and purge flow. The latter demonstrated to be sensitive to the inlet boundary layer, and therefore, improving the experimental characterization of the inlet boundary layer must be sought to assess the capability of correlations to predict secondary loss correctly.

Dedication

Dedico este trabalho à minha avó, que partiu do mundo físico antes que pudéssemos comemorar esta vitória juntos.

"Metidos nesta pele que nos refuta,
Dois somos, o mesmo que inimigos.
Grande coisa, afinal, é o suor
(Assim já o diziam os antigos):
Sem ele, a vida não seria luta,
Nem o amor amor."
José Saramago, in "Os Poemas Possíveis"

Acknowledgments

It has been a long journey since I arrived in Brussels in 2019. As usual, I find myself with the challenging task of successfully conveying what I must while keeping it concise. It is impossible to recall and acknowledge everyone who has been part of this journey individually. Please do not think less of me. However, I will recall people who have had a lasting impact on my past, present, and hopefully future.

It makes sense to start with people who saw my professional development over the last five years at VKI. It's only reasonable to begin with Fede and Miz, as we have been together nearly since the beginning of our stay in Belgium. We've shared many professional and personal moments, and our relationship is perhaps the central point of this experience. Thank you for all the fun working days (even at times when fun is not the word that describes the mindset), the climbing sessions, and the road trips. Having seen the project in which my PhD fits from beginning to end, lots of people came and went. The first was Sam, who received me in Belgium and the SPLEEN project. Thank you for your guidance while keeping it as humane as possible and following up with Loris, who integrated the project later. I'm not sure I should thank you for all the late nights we tested, prepared to test, or wrote articles, but I'm sure you made it bearable enough that I don't resent these moments. I appreciate interacting with you and have been a victim of your energy and enthusiasm. I also extend my appreciation to Marios, who joined the project at a critical phase and from whom I've learned a lot from his approach to work and leadership. As for the remaining colleagues with whom I've had great times at and off work, thank you, Gonçalo, Ricci, Cansev, Lore, Schena, Bertelli, Filippo, Bogdan, Eli, Giacomo, Jorge, Tânia, Marios, Bora, Nik, Rosafio, Peter, Terezie, Antoine. I apologize if I forgot anyone, and I also thank them. I've co-supervised more than twenty students during my stay at VKI, and I cannot possibly name them individually. I'd still like to thank all the students I interacted with for their patience and what I learned from them. I'll extend a particular token of appreciation to Mariana, Filippo, and Gene, with whom I still hold close contact (and possibly some of whom suffered the most with my attention to detail and persistence). I must thank Christine for supporting me and helping me get through a considerable part of my PhD.

I must thank my supervisors, Prof. Sergio Lavagnoli and Prof. Koen Hillewaert, for their guidance and support throughout the PhD. The impact that their advice had is unquantifiable. In particular, I have worked closely with Prof. Sergio Lavagnoli from the beginning. Therefore, he greatly greatly influenced my way of working, attention to detail, and soundness of my work methodology. He always allowed me to conduct research my way, even when it was not the most direct path; he always respected my research curiosity and approach when I made an easy task nearly impossible. I acknowledge his guidance and openness and thank him for that. The support of Prof. Fabrizio Fontaneto is also greatly acknowledged for his availability to discuss and help with research-related questions and for the great moments

spent as a team at international conferences. I thank Terence Boyen for assisting with the extensive list of instrumentation used throughout my work. I extend my gratitude to Prof. Tony Arts, who provided valuable feedback upon arrival at VKI, impacting my professional practices and the project. I also thank the doctoral committee for reviewing the manuscript and providing valuable and insightful feedback and comments.

Life is not only made of work; therefore, I must thank everyone who made my stay in Brussels memorable and enjoyable. Thank you to Sanja, Ricci, Matteo, Ale, Chiara, Nick, Giacomo, Babi, and Thomas for our great time at the park, having a drink, going on road trips, and climbing. You strongly contributed to calling Brussels home and a place where to return and looking forward to meeting again.

The portion of the PhD required to write the thesis and prepare the defense is not negligible. You have been inspiring and supportive over the last few months, during which life has posed me with unexpected personal and professional barriers. You have helped me manage my sanity, encouraged me out of my comfort zone, and supported me unconditionally. I'm forever grateful, Fanny.

Last but not least, this long journey was as challenging for me as it was for my parents. They are one of the main reasons why I keep pushing myself professionally. You have been supportive and loving since I left home to grow personally and professionally. With this, I send my gratitude and pride for having the privilege of calling you my parents. I extend my appreciation to my dear family. A last token of appreciation goes to my friends in Portugal for being a constant source of support and receiving me back home like we never grew up.

Brussels, August 2024
Gustavo Lopes

Table of Contents

Summary i

Dedication i

Acknowledgments i

1 Introduction 1-1
- 1.1 Motivation . . . 1-1
- 1.2 State of the Art . . . 1-6
  - 1.2.1 Two-Dimensional Profile Aerodynamics . . . 1-7
  - 1.2.2 Secondary Flows . . . 1-11
  - 1.2.3 Loss Modeling . . . 1-15
- 1.3 Research Objectives . . . 1-16
- 1.4 Thesis Outline . . . 1-17

References . . . 1-19

2 Experimental Methodology 2-1
- 2.1 The VKI S-1/C Linear Cascade . . . 2-1
- 2.2 The SPLEEN Test Case . . . 2-5
- 2.3 The SPLEEN C1 Cascade . . . 2-7
  - 2.3.1 Scaling of Airfoil-Cavity Arrangement . . . 2-9
  - 2.3.2 High-Speed Wake Generator . . . 2-10
  - 2.3.3 Engine-Representative Cavity Geometry . . . 2-12
- 2.4 Measurement Techniques . . . 2-13
  - 2.4.1 Measurement Planes . . . 2-15
  - 2.4.2 Reference Quantities . . . 2-16
    - 2.4.2.1 Reference Total Pressure . . . 2-17
    - 2.4.2.2 Reference Total Temperature . . . 2-17
    - 2.4.2.3 Inlet and Outlet Static Pressure . . . 2-17
    - 2.4.2.4 Cascade Far Exit . . . 2-18
    - 2.4.2.5 Wake Generator Speed and Position . . . 2-18
    - 2.4.2.6 Purge Flow System Massflow . . . 2-20
  - 2.4.3 Preston Boundary Layer Tube . . . 2-21
  - 2.4.4 Cobra-Shaped Five-Hole Probe . . . 2-22
  - 2.4.5 L-Shaped Five-Hole Probe . . . 2-25
  - 2.4.6 Twin Pneumatic and Fast-Response Virtual Four-Hole Probes . . . 2-26
    - 2.4.6.1 Reynolds Effects in Calibration . . . 2-28
    - 2.4.6.2 PV4HP vs. FRV4HP . . . 2-30
    - 2.4.6.3 Static Calibration . . . 2-31

2.4.6.4 Probe Bandwidth . . . 2-33
2.4.7 Cross-Wire Probe . . . 2-34
2.4.8 Blade Pneumatic Static Pressure Taps . . . 2-35
2.4.9 Endwall Pneumatic Static Pressure Taps . . . 2-35
2.4.10 Blade Fast-Response Pressure Taps . . . 2-36
2.4.11 Blade Surface Mounted Hot-Film Sensors . . . 2-39
2.5 Definition of Operating Point . . . 2-40
2.5.1 Cascade Mach and Reynolds Numbers . . . 2-40
2.5.2 Reduced Frequency and Flow Coefficient . . . 2-41
2.5.3 Purge Massflow Ratio . . . 2-42
2.6 Data Reduction . . . 2-45
2.6.1 Cascade Metrics and Performance . . . 2-45
2.6.1.1 Boundary Layer Integral Parameters . . . 2-45
2.6.1.2 Flow Angles . . . 2-45
2.6.1.3 Kinetic Energy Loss Coefficient . . . 2-47
2.6.1.4 Streamwise Vorticity Coefficient . . . 2-47
2.6.1.5 Secondary Kinetic Energy Coefficient . . . 2-47
2.6.2 Area- and Mass-Averaging . . . 2-48
2.6.3 Phase-Locked Averaging . . . 2-49
2.6.4 Statistical Moments . . . 2-53
2.6.5 Turbulence Estimation with Hot-Wire Probes . . . 2-53
2.6.6 Turbulence Estimation with Fast-Response Probes . . . 2-55
2.7 Uncertainty Quantification . . . 2-56
2.7.1 Definitions and Error Propagation . . . 2-56
2.7.2 Sources of Uncertainty . . . 2-57
2.7.3 Measurement Uncertainties . . . 2-58
2.8 Phases of Testing . . . 2-60
References . . . 2-61

3 Numerical Methods 3-1
3.1 Coupled Viscous-Inviscid Computations . . . 3-1
3.1.1 Boundary Conditions . . . 3-2
3.1.2 Mesh . . . 3-2
3.1.3 Incidence Sensitivity . . . 3-5
3.1.4 Sensitivity to Turbulence . . . 3-8
3.2 Reynolds-Averaged Navier-Stokes . . . 3-9
3.2.1 Numerical Parameters . . . 3-10
3.2.2 Mesh . . . 3-11
3.2.3 Incidence Sensitivity . . . 3-14
3.2.4 Definition of Inlet Turbulent Quantities . . . 3-15
References . . . 3-18

4 Characterization of Flow Conditions in High-Speed Linear Cascade 4-1
4.1 Stability of Flow Conditions . . . 4-1
4.2 Determination of Cascade Inlet Total Pressure . . . 4-3
4.2.1 Turbulence Grid Loss Coefficient . . . 4-4
4.2.2 Turbulence Grid + Wake Generator Loss Coefficient . . . 4-7
4.3 Periodicity . . . 4-9
4.3.1 Plane 01 . . . 4-9

4.3.2 Plane 02 . . . 4-10
4.3.3 Plane 03 . . . 4-12
4.3.4 Plane 06 . . . 4-14
4.4 Probe Interference . . . 4-21
4.4.1 Inlet Measurements . . . 4-24
4.4.2 Outlet Measurements . . . 4-25
4.4.3 Blade . . . 4-26
4.4.4 Compensation . . . 4-28
4.4.5 Monitoring of Operating Point . . . 4-32
4.5 Conclusions . . . 4-34
References . . . 4-36

5 Profile Aerodynamics 5-1
5.1 Flow Conditions . . . 5-1
5.2 Time-Averaged Results . . . 5-2
5.2.1 Cascade Inlet . . . 5-2
5.2.1.1 Cascade Inlet with Steady Flow . . . 5-2
5.2.1.2 Cascade Inlet with Unsteady Wakes . . . 5-3
5.2.1.3 Turbulent Quantities . . . 5-5
5.2.2 Blade Loading and Boundary Layer . . . 5-6
5.2.2.1 Steady Inlet Flow . . . 5-6
5.2.2.2 Impact of Unsteady Wakes . . . 5-26
5.2.3 Profile wake and Loss . . . 5-32
5.2.3.1 Steady Inlet Flow . . . 5-32
5.2.3.2 Impact of Unsteady Wakes . . . 5-33
5.3 Time-Resolved Measurements . . . 5-36
5.3.1 Bar Wake Characterization . . . 5-36
5.3.2 Wake-Boundary Layer Interaction . . . 5-40
5.3.3 Blade Wake Aerodynamics . . . 5-48
5.4 Spectral Analysis . . . 5-56
5.4.1 Rig Characteristic Frequencies . . . 5-56
5.4.2 Blade Surface Frequencies . . . 5-59
5.5 Conclusions . . . 5-66
References . . . 5-69

6 Secondary Flows 6-1
6.1 Flow Conditions . . . 6-1
6.2 Time-Averaged Measurements . . . 6-2
6.2.1 Inlet Boundary Layer Characterization . . . 6-2
6.2.1.1 Steady Inlet Flow . . . 6-2
6.2.1.2 Turbulent Quantities . . . 6-4
6.2.1.3 Unsteady Inlet Flow with Flat Endwall . . . 6-4
6.2.1.4 Unsteady Inlet Flow with Cavity Slot . . . 6-7
6.2.2 Blade Aerodynamics . . . 6-9
6.2.2.1 On- and Off-Design Impact . . . 6-9
6.2.2.2 Impact of Unsteady Wakes . . . 6-11
6.2.2.3 Impact of Purge Flow on Blade Loading . . . 6-11
6.2.3 Characterization of Secondary Flows . . . 6-13
6.2.3.1 Off-Design Performance under Steady Inlet Flow . . . 6-15

6.2.3.2 Impact of Unsteady Wakes . . . 6-19
6.2.3.3 Impact of Purge Flow . . . 6-21
6.3 Time-Resolved Measurements . . . 6-25
6.3.1 Unsteadiness of the Inlet Boundary Layer . . . 6-25
6.3.2 Unsteadiness of the Inlet Purge Flow . . . 6-29
6.3.3 Unsteadiness on Blade Surface . . . 6-31
6.3.4 Secondary Flows . . . 6-35
6.4 Spectral Analysis . . . 6-46
6.4.1 Blade Surface . . . 6-46
6.4.2 Secondary flows . . . 6-47
6.5 Conclusions . . . 6-49
References . . . 6-52

7 Loss Modeling **7-1**
7.1 Profile Loss . . . 7-1
7.1.1 Past models . . . 7-1
7.1.2 Model of Coull & Hodson . . . 7-2
7.1.2.1 Estimation of Separation Location . . . 7-5
7.1.2.2 Comparison of Model with Calibrated MISES . . . 7-8
7.1.2.3 Comparison of Loss Breakdown Schemes . . . 7-13
7.1.2.4 Loss Breakdown . . . 7-17
7.2 Secondary Loss . . . 7-23
7.2.1 Model of Coull, 2017 . . . 7-24
7.2.2 Model of Coull and Clark, 2022 . . . 7-28
7.3 Conclusions . . . 7-29
References . . . 7-32

8 Conclusions **8-1**
8.0.1 Future Work and Remarks . . . 8-3

A Publications **A-1**
A.1 Journal Publications . . . A-1
A.2 Conference Proceedings . . . A-2
A.3 Data Sets . . . A-2

B Calibration of Instrumentation **B-1**
B.1 Static Calibration of reference K-type Thermocouple . . . B-1
B.2 Static Calibration of Injection Circuit K-type Thermocouple . . . B-2
B.3 Static Calibration of Injection Circuit Validynes . . . B-3
B.4 Aerodynamic Calibration of C5HP . . . B-4
B.4.1 Sensitivity of the Aerodynamic Calibration Coefficients to P_{ave} . . . B-4
B.4.2 Aerodynamic Calibration Coefficients . . . B-6
B.4.3 Orthogonality Map . . . B-6
B.5 Aerodynamic Calibration of L5HP . . . B-8
B.5.1 Sensitivity of the Aerodynamic Calibration Coefficients to P_{ave} . . . B-8
B.5.2 Aerodynamic Calibration Coefficients . . . B-8
B.5.3 Orthogonality Map . . . B-9
B.6 Aerodynamic Calibration of PV4HP . . . B-11
B.6.1 Aerodynamic Calibration Coefficients . . . B-11

B.7 Static Calibration of FRV4HP Sensors B-13
B.7.1 Pressure B-13
B.7.2 Temperature B-13
B.8 Static Calibration of Blade FR Pressure Sensors B-14
B.8.1 Pressure B-14
B.8.2 Temperature B-15

C Location of instrumentation **C-1**
C.1 Blade SS: pneumatic taps C-1
C.2 Blade PS: pneumatic taps C-2
C.3 Endwall Insert 1: pneumatic taps C-2
C.4 Endwall Insert 2: pneumatic taps C-3
C.5 Blade SS: fast-response taps C-3
C.6 Blade PS: fast-response taps C-3
C.7 Endwall Insert 1: fast-response taps C-4
C.8 Endwall Insert 2: fast-response taps C-4
C.9 Blade SS: surface mounted hot-films C-4
C.10 Blade PS: surface mounted hot-films C-5

D Detailed Breakdown of Uncertainty Estimation **D-1**
D.1 Loss Correlation for Turbulence Grid and Wake Generator D-1
D.2 Flow Conditions and Surface Measurements D-2
D.2.1 Uncertainty of isentropic Mach number D-2
D.2.2 Uncertainty of static temperature D-2
D.2.3 Uncertainty of isentropic velocity D-2
D.2.4 Uncertainty of density D-2
D.2.5 Uncertainty of dynamic viscosity D-3
D.2.6 Uncertainty of isentropic Reynolds number D-3
D.3 Quantities Retrieved with Directional Multi-Hole Probes D-3
D.3.1 Probe yaw angle D-3
D.3.2 Probe pitch angle D-4
D.3.3 Total pressure D-4
D.3.4 Static pressure D-5
D.3.5 Mach number D-6
D.3.6 System of equations to retrieve unknown uncertainties D-6
D.4 Quantities Describing Cascade Performance D-7
D.4.1 Primary flow direction D-7
D.4.2 Cascade pitch angle D-7
D.4.3 Normalized static pressure D-8
D.4.4 Normalized total pressure D-8
D.4.5 Total pressure loss coefficient without static pressure D-8
D.4.6 Total pressure loss coefficient with static pressure D-8
D.4.7 Kinetic energy loss coefficient D-8

E Comparison of Blade Loading and Hot-Film Measurements for Steady and Unsteady Inlet Flow **E-1**
E.1 Steady Inlet Flow E-1
E.2 Unsteady Inlet Flow E-4

F Boundary layer parameters **F-1**
F.1 Plane 01 . . . . . F-1
F.2 Plane 02 . . . . . F-1

G Experimental Loss Breakdown **G-1**
G.1 Mass-Averaged G-1
G.2 Mixed-Out-Averaged G-3

H Error from Different Methods of Estimating the Separation Location **H-1**

I Boundary Layer Integral Parameters at Blade Trailing Edge **I-1**

List of Figures

1.1 Comparison of the evolution of CO_2 emissions for different scenarios: fleet with 1990 efficiency, fleet with current characteristics; in relation to net-zero target [5]. . . . 1-2
1.2 The Pratt & Whitney PW1100G (source: Pratt & Whitney). . . . 1-3
1.3 Specific fuel consumption vs. by-pass ratio for direct drive and geared architectures [6]. . . . 1-3
1.4 Axial turbine stage efficiency in function of stage loading and flow coefficient [12]. . . . 1-4
1.5 Airfoils and velocity triangles of conventional LPT (left) and equivalent to high-speed LPT (right) [13]. . . . 1-5
1.6 Reynolds number regime encountered in LPT during flight cycle [21]. . . . 1-7
1.7 Schematic representation of laminar separation bubble [39] (a) and signature on turbine blade loading [40] (b). . . . 1-8
1.8 Sketch of wake in LPT (a) and velocity triangles in the freestream and wake (b) [66]. . . . 1-9
1.9 Schematic of the transition mechanism resulting from wake-separated boundary layer interaction. [72] . . . 1-10
1.10 Interaction of negative jet with inflectional boundary and generation of Kelvin-Helmholtz instabilities [71] (a) and pressure fluctuating traces in separation bubble [72] (b). . . . 1-11
1.11 Secondary flow model of Wang et al. [85] 1-12
1.12 Schematic representation of secondary flows in turbine after Coull [14]. . . . 1-13
1.13 Rim seal aero-thermodynamics in terms of streamlines in meridional plane [110] and ISO-surface of constant turbulent kinetic energy and surface streamlines showing the secondary flow vortices for the cavity case [112]. . . . 1-15

2.1 The VKI S-1/C wind tunnel. . . . 2-2
2.2 Elbow of VKI S-1/C equipped with linear cascade (a) and cut of cascade used during the EU SPLEEN campaign (b). . . . 2-2
2.3 Turbulence grid in relation to cascade with detail characterizing TG key parameters (a) and isolated TG (b). . . . 2-3
2.4 Technical drawing of generic cascade with wake generator bars (a), detailed view of wake generator bars relative to cascade (b) and wake generator casing (c). . . . 2-4
2.5 Purge flow circuit constituents in relation to the upper loop of VKI S-1/C. . . . 2-4
2.6 Implemented secondary air system in relation to the VKI S-1/C: Orifice plate (a) and purge flow splitter (b). . . . 2-5
2.7 Probe traversing unit (a) mounted in the VKI S-1/C (b). . . . 2-6
2.8 Blade traversing unit (a) mounted in the VKI S-1/C (b). . . . 2-6

2.9 Schematic view of 1.5 low-pressure turbine stages with identified regions of interest. 2-7
2.10 SPLEEN cascade complete test section setup(a) and detail of WG slot (b). . . 2-8
2.11 SPLEEN C1 installed in the VKI S-1/C without WG and cavity slot (a), and test section equipped with WG bars and cavity slot (b). 2-8
2.12 SPLEEN Cascade C1 geometry. 2-9
2.13 Wake generator assembly in relation to linear cascade (a) and wake generator bars in test section (b). 2-11
2.14 Wake generator bar support used during tests performed without purge flow. 2-11
2.15 Wake generator bar support used during tests performed with purge flow. . . 2-11
2.16 View of the test section with detail of wake generator bar support and cavity structural elements: (1) buffer plate and (2) NACA0024 (a) and cavity geometry key dimensions (b). 2-12
2.17 Cavity endwall tested alongside cascade: central/sliding blade, WG slot. . . 2-13
2.18 Meridional view of linear cascade test section highlighting the distribution of instrumentation used in this investigation. 2-14
2.19 Cartesian reference system of SPLEEN C1 cascade. 2-15
2.20 Blade-to-blade view of cascade highlighting the measurements planes. Plane Ref. is omitted. 2-16
2.21 Location of the pitot tubes upstream of the test section. 2-17
2.22 Location of cascade far exit pressure tap. 2-18
2.23 Phasing of the wake generator bars with the central blade leading edge: wake generator bar aligned with the central airfoil LE along the projection of the airfoil metal angle (a) and practical application in the VKI S-1/C (b). 2-19
2.24 Photo-diode signal and wake generator toothed wheel position. The second edge of the short tooth in the direction of rotation is the reference for the bar #1 aligned with the central blade LE (corresponding to a bar phase of 0). . . 2-19
2.25 Schematic of orifice plate geometry. 2-20
2.26 Schematic of instrumentation in the vicinity of the orifice plate. 2-21
2.27 Purge flow splitter. 2-21
2.28 Preston boundary layer probe geometry and dimensions. 2-22
2.29 Cobra-shaped five-hole probe geometry and dimensions. 2-23
2.30 Iterative cycle used to retrieve flow quantities [14]. 2-24
2.31 L-shaped five-hole probe geometry and dimensions. 2-25
2.32 Virtual four-hole probe geometry and dimensions. 2-26
2.33 Pressure coefficients obtained for a probe used in a virtual mode in the function of the probe yaw angle. 2-27
2.34 Heads of virtual four-hole probe to be installed with pneumatic lines and fast-response sensors. 2-27
2.35 Comparison between the aerodynamic calibration coefficients of pneumatic virtual four-hole probe obtained ex-situ and in-situ at fixed γ=0°: (a) K_α, (b) K_γ, (c) K_{tot} and (d) K_{stat}. 2-29
2.36 Difference in retrieved P_0 (a) and P (b) between in-situ and ex-situ calibrations for γ=0°. 2-29
2.37 Comparison between the aerodynamic calibration coefficients of fast-response and pneumatic virtual four-hole probe obtained at fixed γ=0°: (a) K_α, (b) K_γ, (c) K_{tot} and (d) K_{stat}. 2-30

2.38 Deficit in perceived P_0 (a) and P between the in-situ calibrations of fast-response and virtual four-hole probe probes for a dynamic head typically encountered at the inlet of the test section for γ=0°. 2-31
2.39 Schematic highlighting possible probe head difference to justify the difference in perceived pitch angle. 2-31
2.40 Fitted calibration surface to P=f(V_P, V_S) (a) and to T=f(V_P, V_S) (b) for the second sensor on the blade suction side during the second phase of testing. . . 2-32
2.41 Sketch of virtual four-hole probe head instrumented with fast-response sensors and resulting line-cavity system. 2-33
2.42 Schematic of line-cavity system highlighting sensor recess for down tap of virtual four-hole probe. 2-34
2.43 Geometry and dimensions of the cross hot-wire probe. 2-35
2.44 Location of pressure taps on blade suction side (a) and pressure side (b). The milled grooves on the non-measuring side are filled with epoxy to ensure a smooth surface. 2-35
2.45 Combination of insert 1 and 2 to create a virtual insert with higher spatial resolution. 2-36
2.46 Instrumented endwall inserts: Insert 1 with 30 pneumatic taps (a) and Insert 2 with 36 pneumatic taps (b). 2-37
2.47 Location of fast-response pressure taps on blade suction side. 2-37
2.48 Surface-mounted hot-film sensors on the blade surface. 2-40
2.49 Iterative procedure employed in determining the mass flow rate across the orifice plate. 2-43
2.50 Discharge coefficient as a function of the Reynolds number. The ISO 5167 - 3 standard [36] is plotted against the Johansen interpolation [38] that enables finding the peak of the discharge coefficient. 2-44
2.51 Discharge coefficient as a function of the Reynolds number obtained with ISO standard and extended correlation. 2-45
2.52 Primary flow direction and cascade pitch angle in the cascade reference system.2-46
2.53 Breakdown of WG disk revolutions into periodic events (a) and re-phasing of the WG repeating events over one disk revolution period (b). 2-50
2.54 Comparison of a signal phase-lock averaged over one disk revolution against one bar passing multiplied by the number of bars in the disk (a) and error from assuming similarity between each bar (b). 2-51
2.55 Impact of reducing the number of points/per class on PLA signal error. 2-52
2.56 Evolution of a phase-lock averaged signal as a function of the number of averaged events (a) and difference between the phase-lock average performed with the maximum number of events and the phase-lock average performed with increasing number of events over one bar passing period (b). 2-52
2.57 Re-phased points for two bar passing periods along the phase-lock average (a) and histogram describing the normal distribution of a set of points belonging to class #40 (b). 2-53

3.1 MISES flow domain and mesh. 3-3
3.2 Blade surface isentropic Mach number for a case with closed laminar separation bubble (a) and nominal flow case (b). 3-4
3.3 Mesh sensitivity: relative error in blade isentropic Mach number compared to mesh M5. 3-5

3.4 MISES with AGS transition model: Blade surface isentropic Mach number as a function of incidence for M=0.70; Re=120k flow case. 3-6
3.5 Relative error in isentropic Mach number between MISES and experimental loading for the transitional case at M=0.70; Re=120k. 3-6
3.6 MISES with tripped boundary layer (fully turbulent): Blade surface isentropic Mach number as a function of incidence for M=0.70; Re=120k flow case. 3-7
3.7 Relative error in isentropic Mach number between MISES and experimental loading for the transitional case at M=0.70; Re=120k. 3-7
3.8 Turbulence sensitivity: surface isentropic Mach number distribution along the normalized surface length. Zoomed-in regions of suction side laminar separation bubble (top-right) and pressure side separation (bottom-right). . . 3-8
3.9 Turbulence sensitivity: relative error in isentropic Mach number between MISES and experiments. 3-9
3.10 Flow domain used in 2D RANS CFD. 3-10
3.11 Mesh M3 and details of the leading edge and trailing edge region. 3-12
3.12 CFD mesh sensitivity for M=0.70; Re=120k: surface isentropic Mach number distribution along normalized surface length. Zoomed-in regions of suction side laminar separation bubble (top-right) and pressure side separation (bottom-right). 3-13
3.13 CFD mesh sensitivity for M=0.70; Re=120k: Pitchwise distribution of total pressure loss coefficient, ζ (a) and mass-averaged total pressure loss coefficient (b). 3-13
3.14 CFD mesh sensitivity for M=0.90; Re=70k: surface isentropic Mach number distribution along normalized surface length. Zoomed-in regions of SS laminar separation bubble (top-right) and PS separation (bottom-right). . . . 3-14
3.15 CFD mesh sensitivity for M=0.90; Re=70k: Pitchwise distribution of total pressure loss coefficient, Y_{tot}, (a) and mass-averaged total pressure loss coefficient, ζ (b). 3-15
3.16 CFD incidence sensitivity for M=0.70; Re=500k: Blade surface isentropic Mach number as a function of incidence (a) the relative error in isentropic Mach number between CFD and experimental loading (b). 3-16
3.17 CFD: Turbulence decay fine-tuning against experimental data. 3-16
3.18 Turbulence decay obtained for the productive cases compared against the experimental one. 3-17

4.1 Stability of the Mach number (a) and Reynolds number (b) during the first phase of testing. 4-2
4.2 Stability of the WG rotational speed (a) and Strouhal number (b) during the second phase of testing. 4-2
4.3 Stability of the PMFR during the third phase of testing. 4-3
4.4 Procedure to retrieve cascade inlet total pressure. 4-4
4.5 Pitchwise distribution of turbulence grid loss coefficient for the different investigated flow conditions (a) and normalized distributions (b). 4-5
4.6 Turbulence grid loss coefficient correlation as a function of inlet flow conditions (a) and outlet flow conditions (b) 4-6
4.7 Pitchwise distribution of inlet total pressure loss coefficient for the different investigated flow conditions (a) and normalized distributions (b). 4-7

4.8 Turbulence grid + wake generator loss coefficient correlation in the function of inlet flow conditions (a) and outlet flow conditions (b). 4-8
4.9 Spanwise distribution of normalized total pressure at Plane 01. 4-9
4.10 Pitchwise distribution of BL integral parameters measured at Plane 01: displacement thickness (a), momentum thickness (b), and shape factor (c). The true chord normalizes the displacement and momentum thickness. 4-10
4.11 Spanwise distributions at Plane 02 during the first phase of testing: inlet flow incidence (a), cascade pitch angle (b), and normalized total pressure (c). . . . 4-11
4.12 Schematic representation of the impact of wake generator on inlet velocity vectors. 4-11
4.13 Contours of angular quantities at Plane 02 with WG: primary flow direction (a) and cascade pitch angle (b). 4-12
4.14 Spanwise distributions at Plane 02 during the second phase of testing: inlet flow incidence (a), cascade pitch angle (b), and normalized total pressure (c). 4-13
4.15 Pitchwise virtual shift at Plane 03. 4-13
4.16 Pitchwise distribution of normalized total pressure using re-shifted measurements at Plane 03: z/H=2.61% (a), z/H=5.03% (b) z/H=9.88% (c) and z/H=46.36% (d). 4-14
4.17 Pitchwise distribution of flow incidence using re-shifted measurements at Plane 03: z/H=2.61% (a) and z/H=46.36% (b). 4-15
4.18 Pitchwise virtual shift at Plane 06. 4-15
4.19 Downstream flowfield measured during productive tests: primary flow direction (a), cascade pitch angle (b), and kinetic energy loss coefficient (c). . . . 4-16
4.20 Pitchwise mass-averaged profiles obtained for different wakes downstream of the cascade: primary flow direction (a), cascade pitch angle (b), and kinetic energy loss coefficient (c). 4-17
4.21 Re-shifted pitchwise distribution of kinetic energy loss coefficient measured during the first phase: z/H=0.05 (a), z/H=0.10 (b), and z/H=0.50 (c). 4-17
4.22 Downstream flowfield measured during periodicity surveys for the second phase: primary flow direction (a), cascade pitch angle (b), and kinetic energy loss coefficient (c). Refer to the legend of the previous figure. 4-19
4.23 Pitchwise mass-averaged profiles obtained for different wakes downstream of the cascade during the second phase: primary flow direction (a), cascade pitch angle (b), and kinetic energy loss coefficient (c). 4-20
4.24 Schematic representation of inlet boundary layer skewness from [2]. 4-20
4.25 Re-shifted pitchwise distribution of loss coefficient at z/H=0.50 measured during the second phase. 4-21
4.26 Downstream flowfield measured during periodicity surveys for the third phase: primary flow direction (a), cascade pitch angle (b), and kinetic energy loss coefficient (c) 4-22
4.27 Pitchwise mass-averaged profiles obtained for different wakes downstream of the cascade during the third phase: primary flow direction (a), cascade pitch angle (b), and kinetic energy loss coefficient (c). 4-23
4.28 Schematic representation of probe movement during probe interference investigations: impact of C5HP on endwall taps (a), impact of L5HP on endwall taps (b), and impact of L5HP on blade taps (c). 4-23
4.29 Sketch of spanwise location of C5HP relative to the cascade: z_{L5HP}/H=0.01 (a) and z_{L5HP}/H=0.50 (b). 4-24

4.30 Pitchwise distribution of the isentropic Mach number at Plane 01 when the C5HP is inserted at Plane 02 and position is varied: near the endwall (a) and at midspan (b), and isentropic Mach number at Plane 06 when the probe is near the endwall (c) and at midspan (d). 4-25
4.31 Sketch of spanwise location of L5HP relative to the cascade: z_{L5HP}/H=0.01 (a) and z_{L5HP}/H=0.50 (b). 4-26
4.32 Pitchwise distribution of the isentropic Mach number at Plane 01 when the L-shaped five-hole probe is measured at Plane 06 and position is varied: near the endwall (a) and at midspan (b), and isentropic Mach number at Plane 06 when the probe is near the endwall (c) and at midspan (d). 4-27
4.33 Impact of traversing the L-shaped five-hole probe at z_{L5HP}/H=0.50 on suction side blade loading at z/H=0.50: overall loading (a) and zoomed-in portion highlighting rear portion of suction side (b). 4-28
4.34 Impact of traversing the L-shaped five-hole probe when the blade taps are at z/H=0.50: near the endwall at z/H=0.10 (a) and midspan (b). 4-29
4.35 Impact of increasing the outlet Mach number to retrieve nominal blade loading when the blade taps are at z/H=0.50: L5HP sits at y_{L5HP}/g=-1.00 near the endwall at z_{L5HP}/H=0.05 (a) and at midspan (b). 4-30
4.36 Impact of increasing the Mach number on pitchwise distribution of primary flow direction near the endwall (a) and at midspan (b), and kinetic energy loss coefficient near the endwall (a) and at midspan (b). 4-31
4.37 Impact of increasing the Mach number on mass-averaged quantities: primary flow direction (a) and kinetic energy loss coefficient (b). 4-32
4.38 Impact of measuring probes on inlet and outlet isentropic Mach number: Cobra five-hole probe (a) and L-shaped five-hole probe (b). 4-33
4.39 Variation of outlet isentropic Mach number during L-shaped five-hole probe traverse: taps used for averaging (a) and time-history of averaged outlet Mach number (b). 4-34

5.1 Characterization of midspan inlet flowfield at Plane 02 in the absence of wake generator: inlet flow incidence (a), cascade pitch angle (b), and normalized Mach number (c). 5-2
5.2 Velocity triangles resultant from the variation of flow incidence with outlet Mach number. 5-4
5.3 Characterization of midspan inlet flowfield at Plane 02 in the presence of wake generator: inlet flow incidence (a), cascade pitch angle (b), and normalized Mach number (c). 5-4
5.4 Pitchwise distribution of turbulent quantities in the absence of wake generator: turbulence intensity (a), and integral length scale (b). 5-6
5.5 Suction side and pressure side flow topology for several flow conditions. . . 5-8
5.6 Blade loading: experimental (markers), CFD γ-$\tilde{Re}_{\theta t}$ (solid line) and MISES AGS (dashed line); Re=65k (a), Re=70k (b), Re=100k (c) and Re=120k (d). . 5-9
5.7 Blade loading zoomed-in SS region: experimental (markers), CFD γ-$\tilde{Re}_{\theta t}$ (solid line) and MISES AGS (dashed line); Re=65k (a), Re=70k (b), Re=100k (c) and Re=120k (d). 5-10
5.8 Blade loading zoomed-in PS region: experimental (markers), CFD γ-$\tilde{Re}_{\theta t}$ (solid line) and MISES AGS (dashed line); Re=65k (a), Re=70k (b), Re=100k (c) and Re=120k (d). 5-11

5.9 Blade skin friction: experimental (markers), CFD γ-$\tilde{Re}_{\theta t}$ (solid line) and MISES AGS (dashed line); M=0.70; Re=65k (a), M=0.90; Re=70k (b), M=0.95; Re=70k (c), M=0.70; Re=120k (d) and M=0.90; Re=120k (e). 5-13
5.10 Blade isentropic Mach number along SS surface plotted on the left y-axis (solid black line), acceleration parameter plotted on the right y-axis (solid red line) and scaled local derivative of acceleration parameter plotted on the right y-axis (solid blue line): M=0.70; Re=120k (a) and M=0.95; Re=70k (b). 5-14
5.11 Relation between separation location computed with skin friction and with the acceleration parameter methodology. 5-14
5.12 Acceleration parameter versus surface length based Reynolds number at the separation location for experimentally investigated cases: without (a) and with (b) correcting the separation location obtained from the acceleration parameter methodology. 5-15
5.13 Surface length-based Reynolds number at reattachment versus at the separation location. 5-16
5.14 Normalized density gradient inside passage: M=0.90; Re=120k (a) and M=0.95; Re=120k (b). 5-17
5.15 Sketch of shock-boundary layer interaction after Boerner and Niehuis [11] . 5-17
5.16 Normalized density gradient inside passage at M=0.95; Re=120k: g/C=0.63 (a) and g/C=0.78 (b). 5-18
5.17 Blade SS isentropic Mach number for g/C=0.63 (a) and g/C=0.78 (b), skin friction coefficient for g/C=0.63 (c) and g/C=0.78 (d), and boundary layer integral parameters for g/C=0.63 (e) and g/C=0.78 (f). Displacement thickness ($-$) and momentum thickness ($--$) are plotted on the left y-axis in black, and the shape factor is plotted on the right y-axis in red. 5-20
5.18 Blade isentropic Mach number for M=0.70; Re=120k (a) and M=0.95; Re=70k (b), standard deviation of HF bridge voltage for M=0.70; Re=120k (c) and M=0.95; Re=70k (d), skewness of HF bridge voltage for M=0.70; Re=120k (e) and M=0.95; Re=70k (f), and kurtosis of HF bridge voltage for M=0.70; Re=120k (g) and M=0.95; Re=70k (h). 5-22
5.19 PDF of hot-film bridge voltage for M=0.70; Re=120k: in the laminar region at s/S_L=0.22, in the early transitional region at s/S_L=0.72, near the transition location at s/S_L=0.81, and in a late transitional region at s/S_L=0.93. 5-23
5.20 Comparison of transition point between model of Hatman and Wang [8] and current experimental data. 5-23
5.21 Acceleration parameter on the pressure side: Re=65k (a), Re=70k (b), Re=100k (c) and Re=120k (d). 5-25
5.22 Impact of introducing unsteady wakes on the overall surface isentropic Mach number distribution: Re=65k (a), Re=70k (b), Re=100k (c), and Re=120k (d). 5-27
5.23 Impact of introducing unsteady wakes on the laminar separation bubble region: Re=65k (a), Re=70k (b), Re=100k (c) and Re=120k (d). 5-28
5.24 Blade isentropic Mach number for M=0.70; Re=120k (a) and M=0.95; Re=70k (b), pseudo skin friction coefficient for M=0.70; Re=120k (c) and M=0.95; Re=70k (d), standard deviation of HF bridge voltage for M=0.70; Re=120k (e) and M=0.95; Re=70k (f), skewness of HF bridge voltage for M=0.70; Re=120k (g) and M=0.95; Re=70k (h), and kurtosis of HF bridge voltage for M=0.70; Re=120k (i) and M=0.95; Re=70k (j). 5-30

5.25 Pitchwise distribution of kinetic energy loss coefficient during the first phase of testing: Re=70k (a) and Re=120k (b). 5-33
5.26 Mass-averaged profile loss in terms of kinetic energy loss coefficient obtained during the first testing phase. 5-34
5.27 Comparison of pitchwise distributions of kinetic energy loss coefficient with and without wakes: Re=70k (a) and Re=120k (b). 5-35
5.28 Comparison of mass-averaged profile loss in terms of kinetic energy loss coefficient with and without wakes. 5-35
5.29 Pitch-to-pitch phase-resolved normalized total pressure fluctuations as a function of the Reynolds number at M=0.70 measured experimentally. 5-36
5.30 Pitch-to-pitch phase-resolved normalized total pressure fluctuations as a function of the Mach number at Re=70k measured experimentally. 5-37
5.31 Experimental wakes measured at y/g=0.00 for M=0.70: normalized total pressure fluctuations (a) and angular fluctuations (b). 5-37
5.32 Experimental phase-averaged wakes measured at y/g=0.00 with varying Mach number at Re=70k: normalized total pressure fluctuations (a) and angular fluctuations (b). 5-38
5.33 Experimental phase-averaged wakes measured at y/g=0.00 characterized in terms of turbulence intensity: at M=0.70 (a) and Re=70k (b). 5-39
5.34 Wake relative position of pressure deficit in relation to angular fluctuations (a) and turbulence intensity (b). 5-39
5.35 Schematic space-time diagrams for M=0.70; Re=70k case: quasi-wall shear stress normalized by a local maximum at which surface coordinate (a) and standard deviation of bridge voltage normalized by leading edge time-averaged value (b). 5-41
5.36 Quasi-wall shear stress (a, b), standard deviation of bridge voltage (c, d), and skewness of bridge voltage (e, f) for M=0.70 and M=0.90 at Re=70k. 5-43
5.37 Quasi-wall shear stress (a, b), standard deviation of bridge voltage (c, d), and skewness of bridge voltage (e, f) for Re=70k and Re=120k at M=0.90. 5-45
5.38 Phase-averaged normalized pressure traces along the blade SS with varying Reynolds number: M=0.70 (a) and M=0.90 (b). 5-46
5.39 Phase-averaged normalized pressure traces (solid line) and standard deviation (dashed line) along the blade SS with varying Mach number: M=0.70; Re=70k (a) and M=0.95; Re=70k (b). 5-47
5.40 Phase-averaged normalized pressure traces (solid line) and standard deviation (dashed line) along the blade SS with varying Reynolds number: M=0.90; Re=70k (a) and M=0.90; Re=120k (b). 5-47
5.41 Space-time diagram of kinetic energy loss coefficient at Re=70k: M=0.70 (a) and M=0.90 (b). 5-48
5.42 Phase-averaged kinetic energy loss coefficient at on- and off-design flow conditions: y/g=-0.58 (a), y/g=-0.18 (a), and y/g=+0.03 (c). 5-49
5.43 Phase-resolved kinetic energy loss coefficient mass-averaged over one blade pitch. 5-50
5.44 Space-time diagram of angular fluctuations at Re=70k: M=0.70 (a) and M=0.90 (b). 5-51
5.45 Phase-averaged angular fluctuations at on- and off-design flow conditions: y/g=-0.58 (a), y/g=-0.18 (a) and y/g=+0.03 (c). 5-52

5.46 Phase-resolved deviation from primary flow direction mass-averaged over one blade pitch. 5-52
5.47 Space-time diagram of turbulence intensity at Re=70k: M=0.70 (a) and M=0.90 (b). 5-53
5.48 Pitchwise profiles of turbulence intensity measured experimentally downstream of the cascade at fixed: M=0.70 (a), M=0.90 (b), and Re=70k (c). 5-54
5.49 Phase-averaged turbulence intensity fluctuations at on- and off-design flow conditions: $y/g = -0.58$ (a), $y/g = -0.18$ (a) and $y/g = +0.03$ (c). 5-55
5.50 Power spectral density of cross-wire voltage with and without grid at M=0.70; Re-70k. 5-56
5.51 Power spectral density of cross-wire voltage with turbulence grid: sensitivity to Mach number (a) and zoomed detail (c), sensitivity to Reynolds number (b), and zoomed detail (d). 5-57
5.52 Location of inlet and outlet fast-response probe measurement locations. . . . 5-57
5.53 Sensitivity of power spectral density at Plane 02: without wake generator (a) and with wake generator (b). 5-58
5.54 Sensitivity of power spectral density at Plane 06: without wake generator (a) and with wake generator (b). 5-59
5.55 Location of blade fast-response pressure sensors on the blade surface. 5-61
5.56 Power spectral density on blade pressure side sensor at s/S_L=0.214: sensitivity to Reynolds number (a) and sensitivity to Mach number (b). 5-62
5.57 Power spectral density on blade suction side sensor at s/S_L=0.532: sensitivity to Reynolds number (a) and sensitivity to Mach number (b). 5-63
5.58 Power spectral density on blade suction side sensor at s/S_L=0.872: sensitivity to Reynolds number (a) and sensitivity to Mach number number (b). 5-63
5.59 Power spectral density on blade suction side sensor at Re=100k: s/S_L=0.637 (a) and s/S_L=0.753 (b). 5-64
5.60 Power spectral density of hot-film voltage at M=0.95; Re=70k. 5-64
5.61 Power spectral density on blade pressure side sensor at s/S_L=0.214: sensitivity to Reynolds number number at M=0.90 (a) and sensitivity to Mach number at Re=70k (b). 5-65
5.62 Sensitivity of power spectral density to unsteady wakes at M=0.70; Re=120k for suction side sensor 2 (a) and 7 (c), and at M=0.70; Re=120k for suction side sensor 2 (b) and 7 (d). 5-66

6.1 Inlet boundary layer profiles: all flow cases (a) and mean level with shaded area (b). 6-3
6.2 Variation of boundary layer integral parameters with Mach and Reynolds numbers: displacement thickness (a), momentum thickness (b), and shape factor (c). 6-3
6.3 Radial profiles of turbulence: turbulence intensity (a) and integral length scale (b). 6-4
6.4 Contours of inlet kinetic energy loss coefficient: without wake generator (a) and with wake generator (b). 6-5
6.5 Comparison between mass-averaged radial profiles with steady and unsteady inlet flow: pressure coefficient (a) and kinetic energy loss coefficient (b), and pitch-to-pitch variation of kinetic energy loss coefficient (c). 6-6

6.6 Pitchwise distribution of boundary layer integral parameters measured for steady and unsteady inlet flow cases: displacement thickness (a), momentum thickness (b), and shape factor (c). 6-7
6.7 Radial profiles of cascade inlet incidence for steady and unsteady inlet flow cases: y/g=-0.50 (a), y/g=0.00 (b), and y/g=+0.50 (c). 6-7
6.8 Comparison between mass-averaged radial profiles with and without cavity slot with increasing purge massflow ratio: pressure coefficient (a) and kinetic energy loss coefficient (b), and pitch-to-pitch variation of kinetic energy loss coefficient (c). 6-8
6.9 Pitchwise distribution of boundary layer integral parameters measured for cases with and without cavity slot: displacement thickness (a), momentum thickness (b), and shape factor (c). 6-9
6.10 Radial profiles of cascade inlet incidence for cases with and without cavity slot and increasing purge massflow ratio: y/g=-0.50 (a), y/g=0.00 (b) and y/g=+0.50 (c). 6-10
6.11 Radial profiles of cascade pitch angle for cases with and without cavity slot and increasing purge massflow ratio: y/g=-0.50 (a), y/g=0.00 (b), and y/g=+0.50 (c). 6-10
6.12 Variation of blade loading along span for M=0.70; Re=120k (a) and sensitivity of near-wall loading at z/H=0.05 to Reynolds number at M=0.80 (b). 6-11
6.13 Sensitivity of unsteady wake radial profile on blade loading: z/H=0.02 (a), z/H=0.05 (b), z/H=0.10 (c), z/H=0.50 (d). 6-12
6.14 Contours of difference in surface isentropic Mach number in relation to the case without cavity slot: PMFR=0.00% (a), PMFR=0.50% (b), and PMFR=0.90% (c). 6-13
6.15 Blade surface isentropic Mach number distributions for cases with and without cavity sot and varying purge massflow ratio: z/H=1.52% (a), z/H=5.15% (b), z/H=10.00% (c) and z/H=50.00% (d). 6-14
6.16 Representation of primary and secondary flow structures with Q-criterion. . . 6-15
6.17 Characterization of secondary flow structures downstream for nominal flow case: kinetic energy loss coefficient (a), streamwise vorticity coefficient superimposed with isolines of kinetic energy loss coefficient (b) and secondary kinetic energy coefficient superimposed with secondary velocity vectors (c). The observer looks upstream. 6-16
6.18 Impact of Reynolds number on kinetic energy loss coefficient at Re=70k: M=0.70 (a), M=0.90 (b) and M=0.95 (c). 6-17
6.19 Radial profiles for Re=70k: secondary kinetic energy loss coefficient (a), deviation from primary flow direction (b), and secondary kinetic energy coefficient (c). 6-18
6.20 Radial profiles for M=0.90: secondary kinetic energy loss coefficient (a), deviation from primary flow direction (b), and secondary kinetic energy coefficient (c). 6-18
6.21 Breakdown of the planewise mass-averaged losses for the steady inlet flow cases. 6-19
6.22 Contours obtained with unsteady inlet flow: kinetic energy loss coefficient (a) and secondary kinetic energy coefficient superimposed with secondary velocity vectors (b). 6-20

6.23 Impact of unsteady wakes on radial profiles of mass-averaged quantities: secondary kinetic energy loss coefficient (a), deviation from primary flow direction (b), and secondary kinetic energy coefficient (c). 6-20
6.24 Breakdown of the planewise mass-averaged losses for steady and unsteady inlet flow cases. 6-21
6.25 Contours of kinetic energy loss coefficient at M=0.90; Re=70k for cases with and without cavity slot and varying purge flow: no cavity slow (a), PMFR=0.00% (b), PMFR=0.50% (c) and PMFR=0.90% (d). 6-22
6.26 Contours of streamwise vorticity coefficient for cases with and without cavity slot and varying purge flow: no cavity slow (a), PMFR=0.00% (b), PMFR=0.50% (c) and PMFR=0.90% (d). 6-22
6.27 Contours of secondary kinetic energy coefficient for cases with and without cavity slot and varying purge massflow ratio: no cavity slow (a), PMFR=0.00% (b), PMFR=0.50% (c) and PMFR=0.90% (d). 6-23
6.28 Impact of endwall geometry and purge flow on radial profiles of mass-averaged quantities: secondary kinetic energy loss coefficient (a), deviation from primary flow direction (b), and secondary kinetic energy coefficient (c). 6-24
6.29 Breakdown of the planewise mass-averaged losses for cases with and without cavity slot and varying purge flow. 6-25
6.30 Inlet quantities measured with Cobra five-hole probe and fast-response virtual four-hole probe at Plane 02 and y/g=0.00: inlet normalized total pressure (a) and primary flow direction (b). 6-26
6.31 Radial profiles of turbulence intensity measured with the fast-response virtual four-hole probe at Plane 02. 6-26
6.32 Inlet mapping at t/T=0: normalized total pressure fluctuations (a), angular fluctuations (b), turbulent intensity (c), and correlation coefficient (d). 6-28
6.33 Phase-resolved inlet quantities with varying spanwise location: normalized total pressure fluctuations (a), angular fluctuations (b), and turbulent intensity (c). 6-28
6.34 Phase-resolved boundary layer thickness at Plane 02. 6-29
6.35 Comparison between inlet quantities measured with PV4HP and fast-response virtual four-hole probe at Plane 03 and y/g=-0.83: inlet normalized total pressure (a) and deviation from primary flow direction (b). 6-30
6.36 Inlet radial profiles of turbulent quantities at y/g=-0.83: turbulent kinetic energy (a) and turbulence intensity (b). The blue data points with lower magnitude represent the profile at Plane 02 normalized to match the midspan value at Plane 03. 6-30
6.37 Phase-averaged traces of normalized total pressure fluctuatiIdentifyingions, and turbulence intensity at Plane 03, y/g=-0.83: z/H=0.03 (a–c), z/H=0.06 (d–f), z/H=0.10 (g–i) and z/H=0.50 (j–l). 6-32
6.38 Contour of skin friction coefficient superimposed with viscous stress streamlines (a) and identification of stagnation lines of secondary flow structures (b). 6-33
6.39 Contours for cases with unsteady inlet flow, without and with cavity and purge flow: normalized quasi-wall shear stress (a–c), standard deviation of bridge voltage (d–f), skewness of bridge voltage (g–i), and correlation coefficient (j–l). 6-34

6.40 Contour of normalized surface pressure fluctuations: no cavity (a), PMFR=0.50% (b), and PMFR=0.90% (c). 6-35
6.41 Contours obtained with FRV4HP superimposed with isolines of L5HP for PMFR=0.90% case: kinetic energy loss coefficient (a), streamwise vorticity coefficient (b) and secondary kinetic energy (c). 6-36
6.42 Pitchwise distribution measured with L5HP and FRV4HP: deviation from primary flow direction (a), cascade pitch angle (b), and kinetic energy loss coefficient (c). 6-37
6.43 Mass-averaged quantities measured with L5HP and FRV4HP: deviation from primary flow direction (a), cascade pitch angle (b), kinetic energy loss coefficient (c), and secondary kinetic energy (d). 6-38
6.44 Contours of turbulence intensity superimposed with the kinetic energy loss coefficient isolines: NC (a), PMFR=0.50% (b) and PMFR=0.90% (c). 6-39
6.45 Phase-averaged pitchwise mass-averaged kinetic energy loss coefficient (a–c), deviation from primary flow direction (d–f), and turbulence intensity (g–i) for the case without the cavity, and cases with increasing PMFR. 6-41
6.46 Instantaneous contours of kinetic energy loss coefficient at time instants of minimum (top row) and maximum (bottom row) secondary loss. 6-42
6.47 Instantaneous contours of turbulence intensity at time instants of minimum (top row) and maximum (bottom row) secondary loss. 6-44
6.48 Correlation coefficient of center tap pressure (top-row) and kinetic energy fluctuations (bottom-row). 6-45
6.49 Breakdown of kinetic energy loss coefficient fluctuations. A corresponds to the freestream region near the blade SS, B corresponds to the core of the PV, and C corresponds to the interface of the TSV and near-SS wake. 6-46
6.50 Locations of investigated spectra in relation to secondary flow structures at PMFR=0.90%. 6-47
6.51 Power spectral density of blade static pressure fluctuations: in reattachment line of wall induced vortex (a), in the trajectory of wall induced vortex (b), in separation line of passage vortex (c), and trajectory of passage vortex (d). . . 6-48
6.52 Regions of interest for investigation of spectra. 6-48
6.53 Power spectral density of flow total pressure fluctuations: in the 2D flow region near the SS (a), in the passage vortex core (b), in the interface between SS wake and trailing shed vorticity region (c), and the trailing shed vorticity region (d). 6-49

7.1 Comparison between experimental and predicted profile loss using different models: steady flow cases (a) and unsteady flow cases (b). 7-2
7.2 Comparison between experimental and predicted profile loss using the model of Benner et al. [5, 6]. 7-3
7.3 Impact of boundary layer tripping location on blade loading obtained with MISES: pressure side and suction side (a) and zoomed-in region of SS (b). . 7-3
7.4 Comparison between MISES computations tripped near the leading edge and fully turbulent RANS: M=0.90; Re=120k (a) and M=0.95; Re=120k (b). . . 7-4
7.5 Relationship between loss computed using model of Coull & Hodson [9] for fully turbulent MISES and RANS loadings. 7-4
7.6 Comparison of experimentally obtained separation locations against those estimated with different Thwaites-derived methods. 7-6

7.7 Comparison of experimentally obtained separation locations against those estimated with different Stratford-derived methods. 7-6
7.8 Comparison of experimentally obtained separation location against the one estimated with the best method of the Thwaites and Stratford type methods. . 7-8
7.9 Comparison of profile loss obtained experimentally and one obtained from transitional MISES. 7-9
7.10 Comparison between pressure side boundary lower obtained with transitional MISES and model of Coull & Hodson: displacement thickness (a) and momentum thickness (b). 7-10
7.11 Comparison between momentum thickness at the separation location for transitional MISES and CH model: impact of separation location (a) and dependence from flow condition using the method of Stratford (b). 7-11
7.12 Comparison between SS boundary layer obtained with transitional MISES and model of Coull & Hodson, estimating the separation location with the method of Stratford with m=3: displacement thickness (a) and momentum thickness (b). 7-12
7.13 Comparison of profile loss obtained experimentally and predicted by incorporating boundary layer parameters from MISES computations and estimated with the model of Coull & Hodson [9], in the breakdown scheme of Denton [18]. 7-13
7.14 Impact of increasing the blade loading on the $V_{TE,SS}/V_{out}$ ratio (a) and ratio as a function of normalized cascade pitch (b). 7-15
7.15 Pitchwise distribution of velocity ratio inside the passage in the vicinity of the TE obtained with MISES: M=0.70 (a), M=0.80 (b), M=0.90 (c), and M=0.95 (d). 7-15
7.16 Impact of $V_{TE,SS}/V_{out}$ and loss breakdown scheme on profile loss prediction against experimental data: steady flow cases (a) and unsteady flow cases (b). 7-16
7.17 Loss breakdown by flow condition (a), and contributions of BL on SS (b) for steady inlet flow cases. 7-18
7.18 Loss breakdown by flow condition (a), and contributions of BL on SS (b) for unsteady inlet flow cases. 7-19
7.19 Breakdown of loss contributions of profile loss for steady and unsteady inlet flow from Eq. 7.16–Eq. 7.19: mixing loss (a, b), blockage loss (c, d), trailing edge wedge angle loss (e, f), and base pressure loss (g, h). 7-21
7.20 Loss breakdown relative to total loss for each flow case. 7-22
7.21 Comparison between experimentally measured and predicted secondary loss with different models (a) and the highlight of most accurate models in the family of models of Ainley and Mathieson models, Craig and Cox model, and Coull. Only the steady cases without purge are included. 7-23
7.22 Streamlines along the passage used to compare endwall experimental quantities against ones retrieved from MISES (a) and isentropic Mach number distribution along the normalized axial direction (b). 7-25
7.23 Endwall loss computed with experimental data against one compute with MISES results. Loss integral is solved in an experimentally delimited area. . 7-25
7.24 Sensitivity of experimental loss to inlet kinetic energy loss coefficient (a), and impact of Mach and Reynolds numbers if inlet kinetic energy at Plane 01 is accounted for (b). 7-27

7.25 Breakdown of contribution by secondary flow structure (a) and breakdown of loss into endwall dissipation and mixing (b) for steady flow cases. 7-28
7.26 Sensitivity of experimental loss to inlet boundary layer parameters (a) and impact of Mach and Reynolds numbers if inlet boundary layer at Plane 01 is accounted for (b). 7-29

B.1 Reference K-type thermocouple calibration curves for the various phases of testing (a) and residuals for the obtained calibrations (b). B-2
B.2 Injection K-type thermocouple calibration curve (a) and residuals for the obtained calibration (b). B-2
B.3 Validyne 1 calibration curve (a) and residuals for the obtained calibration (b). B-3
B.4 Validyne 2 calibration curve (a) and residuals for the obtained calibration (b). B-4
B.5 Comparison of the sensitivity of the aerodynamic coefficients of the C5HP to P_{ave}: (a) K_α in function of the yaw angle and (b) K_γ in function of the pitch angle. B-5
B.6 Orthogonality map resultant from the calibration of the C5HP at M=0.40. . . B-5
B.7 Aerodynamic calibration coefficients of C5HP for the calibrated Mach numbers: (a) K_α as function of α and γ, (c) K_γ as function of α and γ, (e) K_{tot} as function of α and γ and (g) K_{stat} as function of α and γ; and cuts of the surfaces at fixed α or γ for (b) K_α, (d) K_γ, (f) K_{tot} and (h) K_{stat}. B-7
B.8 Orthogonality maps for the range of M for which the C5HP was calibrated. . B-8
B.9 Comparison of the sensitivity of the aerodynamic coefficients of the L5HP to P_{ave}: (a) K_α in function of the yaw angle and (b) K_γ in function of the pitch angle. B-8
B.10 Orthogonality map resultant from the calibration of the L5HP at M=0.80. . . B-9
B.11 Aerodynamic calibration coefficients of L5HP for the calibrated Mach numbers: (a) K_α as function of α and γ, (c) K_γ as function of α and γ, (e) K_{tot} as function of α and γ and (g) K_{stat} as function of α and γ; and cuts of the surfaces at fixed α or γ for (b) K_α, (d) K_γ, (f) K_{tot} and (h) K_{stat}. B-10
B.12 Orthogonality maps for the range of M for which the L5HP was calibrated. . B-11
B.13 Aerodynamic calibration coefficients of Pneumatic V4HP for the calibrated Mach numbers: (a) K_α as function of α and γ, (c) K_γ as function of α and γ, (e) K_{tot} as function of α and γ and (g) K_{stat} as function of α and γ; and cuts of the surfaces at fixed α or γ for (b) K_α, (d) K_γ, (f) K_{tot} and (h) K_{stat}. . . . B-12

E.1 Blade isentropic Mach number for M=0.70; Re=70k (a) and M=0.90; Re=70k (b), standard deviation of HF bridge voltage for M=0.70; Re=70k (c) and M=0.90; Re=70k (d), skewness of HF bridge voltage for M=0.70; Re=70k (e) and M=0.90; Re=70k (f), and kurtosis of HF bridge voltage for M=0.70; Re=70k (g) and M=0.90; Re=70k (h). E-2
E.2 Quantities for M=0.90; Re=120k: Blade isentropic Mach number(a), standard deviation of HF bridge voltage (b), skewness of HF bridge voltage (c), and kurtosis of HF bridge voltage (d). E-3
E.3 Blade isentropic Mach number for M=0.90; Re=70k (a) and M=0.90; Re=120k (b), pseudo skin friction coefficient for M=0.90; Re=70k (c) and M=0.90; Re=120k (d), standard deviation of HF bridge voltage for M=0.90; Re=70k (e) and M=0.90; Re=120k (f), skewness of HF bridge voltage for M=0.90; Re=70k (g) and M=0.90; Re=120k (h), and kurtosis of HF bridge voltage for M=0.90; Re=70k (i) and M=0.90; Re=120k (j). E-5

List of Tables

1.1 Design parameters of a modern direct drive turbofan LPT and a high-speed LPT for a geared architecture after [13]. 1-5
1.2 Investigations on the impact of unsteady wakes on secondary flows. 1-14
1.3 Investigations on the impact of purge flow on secondary flows. 1-14

2.1 Characteristic geometry features of the passive turbulence grid. 2-3
2.2 Geometry of SPLEEN Cascade C1. 2-10
2.3 Key dimensions of cavity geometry. 2-13
2.4 Types of instrumentation used for aerothermal measurements. 2-14
2.5 Location of measurement planes as a function of the axial chord. 2-16
2.6 Orifice geometrical characteristics. 2-20
2.7 Instrumentation used to monitor secondary air system flow properties. 2-21
2.8 Fast-response probe taps' line-cavity dimensions in mm. 2-33
2.9 Dynamic response of virtual four-hole probe fast-response pressure sensors computed with the Helmholtz [24], Hougen [25] and Bergh and Tijdeman [27] models, with and without end correction [26]. 2-34
2.10 Fast-response blade taps line-cavity dimensions in mm. 2-38
2.11 Dynamic response of Blade fast-response pressure sensors computed with the Helmholtz [24], Hougen [25] and Bergh and Tijdeman [27] models, with and without end correction [26]. 2-38
2.12 Coefficients obtained through the minimization of the objective functions built to extend ISO standard with the formulation of Jankowsky et al. [37]. . . 2-45
2.13 Uncertainty sources of thermocouple calibration. 2-57
2.14 Uncertainty sources of Kulite calibration. 2-58
2.15 Uncertainty sources of Validyne calibration. 2-58
2.16 Breakdown of uncertainty expanded with 95% confidence interval. 2-58
2.17 Experimental campaign phases. 2-60

3.1 Inlet boundary conditions to MISES flow solver. 3-2
3.2 Mesh parameters for MISES computations. 3-4
3.3 Mesh properties for sensitivity study. 3-11
3.4 Mesh properties for sensitivity study. 3-11
3.5 Turbulence model parameters. 3-17

4.1 Standard deviation with 95% confidence interval resultant from variation in flow conditions from the nominal point. 4-3
4.2 Calibration coefficients, goodness of fitting, and standard error of fittings performed to turbulence grid loss coefficient. 4-6

4.3 Turbulence grid loss coefficient as a function of the flow Mach and Reynolds numbers. . . . 4-7
4.4 Calibration coefficients, goodness of fitting, and standard error of fittings performed to turbulence grid + wake generator loss coefficient. . . . 4-8
4.5 TG+WG loss coefficient as a function of the flow Mach and Reynolds numbers. 4-9
4.6 Calibration coefficients, goodness of fitting, and standard error of far exit flow correlation. . . . 4-34

5.1 Variation of the Strouhal number with the outlet Mach number. . . . 5-1
5.2 Wake generator-induced flow turning computed with the model and estimated experimentally, and absolute and relative Mach number. . . . 5-5
5.3 Power law coefficients fitted to HW data. . . . 5-6
5.4 Separation location, s_{sep}/S, obtained experimentally, with CFD and MISES under steady inlet flow. . . . 5-24
5.5 Reattachment location, s_{reatt}/S, obtained experimentally, with CFD and MISES. 5-25
5.6 PS laminar separation bubble reattachment location against relaminarization location. . . . 5-26
5.7 Separation location, s_{sep}/S, obtained experimentally under unsteady inlet flow. 5-31
5.8 Reattachment location, s_{sep}/S, obtained experimentally under unsteady inlet flow. . . . 5-31
5.9 Separation, s_{sep}/S, and reattachment location, s_{reatt}/S, obtained experimentally for the inlet steady and unsteady flow cases. . . . 5-32
5.10 Rig characteristic frequencies in Hz. . . . 5-59
5.11 Dominant frequency in Hz associated with the growth of Tollmien-Schlichting waves on blade suction side. . . . 5-60
5.12 Frequency range in Hz associated with Kelvin-Helmholtz instability related to suction side separation bubble. . . . 5-60
5.13 Estimated shock-related frequencies in Hz on blade suction side. . . . 5-61

6.1 Flow conditions exploited with steady inlet flow. . . . 6-1
6.2 Flow conditions exploited with wake generator and purge flow. . . . 6-2
6.3 Phase instants at which the minimum and maximum of the loss core are observed for the case without cavity slot and with increasing purge massflow ratio. . . . 6-39

7.1 Constants for each of the methods based on the Thwaites parameter. . . . 7-5
7.2 Constants for each of the methods based on the Stratford parameter. . . . 7-5
7.3 Summary of blade loading parameters. . . . 7-7
7.4 Mean error in estimating separation location for each method. . . . 7-7
7.5 Mean error in estimating separation location for each Mach number for the methods of Pohlhausen and Stratford . . . 7-8
7.6 RMSE in estimating profile loss with breakdown of Denton [18], and Senior & Miller [16] with varying velocity ratio. . . . 7-17

B.1 Calibration coefficients, goodness of fitting, and standard error of calibrations performed of reference thermocouple for each phase of testing. . . . B-2
B.2 Calibration coefficients, goodness of fitting and standard error of calibrations performed of injection thermocouple. . . . B-3

B.3 Calibration coefficients, goodness of fitting and standard error of calibrations performed for Validynes. B-4
B.4 Calibration coefficients, goodness of fitting, and standard error of pressure calibrations performed for V4HP FR sensors throughout different phases of testing. B-13
B.5 Calibration coefficients, goodness of fitting, and standard error of temperature calibrations performed for V4HP FR sensors throughout different phases of testing. B-13
B.6 Calibration coefficients, goodness of fitting, and standard error of pressure calibrations performed for Blade FR sensors throughout different phases of testing. B-14
B.7 Calibration coefficients, goodness of fitting, and standard error of temperature calibrations performed for Blade FR sensors throughout different phases of testing. B-15

C.1 Location of pneumatic static pressure taps on Blade SS. C-1
C.2 Location of pneumatic static pressure taps on Blade PS. C-2
C.3 Location of pneumatic static pressure taps on Endwall Insert 1. . . . . C-2
C.4 Location of pneumatic static pressure taps on Endwall Insert 2. . . . . C-3
C.5 Location of fast-response static pressure taps on Blade SS. C-3
C.6 Location of fast-response static pressure taps on Blade PS. C-3
C.7 Location of fast-response static pressure taps on Endwall insert 1. . . . . C-4
C.8 Location of fast-response static pressure taps on Endwall insert 2. . . . . C-4
C.9 Location of surface mounted hot-films on Blade SS. C-4
C.10 Location of surface mounted hot-films on Blade PS. C-5

D.1 Uncertainty of sources used to build map of K_{tot}. D-5
D.2 Uncertainty of sources used to build map of K_{stat}. D-5

F.1 Boundary layer integral parameters measured at Plane 01. . . . . F-1
F.2 Boundary layer integral parameters measured at Plane 02. . . . . F-2

G.1 Experimental loss breakdown in terms of mass-averaged quantities. G-2
G.2 Experimental loss breakdown in terms of mixed-out-averaged quantities. . . . G-3

H.1 Error from the family of Thwaites parameter methods in estimating the separation location with respect to experimental prediction. H-1
H.2 Error from the family of Stratford methods in estimating the separation location with respect to experimental prediction. H-2

I.1 Boundary layer integral parameters on the pressure side near the trailing edge from the model of Coull. I-2
I.2 Boundary layer integral parameters on the suction side near the trailing edge from the model of Coull. I-3

List of Acronyms

AM	Ainley and Mathieson
ASME	The American Society of Mechanical Engineers
ATAG	Air Transport Action Group
BL	Boundary layer
BPR	Bypass ratio
CC	Craig and Cox
CFD	Computational fluid dynamics
CH	Coull and Hodson
CTA	Constant temperature anemometry
CV	Suction side corner vortex
C5HP	Cobra-shaped five-hole probe
DC	Dunham and Came
DDTF	Direct drive turbofan
DP	Design point
EU	European Union
FSTI	Freestream turbulence intensity
GE	General Electric
GTF	Geared turbofan
HW	Hot-wire probe
HF	Surface mounted hot-film sensor
HPT	High-pressure turbine
IATA	International Air Transport Association
ISO	International Organization for Standardization
KO	Kacker and Okapuu
LE	Leading edge
LPT	Low-pressure turbine
L5HP	L-shaped five-hole probe
PLA	Phase-lock average
PMFR	Purge massflow ratio
PS	Pressure side
PT	Preston tube
PV	Passage vortex
RANS	Reynolds-averaged Navier-Stokes
RMS	Root-mean square level
RMSE	Root-mean square error
RPM	Revolutions per minute
SAE	Safran aircraft engines
SFC	Specific fuel consumption
SS	Suction side

TE	Trailing edge
TSM	Taylor series method
TSV	Trailing shed vortex
VKI	von Karman Institute
V4HP	Virtual four-hole probe
WG	Wake generator
WIV	Wall induced vortex
WP	Work package
XW	Cross-wire probe
ZS	Zhu and Sjolander

List of Roman Letters

c	Local speed of sound
C	Airfoil true chord, Coefficient
C_{ax}	Airfoil axial chord
C_d	Discharge coefficient
d	Orifice plate inner diameter
d_w	Hot-wire diameter
D	Orifice pipe inner diameter, Probe head diameter
D_L	Line diameter in line-cavity system
E	Voltage
EW	Endwall
F_{bar}	Bar passing frequency
F_s	Sampling frequency
g	Cascade pitch
H	Cascade span, Total enthalpy, Height of Preston tube head
H_{12}	Boundary layer shape factor
i	Incidence
K	Coefficient
Kn	Knudsen number
K_M	Mach number coefficient
$K_{P,Center}$	Probe center tap pressure coefficient
K_{tot}	Probe total pressure coefficient
K_{stat}	Probe static pressure coefficient
l_W	Effective wire length
L	Line length in line-cavity system
L_e	Equivalent line length in line-cavity system
l_{in}	Distance from orifice plate to pressure tap at inlet
L_{in}	Length of inlet pipe
l_{out}	Distance from orifice plate to pressure tap at outlet
L_{out}	Length of outlet pipe
M	Mach number
N_{bars}	Number of bars of wake generator
Nu	Nusselt number
o	Blade passage throat
P	Pressure, Electrical power supplied to surface mounted hot-film sensor
R	Rotor
R	Gas constant
R_s	Support resistance
R_S	Surface mounted hot-film sensor resistance

R_t	Total resistance
R_W	Wire resistance
Ra	Averaged roughness
Re	Reynolds number
Re_D	Orifice pipe outer diameter based Reynolds number
Re_w	Hot-wire diameter based Reynolds number
R^2	Goodness of fitting
s	Location along the surface length, Sensitivity
S_L	Pressure or suction side surface length
t	Blade maximum thickness
T	Temperature
T_w	Effective wire temperature
u	Streamwise velocity
U	Uncertainty, Rotational velocity of turbine stage, Voltage
V	Vane
V_{ax}	Axial velocity in turbine stage
V_C	Cavity volume in line-cavity system
V_e	Mass-averaged engine exhaust velocity
V_f	Mass-averaged fan exhaust velocity
V_L	Line volume in line-cavity system
V_P	Pressure sensitive voltage
V_S	Temperature sensitive voltage
V_0	Flight velocity
W	Width of Preston tube head
x	Location along axial chord
y	Location along pitchwise direction
Y	Turbulence grid (and wake generator) total pressure loss coefficient
z	Location along spanwise direction

List of Greek Letters

α	Probe yaw angle
β	Primary flow direction, Ratio of orifice pipe inner to outer diameter
γ	Ratio of specific heats, Probe pitch angle
δ	Displacement thickness
Δ	Variation
ϵ	Expansibility factor
ζ	Stagger angle, Total pressure loss coefficient
η	Efficiency, Recovery factor
θ	Momentum thickness
κ	Thermal conductivity
λ	Lambda parameter
μ	Dynamic viscosity
ν	Kinematic viscosity, degrees of freedom
ξ	Kinetic energy loss coefficient
ρ	Density
σ	Turbulence grid solidity
τ	Wall shear stress
ϕ	Dewey's corrective factor
Φ	Flow coefficient

List of Subscripts and Superscripts

a	ambient
ave	averaged
ax	axial
C	center
corr	corrected
D	down
eff	effective
end	endwall
fs	freestream
in	inlet
inj	injection
is	isentropic
L	left
met	metallic
nom	nominal
O	overall
P	propulsive
prof	profile
PV	passage vortex
R	right
rand	random
ref	reference
sys	systematic
T	thermal
TE	trailing edge
tot	total
TSV	trailing shed vorticity
w	wire
WIV	wall induced vortex
0	total, reference
a	area-averaged
m	mass-averaged
$'$	fluctuating component

1 Introduction

1.1 Motivation

Aviation currently accounts for 2%–3% of global CO_2 emissions [1], and 4% in Europe [2]. The Flightpath2050 initiative aims to mitigate the environmental impact of aviation to meet the international efforts of limiting global warming of $1.50°$ [3]. Achieving net-zero aviation will require a reduction of CO_2, NOx, and sound level by 75%, 90%, and 65% compared to the 2000 levels.

The decrease in emissions is counter-balanced by the air traffic growth, which has proven to be resilient to external factors such as the economy, politics, pandemics, and war. A recent communication by the International Air Transport Association (IATA) stated that as of September 2023, air traffic is at 95.6% of pre-COVID levels [1]. The slowdown in growth resulting from the COVID pandemic is insufficient to meet aviation's climate goals without pursuing further action [4].

It is estimated that increases in operational efficiency have reduced the CO_2 produced by modern flights by 54.3% compared to the same flight in 1990 [5]. Modern turbofan engines result from decades of research and development and can be considered efficient machines. Nonetheless, the Air Transport Action Group (ATAG) estimates that with the current fleet and operational efficiency, an estimated 2,000 Mt of CO_2 would be output by 2050 if nothing was done (see Fig. 1.1).

Based on a report from Clean Sky [2], flights covering distances smaller than 3,000 kilometers will contribute to $\sim$60% of the overall aviation CO_2 emissions while encompassing more than 90% of all flights. The medium and large aircraft categories operating on short to medium-haul flights ($<$4,000 kilometers) are projected to contribute to 55% of the CO_2 emis-

[1] https://www.iata.org/en/pressroom/2023-releases/2023-09-06-01

[2] https://www.clean-aviation.eu/media/publications/technology-evaluator-first-global-assessment-2020-technical-report

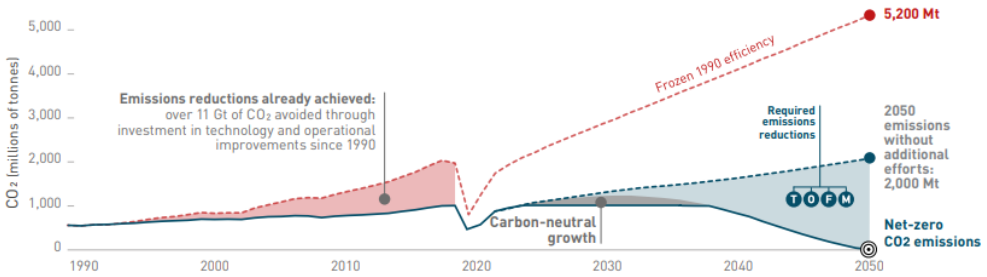

Figure 1.1: Comparison of the evolution of CO_2 emissions for different scenarios: fleet with 1990 efficiency, fleet with current characteristics; in relation to net-zero target [5].

sions. The flight volume forecast and the technologies employable for each market segment indicate that gas turbines will be a crucial element in decarbonizing aviation.

Improvements in the turbofan propulsive efficiency constitute a key pathway to reduce the overall engine efficiency [6], namely through an increase of the engine by-pass ratio (BPR). However, the fan size is limited by the low-pressure turbine (LPT). In a direct drive turbofan (DDTF), the work extracted by the low-pressure turbine must increase to satisfy the power requirements of a bigger fan. The latter can be achieved by increasing the number of stages. An excessive number of stages would be required to further decrease the specific fuel consumption (SFC) for an increasing by-pass ratio. On the other hand, the low-pressure turbine efficiency can be improved by operating at higher rotational velocities. Decreasing the spool speed due to increasing the fan size would result in penalties for the low-pressure turbine efficiency. Increasing the stage number (stage loading) can partially compensate for the effect. However, the designer faces a compromise between the part count and efficiency. Historically, increasing the low-pressure turbine efficiency by 1% improved the engine overall efficiency by $\sim$1%. [7]

The efficiency of the fan and low-pressure turbine can be independently addressed by decoupling the spool speeds employing a power gearbox, resulting in a geared turbofan (GTF) architecture. Fig. 1.2 displays a Pratt & Whitney PW1000G cut highlighting the characteristics of a modern geared turbofan.

Considering the same hot core, a geared turbofan offers benefits compared to a direct-drive turbofan when the by-pass ratio exceeds 10 [6]. Both architectures will feature a similar specific fuel consumption for the same by-pass ratio. However, the part count and engine modules' dimensions are significantly reduced. However, the weight of the gearbox and cooling system can exceed weight savings. In sum, the main advantage of geared architectures is the capability to explore higher by-pass ratios without compromising the fan and low-pressure turbine performance. As a result, a significant reduction in specific fuel consumption is achievable (see Fig. 1.3).

Even though aviation has a clear trend of increasing the by-pass ratio, the latter cannot be increased indefinitely. The increase in the fan size results in the rise of the nacelle drag and weight [6, 8, 9], which have detrimental effects on specific fuel consumption. Furthermore, the integration into the airframe is complicated and can generate coupling effects between the aerodynamics of the nacelle and the wing/airframe [9–11].

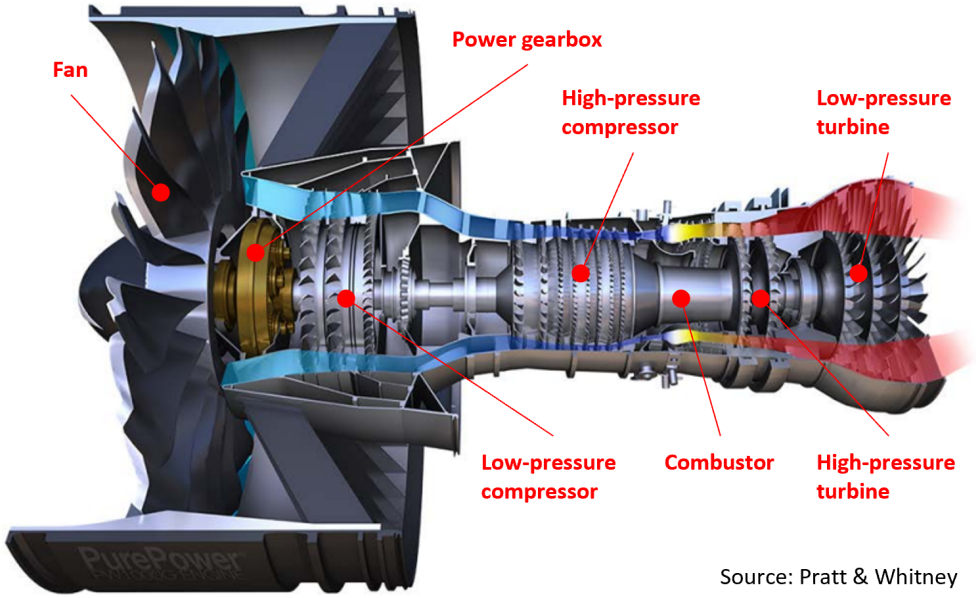

Figure 1.2: The Pratt & Whitney PW1100G (source: Pratt & Whitney).

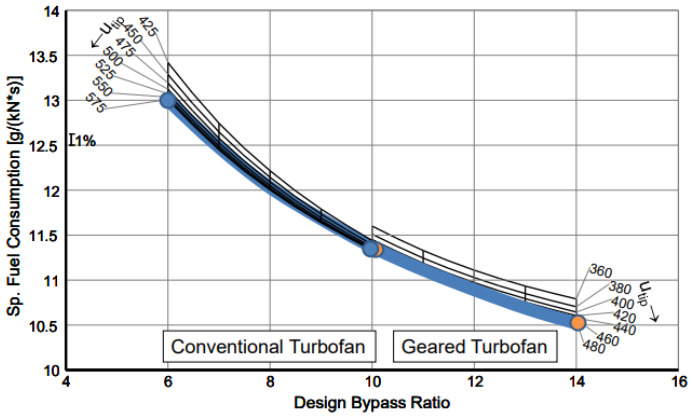

Figure 1.3: Specific fuel consumption vs. by-pass ratio for direct drive and geared architectures [6].

The low-pressure turbine is one of the modules that undergoes the most significant change in geared turbofans. The gearbox enables an increase in blade peripheral speed, which allows for reduced loading and flow coefficient. The shift in the design space is schematically highlighted in the Smith chart [12] displayed in Fig. 1.4. The lower stage loading and flow coefficient in geared turbofans allows for reduced low-pressure turbine part count (∼87% for a turbofan with the same by-pass ratio and thrust).

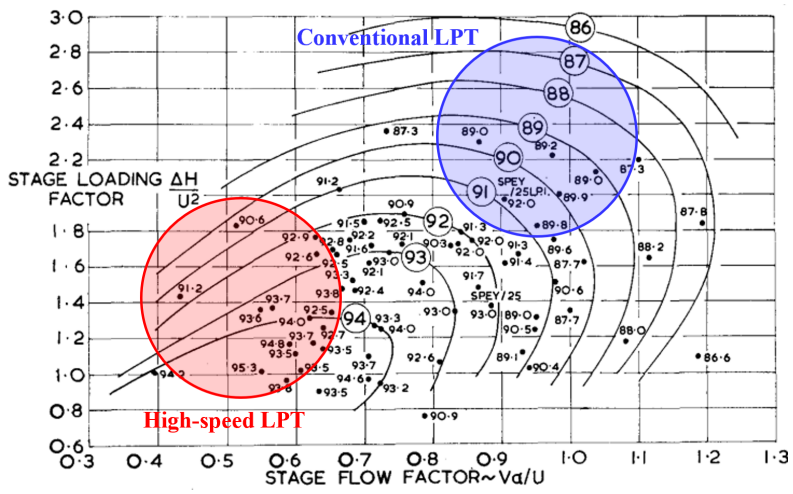

Figure 1.4: Axial turbine stage efficiency in function of stage loading and flow coefficient [12].

Several changes occur at aerodynamic, geometrical, and mechanical levels due to operating at higher peripheral velocities. Torre et al. [13] tested a multi-stage high-speed low-pressure turbine. The work highlights key characteristics that vary from a conventional low-pressure turbine to a high-speed low-pressure turbine. A higher expansion ratio through the machine was also highlighted. The latter promotes more significant variations of the density, which spread the range of Reynolds numbers encountered in the turbine.

The work also highlighted a pair of relevant blading alongside their velocity triangles for a conventional low-pressure turbine vs. a high-speed low-pressure turbine (see Fig. 1.5). The high peripheral velocity enables the blades to be designed with lower inlet metal angles (in the rotor frame of reference). The latter leads to higher velocity ratios. Both of these effects lead to a reduction of secondary loss [14].

Table 1.1 summarizes the design parameters encountered in a modern low-pressure turbine against the ones in a high-speed low-pressure turbine.

The blades are subjected to higher mechanical loads: centrifugal load [15] and higher pressure loads due to higher stage pressure ratio [16]. This impacts the design of the blades, whose thickness must be increased to withstand the maximum load at the root, and the disk, which must have a smaller bore radius and bigger bore width [6].

Rapidly developing efficient low-pressure turbines for geared architectures relies on low-order models used in the preliminary design stages. Often empirical or semi-empirical, these tools depend on their underlying assumptions and training data. Experimentally, the existing knowledge in the field has relied on flat plate testing, linear/annular cascade testing, and full-

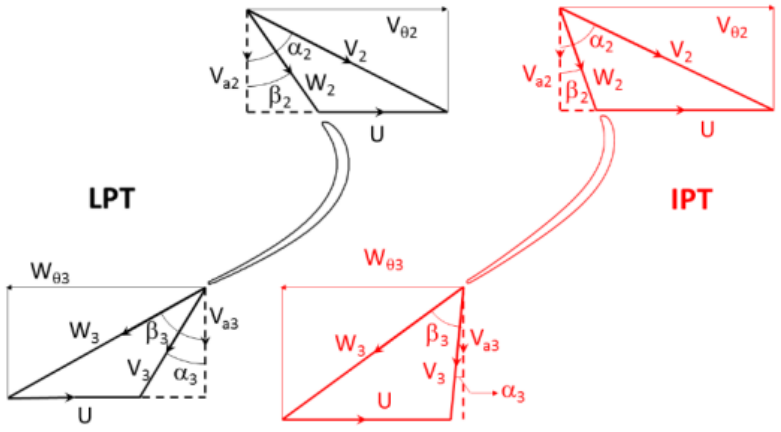

Figure 1.5: Airfoils and velocity triangles of conventional LPT (left) and equivalent to high-speed LPT (right) [13].

Table 1.1: Design parameters of a modern direct drive turbofan LPT and a high-speed LPT for a geared architecture after [13].

Parameter	Unit	DDTF	GTF
Inlet angle	[°]	40	20
Outlet angle	[°]	65	65
Velocity ratio	[−]	1.75	2.30
Outlet Mach number	[−]	0.5–0.6	0.7–0.9
Outlet Reynolds number ($\times 10^3$)	[−]	400–100	1,000–100
Flow coefficient, V_{ax}/U	[−]	0.7–1.2	0.3–0.7
Stage loading, $\Delta H_0/U^2$	[−]	1.7–3.0	0.9–1.7

stage testing. This data is commonly used to complement training datasets for loss prediction, calibrate numerical models in Reynolds-Averaged Navier-Stokes (RANS) applications, and validate high-order numerical Direct Numerical Simulation (DNS) codes.

The underlying assumption of using such data to predict the performance of high-speed low-pressure turbine geometries is that state-of-the-art knowledge provides a good representation of the flow physics occurring in high-speed low-pressure turbines. At the time of writing of this thesis, there is a critical lack of high-speed low-pressure turbine research to accelerate the research and development of greener propulsive units. In particular, the gap concerns measurements at engine-relevant conditions.

Investigations concerning the time-averaged blade aerodynamics and profile loss at engine-relevant Mach and Reynolds numbers are reported. However, measurements with high-speed low-pressure turbine-relevant wake characteristics are lacking. The lack of data concerns the time-resolved aerodynamics of the inlet and outlet flow in a transonic low-Reynolds number environment. More importantly, the transition mechanisms at high-transonic Mach number, low-Reynolds, and large wake reduced frequency have not been addressed in the scope of low-pressure turbine blading where shocks can occur.

The lack of investigations of high-speed low-pressure turbines extends to secondary flows. Apart from a handful of studies performed in annular cascades, the impact of unsteady wakes on secondary flows at conditions representative of high-speed low-pressure turbines has not been addressed. Unsteady inflow cases usually concern low-speed conditions with matched wake characteristics or high-speed applications with off-design wake velocity triangles. In addition, studies with the combined effect of cavity purge flows are not available in the open literature—-the lack of literature concerns time-averaged and time-resolved investigations.

1.2 State of the Art

Loss in axial turbines can be generally split into three terms: two-dimensional profile loss, endwall loss, and tip leakage loss [17]. Due to the high-aspect ratio encountered in low-pressure turbines [18, 19], the profile loss, in particular the suction side (SS) related one [20], is a dominant term in the overall loss budget. Nonetheless, the endwall-related loss can amount to one-third of the overall loss [17].

Conventional axial low-pressure turbines in aeronautical applications operate under low-Reynolds numbers at cruise conditions [21, 22]. Fig. 1.6 displays the typical flight envelope of a low-pressure turbine.

In geared low-pressure turbines, higher expansion ratios through the machine are encountered [13]. The latter promotes more significant variations of the density, which spread the range of Reynolds numbers encountered in the turbine. Nonetheless, the blade design drives the Reynolds number, which can still be low.

Due to the increase in rotational velocity of the low-pressure spool imposed by the gearbox, the low-pressure turbine operates at transonic exit Mach numbers that can exceed 0.70 in the relative frame of reference [13]. The spool speed also results in decreased flow coefficient and increased blade wake reduced frequency.

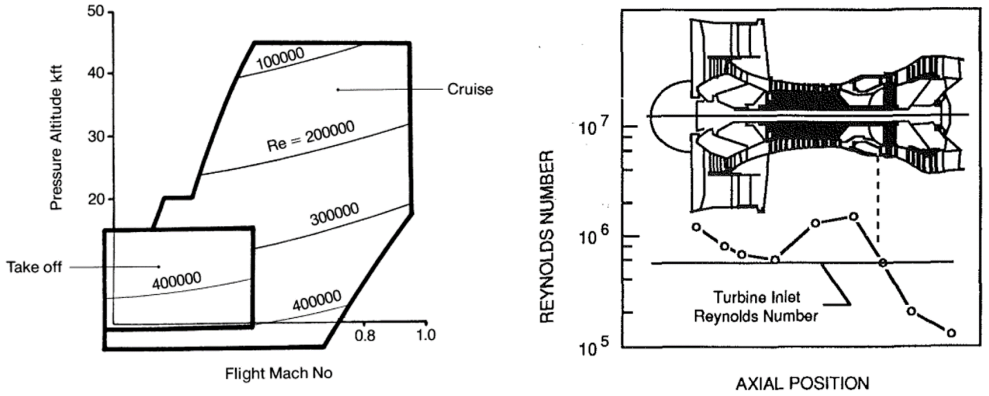

Figure 1.6: Reynolds number regime encountered in LPT during flight cycle [21].

1.2.1 Two-Dimensional Profile Aerodynamics

In low-pressure turbines, the boundary layer (BL) is laminar for most of the blade surface and typically separates in the adverse pressure gradient portion of the blade suction side. Transition in axial turbines has been a critical research topic for decades [23]. Transition in axial turbines is driven by:

- Surface roughness [24–26],
- Pressure gradient [27, 28],
- Compressibility [29–31],
- Heat transfer [32, 33],
- Turbulence intensity and length scale [23, 34–38].

The freestream turbulence and pressure gradient are significant parameters in low-pressure turbines. In low-pressure turbines, the boundary layer usually undergoes transition in the separated shear layer. The boundary layer reattaches before the blade trailing edge unless the transition process is too slow. As a result, a laminar separation bubble (LSB) is formed. Fig. 1.7(a) shows a sketch of the formed laminar separation bubble. The laminar separation bubble is visible on the turbine blade loading as a local "bump" as displayed in Fig. 1.7(b).

The extent of the laminar separation bubble defines its type. Hatman and Wang [41] separated the laminar separation bubble into short and long bubbles in cases for which transition occurs after the separation. The bubble type depends on the status of the boundary layer at the separation location: acceleration parameter, Reynolds number based on the momentum thickness, and Reynolds number based on the surface length. Short bubbles occur when the momentum thickness Reynolds number is lower than 240 at the separation location.

Controlling the extent of the laminar separation bubble on the suction side is critical to the low-pressure turbine performance. The laminar separation bubble can contribute up

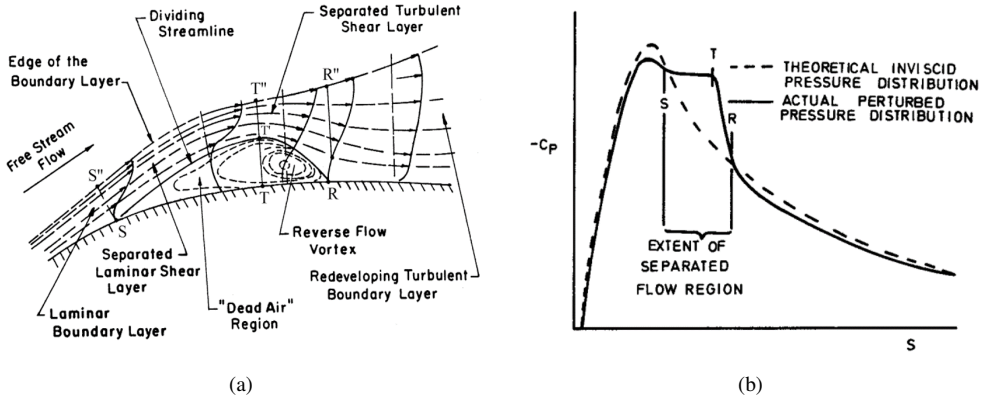

(a) (b)

Figure 1.7: Schematic representation of laminar separation bubble [39] (a) and signature on turbine blade loading [40] (b).

to 60% of the suction side-related loss [18]. Over the years, researchers have developed empirical correlations to predict better the laminar separation bubble extent and its transition properties. Numerical tools, namely RANS, remain the most used tool in the design of a turbine. However, the existing transition models employed in RANS frameworks still struggle to capture the underlying flow physics [42–44]. Improving transition models is an ongoing necessity. Research on the topic is often conducted in low-speed wind tunnels by varying the turbulence level and pressure gradient [27, 28, 34, 45–47]. Studies including blade-relevant pressure gradients at engine-representative Mach numbers are scarce.

An additional downfall of RANS is the wake mixing sensitivity to the mesh density when compared against higher-order methods such as Large Eddy Simulation (LES) [44, 48–50]. Recent efforts have been put into data-driven approaches to train transition closures through machine learning approaches [51–54]. The models are often trained with LES and DNS data to improve the prediction of the transition extent and create wake detection functions to improve the wake prediction and, hence, profile loss. The computational cost of running high-order CFD limits the variation of critical parameters such as the pressure gradient (blade geometry), turbulence intensity, roughness, trailing edge geometry, etc. To the author's knowledge, similar machine learning frameworks that use highly modular wind tunnels have not yet been implemented.

At a larger level, researchers have addressed the impact of the Reynolds number on the blade performance. The early work of Hourmouziadis [21] on controlled diffusion airfoils set the stage for upcoming decades of research. A turning point in low-pressure turbine blading occurred with the advent of (ultra-)high-lift profiles. These profiles are characterized by increased loading and were developed to reduce the low-pressure turbine part count (and weight). These geometries were heavily investigated in low-speed [55–57] and high-speed [58–61] linear cascades at engine-relevant Reynolds number. Common findings were achieved. Increasing the Reynolds number promotes a decrease in the laminar separation bubble extent and consequent profile loss.

High-speed testing of high-lift profiles has considered Mach number up to $\sim$0.70. Open

literature for high-transonic Mach numbers is lacking. Vera et al. [58] investigated the impact of the Mach number on the performance of two low-pressure turbine linear cascades designed to have the same loading and to operate at Re=190k. They found the profile loss independent of the Mach number for the high-speed testing case up to M=0.76. In their case, a passage shock formed at M=0.83. Vazquez et al. [62] also found increasing profile loss with Mach number in annular cascade surveys. The authors displayed a decrease in the blade loading and shift of the velocity peak towards the trailing edge [62, 63]. The latter effect is attributed to the change in the loading at the off-design Mach number. Redesigning the profile to retrieve the on-design loading would result in an identical profile loss.

The flow in low-pressure turbines is inherently unsteady due to the rotor-stator relative motion. In the relative frame of reference, the wake can be seen as a negative jet [64]. The wake convection is described by simple kinematics [65]. The wake is bowed, reoriented, elongated, and stretched, as it conveys in the passage. The wake low momentum fluid accumulates near the suction side due to the cross-passage pressure gradient. The process is schematically represented in Fig. 1.8(a). The negative jet reduces the flow incidence (see Fig. 1.8(b)) due to its lower relative velocity than the freestream.

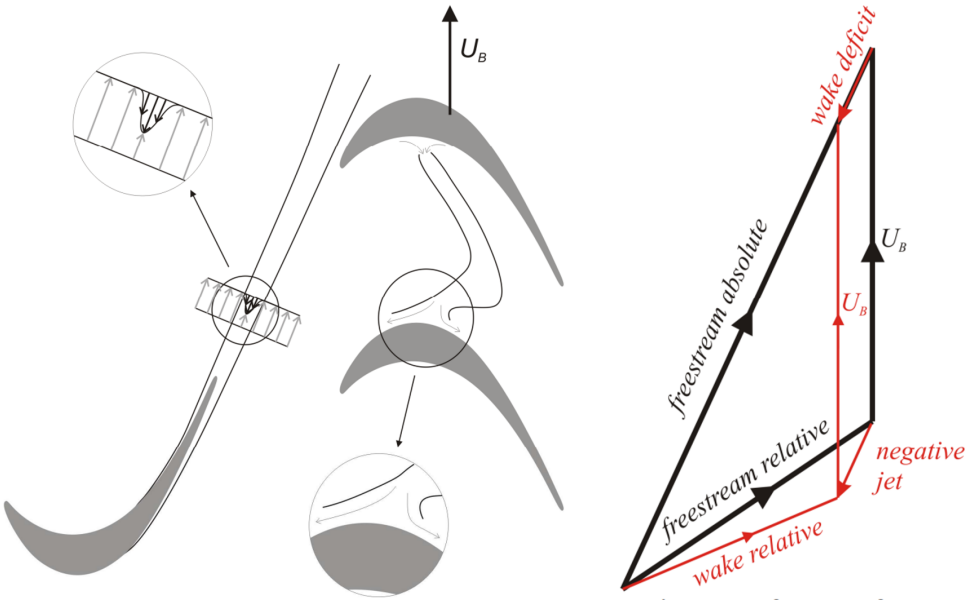

Figure 1.8: Sketch of wake in LPT (a) and velocity triangles in the freestream and wake (b) [66].

The perturbations that travel with the wake interact with the suction side boundary layer and can trigger an early transition. This transition mechanism is named wake-induced transition and is one of many transition mechanisms that can co-exist in low-pressure turbine boundary layers [67]. Early research highlighted the effect of the wake in triggering the formation of turbulent spots in the boundary layer, followed by the so-called becalmed region in the attached boundary layer [18, 68, 69]. Additional research considered the for-

mation of turbulent spots upstream of the laminar separation bubble for cases with separation [69, 70]. Consequent works described the wake-induced transition in the separated flow region [67, 71]. The wake-boundary layer interaction in separated flows can be represented with a space-time diagram (see Fig. 1.9). The wake perturbations generate turbulent perturbations that propagate slower than the wake itself. The leading edge of the turbulent region propagates at 88% of the freestream velocity. The trailing edge of the turbulent spot propagates at 50% of the freestream velocity. After the turbulent portion, a becalmed region is formed. The trailing edge of this region propagates at 0.30% of the freestream velocity. The becalmed region is characterized by a full boundary layer resistant to adverse pressure gradients. The laminar separation bubble then reestablishes itself until the following wake arrives, restarting the process.

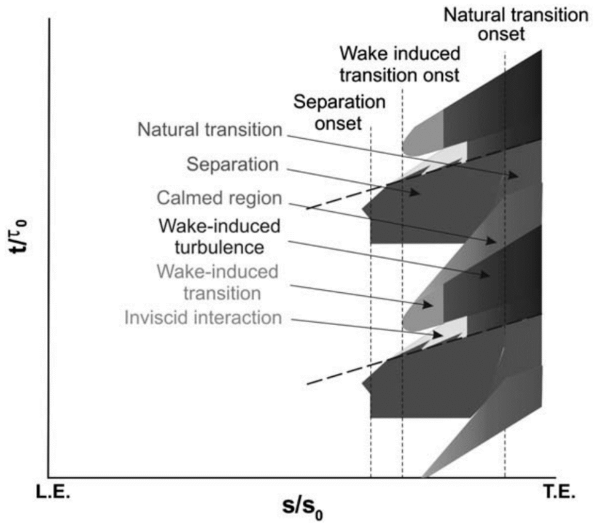

Figure 1.9: Schematic of the transition mechanism resulting from wake-separated boundary layer interaction. [72]

In separated flows and with low freestream turbulence and low surface roughness, the mechanism through which transition is triggered is the formation of spanwise Kelvin-Helmholtz (KH) roll-ups [72]. In reality, increasing the turbulence level and having surface discontinuities near the leading edge can trigger the formation of Klebanoff streaks through a shear sheltering process. The Klebanoff streaks break down the Kelvin-Helmholtz spanwise structures and trigger the formation of Lambda-vortices that further contribute to the turbulence breakdown. A simplified representation of the process is illustrated in Fig. 1.10(a). These roll-ups travel at half of the wake velocity. Similar to the attached wake-induced transition, a becalmed region is formed after the Kelvin-Helmholtz disturbances have exited the passage. The perturbations penetrate the boundary layer and can be perceived as local pressure fluctuations (see Fig. 1.10(b)) as highlighted by Stieger et al. [72]. Due to the double-sided effect of the wake negative jet, the pressure fluctuations resemble a local sine-wave fluctuation.

Wake-induced transition mechanisms have been investigated mainly in low-speed linear cascades [73] and flat plates [66, 67] under pressure gradients at engine-realistic wake veloc-

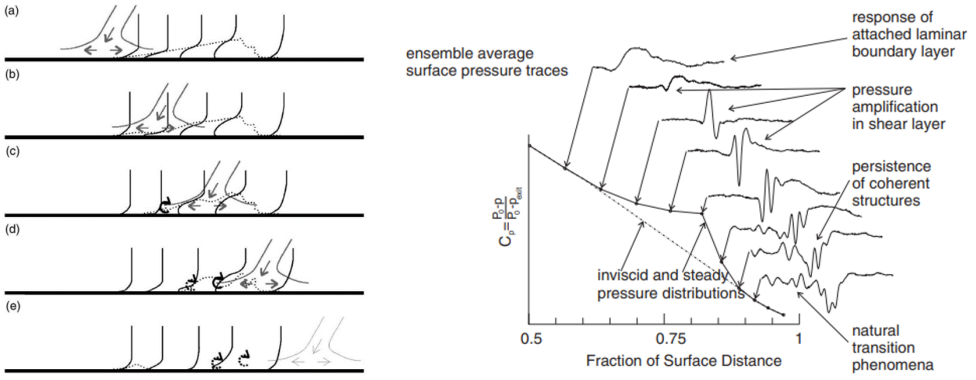

Figure 1.10: Interaction of negative jet with inflectional boundary and generation of Kelvin-Helmholtz instabilities [71] (a) and pressure fluctuating traces in separation bubble [72] (b).

ity triangles. Similar transition mechanisms have been detected in linear cascade testing of direct-drive turbofan low-pressure turbines at high-subsonic Mach numbers, engine-relevant Reynolds number, and wake reduced frequency [74]. The author is unaware of works investigating the transition mechanisms in cases characterized by passage shocks. The latter can occur in geared low-pressure turbines operating at off-design conditions. Boerner et al. [75] investigated transition under steady inlet flow conditions at low-pressure turbine-representative Reynolds number. The linear cascade was designed to trigger shock-boundary layer interactions and examine its impact on transition.

In general, the wake reduces the laminar separation bubble extent in the time-averaged flow, which reduces the profile loss. The latter effect has been both observed in low-speed [56, 69, 76] and high-speed [26, 74] cascade testing. The impact is dependent on the Reynolds number and flow coefficient. Increasing the wake reduced frequency can result in a larger turbulent wetted area and suppress the wake-induced benefit of reducing the laminar separation bubble extent [26, 56, 69, 74].

Based on the parameters above impacting transition and the profile aerodynamics, it is crucial to complement literature with geared turbofan engine-representative cases. There is a critical lack of accurate measurements addressing the transition mechanisms and loss at high transonic Mach number, preferably in the presence of shocks for off-design conditions, combined with low Reynolds numbers and high wake reduced frequency.

1.2.2 Secondary Flows

Secondary flows are formed at the endwall of a linear turbine cascade. The inlet boundary layer experiences an adverse pressure gradient while approaching the leading edge and separates. The separated boundary layer rolls into a double-sided horseshoe vortex (HV) [77]. The two legs of the horseshoe vortex, the pressure side (HV_{PS}) and suction side leg (HV_{SS}) have opposite vorticity. Different models over decades of research have characterized the development of the HV into primary and secondary flow structures. Sieverding [78] reviewed

secondary flow literature, including works up to 1985. Langston [79] extended the literature review to include works up to 2001. Ligrani et al. [80] review endwall flows up to 2017.

Generally, existing models agree on what concerns the formation of the passage vortex (PV). The pressure side (PS) leg of the horseshoe vortex migrates towards the adjacent blade suction side due to the cross-passage pressure gradient. Doing so entrains low-momentum fluid in the endwall and forms the PV. The latter corresponds to the most dominant secondary flow structure in the turbine passage. The development of the suction side leg of the HV varies from model to model. Some models highlight the lift-off of this structure above the PV as it conveys attached to the suction side [81, 82], while others defend that it wraps itself around the PV though a helical motion [83–85]. Arguably, the most comprehensive model is the one of Wang [85]. The authors used smoke visualization in a low-speed linear cascade to characterize the developing secondary flow structures across the cascade. The authors detected a wall-induced vortex (WIV) generated by the impingement of the pressure side leg of the horseshoe vortex on the blade suction side. The WIV has the opposite vorticity of the PV. In addition, the formation of the suction side corner vortex with counter vorticity with respect to the PV is highlighted. The secondary flow structures recognized in the model are schematically represented in Fig. 1.11.

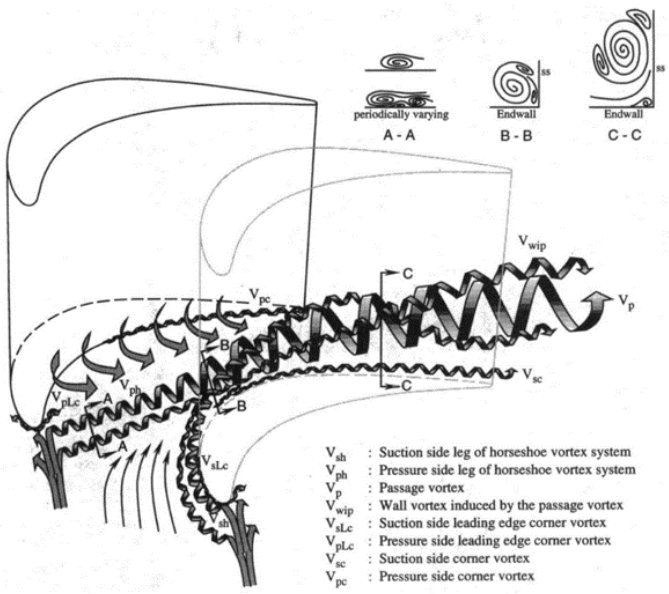

Figure 1.11: Secondary flow model of Wang et al. [85] .

The spanwise variation of the blade loading gives rise to trailing shed vorticity (TSV) that rotates in the opposite direction of the passage vortex [86]. The trailing shed vorticity typically sits above the PV and around the location as the WIV and HV_{SS}, characterized by the same vorticity. The challenge of decoupling the above flow structures led researchers to denominate their combination as a counter-vortex. The primary secondary flow structures are displayed in Fig 1.12 after Coull [14]. The formation of the secondary flow structures mainly depends on the blade design, flow condition, and inlet boundary layer.

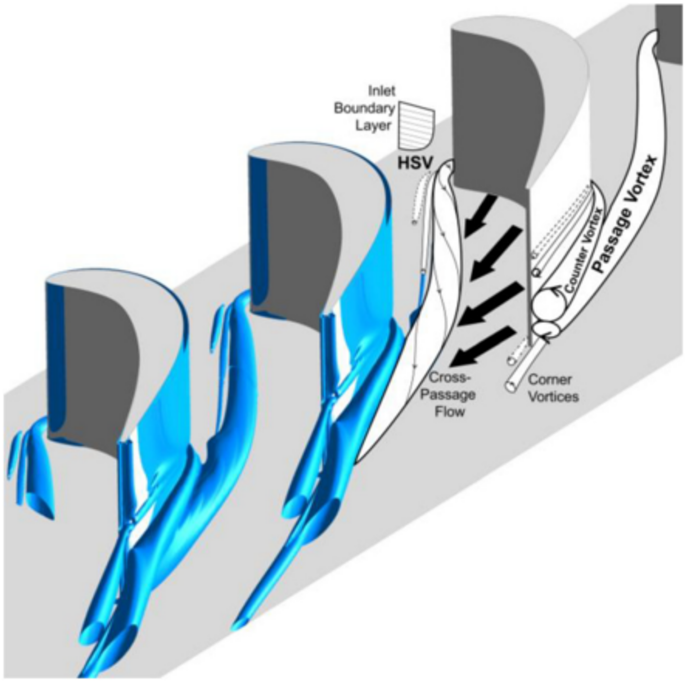

Figure 1.12: Schematic representation of secondary flows in turbine after Coull [14].

Perdichizzi [87] investigated the influence of off-design Mach numbers on developing secondary flow in a high-pressure turbine (HPT) linear cascade. The Mach number was varied in the range of 0.20–1.55. The Reynolds number was representative of those found in high-pressure turbines. An increase in the outlet Mach number resulted in weaker secondary flows and migration of the flow structures toward the endwall. Similar findings were achieved by Vazquez et al. [62] during their annular cascade testing with the Mach numbers in the range of 0.50–0.90. In a follow-up study performed in a multi-row high-speed low-pressure turbine, Vazquez and Torre [63] established that the variation in secondary loss with Mach number resulted from altering blade loading at off-design conditions.

Hodson and Dominy [88] investigated the impact of the Reynolds number on secondary flow loss in a low-pressure turbine linear cascade operating at M_{out}=0.70. Three Reynolds numbers were investigated: 150,000, 300,000, 600,000. The inlet boundary layer was conserved between the cases. They found increasing secondary loss with Reynolds number.

The formation of secondary flows largely depends on the inlet boundary layer since most of the lower momentum fluid in the boundary layer is entrained into the horseshoe vortex system. The properties of the inlet boundary layer that impact the secondary flows are mainly the thickness, shape factor, and skewness.

Perdichizzi and Dossena [89] addressed the impact of the inlet incidence on the secondary flow loss of a high-pressure turbine linear cascade operated at an outlet Mach number of 0.70. He found that the secondary flow structures migrate toward the center of the passage with increasing incidence.

Due to the change of the frame of reference from stator to rotor, and vice-versa, in an

actual stage, the boundary layer is skewed. Walsh and Gregory-Smith [90] found the inlet skew to modify the vorticity distribution at the outlet. They found increasing endwall loss with boundary layer skewness. The previous work also defended the inlet skew as more significant than the boundary layer thickness on the endwall loss. Coull [91] argued that the shape factor of the inlet boundary layer contributed more to endwall loss than the boundary layer skewness. The statement aligns with the findings in [88, 92]. The statement also agrees with the work of de la Rosa Blanco et al. [93], where a higher secondary loss was found for turbulent boundary layers.

Studies dealing with the impact of unsteadiness on the secondary loss in a linear cascade environment are scarce. Infantino et al. [94] highlighted the importance of accounting for the impact of unsteadiness in the early design procedures of low-pressure turbine blades. Literature can be split into tests performed in low-speed linear cascades at engine-relevant Reynolds number and wake reduced frequency [94–96] and studies at engine-relevant Mach number and Reynolds number with unrealistic wake velocity triangles [97]. Table 1.2 gathers the flow conditions for studies relevant to this work. At the time of writing of this thesis, research combining geared turbofan-relevant Mach number, Reynolds number, and velocity triangles is not available.

Table 1.2: Investigations on the impact of unsteady wakes on secondary flows.

	Type	M	Re	f^+	V_{ax}/U
Satta et al. [95]	LS LPT	–	100,000, 300,000	0.62	0.675
Volino et al. [96]	LS HPT	–	30,000	1.05	1.00
Infantino et al. [94]	LS LPT	–	300,000	0.62	0.675
Ciorciari et al. [97]	HS LPT	0.59	200,000	0.33–0.66	1.90–3.80

Generally, the low-speed investigations found the unsteady wakes to reduce the secondary loss by reducing their intensity. However, no data concerning the inlet boundary layer was reported in [95]. Opposite findings are reported in [96] for which the boundary layer was similar for the steady and unsteady flow cases. The investigations of Infantino et al. [94] and Ciorciari [97] used phase-resolved data to investigate the modulation of the secondary flow structures. The PV and TSV were periodically distorted and weakened during a wake-passing period. The most significant loss happened when the wake of the bar was passing through the measurement plane.

Cavity purge flows are another aspect impacting secondary flow development, often overseen in linear cascade testing. Turbine investigations commonly report an increase of the secondary loss and displacement of secondary flow structures away from the endwall as the purge massflow rate is increased [98–107]. Linear cascade investigations of purge flow effects are generally conducted under steady inlet flow and low-speed conditions. Table 1.3 highlights two investigations relevant to this work.

Table 1.3: Investigations on the impact of purge flow on secondary flows.

	Type	M	Re	PMFR
Barigozzi et al. [108]	LS HPT	0.17	740,000	0.50%–2.00%
de la Rosa Blanco et al. [109]	LS LPT	0.07	232,000	0.00%, 0.30%, 0.70%

de la Rosa Blanco et al. [109] found that the endwall flows and mixed-out losses were influenced by the exchange of mass and momentum between the recirculating fluid in the gap geometry and the main flow, even when no purge flow was injected. This finding was further exploited by Popovic and Hodson [110] through a numerical framework. The work characterized the leakage vortex and its entertainment in the passage (see Fig. 1.13(a)). Near the pressure side (Plane-1), there is an exchange of entrainment from the main flow into the cavity slot due to the static pressure gradient experienced by the incoming flow. Along the purge flow, this fluid develops into a vortex and moves toward the suction side of the adjacent blade (Plane-3), where the cascade-imposed static pressure increases again. The leakage vortex exits the cavity somewhere in the middle of the passage (between Plane-2 and Plane-3) in a region of lower static pressure. Once in the passage, it is transported until it merges with the passage vortex. The merging location depends on the purge massflow ratio.

Due to the significant impact of gap geometry on secondary flow strength and losses, even in cases where no purge flow is injected, some studies have emphasized the importance of including endwall gap geometry in the early design stages of turbines [98, 111]. While detailed geometry inclusion can be challenging in the early design phase, MacIsaac et al. [112] have demonstrated that the use of a simplified geometry is still highly impactful, especially for optimization schemes, since the losses are enhanced with a cavity endwall. Fig. 1.13(b) displays iso surfaces highlighting the secondary flow structures present in their work. The streamlines display the formation of the leakage vortex and its entrainment in the passage near the suction side of the adjacent blade.

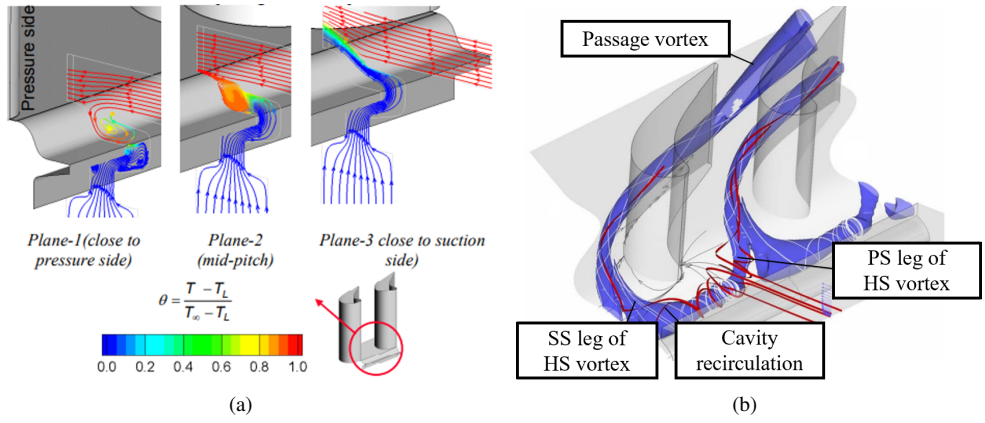

Figure 1.13: Rim seal aero-thermodynamics in terms of streamlines in meridional plane [110] and ISO-surface of constant turbulent kinetic energy and surface streamlines showing the secondary flow vortices for the cavity case [112].

1.2.3 Loss Modeling

Low-order correlations are still paramount in the early design stages of axial turbines to provide initial design guidance and to estimate the loss and efficiency of the machine. The mean-line prediction method of Ainley and Mathieson [113] served as the basis for following

improved correlations: Dunham and Came (DC) [114], Kacker and Okapuu [115], Zhu and Sjolander [116], Benner et al. [117, 118]. The methods of Zhu and Sjoladner, and Benner et al. included high-lift design profiles in the training data. The model of Craig and Cox [119] can be regarded as a standalone in its approach and training dataset. Both families of Ainley and Mathieson [113–115, 117–119], and Craig and Cox [119] models provide correlations for the estimation of the profile and secondary loss. They also include the tip leakage loss term not addressed in this work.

Coull [14] pointed out that existing models by 2017 had little physical basis. Coull and Hodson [120] developed a physics-based empirical model applicable to (ultra-)high-lift low-pressure turbine blading. The model predicts the boundary layer integral parameters at the pressure and suction sides trailing edge, allowing us to estimate the profile loss. The boundary layer integral parameters account for the impact of unsteady wakes, turbulent wetted area, and separation bubble development. The model was developed considering high-lift designs. Flat plate low-speed tests were performed. The model does not account for compressible effects in high-speed low-pressure turbines.

Following the development of their comprehensive profile loss model, Coull [14] developed a physics-based secondary loss correlation. The research significantly contributed to understanding the sensitivity of secondary loss to crucial design parameters through a parametric approach. The boundary layer was kept similar so its contribution could be isolated. Coull [14] used classical secondary flow theory to divide secondary loss into two primary constituents: endwall loss due to the boundary layer dissipation and loss due to the mixing of the secondary flow structures. The impact of the secondary flow structures is considered through vortex amplification factors.

In a consequential work, Coull and Clark [91] extended the previous work to consider the inlet boundary layer status and thickness. The secondary loss coefficient was inversely proportional to the aspect ratio and proportional to the square of non-dimensional circulation (blade profile design). The vorticity distribution was considered through a parameter built with secondary flow theory to cover a range of boundary layer parameters representative of engine and cascade data. The model constitutes the most advanced secondary loss model to date. The model is also unique in considering the loss as a dissipation of secondary kinetic energy rather than a conventional loss coefficient.

1.3 Research Objectives

The current research serves multiple purposes. A transonic linear cascade present at the von Karman Institute was adapted to enable testing quasi-3D flows. The work provides an in-depth characterization of the experimental methods developed and employable. A comprehensive characterization of the revamped rig is provided before considering the aerodynamics of high-speed, low-pressure turbines. The rig commission aims to demonstrate the rig's capabilities to test high-speed, low-pressure turbines under the impact of unsteady wakes and purge flows.

In light of the knowledge gaps and ongoing challenges to improve design tools for greener propulsive units, the main objectives of the current study are:

- To commission a revamped transonic low-Reynolds number linear cascade and prove

its applicability in testing high-speed low-pressure turbines under the impact of unsteady wakes and purge flows,

- To develop advanced time-averaged and time-resolved flowfield and surface experimental techniques for the comprehensive characterization of the profile and endwall aerodynamics of the high-speed linear cascade,
- To compare the experimental results against numerical frameworks and challenge the applicability of the latter to high-speed low-pressure turbine designs,
- To describe the on- and off-design profile performance and draw considerations on the impact of shocks in existing transition correlations,
- To address the wake-induced transition mechanisms at engine-relevant Mach and Reynolds numbers in the presence of compressible effects,
- To quantify the impact of unsteady wakes and purge flows on the secondary flow development and loss in the time-averaged and time-resolved frame of reference,
- To challenge the fitting of existing low-order models for profile and secondary loss correlation obtained at low-speed conditions,
- To ultimately generate a high-fidelity database of geared turbofan relevant data that can be used to develop low-speed testing setups to validate compressibility effects in experimental environments, increase the dataset used in profile loss and secondary loss low-order models, improve/mature transition models in numerical frameworks, validate new low-order and high-order numerical solvers.

1.4 Thesis Outline

The thesis is divided into eight chapters describing the research methodologies, characterizing a revamped high-speed linear cascade for testing quasi-3D flows, and detailing the research results.

Chapter 1 introduces the motivation for the research addressed in this manuscript. It also presents the topic and the current state-of-the-art. The existing literature and gaps in geared low-pressure turbine research are highlighted. Finally, the research objectives are stated.

Chapter 2 describes the experimental apparatus and introduces the reader to the EU project SPLEEN, of which the high-speed low-pressure turbine geometry under investigation is part. It also describes the facility where the geometry was investigated and its constituents. The measurement techniques and data reduction techniques are also depicted.

Chapter 3 highlights the numerical tools used in this work. It highlights the sensitivity to several parameters, including mesh size, incidence, and turbulent quantities, to justify the choice of modeling parameters.

Chapter 4 characterizes the rig performance in terms of the stability of the operating point and the periodicity of the flow conditions in the test section. Probe interference, which arises when measuring with finite-size probes in transonic flowfields, is exposed. The interference is quantified, and a methodology for correcting intrusiveness is presented.

Chapter 5 addresses the profile aerodynamics at on- and off-design flow conditions. The inlet boundary conditions with and without unsteady wakes are provided. The steady-state aerodynamics are compared against numerical schemes. The impact of unsteadiness on the blade loading is depicted. The blade surface boundary layer is described thoroughly for steady and unsteady inlet flowfields. The profile loss is reported as well. The time-resolved flowfield is investigated. The inlet bar wake is characterized by pressure loss and turbulence signature. Wake-boundary layer interaction at off-design conditions is reported to address transition mechanisms. Finally, the outlet flowfield is scrutinized in terms of its unsteadiness.

Chapter 6 highlights the secondary flows in the linear cascade tests. The on- and off-design aerodynamics with steady inlet flow are addressed. Both the inlet boundary layer and outlet flowfield are exploited. The impact of introducing the wake generator on the inlet boundary layer and secondary flow signature is depicted. Lastly, the effect of replacing the flat endwall with a cavity slot and injecting purge flow is addressed on the secondary flow losses. For cases with unsteady inlet flow, the inlet and outlet flowfields are characterized by their unsteadiness: loss, angles, and turbulence intensity.

Chapter 7 challenges existing profile and secondary floss correlations and their applicability to the high-speed low-pressure turbine geometry tested in this work. The time-averaged loss data depicted in the previous chapters is compared against loss correlations in the literature. Based on the experimental and numerical data obtained in the scope of this work, the underlying assumptions of the most advanced loss models are challenged. Both profile and secondary loss are broken down to explain the trends observed experimentally.

Chapter 8 summarizes the main findings of the thesis. The rig performance parameters are recalled. The two-dimensional profile performance impact on the engine-representative flow conditions is scrutinized. The flow mechanisms encountered during the study are compared against existing literature. Considerations are drawn on the experimental secondary loss breakdown. The validity of existing correlations in the scope of high-speed low-pressure turbine geometries is recalled.

References

[1] IEA. *CO2 Emissions in 2022*. IEA, Paris, 2023.

[2] European Commission, Directorate-General for Research, and Innovation. *Fly the Green Deal – Europe's vision for sustainable aviation*. Publications Office of the European Union, 2022.

[3] Intergovernmental Panel on Climate Change (IPCC). *Global Warming of 1.5°C: IPCC Special Report on Impacts of Global Warming of 1.5°C above Pre-industrial Levels in Context of Strengthening Response to Climate Change, Sustainable Development, and Efforts to Eradicate Poverty*. Cambridge University Press, 2022.

[4] A. Muller, J.L. Walls, and A. Wittmer. *Sustainable Aviation: An Introduction*, pages 1–22. Springer International Publishing, Cham, 2022.

[5] Air Transport Action Group (ATAG). *Waypoint 2050.Balancing growth in connectivity with a comprehensive global air transport response to the climate emergency: a vision of net-zero aviation by mid-century.* 2021.

[6] J. Kurzke. *Fundamental Differences Between Conventional and Geared Turbofans*. volume Volume 1: Aircraft Engine; Ceramics; Coal, Biomass and Alternative Fuels; Controls, Diagnostics and Instrumentation; Education; Electric Power; Awards and Honors of *Turbo Expo: Power for Land, Sea, and Air*, pages 145–153, 06 2009.

[7] D.C. Wisler. *The technical and economic relevance of understanding blade row interaction effects in turbomachinery*. Lecture series-van Kareman Institute for fluid dynamics, 2:H1–H17, 1998.

[8] W. Lu, G. Huang, X. Xiang, J. Wang, and Y. Yang. *Thermodynamic and Aerodynamic Analysis of an Air-Driven Fan System in Low-Cost High-Bypass-Ratio Turbofan Engine*. Energies, 12(10), 2019.

[9] C. Hughes, D. Van Zante, and J. Heidmann. *Aircraft engine technology for green aviation to reduce fuel burn*. In 3rd AIAA Atmospheric Space Environments Conference, page 3531, 2011.

[10] T.P. Stankowski, D.G. MacManus, M. Robinson, and C.T. Sheaf. *Aerodynamic Effects of Propulsion Integration for High Bypass Ratio Engines*. Journal of Aircraft, 54(6):2270–2284, 2017.

[11] R. Rudnik, C. Rossow, and H. Frhr.v.Geyr. *Numerical simulation of engine/airframe integration for high-bypass engines*. Aerospace Science and Technology, 6(1):31–42, 2002.

[12] S.F. Smith. *A Simple Correlation of Turbine Efficiency*. The Aeronautical Journal, 69(655):467–470, 1965.

[13] D. Torre, G. GarcIa-Valdecasas, A. Puente, D. HernAndez, and S. Luque. *Design and Testing of a Multi-Stage Intermediate Pressure Turbine for Future Geared Turbofans*. Journal of Turbomachinery, 144(9):091008, 03 2022.

[14] J.D. Coull. *Endwall Loss in Turbine Cascades*. Journal of Turbomachinery, 139(8):081004, 03 2017.

[15] M. Giovannini, F. Rubechini, M. Marconcini, A. Arnone, and F. Bertini. *Analysis of a LPT Rotor Blade for a Geared Engine: Part I — Aero-Mechanical Design and Validation*. volume Volume 2B: Turbomachinery of *Turbo Expo: Power for Land, Sea, and Air*, page V02BT38A053, 06 2016.

[16] F.J. Malzacher, J. Gier, and F. Lippl. *Aerodesign and Testing of an Aeromechanically Highly Loaded LP Turbine*. Journal of Turbomachinery, 128(4):643–649, 12 2003.

[17] J.D. Denton. *The 1993 IGTI Scholar Lecture: Loss Mechanisms in Turbomachines*. Journal of Turbomachinery, 115(4):621–656, 10 1993.

[18] R.J. Howell, O.N. Ramesh, H.P. Hodson, N.W. Harvey, and V. Schulte. *High Lift and Aft-Loaded Profiles for Low-Pressure Turbines*. Journal of Turbomachinery, 123(2):181–188, 02 2000.

[19] H.P. Hodson and R.J. Howell. *BLADEROW INTERACTIONS, TRANSITION, AND HIGH-LIFT AEROFOILS IN LOW-PRESSURE TURBINES*. Annual Review of Fluid Mechanics, 37(1):71–98, 2005.

[20] E.M. Curtis, H.P. Hodson, M.R. Banieghbal, J.D. Denton, R.J. Howell, and N.W. Harvey. *Development of Blade Profiles for Low-Pressure Turbine Applications*. Journal of Turbomachinery, 119(3):531–538, 07 1997.

[21] J. Hourmouziadis. *Aerodynamic design of low pressure turbines*. AGARD, Blading Design for Axial Turbomachines 40 p(SEE N 89-27661 22-07), 1989.

[22] W. Lou and J. Hourmouziadis. *Separation Bubbles Under Steady and Periodic-Unsteady Main Flow Conditions*. Journal of Turbomachinery, 122(4):634–643, 02 2000.

[23] R.E. Mayle. *The 1991 IGTI Scholar Lecture: The Role of Laminar-Turbulent Transition in Gas Turbine Engines*. Journal of Turbomachinery, 113(4):509–536, 10 1991.

[24] R. Vazquez and D. Torre. *The Effect of Surface Roughness on Efficiency of Low Pressure Turbines*. Journal of Turbomachinery, 136(6):061008, 11 2013.

[25] F. Montomoli, H. Hodson, and F. Haselbach. *Effect of Roughness and Unsteadiness on the Performance of a New Low Pressure Turbine Blade at Low Reynolds Numbers*. Journal of Turbomachinery, 132(3):031018, 04 2010.

[26] M. Vera, H.P. Hodson, and R. Vazquez. *The Effects of a Trip Wire and Unsteadiness on a High-Speed Highly Loaded Low-Pressure Turbine Blade*. Journal of Turbomachinery, 127(4):747–754, 03 2004.

[27] M. Dellacasagrande, D. Barsi, D. Lengani, D. Simoni, and J. Verdoya. *Response of a flat plate laminar separation bubble to Reynolds number, free-stream turbulence and adverse pressure gradient variation*. Experiments in Fluids, 61:1–17, 2020.

[28] M. Dellacasagrande, D. Lengani, D. Simoni, M. Ubaldi, and P. Zunino. *Evaluation of Turbulent Spot Production Rate in Boundary Layers Under Variable Pressure Gradients for Gas Turbine Applications*. Journal of Turbomachinery, 142(6):061003, 05 2020.

[29] R.Narasimha. *The laminar-turbulent transition zone in the boundary layer*. Progress in Aerospace Sciences, 22(1):29–80, 1985.

[30] D.H. Choi and E.H. Lee. *Prediction of separation bubbles using improved transition criterion with two-equation turbulence model*. AIAA Journal, 33(8):1512–1514, 1995.

[31] J.P. Clark, T.V. Jones, and J.E. LaGraff. *On the propagation of naturally-occurring turbulent spots*. Journal of Engineering Mathematics, 28(1):1–19, 1994.

[32] T.S. Cação Ferreira, N. Vasilakopoulos, and T. Arts. *Investigation of Thermal Effect on Bypass Transition on a High-Pressure Turbine Guide Vane*. Journal of Turbomachinery, 141(5):051006, 01 2019.

[33] T.S. Cação Ferreira. *Boundary layer transition and convective heat transfer of the high-pressure turbine vane LS89*. PhD thesis, von Karman Institute for Fluid Dynamics & Ecole Polytechnique de Louvain, 2021.

[34] M. Dellacasagrande, D. Lengani, D. Simoni, J.O. Pralits, K. Durovich, A. Hanifi, and D. Henningson. *Statistical characterization of free-stream turbulence induced transition under variable Reynolds number, free-stream turbulence, and pressure gradient*. Physics of Fluids, 33(9):094115, 09 2021.

[35] R.E. Mayle. *A Theory for Predicting the Turbulent-Spot Production Rate*. Journal of Turbomachinery, 121(3):588–593, 07 1999.

[36] R.J. Volino. *An investigation of the scales in transitional boundary layers under high free-stream turbulence conditions*. Experiments in fluids, 38:516–533, 2005.

[37] S.K. Roberts and M.I. Yaras. *Measurements and Prediction of Free-Stream Turbulence and Pressure-Gradient Effects on Attached-Flow Boundary-Layer Transition*. volume Volume 5: Turbo Expo 2003, Parts A and B of *Turbo Expo: Power for Land, Sea, and Air*, pages 729–743, 06 2003.

[38] M.I. Yaras. *Measurements of the Effects of Freestream Turbulence on Separation-Bubble Transition*. volume Volume 3: Turbo Expo 2002, Parts A and B of *Turbo Expo: Power for Land, Sea, and Air*, pages 647–660, 06 2002.

[39] M.M. O'Meara and T.J. Mueller. *Laminar separation bubble characteristics on an airfoil at low Reynolds numbers*. AIAA Journal, 25(8):1033–1041, 1987.

[40] T. Coton. *Unsteady wake-boundary layer interaction on advanced high lift low pressure turbine airfoils*. PhD thesis, von Karman Institute for Fluid Dynamics & University of Liege, 2004.

[41] A. Hatman and T. Wang. *A Prediction Model for Separated-Flow Transition*. Journal of Turbomachinery, 121(3):594–602, 07 1999.

[42] T.J. Praisner and J.P. Clark. *Predicting Transition in Turbomachinery—Part I: A Review and New Model Development*. Journal of Turbomachinery, 129(1):1–13, 03 2004.

[43] T.J. Praisner, E.A. Grover, M.J. Rice, and J.P. Clark. *Predicting Transition in Turbomachinery—Part II: Model Validation and Benchmarking*. Journal of Turbomachinery, 129(1):14–22, 03 2004.

[44] N. Rosafio, G. Lopes, S. Salvadori, S. Lavagnoli, and D.A. Misul. *RANS Prediction of Losses and Transition Onset in a High-Speed Low-Pressure Turbine Cascade*. Energies, 16(21), 2023.

[45] M. Dellacasagrande, D. Lengani, D. Simoni, and S. Yarusevych. *A data-driven analysis of short and long laminar separation bubbles*. Journal of Fluid Mechanics, 976:R3, 2023.

[46] M. Dellacasagrande, D. Lengani, D. Simoni, and M. Ubaldi. *An Experimental Database for the Analysis of Bursting of a Laminar Separation Bubble*. International Journal of Turbomachinery, Propulsion and Power, 9(1), 2024.

[47] D. Petronio, M. Dellacasagrande, D. Simoni, and D. Lengani. *A New Empirical Correlation for Transition in Both Short and Long Separation Bubbles*. volume Volume 13C: Turbomachinery — Deposition, Erosion, Fouling, and Icing; Design Methods and CFD Modeling for Turbomachinery; Ducts, Noise, and Component Interactions of *Turbo Expo: Power for Land, Sea, and Air*, page V13CT32A028, 06 2023.

[48] R. Pichler, Y. Zhao, R. Sandberg, V. Michelassi, R. Pacciani, M. Marconcini, and A. Arnone. *Large-Eddy Simulation and RANS Analysis of the End-Wall Flow in a Linear Low-Pressure Turbine Cascade, Part I: Flow and Secondary Vorticity Fields Under Varying Inlet Condition*. Journal of Turbomachinery, 141(12):121005, 11 2019.

[49] M. Marconcini, R. Pacciani, A. Arnone, V. Michelassi, R. Pichler, Y. Zhao, and R. Sandberg. *Large Eddy Simulation and RANS Analysis of the End-Wall Flow in a Linear Low-Pressure-Turbine Cascade—Part II: Loss Generation*. Journal of Turbomachinery, 141(5):051004, 01 2019.

[50] V. Michelassi, J. Wissink, and W. Rodi. *Analysis of DNS and LES of flow in a low pressure turbine cascade with incoming wakes and comparison with experiments*. Flow, turbulence and combustion, 69:295–329, 2002.

[51] R. Pacciani, M. Marconcini, A. Arnone, F. Bertini, E. Spano, S. Rosa Taddei, and R.D. Sandberg. *Improvements in the Prediction of Steady and Unsteady Transition and Mixing in Low-Pressure Turbines by Means of Machine-Learnt Closures*. Journal of Turbomachinery, 146(5):051009, 01 2024.

[52] H.D. Akolekar, F. Waschkowski, R. Pacciani, Y. Zhao, and R.D. Sandberg. *Multi-Objective Development of Machine-Learnt Closures for Fully Integrated Transition and Wake Mixing Predictions in Low Pressure Turbines*. volume Volume 10C: Turbomachinery — Design Methods and CFD Modeling for Turbomachinery; Ducts, Noise, and Component Interactions of *Turbo Expo: Power for Land, Sea, and Air*, page V10CT32A013, 06 2022.

[53] Y. Fang, Y. Zhao, H.D. Akolekar, A.S.H. Ooi, R.D. Sandberg, R. Pacciani, and M. Marconcini. *A Data-Driven Approach for Generalizing the Laminar Kinetic Energy Model for Separation and Bypass Transition in Low- and High-Pressure Turbines*. volume Volume 13C: Turbomachinery — Deposition, Erosion, Fouling, and Icing; Design Methods and CFD Modeling for Turbomachinery; Ducts, Noise, and Component Interactions of *Turbo Expo: Power for Land, Sea, and Air*, page V13CT32A025, 06 2023.

[54] R. Pacciani, M. Marconcini, F. Bertini, S. Rosa Taddei, E. Spano, Y. Zhao, H.D. Akolekar, R.D. Sandberg, and A. Arnone. *Assessment of Machine-Learned Turbulence Models Trained for Improved Wake-Mixing in Low-Pressure Turbine Flows*. Energies, 14(24), 2021.

[55] X.F. Zhang, M. Vera, H. Hodson, and N. Harvey. *Separation and Transition Control on an Aft-Loaded Ultra-High-Lift LP Turbine Blade at Low Reynolds Numbers: Low-Speed Investigation*. Journal of Turbomachinery, 128(3):517–527, 02 2005.

[56] A. Mahallati, B.R. McAuliffe, S.A. Sjolander, and T.J. Praisner. *Aerodynamics of a Low-Pressure Turbine Airfoil at Low Reynolds Numbers—Part I: Steady Flow Measurements*. Journal of Turbomachinery, 135(1):011010, 11 2012.

[57] R.J. Volino. *Separated Flow Measurements on a Highly Loaded Low-Pressure Turbine Airfoil*. volume Volume 6: Turbomachinery, Parts A, B, and C of *Turbo Expo: Power for Land, Sea, and Air*, pages 1427–1437, 06 2008.

[58] M. Vera, X.F. Zhang, H. Hodson, and N. Harvey. *Separation and Transition Control on an Aft-Loaded Ultra-High-Lift LP Turbine Blade at Low Reynolds Numbers: High-Speed Validation*. Journal of Turbomachinery, 129(2):340–347, 05 2006.

[59] J. Michalek, M. Monaldi, and T. Arts. *Aerodynamic Performance of a Very High Lift Low Pressure Turbine Airfoil (T106C) at Low Reynolds and High Mach Number With Effect of Free Stream Turbulence Intensity*. Journal of Turbomachinery, 134(6):061009, 08 2012.

[60] J. Babajee and T. Arts. *Investigation of the Laminar Separation-Induced Transition With the -Re t Transition Model on Low-Pressure Turbine Rotor Blades at Steady Conditions*. volume Volume 8: Turbomachinery, Parts A, B, and C of *Turbo Expo: Power for Land, Sea, and Air*, pages 1167–1178, 06 2012.

[61] S. Brunner, L. Fottner, and H. Schiffer. *Comparison of Two Highly Loaded Low Pressure Turbine Cascades Under the Influence of Wake-Induced Transition*. volume Volume 3: Heat Transfer; Electric Power; Industrial and Cogeneration of *Turbo Expo: Power for Land, Sea, and Air*, page V003T01A073, 05 2000.

[62] R. Vazquez, A. Antoranz, D. Cadrecha, and L. Armananzas. *The Influence of Reynolds Number, Mach Number and Incidence Effects on Loss Production in Low Pressure Turbine Airfoils*. volume Volume 6: Turbomachinery, Parts A and B of *Turbo Expo: Power for Land, Sea, and Air*, pages 949–960, 05 2006.

[63] R. Vazquez and D. Torre. *The Effect of Mach Number on the Loss Generation of LP Turbines*. volume Volume 8: Turbomachinery, Parts A, B, and C of *Turbo Expo: Power for Land, Sea, and Air*, pages 1131–1142, 06 2012.

[64] R.X. Meyer. *The effect of wakes on the transient pressure and velocity distributions in turbomachines*. Transactions of the American Society of Mechanical Engineers, 80(7):1544–1551, 1958.

[65] R.D. Stieger and H.P. Hodson. *The Unsteady Development of a Turbulent Wake Through a Downstream Low-Pressure Turbine Blade Passage*. Journal of Turbomachinery, 127(2):388–394, 05 2005.

[66] J.D. Coull. *Wake induced transition in low pressure turbines*. PhD thesis, University of Cambridge, 2010.

[67] J.D. Coull and H.P. Hodson. *Unsteady boundary-layer transition in low-pressure turbines*. Journal of Fluid Mechanics, 681:370–410, 2011.

[68] D.E. Halstead, D.C. Wisler, T.H. Okiishi, G.J. Walker, H.P. Hodson, and H.-W. Shin. *Boundary Layer Development in Axial Compressors and Turbines: Part 1 of 4—Composite Picture*. Journal of Turbomachinery, 119(1):114–127, 01 1997.

[69] V. Schulte and H.P. Hodson. *Unsteady Wake-Induced Boundary Layer Transition in High Lift LP Turbines*. Journal of Turbomachinery, 120(1):28–35, 01 1998.

[70] R.D. Stieger and H.P. Hodson. *Unsteady dissipation measurements on a flat plate subject to wake passing*. Proceedings of the Institution of Mechanical Engineers, Part A: Journal of Power and Energy, 217(4):413–419, 2003.

[71] R.D. Stieger and H.P. Hodson. *The Transition Mechanism of Highly Loaded Low-Pressure Turbine Blades*. Journal of Turbomachinery, 126(4):536–543, 12 2004.

[72] R.D. Stieger, D. Hollis, and H.P. Hodson. *Unsteady Surface Pressures Due to Wake-Induced Transition in a Laminar Separation Bubble on a Low-Pressure Cascade*. Journal of Turbomachinery, 126(4):544–550, 12 2004.

[73] L. Davide, D. Simoni, M. Ubaldi, P. Zunino, and F. Bertini. *Coherent structures formation during wake-boundary layer interaction on a LP turbine blade*. Flow, Turbulence and Combustion, 98:57–81, 2017.

[74] J. Clinckemaillie, L. Fattorini, T. Fontani, C. Nuyts, G. Wain, and T. Arts. *Aerodynamic performance of a very-high-lift low-pressure turbine airfoil (T106C) at low Reynolds and high Mach number including the effect of incoming periodic wakes*. In 11 th European Conference on Turbomachinery Fluid dynamics & Thermodynamics. EUROPEAN TURBOMACHINERY SOCIETY, 2015.

[75] M. Boerner and R. Niehuis. *Dynamics of Shock Waves Interacting With Laminar Separated Transonic Turbine Flow Investigated by High-Speed Schlieren and Surface Hot-Film Sensors*. Journal of Turbomachinery, 143(5):051010, 04 2021.

[76] X.F. Zhang, H.P. Hodson, and N.W. Harvey. *Unsteady boundary layer studies on ultra-high-lift low-pressure turbine blades*. Proceedings of the Institution of Mechanical Engineers, Part A: Journal of Power and Energy, 219(6):451–460, 2005.

[77] W.A. Eckerle and L.S. Langston. *Horseshoe Vortex Formation Around a Cylinder*. Journal of Turbomachinery, 109(2):278–285, 04 1987.

[78] C.H. Sieverding. *Recent Progress in the Understanding of Basic Aspects of Secondary Flows in Turbine Blade Passages*. Journal of Engineering for Gas Turbines and Power, 107(2):248–257, 04 1985.

[79] L.S. Langston. *Secondary Flows in Axial Turbines—A Review*. Annals of the New York Academy of Sciences, 934(1):11–26, 2001.

[80] P. Ligrani, G. Potts, and A. Fatemi. *Endwall aerodynamic losses from turbine components within gas turbine engines*. Propulsion and Power Research, 6(1):1–14, 2017.

[81] L.S. Langston. *Crossflows in a Turbine Cascade Passage*. Journal of Engineering for Power, 102(4):866–874, 10 1980.

[82] R.J. Goldstein and R.A. Spores. *Turbulent Transport on the Endwall in the Region Between Adjacent Turbine Blades*. Journal of Heat Transfer, 110(4a):862–869, 11 1988.

[83] C.H. Sieverding and P. Van den Bosche. *The use of coloured smoke to visualize secondary flows in a turbine-blade cascade*. Journal of Fluid Mechanics, 134:85–89, 1983.

[84] O.P. Sharma and T.L. Butler. *Predictions of Endwall Losses and Secondary Flows in Axial Flow Turbine Cascades*. Journal of Turbomachinery, 109(2):229–236, 04 1987.

[85] H.P. Wang, S.J. Olson, R.J. Goldstein, and E.R.G. Eckert. *Flow Visualization in a Linear Turbine Cascade of High Performance Turbine Blades*. Journal of Turbomachinery, 119(1):1–8, 01 1997.

[86] G. Pullan, J. Denton, and M. Dunkley. *An Experimental and Computational Study of the Formation of a Streamwise Shed Vortex in a Turbine Stage*. Journal of Turbomachinery, 125(2):291–297, 04 2003.

[87] A. Perdichizzi. *Mach Number Effects on Secondary Flow Development Downstream of a Turbine Cascade*. Journal of Turbomachinery, 112(4):643–651, 10 1990.

[88] H.P. Hodson and R.G. Dominy. *The Off-Design Performance of a Low-Pressure Turbine Cascade*. Journal of Turbomachinery, 109(2):201–209, 04 1987.

[89] A. Perdichizzi and V. Dossena. *Incidence Angle and Pitch–Chord Effects on Secondary Flows Downstream of a Turbine Cascade*. Journal of Turbomachinery, 115(3):383–391, 07 1993.

[90] J.A. Walsh and D.G. Gregory-Smith. *Inlet Skew and the Growth of Secondary Losses and Vorticity in a Turbine Cascade*. Journal of Turbomachinery, 112(4):633–642, 10 1990.

[91] J.D. Coull and C.J. Clark. *The Effect of Inlet Conditions on Turbine Endwall Loss*. Journal of Turbomachinery, 144(10):101011, 06 2022.

[92] D.G. Gregory-Smith, C.P. Graves, and J.A. Walsh. *Growth of Secondary Losses and Vorticity in an Axial Turbine Cascade*. Journal of Turbomachinery, 110(1):1–8, 01 1988.

[93] E.Rosa de la Blanco, H.P.Hodson, R. Vazquez, and D. Torre. *Influence of the state of the inlet endwall boundary layer on the interaction between pressure surface separation and endwall flows*. Proceedings of the Institution of Mechanical Engineers, Part A: Journal of Power and Energy, 217(4):433–441, 2003.

[94] D. Infantino, F. Satta, D. Simoni, M. Ubaldi, P. Zunino, and F. Bertini. *Phase-Locked Investigation of Secondary Flows Perturbed by Passing Wakes in a High-Lift LPT Turbine Cascade*. volume Volume 2C: Turbomachinery of *Turbo Expo: Power for Land, Sea, and Air*, page V02CT44A008, 06 2015.

[95] F. Satta, D. Simoni, M. Ubaldi, P. Zunino, and F. Bertini. *Profile and secondary flow losses in a high-lift LPT blade cascade at different reynolds numbers under steady and unsteady inflow conditions*. Journal of Thermal Science, 21:483–491, 2012.

[96] R.J. Volino, C.D. Galvin, and M.B. Ibrahim. *Effects of Periodic Unsteadiness on Secondary Flows in High Pressure Turbine Passages*. volume Volume 6C: Turbomachinery of *Turbo Expo: Power for Land, Sea, and Air*, page V06CT42A042, 06 2013.

[97] R. Ciorciari, I. Kirik, and R. Niehuis. *Effects of Unsteady Wakes on the Secondary Flows in the Linear T106 Turbine Cascade*. Journal of Turbomachinery, 136(9):091010, 05 2014.

[98] S.D. Hunter and S.R. Manwaring. *Endwall Cavity Flow Effects on Gaspath Aerodynamics in an Axial Flow Turbine: Part I — Experimental and Numerical Investigation*. volume Volume 1: Aircraft Engine; Marine; Turbomachinery; Microturbines and Small Turbomachinery of *Turbo Expo: Power for Land, Sea, and Air*, page V001T03A111, 05 2000.

[99] J. Gier, B. Stubert, B. Brouillet, and L. de Vito. *Interaction of Shroud Leakage Flow and Main Flow in a Three-Stage LP Turbine*. Journal of Turbomachinery, 127(4):649–658, 03 2003.

[100] J. Schlienger, A. Pfau, A.I. Kalfas, and R.S. Abhari. *Effects of Labyrinth Seal Variation on Multistage Axial Turbine Flow*. volume Volume 6: Turbo Expo 2003, Parts A and B of *Turbo Expo: Power for Land, Sea, and Air*, pages 173–185, 06 2003.

[101] D. Bohn. *Investigation of two different axial s̈upersonic compressor stages with special consideration of the interactions between air impeller and guide wheel*. Technical report, 1977.

[102] C. McLean, C. Camci, and B. Glezer. *Mainstream Aerodynamic Effects Due to Wheelspace Coolant Injection in a High-Pressure Turbine Stage: Part I—Aerodynamic Measurements in the Stationary Frame*. Journal of Turbomachinery, 123(4):687–696, 02 2001.

[103] S. Schrewe, H. Werschnik, and H. Schiffer. *Experimental Analysis of the Interaction Between Rim Seal and Main Annulus Flow in a Low Pressure Two Stage Axial Turbine*. Journal of Turbomachinery, 135(5):051003, 06 2013.

[104] P. Schuepbach, R.S. Abhari, M.G. Rose, and J. Gier. *Influence of Rim Seal Purge Flow on the Performance of an Endwall-Profiled Axial Turbine*. Journal of Turbomachinery, 133(2):021011, 10 2010.

[105] P. Schuepbach, R.S. Abhari, M.G. Rose, T. Germain, I. Raab, and J. Gier. *Effects of Suction and Injection Purge-Flow on the Secondary Flow Structures of a High-Work Turbine*. Journal of Turbomachinery, 132(2):021021, 01 2010.

[106] B.D.J Schreiner, M. Wilson, Y.S. Li, and C.M. Sangan. *Effect of Purge on the Secondary Flow-Field of a Gas Turbine Blade-Row*. Journal of Turbomachinery, 142(10):101006, 09 2020.

[107] G. Paniagua, R. Denos, and S. Almeida. *Effect of the Hub Endwall Cavity Flow on the Flow-Field of a Transonic High-Pressure Turbine*. Journal of Turbomachinery, 126(4):578–586, 12 2004.

[108] Giovanna B., Giuseppe F., Antonio P., Massimiliano M., and Roberto A. *Purge flow and interface gap geometry influence on the aero-thermal performance of a rotor blade cascade*. International Journal of Heat and Fluid Flow, 44:563–575, 2013.

[109] E. de la Rosa Blanco, H.P. Hodson, and R. Vazquez. *Effect of the Leakage Flows and the Upstream Platform Geometry on the Endwall Flows of a Turbine Cascade*. Journal of Turbomachinery, 131(1):011004, 10 2008.

[110] I. Popovic and H.P. Hodson. *The Effects of a Parametric Variation of the Rim Seal Geometry on the Interaction Between Hub Leakage and Mainstream Flows in HP Turbines*. volume Volume 4: Heat Transfer, Parts A and B of *Turbo Expo: Power for Land, Sea, and Air*, pages 1823–1833, 06 2012.

[111] D. Cherry, A. Wadia, R. Beacock, M. Subramanian, and P. Vitt. *Analytical Investigation of a Low Pressure Turbine With and Without Flowpath Endwall Gaps, Seals and Clearance Features*. volume Volume 6: Turbo Expo 2005, Parts A and B of *Turbo Expo: Power for Land, Sea, and Air*, pages 1099–1105, 06 2005.

[112] G.D. MacIsaac, S.A. Sjolander, T.J. Praisner, E.A. Grover, and R. Jurek. *Effects of Simplified Platform Overlap and Cavity Geometry on the Endwall Flow: Measurements and Computations in a Low-Speed Linear Turbine Cascade*. volume Volume 6A: Turbomachinery of *Turbo Expo: Power for Land, Sea, and Air*, page V06AT36A035, 06 2013.

[113] D.G. Ainley and G.C.R. Mathieson. *A method of performance estimation for axial-flow turbines*. 1951.

[114] J. Dunham and P.M. Came. *Improvements to the Ainley-Mathieson Method of Turbine Performance Prediction*. Journal of Engineering for Power, 92(3):252–256, 07 1970.

[115] S.C. Kacker and U. Okapuu. *A Mean Line Prediction Method for Axial Flow Turbine Efficiency*. Journal of Engineering for Power, 104(1):111–119, 01 1982.

[116] J. Zhu and S.A. Sjolander. *Improved Profile Loss and Deviation Correlations for Axial-Turbine Blade Rows*. volume Volume 6: Turbo Expo 2005, Parts A and B of *Turbo Expo: Power for Land, Sea, and Air*, pages 783–792, 06 2005.

[117] M.W. Benner, S.A. Sjolander, and S.H. Moustapha. *An Empirical Prediction Method for Secondary Losses in Turbines—Part I: A New Loss Breakdown Scheme and Penetration Depth Correlation*. Journal of Turbomachinery, 128(2):273–280, 02 2005.

[118] M.W. Benner, S.A. Sjolander, and S.H. Moustapha. *An Empirical Prediction Method For Secondary Losses In Turbines—Part II: A New Secondary Loss Correlation*. Journal of Turbomachinery, 128(2):281–291, 02 2005.

[119] H.R.M. Craig and H.J.A. Cox. *Performance Estimation of Axial Flow Turbines*. Proceedings of the Institution of Mechanical Engineers, 185(1):407–424, 1970.

[120] J.D. Coull and H.P. Hodson. *Predicting the Profile Loss of High-Lift Low Pressure Turbines*. Journal of Turbomachinery, 134(2):021002, 06 2011.

2 Experimental Methodology

This chapter describes the experimental apparatus and introduces the reader to the EU project SPLEEN, of which the geometry under investigation is part. It also describes the facility where the geometry was investigated and its constituents. The measurement techniques and data reduction techniques are also depicted.

2.1 The VKI S-1/C Linear Cascade

The experiments presented throughout this thesis were conducted in the high-speed, low Reynolds facility S-1/C of the von Karman Institute. A sketch describing the facility is shown in Fig. 2.1. The wind tunnel is a continuous closed-loop facility driven by a 615 kW 13-stage axial flow compressor. A cooler keeps the flow temperature near the atmospheric one. The mass flow is regulated by adjusting the compressor rotational speed and a pressure regulation valve. A vacuum pump allows lowering the tunnel absolute pressure to below 8,000 Pa. Linear cascades can be installed in the upper left elbow in Fig. 2.1. Wire meshes and honeycombs upstream of the test section ensure homogeneous flow conditions.

The elbow of the VKI S-1/C equipped with a linear cascade is depicted in Fig. 2.2(a). Fig. 2.2(b) highlights a cut of the test section for a cascade equipped with the SPLEEN C1 blades. A bell mouth and vertical and lateral contractions provide the transition between the original circular parts of the wind tunnel to the cascade. The latter entrance height can be adjusted between 375 and 650 mm. The maximum airfoil span is 225 mm. The linear cascade ensemble is made up of several full blades (depending on the pitch and chord length) plus two end-blocs at the upper and lower extremities of the cascade, shaped respectively according to the suction and pressure side profiles of the blades (see Fig. 2.2(a)). The cascade is mounted between two large circular sidewalls (1.12 m diameter), allowing the regulation of the cascade inlet flow angle. Two tailboards guide the outlet flow and tailor the periodicity. Descriptions of the facility can be found in [1, 2].

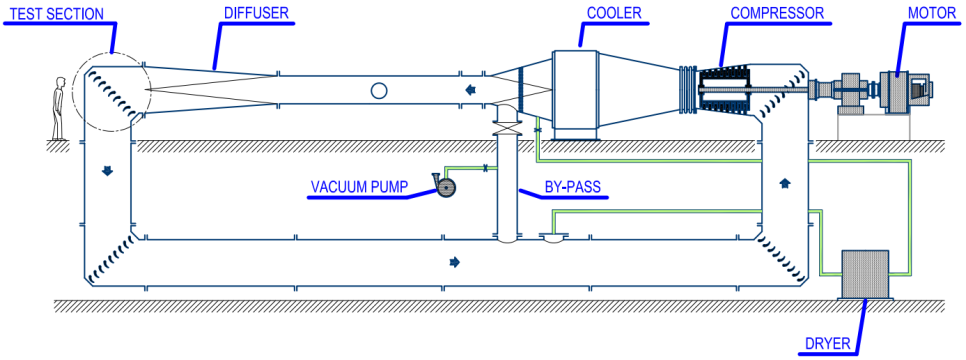

Figure 2.1: The VKI S-1/C wind tunnel.

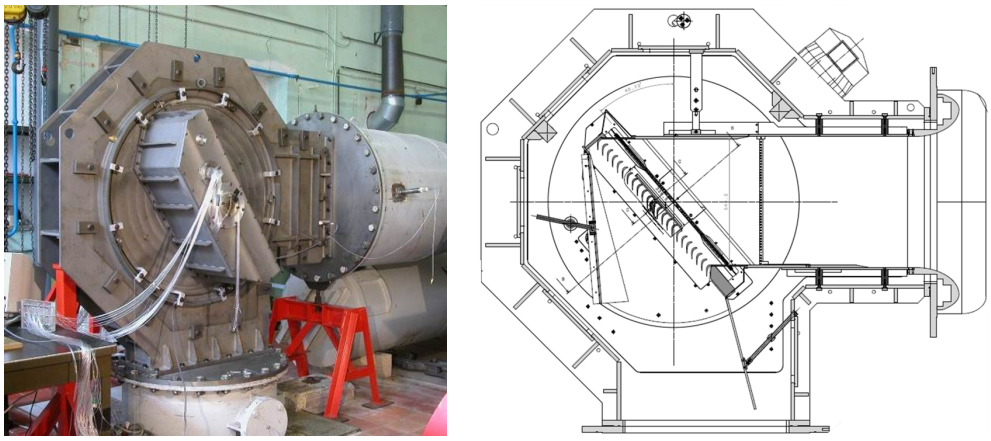

(a) (b)

Figure 2.2: Elbow of VKI S-1/C equipped with linear cascade (a) and cut of cascade used during the EU SPLEEN campaign (b).

The natural level of the freestream turbulence intensity at the cascade inlet is $\sim$0.90% [3]. A passive turbulence grid (TG) can be installed upstream of the test section to increase the freestream turbulence level to values typically found in low-pressure turbines. The turbulence grid consists of an array of parallel cylindrical bars. The geometrical characteristics of the grid are reported in Table 2.1. Each bar is parallel to the cascade central blade leading edge, and the grid is mounted to be orthogonal to the inlet flow to the cascade, hence at an angle relative to the cascade (see Fig. 2.3).

Table 2.1: Characteristic geometry features of the passive turbulence grid.

Bar diameter	3.00	$[mm]$
Mesh size	12.00	$[mm]$
Solidity, σ	0.25	[-]

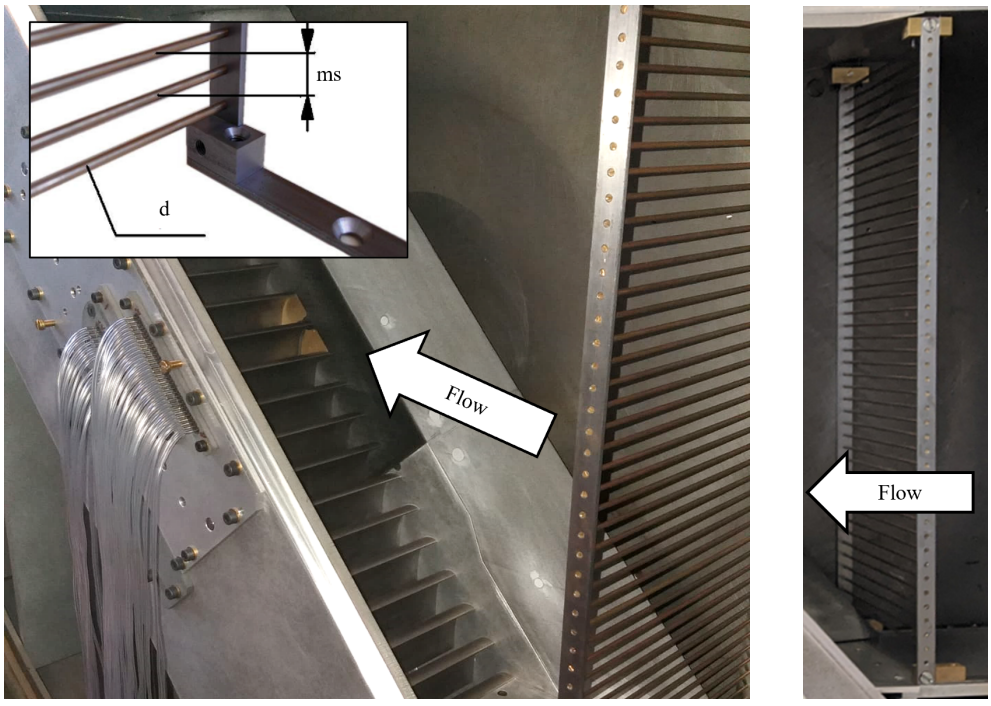

(a) (b)

Figure 2.3: Turbulence grid in relation to cascade with detail characterizing TG key parameters (a) and isolated TG (b).

To simulate the blade-row interference effects due to wake-blade interactions, the test section is equipped with an upstream high-speed rotating bar system (see Fig. 2.4a). The wake generator (WG) consists of a disc of 625 mm diameter equipped with cylindrical bars made of molybdenum at its periphery. The latter material was chosen because of its high yield strength, close to its tensile strength. The number and diameter of the bars and the rotational speed of the disk are adjustable to match a requested Strouhal number and flow

coefficient. The rotating bars are only parallel to the blade leading edge (LE) when passing in front of the central blade (see Fig. 2.4b). A 30 kW electric motor drives the wake generator up to 3500 RPM, corresponding to a bar passing velocity of ∼165 m/s at blade midspan. The wake generator assembly is placed inside an air-tight casing (see Fig. 2.4c).

(a) (b) (c)

Figure 2.4: Technical drawing of generic cascade with wake generator bars (a), detailed view of wake generator bars relative to cascade (b) and wake generator casing (c).

A secondary air system simulates purge/leakage flows upstream of the cascade. The purge system consists of a circuit that uses the pressure drop between a high-pressure region within the rig (immediately downstream of the compressor) and the purge location near the test section. A schematic view of the circuit is displayed in Fig. 2.5.

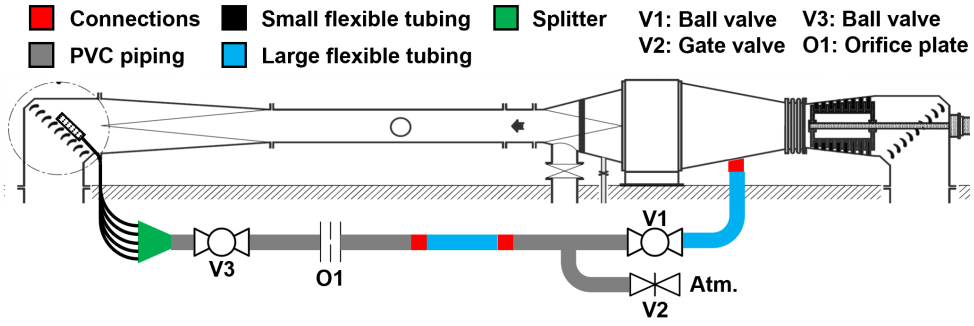

Figure 2.5: Purge flow circuit constituents in relation to the upper loop of VKI S-1/C.

The massflow through the secondary air system is monitored through a standard orifice plate (O1) [4]. Two ball valves (V1 and V3) are used to fine-tune the amount of bypassed flow to be purged upstream of the cascade. Two ball valves were selected to ensure that tests can be performed in case the pipe containing the orifice plate must be accessed for maintenance or calibration of embedded instrumentation. In this case, both valves can be closed to seal the main loop of the VKI S-1/C. An additional gate valve (V2) draws air from the atmosphere if the pressure ratio is insufficient to accomplish the required massflow rate. Downstream the orifice plate, the flow encounters a splitter that guides the flow through 12 small flexible

pipes plugged into the cavity settling chamber. Fig. 2.6(a) and Fig. 2.6(b) highlight the orifice plate and the splitter near the VKI S-1/C test section. Details on the instrumentation used to monitor the massflow are provided in Section 2.4.2.6.

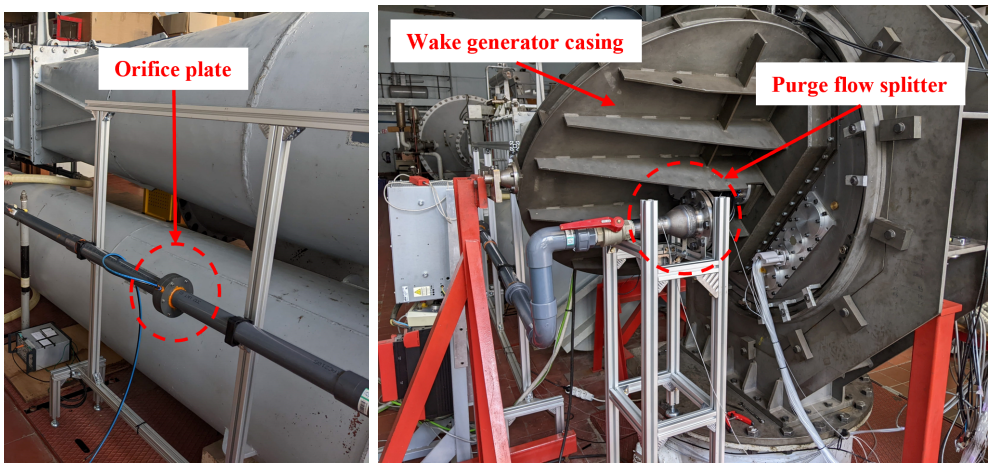

(a) (b)

Figure 2.6: Implemented secondary air system in relation to the VKI S-1/C: Orifice plate (a) and purge flow splitter (b).

Lastly, a traversing unit is used to traverse probes upstream and downstream of the cascade. The traversing unit uses three motors to offer three degrees of freedom: Motor 1 for pitchwise traversing, Motor 2 for spanwise traversing, and Motor 3 for rotation around the probe axis. The latter is helpful for tests performed with cylindrical probes, primarily when operated under virtual mode. The traversing mechanism is displayed in Fig. 2.7(a). Additionally, Fig. 2.7(b) displays the unit mounted in the VKI S-1/C linear cascade. All motors ensure the placement of the probe with a precision of 0.2 mm.

An additional traversing unit allows traversing the cascade central blade. Sliding the blade allows shifting the location of the blade instrumentation from the endwall to the midspan to investigate the blade aerodynamics in the two-dimensional (2D) flow and region impacted by secondary flows. The traversing mechanism is displayed in Fig. 2.8(a). Additionally, Fig. 2.8(b) displays the unit mounted in the VKI S-1/C linear cascade. The motor ensures the placement of the sensors' location with a precision of 0.2 mm in the spanwise direction. The traversing mechanism sits in an air-tight box (see Fig. 2.2(a)). The pressure inside is the static pressure at the cascade inlet or outlet, depending on the probe being traversed at the inlet or outlet, respectively.

2.2 The SPLEEN Test Case

The current dissertation is built on results obtained throughout the EU-funded project SPLEEN (**S**econdary and leakage flow effects in high-s**P**eed **L**ow-pr**E**ssur**E** turbi**N**es) led by the von Karman Institute in collaboration with Safran Aircraft Engines (SAE). The project

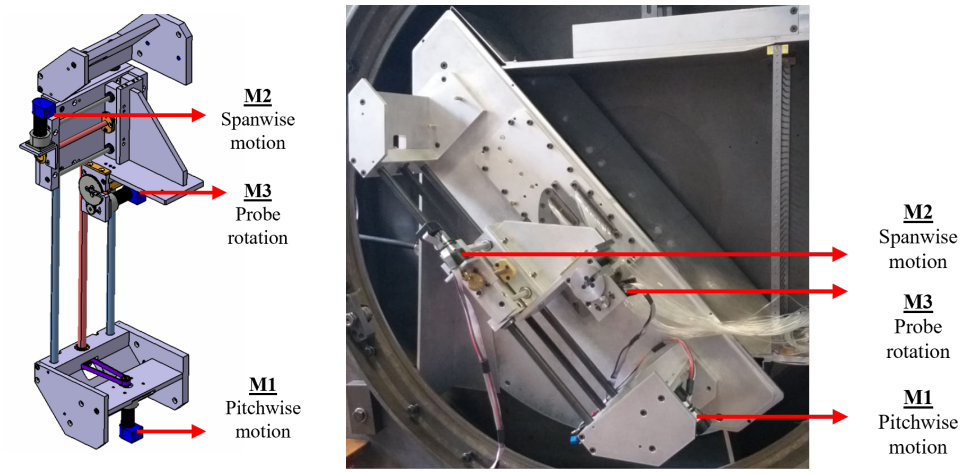

Figure 2.7: Probe traversing unit (a) mounted in the VKI S-1/C (b).

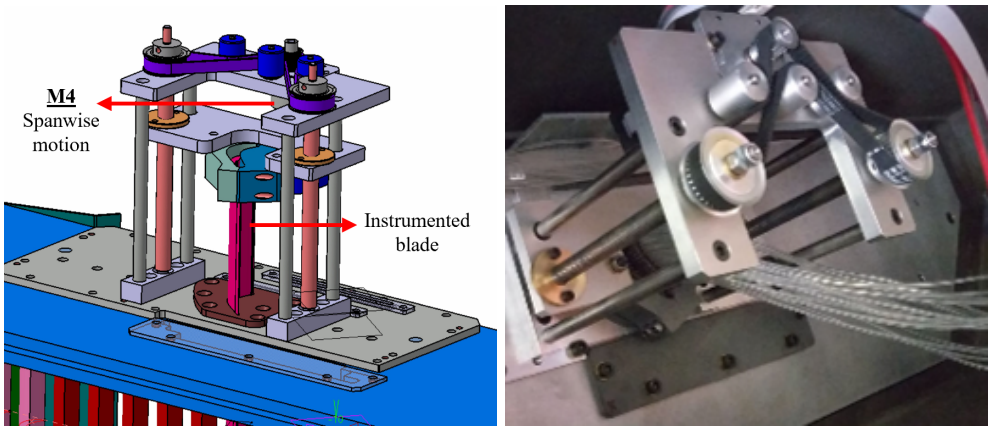

Figure 2.8: Blade traversing unit (a) mounted in the VKI S-1/C (b).

investigated the combined effect of purge flows and secondary flows on the performance of high-speed low-pressure turbines in the presence of unsteady flow effects that result from the stator-rotor relative motion in an actual engine application. A schematic view of a meridional cut of 1.5 stages of a low-pressure turbine is displayed in Fig. 2.9.

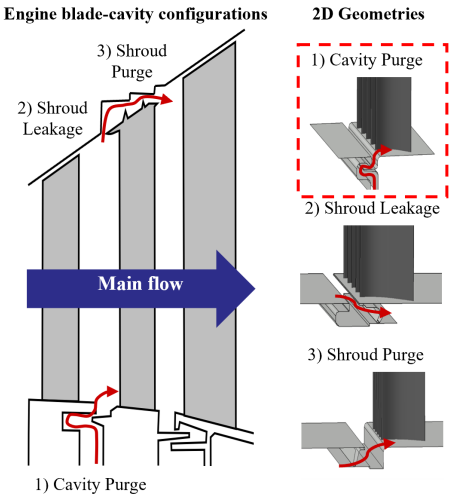

Figure 2.9: Schematic view of 1.5 low-pressure turbine stages with identified regions of interest.

Different regions of interest are highlighted regarding the combined interaction of purge/leakage flow with the mainstream flow and following vane/rotor aerodynamics. This thesis details results concerning the impact of purge flow from the V1-R1 hub platform on the secondary flows and blade performance of the rotor near the endwall. The engine-representative geometry highlighted in Fig. 2.9 was extruded linearly to generate one to be tested in a linear cascade arrangement.

2.3 The SPLEEN C1 Cascade

Testing a cascade under the effect of unsteady wakes and purge flows required translating one of the test-section endwalls to house the engine-representative cavity geometry. The modification of the endwall gave rise to introducing a boundary layer passive control feature (boundary layer lip). Fig. 2.10(a) schematically displays the test section constituents. The BL lip ensures a smooth transition from the full-width channel to the reduced one. The modification of the endwall also resulted in a slot through which the wake generator bar protrudes into the test section. The bar support is recessed from the surface by 10 mm. The slot has a width of 9 mm. Details on the wake generator are provided in Section 2.3.2.

Fig. 2.11(a) highlights the boundary layer lip in relation to the cascade test section in the absence of the wake generator and cavity slot. On the other hand, Fig. 2.11(b) highlights the test section in the presence of the rotating bars protruding from the wake generator slot and the cavity slot from which purge flow is injected.

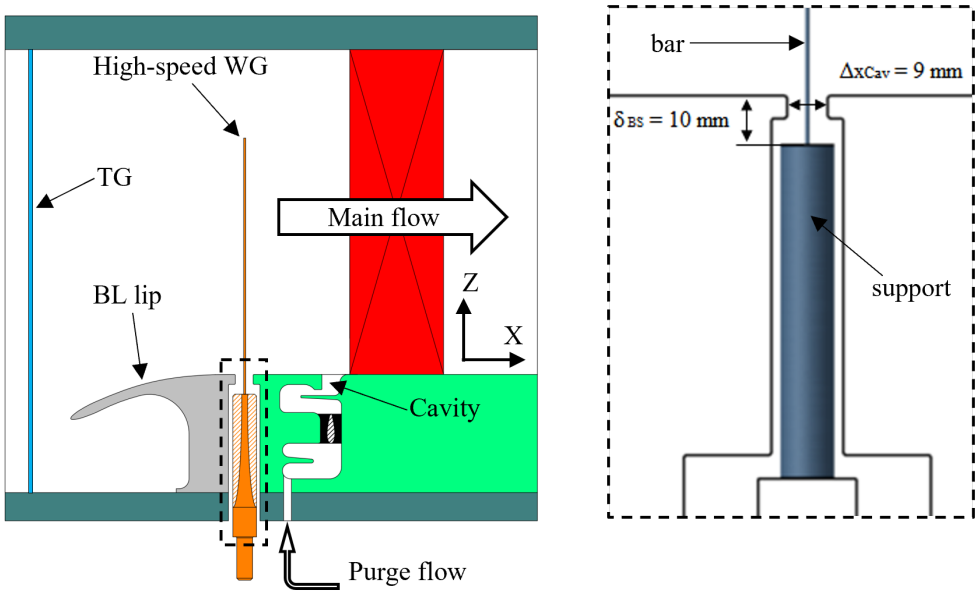

(a) (b)

Figure 2.10: SPLEEN cascade complete test section setup(a) and detail of WG slot (b).

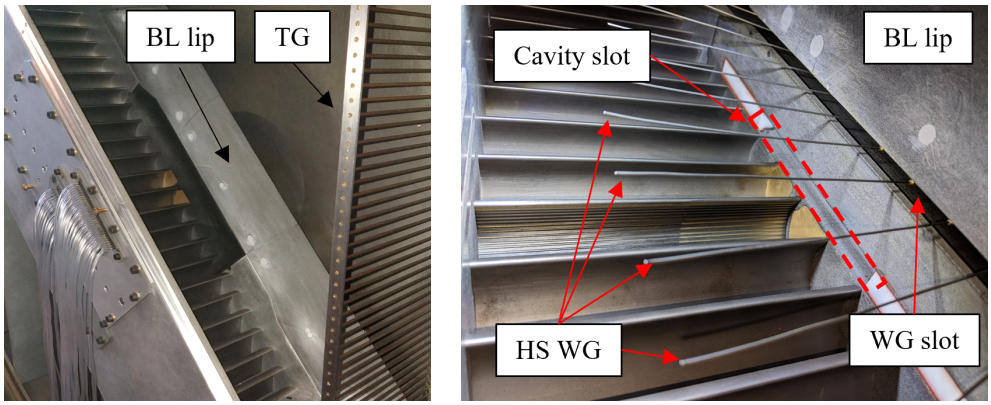

(a) (b)

Figure 2.11: SPLEEN C1 installed in the VKI S-1/C without WG and cavity slot (a), and test section equipped with WG bars and cavity slot (b).

2.3.1 Scaling of Airfoil-Cavity Arrangement

SAE designed the airfoil-cavity arrangement and is of open access. The SPLEEN C1 cascade is representative of a rotor-hub airfoil of a modern high-speed low-pressure turbine. The SPLEEN C1 profile was designed to operate under transonic outlet Mach number, high turning, and low flow acceleration. The blade nominal operating outlet Mach and Reynolds numbers are 0.90 and 70,000, respectively.

The profile maximum thickness of the engine configuration was respected since this parameter plays a significant role in forming secondary flows [5]. On the other hand, the trailing edge radius was increased to permit the installation of pneumatic taps on the suction side close to the trailing edge. A relatively conservative value of pitch-to-chord ratio was chosen to mitigate the flow separation on the suction side. Similar considerations were adopted in the definition of the blade loading distribution. The final blade geometry considered for the experimental campaign presented in this paper is depicted in Fig. 2.12.

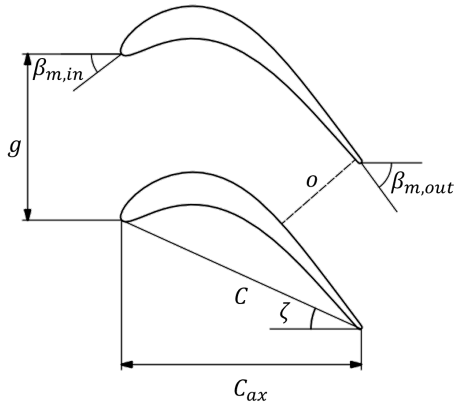

Figure 2.12: SPLEEN Cascade C1 geometry.

The blade was scaled to respect geometric, kinematic, and dynamic similarity by preserving the geometrical characteristics and the engine exit isentropic outlet Mach and Reynolds numbers. A scaling factor of 1.60 with respect to the engine conditions was chosen. The constraining parameter used to define the blade size was the minimum outlet static pressure that ensures a stable and safe operation of the facility, which is close to 5,000 Pa. The highest achievable high scaling factor was preferred to increase the airfoil instrumentation spatial resolution relative to the blade geometry. The scaled geometrical dimensions of the cascade are reported in Table 2.2. The scaling resulted in a cascade consisting of 23 blades with a span of 165 mm. All blades were manufactured with a tolerance inferior to $\pm$0.05 mm. The maximum roughness on the central blade suction side at midspan is Ra=1.67 μm, assessed employing 2D profile measurement. The large number of blades allowed the discard of the use of tailboards to tailor the downstream periodicity of the cascade.

Table 2.2: Geometry of SPLEEN Cascade C1.

Scaling factor	1.60	[-]
True chord, C	52.285	$[mm]$
Axial chord, C_{ax}	47.614	$[mm]$
Camber line length	60.78	$[mm]$
Cascade pitch, g	32.950	$[mm]$
Pitch-to-chord ratio	0.630	[-]
Cascade span, H	165	$[mm]$
Max. thickness, t	6.43	$[mm]$
LE radius/C	0.017	[-]
LE wedge angle	88.59	$[^\circ]$
TE thickness, δ_{TE}	0.86	$[mm]$
TE radius/C	0.0082	[-]
TE wedge angle	4.96	$[^\circ]$
Throat, o	19.400	$[mm]$
Rear SS mean radius of curvature	38.07	$[mm]$
Inlet metal angle, $\alpha_{met,in}$	37.30	$[^\circ]$
Outlet metal angle, $\alpha_{met,out}$	53.80	$[^\circ]$
Stagger angle, ζ	24.40	$[^\circ]$
Rear SS turning angle	4.74	$[^\circ]$

2.3.2 High-Speed Wake Generator

A spoked-wheel type wake generator was used to recreate unsteady wakes representative of the ones shed by the upstream stage in a real machine. The wake generator consists of a brass disk with 625 mm of diameter, on which cylindrical bars are mounted. The wake generator sits 1.12 axial chords upstream of the cascade leading edge plane. A technical drawing highlighting the position of the wake generator (disk and bars) relative to the cascade is provided in Fig. 2.13.

The bars are installed on a brass threaded support which is screwed to the wake generator disk. The bar is fixed to the support by local brazing performed at the end of the bar support. The bars are made of Molybdenum, characterized by a high yield strength close to its tensile strength. The bar geometry is constrained in terms of diameter and length. The length was selected so the bar reaches $\sim$73% of the cascade span. The latter bar length avoids spoiling the midspan flowfield with possible induced bar tip vortices.

The bar diameter was selected to be similar to the trailing edge thickness to produce an airfoil-representative wake of the blade being tested [6]. The bar support has a diameter of 12 mm. The resulting bar+support assembly is displayed in Fig. 2.14.

During the campaign, one of the bar supports suffered a mechanical failure. Upon investigating the cause, it was found that the bar support weight promoted a longitudinal stress superior to its yield strength due to the large centrifugal force resultant from the wake generator rotational velocity used during the experimental campaign. The bar support was redesigned with an elliptical shape to reduce its weight. Therefore, two bar support geometries were used at distinct testing phases (see Section 2.8). The resultant bar-support assembled component is highlighted in Fig. 2.15.

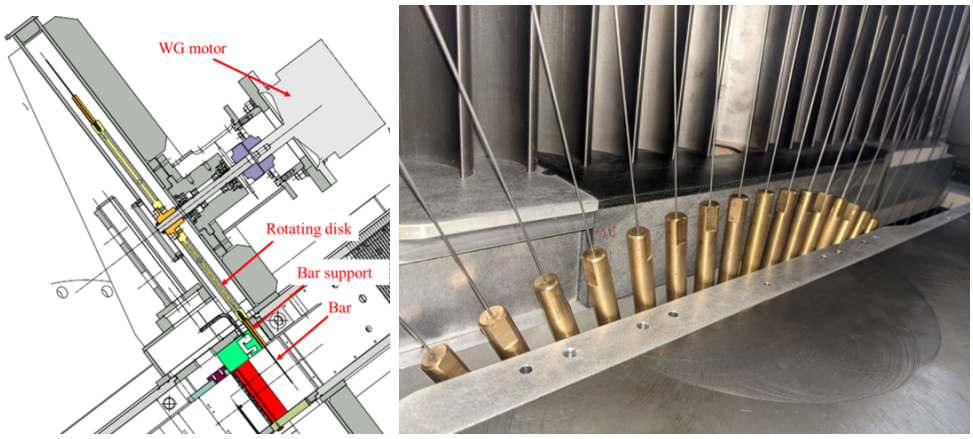

(a) (b)

Figure 2.13: Wake generator assembly in relation to linear cascade (a) and wake generator bars in test section (b).

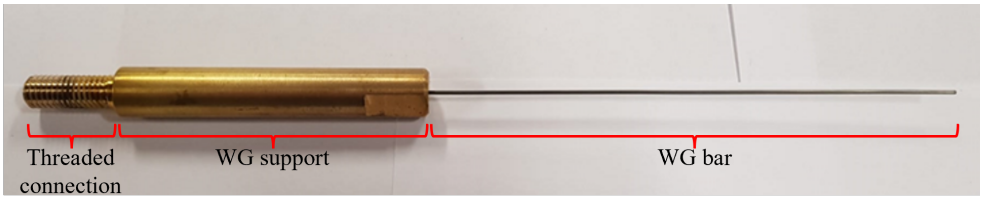

Figure 2.14: Wake generator bar support used during tests performed without purge flow.

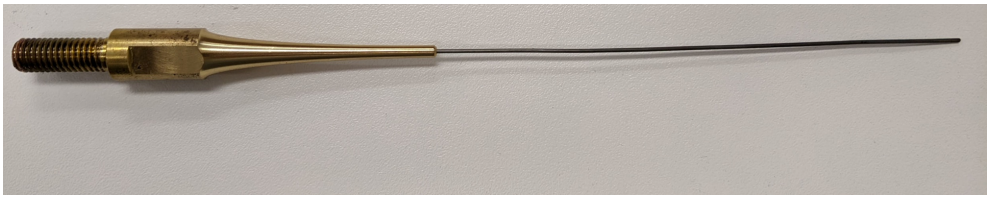

Figure 2.15: Wake generator bar support used during tests performed with purge flow.

2.3.3 Engine-Representative Cavity Geometry

The cavity geometry is representative of one found in a real-engine application. The cavity is placed upstream of the cascade and downstream of the wake generator. The same factor scaled the cavity as the airfoil. Fig. 2.16(a) highlights the relative position between the wake generator bar, cavity, and blade in a meridional view of the cascade test section.

As Section 2.1 mentioned, the splitter fed the cavity settling chamber through 12 equidistant pipes to reduce flow non-uniformity as the flow developed within the cavity. In addition, a buffer plate (element 1 in Fig. 2.16(a)) was introduced to increase mixing and homogenize the flow in the cavity. A CFD investigation on the impact on the buffer plate was performed. It was found that a maximum variation in the non-dimensional total pressure at the cavity outlet can be reduced by a factor of two compared to a case where no buffer plate is used.

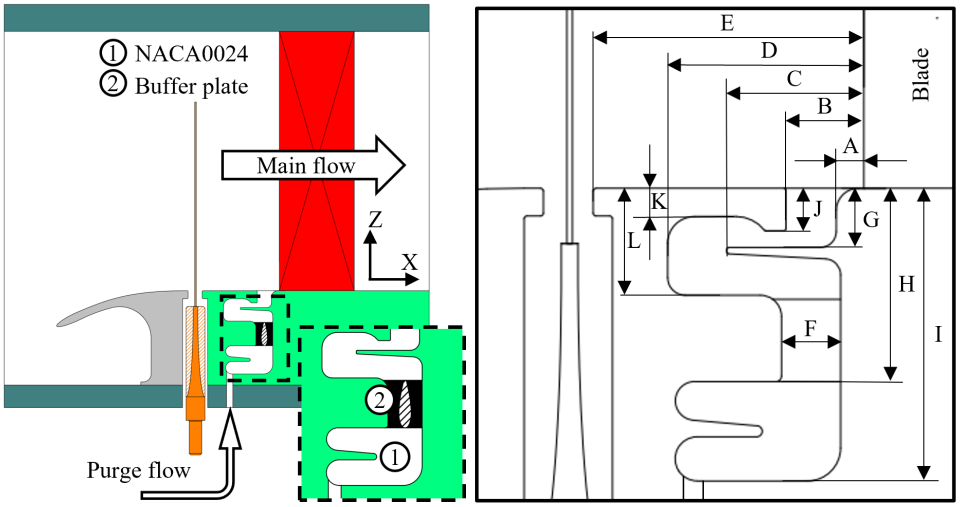

Figure 2.16: View of the test section with detail of wake generator bar support and cavity structural elements: (1) buffer plate and (2) NACA0024 (a) and cavity geometry key dimensions (b).

No swirler was mounted near the cavity outlet to avoid spoiling the purge outlet flow. The only available location for a potential swirler was where a structural element was placed (element 2 in Fig. 2.16a). During the design stage, a CFD study compared the cascade outlet flow field for the cases where a swirler with $45°$ turning versus the case where a symmetrical profile (NACA0024) was used. It was found that the cavity geometry downstream of the structural elements dampened the tangential velocity component imposed by the swirler. For this reason, the symmetrical element was used in this study. An under-prediction of the secondary losses comparatively to a linear cascade setup with the swirled purge flow is expected due to the lack of the tangential momentum [7, 8].

A detailed view of the cavity geometry with key dimensional parameters is displayed in Fig. 2.16(b). The dimensions are reported in Table 2.3 for completeness.

For completeness, Fig. 2.17 displays the hardware installed in the VKI S-1/C. The cavity geometry is contained within a Polyamide 12 (PA12) 3D-printed block on which the blades

Table 2.3: Key dimensions of cavity geometry.

Nom.	Units	Nom.	Units
A	$0.133C_{ax}$	G	$0.285C_{ax}$
B	$0.375C_{ax}$	H	$0.930C_{ax}$
C	$0.660C_{ax}$	I	$1.409C_{ax}$
D	$0.945C_{ax}$	J	$0.204C_{ax}$
E	$1.305C_{ax}$	K	$0.136C_{ax}$
F	$0.285C_{ax}$	L	$0.515C_{ax}$

are mounted. The endwall surface was manually polished to achieve Ra$<0.25\mu m$. The cavity slot covers four passages centered around the central blade.

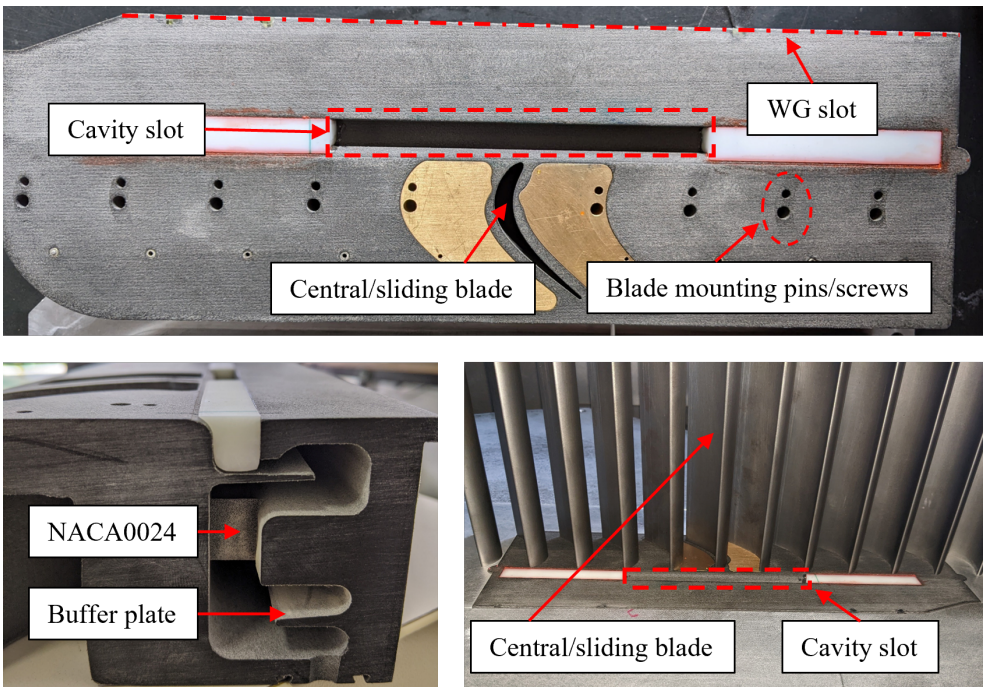

Figure 2.17: Cavity endwall tested alongside cascade: central/sliding blade, WG slot.

2.4 Measurement Techniques

A dense set of instrumentation from the cascade inlet to the outlet was used to characterize the cascade aerodynamics. The instrumentation list comprises pneumatic and fast-response static pressure taps on blade/endwall surfaces, pneumatic and fast-response aerodynamic probes, blade surface-mounted hot-film sensors, and fixed instrumentation. Fig. 2.18 highlights the high density of instrumentation in terms of type and location.

The aerothermal quantities measured for each type of instrumentation are contained in Table 2.4 for completeness.

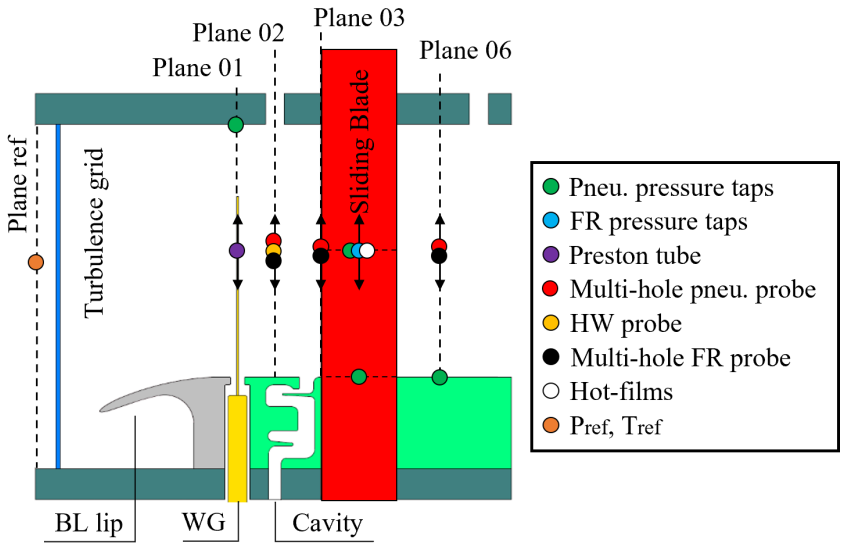

Figure 2.18: Meridional view of linear cascade test section highlighting the distribution of instrumentation used in this investigation.

Table 2.4: Types of instrumentation used for aerothermal measurements.

Instrumentation	Aerothermal quantities
Pneu. pressure taps	Time-averaged surface static pressure
FR pressure taps	Time-resolved surface static pressure
Preston tube	Time-averaged total pressure
Multi-hole pneu.probe	Time-averaged yaw angle, pitch angle, total pressure, static pressure, and Mach number
HW probe	Turbulence intensity and integral length scale
Multi-hole FR probe	Time-resolved yaw angle, pitch angle, total pressure, static pressure, and Mach number
Surface mounted hot-films	Quasi-wall shear stress, statistical moments of wall heat flux
P_{ref}, T_{ref}	Reference inlet total pressure, and temperature

2.4.1 Measurement Planes

The Cartesian reference system used throughout this study is presented in Fig. 2.19. The origin point of the reference system sits at the intersection of the central blade leading edge with the cavity endwall (endwall at the side of boundary layer lip and wake generator). The spanwise coordinate, z, increases from the origin towards the blade midspan. The pitchwise coordinate, y, increases from the pressure side of the central blade to the suction side of the closest blade, and the axial chordwise coordinate, x, increases from the origin towards the trailing edge following a direction perpendicular to the plane containing the leading edge (red surface in Fig. 2.19) of all blades. The trailing edge plane is also identified for completeness (blue surface in Fig. 2.19).

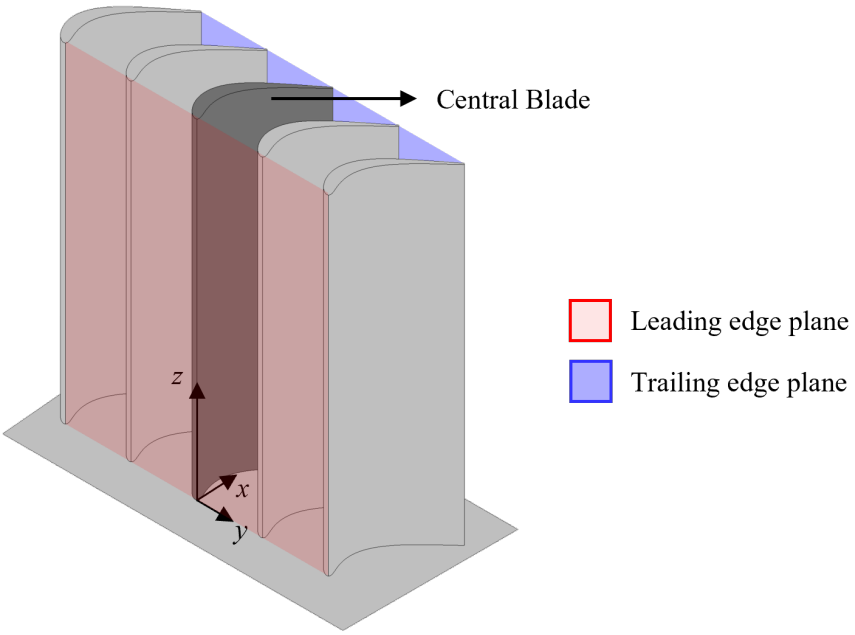

Figure 2.19: Cartesian reference system of SPLEEN C1 cascade.

Several measurement planes upstream and downstream of the cascade are used to traverse probes or identify critical locations of the cascade. A blade-to-blade cut of the cascade highlighting the location of the principal planes in relation to the cascade is displayed in Fig. 2.20.

The planes used in the scope of this thesis are:

- Plane Ref.: measurement plane of the reference total pressure and temperature. The location of this plane depends on the rotation of the whole cascade. It sits at least 1 m upstream of the central blade leading edge (not identified in Fig. 2.20),
- Plane 01: aligned with the plane of rotation of the wake generator and located at x=-1.12C_{ax},
- Plane 02: approximate exit location of the cavity slot. It is located at x=-0.50C_{ax},

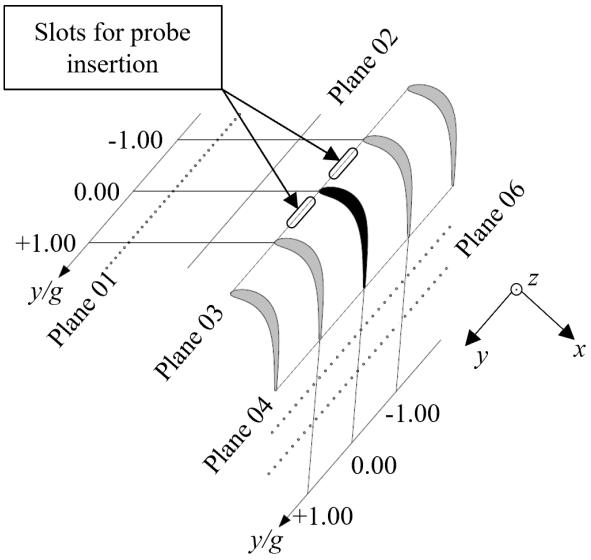

Figure 2.20: Blade-to-blade view of cascade highlighting the measurements planes. Plane Ref. is omitted.

- Plane 03: leading edge plane (located at x=0.00C$_{ax}$ (Plane containing leading edge of all blades),
- Plane 04: trailing edge plane (located at x=1.00C$_{ax}$ (Plane containing trailing edge of all blades),
- Plane 06: parallel to Plane 04 and located at x=1.50C$_{ax}$. Used to characterize outlet flow field.

The location of the measurement planes as a function of the blade axial chord is provided in Table 2.5 for completeness.

Table 2.5: Location of measurement planes as a function of the axial chord.

Upstream of LE		Blade		Downstream of TE
Plane 01	Plane 02	Plane 03	Plane 04	Plane 06
$-1.12C_{ax}$	$-0.50C_{ax}$	$0.00C_{ax}$	$1.00C_{ax}$	$1.50C_{ax}$

One additional plane is defined 0.25C$_{ax}$ downstream of Plane 06, named Plane 07. This plane is used to insert non-cylindrical probes that measure at Plane 06. No measurements are performed in this plane.

2.4.2 Reference Quantities

The cascade is permanently instrumented with pneumatic surface static pressure taps at the inlet and outlet, two Pitot probes, and one K-type thermocouple at the reference plane.

2.4.2.1 Reference Total Pressure

The reference measurements of inlet total pressure, $P_{0,ref}$, are upstream of the turbulence grid. $P_{0,ref}$ is acquired by two Pitot tubes placed upstream of the cascade at different heights and depths. The upper one is at half-height of the diffuser, and the head of the probe is at a third of the width from the sidewall, while the lower one is placed at a third of the height from the bottom of the diffuser, with the head placed at mid-width of the channel (see Fig. 2.21). Doubling the measurement allows the verification that no spanwise pressure gradient is present upstream of the turbulence grid. The upper Pitot tube is connected to an absolute pressure sensor WIKA P-30 that references the remaining pressure instrumentation in the test section. The lower Pitot tube is connected to a Scanivalve MPS4264–1 psi referenced to the pressure measured by the upper Pitot tube.

Figure 2.21: Location of the pitot tubes upstream of the test section.

2.4.2.2 Reference Total Temperature

The total temperature measured at Plane Ref., $T_{0,ref}$, is measured with a K-type bare thermocouple. The total temperature probe is located upstream of the total pressure probes in a low-velocity region to ensure a temperature recovery factor of unity. The thermocouple was calibrated against a PT-100 for temperatures ranging from $\sim$278 K to $\sim$330 K, which are expected to cover the limits encountered in the VKI S-1/C. Details of the calibration can be found in Appendix B.1.

2.4.2.3 Inlet and Outlet Static Pressure

The arrays of static pressure taps, used to monitor inlet and outlet static pressure, sit at Plane 01 (-1.12C_{ax}) and Plane 06 (1.50C_{ax}), respectively. At Plane 01, 31 pneumatic taps with a diameter of 1.00 mm are equally distributed in the pitchwise direction, covering three cascade pitches. This results in a spatial resolution of 3.30 mm between taps. The central tap of this array is contained in a line that follows the inlet metallic flow angle and intersects the central blade leading edge. The Plane 01 taps are connected to a Scanivalve MPS4264–1 psi.

The static pressure taps at Plane 06 are distributed over four-blade pitches. Equally to Plane 01, 31 pressure taps with a diameter of 1.00 mm are used. This arrangement results

in a spatial resolution between taps of 4.40 mm. The central tap in this array is contained in a line parallel to the outlet metallic angle and intersects the central blade trailing edge. The Plane 06 taps are connected to a Scanivalve MPS4264–2.5 psi.

2.4.2.4 Cascade Far Exit

The static pressure in the wind tunnel far downstream of the test section is monitored to control the long-term stability of cascade operating conditions during probe measurements. The tap is connected to a Scanivalve MPS4264–2.5 psi. The far exit pressure tap monitors the flow conditions when performing tests with probes at Plane 06 for probe interference reasons (see Section 4.4).

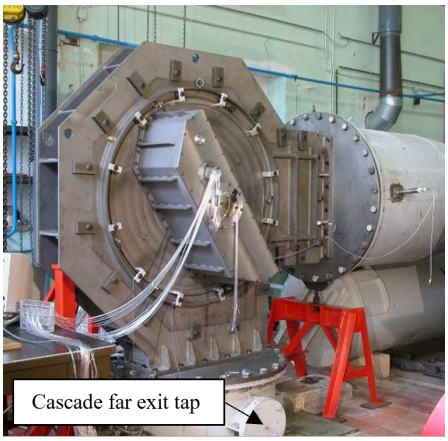

Figure 2.22: Location of cascade far exit pressure tap.

2.4.2.5 Wake Generator Speed and Position

The angular position and velocity of the wake generator are obtained with a photocell combined with a toothed wheel mounted on the wake generator shaft. The toothed wheel presents 29 equally spaced teeth and one smaller tooth. The signal of the photo-diode is 9V when the diode light passes in the empty spaces between the teeth and 0V when the teeth block the space between the photocell. The wake generator bars were phased with respect to the cascade central blade leading edge. The process required the alignment of the bar #1 with the central blade leading edge (following the inlet metallic angle) while positioning the second edge of the small tooth (second in the direction of rotation) in correspondence with the location where the photo-diode signal rises to 9V. A schematic view of the bar alignment and a picture taken during the process are reported in Fig. 2.23.

A schematic example of the signal emitted by the photo-diode is shown in Fig. 2.24 compared with the wheel position.

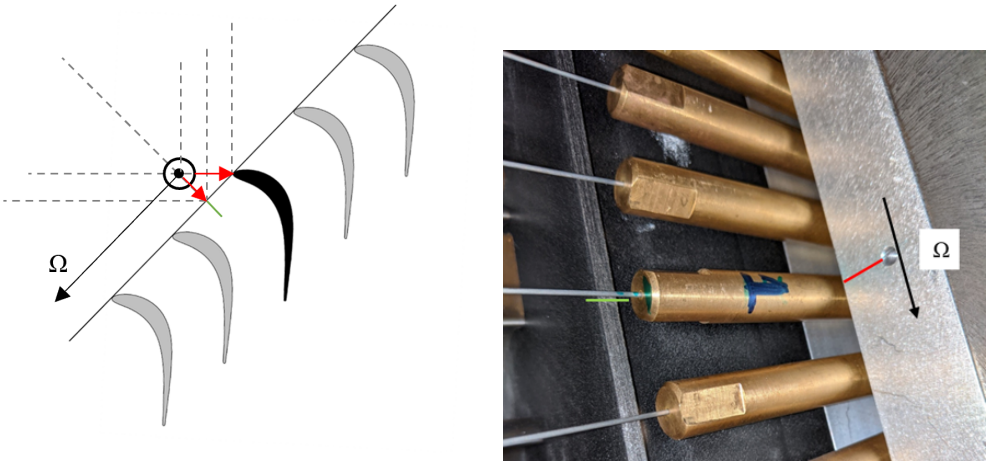

(a) (b)

Figure 2.23: Phasing of the wake generator bars with the central blade leading edge: wake generator bar aligned with the central airfoil LE along the projection of the airfoil metal angle (a) and practical application in the VKI S-1/C (b).

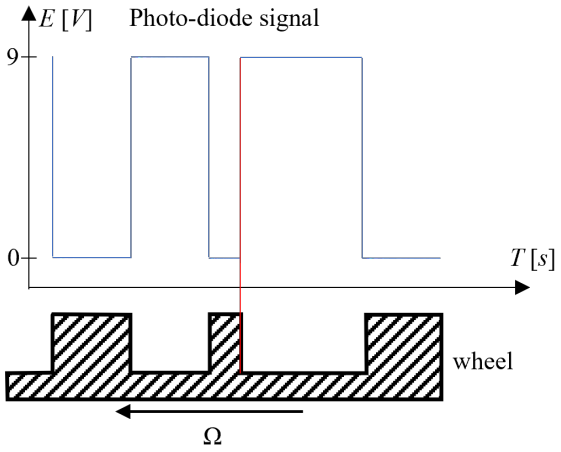

Figure 2.24: Photo-diode signal and wake generator toothed wheel position. The second edge of the short tooth in the direction of rotation is the reference for the bar #1 aligned with the central blade LE (corresponding to a bar phase of 0).

2.4.2.6 Purge Flow System Massflow

The purge mass flow ratio is measured utilizing an orifice plate. The orifice plate was designed according to the standard ASME MFC-3M, 2004 [4]. For a fixed geometry respecting the standard, the massflow past an orifice plate can be computed knowing the pressure drop across it. Other aero-thermodynamic quantities, such as a Reynolds number and density upstream of the orifice plate, must be known (see Section 2.5.3).

The geometry of the orifice plate is fixed throughout the experiments to respect the standard ASME MFC-3M, 2004 [4]. A sketch of the orifice plate along the geometrical characteristics is displayed in Fig. 2.25.

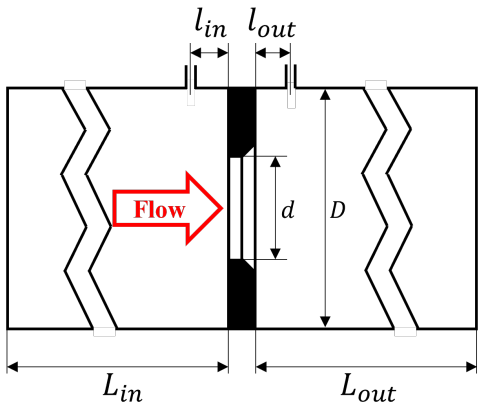

Figure 2.25: Schematic of orifice plate geometry.

The geometrical characteristics are reported in Table 2.6 for completeness.

Table 2.6: Orifice geometrical characteristics.

d	35.00	mm
D	53.00	mm
l_{in}	10.00	mm
L_{in}	3000.00	mm
l_{out}	10.00	mm
L_{out}	1000.00	mm

The massflow measurement past the orifice was done using a differential pressure sensor (Validyne DP45). The inlet aero-thermodynamic conditions were computed utilizing a second Validyne DP45 referenced to the inlet reference pressure (see Section 2.4.2.1) and a K-type thermocouple installed upstream of the orifice plate. A sketch of the instrumentation relative to the VKI S-1/C is displayed in Fig. 2.26.

The instrumentation used to monitor the secondary air system flow properties is contained in Table 2.7.

The thermocouple was calibrated with a similar procedure as the reference thermocouple (see Section 2.4.2.2) was employed. Details can be found in Appendix B.2.

The two Validynes were calibrated using a GE Druck DP1 610 pressure calibrator with a $\pm$70 mbar range. Details of the calibration can be found in Appendix B.3.

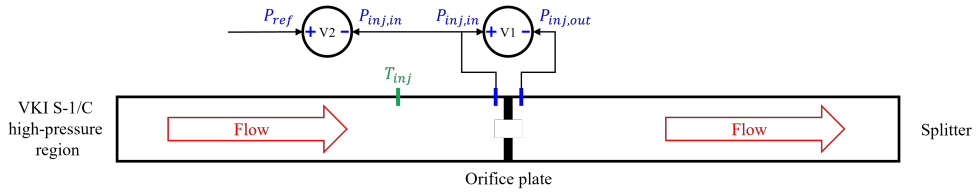

Figure 2.26: Schematic of instrumentation in the vicinity of the orifice plate.

Table 2.7: Instrumentation used to monitor secondary air system flow properties.

Nomenclature	Quantity	Instrument	Range
V1	$\Delta P_{inj} = P_{inj,in} - P_{inj,out}$	Validyne DP45	$\pm$550 Pa
V2	$P_{ref} - P_{inj,in}$	Validyne DP45	$\pm$3500 Pa
T_{inj}	T_{inj}	K-type thermocouple	–

Further downstream of the orifice plate, the flow encounters the splitter. The latter is connected to twelve flexible pipes connected to the cavity plenum chamber. The splitter is displayed alongside a cut view in Fig. 2.27. Inside the splitter, a Pitot tube measures the flow total pressure before being split. This pressure is required to compute the inlet mixed-out total pressure at the cascade inlet (see Section 6.2.3.3).

The total pressure is measured through a differential pressure sensor (Validyne DP45) with a range of $\pm$3500 Pa referenced against the inlet reference total pressure (see Section 2.4.2.1).

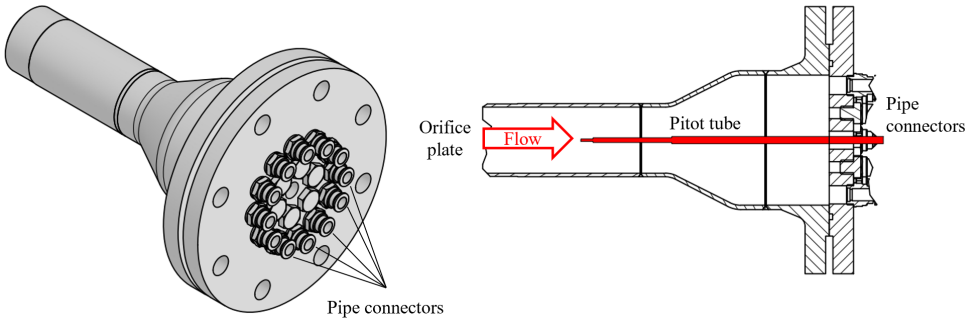

Figure 2.27: Purge flow splitter.

2.4.3 Preston Boundary Layer Tube

A Preston boundary layer tube (PT) measures the inlet total pressure profile at Plane 01. An aspect ratio, W/H, of 2.60 characterizes the probe head. Fig. 2.28 highlights the probe geometry along some key characteristic dimensions.

The probe head is aligned with the inlet metal flow angle. For a conventional round Pitot tube, the range of insensitivity to the inlet flow angle (region where deviation from the flow total pressure is less than 1% of the dynamic head) is $\pm 11^{\circ}$ from Mach numbers ranging

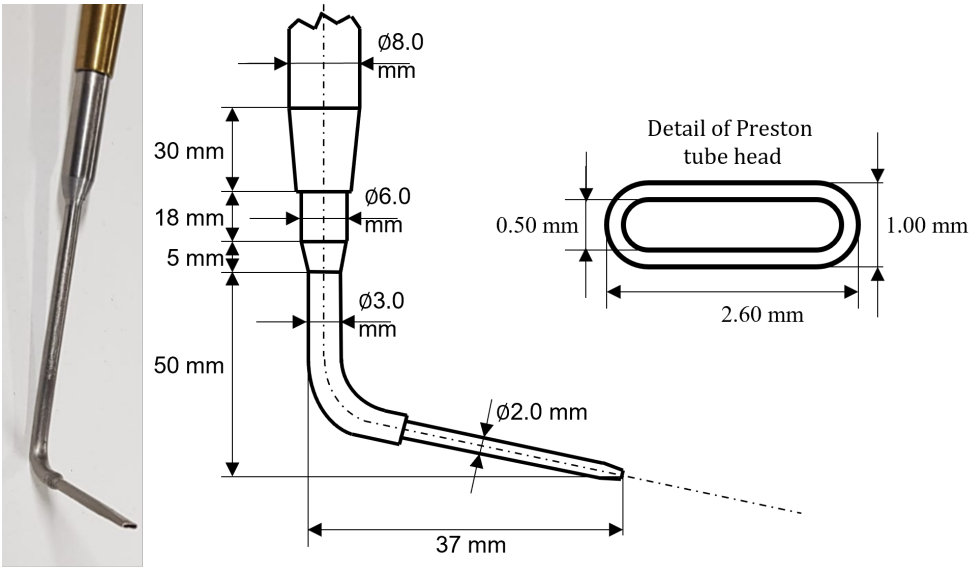

Figure 2.28: Preston boundary layer probe geometry and dimensions.

from 0.26 to 1.62 [9]. It is assumed that the range of a flat-head Pitot probe (Preston tube) is similar. Another source of error in measurements with Pitot tubes is one caused by viscosity. The latter was first exposed by Barker [10] and is named after him. Based on the aspect ratio of the Preston tube head and the flow conditions measured in the VKI S-1/C, a maximum error due to the "Barker effect" of 0.1% of the inlet freestream total pressure is expected.

A second source of error is attributed to wall proximity. The effect is reported in [11] for circular Pitot tubes. The error becomes non-negligible for distances to the endwall below two probe head diameters (z/D$<$2). Based on the hydraulic diameter of the Preston tube head and the flow conditions investigated in the scope of this work, the maximum error in the velocity due to wall proximity effects is 0.6% of the inlet freestream isentropic velocity. This effect is assumed to have the same magnitude for flattened Pitot tubes (Preston tubes). For this reason, no correction was applied.

The Preston tube is connected to the Scanivalve MPS4264–1 psi. During testing, the signal is sampled at 300 Hz for a sampling time of 3 s.

2.4.4 Cobra-Shaped Five-Hole Probe

A cobra five-hole probe (C5HP) was used to characterize the inlet flowfield at Plane 02. The probe is characterized by a pyramidal head shape with a diagonal of 2.20 mm. The probe geometry and its key characteristics are displayed in Fig. 2.29.

The probe was used in non-nulled (calibrated) mode. An aerodynamic calibration in an open jet was performed to investigate the angular sensitivity of the probe at different flow Mach numbers. The probe has been calibrated for yaw and pitch angles in the range of $\pm 30^\circ$ and $\pm 20^\circ$ in increments of 1°, respectively. The angular sensitivity of the probe to the incoming flow field was investigated for flow Mach numbers of 0.20, 0.40, and 0.60 to cover

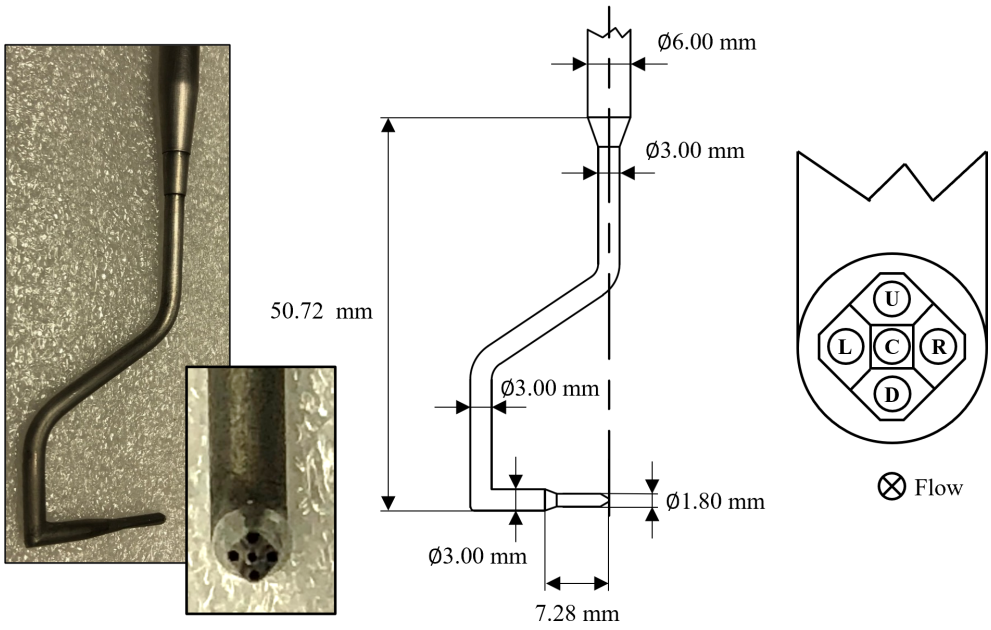

Figure 2.29: Cobra-shaped five-hole probe geometry and dimensions.

the expected range of Mach numbers at the inlet of the cascade for the current investigation.

Aerodynamic coefficients that are a function of the flow angles and Mach number were used to relate the probe-measured pressures with the local flow variables. The coefficients proposed by Treaster et al. [12] were chosen in this investigation.

$$K_\alpha\left(K_\alpha, K_\gamma, M\right) = \frac{P_L - P_R}{P_C - P_{ave}} \tag{2.1}$$

$$K_\gamma\left(K_\alpha, K_\gamma, M\right) = \frac{P_D - P_U}{P_C - P_{ave}} \tag{2.2}$$

$$K_{tot}\left(K_\alpha, K_\gamma, M\right) = \frac{P_C - P_0}{P_C - P_{ave}} \tag{2.3}$$

$$K_{stat}\left(K_\alpha, K_\gamma, M\right) = \frac{P_{ave} - P}{P_C - P_{ave}} \tag{2.4}$$

Where $P_{ave} = \left(P_L + P_R + P_D + P_U\right)/4$. This definition maximizes the sensitivity of the retrieved yaw/pitch to the measured pressures, resulting in lower measurement uncertainties as well [13]. A sensitivity survey to different definitions of P_{ave} was performed and can be found in Appendix B.4.1. A visualization of the aerodynamic calibration coefficients and orthogonality map is contained in Appendix B.5.2 and Appendix B.5.3, respectively.

Since the coefficients are a function of K_α, K_γ, and M, the retrieval of the local flow quantities requires an interpolation in the three-dimensional (3D) space that constitutes the calibration maps. An iterative cycle based on the local Mach number retrieves α and γ in

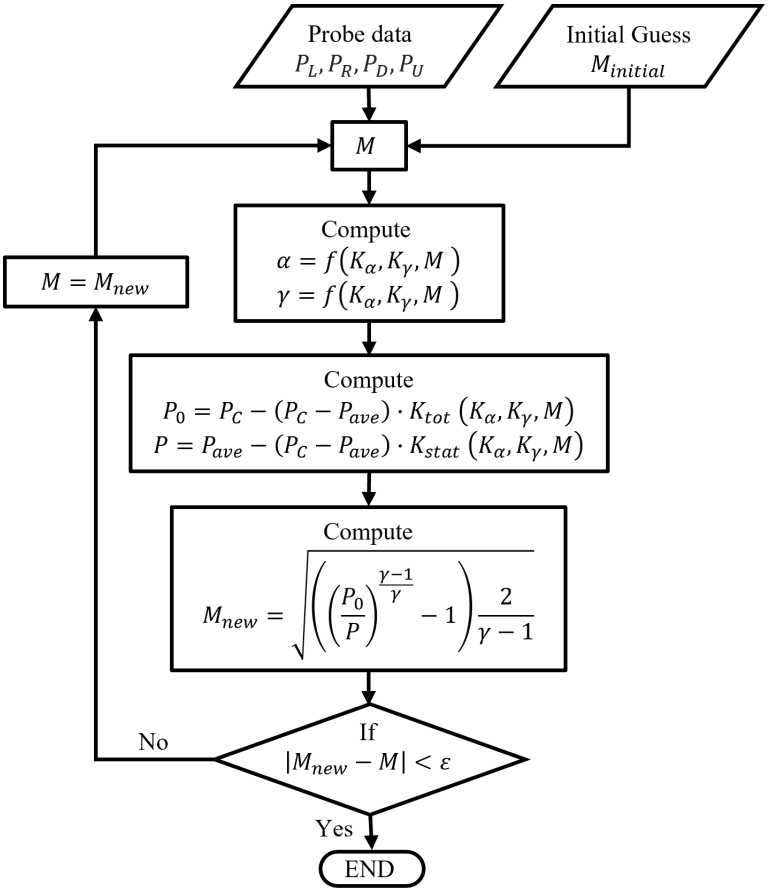

Figure 2.30: Iterative cycle used to retrieve flow quantities [14].

the probe head reference system, P_0, P, and consequently M [14]. A chart highlighting the procedure is depicted in Fig. 2.30.

For the measurements performed with the cobra five-hole probe, the maximum allowable error, ϵ, for the iterating Mach number was set to 1e-07. The taps are connected to the Scanivalve MPS4264–1 psi. During testing, the signal is sampled at 300 Hz for a sampling time of 3 s.

2.4.5 L-Shaped Five-Hole Probe

An L-shaped five-hole probe (L5HP) was used to measure downstream of the cascade at Plane 06. The probe is characterized by a hemispherical head with a diameter of 2.20 mm. The probe geometry and pressure tap convention are presented in Fig. 2.31.

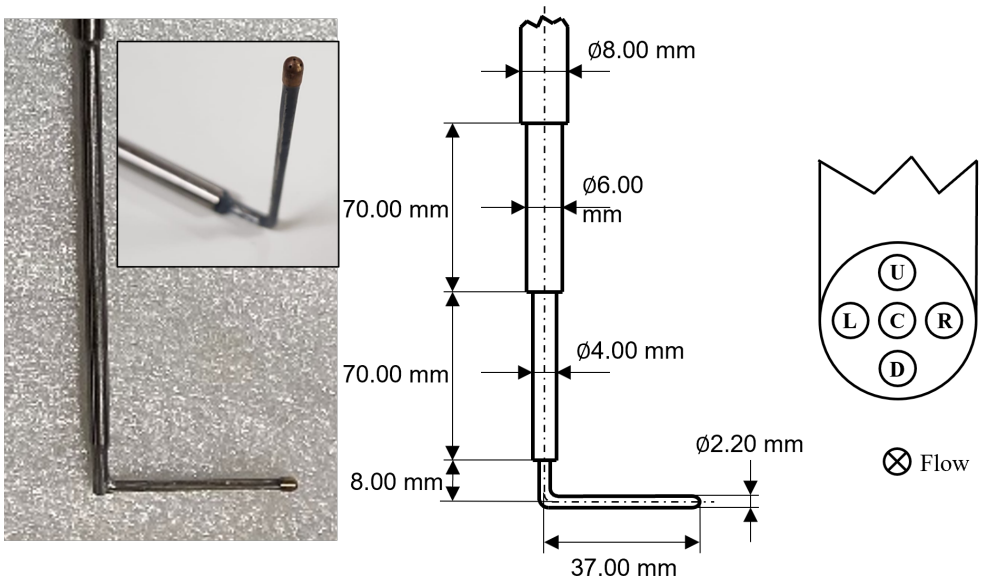

Figure 2.31: L-shaped five-hole probe geometry and dimensions.

The probe was calibrated like the cobra five-hole probe detailed in section 2.4.5. The same calibration coefficients were employed. The L-shaped five-hole probe was calibrated for a range of α and γ between $\pm 30°$, and for M $\in \{0.20, 0.40, 0.60, 0.80, 0.90, 0.95\}$. A similar effect from the P_{ave} definition was found for this probe head geometry as for the cobra five-hole probe, and therefore, the same definition was adopted. The sensitivity study to the P_{ave} definition can be found in Appendix B.5.1. A visual interpretation of the aerodynamic coefficients and orthogonality maps can be found in Appendix B.5.2 and Appendix B.5.3.

The taps are connected to the Scanivalve MPS4264–1 psi. During testing, the signal is sampled at 300 Hz for a sampling time of 3 s. Before the acquisition, the probe rests at the measuring location for 8 s to ensure the pressure has settled.

2.4.6 Twin Pneumatic and Fast-Response Virtual Four-Hole Probes

A virtual four-hole probe (V4H) was designed to measure at Plane 02, Plane 03, and Plane 06. The probe was designed to be instrumented with fast-response sensors. Operating it in virtual mode offered the possibility to reduce the number of used sensors and, hence, the probe head dimensions. The probe design was inspired by the probe used in [15, 16]. The probe head was instrumented with two commercially available Kulite® LQ–062–5A with a range of 35 kPa and an estimated bandwidth of 150 kHz. The probe has a head diameter of 2.65 mm. The probe geometry and pressure tap convention are presented in Fig. 2.32.

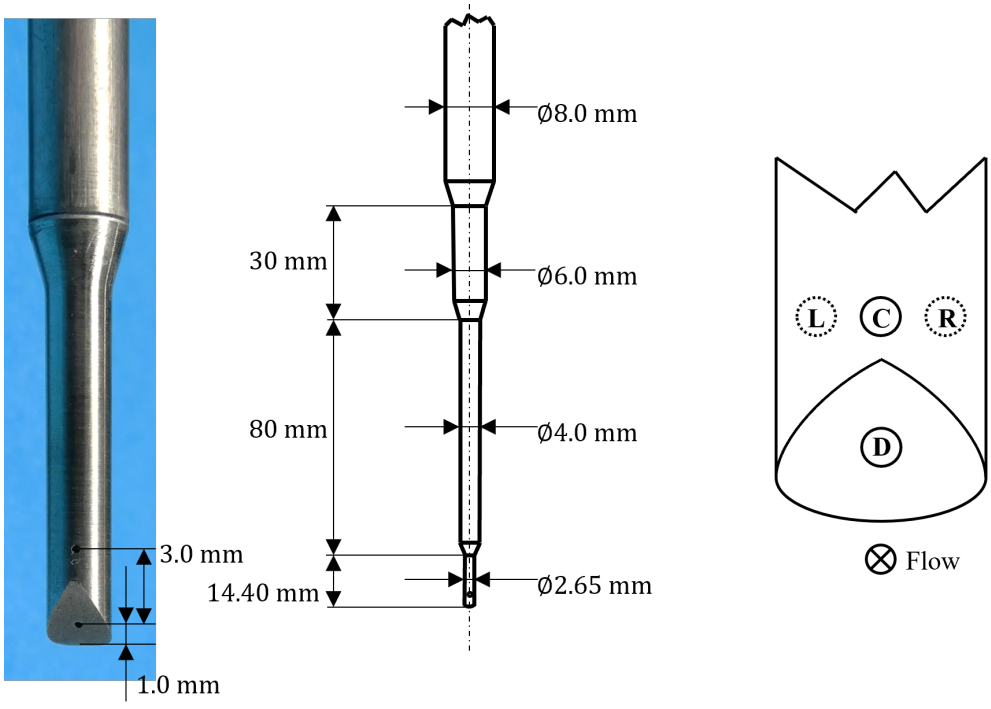

Figure 2.32: Virtual four-hole probe geometry and dimensions.

The principle of operating probes in virtual mode is well established [16–19]. The probe head is rotated around its axisymmetric axis. As a result, the center tap is rotated, and a virtual left and right tap are recreated. A tap pressure coefficient can be defined to illustrate the operating principle:

$$K_{P,Center} = \frac{P_{Center} - P}{P_0 - P} \tag{2.5}$$

The coefficient takes its maximum value when the tap is aligned with the flow. When the probe is rotated towards positive yaw angles, the pressure measured by the center tap decreases. The pressure that would have been measured by a physical right tap increases and vice-versa for the left tap. This behavior is highlighted in Fig. 2.33. A virtual displacement of $\pm 30^\circ$ is used.

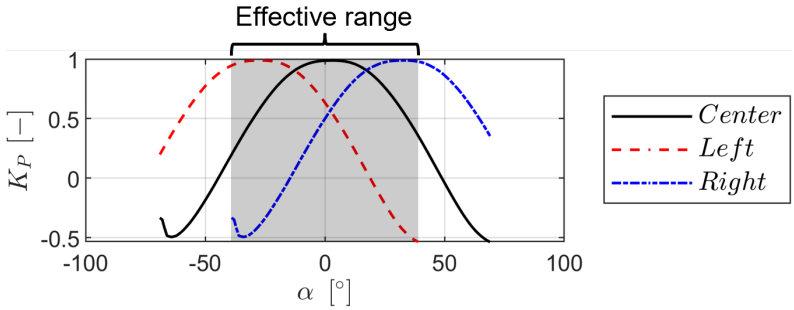

Figure 2.33: Pressure coefficients obtained for a probe used in a virtual mode in the function of the probe yaw angle.

Measurements of the center tap and resultant left and right taps are not correlated in time. Therefore, aerothermodynamic quantities that rely on measured pressures (yaw angle, pitch angle, total and static pressures) cannot be obtained as a time series.

The fast-response pressure sensors used in this work have a range of 35 kPa. Consequently, the probe cannot be aerodynamically calibrated in an open jet like the cobra five-hole probe and L-shaped five-hole probe. A twin probe head instrumented with pneumatic taps was used to calibrate the probe accurately. The calibration maps can then be used on the head instrumented with the fast-response sensors, assuming the manufacturing tolerances are low enough to produce identical head geometries. This ensured that the fast-response probe could measure independently of measurements performed by the pneumatic probe. Fig. 2.34 displays both probe heads side-by-side before being installed in their respective stem.

Figure 2.34: Heads of virtual four-hole probe to be installed with pneumatic lines and fast-response sensors.

The pneumatic V4HP was calibrated for a range of α and γ between $\pm 70°$ and $\pm 30°$, respectively, and for M$\in$ $\{0.20, 0.40, 0.60, 0.80, 0.90, 0.95\}$. Therefore, the probe has a valid calibration range of $\pm 40°$. Similar to the L-shaped five-hole probe and cobra five-hole probe, aerodynamic coefficients were defined:

$$K_\alpha\left(K_\alpha, K_\gamma, M\right) = \frac{P_L - P_R}{P_C - P_{ave}} \tag{2.6}$$

$$K_\gamma\left(K_\alpha, K_\gamma, M\right) = \frac{P_D - P_C}{P_C - P_{ave}} \tag{2.7}$$

$$K_{tot}\left(K_\alpha, K_\gamma, M\right) = \frac{P_C - P_0}{P_C - P_{ave}} \tag{2.8}$$

$$K_{stat}\left(K_\alpha, K_\gamma, M\right) = \frac{P_C - P}{P_C - P_{ave}} \tag{2.9}$$

Where $P_{ave} = \left(P_L + P_R\right)/2$. The calibration maps obtained for the pneumatic V4HP as a function of α, γ, and M can be found in Section B.6.1.

The transferability of the pneumatic virtual four-hole probe ex-situ calibration to the fast-response virtual four-hole probe was assessed by:

- Calibration of pneumatic virtual four-hole probe at low-Reynolds (in-situ calibration in the VKI S-1/C) to assess Reynolds effects from the ex-situ to in-situ calibration,
- In-situ calibration of fast-response virtual-four hole probe (fast-response virtual four-hole probe) in the VKI S-1/C to compare against in-situ calibration of pneumatic virtual four-hole probe.

2.4.6.1 Reynolds Effects in Calibration

The ex-situ and in-situ aerodynamic coefficients obtained from calibrating the pneumatic virtual four-hole probe are displayed in Fig. 2.35. The yaw angle coefficient is insensitive to the Reynolds number for $\alpha \in [-20°, +20°]$ (see Fig. 2.35(a)). The total pressure coefficient also displays good insensitivity to the Reynolds number (see Fig. 2.35(c)).

The Reynolds impacts the pitch angle coefficient (see Fig. 2.35(b)). In particular for the lowest Mach number. This is attributed to a variation of the probe pitch angle with respect to the incoming flow. Nonetheless, the variation in K_γ amounts to a variation in the perceived pitch angle of less than $1.00°$. For the higher Mach number, this difference is smaller than $0.20°$. No correction was applied to the pitch angle. In addition, the variation in pitch angle produces negligible variations in the retrieved α, P_0, and P.

Fig. 2.35(d) highlights the static pressure coefficient. The maps of K_{stat} show a significant impact by the pressure level at which the probe is calibrated. An underestimation of the static pressure of 300 Pa by the in-situ calibration occurs when the probe is aligned with the incoming flow.

Fig. 2.36(a) and Fig. 2.36(b) display the difference between the probe perceived total pressure and static pressure computed from the in-situ and ex-situ calibration curves. The difference in the retrieved total pressure is within $\pm$20 Pa. On the other hand, the discrepancy in perceived static pressure can reach 300 Pa.

The considerable variation in the retrieved static pressure cannot be directly attributed to a variation of the Reynolds number since the flow regime around a cylinder is the same for Reynolds numbers encountered during the ex-situ and in-situ calibration: fully turbulent vortex street [20]. However, given that the difference between the ex-situ and in-situ calibrations is similar for both Mach numbers, there could be an effect in the static pressure inside at low density causing a “bias”.

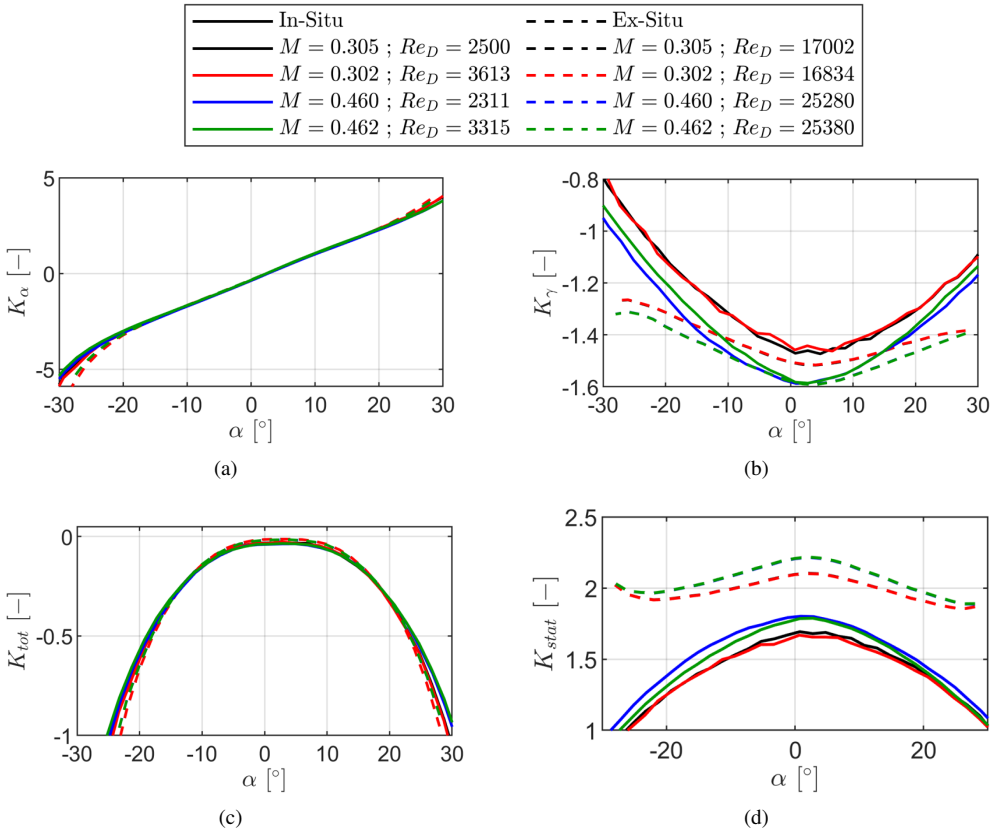

Figure 2.35: Comparison between the aerodynamic calibration coefficients of pneumatic virtual four-hole probe obtained ex-situ and in-situ at fixed γ=0°: (a) K_α, (b) K_γ, (c) K_{tot} and (d) K_{stat}.

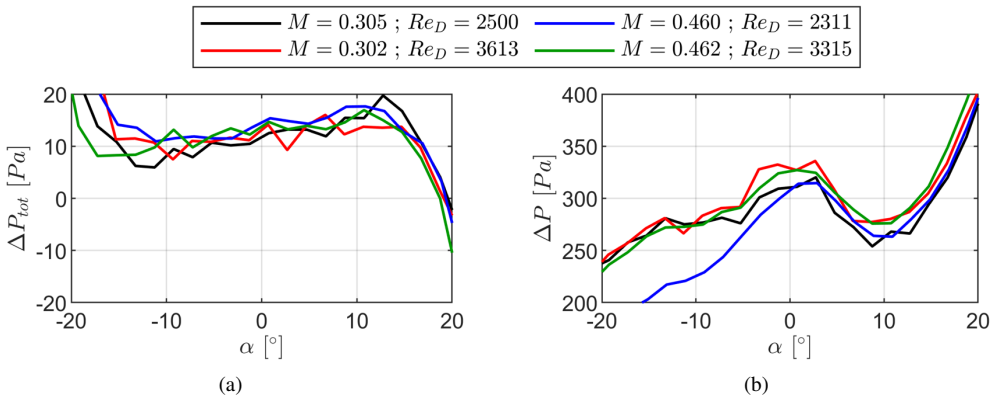

Figure 2.36: Difference in retrieved P_0 (a) and P (b) between in-situ and ex-situ calibrations for γ=0°.

2.4.6.2 PV4HP vs. FRV4HP

The comparison between the aerodynamic coefficients measured in-situ for the pneumatic virtual four-hole probe and the fast-response virtual four-hole probe is reported in Fig. 2.37. The yaw angle (see Fig. 2.37(a)) and total pressure (see Fig. 2.37(c)) coefficients display good agreement between both probe heads. The pitch angle coefficient displays a non-negligible variation between both probes. The static pressure coefficient (see Fig. 2.37(d)) also shows good agreement between both in-situ calibrations.

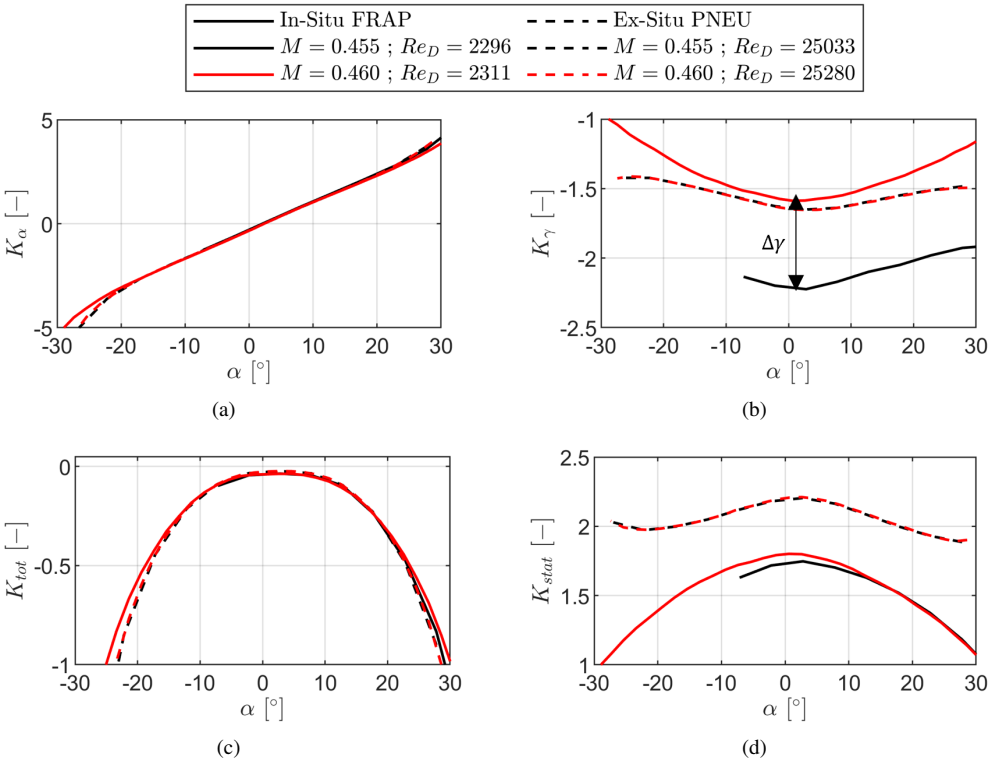

Figure 2.37: Comparison between the aerodynamic calibration coefficients of fast-response and pneumatic virtual four-hole probe obtained at fixed γ=0°: (a) K_α, (b) K_γ, (c) K_{tot} and (d) K_{stat}.

A variation in the angle of the surface containing the down tap (highlighted by $\Delta\gamma$ in Fig. 2.37(b)) could be responsible for the discrepancy between the coefficients for the two probes calibrated in-situ.

The difference between the retrieved total and static pressure by both probes is depicted in Fig. 2.38(a) and Fig. 2.38(b), respectively. The retrieved P_0 between both probes displays a variation within $\pm$10 Pa. On the other hand, the variation in static pressure between both probes can reach up to 60 Pa between both probes for the extremity of α encountered during this work. Nonetheless, the variation is still satisfactory ($\delta P < 0.01 P_{01}$).

The intermediate conclusion of this exercise is that the ex-situ calibration performed to the pneumatic V4HP can be transferred to the fast-response probe measurements performed in the rig since the yaw angle, P_0, and P can be retrieved effectively. On the other hand,

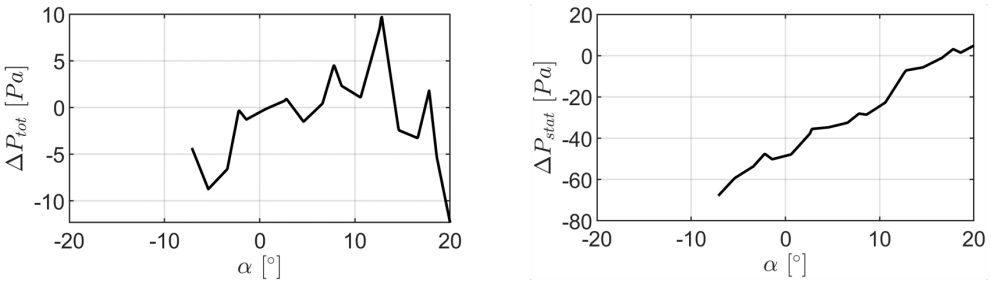

Figure 2.38: Deficit in perceived P_0 (a) and P between the in-situ calibrations of fast-response and virtual four-hole probe probes for a dynamic head typically encountered at the inlet of the test section for γ=0°.

the perceived pitch angle will be different for both probes. For a fixed yaw angle of 0°, a $\Delta\gamma \approx$11.50° would be required to justify the difference in K_γ observable in Fig. 2.37(b). Fig. 2.39 highlights the probable difference between the pneumatic and fast-response probe that could justify the latter effect.

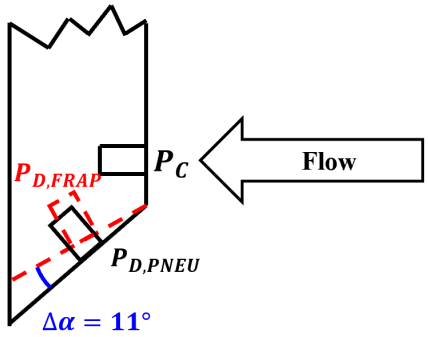

Figure 2.39: Schematic highlighting possible probe head difference to justify the difference in perceived pitch angle.

Throughout the results, a correction of 11.50° has been applied to measurements performed with the fast-response virtual four-hole probe at Plane 06. The correction to the pitch angle alone does not impact the remaining retrieved quantities: α, P_0, P. The maximum difference in total pressure in $\alpha \in [-10°, 10°]$ is within $\pm$10 Pa. The maximum difference in retrieved static pressure is within $\pm$19 Pa for the same angular range.

2.4.6.3 Static Calibration

The fast-response sensors mounted in the V4HP were statically calibrated to relate the output voltage to the local pressure and temperatures. Two calibration surfaces were obtained from the former procedure:

- Static pressure, P, as a function of the pressure-sensitive voltage, V_P, and temperature-sensitive voltage, V_S,
- Temperature, T, as a function of the pressure-sensitive voltage, V_P, and temperature-sensitive voltage, V_S.

Two types of static calibrations were performed: in-situ and ex-situ. An in-situ calibration inside the rig was performed before and after testing for cases with a wake generator. Due to the narrow range of aerothermal conditions encountered in the in-situ calibration, a polynomial surface of the first order in V_P and V_S was chosen to describe the relationship between the sensor pressure-sensitive voltage, V_P, as well as temperature sensitive voltage, V_S, and the aerothermal properties: P and T. The latter are presented in Eq. 2.10 and Eq. 2.11.

$$P\left(V_P, V_S\right) = C_1 V_P + C_2 V_S + C_3 \tag{2.10}$$

$$T\left(V_P, V_S\right) = C_1 V_P + C_2 V_S + C_3 \tag{2.11}$$

The surface fittings are graphically highlighted in Fig. 2.40. The one displayed corresponds to the fitting found for the first sensor (center tap) of the fast-response V4HP during the third testing phase.

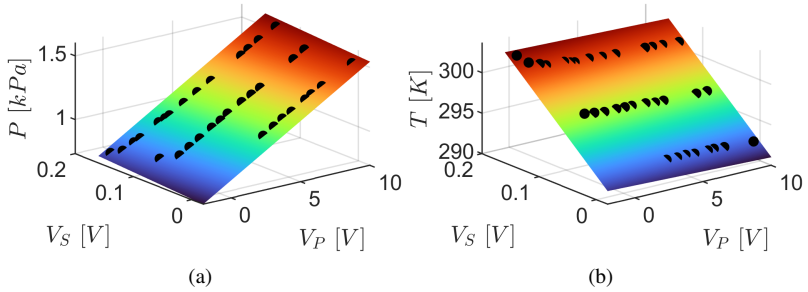

Figure 2.40: Fitted calibration surface to P=f(V_P, V_S) (a) and to T=f(V_P, V_S) (b) for the second sensor on the blade suction side during the second phase of testing.

The ex-situ calibration was conducted in a chamber capable of independently varying the pressure and temperature. This allowed to calibrate the probe in a broader range of pressures (P $\in [2500,\ 30000]$ Pa every 2500 Pa) and temperatures (T $\in [5,\ 45]$ °C every 5 °C). Due to the broader range of aerothermal properties in the ex-situ calibration, the order of the fitted polynomials was increased in V_S to correlate V_P and V_S as follows:

$$P\left(V_P, V_S\right) = C_1 V_P + C_2 V_S + C_3 + C_4 V_P V_S + C_5 V_S^2 \tag{2.12}$$

$$T\left(V_P, V_S\right) = C_1 V_P + C_2 V_S + C_3 + C_4 V_P V_S + C_5 V_S^2 \tag{2.13}$$

The fitted coefficients obtained throughout the experimental campaign are in Appendix B.7.

It is worth mentioning that the temperature-sensitive voltage results from an in-house active compensation circuit that aims at correcting the measured pressure. The sensor manufacturer reports a sensor bandwidth of ∼150 kHz. However, this bandwidth corresponds to one of the pressure-sensitive voltages that mainly impacts the pressure fluctuations due to the calibration linearity and low weight of the temperature-sensitive voltage-associated coefficients. The temperature-sensitive voltage is estimated to be measured with a bandwidth of ∼10 Hz. Therefore, this term is averaged in Eq. 2.10 and Eq. 2.11, and the instantaneous pressure is strongly linked to the instantaneous pressure-sensitive voltage signal.

2.4.6.4 Probe Bandwidth

The sensors installed in the probe head have a natural bandwidth of 150 kHz. In the scope of this work, the sensors have been recessed from the surface to improve the spatial resolution. Fig. 2.41 presents a sketch of the sensors installed in the V4HP head.

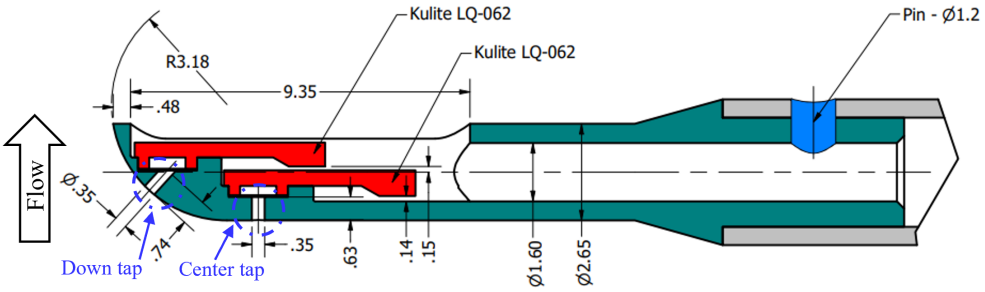

Figure 2.41: Sketch of virtual four-hole probe head instrumented with fast-response sensors and resulting line-cavity system.

The resulting line-cavity system reduces the bandwidth of the sensor due to its acoustic performance [21]. A dynamic calibration [19, 22, 23] was not employed due to the range of the sensors. Models [24–27] describing the dynamics of the line-cavity system were used to estimate the probe bandwidth. In addition to the line-cavity system, an extra recess was considered. The recess accounts for the distance the sensor is mounted from the surface of a cylindrical casing (highlighted in black in Fig. 2.42). A recess of ∼0.10 mm was accounted for based on the experience of the technician who instrumented the probe.

The dimensions characterizing the line, cavity, and recess are contained in Table 2.8.

Table 2.8: Fast-response probe taps' line-cavity dimensions in mm.

	Down tap			Center tap		
	Line	Cavity	Recess	Line	Cavity	Recess
Diameter	0.35	1.64	1.00	0.35	1.64	1.00
Length	0.74	0.05	0.10	0.64	0.05	0.10

The line-cavity system natural frequency estimated with the models above is contained in Table 2.9.

The lowest natural frequency was found for the Hougen model with end correction. Frequencies of 31 kHz and 30 kHz have been found for the center and down tap if consider-

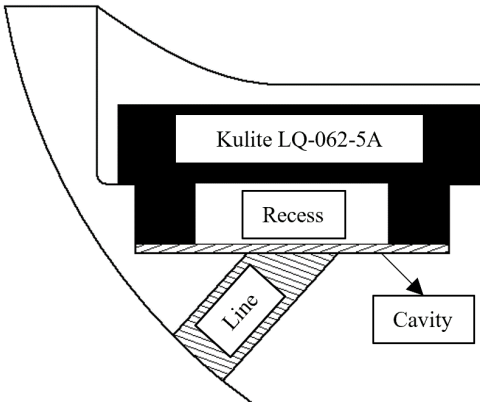

Figure 2.42: Schematic of line-cavity system highlighting sensor recess for down tap of virtual four-hole probe.

Table 2.9: Dynamic response of virtual four-hole probe fast-response pressure sensors computed with the Helmholtz [24], Hougen [25] and Bergh and Tijdeman [27] models, with and without end correction [26].

	Helmholtz		Hougen		
Sensor	w/o corr.	w/ corr.	w/o corr.	w/ corr.	Bergh and Tjideman
1	49	40	45	31	41
2	46	39	42	30	38

ing flow conditions typically encountered at the cascade inlet (M$\sim$0.45), respectively. The bandwidth is reduced by 1 kHz if the flow conditions at the cascade outlet are considered (M$\sim$0.90). The latter bandwidths enable resolving up to four harmonics of the bar passing frequency.

2.4.7 Cross-Wire Probe

A cross-wire probe (XW) was used to survey the inlet flowfield regarding turbulence characteristics, such as intensity and length scale. Fig. 2.43 displays the probe along characteristic dimensions. The probe is defined by two slanted wires forming an angle of 120° between them, with diameters of 5 μm and 9 μm. The total wire length is $\sim$3 mm, while the active length is $\sim$1 mm. This probe was used to characterize the inlet flow field at Plane 02 in the absence of the wake generator, both with and without a turbulence grid.

Both wires are connected to a Dantec Dynamics StreamLine Pro anemometer. Before the acquisition, the signals go through a 100 kHz analog low-pass filter. A 16-bit NI board was used to sample the signals. The signals are acquired at 300 kHz during tests performed without the wake generator and 1,200 kHz for experiments with the wake generator. The cutoff frequency of both wires was optimally adjusted with a square-wave test performed at engine-representative conditions and was found to be around 10 and 20 kHz for the 9 μm and 5 μm wires, respectively. A thorough probe calibration and methodology description can be found in [28].

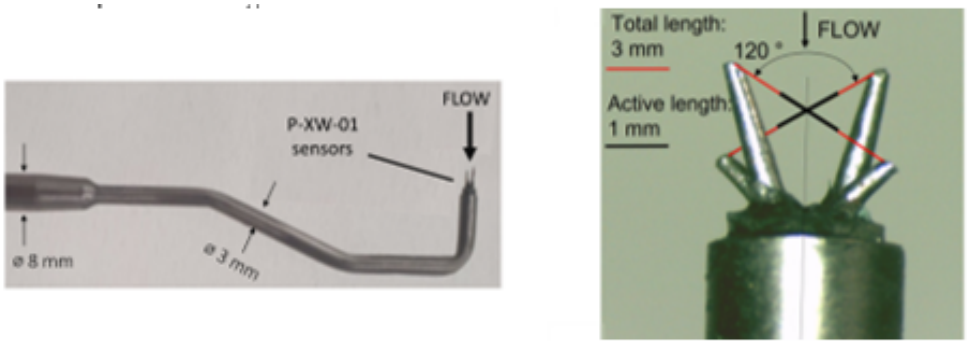

Figure 2.43: Geometry and dimensions of the cross hot-wire probe.

2.4.8 Blade Pneumatic Static Pressure Taps

Two blades were used to address the blade aerodynamics. One blade was instrumented with 24 pressure taps on the suction side, while a second blade was instrumented with 17 pressure taps on the pressure side. Fig. 2.44(a) displays the location of the pressure taps on the blade suction side, while Fig. 2.44(b) displays the location of the pressure taps on the blade pressure side. Both figures highlight varying type diameters along the blade surface. To maximize the spatial resolution, the tap diameter and the groove to install the pneumatic line had to be reduced near the trailing edge. One can also notice a larger groove on the blade pressure side. This groove was used to install a fast-response pressure sensor (see Section 2.4.10). The location of the pressure taps on the blade surface is reported in Appendix C.1 and Appendix C.2. The taps are connected to the Scanivalve MPS4264–1 psi. During testing, the signal is sampled at 300 Hz for a sampling time of 3 s.

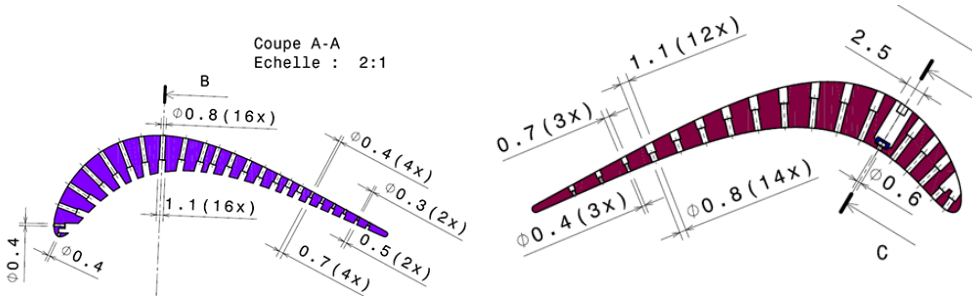

Figure 2.44: Location of pressure taps on blade suction side (a) and pressure side (b). The milled grooves on the non-measuring side are filled with epoxy to ensure a smooth surface.

2.4.9 Endwall Pneumatic Static Pressure Taps

The two endwall (EW) passages adjacent to the central blade are instrumented with pneumatic (and fast-response taps). The latter combines 66 measurement taps and maps the

endwall static pressure in a virtual passage with higher spatial resolution, as highlighted in Fig. 2.45. The figure also includes the fast-response pressure taps installed in the scope of the project SPLEEN. Results on the latter will not be presented in this thesis.

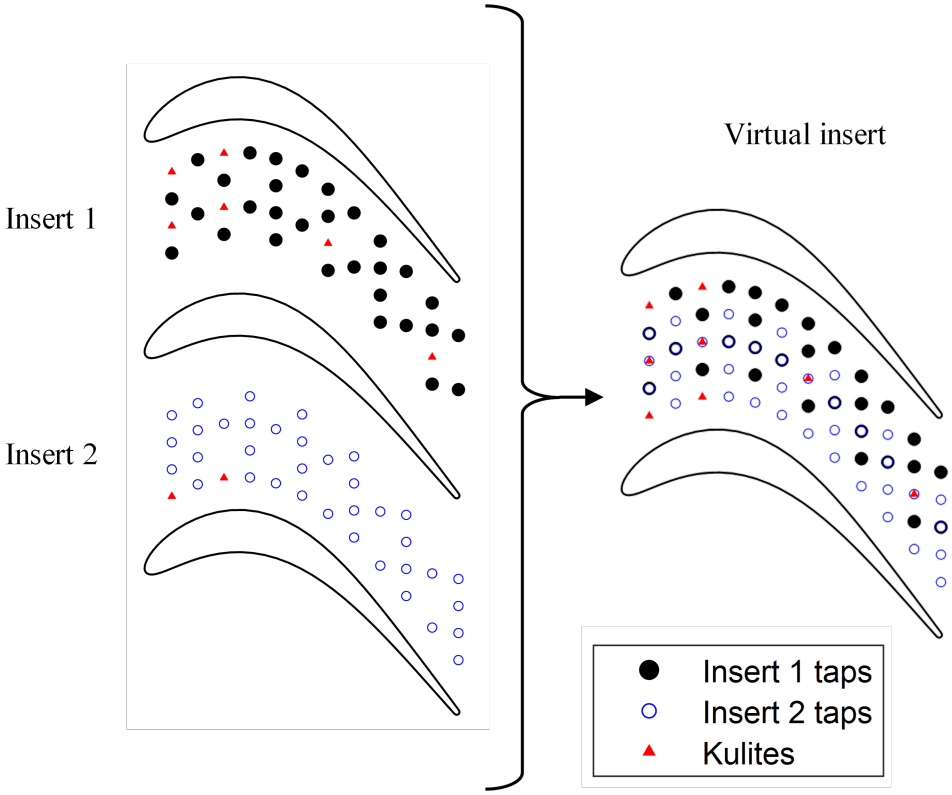

Figure 2.45: Combination of insert 1 and 2 to create a virtual insert with higher spatial resolution.

The finalized instrumented endwall inserts with pneumatic and fast response taps are shown in Fig. 2.46. The inserts on the suction and pressure sides of the central blade are named “Insert 1” and “Insert 2”, respectively. Insert 1, located in the upper passage, includes the suction side of the central blade, which contains 30 pneumatic taps. The insert on the lower passage, which consists of the central blade pressure side, is instrumented with 36 pneumatic taps. The location of the pressure taps on the endwall inserts is reported in Appendix C.3 and Appendix C.4. The taps are connected to the Scanivalve MPS4264–2.5 psi. During testing, the signal is sampled at 300 Hz for a sampling time of 3 s.

2.4.10 Blade Fast-Response Pressure Taps

An extra blade measured time-resolved pressure fluctuations along the suction side. It is recalled that the blade instrumented with pressure taps on the pressure side is also equipped with a fast-response pressure transducer. Fig. 2.47 highlights the location of the pressure taps on the suction side. The location of the fast-response pressure taps on the blade surface is reported in Appendix C.5 and Appendix C.6.

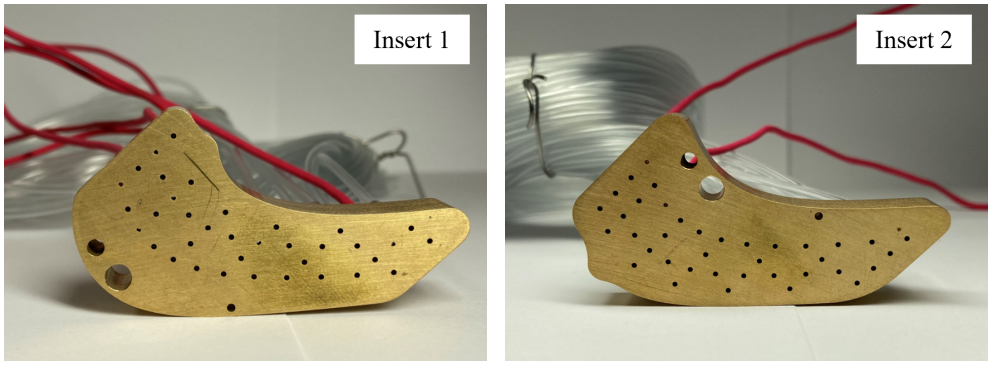

(a) (b)

Figure 2.46: Instrumented endwall inserts: Insert 1 with 30 pneumatic taps (a) and Insert 2 with 36 pneumatic taps (b).

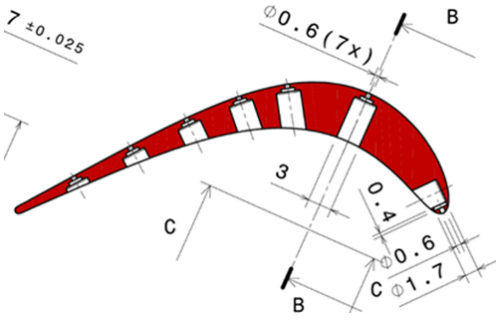

Figure 2.47: Location of fast-response pressure taps on blade suction side.

The fast-response sensors mounted on the blade suction side and pressure side are Kulite® LQ–062–5A with an absolute range of 35 kPa and an announced bandwidth of 150 kHz. The relationship between the pressure and temperature sensed by the sensors and the measured V_P and V_S was performed with in-situ calibrations as described in Section 2.4.6. The calibration coefficients resultant from the static calibration can be found in Appendix B.8.

The blade sensors have been recessed to increase the spatial resolution. The sensing tap area has thus been reduced from 1.70 mm (diameter of the sensor) to 0.60 mm. The dimensions of the line-cavity system for each sensor on the SS and PS are contained in Table 2.10.

Table 2.10: Fast-response blade taps line-cavity dimensions in mm.

		SS1	SS2	SS3	SS4	SS5	SS6	SS7	PS1
line	length	0.70	0.67	0.51	0.43	0.48	0.56	0.48	0.50
	diameter	0.60							
cavity	length	0.20							
	diameter	1.70							
recess	length	0.20							
	diameter	1.00							

The same models as depicted before have been used to estimate the line-cavity system's natural frequency. The latter is the same for all sensors. The local speed of sound has been computed based on a fully turbulent CFD 2D RANS computation (see Section 3.2). The line-cavity system natural frequency estimated with the models mentioned above is contained in Table 2.11.

Table 2.11: Dynamic response of Blade fast-response pressure sensors computed with the Helmholtz [24], Hougen [25] and Bergh and Tijdeman [27] models, with and without end correction [26].

		Helmholtz		Hougen		
Blade	Sensor #	w/o corr.	w/ corr.	w/o corr.	w/ corr.	Bergh and Tijdeman
SS	1	51	39	79	46	39
SS	2	48	36	77	44	39
SS	3	55	39	99	50	46
SS	4	59	40	117	54	50
SS	5	56	39	105	51	47
SS	6	52	38	91	48	44
SS	7	57	40	107	52	48
PS	1	60	42	110	55	47

Regardless of the model, the minimum natural frequency found between the sensors was estimated to be $\sim$36 kHz. The latter was sufficient to resolve up to five harmonics of the bar passing frequency for the tests performed with the wake generator. Each sensor was sampled with a NI6253–USB data acquisition board. Signals were acquired at 1.2 MHz and sampled for 3 s. Before the acquisition, the signals go through an analog low-pass filter of 250 kHz.

2.4.11 Blade Surface Mounted Hot-Film Sensors

Hot-films use the established relationship between convective heat flux and wall shear stress (τ_w) proposed by Bellhouse and Schultz [29]. Knowing the temperature difference between the sensor and the flow, one can express the following relationship [29]:

$$\tau_w = A\left(\frac{U\left(t\right)^2 - B^2}{\Delta T}\right)^3 \tag{2.14}$$

U(t) is the sensor voltage. A and B are functions of the temperature difference and can be obtained through calibration. For slight variations of ΔT, it is reasonable to regard A and B as constants.

A practical calibration of hot-film sensors is troublesome and time-consuming since the sensors must be calibrated for a known boundary layer state. For this reason, the hot-film technique is often used to estimate the quasi-wall shear stress (τ_q) that still provides information on the state of the boundary layer and does not require calibration of the sensors [30–34]:

$$\tau_w \sim \tau_q = \left[\frac{E_b^2 - \bar{E_{b,0}^2}}{\bar{E_{b,0}^2}}\right]^3 \tag{2.15}$$

Where E_b is the measured bridge voltage during the experiment and $\bar{E_{b,0}^2}$ is the average value of the square of the bridge voltage without incoming flow with the same sensor-to-gas driving temperature. The latter is obtained after the rig shutdown, so the gas temperature during the test and flow-off are similar. The temperature decreases when the rig compressor is slowed, and the flow stops circulating. Thus, the sensor-to-gas temperature difference during the test and the flow-off phases differ. For this reason, the flow-off voltage is compensated with the correction proposed by Hultmark and Smits [35]:

$$E_{b,corr} = E_b\sqrt{\frac{T_S - T_0}{T_S - T_a}} \tag{2.16}$$

T_S is the sensor temperature during operation, T_a is the gas temperature during the measurement, and T_0 is the reference temperature to which the over-temperature resultant from the overheat ratio is applied during the setup.

Senflex® surface-mounted hot-films were used for blade measurements. The nickel sensor elements and the cooper leads were printed on a *Upilex S polyamide film*®. The sensor geometry has a sensing element with width, thickness, and length of 0.1016 mm $\times$ 0.0002 mm $\times$ 1.4478 mm, respectively. A cold resistance of $\sim$9.90 Ω was measured at 20 °C for all sensors. The leads have width, thickness, and length of 0.60 mm $\times$ 0.0127 mm $\times$ 215 mm, respectively. The total number of sensors, equally spaced by 2 mm, on the suction and pressure sides was 31 and 21, respectively. The location of the sensors on the suction side and pressure side can be found in Appendix C.9 and Appendix C.10, respectively. The hot-film array, designed in-house and produced by Tao Systems, was wrapped around the leading edge and cut to fit a recess on the blade suction side and pressure side to avoid steps on the blade profile. Fig. 2.48 displays the final substrate wrapped around the blade.

The sensors were operated in constant temperature anemometry mode. A Dantec Streamline Pro chassis with six Wheatstone bridges was used to sample all the sensors. The sensors

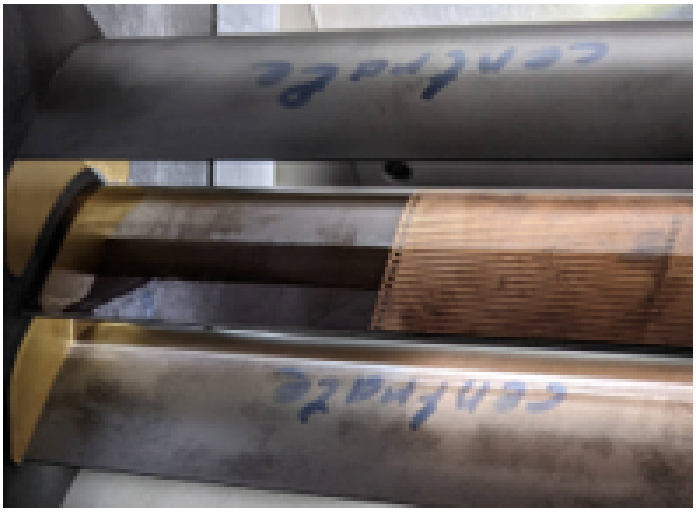

Figure 2.48: Surface-mounted hot-film sensors on the blade surface.

were acquired in groups of five or six, and the distance between operating sensors was maximized to reduce the heating effects from neighboring sensors.

The sensors were operated with an overheat ratio of 0.50, resulting in an over-temperature of ∼60 K. Before testing, a square-wave test was performed to maximize the bandwidth of the sensors. A minimum bandwidth of 50 kHz was found between all the sensors. During testing, the signals were sampled with a NI6253-USB data acquisition board. Signals were acquired at 1,200 kHz for a sampling time of 3 s. Before the acquisition, the signals go through an analog low-pass filter of 100 kHz.

2.5 Definition of Operating Point

The flow conditions in the test section are estimated by live-monitoring the inlet reference total pressure (see Section 2.4.2.1) and temperature (see Section 2.4.2.2), and static pressure at the inlet and outlet of the cascade (see Section 2.4.2.3). The procedure employed to estimate the operating flow conditions is depicted in the following sections.

2.5.1 Cascade Mach and Reynolds Numbers

Evaluating the inlet total pressure downstream of the grid at Plane 01, P_{01}, allows the computation of the other flow conditions. The inlet total pressure is estimated using a correlation in Section 4.2.

The $M_{1,is}$ is computed from the measured static pressure at Plane 01, P_1, and the inlet total pressure, P_{01}, by Eq. 2.17.

$$M_{1,is} = \sqrt{\frac{2}{\gamma - 1}\left[\left(\frac{P_{01}}{P_1}\right)^{-\frac{\gamma-1}{\gamma}} - 1\right]} \tag{2.17}$$

Since the cascade does not extract work from the flow, the inlet total pressure in the freestream region is conserved from inlet to outlet. The computation of the cascade outlet isentropic Mach number, $M_{is,out}$, is performed with Eq. 2.18:

$$M_{6,is} = \sqrt{\frac{2}{\gamma - 1}\left[\left(\frac{P_{01}}{P_6}\right)^{-\frac{\gamma-1}{\gamma}} - 1\right]} \tag{2.18}$$

Assuming that the total temperature, T_0, is conserved from the cascade inlet to the cascade outlet for the same reason depicted above, the static pressure at the inlet and outlet can be computed using Eq. 2.19 by using the inlet or outlet isentropic Mach number.

$$T = \frac{T_0}{1 + \frac{\gamma-1}{2}M_{is}^2} \tag{2.19}$$

The isentropic flow velocity at the inlet and outlet is computed with Eq. 2.20.

$$V_{is} = M_{is}a = M_{is}\sqrt{\gamma RT} \tag{2.20}$$

Where a is the speed of sound, R=287.05 J/kg K is the gas constant, and γ=1.40 is the ratio of specific heats. The density is then computed with Eq. 2.21.

$$\rho = \frac{P}{RT} \tag{2.21}$$

From the static pressure, Sutherland's equation retrieves the dynamic viscosity, μ (see Eq. 2.22).

$$\mu = \frac{1.458 \times 10^{-6} T^{3/2}}{T + 110.40} \tag{2.22}$$

Finally, the Reynolds number at the inlet or outlet is computed with Eq. 2.23.

$$Re = \frac{\rho V_{is} C}{\mu} \tag{2.23}$$

2.5.2 Reduced Frequency and Flow Coefficient

The computation of the reduced frequency requires the wake generator's rotational velocity and the outlet isentropic velocity. The number of bars and the blade chord are fixed. The rotational velocity of the wake generator is monitored utilizing a photo-diode (see Section 2.4.2.5), while the outlet isentropic velocity is estimated as presented in the previous section. The reduced frequency, f^+, is computed with Eq. 2.24.

$$f^+ = \frac{RPM}{60} N_{bars} \frac{C}{V_{6,is}} \tag{2.24}$$

The computation of the flow coefficient requires the bar peripheral velocity at midspan and the inlet axial velocity. The latter is immeasurable in real-time. However, an estimation is obtained by decomposing the inlet isentropic velocity with the inlet metallic angle of the cascade. Therefore, the flow coefficient, Φ, can be estimated with Eq. 2.25.

$$\Phi = \frac{U}{V_{1,ax,is}} = \frac{U}{V_{1,is} cos\left(\alpha_{met,in}\right)} \tag{2.25}$$

The bar peripheral velocity, U, is computed as U=2·π·r·RPM/60, where r is the distance from the wake generator's center of rotation to the cascade midspan.

2.5.3 Purge Massflow Ratio

The purge mass flow ratio is measured employing an orifice plate and controlled by regulating valves in the secondary air system presented in Section 2.1.

During the experiments, the required mass flow is achieved by adjusting a gate valve upstream of the orifice plate, which modifies the ΔP_{inj}. An additional needle valve that allows fine adjustment allows the drawing of small fractions of air from the atmosphere for further regulation of the massflow. By measuring the aero-thermodynamic quantities using the instrumentation reported in Section 2.4.2.6, the ISO 5167–3 standard [36] can be used to compute the mass flow rate according to Eq. 2.26.

$$\dot{m} = C_d \varepsilon \frac{\pi d^2}{4} \sqrt{\frac{2\rho_{inj,in}\left(P_{inj,in} - P_{inj,out}\right)}{\left(1-\beta^4\right)}} \tag{2.26}$$

Where for Reynolds numbers based on the outer diameter, D, of the orifice pipe, Re_D, higher than 5,000, the discharge coefficient, C_d, is computed with Eq. 2.27.

$$\begin{aligned} C_{d,gen} = 0.5961 + 0.0261\beta^2 - 0.216\beta^8 + 0.000521 \left(\frac{10^6\beta}{Re_D}\right)^{0.7} \\ + \left(0.0188 + 0.0063A\right)\beta^{3.5} \left(\frac{10^6}{Re_D}\right)^{0.3} \\ + \left(0.043 + 0.080e^{-10L_1} - 0.123e^{-7L_1}\right)\left(1 - 0.11A\right)\frac{\beta^4}{1-\beta^4} \\ - 0.031\left(M_2 - 0.8M_2^{1.1}\right)\beta^{1.3} \end{aligned} \tag{2.27}$$

Since the orifice pipe's outer diameter is smaller than 71.12 mm, the following extra term is added to Eq. 2.27:

$$C_{D,extra} = 0.011\left(0.75 - \beta\right)\left(2.8 - \frac{D}{25.4}\right) \tag{2.28}$$

The final discharge coefficient is then obtained by combining Eq. 2.27 and Eq. 2.28 as:

$$C_d = C_{d,gen} + C_{d,extra} \tag{2.29}$$

The expansibility factor, ϵ, is computed according to Eq. 2.30

$$\epsilon = 1 - \left(0.351 + 0.256\beta^4 + 0.93\beta^8\right)\left[1 - \left(\frac{P_{inj,out}}{P_{inj,in}}\right)^{1/\gamma}\right] \tag{2.30}$$

The term β is the ratio of the inner to the outer diameter of the orifice pipe (i.e., β=d/D), which in the current application equals 0.66. The terms A and M_2 are computed according to Eq. 2.31 and Eq. 2.32.

$$A = (19000\beta/Re_D)^{0.8} \tag{2.31}$$

$$M_2 = 2L_2/(1-\beta) \tag{2.32}$$

For corner taps, L_2 equals zero. The orifice inlet static temperature is not measurable. Therefore, calculating the mass flow relies on an iterative process using measured aero-thermodynamic quantities. A schematic view of the iterative cycle is displayed in Fig. 2.49.

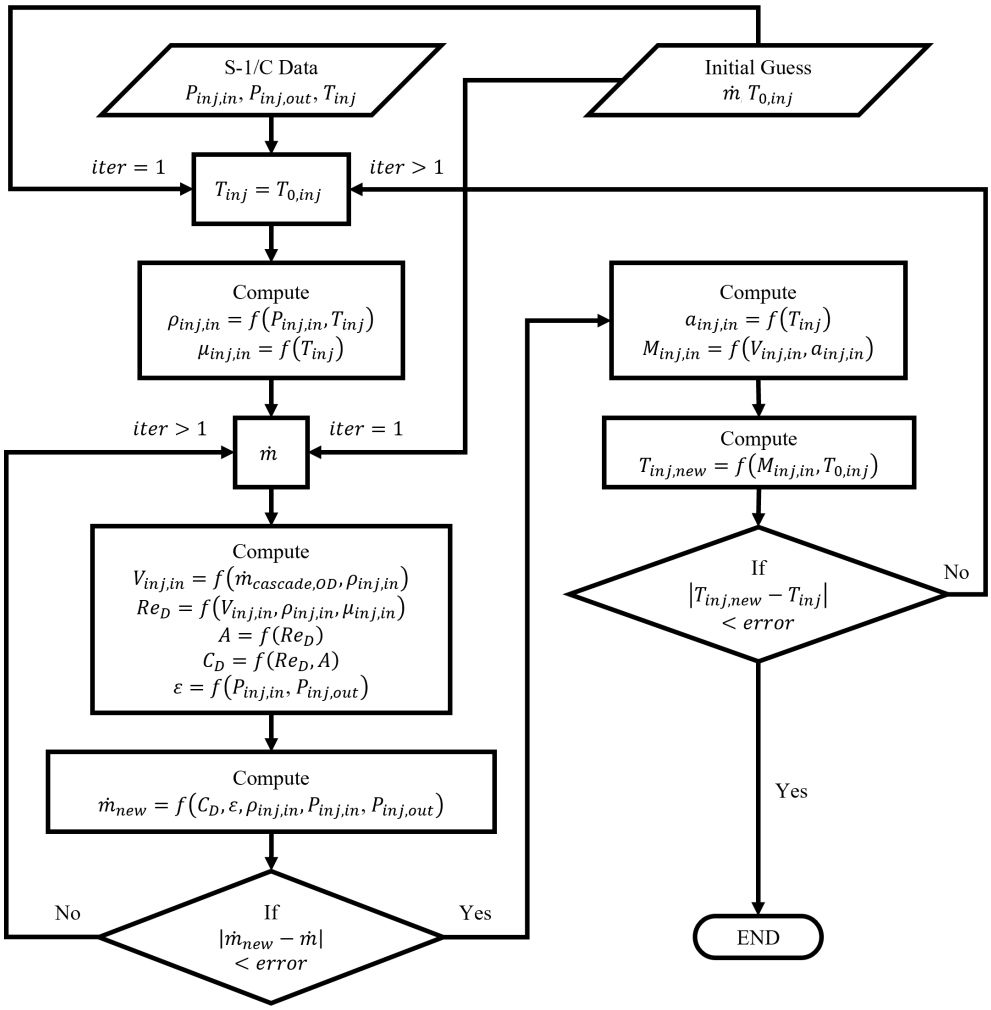

Figure 2.49: Iterative procedure employed in determining the mass flow rate across the orifice plate.

An issue with the previous approach is the range of Re_D for which the ISO 5167–3 standard [36] is applicable (Re_D >5,000). Due to the upgrades performed to the secondary air

system, the Re_D encountered during testing is between 1,500 and 5,000 for the lowest and highest mass flow rates investigated, respectively. For low values of $\Delta \mathrm{P}_{inj}$, the discharge coefficient tends to infinity as $\Delta \mathrm{P}_{inj}$ tends to zero (i.e., $\lim_{\Delta P \to 0} C_D = +\infty$). The work of Jankowsky et al. [37] describes the methodology of finding an empirical correlation describing C_D as a function of $\Delta \mathrm{P}_{inj}$. The methodology relies on using the following equation:

$$C_D = A_0 \left(1 + A_1 \, e^{\left(-A_2 \sqrt{Re_D}/A_0\right)} + A_3 \, e^{\left(-A_4 \sqrt{Re_D}/A_0\right)}\right) \tag{2.33}$$

The coefficients are determined by utilizing a dataset by Johansen [38] that explores the usage of orifice plates at low Reynolds numbers. The data is used to find the peak in the discharge coefficient that occurs at low Reynolds numbers (see Fig. 2.50).

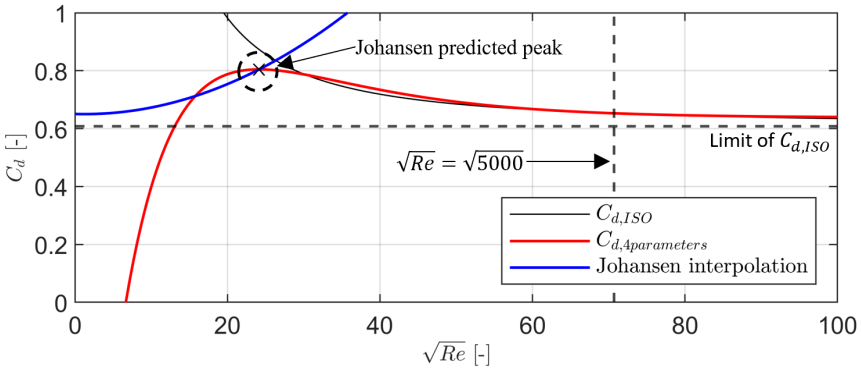

Figure 2.50: Discharge coefficient as a function of the Reynolds number. The ISO 5167 - 3 standard [36] is plotted against the Johansen interpolation [38] that enables finding the peak of the discharge coefficient.

The coefficients can then be obtained with the *fsolve* function in MATLAB with four objective functions to be minimized. The four objective functions are:

1. Function intersects with ISO correlation at the intersection point (Re_D=5,000),
2. Derivative of function intersects with a derivative of ISO correlation at the intersection point,
3. Function intersects with the peak value predicted by Johansen [38],
4. Derivative of function is zero at the peak value predicted by Johansen [38].

This represents an adaptation to the method of Jankowsky et al. [37], as the correlation proposed in the original paper must respect the condition $\mathrm{C}_D = 0$ for Re_D=0. This condition was removed in favor of first-order continuity in the intersection point between the ISO 5167–3 standard [36] and the Jankowsky correlation (Re_D=5,000). The cost of this modification is a slight inaccuracy at very low massflows. The error is about 0.03 g/s at 0 g/s, which is considered negligible as it is far outside the required mass flow working range. The coefficients of Eq. 2.33 found from the minimization of the objective functions are reported in Table 2.12.

Finally, the extended correlation plotted alongside the ISO standard is displayed in Fig. 2.51.

Table 2.12: Coefficients obtained through the minimization of the objective functions built to extend ISO standard with the formulation of Jankowsky et al. [37].

A_0	0.6378525722081
A_1	2.501863938899
A_2	0.04189076955453
A_3	-6.395452928903
A_4	0.08553907175406

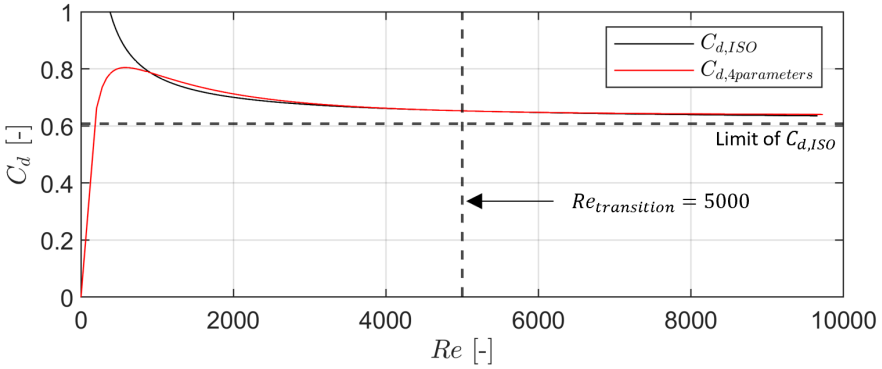

Figure 2.51: Discharge coefficient as a function of the Reynolds number obtained with ISO standard and extended correlation.

2.6 Data Reduction

2.6.1 Cascade Metrics and Performance

2.6.1.1 Boundary Layer Integral Parameters

The boundary layer integral parameters have been using a compressible approach. As such the displacement thickness, δ^*, and momentum thickness, θ, are computed as:

$$\delta^* = \int \left(1 - \frac{\rho(z)\,U(z)}{\rho_{fs}U_{fs}}\right) dz \tag{2.34}$$

$$\theta = \int \frac{\rho(z)\,U(z)}{\rho_{fs}U_{fs}} \left(1 - \frac{\rho(z)\,U(z)}{\rho_{fs}U_{fs}}\right) dz \tag{2.35}$$

The shape factor, H_{12}, is consequently computed as the ratio of displacement thickness to momentum thickness:

$$H_{12} = \delta^*/\theta \tag{2.36}$$

2.6.1.2 Flow Angles

The quantities describing the inlet and outlet flow angle are the primary flow direction, β, and the cascade pitch angle, γ. Fig. 2.52 displays the positive orientation of the primary flow direction and the cascade pitch angle in the cascade reference system. The primary flow

direction can be seen as a projection of the inlet or outlet flow angle on the XY plane. On the other hand, the cascade pitch angle is the projection of the inlet or outlet flow angle on the XZ plane. The primary flow direction, β, and the cascade pitch angle, γ, are determined from the flow angles measured by the multi-hole probe to reconcile the reference system of the probe angular calibration and the cascade reference system of Fig. 2.52.

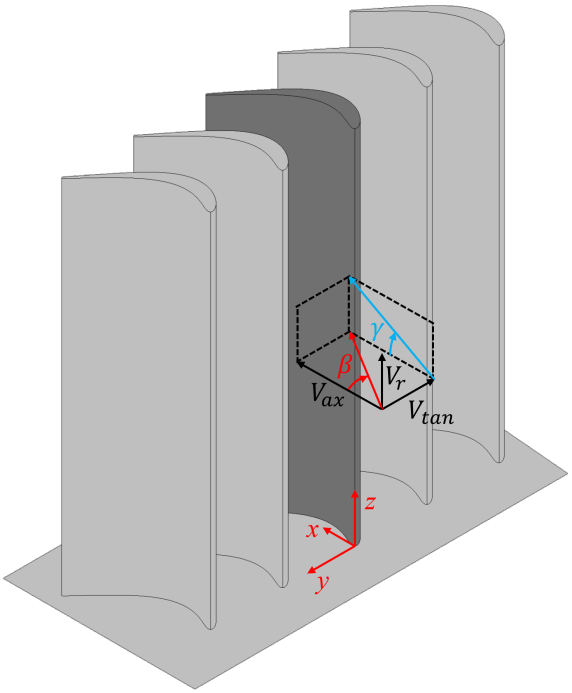

Figure 2.52: Primary flow direction and cascade pitch angle in the cascade reference system.

The main quantity used to quantify the outlet flow angle is the primary flow direction at which point:

$$\beta = \tan^{-1} \frac{V_{tan}}{V_{ax}} \tag{2.37}$$

If one is interested in the outlet flow under/overturning, the deviation, d, can be computed as $d = \beta - \alpha_{m,outlet}$. Overturning occurs when d>0. The incidence at the inlet of the cascade, i, can be computed as $i = \beta - \alpha_{m,inlet}$. The quantity describing the deviation from two-dimensionality is the cascade pitch angle. The latter can be computed as:

$$\gamma = \tan^{-1} \frac{V_r}{V_{ax}} \tag{2.38}$$

Note that γ also denotes the pitch in the probe head reference system. Whenever probe measurements concerning the pitch angle are presented throughout this thesis, they refer to the cascade pitch angle computed from the velocity components.

2.6.1.3 Kinetic Energy Loss Coefficient

The losses are characterized by the energy loss coefficient described by Denton [39]. This coefficient is less sensitive to Mach number than the total pressure and entropy loss coefficients [40].

$$\xi = 1 - \frac{1 - \left(\frac{P_6}{P_{06}}\right)^{\frac{\gamma-1}{\gamma}}}{1 - \left(\frac{P_6}{P_{01}}\right)^{\frac{\gamma-1}{\gamma}}} \tag{2.39}$$

Throughout the results, the outlet total pressure is measured locally by the L-shaped five-hole probe or fast-response virtual four-hole probe. The static pressure at the outlet has been obtained from the endwall tap measurements during tests when no probe was inserted in the test section. The inlet freestream total pressure is retrieved with the inlet loss correlations (see Section 4.2).

2.6.1.4 Streamwise Vorticity Coefficient

The streamwise vorticity was used to highlight the sense of rotation of secondary flow structures downstream of the cascade and their relative intensity. The streamwise vorticity described by Gregory-Smith al. [41] is multiplied by the chord-to-outlet isentropic velocity ratio. The normalization is the same as employed by Taremi [42] and El Ella and Hamza [43]:

$$K_\omega = \frac{C}{V_{6,is}} \left(\omega_{ax} cos\beta_{MS} + \omega_{tan} sin\beta_{MS}\right) \tag{2.40}$$

The axial vorticity can be directly computed with the L-shaped five-hole probe or fast-response virtual four-hole probe data using Eq. 2.41. Since the downstream measurements were performed on a single plane, the tangential vorticity component, ω_{tan}, is estimated using the Crocco's relation as suggested in [41, 44] according to Eq. 2.42.

$$\omega_{ax} = \frac{\partial V_{rad}}{\partial y} - \frac{\partial V_{tan}}{\partial z} \tag{2.41}$$

$$\omega_{tan} = \frac{1}{V_{ax}} \left(V_{tan}\omega_{ax} + \frac{a^2}{\gamma} \frac{\partial \left(lnP_{06}\right)}{\partial z} \right) \tag{2.42}$$

2.6.1.5 Secondary Kinetic Energy Coefficient

The secondary kinetic energy was used to highlight regions of shear interaction (mixing) of secondary flow structures downstream of the cascade. The secondary kinetic energy coefficient, K_{SKE}, is defined as:

$$K_{SKE} = \frac{\rho_6 \left(v_{y,sec}^2 + v_{z,sec}^2\right)}{\gamma P_6 M_{6,is}^2} \tag{2.43}$$

Where the secondary velocity components, $v_{y,sec}$ and $v_{z,sec}$, are computed locally as projections of the local velocity vector on a plane normal to the local primary flow direction (see Eq. 2.37) as:

$$v_{y,sec} = V_{tan} \cos\beta - V_{ax} \sin\beta \tag{2.44}$$

$$v_{z,sec} = V_{rad} \tag{2.45}$$

2.6.2 Area- and Mass-Averaging

Area-averaging is typically employed to average the static pressure field. The mathematical definitions of a generic quantity, Φ, area-averaged over the pitchwise direction, as well as over the pitch and spanwise directions (planewise averaged), are as follows:

$$pitchwise, \Phi^a = \frac{1}{g} \int_{-g}^{g} \Phi(y)\, dy \tag{2.46}$$

$$planewise, \Phi^a = \frac{1}{gH} \int_{0}^{H} \int_{-g}^{g} \Phi(y,z)\, dydz \tag{2.47}$$

The mass-averaging procedure allows for accounting for the mass deficit in boundary and/or shear layers as a reduction in the enthalpy flux instead of a direct loss. This becomes useful when a loss definition derived from enthalpy conservation is used. Consequently, this procedure is recommended for averaging total temperatures and total pressures. The mathematical definitions of a generic quantity, Φ, mass-averaged over the pitchwise direction and the pitch and spanwise directions (planewise averaged) are as follows:

$$pitchwise, \Phi^m = \frac{\frac{1}{g}\int_{-g}^{g} \rho(y)\, V_{ax}(y)\, \Phi(y)\, dy}{\frac{1}{g}\int_{-g}^{g} \rho(y)\, V_{ax}(y)\, dy} \tag{2.48}$$

$$planewise, \Phi^m = \frac{\frac{1}{gH}\int_{0}^{H}\int_{-g}^{g} \rho(y,z)\, V_{ax}(y,z)\, \Phi(y,z)\, dydz}{\frac{1}{gH}\int_{0}^{H}\int_{-g}^{g} \rho(y,z)\, V_{ax}(y,z)\, dydz} \tag{2.49}$$

In a case where a quantity is computed by combining static and total quantities, each one of the quantities constituting the final quantity area- or mass-averaged. This is the case for the kinetic energy loss coefficient to characterize the cascade losses. The mass-averaged energy loss coefficient is computed as follows:

$$\xi^m = 1 - \frac{1 - \left(\frac{P_6^a}{P_{06}^m}\right)^{\frac{\gamma-1}{\gamma}}}{1 - \left(\frac{P_6^a}{P_{01}^m}\right)^{\frac{\gamma-1}{\gamma}}} \tag{2.50}$$

In the subsequent section dealing with loss modeling (see Section 7), the mixed-out averaged loss was also compared against existing models in the literature. The mixed-out averaging procedure was provided by SAE and will not be shared in this thesis. The reader is referred to a similar procedure [45]. In the scope of this work, the mixed-out averaged loss displayed a similar topology to the mass-averaged one.

2.6.3 Phase-Locked Averaging

The phase-locked average (PLA) technique has been used to extract the time-resolved fluctuations periodic with the bar passing frequency from fast-response instrumentation. For a periodic quantity Φ(t), the method consists of averaging the signals over several repeating periods, N_{per}. Each period is discretized in several classes, N_{class}, that discretize the period of the repeating event into smaller portions. The original signal is broken down into repeating events, and points of the same class are averaged to obtain the final ensemble-average signal. The PLA method can be defined mathematically by the following equation:

$$\widetilde{\Phi}\left(t_i\right) = \frac{1}{N_{per}} \sum_{j=1}^{N_{per}} \Phi_j\left(t_i\right), \;\; i = 1...N_{class} \tag{2.51}$$

The fluctuations in each class can be estimated as:

$$\Phi\prime\left(t_i\right) = \frac{1}{N_{per}} \sum_{j=1}^{N_{per}} \left(\Phi_j\left(t_i\right) - \widetilde{\Phi}\left(t_i\right)\right), \;\; i = 1...N_{class} \tag{2.52}$$

Lastly, the RMS of each class can be estimated by:

$$RMS(t_i) = \sqrt{\Phi\prime^2\left(t_i\right)}, \;\; i = 1 \ldots N_{class} \tag{2.53}$$

The latter is equivalent to computing the standard deviation of $\Phi_j\left(t_i\right)$. The skewness of the fluctuations in each class is also determined and reported. Statistical moments are defined as applied to each class composing the ensemble-averaged signal.

Fig. 2.53 provides a visual interpretation of the PLA. Fig. 2.53(a) displays the calibrated pressure signal measured by the fast response Kulite sensor $\#4$ on the blade suction side. The signal was acquired during measurements performed at midspan for the case of M=0.95; Re=70k. This flow condition will be used for the explanatory purpose of this section.

The signal can be broken down in every wake generator disk revolution, which in this case is periodic. The repeated signals can then be re-phased with a triggering event (1^{st} wake generator bar) to be averaged and reduce the measurement random error. Fig. 2.53(b) displays the re-phased periodic signals in one wake generator disk revolution period featuring 96 bar passing events.

The repeating event can be one bar passing or the entire disk revolution (i.e., 96 bar passing events). Averaging over one bar passing period increases the number of events to be averaged. For this to be possible, all bars must be similar. To assess this assumption, the PLA of a signal averaged over one disk revolution has been compared with the PLA of a signal averaged for one bar passing and multiplied by 96 events. If the bars are identical, they generate repeatable wakes with wake-induced flow fluctuations that are also periodic.

Fig. 2.54(a) displays the back-to-back comparison of the normalized pressure measured by the 4^{th} fast-response Kulite pressure sensor on the blade suction side, averaged over a disk revolution against the same signal averaged over a bar passing period and repeated 96 times. The signal is shown for the first 40 bars. The ensemble average periodic signal difference obtained through the two approaches is displayed in Fig. 2.54(b). The maximum difference between the two cases is $\sim$0.005P_{01} ($\sim$50 Pa). The standard deviation of their difference

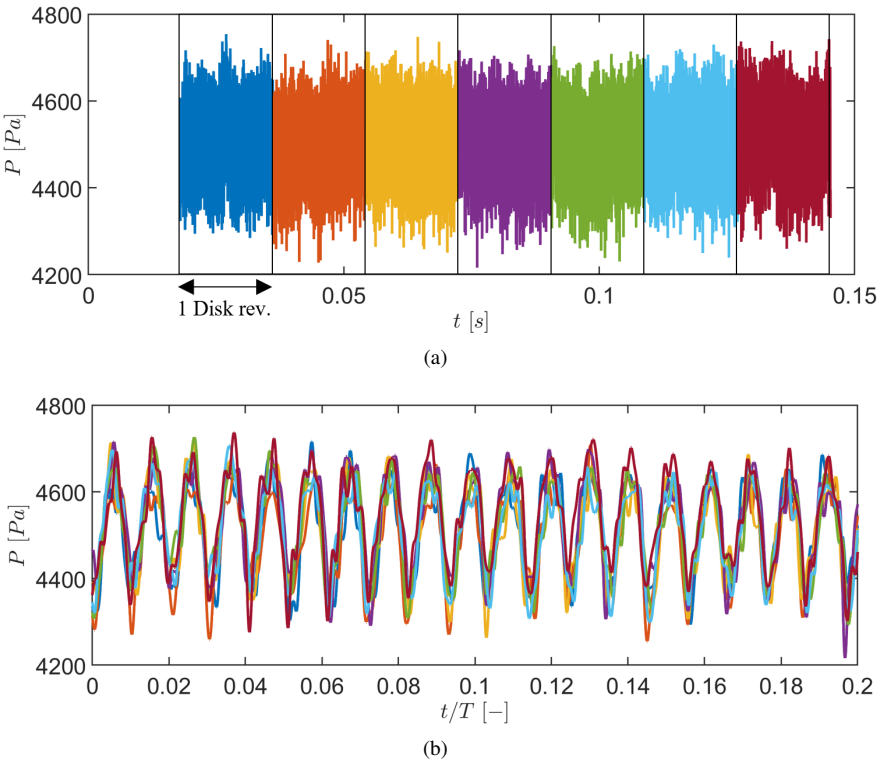

Figure 2.53: Breakdown of WG disk revolutions into periodic events (a) and re-phasing of the WG repeating events over one disk revolution period (b).

over a disc revolution is $\sim$0.0016P_{01} ($\sim$15 Pa). Even though not reported in this thesis, this exercise has been done for different instrumentation, including the fast-response virtual four-hole probe. The maximum difference is of the same order of magnitude for all the fast-response pressure sensors used in the results of this thesis.

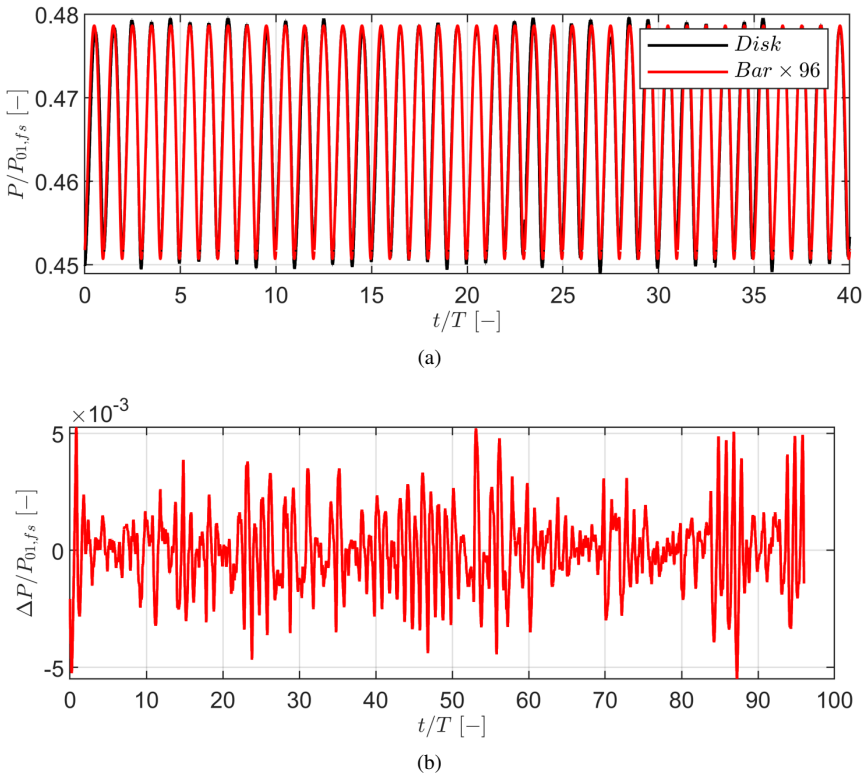

Figure 2.54: Comparison of a signal phase-lock averaged over one disk revolution against one bar passing multiplied by the number of bars in the disk (a) and error from assuming similarity between each bar (b).

The bar passing period is discretized with 227 classes, such that there is at least one point per class at the given sampling frequency and bar passing frequency ($N_{class,opt}$=F_s/F_{bar}). Reducing the number of classes results in more points per class. Fig. 2.55 displays the difference between ensemble-averaged signals with different number of classes against the ensemble-averaged signal with the optimal number of classes (227). As the number of classes is increased above 75, the ensemble-averaged signal has virtually no variation.

The ensemble-averaged periodic component from all time-accurate measurements acquired in the presence of incoming periodic wakes was discretized by 227 classes.

The averaging of a different number of bar passing events has also been addressed in the scope of this work. This was accomplished by studying the evolution of the PLA signal as more repeating events are added to the average. For typical acquisitions of time-accurate measurements, around 15,000 events occur during a sampling time of 3 s. Fig. 2.56(a) displays the evolution of the PLA signal over one bar passing period as the number of averaged

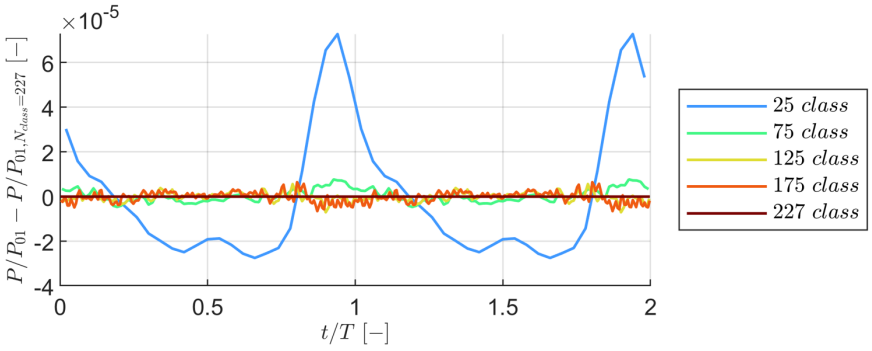

Figure 2.55: Impact of reducing the number of points/per class on PLA signal error.

events increases. The difference between the PLA using the maximum number of events and the PLA using an increasing number of events is displayed in Fig. 2.56(b). The ensemble-average signal has already statistically converged after 200 bar passing events. The maximum number of available events is always used to ensemble-average all the acquired signals. Therefore, the error induced by averaging over a finite signal duration is considered negligible for instantaneous pressure and shear stress measurements.

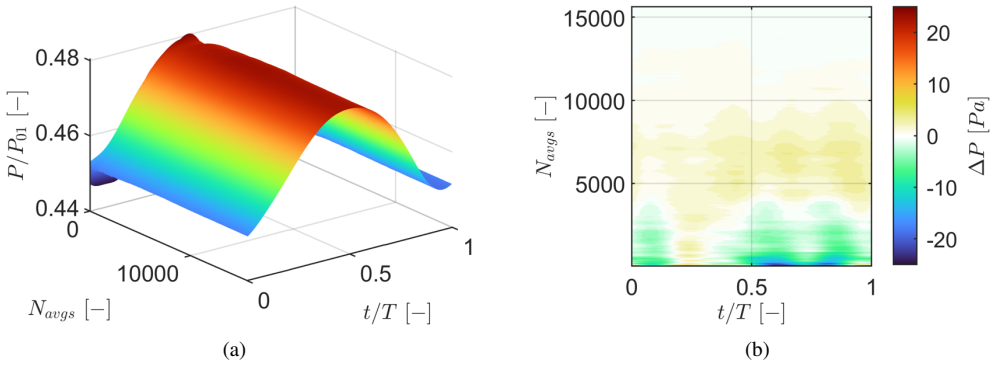

Figure 2.56: Evolution of a phase-lock averaged signal as a function of the number of averaged events (a) and difference between the phase-lock average performed with the maximum number of events and the phase-lock average performed with increasing number of events over one bar passing period (b).

The signal of each bar passing event is compared against the final ensemble-averaged signal in Fig. 2.57(a). For each class, the scattered points from the 15,648 bar passing events were verified to follow a Gaussian distribution as suggested in Fig. 2.57(b) for the class #40.

The person correlation coefficient is used to quantify the correlation between measurements performed with fast-response instrumentation and the wake passing:

$$R^2 = \frac{\sum_{i=1}^{n}(x_i - \bar{x})(y_i - \bar{y})}{\sqrt{\sum_{i=1}^{n}(x_i - \bar{x})^2}\sqrt{\sum_{i=1}^{n}(y_i - \bar{y})^2}} \tag{2.54}$$

The coefficient ranges from zero if an aerothermal quantity is not correlated with the deterministic event to unity if it is perfectly described or modulated by the wake generator

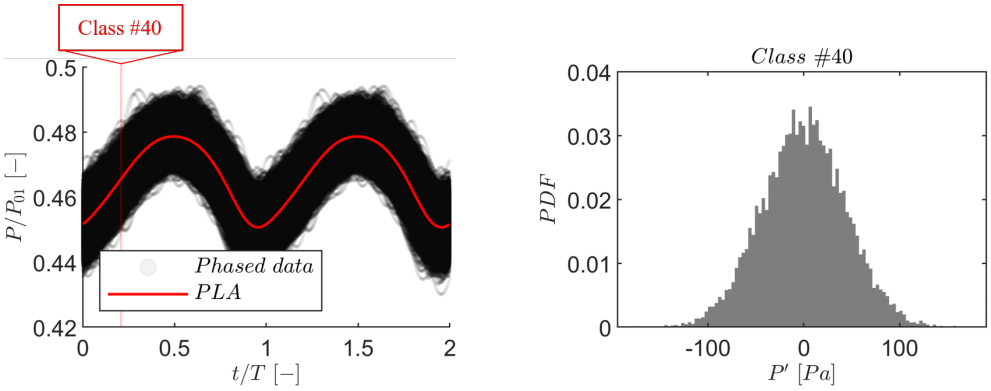

Figure 2.57: Re-phased points for two bar passing periods along the phase-lock average (a) and histogram describing the normal distribution of a set of points belonging to class #40 (b).

bar passing period.

2.6.4 Statistical Moments

The raw/calibrated signals obtained during tests performed with fast-response instrumentation are often characterized through their statistical moments. The definitions of the used statistical moments for a generic quantity Φ(t) are recalled below. The standard deviation used in the scope of this work is defined as:

$$std\left(\Phi(t)\right) = \sqrt{\frac{1}{N-1}\sum_{t=1}^{N}\left|\Phi\left(t\right)-\bar{\Phi}\right|^{2}} \tag{2.55}$$

$\bar{\Phi}$ is the time-mean of $\Phi\left(t\right)$, and N is the number of signal samples. The skewness is defined as:

$$skew\left(\Phi(t)\right) = \frac{\frac{1}{n}\sum_{t=1}^{N}\left(\Phi\left(t\right)-\bar{\Phi}\right)^{3}}{\left(\sqrt{\frac{1}{n}\sum_{t=1}^{N}\left(\Phi\left(t\right)-\bar{\Phi}\right)^{2}}\right)^{3}} \tag{2.56}$$

Lastly, the kurtosis is defined as:

$$kurt\left(\Phi\left(t\right)\right) = \frac{\frac{1}{n}\sum_{t=1}^{N}\left(\Phi\left(t\right)-\bar{\Phi}\right)^{4}}{\left(\frac{1}{n}\sum_{t=1}^{N}\left(\Phi\left(t\right)-\bar{\Phi}\right)^{2}\right)^{2}} \tag{2.57}$$

2.6.5 Turbulence Estimation with Hot-Wire Probes

In transonic and rarefied regimes, the hot-wire output voltage strongly depends on the fluctuations of velocity, density, and total temperature:

$$E_b = f\left(V, \rho, T_0\right) \tag{2.58}$$

A non-dimensional calibration was coupled with a sensitivity analysis and employed to post-process the experimental data, extending the data-reduction methodology described by Cukurel et al. [46]. The fluctuations of flow total temperature were neglected. The sensitivity of the hot-wire to density and velocity fluctuations was obtained through an in-situ calibration performed at relevant Mach and Reynolds numbers. The following sensitivity matrix was used to decouple the velocity and density fluctuations.

$$\begin{bmatrix} S_{\rho 1} & S_{v1} \\ S_{\rho 2} & S_{v2} \end{bmatrix} \begin{bmatrix} \frac{\rho'}{\rho} \\ \frac{V'}{V} \end{bmatrix} = \begin{bmatrix} \frac{E_1'}{E_1} - S_{\alpha 1} * \alpha' \\ \frac{E_2'}{E2} - S_{\alpha 2} * \alpha' \end{bmatrix} \tag{2.59}$$

Subscripts 1 and 2 refer to the two wires of the cross-wire probe. The terms S_α and α' are the wire sensitivity to the yaw angle and the yaw angle fluctuations, respectively. These values were computed before applying the sensitivity system, exploiting the in-situ angular calibration. The fluctuating angle α' is a function of the ratio of the two wires' Nusselt numbers, while the sensitivities S_α for both wires can be computed from the bridge voltage and the knowledge of the local flow angle α:

$$\alpha' = f\left(\frac{Nu_{w1}}{Nu_{w2}}\right) \tag{2.60}$$

$$S_\alpha = f\left(E_{b1,2},\ \alpha\right) \tag{2.61}$$

This methodology provides both velocity fluctuations V' and angle fluctuations α'. The probe head was aligned with the incoming flow; thus, the measured velocity fluctuations are in the mean flow direction. From the knowledge of the instantaneous yaw angle fluctuations, it is possible to decompose the computed velocity in two directions in the blade-to-blade plane, namely V_x'=V' and the perpendicular component V_y'.

Based on the definition of turbulent intensity:

$$TI = \frac{\sqrt{\frac{1}{3}({V_x}'^2 + {V_y}'^2 + {V_z}'^2)}}{V} \tag{2.62}$$

V' corresponds to the root-mean-square level of the fluctuating velocity. The velocity in the denominator is measured at the same location as the fluctuations. Two definitions of turbulence intensity have been derived. The first one assumes that the flow is isotropic (V_x'=V_y'=V_z'). The second one assumes that the third component of turbulence (not obtainable with two wires) is the mean sum of the squares of the measured components. Both definitions are reported in Eq. 2.63 and Eq. 2.64, respectively.

$$TI_{iso} = \frac{\sqrt{{V_x}'^2}}{V} \tag{2.63}$$

$$TI_{aniso} = \frac{\sqrt{\frac{1}{2}({V_x}'^2 + {V_y}'^2)}}{V} \tag{2.64}$$

The integral length scale is considered a measure of the largest eddy size in a turbulent flow. Under the assumption of isotropic turbulence, the integral length scales were computed from the Power Spectral Density function (PSD) of the velocity fluctuations, as proposed by Roach [47]:

$$ILS = V\left[\frac{E\left(f\right)}{4V'^{2}}\right]_{f\to 0} \tag{2.65}$$

To compute $\left[E\left(f\right)\right]_{f\to 0}$, the power spectrum is averaged up to the frequency before the decay.

A thorough description of the hot-wire methodology can be found in [28].

2.6.6 Turbulence Estimation with Fast-Response Probes

The measurement of turbulence with fast-response pressure probes relies on the capability of the probe to measure flow pressure fluctuations, which can be related to velocity fluctuations and, therefore, turbulence.

Wallace and Davis [48] derived a relation between the root mean square of the pressure fluctuations, $\overline{P_0'^2}$, and the flow velocity fluctuations, $\overline{u'^2}$, for compressible flow.

$$\overline{P_0'^2} = 0.49\rho^2\left(1-0.175M^4\right)^2\overline{u'^2}^2 + \rho^2U^2\left(1+0.5M^2\right)^2\overline{u'^2} + 0.7\rho\left(1-0.175M^4\right)\left(1+0.5M^2\right)\overline{u'^3} \tag{2.66}$$

Persico et al. [49] simplified the previous equation by neglecting the term with $\overline{u'^3}$. Since there is only one measuring tap in the yaw plane (left and right tap measurements are obtained at different time instants and therefore flow fluctuations are uncorrelated), turbulence must be assumed isotropic:

$$TI_{iso} = \sqrt{\frac{\overline{u'^2}}{V_{det}^2}} \tag{2.67}$$

In a following work, Persico et al. [50] argued that the sensor senses all three turbulence components rather than the streamwise component. A $\sqrt{3}$ correction factor is applied, assuming isotropic turbulence. Therefore, the turbulence intensity obtained in Eq. 2.67 is divided by the proposed corrective factor to get the final quantity.

The density and Mach number in Eq. 2.66 were replaced by the phase-lock averaged ones. The time-resolved density and Mach number were obtained with the isentropic relations based on the local phase-locked averaged total pressure obtained with the fast-response virtual-four probe. For outlet measurements, the static pressure was the steady endwall static pressure measured at Plane 06. For measurements at Planes 02 and 03, where endwall static pressure taps are unavailable, the local time-averaged static pressure measured at midspan was used instead. The steady inlet total temperature was used alongside the previous quantities. The aero-thermodynamic quantities were computed as:

$$M(\phi) = \sqrt{\frac{2}{\gamma-1}\left[\left(\frac{P_{01}(\phi)}{P_{steady}}\right)^{-\frac{\gamma-1}{\gamma}} - 1\right]} \tag{2.68}$$

$$T(\phi) = \frac{T_{0,steady}}{1 + \frac{\gamma-1}{2} M(\phi)^2} \tag{2.69}$$

$$V(\phi) = M(\phi)a = M(\phi)\sqrt{\gamma RT(\phi)} \tag{2.70}$$

$$\rho(\phi) = \frac{P_{steady}}{RT(\phi)} \tag{2.71}$$

Where ϕ denotes the phase of the quantity. Hence, the term $\overline{P_0'^2}$ is also phase-locked averaged. The latter assumption enables the computation of the turbulence intensity for each phase of the wake generator bar, assuming that the signal at each bar phase for different bar events is correlated. It is recalled that the velocity used to compute the turbulence intensity in Eq. 2.67 is phase-locked averaged and computed according to Eq. 2.70. It is impossible to estimate if the instantaneous flow angle is within the range of insensitive of the probe. Throughout the measurements, the angle deterministic fluctuations in the probe reference system were kept below $\pm 4^\circ$. It is estimated that the stochastic angle fluctuations do not exceed $\pm 1^\circ$, and therefore, the turbulence measurements are performed within the range of insensitivity of the probe.

2.7 Uncertainty Quantification

2.7.1 Definitions and Error Propagation

The measurement uncertainty, U, is evaluated according to the ASME uncertainty method [51]. The errors have been categorized as "random" for errors that varied during the measurement period and as "systematic" for invariant errors during the measurement period. The non-propagated total uncertainty of a measured quantity is estimated according to Equation 2.72.

$$U_{tot} = \sqrt{U_{sys}^2 + U_{rand}^2} \tag{2.72}$$

The expanded uncertainty with a 95% confidence interval can be computed as:

$$U_{tot,95\%} = \pm t_{95}(\nu) \times U_{tot} \tag{2.73}$$

Where $t_{95}(\nu)$ is the t-student distribution and relies on the combined degrees of freedom of the measured quantity. In the scope of this work, the degrees of freedom for systematic uncertainty were assumed to be infinite. For quantities deriving from signals, at least 600 samples were used. There are enough degrees of freedom to consider $t_{95}(\nu) = 2$ in the scope of this work.

For a generic quantity q that is a function of n independent parameters:

$$q = f(\Phi_1, \Phi_1, \Phi_1, ..., \Phi_n) \tag{2.74}$$

The uncertainty propagation into the derived quantity q due to the uncertainty of its parameters is determined through a Taylor Series Method (TSM) by neglecting higher-order terms:

$$U_q = \sqrt{\sum_{n=1}^{n} \left(\frac{\partial q}{\partial \Phi_i} \right)^2} \tag{2.75}$$

The $\partial q/\partial \Phi_i$ represents the sensitivity coefficient expressing the dependence of Φ_i on q. A detailed uncertainty breakdown for the quantities used in this work can be found in Appendix D.

2.7.2 Sources of Uncertainty

The sources of uncertainty derive from the calibration of instrumentation and reference instrumentation used throughout the measurements. The calibration uncertainty is reflected in the measured quantities. The calibration-related sources concern the thermocouple used to measure the inlet temperature (see Section 2.4.2.2), Validyne differential pressure sensors used to monitor the purge flow conditions (see Section 2.4.2.6), and fast-response pressure sensors mounted on the blade, endwall, and fast-response probe.

The thermocouple was calibrated against a reference PT-100 thermocouple. The final calibration uncertainty depends on random and systematic terms. The goodness of fitting mainly impacts the random term, while the systematic terms depend on the hardware used to calibrate the thermocouple: reference PT-100 thermocouple, Isotech Hyperion. Table 2.13 summarizes the uncertainty sources in the thermocouple calibration.

Table 2.13: Uncertainty sources of thermocouple calibration.

Random	$S_{\bar{\mathbb{M}}}$	0.063 K
Systematic	Uncertainty of cold junction	0.26 K
	Readout accuracy for reference probe	0.01 K
	Reference probe calibration uncertainty	0.03 K
	Isotech Hyperion axial uniformity	0.01 K
	Isotech Hyperion radial uniformity	0.01 K
	Total unc.	0.27 K
	Expanded unc. with 95% confidence	0.52 K

The calibration uncertainty of the fast-response pressure sensors, used as a bias during the measurements, was obtained similarly. The calibration uncertainty was split into random and systematic terms. The Kulite sensors were calibrated against the WIKA–P30 as a reference. The uncertainty provided by the manufacturer (25 Pa) was assumed to be expanded with 95% confidence. Therefore, the uncertainty in the Kulite calibration was "non-expanded," assuming a Gaussian distribution. The Kulite manufacturer's reported bias assumed the same. Table 2.14 summarizes the sources of uncertainty for the blade, endwall, and fast-response sensors. The uncertainty is displayed for the severest sensor for the sake of simplicity.

The calibration uncertainty of the Validynes (see Section 2.4.2.6) was obtained similarly to the Kulite. The uncertainty of the GE-Druck calibrator was considered instead of the WIKA–P30. Table 2.15 summarizes the sources of uncertainty in the Validyne calibration.

The calibration uncertainty of the thermocouple, Kulites, and Validynes was propagated into the measured uncertainty as a systematic error. The scanners used to measure the endwall

Table 2.14: Uncertainty sources of Kulite calibration.

		Blade	FRV4H	Endwall
Random	$S_{\bar{\mathbb{M}}}$	2.87 Pa	2.98 Pa	8.97 Pa
Systematic	Accuracy of WIKA–P30	12.76 Pa	12.76 Pa	12.76 Pa
	Sensor bias - Manufacturer	17.86 Pa	17.86 Pa	17.86 Pa
	Total unc.	22.13 Pa	22.15 Pa	23.71 Pa
	Expanded unc. with 95% confidence	43.38 Pa	43.41 Pa	46.46 Pa

Table 2.15: Uncertainty sources of Validyne calibration.

		V1	V2
Random	$S_{\bar{\mathbb{M}}}$	0.02 Pa	2.97 Pa
Systematic	Accuracy of Calibrator	0.06 Pa	3.50 Pa
	Sensor bias - Manufacturer	1.40 Pa	8.93 Pa
	Total unc.	1.41 Pa	10.04 Pa
	Expanded unc. with 95% confidence	2.81 Pa	20.08 Pa

static pressure at Planes 02 and 06 were not calibrated in-house. The manufacturer's bias was taken to be expanded with a Gaussian distribution. The unexpanded uncertainty, 2.11 Pa for the Scanivalve MPS4264–1 psi and 7.04 Pa for Scanivalve MPS4264–2.5 psi, was used as a source for pneumatic measurements.

Lastly, the probe positioning in the test rig was achieved employing a Mitutoyo inclinometer with a precision of $\pm 0.10^{\circ}$. The latter was taken as a source of uncertainty as well.

2.7.3 Measurement Uncertainties

Table 2.16 contains the expanded uncertainty with a 95% confidence interval of quantities used in this work. The uncertainties reported in Table 2.16 show that systematic terms contribute the most to the overall measurement uncertainty. As a general consideration, the difference between the same measurement performed at different operating points (in terms of cascade operating exit Mach number and Reynolds number) and/or pitch and span locations is not markedly affected by systematic errors, being the quantities measured by the same calibrated transducers and measurement chains over a relatively unchanged experimental setup [52]. For these reasons, the uncertainty in comparing the measurements in this work is dominated by random error terms with minimal systematic uncertainty.

Table 2.16: Breakdown of uncertainty expanded with 95% confidence interval.

Quantity	Symbol	Unit	Value	U_{rand}	U_{sys}
Fixed instrumentation/Blade/Endwalls - Pneumatic					
Inlet total temperature	T_{ref}	K	304.90	0.002	0.518
Static pressure	P	Pa	5820	0.95	28.55
Isentropic Mach number	M_{is}	–	0.905	0.0007	0.0054
Blade chord	C	m	0.052285	0.000	0.001
Isentropic Reynolds number	Re_{is}	–	71611	59	1438

Rotational velocity of WG	Ω	RPM	3300	0.003	0.098
WG bar phase	t/T	–	–	0.004	0.003
Strouhal number	f^+	–	0.94	0.0007	0.0185
Purge massflow rate	PMFR	Abs. %	0.90	0.0020	0.0020
Blade - Fast-Response					
Static pressure	P	Pa	4612	0.11	43.22
Norm. pressure fluctuations	$\Delta P/P_{01}$	–	0.100	0.000	0.004
Isentropic Mach number	M_{is}	–	0.495	0.0006	0.0082
Endwall - Fast-Response					
Static pressure	P	Pa	4612	0.13	46.04
Isentropic Mach number	M_{is}	–	0.495	0.0006	0.0087
Preston tube					
Total pressure	P_{BL}	Pa	9307	0.95	25.36
PBl over P01	P_{BL}/P_{01}	–	0.9996	0.0007	0.0040
PBl over P1stat	P_{BL}/P_1	–	1.1518	0.0002	0.0054
Mach number	M_{BL}	–	0.455	0.0006	0.0031
VBL over Vfs	V_{BL}/V_{fs}	–	1.000	0.001	0.008
C5HP					
Probe placement angle in rig		$^\circ$	30.40	0.0000	0.1960
Total pressure	P_{02}	Pa	9715	5.57	36.83
Static pressure	P_2	Pa	8520	5.57	28.67
Yaw angle	α	$^\circ$	4.77	0.20	1.45
Pitch angle	γ	$^\circ$	0.83	0.20	0.82
Mach number	M_2	–	0.437	0.00159	0.00834
FRV4HP					
Probe placement angle in rig		$^\circ$	54.00	0.0000	0.1960
Total pressure	P_{06}	Pa	10032	8.72	47.33
Static pressure	P_6	Pa	6333	8.74	89.09
Yaw angle	α	$^\circ$	2.24	0.22	0.71
Pitch angle	γ	$^\circ$	-0.32	0.10	2.24
Mach number	M_6	–	0.838	0.00208	0.01778
L5HP					
Probe placement angle in rig		$^\circ$	54.00	0.0000	0.1960
Total pressure	P_{06}	Pa	10032	5.96	35.94
Static pressure	P_6	Pa	6333	5.96	22.87
Yaw angle	α	$^\circ$	2.24	0.20	0.36
Pitch angle	γ	$^\circ$	-0.32	0.20	0.31
Mach number	M_6	–	0.838	0.00138	0.00511
Derived Quantities					
Turbulence grid loss coeff.	Y_{TG+WG}	–	0.0590	0.00070	0.00174
Inlet total pressure - Correlation	P_{01}	Pa	9901	7.09	29.82
With C5HP					
Inlet Primary flow direction	β_{in}	$^\circ$	35.18	0.24	0.96
Inlet cascade pitch angle	γ_{in}	$^\circ$	1.02	0.24	0.73
Inlet incidence	i	$^\circ$	2.12	0.31	0.98
P02 over P01	P_{02}/P_{01}	–	1.0005	0.001	0.005

P2stat over P01	P_2/P_{01}	–	0.8774	0.001	0.004
With FRV4HP					
Inlet Primary flow direction	β_{in}	°	35.18	0.23	1.65
Inlet cascade pitch angle	γ_{in}	°	1.02	0.24	2.75
Inlet incidence	i	°	2.12	0.30	1.66
P02 over P01	P_{02}/P_{01}	–	1.0005	0.001	0.006
P2stat over P01	P_2/P_{01}	–	0.8774	0.001	0.011
Outlet Primary flow direction	β_{out}	°	51.76	0.16	1.00
Outlet cascade pitch angle	γ_{out}	°	-0.52	0.13	1.24
Outlet deviation	d	°	-2.04	0.25	1.02
P06 over P01	P_{06}/P_{01}	–	1.0017	0.001	0.006
P6stat over P01	P_6/P_{01}	–	0.6324	0.001	0.009
Energy loss coefficient	ξ	–	0.1500	0.0023	0.0114
Secondary kinetic energy coeff.	K_{SKE}	–	0.0097	0.0001	0.0021
With L5HP					
Outlet Primary flow direction	β_{out}	°	51.7601	0.15	0.33
Outlet cascade pitch angle	γ_{out}	°	-0.5188	0.13	0.21
Outlet deviation	d	°	-2.04	0.25	0.38
P06 over P01	P_{06}/P_{01}	–	1.0017	0.001	0.005
P6stat over P01	P_6/P_{01}	–	0.6324	0.001	0.003
Energy loss coefficient	ξ	–	0.1500	0.0019	0.0095
Secondary kinetic energy coeff.	K_{SKE}	–	0.03	0.0015	0.0020
Hot wire anemometry					
Velocity	u	$\% \overline{U}$	150.30	0.002%	2.33%
Turbulence intensity	TI	% u	2.40	–	0.20%
Integral length scale	ILS	mm	12	–	3.92

2.8 Phases of Testing

During the SPLEEN experimental campaign, the measurements were divided into three phases with increasing engine-resemblance. The first test consisted of on- and off-design tests under steady inlet flow. The wake generator was then introduced during the second phase of testing. On- and off-design measurements were performed at midspan. The secondary flows were investigated at the design point. Lastly, the cavity purge flow system was introduced and tested alongside the wake generator during the third phase. Measurements were performed at different purge massflow ratios. The testing phases are summarized in Table 2.17.

Table 2.17: Experimental campaign phases.

Phase.	WG	WG support	Cavity slot
1	No	–	No
2	Yes	Cylindrical	No
3	Yes	Elliptical	Yes

References

[1] T. Arts. *Aerodynamic performance of two very high lift low pressure turbine airfoils (T106C–T2) at low Reynolds and high Mach numbers*. In 5th European Conference for Aerospace Sciences, Munich, Germany, 2013.

[2] J. Clinckemaillie, L. Fattorini, T. Fontani, C. Nuyts, G. Wain, and T. Arts. *Aerodynamic performance of a very-high-lift low-pressure turbine airfoil (T106C) at low Reynolds and high Mach number including the effect of incoming periodic wakes*. 11th European Conference on Turbomachinery Fluid Dynamics and Thermodynamics, ETC 2015, 01 2015.

[3] J. MichAlek, M. Monaldi, and T. Arts. *Aerodynamic Performance of a Very High Lift Low Pressure Turbine Airfoil (T106C) at Low Reynolds and High Mach Number With Effect of Free Stream Turbulence Intensity*. Journal of Turbomachinery, 134(6), 08 2012. 061009.

[4] ASME. *Measurement of Fluid Flow in Pipes Using Orifice, Nozzle, and Venturi*. MFC-3M, 2004.

[5] M.J. Brear, H.P. Hodson, P. Gonzalez, and N.W. Harvey. *Pressure Surface Separations in Low-Pressure Turbines—Part 2: Interactions With the Secondary Flow*. Journal of Turbomachinery, 124(3):402–409, 07 2002.

[6] H. Pfeil and J. Eifler. *On the question of the shear stress distribution for the plane free turbulent flows*. Research in Engineering A, 41:105–112, 1975.

[7] Giovanna B., Giuseppe F., Antonio P., Massimiliano M., and Roberto A. *Purge flow and interface gap geometry influence on the aero-thermal performance of a rotor blade cascade*. International Journal of Heat and Fluid Flow, 44:563–575, 2013.

[8] E. de la Rosa Blanco, H.P. Hodson, and R. Vazquez. *Effect of the Leakage Flows and the Upstream Platform Geometry on the Endwall Flows of a Turbine Cascade*. Journal of Turbomachinery, 131(1), 10 2008. 011004.

[9] W. Gracey, W. Letko, and W.R Russell. *Wind-tunnel investigation of a number of total-pressure tubes at high angles of attack subsonic speeds*. Technical report, NATIONAL AERONAUTICS AND SPACE ADMINISTRATION HAMPTON VA LANGLEY RESEARCH CENTER, 1951.

[10] M. Barker. *On the use of very small pitot-tubes for measuring wind velocity*. Proceedings of the Royal Society of London.Series A, Containing Papers of a Mathematical and Physical Character, 101(712):435–445, 1922.

[11] F.A. MacMillan. *Experiments on Pitot-tubes in shear flow*. 1956.

[12] A.L. Treaster and A.M. Yocum. *The calibration and application of five-hole probes*. Technical report, Pennsylvania State Univ University Park Applied Research Lab, 1978.

[13] B.F. Hall and T. Povey. *The Oxford Probe: an open access five-hole probe for aerodynamic measurements*. Measurement Science and Technology, 28(3):035004, jan 2017.

[14] T. Yasa and G. Paniagua. *Robust procedure for multi-hole probe data processing*. Flow Measurement and Instrumentation, 26:46–54, 2012.

[15] I. Bosdas, M. Mansour, A.I. Kalfas, R.S. Abhari, and S. Senoo. *Unsteady Wet Steam Flow Field Measurements in the Last Stage of Low Pressure Steam Turbine*. Journal of Engineering for Gas Turbines and Power, 138(3), 09 2015. 032601.

[16] C. Lenherr, A.I. Kalfas, and R.S. Abhari. *High temperature fast response aerodynamic probe*. Journal of engineering for gas turbines and power, 133(1), 2011.

[17] J. Clinckemaillie and T. Arts. *Characterization of Periodic Incoming Wakes in a Low-Pressure Turbine Cascade Test Section by Means of a Fast-Response Single Sensor Virtual Three-Hole Probe*. International Journal of Turbomachinery, Propulsion and Power, 4(3), 2019.

[18] P. Gaetani and G. Persico. *Technology Development of Fast-Response Aerodynamic Pressure Probes*. International Journal of Turbomachinery, Propulsion and Power, 5(2), 2020.

[19] A. Pfau, J. Schlienger, A. I Kalfas, and R.S. Abhari. *Virtual four sensor fast response aerodynamic probe (FRAP®)*. In E3S Web of Conferences, volume 345, page 01014. EDP Sciences, 2022.

[20] R.D. Blevins. *Flow-induced vibration*. 1977.

[21] E. Boufidi, M. Alati, F. Fontaneto, and S. Lavagnoli. *Design and Testing of a Miniaturized Five-Hole Fast Response Pressure Probe With Large Frequency Bandwidth and High Angular Sensitivity*. Journal of Engineering for Gas Turbines and Power, 141(10), 09 2019.

[22] G. Persico, P. Gaetani, and A. Guardone. *Design and analysis of new concept fast-response pressure probes*. Measurement Science and Technology, 16(9):1741, 2005.

[23] A.C. Chasoglou, M. Mansour, A.I. Kalfas, and R.S. Abhari. *A novel 4-sensor fast-response aerodynamic probe for non-isotropic turbulence measurement in turbomachinery flows*. Journal of the Global Power and Propulsion Society, 2:362–375, 2018.

[24] J.F. Brouckaert. *Development of Fast Response Aerodynamic Pressure Probes for Time-resolved Measurements in Turbomachines: Thesis Presented in Order to Obtain the Degree of Docteur en Sciences Appliquées, Université Libre de Bruxelles, October 2002*. Von Karman institute for fluid dynamics, 2004.

[25] J.O. Hougen, O.R. Martin, and R.A. Walsh. *Dynamics of pneumatic transmission lines*. Control Engineering, 10(9):114–117, 1963.

[26] U. Ingard. *On the theory and design of acoustic resonators*. The Journal of the acoustical society of America, 25(6):1037–1061, 1953.

[27] H. Bergh and H. Tijdeman. *Theoretical and experimental results for the dynamic response of pressure measuring systems*. 1965.

[28] G. Pastorino, L. Simonassi, G. Lopes, E. Boufidi, F. Fontaneto, and S. Lavagnoli. *Measurements of Turbulence in Compressible Low-Density Flows at the Inlet of a Transonic Linear Cascade With and Without Unsteady Wakes*. Journal of Turbomachinery, pages 1–26, 12 2023.

[29] B.J. Bellhouse and D.L. Schultz. *Determination of mean and dynamic skin friction, separation and transition in low-speed flow with a thin-film heated element*. Journal of Fluid Mechanics, 24(2):379–400, 1966.

[30] D.E. Halstead, D.C. Wisler, T.H. Okiishi, G.J. Walker, H.P. Hodson, and H.W. Shin. *Boundary Layer Development in Axial Compressors and Turbines: Part 1 of 4—Composite Picture*. Journal of Turbomachinery, 119(1):114–127, 01 1997.

[31] M.L.G. Oldfield, R. Kiock, A.T. Holmes, and C.G. Graham. *Boundary Layer Studies on Highly Loaded Cascades using Heated Thin Films and a Traversing Probe*. Journal of Engineering for Power, 103(1):237–246, 01 1981.

[32] P. Pucher and R. Gohl. *Experimental Investigation of Boundary Layer Separation With Heated Thin-Film Sensors*. Journal of Turbomachinery, 109(2):303–309, 04 1987.

[33] H.P. Hodson. *The detection of boundary layer transition and separation in high speed turbine cascades*. 1983.

[34] H.P. Hodson, I. Huntsman, and A.B. Steele. *An Investigation of Boundary Layer Development in a Multistage LP Turbine*. Journal of Turbomachinery, 116(3):375–383, 07 1994.

[35] M. Hultmark and A.J. Smits. *Temperature corrections for constant temperature and constant current hot-wire anemometers*. Measurement Science and Technology, 21(10):105404, aug 2010.

[36] ISO. *Measurement of fluid flow by means of pressure differential devices inserted in circular-cross section conduits running full - Part 2: Orifice plates*. 5167-2, 2003.

[37] T.A. Jankowski, E.N. Schmierer, F.C. Prenger, and S.P. Ashworth. *A Series Pressure Drop Representation for Flow Through Orifice Tubes*. Journal of Fluids Engineering, 130(5), 05 2008. 051204.

[38] F.C. Johansen. *Flow through pipe orifices at low Reynolds numbers*. Proceedings of the royal society of London.series A, containing Papers of a Mathematical and Physical character, 126(801):231–245, 1930.

[39] J.D. Denton. *The 1993 IGTI Scholar Lecture: Loss Mechanisms in Turbomachines*. Journal of Turbomachinery, 115(4):621–656, 10 1993.

[40] L.E. Brown. *Axial Flow Compressor and Turbine Loss Coefficients: A Comparison of Several Parameters*. Journal of Engineering for Power, 94(3):193–201, 07 1972.

[41] D.G. Gregory-Smith, C.P. Graves, and J.A. Walsh. *Growth of Secondary Losses and Vorticity in an Axial Turbine Cascade*. Journal of Turbomachinery, 110(1):1–8, 01 1988.

[42] F. Taremi. *Endwall flows in transonic turbine cascades*. PhD thesis, Carleton University, 2013.

[43] A. El Ella and M.M. Hamza. *Investigation of the Effects of an Upstream Cavity on the Secondary Flow in Transonic Turbine Blade Passages with Endwall Contouring*. PhD thesis, Carleton University, 2015.

[44] M. Yaras and S.A. Sjolander. *Development of the Tip-Leakage Flow Downstream of a Planar Cascade of Turbine Blades: Vorticity Field*. Journal of Turbomachinery, 112(4):609–617, 10 1990.

[45] A. Prasad. *Calculation of the Mixed-Out State in Turbomachine Flows*. Journal of Turbomachinery, 127(3):564–572, 03 2004.

[46] B. Cukurel, S. Acarer, and T. Arts. *A novel perspective to high-speed cross-hot-wire calibration methodology*. Experiments in fluids, 53:1073–1085, 2012.

[47] P.E. Roach. *The generation of nearly isotropic turbulence by means of grids*. International Journal of Heat and Fluid Flow, 8(2):82–92, 1987.

[48] J.D. Wallace and M.R.D. Davis. *Turbulence measurements with a calibrated pitot mounted pressure transducer*. In 13th Symposium on Measuring Techniques in Turbomachinery, Zürich, 1996.

[49] G. Persico, P. Gaetani, and B. Paradiso. *Estimation of turbulence by single-sensor pressure probes*. In Proceedings of the XIX Biannual Symposium on Measuring Techniques in Turbomachinery Transonic and Supersonic Flow in Cascades and Turbomachines, 2008.

[50] G. Persico, V. Dossena, and P. Gaetani. *On the Capability of Fast Response Total Pressure Probes toMeasure Turbulence Kinetic Energy*. In XX Biannual Symposium on Measuring Techniques in Turbomachinery, Milano, Italy, 2010.

[51] R.B. Abernethy, R.P. Benedict, and R.B. Dowdell. *ASME Measurement Uncertainty*. Journal of Fluids Engineering, 107(2):161–164, 06 1985.

[52] h.W. Coleman and W.G. Steele. *Experimentation, validation, and uncertainty analysis for engineers*. John Wiley & Sons, 2018.

3 Numerical Methods

Numerical methods have been employed to complement the experiments. In particular, the numerical tools were used to obtain the blade loading and boundary layer parameters required for loss modeling applications. The implicit solver MISES was used to get calibrated blade loadings that accurately predict the laminar separation bubble. The loss breakdown section uses the boundary layer parameters (see Section 7.1). In addition, transitional RANS simulations were used to address the capability of current transition models to capture the extent of the laminar separation bubble on the suction side. The RANS results were also used to get insight into the passage flow in the presence of a shock.

This chapter highlights the numerical tools used in the scope of this work. It highlights the sensitivity to several parameters, including mesh size, incidence, and turbulent quantities, to justify the choice of modeling parameters.

3.1 Coupled Viscous-Inviscid Computations

MISES is a coupled viscous-inviscid flow solver that models the flow with the steady Euler equations and integral boundary layer equations. The solver and assumptions are described in [1]. A particularity of the code is that it employs a modified version of the Abu-Ghannam and Shaw (AGS) [2] transition model depicted by Drela [3]. Transition onset is defined in terms of momentum thickness, Reynolds number, freestream turbulence intensity, and the Thwaites parameter.

The Abu-Ghannam and Shaw model does not explicitly account for the effect of the length scale. Several authors attempted to define an effective turbulence that relies on the length scale. However, Dick and Kubacki [4] defended that no correction based on the length scale should be applied based on the state-of-the-art in transition modeling. In addition, the location at which the turbulence is defined on the blade surface is ambiguous.

MISES requires the specification of a blunt trailing edge. The influence of blunt trailing

edges is treated with a two-equation lag-dissipation closure integral boundary layer formulation that treats the wake as a viscous layer and matches the viscous layer at the pressure and suction sides boundary layer at the trailing edge [5].

3.1.1 Boundary Conditions

The definition of boundary conditions is case-dependent. In the scope of this work, the ratio of outlet static pressure to inlet total pressure ratio has been forced to be the same as the experimentally measured ones. The solver also requires the inlet Reynolds number based on the axial chord as an input boundary condition. The Reynolds number was computed using the pressure ratio and fixed experimental-relevant total temperature. A total temperature of 300 K was used.

MISES has been used solely for the steady flow cases. The flow boundary conditions imposed are contained in Table 3.1.

Table 3.1: Inlet boundary conditions to MISES flow solver.

$M_{out}\,[-]$	$Re_{out}\,[-]$	$P/P_{01}\,[-]$	$Re_{in} = V_{in}C_{ax}\rho_{in}/\mu_{in}\,[-]$
0.70	65000	0.721	59193
0.80	65000	0.655	59193
0.90	65000	0.592	59193
0.70	70000	0.720	63746
0.80	70000	0.653	63746
0.90	70000	0.592	63746
0.95	70000	0.557	63746
0.70	100000	0.719	91066
0.80	100000	0.658	91066
0.90	100000	0.591	91066
0.95	100000	0.559	91066
0.70	120000	0.719	109280
0.80	120000	0.656	109280
0.90	120000	0.592	109280
0.95	120000	0.561	109280

3.1.2 Mesh

The mesh generated by the MISES grid generator is displayed in Fig. 3.1. The mesh is repeated to aid the visualization. The inlet plane has been extended one axial chord upstream of the blade leading edge, while the outlet plane has been extended one axial chord downstream of the trailing edge.

The mesh-defining parameters are also highlighted:

- N_{strm}: number of stream tubes used to discretize domain in pitchwise direction,
- N_{in}: number of segments to discretize the inlet portion of the flowfield in the axial direction,

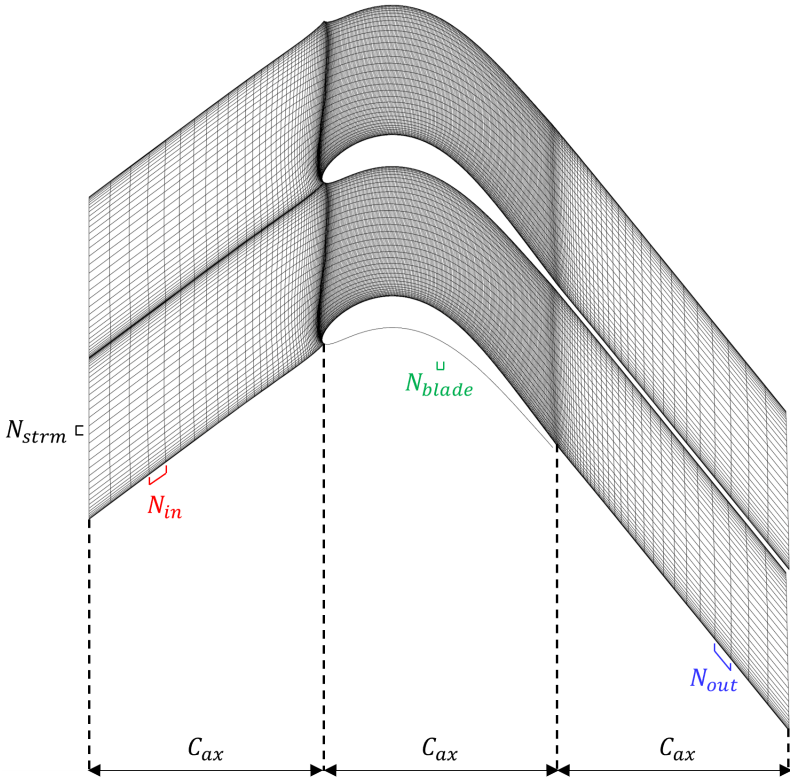

Figure 3.1: MISES flow domain and mesh.

- N_{out}: number of segments to discretize outlet portion of the flowfield in the axial direction,
- N_{blade}: number of segments to discretize blade surface portion of the flowfield in the axial direction.

A mesh sensitivity study has been performed to address the dependency of mesh refinement on blade loading. Five meshes were investigated (see Table 3.2).

Table 3.2: Mesh parameters for MISES computations.

Name	N_{strm}	N_{in}	N_{out}	N_{blade}	Total elements
M1	20	20	20	25	1178
M2	30	30	30	50	3103
M3	40	40	40	100	6903
M4	40	40	40	200	10803
M5	40	40	40	400	18603

The flow incidence and turbulence intensity used in the mesh sensitivity study were $0°$ and 0.40%, respectively. The turbulence intensity differs from the one measured experimentally at the cascade inlet ($\sim$2.50%). However, the lower turbulence intensity improved the agreement between the experimental data and the MISES results (see Section 3.1.4).

Fig. 3.2(a) displays the surface isentropic Mach number along the normalized surface length, s/S_L, for a flow case characterized by a pronounced laminar separation bubble (M=0.70; Re=120k). The bubble extends from s/$S_L\approx$0.60 to 0.77. Differences in the loading are barely perceived. The same can be concluded for the nominal flow case in Fig. 3.2(b).

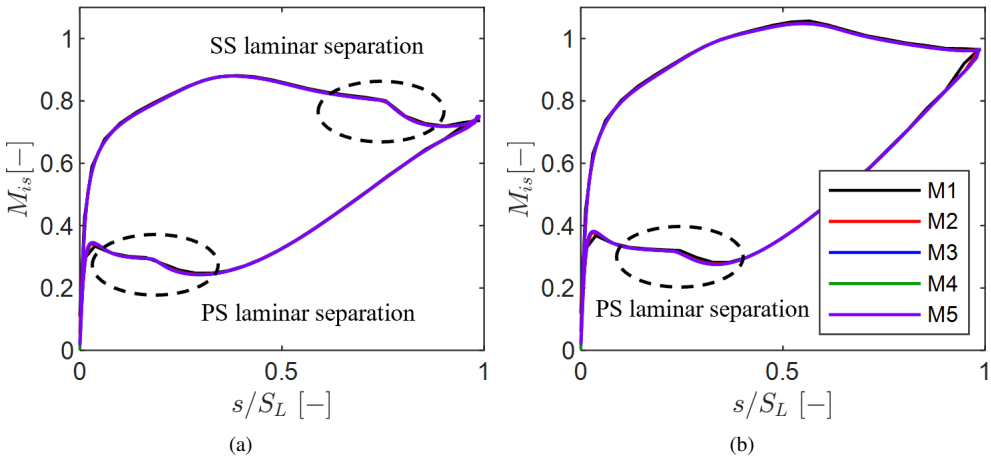

Figure 3.2: Blade surface isentropic Mach number for a case with closed laminar separation bubble (a) and nominal flow case (b).

The relative error, ϵ, in the surface isentropic Mach number between the most refined mesh (M5) and the remaining for the M=0.70; Re=120k flow case is displayed in Fig. 3.3.

The relative error was computed locally for each spatial location. The error is expressed along the normalized surface length, where the negative coordinate represents the blade pressure side. Errors in the isentropic Mach number are restrained within $\pm 1\%$ except near the leading edge. The error decreases with the mesh density. For the second-to-most refined mesh, errors in the region of the pressure side separation bubble ($s/S_L \in$ [-0.21, -0.08]) are still present. However, an error below 0.005 has been considered satisfactory in the scope of this work. Therefore, the mesh M4 has been selected to proceed with the MISES computations.

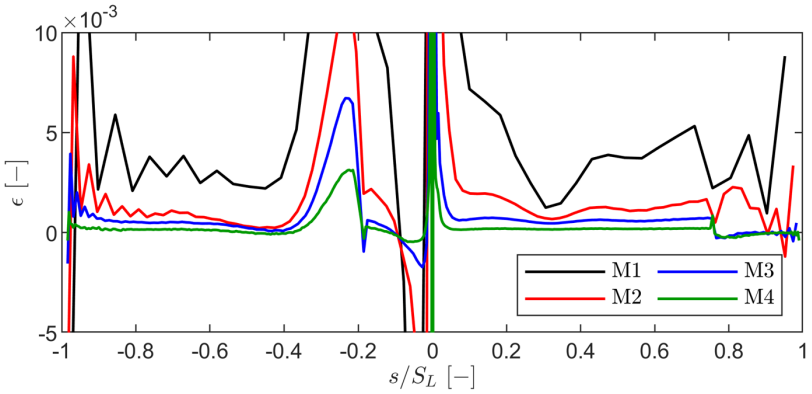

Figure 3.3: Mesh sensitivity: relative error in blade isentropic Mach number compared to mesh M5.

3.1.3 Incidence Sensitivity

An incidence sensitivity study was performed to estimate the inlet flow incidence that best matched the front portion of the experimental blade loading. The status of the boundary layer in the aft portion of the blade suction side can detriment the blade loading past the velocity peak due to the laminar separation bubble often present in low-pressure turbine blading.

Typically, as the extent of the laminar separation bubble increases (due to a reduction of the flow Reynolds number), the suction side loading collapses due to the non-local effect of the separated region [6]. Therefore, the incidence study was performed for the lowest Mach number and highest Reynolds number investigated: M=0.70; Re=120k. The incidence has been varied in the $\pm 2.00°$ range in steps of $0.10°$.

Fig. 3.4 displays the surface isentropic Mach number distribution on the blade pressure and suction sides. The blade loadings are colored according to the flow incidence where the blue end denotes an incidence of -2° and red indicates an incidence of +2°. The MISES computation performed with the AGS model and freestream turbulence of 0.40% manages to retrieve the laminar separation bubble. However, the front part of the loading up to the velocity peak is still reduced compared to the experimental one (see the zoomed region in Fig. 3.4). The laminar separation bubble has a non-local effect on the loading. The pressure side separation bubble was also successfully captured. The sensitivity of the pressure side separation bubble to incidence can be perceived in the second zoomed insert in Fig. 3.4.

Fig. 3.5 contains the relative error in the isentropic Mach number between the MISES results and the experimental loading. Concerning the suction side, the portion of the blade

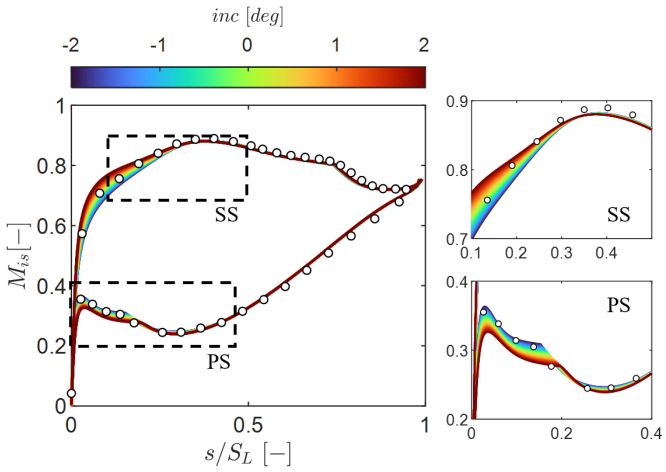

Figure 3.4: MISES with AGS transition model: Blade surface isentropic Mach number as a function of incidence for M=0.70; Re=120k flow case.

loading from the leading edge to the velocity peak was used to compute the error as a sum of the contribution of each spatial location:

$$\epsilon = \sqrt{\frac{1}{N}\sum_{i=0}^{N}\left(M_{exp,i} - M_{MISES,i}\right)^2} \tag{3.1}$$

Where N is the number of experimental data points up to the velocity peak (the MISES results have been interpolated at the locations). On the pressure side, the error was computed using sensors ranging from the second one up to the one where the lowest Mach number was measured.

For the chosen boundary conditions, the lowest error to the suction side experimental loading was found to be near 0.007 and was retrieved for an incidence of -0.10°. However, if the pressure side loading is accounted for instead, the incidence that best represents the loading is -1.00°, with an error of 0.008. Using the incidence that provides the best pressure side matching would imply that modeling the pressure side separation bubble is trustworthy. Due to the transition model limitations, the incidence that provides the best agreement of the suction side portion of the loading was preferred.

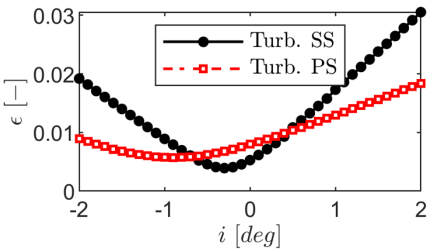

Figure 3.5: Relative error in isentropic Mach number between MISES and experimental loading for the transitional case at M=0.70; Re=120k.

To decouple the effect that the laminar separation has on the overall suction side loading, a MISES computation with a tripped boundary layer was performed for the same flow condition as above. The isentropic Mach number distribution along the normalized pressure side and suction side surfaces is displayed in Fig. 3.6. In the suction side zoomed region (top-right), one can observe that the velocity peak was retrieved. A zoomed insert on the PS is included for completeness. However, no pressure side separation bubble is formed due to the boundary layer tripping.

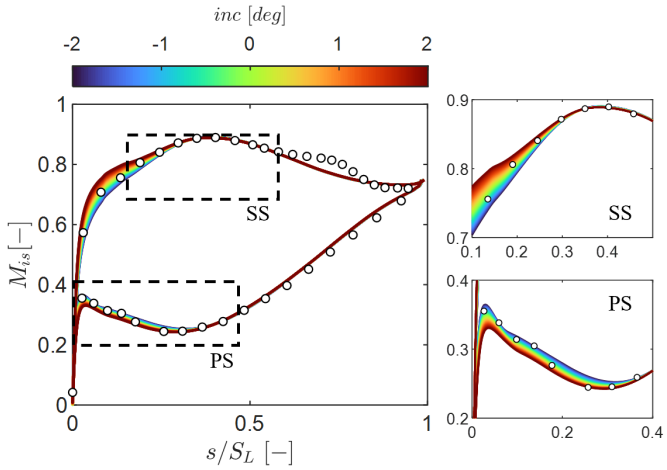

Figure 3.6: MISES with tripped boundary layer (fully turbulent): Blade surface isentropic Mach number as a function of incidence for M=0.70; Re=120k flow case.

Fig. 3.7 displays the relative error in the blade loading between the MISES and experimental data. As a result of tripping the boundary layer at the leading edge, the relative error between the MISES and experiments has been reduced further (below 0.005). A shift of the incidence towards -0.30° that allows the best loading also occurred.

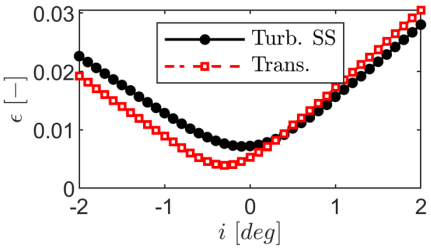

Figure 3.7: Relative error in isentropic Mach number between MISES and experimental loading for the transitional case at M=0.70; Re=120k.

The subtle variation in incidence between the transitional and turbulent cases does not significantly impact the boundary layer quantities along the blade surface. An incidence of -0.30° was used throughout the MISES computations used in this work.

3.1.4 Sensitivity to Turbulence

The Abu-Ghannam Shaw transition model was developed with low-speed testing data under adverse pressure gradients and turbulence levels in the ∼1.00–9.00%. Its implementation into MISES relies solely on the turbulence intensity as an input boundary condition. The solver computes the momentum thickness Reynolds number and Thwaites parameter that completes the model.

A turbulence intensity sensitivity study challenged the model's applicability to the current test case. The turbulence intensity was varied between 0.10% and 3.00% in increments of 0.10%. The M=0.70; Re=120k flow case was considered due to the closed laminar separation bubble.

Fig. 3.8 displays the surface Reynolds number on the blade pressure and suction sides. The color of each loading is associated with the input turbulence intensity. The turbulence intensity significantly impacts the aft portion of the suction side loading. A zoomed-in region on the top-right of Fig. 3.8 highlights the loading topology with varying turbulence intensity. For the turbulence level measured experimentally (∼2.40%), a separation bubble is still present even though its extent is considerably lower than the experimentally measured loading. A decrease in turbulence intensity increases the laminar separation bubble extent and improves the agreement between the MISES and experiments.

The turbulence level also impacts the pressure side (see the zoomed-in region on the bottom-right of Fig. 3.8). Opposite to the suction side findings, the agreement between the experiments and MISES decreases with the decrease in turbulence level. The same effect was found for all the investigated flow conditions.

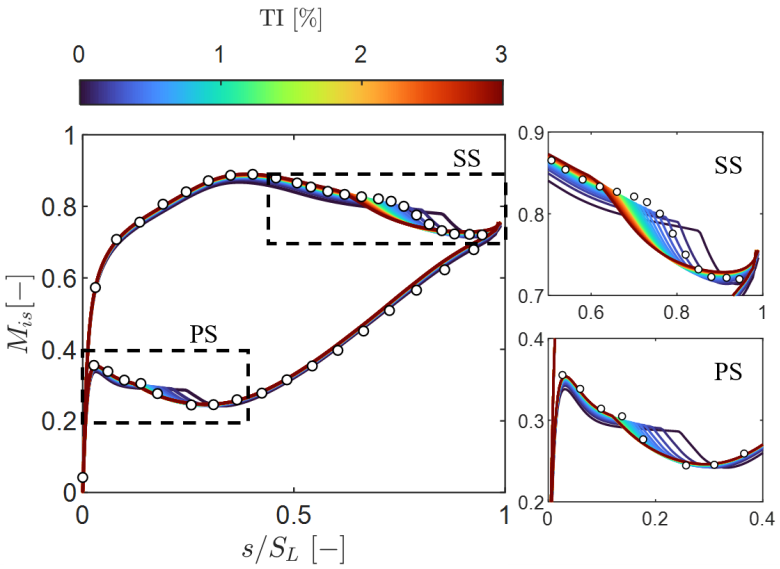

Figure 3.8: Turbulence sensitivity: surface isentropic Mach number distribution along the normalized surface length. Zoomed-in regions of suction side laminar separation bubble (top-right) and pressure side separation (bottom-right).

The suction side loading relative error between the experiments and MISES was com-

puted as the sum of contributions from the data points ranging from the velocity peak to the last sensor near the trailing edge on the suction side (see Eq. 3.1). The pressure side loading relative error accounted for sensors ranging from the second sensor on the pressure side to the one recording the lowest Mach number.

The suction and pressure side loading relative error in the function of the input turbulence intensity is displayed in Fig. 3.9. For the investigated flow case, a turbulence intensity of 0.40% was found to keep the relative error of the suction side loading below 0.01. The lowest error is achieved if the pressure side loading is considered. For a turbulence intensity of 1%, an error of 0.005 was recorded.

In the scope of this work, it was considered that matching the suction side loading was of high relevance due to the higher contribution of the suction side boundary layer on the profile loss in low-pressure turbines compared to the pressure side [7]. The same exercise was performed for the remaining flow conditions, and the same conclusions were attained. For this reason, a turbulence intensity of 0.40% was used as a boundary condition for the MISES computations reported in the results.

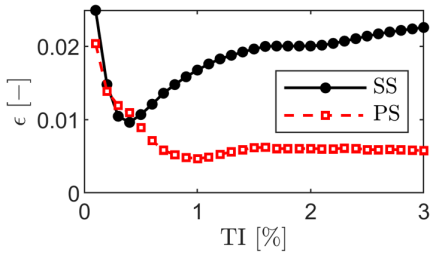

Figure 3.9: Turbulence sensitivity: relative error in isentropic Mach number between MISES and experiments.

3.2 Reynolds-Averaged Navier-Stokes

Reynolds-averaged Navier-Stokes (RANS) computations have been performed with the commercially available *Cadence Fine™/Turbo 16.1*, a time-marching explicit cell-centered finite volume solver.

The solver was used for 2D steady-state computations. Computations of the 3D aerodynamics and 2D unsteady aerodynamics were not performed. A slice with 0.80 mm of thickness throughout the axial coordinate was used (axial velocity density ratio of unity). The flow domain is discretized by a single cell in the spanwise direction. Periodicity is imposed over the lateral boundaries. The inlet of the flow domain has been extended $0.75C_{ax}$ upstream of the blade leading edge. The outlet of the flow domain has been extended one axial chord downstream of the trailing edge so that measurements at the experimental Plane 06 were not impacted by the outlet boundary conditions imposed at the outlet of the flow domain. The flow domain is displayed in Fig. 3.10.

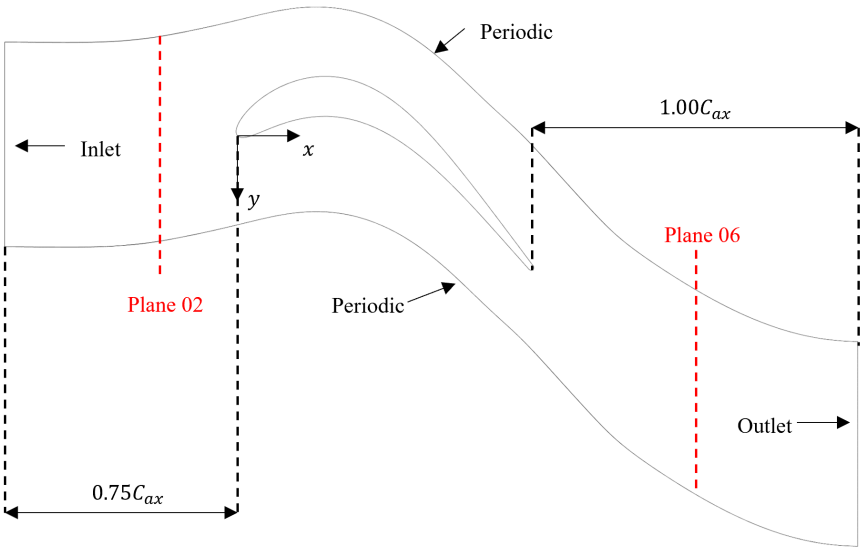

Figure 3.10: Flow domain used in 2D RANS CFD.

3.2.1 Numerical Parameters

In the current work, viscous fluxes were discretized using a central scheme. Convective fluxes were discretized utilizing a second-order accurate Roe-upwind scheme. A second-order symmetric total variation diminishing (STVD) scheme coupled with Van Albada limiters has been used. An explicit multistage Runge-Kutta scheme with local time stepping was used for time discretization.

The κ-ω SST was used for turbulence closure. The model was coupled with the γ-$\tilde{R}e_{\theta t}$ transition model developed by Langtry and Menter [8]. The authors recommended a first cell y^+<5, with preference for values below unity, to resolve the log-layer. A y^+ below five is sufficient to determine the viscous sub-layer. The expansion ratio near the blade surface was kept below ∼1.20.

Total quantities were prescribed at the inlet of the flow domain: pressure and temperature. The flow angle was also set. Static pressure was imposed at the outlet. The total pressure at the inlet and static pressure at the outlet were computed to respect the required outlet Mach and Reynolds numbers for a total temperature of 300 K. The resulting pressure ratio for the investigated cases is the same as for the MISES computations (see Section 3.1.1).

The turbulence quantities at the inlet were prescribed with turbulent kinetic energy, κ, and turbulent kinetic energy dissipation rate, ϵ. The turbulent kinetic energy is related to the inlet velocity, U_{in}, and turbulent intensity as:

$$\kappa = \frac{3}{2}\left(U_{in} TI\right)^2 \tag{3.2}$$

The turbulent kinetic energy dissipation rate is described as:

$$\epsilon = C_{\mu}^{3/4} \frac{\kappa^{3/2}}{ILS} \tag{3.3}$$

C_{μ}=0.09 is a model coefficient for the turbulent viscosity, and ILS is the integral length scale. The inlet turbulence decay during the experiments was used to inform the values of κ and ϵ required to match the experimental turbulence intensity and turbulence decay.

All the γ-$\tilde{Re}_{\theta t}$ computations were started from a transitional computation performed with the AGS model. A CFL=3 was used to ensure numerical stability. A global residual below 1e-7 was achieved for all cases.

3.2.2 Mesh

Structured meshes were generated with the commercially available software *Autogrid5*. The generated meshes are of the O4H type: O-block around the blade and four H-block around the skin block. The number of elements on the blade suction and pressure sides are part of the parameters defining the O-block mesh. A mesh sensitivity study was performed on five meshes with increasing density, ranging from a mesh with $50k$ to $180k$ elements. Attention was taken to achieve an expansion ratio compatible with the γ-$\tilde{Re}_{\theta t}$ model (see Section 3.2.1): namely a $y^+ < 1$ and an expansion ratio (ER) near the blade surface within $\sim$1.20. The parameters of each mesh are reported in Table 3.3.

Table 3.3: Mesh properties for sensitivity study.

Name	N_{SS}	N_{PS}	N_{tot} $[\times 10^{-3}]$	Max. ER	Max. y^+
M1	137	121	$\sim$50	1.20	1.02
M2	177	157	$\sim$80	1.20	0.64
M3	209	189	$\sim$115	1.20	0.38
M4	241	213	$\sim$150	1.20	0.26
M5	261	229	$\sim$180	1.20	0.13

Where N_{SS} and N_{PS} are the number of cells on the suction side and pressure side surfaces, and N_{tot} is the total number of cells. The resulting mesh is similar to the one displayed in Fig. 3.11, which shows the final mesh used in the scope of this work (M3).

The mesh dependency on the blade and flow quantities was assessed for the M=0.70; Re=120k (characterized by a closed laminar separation bubble) and checked for the M=0.90; Re=70k (design point) flow case a-posteriori. No incidence has been imposed. A low turbulence level was used to ensure the activation of the transition model. The turbulent parameters and resulting turbulence intensity are reported in Table 3.4.

Table 3.4: Mesh properties for sensitivity study.

Case	κ $[m^2/s^2]$	ϵ $[m^2/s^3]$	Inlet TI $[\%]$	ILS $[mm]$
$M = 0.70; Re = 120k$	25.07	22175	$\sim$2.62	~ 0.96
$M = 0.90; Re = 70k$	21.59	17718	$\sim$2.65	~ 0.96

Fig. 3.12 displays the isentropic Mach number along the pressure side and suction side surfaces for the M=0.70; Re=120k case. From an overall point of view, the mesh density does

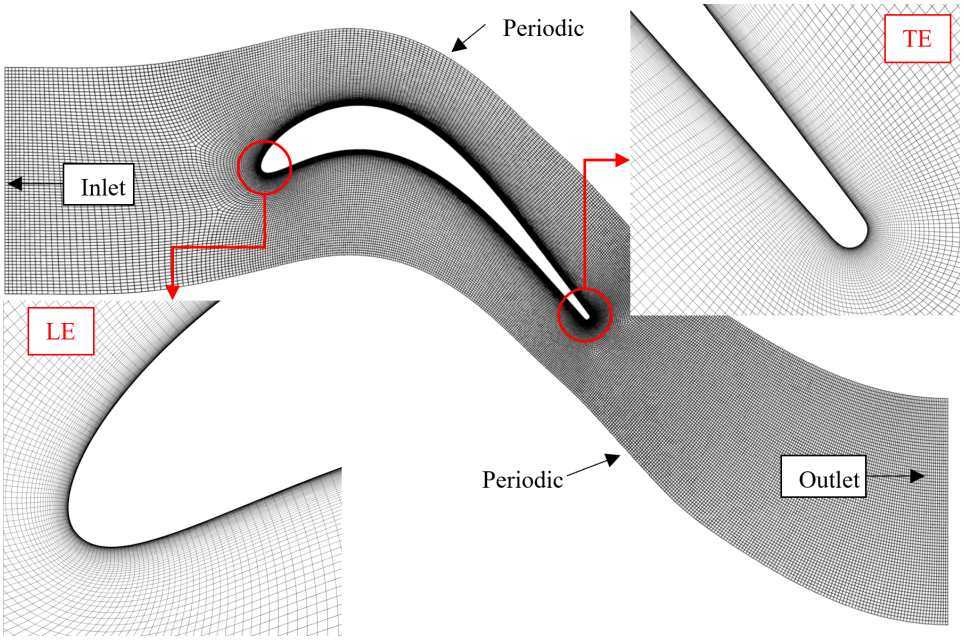

Figure 3.11: Mesh M3 and details of the leading edge and trailing edge region.

not impact the loading. A zoomed-in region of a suction side region near the trailing edge highlights the dependency of mesh on the laminar separation bubble topology. The coarsest mesh displays an oscillatory behavior. However, for the remaining meshes, the difference is subtle. On the pressure side separation region, the loading displays oscillations for the coarsest and finest mesh due to the unsteady nature of the separation bubble.

The pitchwise distribution of the total pressure loss coefficient at $0.50C_{ax}$ downstream of the cascade for the surveyed meshes is displayed in Fig. 3.13(a). The wake thickness was found to decrease with increasing mesh density. Additionally, an increase in the peak loss occurs. This has been pointed out as a shortcoming of RANS in past numerical works [9–11]. Conventional RANS turbulence closures fail to predict turbulent mixing accurately due to using the Boussinesq approximation that suggests a linear coupling of the mean strain field and the Reynolds stress [12]. The shortcomings of the Boussinesq approximation can be addressed by a class of turbulence closures named explicit algebraic Reynolds stress models (EARSM) [13–15], which were not used in this work.

Fig. 3.13(b) displays the mass-averaged total pressure loss coefficient for the different investigated meshes. The loss does not display a monotonic behavior as the mesh density increases. This can be observed in Fig. 3.13(a) by observing that the rise in peak (and decrease in wake thickness) is not monotonic either. The relative error between M3 and M4 to the most refined mesh is 2.62% and 0.69%, respectively. For mesh M3, the absolute error amounts to $\Delta\zeta$=3e-4, which is considered sufficiently small to consider the mesh refined enough for the current test case.

The nominal flow case's blade loading and total pressure loss coefficient were also checked for completeness. Using the meshes M4 and M5 resulted in a non-converged solution due

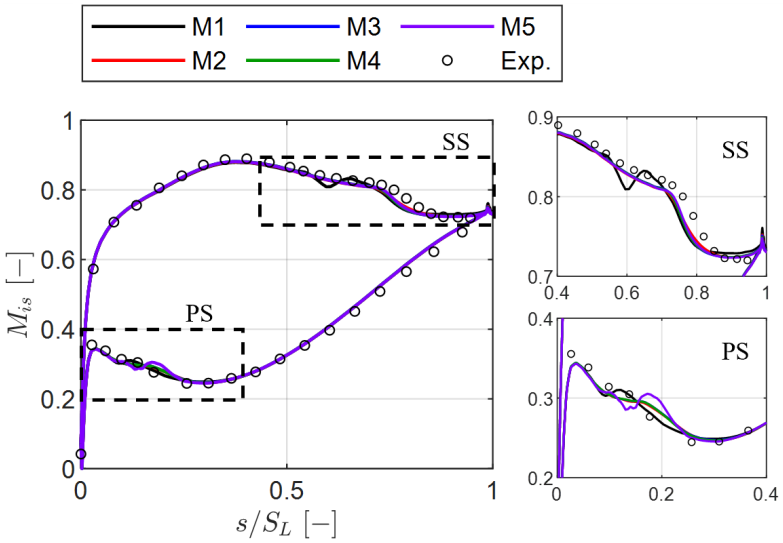

Figure 3.12: CFD mesh sensitivity for M=0.70; Re=120k: surface isentropic Mach number distribution along normalized surface length. Zoomed-in regions of suction side laminar separation bubble (top-right) and pressure side separation (bottom-right).

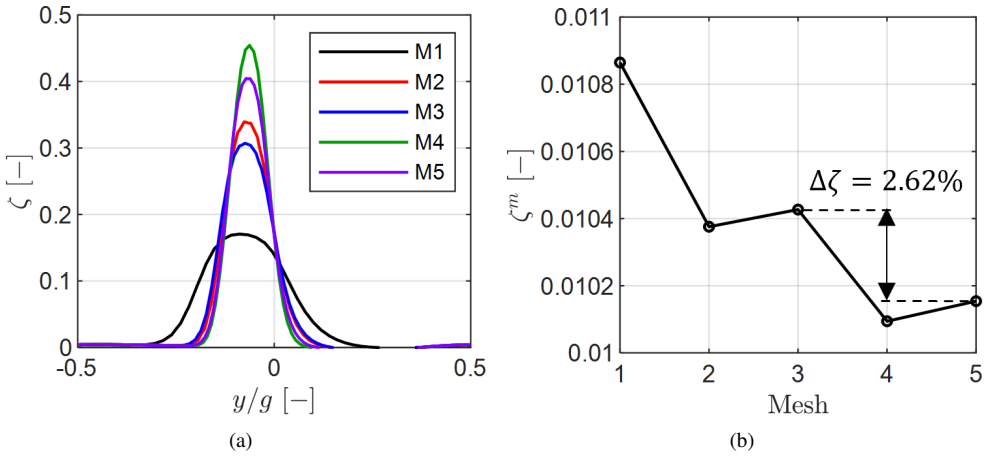

(a) (b)

Figure 3.13: CFD mesh sensitivity for M=0.70; Re=120k: Pitchwise distribution of total pressure loss coefficient, ζ (a) and mass-averaged total pressure loss coefficient (b).

to the large unsteadiness in the rear portion of the suction side due to an open separation. For such cases, URANS should be selected to account for a global time step-—the meshes for which significant unsteadiness impacted convergence were discarded from the comparison. Fig. 3.14 displays the isentropic Mach number along the pressure side and suction side surfaces for the M=0.90; Re=70k case. The suction side loading is independent of the mesh density. On the pressure side, one can see a slight discrepancy in the region of the pressure side separation bubble for the mesh M3. Nonetheless, these oscillations were not present for the productive computations where the incidence has been corrected.

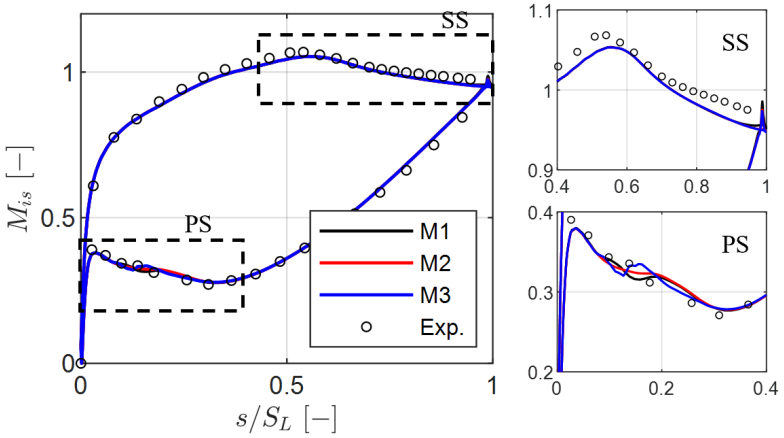

Figure 3.14: CFD mesh sensitivity for M=0.90; Re=70k: surface isentropic Mach number distribution along normalized surface length. Zoomed-in regions of SS laminar separation bubble (top-right) and PS separation (bottom-right).

The pitchwise distribution of the total pressure loss coefficient (total pressure loss normalized by inlet total pressure) at 0.50C_{ax} downstream of the cascade for the surveyed meshes is displayed in Fig. 3.15(a). Experimental data is added for completeness. Like the previous flow case, the wake became thinner and more profound with increasing mesh density. For both meshes M2 and M3, the wakes obtained with CFD are thinner and have higher peaks than the experimental results. There is virtually no difference in the mass-averaged total pressure loss coefficient between mesh M2 and M3 (see Fig. 3.15(b)). Nonetheless, mesh M3 has been considered suitable for productive computations based on the findings for both flow conditions.

3.2.3 Incidence Sensitivity

A similar study performed with MISES was done for the CFD case (see Section 3.1.3). The CFD computations were run without activating the transitional model for high Reynolds number (500,000), ensuring no laminar separation occurred. The incidence has been varied in the range of -2.00°–0.00° in increments of 0.20°. Fig. 3.16(a) displays the isentropic Mach number along the pressure and suction sides. The detailed view highlights that the loading is impacted by the incidence up to $s/S_L \approx$0.30. The relative error between the CFD and experiments (see Fig. 3.16(b)) has been computed using the suction side blade loading

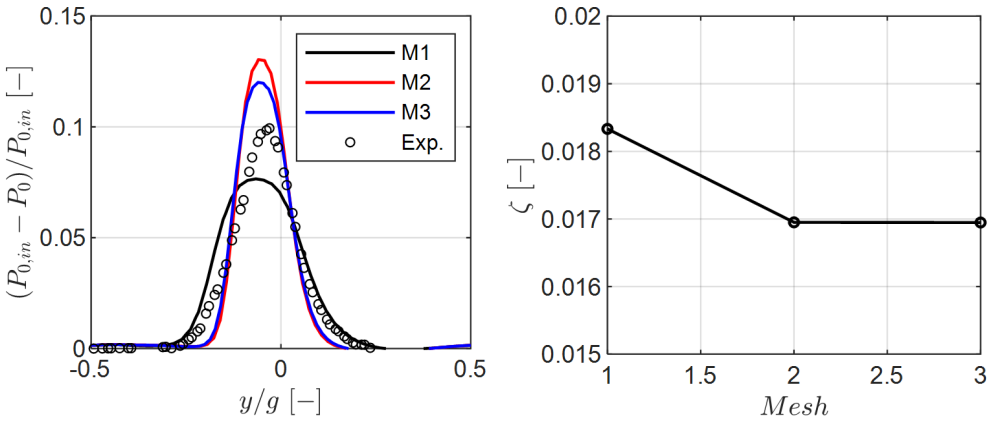

Figure 3.15: CFD mesh sensitivity for M=0.90; Re=70k: Pitchwise distribution of total pressure loss coefficient, Y_{tot}, (a) and mass-averaged total pressure loss coefficient, ζ (b).

portion from the leading edge to the velocity peak. An incidence of -0.60° provided the best agreement between the CFD and experimental loading, having been used for the productive computations.

3.2.4 Definition of Inlet Turbulent Quantities

In two-equation turbulence models, in which the κ-ω SST model falls within, the specification of the turbulence kinetic energy and dissipation parameter at the inlet is required. Praisner and Clark [16] pointed out different methodologies to prescribe inlet turbulence disturbances in case the experimental quantities are unknown. In the scope of this work, the inlet turbulent parameters defining the model, κ, and ϵ, were specified to match the turbulence intensity and local decay measured experimentally by the cross-wire (XW) probe.

Fig. 3.17 displays the turbulence intensity experimental values and their fitted power law, measured with the cross-wire upstream of the cascade. The correlation of Roach [17] is added for completeness and represented by the dashed line. The central blade leading edge is 0.40 m away from the grid. The point corresponding to y/g=0 at Plane 02 is highlighted. Initially, the κ and ϵ were defined to match the turbulence intensity and integral length scale computed with the cross-wire (red curve). It was found that the experimental integral length scale ($\sim$12 mm) resulted in a slower turbulence decay compared to the cross-wire fitted one. A fine-tuning of the turbulence parameters allowed the matching of the experimental decay and turbulence intensity (blue curve). A similar approach has been reported in [18]. A turbulence intensity of $\sim$2.60% and an integral length scale of $\sim$0.93 mm enabled retrieving the magnitude and slope of the experimental turbulence decay.

The increase in the CFD turbulence level towards the blade leading edge, while the experimental curve does not, is due to how the axial distance to the grid was considered. In the CFD analysis, the decay is calculated on a line perpendicular to the turbulence grid and the intersection of the blade leading edge. In the experiments, the angle of the turbulence

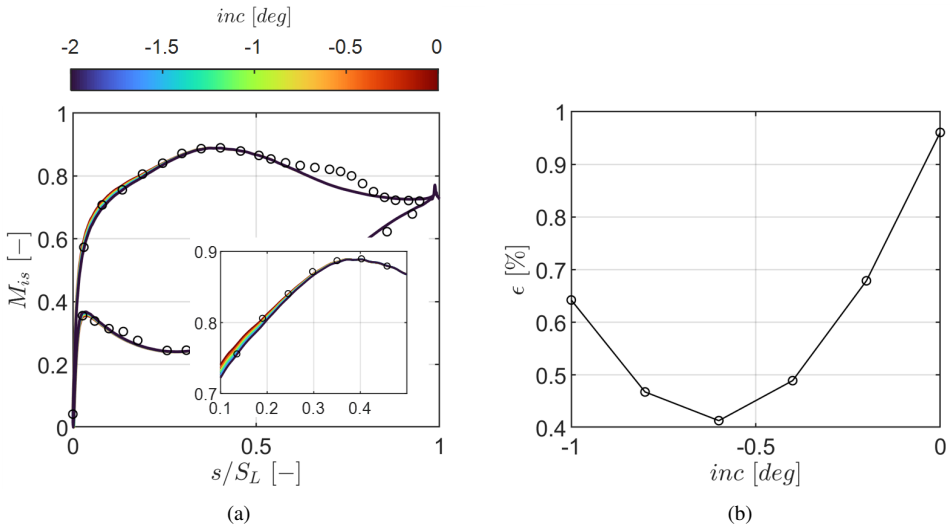

Figure 3.16: CFD incidence sensitivity for M=0.70; Re=500k: Blade surface isentropic Mach number as a function of incidence (a) the relative error in isentropic Mach number between CFD and experimental loading (b).

grid with respect to the cascade is utilized. The distance to the grid is adjusted by moving the probe in the pitchwise direction, and as a result, it is always parallel to the leading edge plane.

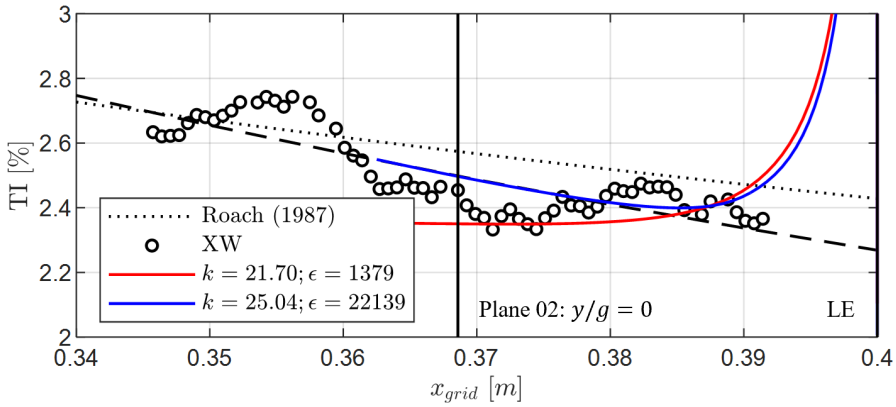

Figure 3.17: CFD: Turbulence decay fine-tuning against experimental data.

The exercise was performed for all flow conditions investigated. The turbulence decay obtained for each is compared with experiments in Fig. 3.18. The turbulence intensity is bounded within ±0.5% around the experimental value at y/g=0.

The turbulence model parameters applied as inlet boundary conditions to match the turbulence decay and intensity for each flow case are reported in Table 3.5.

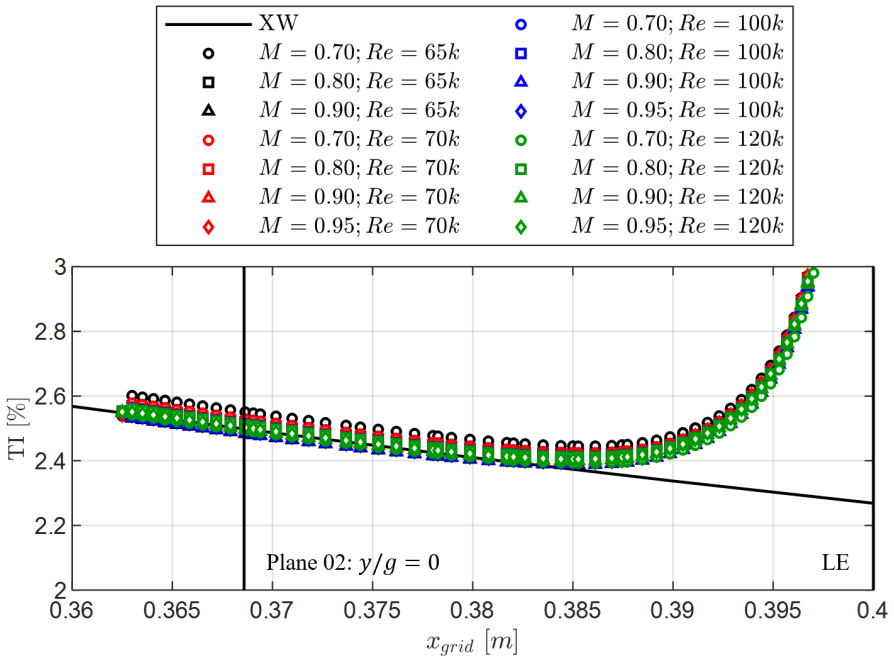

Figure 3.18: Turbulence decay obtained for the productive cases compared against the experimental one.

Table 3.5: Turbulence model parameters.

M_{out} $[-]$	Re_{out} $[-]$	κ $[m^2/s^2]$	ϵ $[m^2/s^3]$	TI $[\%]$	ILS $[mm]$
0.70	$65k$	20.396	16275	2.60	0.93
0.80	$65k$	23.585	20237	2.63	0.93
0.90	$65k$	24.991	22074	2.63	0.93
0.70	$70k$	20.733	16680	2.62	0.93
0.80	$70k$	23.656	20329	2.63	0.93
0.90	$70k$	25.067	22175	2.62	0.93
0.95	$70k$	25.086	22200	2.60	0.93
0.70	$100k$	21.269	17331	2.63	0.93
0.80	$100k$	23.719	20410	2.63	0.93
0.90	$100k$	25.271	22446	2.63	0.93
0.95	$100k$	25.486	22733	2.63	0.93
0.70	$120k$	21.585	17718	2.65	0.93
0.80	$120k$	24.066	20859	2.64	0.93
0.90	$120k$	25.370	22578	2.62	0.93
0.95	$120k$	25.600	22885	2.61	0.93

References

[1] H. Youngren and M. Drela. *Viscous/inviscid method for preliminary design of transonic cascades*. In 27th Joint Propulsion Conference, page 2364, 1991.

[2] B. J. Abu-Ghannam and R. Shaw. *Natural Transition of Boundary Layers—The Effects of Turbulence, Pressure Gradient, and Flow History*. Journal of Mechanical Engineering Science, 22(5):213–228, 1980.

[3] M. Drela. *MISES implementation of modified Abu-Ghannam/Shaw transition criterion*. Mises User's Guide, MIT, 1995.

[4] E. Dick and S. Kubacki. *Transition models for turbomachinery boundary layer flows: a review*. International Journal of Turbomachinery, Propulsion and Power, 2(2):4, 2017.

[5] Mark Drela. *Integral boundary layer formulation for blunt trailing edges*. In 7th Applied Aerodynamics Conference, page 2166, 1989.

[6] M. Gaster. *The structure and behaviour of separation bubbles*. 1967.

[7] J.D. Coull and H.P. Hodson. *Predicting the Profile Loss of High-Lift Low Pressure Turbines*. Journal of Turbomachinery, 134(2):021002, 06 2011.

[8] R.B. Langtry and F.R. Menter. *Correlation-Based Transition Modeling for Unstructured Parallelized Computational Fluid Dynamics Codes*. AIAA Journal, 47(12):2894–2906, 2009.

[9] H.D. Akolekar, F. Waschkowski, Y. Zhao, R. Pacciani, and R.D. Sandberg. *Transition Modeling for Low Pressure Turbines Using Computational Fluid Dynamics Driven Machine Learning*. Energies, 14(15), 2021.

[10] H.D. Akolekar, Y. Zhao, R.D. Sandberg, and R. Pacciani. *Integration of Machine Learning and Computational Fluid Dynamics to Develop Turbulence Models for Improved Low-Pressure Turbine Wake Mixing Prediction*. Journal of Turbomachinery, 143(12):121001, 06 2021.

[11] N. Rosafio, G. Lopes, S. Salvadori, S. Lavagnoli, and D.A. Misul. *RANS Prediction of Losses and Transition Onset in a High-Speed Low-Pressure Turbine Cascade*. Energies, 16(21), 2023.

[12] H. D. Akolekar, J. Weatheritt, N. Hutchins, R. D. Sandberg, G. Laskowski, and V. Michelassi. *Development and Use of Machine-Learnt Algebraic Reynolds Stress Models for Enhanced Prediction of Wake Mixing in Low-Pressure Turbines*. Journal of Turbomachinery, 141(4):041010, 03 2019.

[13] W Rodi. *A new algebraic relation for calculating the Reynolds stresses*. In Gesellschaft Angewandte Mathematik und Mechanik Workshop Paris France, volume 56, page 219, 1976.

[14] T. B. Gatski and C. G. Speziale. *On explicit algebraic stress models for complex turbulent flows*. Journal of Fluid Mechanics, 254:59–78, 1993.

[15] Stefan Wallin and Arne V. Johansson. *An explicit algebraic Reynolds stress model for incompressible and compressible turbulent flows*. Journal of Fluid Mechanics, 403:89–132, 2000.

[16] T.J. Praisner and J.P. Clark. *Predicting Transition in Turbomachinery—Part I: A Review and New Model Development*. Journal of Turbomachinery, 129(1):1–13, 03 2004.

[17] P.E. Roach. *The generation of nearly isotropic turbulence by means of grids*. International Journal of Heat and Fluid Flow, 8(2):82–92, 1987.

[18] J. Babajee and T. Arts. *Investigation of the Laminar Separation-Induced Transition With the -Re t Transition Model on Low-Pressure Turbine Rotor Blades at Steady Conditions*. volume Volume 8: Turbomachinery, Parts A, B, and C of *Turbo Expo: Power for Land, Sea, and Air*, pages 1167–1178, 06 2012.

4 Rig Characterization

In this chapter, the rig performance is evaluated in terms of the stability of the operating point and the periodicity of the flow conditions in the test section. The development of a correlation to monitor the cascade inlet total pressure without local instrumentation is highlighted. Probe interference is exposed, which is the difficulty of measuring with finite-size probes in transonic flowfields. The interference is quantified, and a methodology for the probe downstream of the test article is presented.

4.1 Stability of Flow Conditions

The stability of the rig operating conditions was assessed for each phase of testing. The data includes multiple days of testing throughout the project. Due to the intrusiveness of the L-shaped five-hole probe at Plane 06 (see Section 4.4), the stability of the flow in terms of Mach and Reynolds numbers considered the static pressure measured at the cascade far exit (see Section 2.4.2.4). It is worth noting that the temperature variation during a day of testing can increase by as much as 8 K. The rig was adjusted to keep the Mach and Reynolds numbers nearly constant.

Fig. 4.1(a) displays the normalized probability density function (PDF) of the deviation from the nominal isentropic Mach number computed at the cascade far exit for all measurement points acquired during the first phase of testing (in the absence of wake generator and purge flow). The same type of plot for the Reynolds number is shown in Fig. 4.1(b). For a generic quantity, Φ, the deviation is normalized by the nominal value:

$$\Delta\Phi = \frac{\Phi - \Phi_{nominal}}{\Phi_{nominal}} \tag{4.1}$$

Fig. 4.2(a) displays the probability density function of the wake generator rotational velocity. The standard deviation amounts to a variation of 0.06 RPM. Therefore, the stability

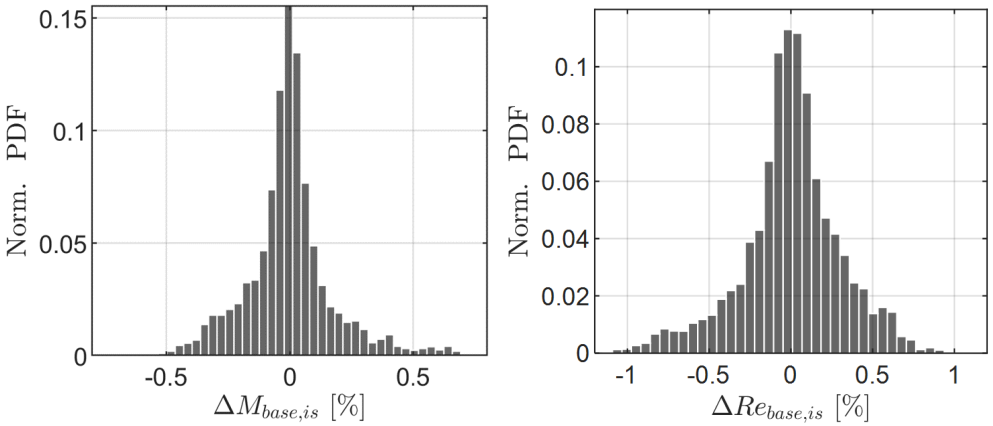

(a) (b)

Figure 4.1: Stability of the Mach number (a) and Reynolds number (b) during the first phase of testing.

of the Strouhal number, for which the probability density function is shown in Fig. 4.2(b), is mainly impacted by the flow conditions (Mach number at the outlet). Nonetheless, the absolute variation for the nominal flow case is within 0.003.

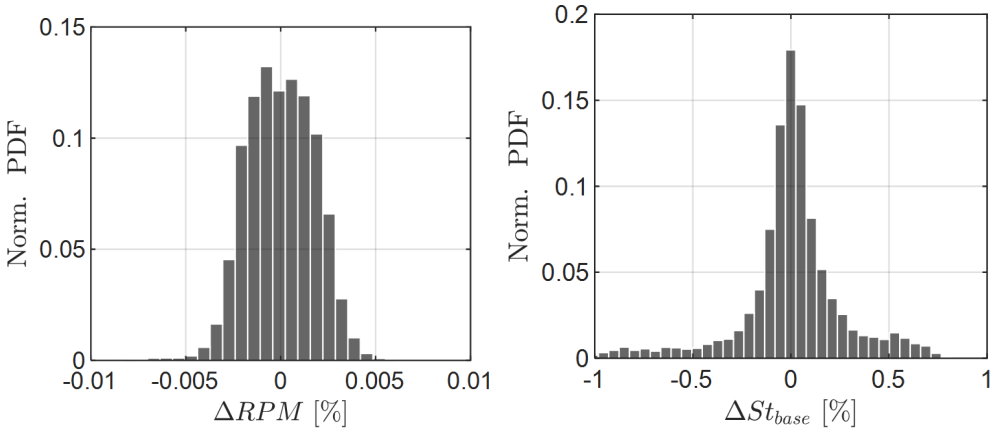

(a) (b)

Figure 4.2: Stability of the WG rotational speed (a) and Strouhal number (b) during the second phase of testing.

Lastly, Fig. 4.3 displays the probability density function of the deviation from the purge massflow ratio=0.90%. The value is not normalized since the purge massflow ratio is already expressed as a percentage. The reported variation is absolute with the nominal value.

The stability of the flow conditions was evaluated in terms of the standard deviation of the probability density function. The standard deviation with a 95% confidence interval (2σ) of the Mach and Reynolds numbers, the wake generator rotational speed and bar reduced

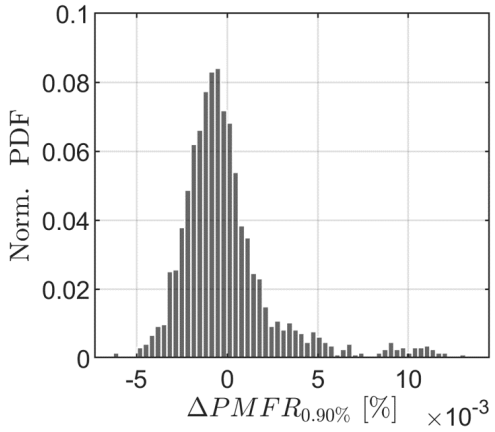

Figure 4.3: Stability of the PMFR during the third phase of testing.

frequency, and the purge massflow ratio for all phases of testing are collected in Table 4.1. Alongside the percentage value, the absolute value for the nominal operating point of the cascade is reported (M=0.90; Re=70k; St=0.95).

Table 4.1: Standard deviation with 95% confidence interval resultant from variation in flow conditions from the nominal point.

Phase		1	2	3
M	rel [%]	0.71	0.92	0.71
	abs [−]	0.006	0.008	0.006
Re	rel [%]	0.61	0.71	0.82
	abs [−]	425	500	574
RPM	rel [%]	–	0.004	0.003
	abs [rpm]	–	0.12	0.11
St	rel [%]	–	0.54	0.32
	abs [−]	–	0.005	0.003
PMFR 0.50%	abs [%]	–	–	0.002
PMFR 0.90%	abs [%]	–	–	0.003

4.2 Determination of Cascade Inlet Total Pressure

The inlet total pressure is not live-monitored during the tests since collocating a probe between the turbulence grid and the wake generator is impossible with the current setup. Instead, a loss coefficient, Y, is defined across the turbulence grid or the turbulence grid in addition to the wake generator. The Y is defined according to Eq. 4.2.

$$Y\left(M, Re\right) = \frac{P_{0,ref} - P_{01}}{P_{0,ref}} \tag{4.2}$$

The coefficient depends on the flow conditions being investigated. For a given flow con-

dition, once the loss coefficient is known, the total pressure at the inlet of the cascade and past the turbulence grid, plus the wake generator if the latter is used, can be obtained by isolating P_{01} in Eq. 4.2, since $P_{0,ref}$ is live-monitored in the rig.

The development of a correlation of the loss across the turbulence grid, including the wake generator for the tests performed with bars, was required. This was achieved by conducting tests at the range of flow conditions expected throughout the project and installing a probe capable of measuring the total pressure at the cascade inlet to compute Y. In the case of the measurements performed with the turbulence grid only, the total pressure was retrieved at Plane 01 utilizing the Preston tube. In the presence of the turbulence grid+wake generator, the total pressure was measured at Plane 02 using the Cobra five-hole probe.

Once the Y=f(M, Re) map was built, an iterative procedure was used during the post-processing phase to estimate the Y during the tests. The procedure is highlighted in the diagram in Fig. 4.4.

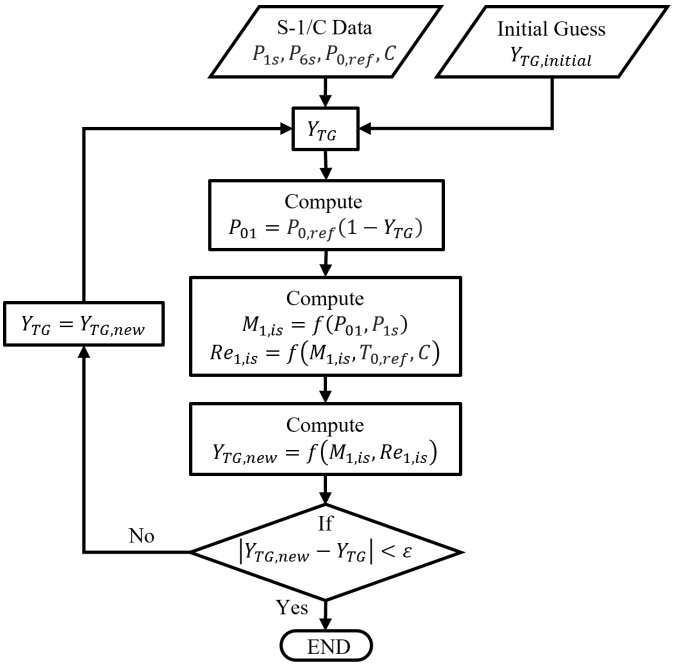

Figure 4.4: Procedure to retrieve cascade inlet total pressure.

4.2.1 Turbulence Grid Loss Coefficient

The Preston tube has been traversed in the pitchwise direction at midspan. The turbulence grid loss coefficient has been evaluated for outlet Mach numbers in the range of 0.70–0.95 and outlet Reynolds numbers in the 65k–120k range. These ranges include all the flow conditions that have been investigated in the scope of this work.

The pitchwise distributions of Y are displayed in Fig. 4.5(a). The loss increases with the Mach number. Four sets of curves at different levels are easily identifiable (the curves for

M=0.95 are close to the ones obtained at M=0.90). In addition, a Reynolds number effect is also present, even though it is much smaller than the one for the Mach number. An increase in the outlet Reynolds number results in increased losses for a fixed Mach number.

The pitchwise distributions display a periodic behavior that scales well with approximately two-blade pitches. The magnitude of the periodic variation is highlighted in Fig. 4.5(b), where the turbulence grid loss coefficient has been normalized by its mean. The pitch-to-pitch variation is within $\pm 0.1\%$ of the inlet total pressure.

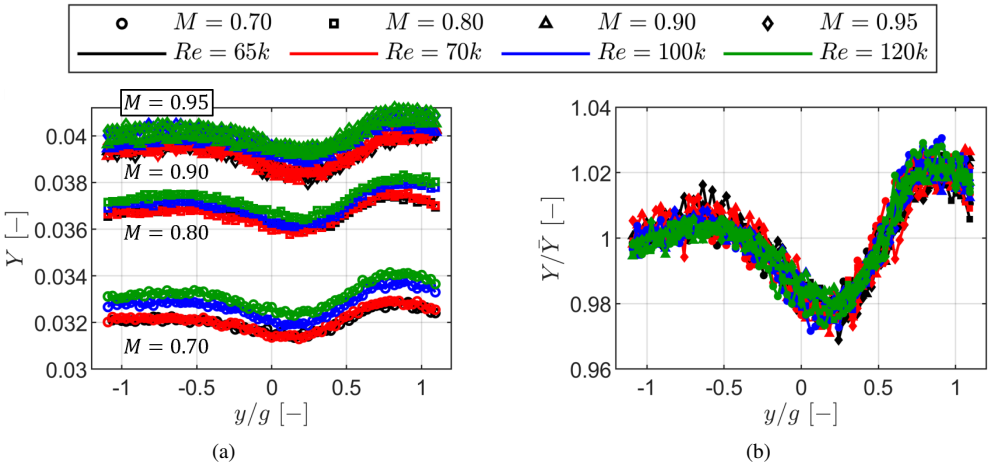

Figure 4.5: Pitchwise distribution of turbulence grid loss coefficient for the different investigated flow conditions (a) and normalized distributions (b).

The turbulence grid loss coefficient has been pitchwise-averaged for each flow condition to obtain a loss correlation as a function of M and Re. Two correlations were obtained: Y as a function of inlet Mach and Reynolds numbers to determine inlet flow conditions and outlet Mach and Reynolds numbers to determine outlet flow conditions. The inlet correlation was built with a 1^{st} order polynomial in $\mathrm{M}_{1,is}$ and $\mathrm{Re}_{1,is}$, while for the outlet flow conditions a 2^{nd} order fitting was used for $\mathrm{M}_{6,is}$. The loss correlations at the inlet and outlet take the form of Eq. 4.3 and Eq. 4.4.

$$Y\left(M_{1,is}, Re_{1,is}\right) = C_1 + C_2 M_{1,is} + C_3 Re_{1,is} \tag{4.3}$$

$$Y\left(M_{6,is}, Re_{6,is}\right) = C_1 + C_2 M_{6,is} + C_3 Re_{6,is} + C_4 M_{6,is}^2 + C_4 M_{6,is} Re_{6,is} \tag{4.4}$$

The coefficients of the fittings alongside the goodness of fitting and fitting error are displayed in Table 4.2.

The turbulence grid loss coefficient diagram in the function of the inlet flow conditions is displayed in Fig. 4.6(a). One can observe that the dependence on the Mach number is larger than the one on the Reynolds number. On the other hand, the sensitivity to Reynolds number, in addition to Mach, increases for the correlation built with the outlet flow conditions (see Fig. 4.6(b)).

Table 4.2: Calibration coefficients, goodness of fitting, and standard error of fittings performed to turbulence grid loss coefficient.

	$Y = f\left(M_{1,is}, Re_{1,is}\right)$	$Y = f\left(M_{6,is}, Re_{6,is}\right)$
C_1 $[-]$	-0.04183	-0.05513
C_2 $[-]$	0.17898	0.18825
C_3 $[-]$	-3.69520e-09	5.04960e-08
C_4 $[-]$	–	-0.09340
C_5 $[-]$	–	-4.53216e-08
R^2	0.99916	0.99953
$S_{\bar{\mathbb{M}}}$ $[-]$	1.15772e-07	6.44884e-08

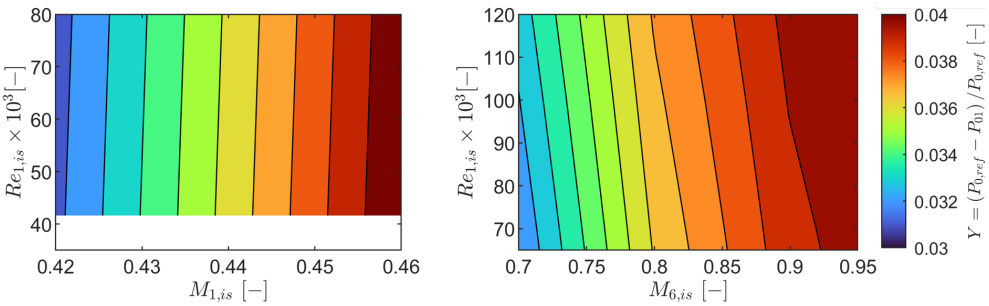

(a) (b)

Figure 4.6: Turbulence grid loss coefficient correlation as a function of inlet flow conditions (a) and outlet flow conditions (b)

The magnitude of the mass-averaged turbulence grid loss coefficient used to build the turbulence grid loss correlation is contained in Table 4.3 for completeness.

Table 4.3: Turbulence grid loss coefficient as a function of the flow Mach and Reynolds numbers.

		Re			
		65k	70k	100k	120k
M	0.70	0.0515	0.0516	0.0523	0.0527
	0.80	0.0567	0.0567	0.0570	0.0572
	0.90	0.0597	0.0597	0.0596	0.0595
	0.95	0.0604	0.0604	0.0600	0.0598

4.2.2 Turbulence Grid + Wake Generator Loss Coefficient

The same exercise was performed when the wake generator was mounted in addition to the turbulence grid. Estimating the loss across both constituents was necessary since no permanent instrumentation exists between them.

The Cobra five-hole probe was traversed at Plane 02. Pitchwise traverses at midspan were performed for outlet Mach and Reynolds numbers in the range expected for the experiments (M$\in$ [0.60, 0.95]; Re$\in$ [65k, 120k]).

The pitchwise distributions of the total pressure loss coefficient (turbulence grid+wake generator) are displayed in Fig. 4.7(a). Adding the wake generator promotes higher loss than for the case with turbulence grid only (around 54% higher for the nominal operating point of the cascade). However, the behavior with the Mach number remains similar: increase of Y with M. Even though less sensitive, the losses also increase with Re for a fixed Mach number. It is worth pointing out that in the presence of the wake generator, the pitchwise distributions also display a periodic topology regardless of the flow condition (see Fig. 4.7(b)). The pitch-to-pitch variation amounts to $\pm 0.1\%$ of the inlet total pressure.

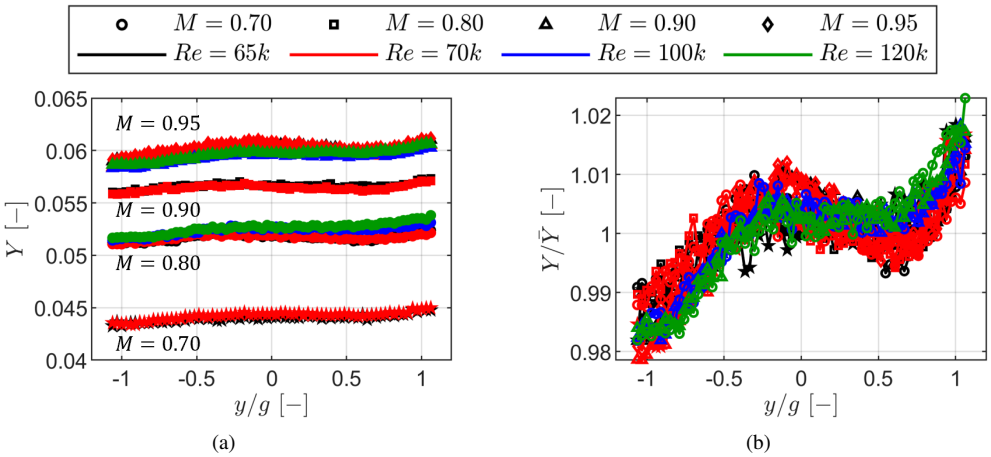

Figure 4.7: Pitchwise distribution of inlet total pressure loss coefficient for the different investigated flow conditions (a) and normalized distributions (b).

Similar to the turbulence grid loss correlation, the inlet total pressure loss correlation was built by fitting a polynomial surface to the data. However, 2^{nd} order for Mach number and 1^{st} order for Reynolds number were used for the inlet and outlet correlation. The resultant equations for the inlet and outlet correlations take the form of Eq. 4.5 and Eq. 4.6, respectively.

$$Y\left(M_{1,is}, Re_{1,is}\right) = C_1 + C_2 M_{1,is} + C_3 Re_{1,is} + C_4 M_{1,is}^2 + C_4 M_{1,is} Re_{1,is} \tag{4.5}$$

$$Y\left(M_{6,is}, Re_{6,is}\right) = C_1 + C_2 M_{6,is} + C_3 Re_{6,is} + C_4 M_{6,is}^2 + C_4 M_{6,is} Re_{6,is} \tag{4.6}$$

The coefficients of the fittings alongside the goodness of fitting and fitting error are displayed in Table 4.4.

Table 4.4: Calibration coefficients, goodness of fitting, and standard error of fittings performed to turbulence grid + wake generator loss coefficient.

	$Y = f\left(M_{1,is}, Re_{1,is}\right)$	$Y = f\left(M_{6,is}, Re_{6,is}\right)$
C_1 $[-]$	-0.05405	-0.05349
C_2 $[-]$	0.27879	0.22443
C_3 $[-]$	5.04281e-07	1.13957e-07
C_4 $[-]$	-0.00236	-0.10919
C_5 $[-]$	-1.33288e-06	-1.32206e-07
R^2 $[-]$	0.99723	0.99907
$S_{\bar{\mathbb{M}}}$ $[-]$	1.07046e-06	3.58202e-07

Lastly, the diagrams of the loss as a function of the inlet and outlet flow conditions are displayed in Fig. 4.8(a) and Fig. 4.8(b), respectively. The dependence of the Mach number on the Y is evident. On the other hand, the loss coefficient displays a higher level of sensitivity to the Reynolds number than for the case with turbulence grid only.

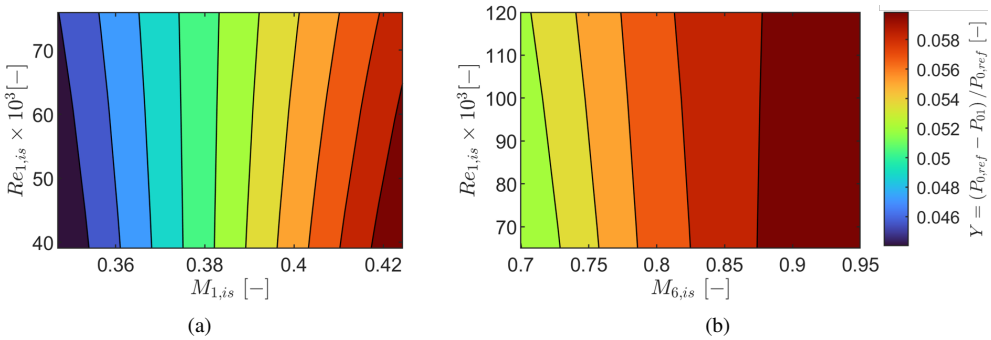

Figure 4.8: Turbulence grid + wake generator loss coefficient correlation in the function of inlet flow conditions (a) and outlet flow conditions (b).

The magnitude of the mass-averaged total pressure loss coefficient (turbulence grid plus wake generator) used to build the turbulence grid loss correlation is contained in Table 4.5 for completeness.

Table 4.5: TG+WG loss coefficient as a function of the flow Mach and Reynolds numbers.

		Re			
		65k	70k	100k	120k
M	0.70	0.1121	0.1099	0.0971	0.0885
	0.80	0.1309	0.1281	0.1113	0.1000
	0.90	0.1498	0.1463	0.1254	0.1115
	0.95	0.1591	0.1553	0.1325	0.1172

4.3 Periodicity

4.3.1 Plane 01

The inlet boundary layer periodicity was surveyed using the Preston tube at Plane 01. Fig. 4.9 displays the inlet total pressure profiles at different pitchwise locations. There is virtually no difference between the profiles. The maximum variation occurs near the endwall and amounts to ∼0.1% of the inlet total pressure.

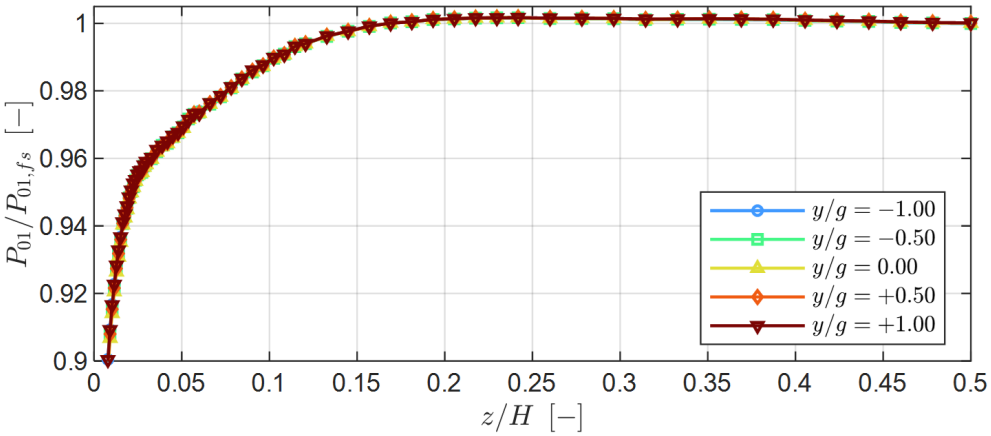

Figure 4.9: Spanwise distribution of normalized total pressure at Plane 01.

The boundary layer pitch-to-pitch periodicity was also characterized in terms of boundary layer integral parameters. Fig. 4.10(a) displays the pitchwise distribution of the boundary layer displacement thickness. The quantity is normalized by the blade true chord. The pitch-to-pitch variation is within ±0.35 mm. Similarly, the pitch-to-pitch variation of the momentum thickness (see Fig. 4.10(b)) was within ±0.26 mm. Since both quantities decrease with increasing pitchwise location, the shape factor remains nearly constant along the cascade pitch as displayed in Fig. 4.10(c). The shape factor indicates that the inlet boundary layer at Plane 01 is fully turbulent [1].

The zig-zag pattern is caused by the specific traversing trajectory chosen for the measurements. In the productive measurements, the probe was first moved in the pitchwise direction, then away from the endwall, and then in the pitchwise direction again until reaching midspan. Inlet or outlet maps were constructed by stacking several pitchwise traverses. Boundary layer measurements were conducted at the beginning of the campaign by performing successive traverses in the spanwise direction. Traverses in adjacent pitchwise locations were performed in the opposite spanwise coordinate in relation to the previous one. The motion of the probe entering or leaving the boundary layer region with low-momentum fluid, combined with a less meticulous analysis of the probe settling time, caused these fluctuations.

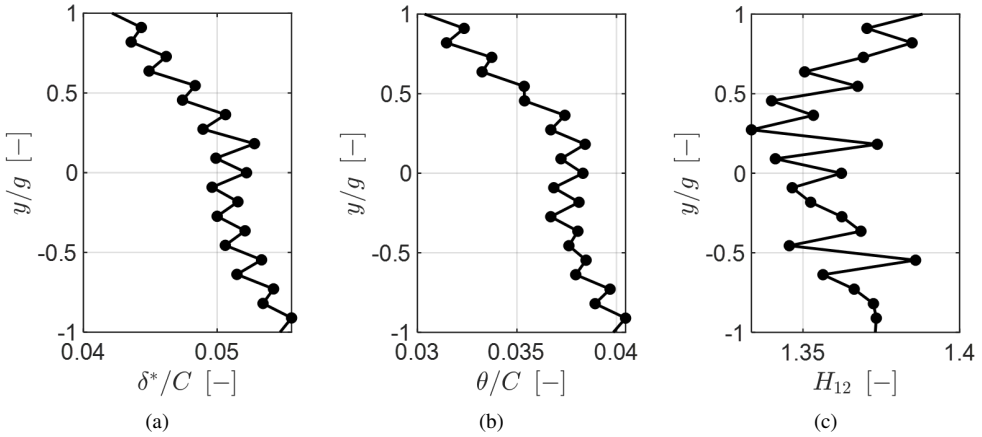

Figure 4.10: Pitchwise distribution of BL integral parameters measured at Plane 01: displacement thickness (a), momentum thickness (b), and shape factor (c). The true chord normalizes the displacement and momentum thickness.

4.3.2 Plane 02

The periodicity of the inlet boundary layer was also characterized at Plane 02, with and without the wake generator. The cobra five-hole probe measurements allowed the characterization of the periodicity in terms of angles, in addition to the total pressure profile. Fig. 4.11 displays the radial profile obtained at different pitchwise locations measured at Plane 02 during the first commissioning phase (absence of wake generator and purge flow).

The incidence is displayed in Fig. 4.11(a). The incidence along the span decreases with the pitchwise location. The variation at y/g=0.00 is within $\pm 1.60^\circ$ near the endwall and three times lower at midspan. The pitch-to-pitch variation of the cascade pitch angle (see Fig. 4.11(b)) does not vary monotonically with the pitch. The variation around the central location is within $\pm 0.25^\circ$ down to the point closest to the endwall. Normalized total pressure characterizes the profile (see Fig. 4.11(c)). The maximum pitch-to-pitch variation occurs near the endwall, corresponds to $\pm 0.5\%$ of the inlet total pressure, and is negligible at midspan.

The relative motion between the wake generator and cascade worsens the inlet flow periodicity. Fig. 4.12 highlights a sketch of the wake generator in relation to the cascade. The

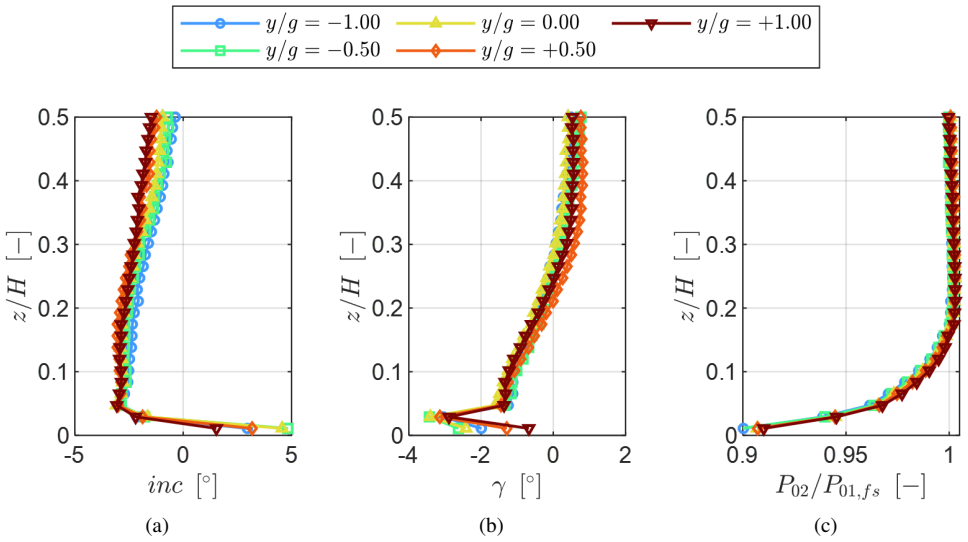

Figure 4.11: Spanwise distributions at Plane 02 during the first phase of testing: inlet flow incidence (a), cascade pitch angle (b), and normalized total pressure (c).

bar rotation imposes a radial velocity component, V_y, that is positive for negative pitchwise locations and vice-versa. The latter effect mainly impacts the angular field.

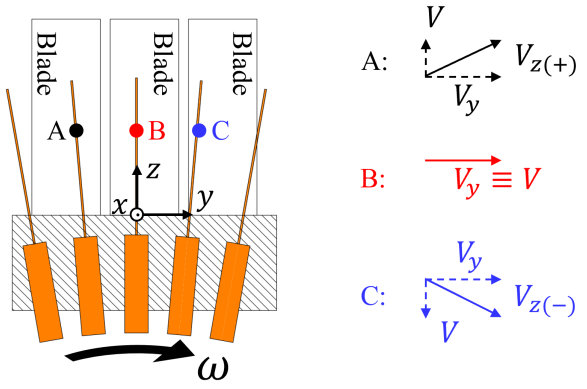

Figure 4.12: Schematic representation of the impact of wake generator on inlet velocity vectors.

The contours of the primary flow direction and cascade pitch angle measured at Plane 02 employing the Cobra five-hole probe in the presence of the wake generator are displayed in Fig. 4.13. The contours focus on the endwall region up to z/H=0.15. Arrows corresponding to the local absolute velocity components are shown for completeness.

The contours highlight that the tangential flow component (V_y=V_{tan}) is dominant with respect to the radial one (V_z=V_{rad}). Even though no upwash and downwash can be explicitly

ascribed, the effect of the wake generator's rotating motion of the flowfield periodicity is demonstrated.

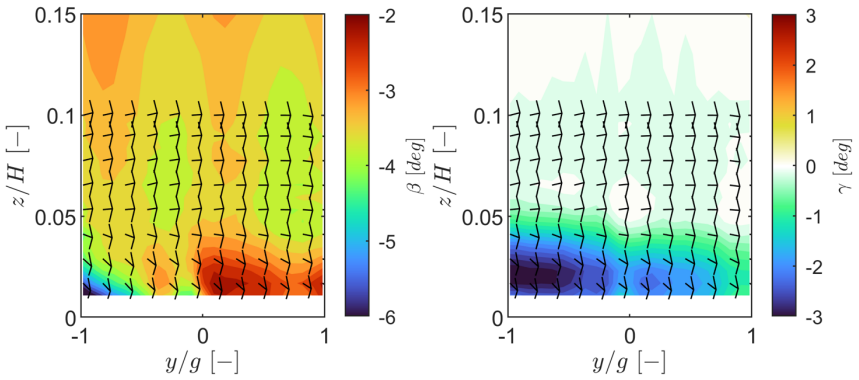

Figure 4.13: Contours of angular quantities at Plane 02 with WG: primary flow direction (a) and cascade pitch angle (b).

Fig. 4.14(a) displays the radial profiles of incidence measured at Plane 02 in the presence of the wake generator. The incidence along the span increases with the pitchwise location. The variation is within $\pm 0.10°$ at midspan. The difference increases towards the endwall. Below z/H=0.05, the variation exceeded $\pm 2.00°$.

The cascade pitch angle (see Fig. 4.14(b)) was found to be impacted by the wake generator at midspan. The variation was within $\pm 0.40°$ along the whole spanwise range.

Lastly, the radial profiles of normalized total pressure are contained in Fig. 4.14(c). The profile displays higher loss towards negative pitchwise locations. Even though the pitch-to-pitch variation is within $\pm 0.1\%$ of the inlet total pressure at midspan, the variation across one blade pitch can reach $\pm 1.25\%$ of the inlet total pressure near the endwall.

4.3.3 Plane 03

The measurements at Plane 03 were performed in two passages. The measurements performed in the passage adjacent to the suction side of the central blade are artificially shifted by one blade pitch. The procedure is highlighted in Fig. 4.15. The pitchwise coordinate y^* denotes that the measurements have been re-shifted to the passage for which the origin of the coordinate system coincides with the intersection of the central blade leading edge with the endwall.

Fig. 4.16(a) displays the pitchwise distribution of the normalized total pressure near the endwall. Two effects can be perceived from the figure: the impact of periodicity and the impact of the purge massflow ratio. The periodicity is better for the lower purge massflow ratio. Nonetheless, pitch-to-pitch variations are within $\pm 0.75\%$ of the inlet total pressure, which is acceptable.

Towards higher spanwise locations, the periodicity significantly improves, and the impact of the purge flow diminishes. At z/H=0.05 (see Fig. 4.16(b)), the pitch-to-pitch variation in

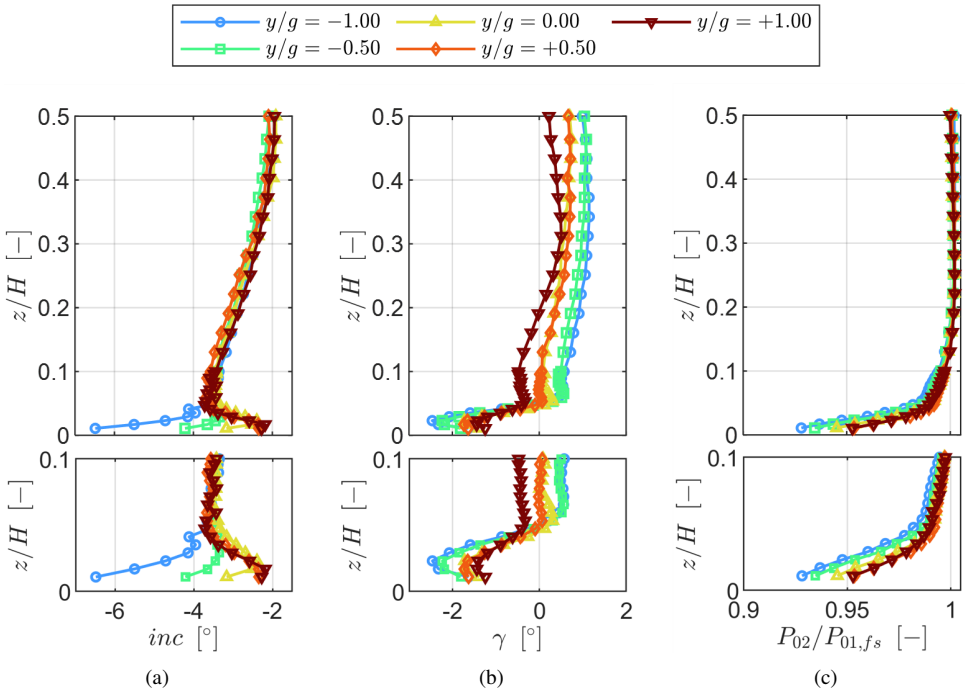

Figure 4.14: Spanwise distributions at Plane 02 during the second phase of testing: inlet flow incidence (a), cascade pitch angle (b), and normalized total pressure (c).

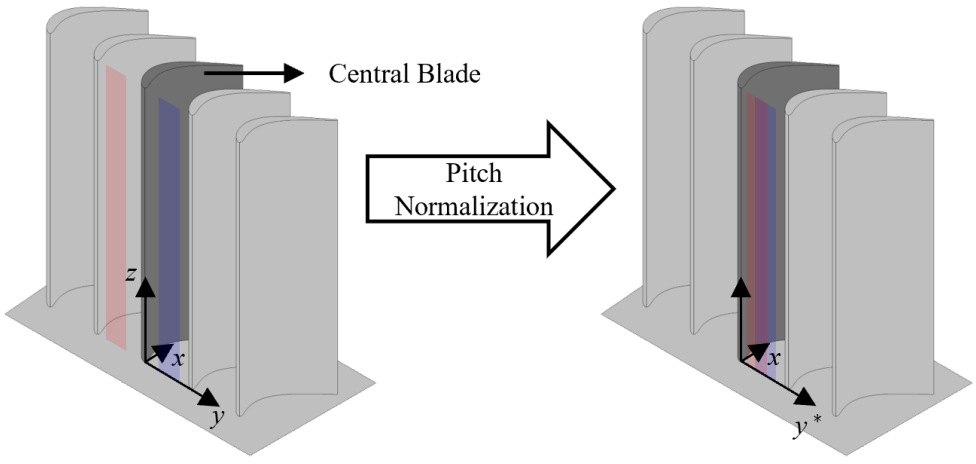

Figure 4.15: Pitchwise virtual shift at Plane 03.

the center of the passage is lower than ±0.37% of the inlet total pressure. Ultimately, the variation is negligible at midspan (see Fig. 4.16(d)).

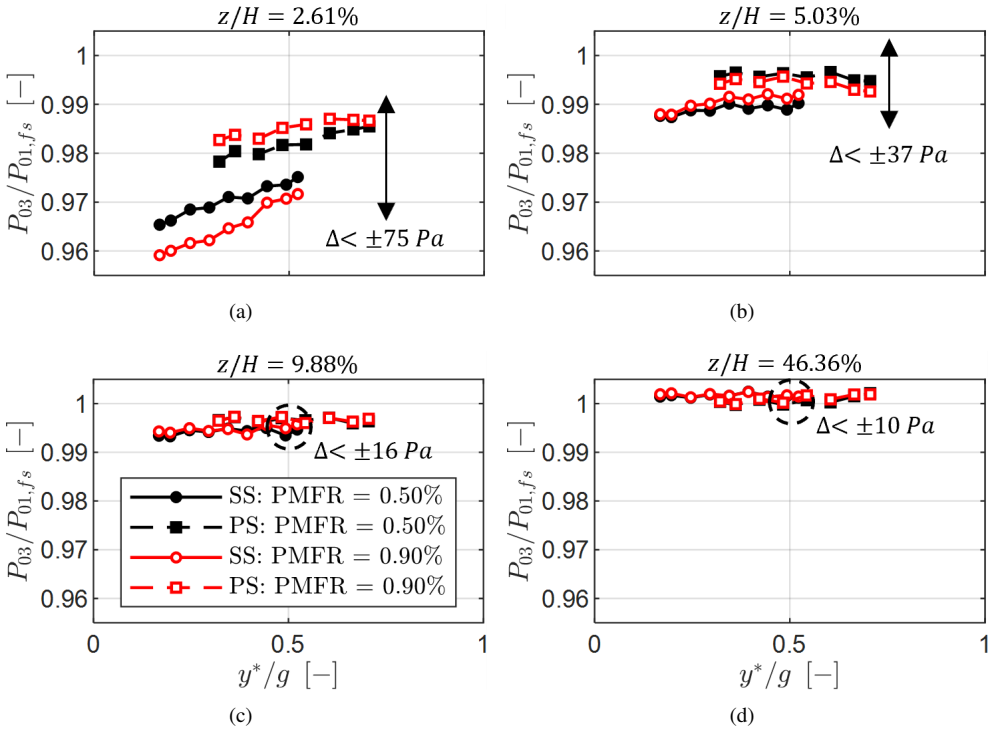

Figure 4.16: Pitchwise distribution of normalized total pressure using re-shifted measurements at Plane 03: z/H=2.61% (a), z/H=5.03% (b) z/H=9.88% (c) and z/H=46.36% (d).

Similar findings were observed in terms of the inlet flow incidence. Near the endwall (see Fig. 4.17(a)), the incidence is practically independent of the purge flow. A maximum angle variation within ±0.60° is present due to the different purge massflow ratios. However, the pitch-to-pitch effect is negligible. The latter effect and the one of the purge do not influence the incidence at midspan (see Fig. 4.17(b)).

4.3.4 Plane 06

The periodicity at Plane 06 was surveyed in the range of y/g∈ [-1.50, +1.50]. The flow domain included three wakes that have been re-shifted similarly to the procedure described in Section 4.3.3. Fig. 4.18 highlights the three domains that assess the pitch-to-pitch downstream periodicity. The pitchwise coordinate y^* denotes that the outlet measurements have been re-shifted by one blade pitch so that the origin of the coordinate system is at the intersection of the line following the outlet metal angle starting from the trailing edge and Plane 06.

Measurements during the first phase were performed at targeted spanwise locations: z/H∈ {0.01, 0.05, 0.10, 0.50}, rather than mapping the whole flow domain. The contours of pri-

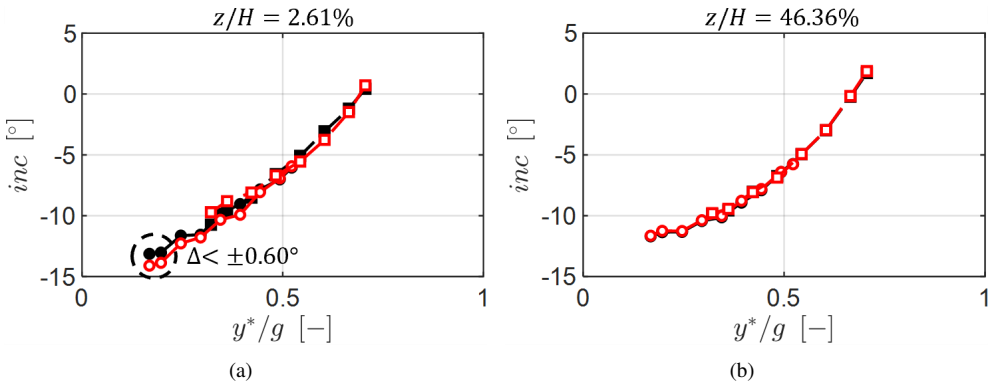

Figure 4.17: Pitchwise distribution of flow incidence using re-shifted measurements at Plane 03: z/H=2.61% (a) and z/H=46.36% (b).

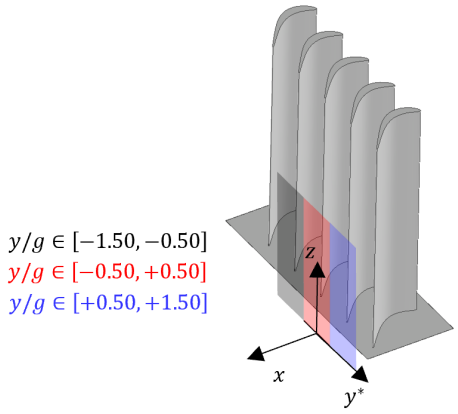

Figure 4.18: Pitchwise virtual shift at Plane 06.

mary flow direction (see Fig. 4.19(a)), cascade pitch angle (see Fig. 4.19(b)) and kinetic energy loss coefficient (see Fig. 4.19(c)) obtained during the productive measurements at the design point (see Section 6.2.3) are presented to aid the description of the periodicity during the first phase. The secondary flow structures present in the flowfield are responsible for the spanwise variation of the presented quantities. Dashed lines highlight the spanwise locations at which the periodicity was investigated.

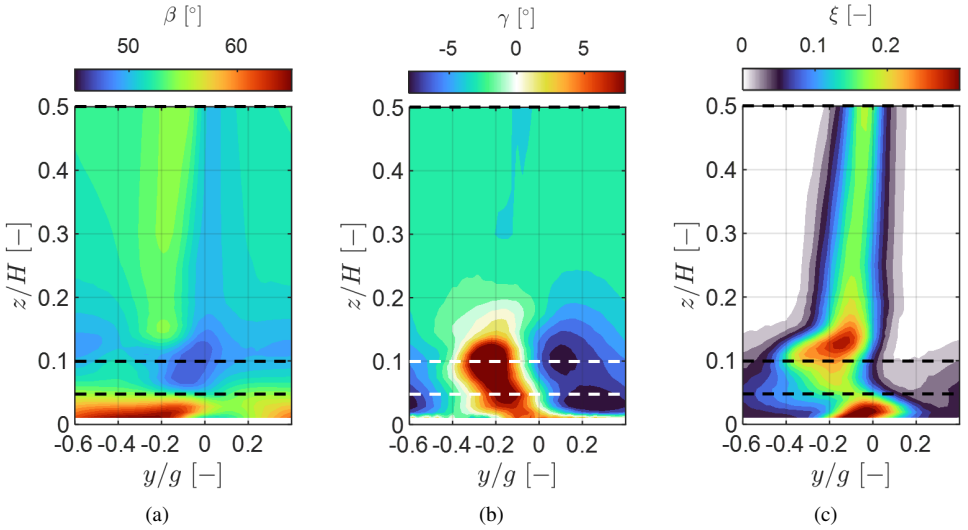

Figure 4.19: Downstream flowfield measured during productive tests: primary flow direction (a), cascade pitch angle (b), and kinetic energy loss coefficient (c).

Fig. 4.20(a) displays the pitchwise mass-averaged primary flow direction for the investigated pitches. The differences are within $\pm 0.30°$. Similar findings are reported for the cascade pitch angle (see Fig. 4.20(b)).

The mass-averaged kinetic energy loss coefficient is presented in Fig. 4.20(c). The pitch-to-pitch variation is negligible. In the secondary flow region, the mass-averaged profiles display discrepancies. At z/H=0.05 (roughly the center of the passage vortex system), a difference in the kinetic energy loss coefficient of 0.012 is present.

The reason for the variation of the mass-averaged loss can be better perceived in the pitchwise distribution of ξ at different spanwise locations displayed in Fig. 4.21. At z/H=0.05, the variation is higher away from the loss peak in the PV region. The loss variation between different wakes is similar in the peak region (impacted by PV and trailing shed vorticity) and the "freestream" region at the following spanwise location. Secondary flow structures do not affect the loss coefficient at midspan. As a result, the cascade outlet flowfield is extremely periodic in the cascade 2D flow region. The slight discrepancy in the freestream region (at y*/g=0.40) is due to the inlet freestream total pressure used to estimate the kinetic energy loss coefficient (see Eq. 2.6.1.3). The inlet freestream total pressure is taken as a single value from a loss correlation (see Section 4.2) that is built by considering a pitchwise range lower than the one measured at the outlet (three blade passages).

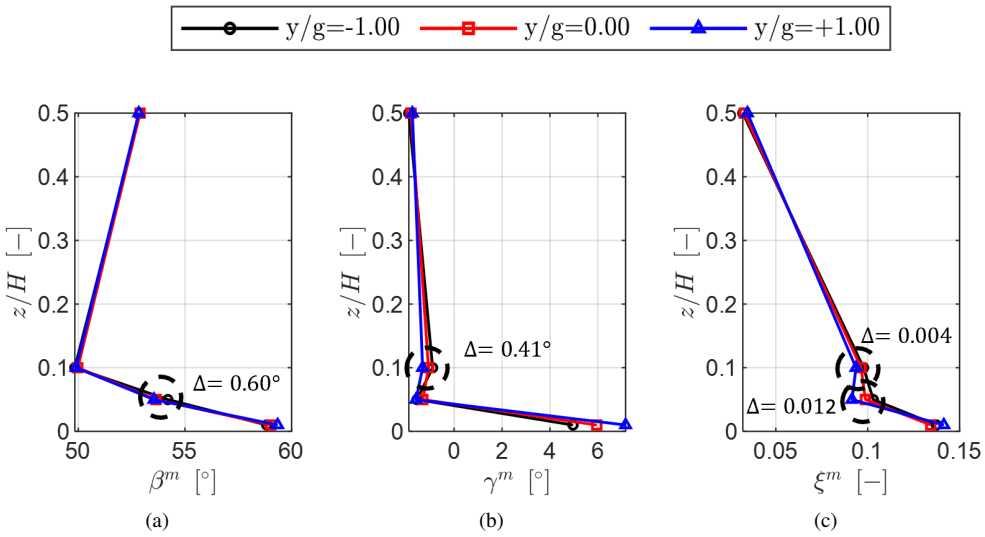

Figure 4.20: Pitchwise mass-averaged profiles obtained for different wakes downstream of the cascade: primary flow direction (a), cascade pitch angle (b), and kinetic energy loss coefficient (c).

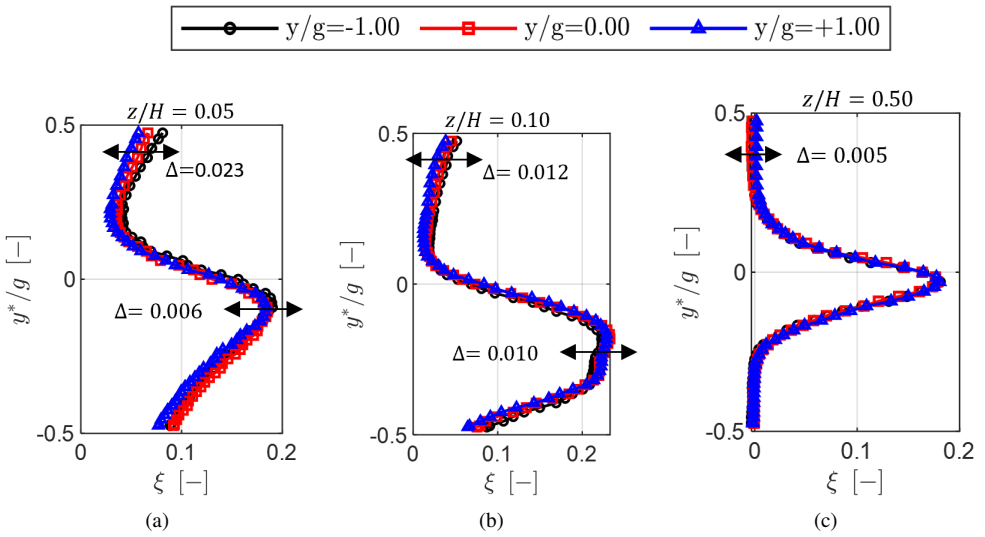

Figure 4.21: Re-shifted pitchwise distribution of kinetic energy loss coefficient measured during the first phase: z/H=0.05 (a), z/H=0.10 (b), and z/H=0.50 (c).

The downstream flowfield was comprehensively mapped during the second testing phase. Fig. 4.22 displays the contours obtained for three blade wakes in terms of primary flow direction (see Fig. 4.22(a), cascade pitch angle (see Fig. 4.22(b) and kinetic energy loss coefficient (see Fig. 4.22(c). The features highlighted are similar for the three wakes.

In the primary flow direction (see Fig. 4.22(a)), two distinct regions are visible: underturning away from the endwall ("A") and overturning near the endwall ("B"); These are mainly linked to the passage vortex. One can see an increase in the intensity of these regions towards the passage above the central blade.

Similar observations can be drawn for the cascade pitch angle (see Fig. 4.22(b)). The regions of downwash ("C") and upwash ("D") result from the PV system as well. The angles are intensified towards passages characterized by negative pitch.

The intensification of the secondary flow structures is also perceived in the kinetic energy loss coefficient displayed in Fig. 4.22(c). Two loss cores are identified. The one near the endwall ("F") sits in the corner vortex region, and the one away from the endwall ("E") results from the presence of the PV and TSV. The intensity of both cores increases towards negative values of y. An additional effect better perceived in the energy loss is the displacement of the loss core away from the endwall—-the latter results from the "stronger" secondary flow structures.

The mass-averaged radial profiles show the intensification of the secondary flow structures and their increased penetration towards the center of the passage. The larger overturning near the endwall ("B") by $\sim$4.00° is visible in Fig. 4.23(a). The magnitude of the underturning peak ("A") increases by $\sim$1.50° as it is displaced away from the endwall.

The pitchwise averaging procedure for the cascade pitch angle includes both regions of upwash and downwash. They cannot be decoupled. However, the higher intensity of the downwash angle ("C" in Fig. 4.23(b)) for the wakes at y/g=-1.00 and y/g=0.00 compared with the remaining one can be seen as increased γ near the endwall. The variation corresponds to $\sim$1.50°.

Lastly, the mass-averaged kinetic energy loss coefficient also supports the previous findings. An increase of the peak intensity of the loss associated with the corner vortex ("F") and PV+TSV ("E") occurs towards negative pitches. An increase of 0.014 is registered. The latter loss peak is also displaced away from the endwall.

The loss variation across different passages is due to the pitchwise variation of the inlet boundary layer thickness (see Section 6.2.1.1). In addition, Walsh and Gregory-Smith [2] found that the inlet boundary layer skewness significantly modifies the inlet vorticity distribution, impacting the secondary flow development. Negatively skewed boundary layers promote higher secondary loss. Fig. 4.24 schematically displays the inlet boundary layer skewness taken from [2]. The inlet boundary layer measured at y/g=-1.00 is characterized by a more negative skewness than at increasing pitchwise locations (see Fig. 4.14). As a result, the secondary loss is higher towards negative pitches.

Despite the impact of the secondary flow structures on the mass-averaged quantities near the endwall, the midspan aerodynamics are characterized by reasonable periodicity as displayed in Fig. 4.25.

In addition to the unsteady wakes, the periodicity was also investigated in the presence of purge flow in the third testing phase. Fig. 4.26 displays the flowfield in terms of primary flow direction (see Fig. 4.26(a)), cascade pitch angle (see Fig. 4.26(b)) and kinetic energy loss

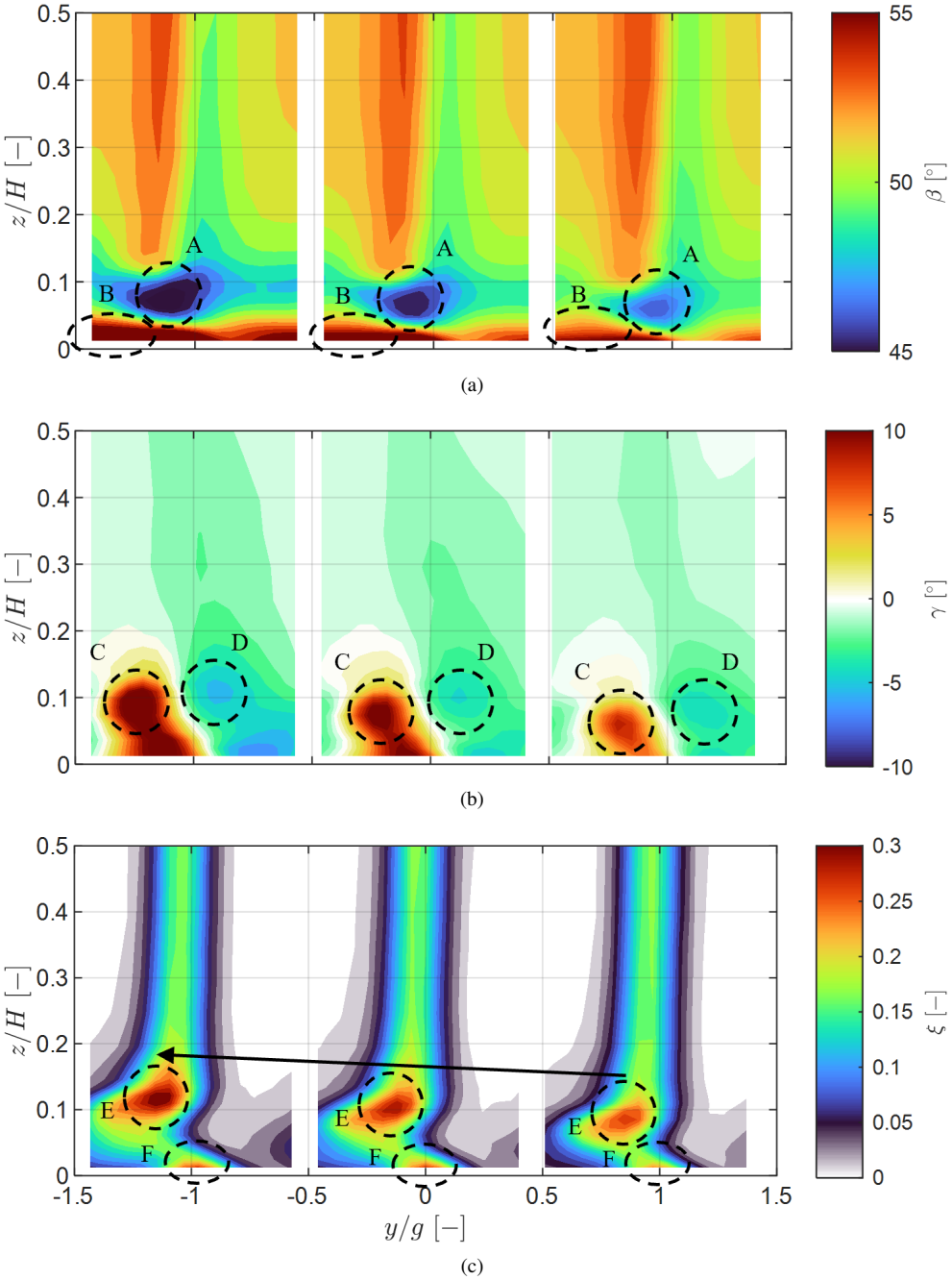

Figure 4.22: Downstream flowfield measured during periodicity surveys for the second phase: primary flow direction (a), cascade pitch angle (b), and kinetic energy loss coefficient (c). Refer to the legend of the previous figure.

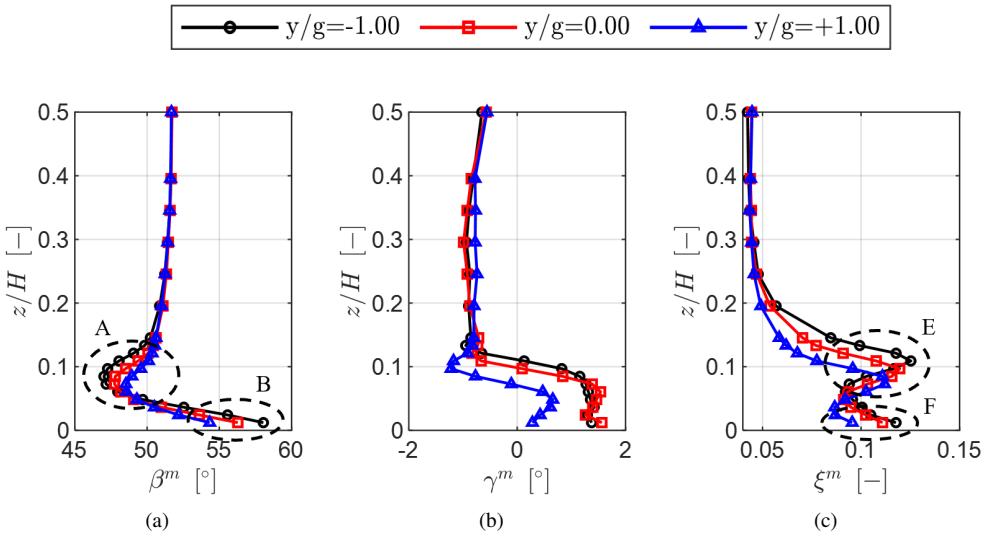

Figure 4.23: Pitchwise mass-averaged profiles obtained for different wakes downstream of the cascade during the second phase: primary flow direction (a), cascade pitch angle (b), and kinetic energy loss coefficient (c).

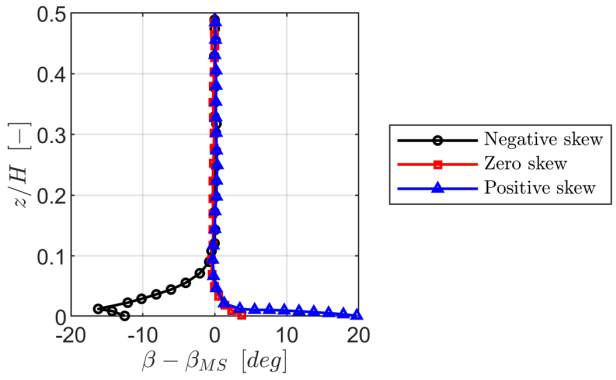

Figure 4.24: Schematic representation of inlet boundary layer skewness from [2].

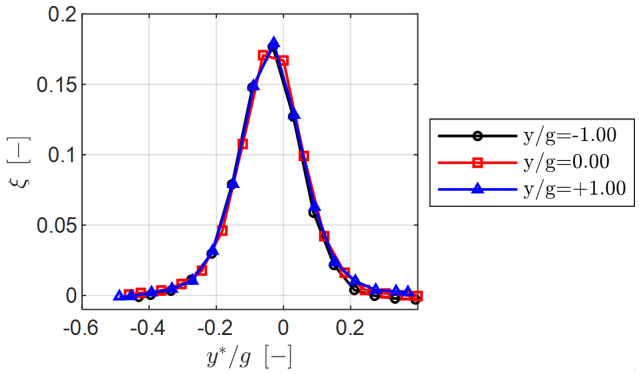

Figure 4.25: Re-shifted pitchwise distribution of loss coefficient at z/H=0.50 measured during the second phase.

coefficient (see Fig. 4.26(c)) at the outlet. The measurements were performed for a purge massflow ratio of 0.90%. Similar flow features as described for Fig. 4.22 are present. The intensity of the secondary flow structures increases towards negative pitchwise locations. However, the secondary flow structures have no significant displacement, as in the case without purge flow. A new loss core is highlighted ("E"). The latter resulted from the intensification of the PV and was also observed during the productive measurements for increasing purge massflow ratio (see Section 6.2.3.3).

The resulting mass-averaged primary flow direction (see Fig. 4.27(a)) displays similar profiles for the regions containing the wakes from the blade at y/g=-1.00 and y/g=0.00. The flow underturning and overturning are reduced for the remaining profile. The periodicity of the cascade pitch angle (see Fig. 4.27(b)) and energy loss coefficient (see Fig. 4.27(c)) radial profiles are also significantly improved compared to the case without purge flow. The more considerable disagreement in the loss profiles lies near the endwall ("C"). The higher peak loss is similar for the wakes from the blade at y/g=-1.00 and y/g=0.00. The increase in magnitude and migration away from the endwall from the peak associated with a stronger PV ("E") can be perceived.

4.4 Probe Interference

Measurements performed with probes introduce non-negligible effects in the aerodynamics of the testing article [3] and the measured flowfield. The measured flowfield is impacted by the interaction of the probe and linear cascade potential fields [4]. In addition, a local blockage can cause massflow redistribution and impact the flowfield upstream of the cascade [5]. According to Truckenmuller and Stetter [3], introducing the probe stem perpendicularly to the flow can modify the dynamic pressure up to 15%.

The probe interference in the scope of this work was addressed by investigating the impact of the measuring probes on the endwall and blade tap measurements. The cobra or L-shaped five-hole probe was traversed at their respective planes. Fig. 4.28 displays the probe locations for the following investigation. The same color code will be used in the figures supporting the findings.

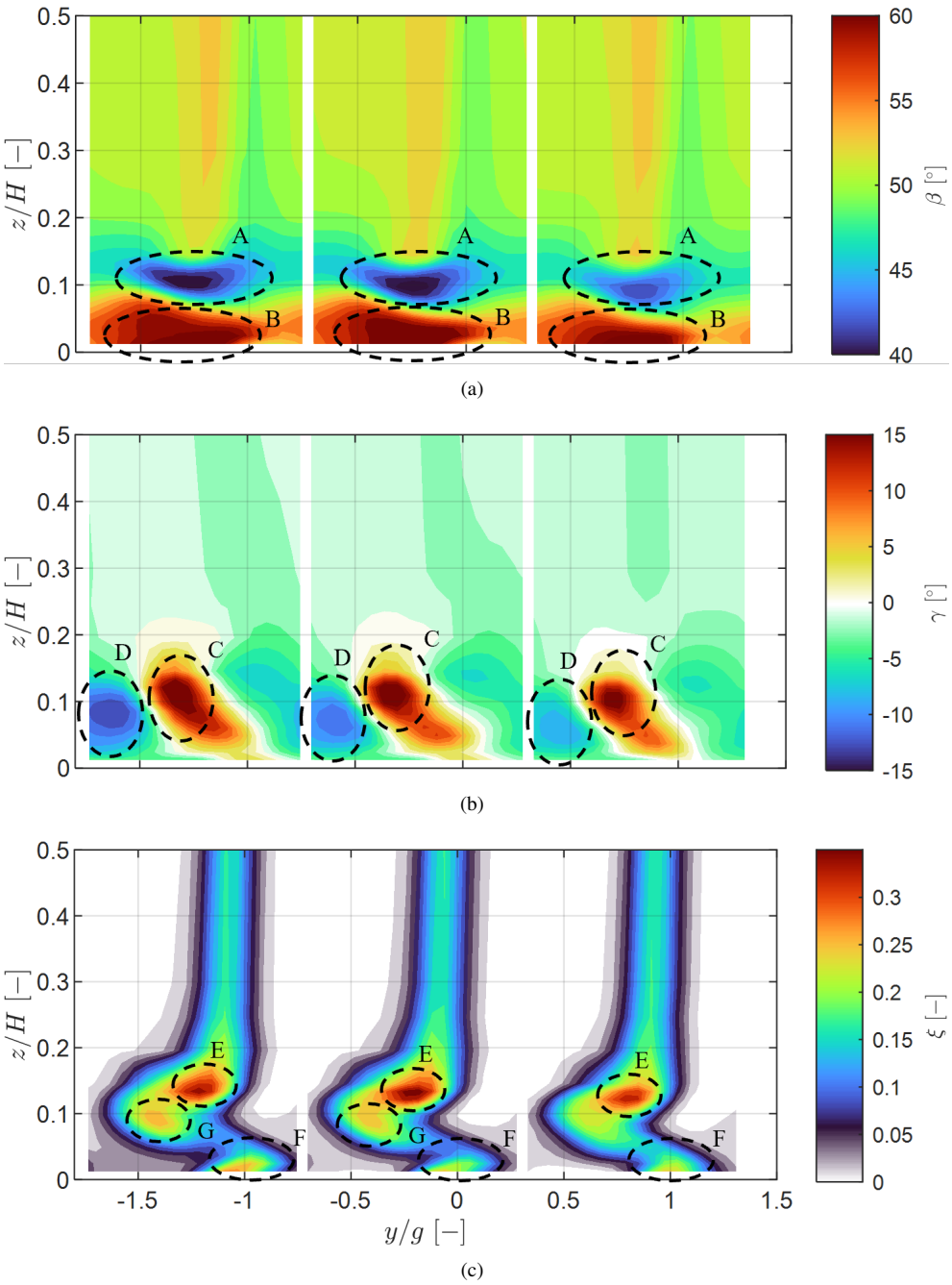

Figure 4.26: Downstream flowfield measured during periodicity surveys for the third phase: primary flow direction (a), cascade pitch angle (b), and kinetic energy loss coefficient (c)

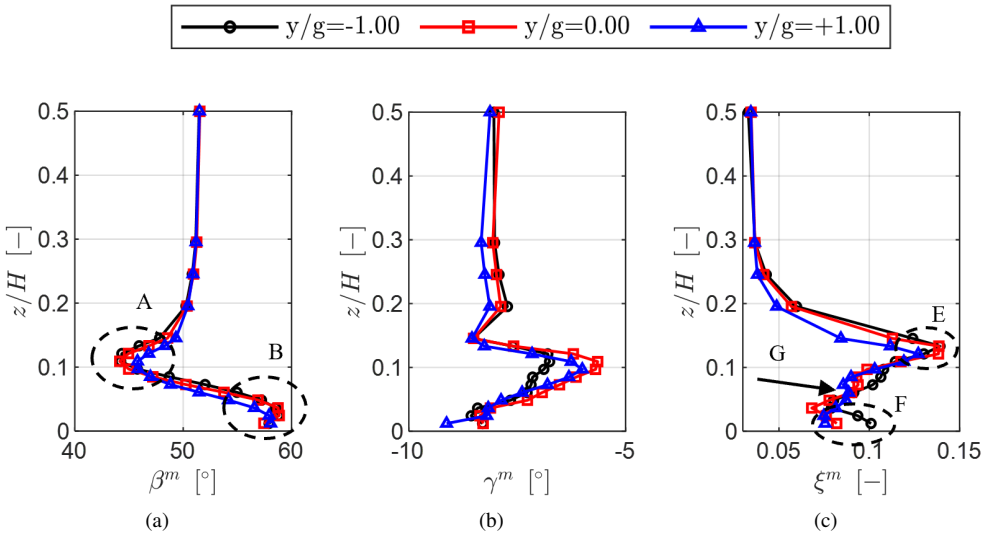

Figure 4.27: Pitchwise mass-averaged profiles obtained for different wakes downstream of the cascade during the third phase: primary flow direction (a), cascade pitch angle (b), and kinetic energy loss coefficient (c).

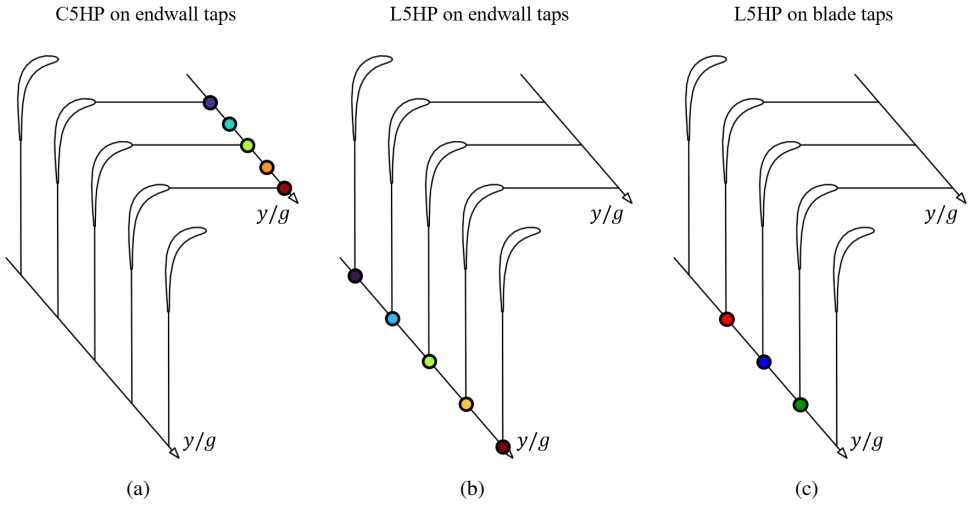

Figure 4.28: Schematic representation of probe movement during probe interference investigations: impact of C5HP on endwall taps (a), impact of L5HP on endwall taps (b), and impact of L5HP on blade taps (c).

4.4.1 Inlet Measurements

The effect of inserting a stem perpendicular to the incoming flow into the flowfield was addressed by inserting the cobra five-hole probe at Plane 02. The inlet and outlet isentropic Mach number measured at the endwall at Planes 01 and 06 through the taps were compared for an undisturbed case and cases where the probe is present. The probe location along the pitch and span was varied. In the following figures, the color of the curve denotes the probe's pitchwise location (see Fig. 4.28(a)). The probe interference is characterized using two sets of figures with the Cobra five-hole probe placed near the endwall (z_{C5HP}/h=0.01) and at midspan (z_{C5HP}/h=0.50). Fig 4.29 highlights the position of the Cobra five-hole probe in the spanwise direction.

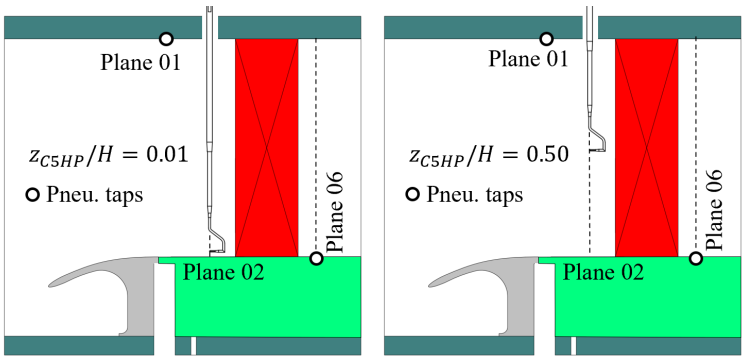

Figure 4.29: Sketch of spanwise location of C5HP relative to the cascade: z_{L5HP}/H=0.01 (a) and z_{L5HP}/H=0.50 (b).

Fig. 4.30 aims at characterizing the impact that the probe location has on the inlet and outlet static pressure. An error bar corresponding to the systematic uncertainty is included to highlight that the variations extend beyond the measurement chain uncertainty. A schematic view of the probe relative to the cascade is displayed in Fig. 4.28(a).

It was found that the insertion of the probe in the flowfield impacts the static pressure at Plane 01 regardless of the probe location. When the probe is near the endwall, the isentropic Mach number decreases in passages blocked by the probe stem. Fig. 4.30(a) highlights that the local isentropic Mach number at y/g=-1.00 can vary by as much as 0.02 when the probe is traversed. The most significant variation in the profile occurred when the probe was at the most positive pitchwise location.

The variations and probe impact are reduced when its penetration into the flowfield is diminished (see Fig. 4.30(a)). When the probe head sits at midspan, the maximum variation in the inlet isentropic Mach number (see Eq. 2.17) is reduced by half. The fact that the Mach number is increasing in passages unobstructed by the probe stem suggests that the probe blockage effect extends to Plane 01. A possible redistribution of massflow to unblocked passages takes place.

The variations in the measured outlet static pressure are lower. When the probe sits near the endwall at Plane 02 (see Fig. 4.30(c)), the outlet isentropic Mach number (see Eq. 2.18)

distribution preserves its shape. Local variations in the order of 0.01 were still observed as the probe was traversed. When the probe is at midspan, the outlet isentropic Mach number is practically unaffected, as shown in Fig. 4.30(d). These findings may be biased because the taps at Plane 06 sit on the endwall instead of the slot where the cobra five-hole probe was inserted (see Fig. 4.31).

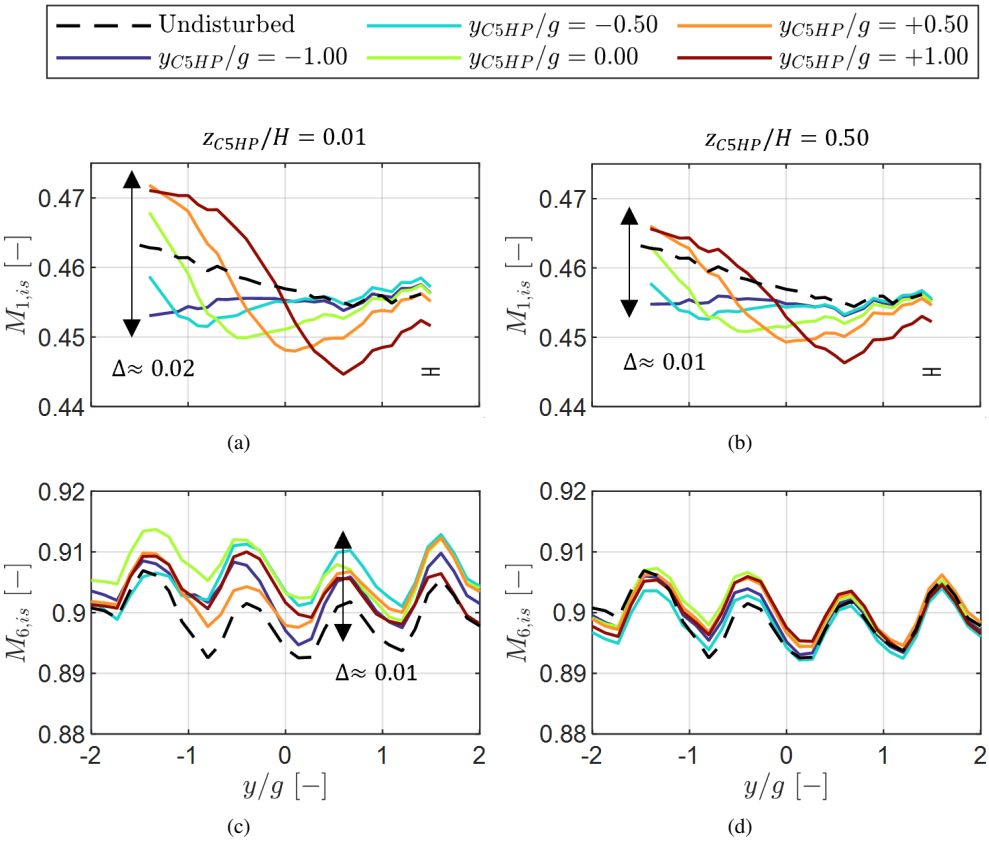

Figure 4.30: Pitchwise distribution of the isentropic Mach number at Plane 01 when the C5HP is inserted at Plane 02 and position is varied: near the endwall (a) and at midspan (b), and isentropic Mach number at Plane 06 when the probe is near the endwall (c) and at midspan (d).

4.4.2 Outlet Measurements

A similar exercise was performed by inserting the L-shaped five-hole probe in a slot downstream of Plane 06. The probe head was situated at Plane 06. The probe traverse covered four passages. In the following figures, the probe pitchwise location is denoted through colors (see Fig. 4.28(b)). The probe interference is characterized utilizing two sets of figures with the L-shaped five-hole probe placed near the endwall (z_{L5HP}/h=0.01) and at midspan (z_{L5HP}/h=0.50). Fig 4.31 highlights the position of the L-shaped five-hole probe in the spanwise direction.

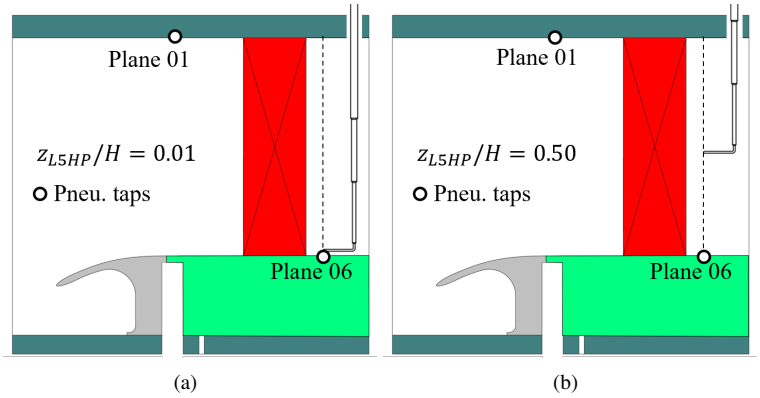

Figure 4.31: Sketch of spanwise location of L5HP relative to the cascade: z_{L5HP}/H=0.01 (a) and z_{L5HP}/H=0.50 (b).

It was found that the downstream inserted probe impacts the flowfield up to Plane 01. The pitchwise distribution of the inlet isentropic Mach number (see Eq. 2.17) could not be recovered regardless of the probe location. The deficit in the inlet isentropic Mach number in the passages instrumented with taps exceeded 0.05. The probe traversing also impacted the pitchwise profiles. Near the endwall (see Fig. 4.32(a)), the local Mach number was higher in passages not blocked by the probe stem. Fig. 4.32(b) highlights that even though the impact from traversing the probe was reduced as the probe immersion was reduced, a systematic deficit in the isentropic Mach number was kept.

The L-shaped five-hole probe had a more significant impact on the static pressure measurements at Plane 06. The probe head sits on the same plane as the pressure taps. When the head is near the endwall taps, a local effect can be observed at the taps below the head (see Fig. 4.32(c)). The probe presence heavily impacts the outlet isentropic Mach number (see Eq. 2.18) profiles. The pitch-to-pitch variation can amount to as much as $\sim$0.23.

A particular feature worth noticing is that the isentropic Mach number is higher in passages below the one where the probe is located (towards positive pitches). This effect is linked to the probe blockage and interaction of the probe with the blade potential field (see Section 4.4.3). When the probe is at its least intrusive location (y_{L5HP}/g=+2.00), the undisturbed isentropic Mach number is still not retrieved.

The pitchwise variation decreases when the probe immersion is reduced (see Fig. 4.32(d)). However, local variations equal to 0.06 are still more significant than the systematic uncertainty.

These results suggest that the probe downstream caused a global redistribution of massflow to passages adjacent to the blocked one. This was previously reported in research dealing with turbine [6] and compressor [5] linear cascades.

4.4.3 Blade

The impact of the L-shaped five-hole probe on the blade suction side aerodynamics was investigated. The L-shaped five-hole probe was traversed in pitch, from y/g=-1.00 to +1.00,

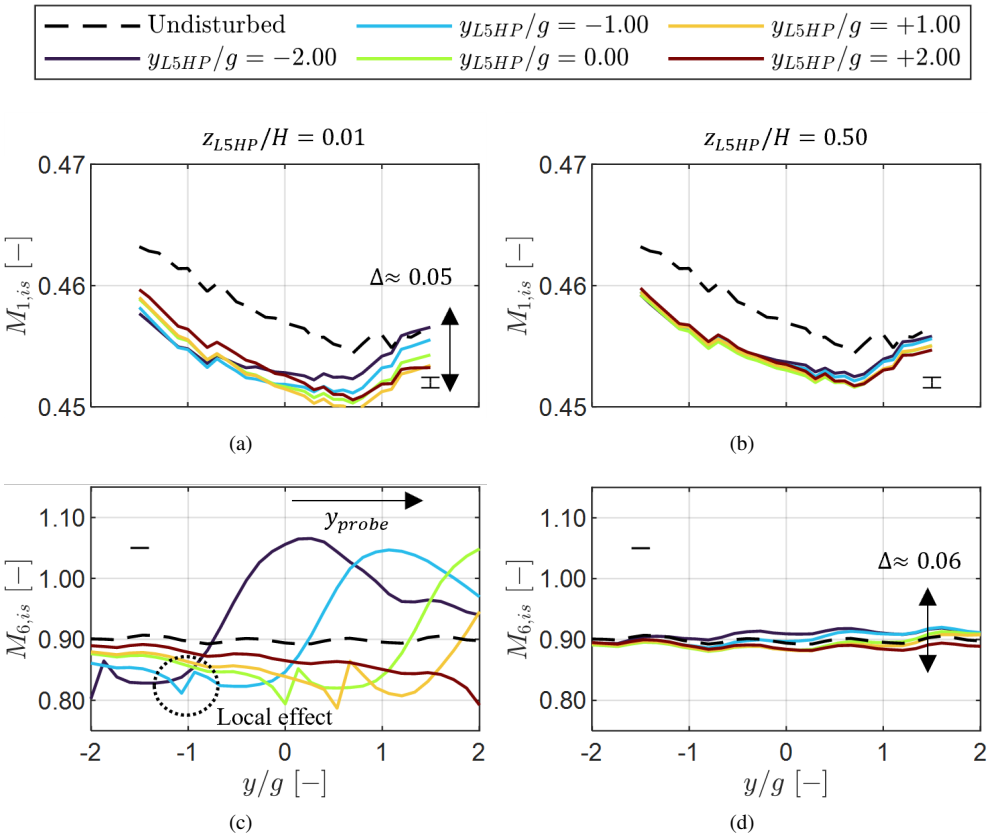

Figure 4.32: Pitchwise distribution of the isentropic Mach number at Plane 01 when the L-shaped five-hole probe is measured at Plane 06 and position is varied: near the endwall (a) and at midspan (b), and isentropic Mach number at Plane 06 when the probe is near the endwall (c) and at midspan (d).

and span, from near the endwall to midspan. A schematic view of the probe relative to the cascade is displayed in Fig. 4.28(c). The blade loading was compared against the reference without the probe for the M=0.90; Re=70k flow case. The suction side instrumented blade was measured with the taps at z/H=0.30 and z/H=0.50.

Fig. 4.33(a) displays the surface isentropic Mach number along the suction side surface length for undisturbed and disturbed cases. The suction side blade loadings were obtained at midspan. The probe presence does not significantly impact the leading edge region. The effects start to be noticeable near the velocity peak, which is lower when the probe is inserted in the flowfield. The lower loading in the presence of the supports the hypothesis that the inlet massflow is redistributed to passages unimpeded by the probe.

If one focuses on the rear portion of the suction side (see Fig. 4.33(b)), the effect of traversing the probe is better perceived. The disturbed loadings were obtained with the probe at z/H=0.50. The loading increased as the probe moved towards positive pitchwise locations (passages below the central blade). This effect has been encountered in the linear cascade experiments of Boerner et al. [6]. A numerical study of Torre et al. [7] found the same effect in an annular configuration.

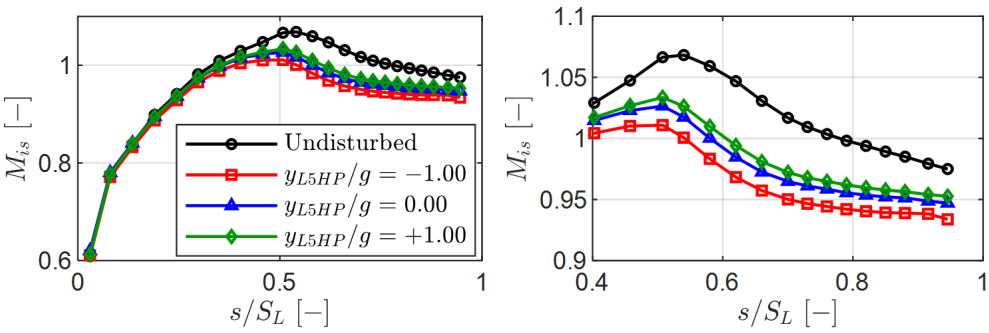

Figure 4.33: Impact of traversing the L-shaped five-hole probe at z_{L5HP}/H=0.50 on suction side blade loading at z/H=0.50: overall loading (a) and zoomed-in portion highlighting rear portion of suction side (b).

Fig. 4.34 displays the deficit in isentropic Mach number relative to the undisturbed case for two cases where the probe immersion was varied. When the probe was positioned near the endwall (see Fig. 4.34(a)), the deficit in the isentropic Mach number increased by ∼60% near the velocity peak region. The effect of the probe pitchwise location also varied, showing higher variation in the loading with the probe location. Reducing the probe immersion (see Fig. 4.34(b)) also reduced the impact on the loading towards the leading edge.

4.4.4 Compensation

Retrieving the original blade loading was attempted by increasing the overall massflow through the cascade. The massflow varied so that the outlet Mach number at Plane 06 was in the range of 0.88 to 0.92. A Mach number of 0.88 corresponds to the case where the cascade is operated to reach the nominal operating point when no probe is introduced downstream.

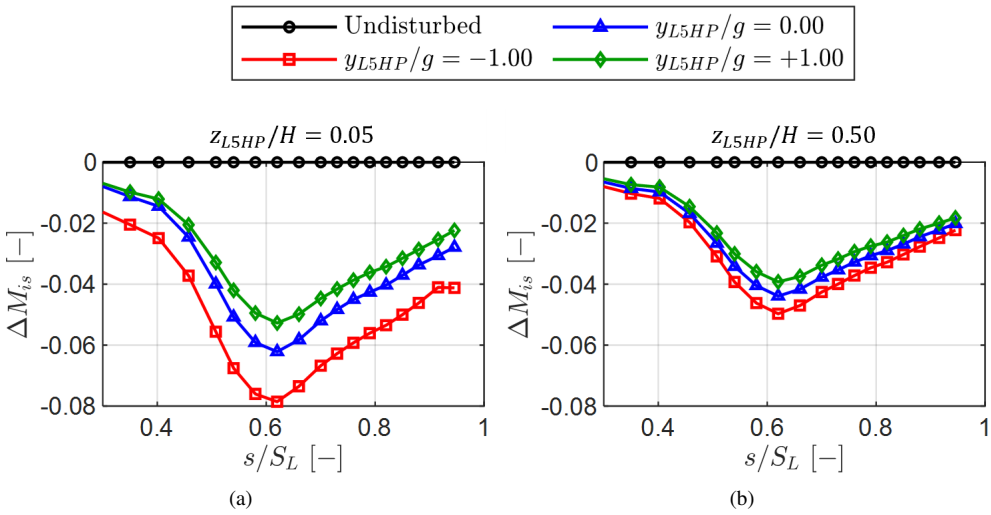

Figure 4.34: Impact of traversing the L-shaped five-hole probe when the blade taps are at z/H=0.50: near the endwall at z/H=0.10 (a) and midspan (b).

Fig. 4.35(a) displays the deficit in the blade isentropic Mach number along the suction side surface for the undisturbed case and three compensated cases when the probe sits at a very intrusive location (y_{L5HP}/g=-1.00; z/H=0.10). The blade loading is the one obtained at midspan. Increasing the outlet Mach number improves the agreement between the undisturbed and disturbed cases. When the probe is near the endwall, the compensation is insufficient to retrieve the nominal blade loading since there is a more significant redistribution of massflow to adjacent passages. When the probe measures at midspan, the compensated cases of M_{out}=0.92 and 0.94 exceed the nominal loading. The variation reached 0.05 near the velocity peak region for the highest Mach number.

As a result of modifying the blade aerodynamics, the outlet flowfield at Plane 06 was also altered. This effect was investigated by performing measurements at Plane 06 utilizing the L-shaped five-hole probe. Pitchwise traverses have been performed in the secondary flow region, z/H=0.10, and midspan, z/H=0.50. The impact was characterized based on the primary flow direction and kinetic energy loss coefficient (see Fig. 4.36).

Fig. 4.36(a) displays the pitchwise distribution of the primary flow direction at 10% span. The topology of the profiles is similar. The main variation due to increasing the outlet Mach number amounts to $\sim$0.30°. Given the local absolute flow angle, this variation is negligible.

The same cannot be concluded for the traverse performed at midspan. The variation between the lower Mach number and intermediate cases is significant. A further increase of the Mach number does not significantly modify the amplitude of the variation. The pitchwise distributions at midspan display a similar topology, a sinusoidal-like shape.

In comparison, the profile obtained with the CFD setup reported in Section 3.2 is included and represented by a black dashed line. The fluctuations are one order of magnitude lower than for the experimental data. The large fluctuations observed experimentally result from the probe measuring in a velocity gradient. The probe head causes a local flow deflection of the blade wake. Recent PIV measurements of Okada et al. [8] using the SPLEEN test case

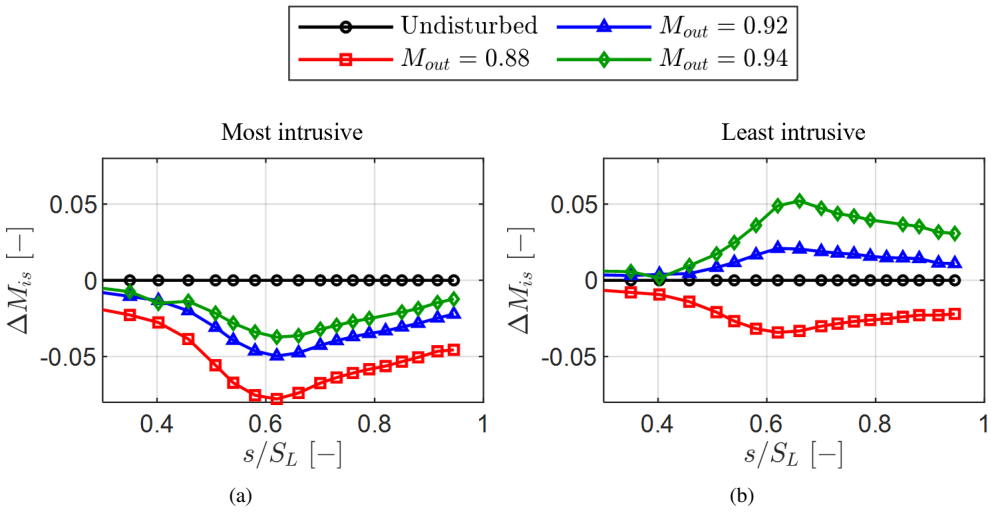

Figure 4.35: Impact of increasing the outlet Mach number to retrieve nominal blade loading when the blade taps are at z/H=0.50: L5HP sits at y_{L5HP}/g=-1.00 near the endwall at z_{L5HP}/H=0.05 (a) and at midspan (b).

captured slightly higher fluctuations than the numerical results, still less than half of the ones measured with the L-shaped five-hole probe. The PIV data is contained in an open-access database [9]. So far, Internal investigations have allowed the conclusion that LES allows capturing the PIV distribution, suggesting that scale-resolving simulations are required to capture the ongoing flow physics.

The impact of probes on measured flow angle was pointed out in previous research works [10, 11]. The pointed-out references presented corrections to address the error imposed by the probe's finite size and the one arising from measuring velocity gradients. Typically, corrections rely on the first corrections proposed by Ligrani [12].

The first correction proposed by Ligrani concerning the probe head finite size was taken into account in this work. Corrections for the velocity gradient depend on the probe head geometry and often rely on experimental and/or numerical calibrations. These were not performed in the scope of this work. Torre et al. [7] concluded that the pitchwise averaged quantity is unaltered inside and outside the secondary flow region.

The pitchwise distribution of the loss coefficient near the endwall is displayed in Fig. 4.36(c). The more significant variations with Mach number occur in the secondary flow cores (i.e., y/g$\in$ [-0.4, 0.0]). The variation can amount to as much as 10% of the local loss.

Variations at midspan are higher, particularly as the Mach number is increased from the lower to the intermediate one. Similar to the flow angle, the variation between the two highest Mach numbers is insignificant.

In terms of averaged flow metrics, the pitchwise mass-averaged primary flow direction variation is displayed in Fig. 4.37(a). The variation for both midspan and near the endwall measurements is negligible. The mass-averaged kinetic energy loss coefficient (see Fig. 4.37(b)) in the secondary flow region is not greatly sensitive to the Mach number variation. However, the mass-averaged profile loss for the uncorrected flow case (M_{out}=0.88)

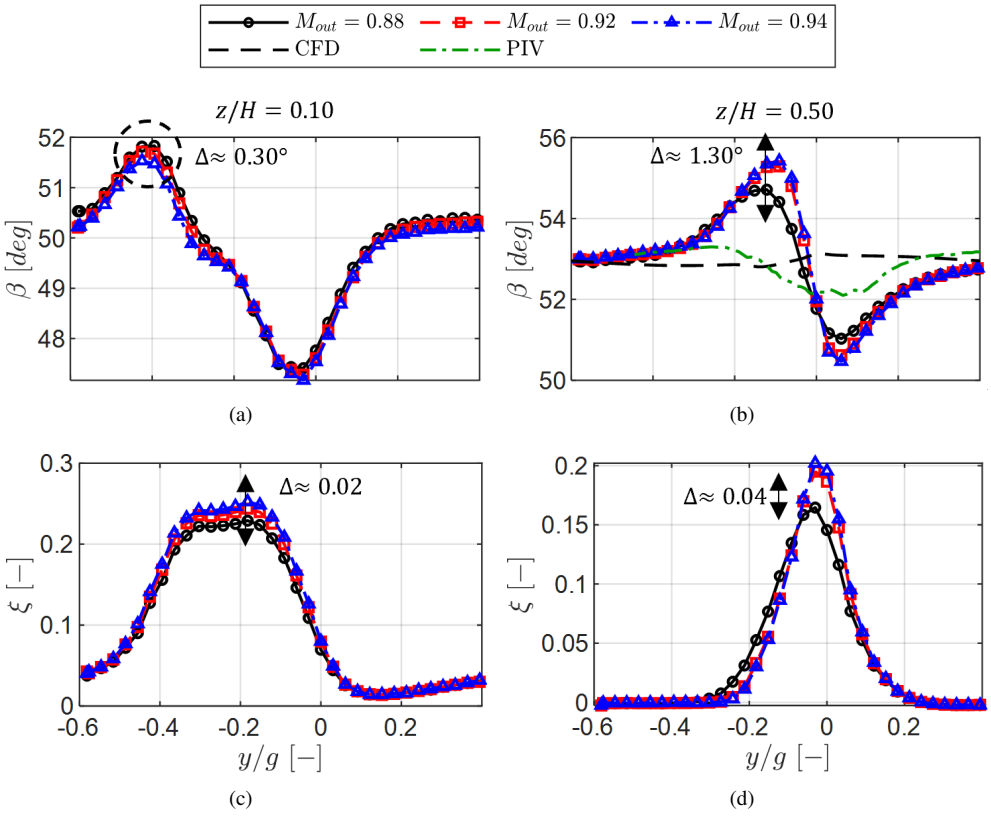

Figure 4.36: Impact of increasing the Mach number on pitchwise distribution of primary flow direction near the endwall (a) and at midspan (b), and kinetic energy loss coefficient near the endwall (a) and at midspan (b).

is nearly 6% lower than for the intermediate Mach number. The profile loss monotonically increases with the Mach number in the investigated range.

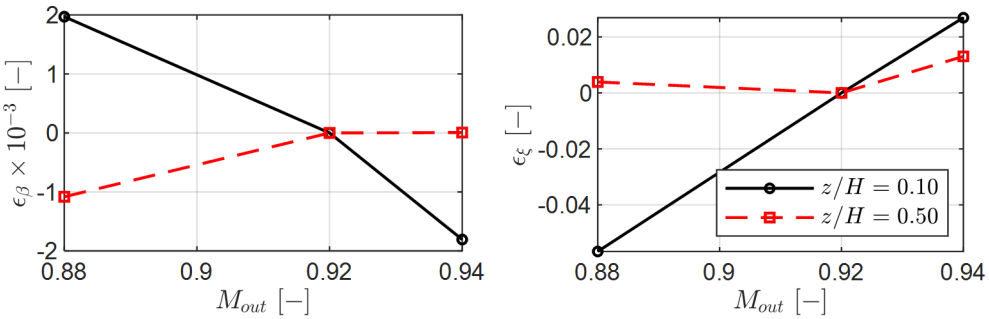

Figure 4.37: Impact of increasing the Mach number on mass-averaged quantities: primary flow direction (a) and kinetic energy loss coefficient (b).

The results from our previous tests, which included blade loading, pitchwise profiles, and mass-averaged quantities, led us to the conclusion that the interference from the probe varies depending on its location. Compensation is necessary to ensure accurate blade aerodynamics and losses. We observed that the loss profile in the uncorrected scenario differs significantly from the cases with increased Mach numbers. Our findings showed that the intermediate case (M_{out}=0.92) had a suitably low deviation for both the most minor and most intrusive scenarios (refer to Fig. 4.35). Additionally, we noted that the mass-averaged loss did not change notably when the Mach number was raised further. Due to the nature of our current measurements, it was impossible to apply location-dependent compensation. Consequently, we determined the kinetic energy loss coefficient by adjusting the cascade operating point ($\Delta M_{6,is}$=+0.02 for the nominal flow case) during testing when the probe was inserted into the test section.

Throughout the manuscript, results obtained with probes at the outlet refer to a nominal Mach number. However, the Mach number in the rig was higher to ensure that the blade loading was near the nominal one.

4.4.5 Monitoring of Operating Point

The probe intrusiveness not only impacts the flow metrics and measurements used to describe the cascade performance. Monitoring the inlet and outlet flow conditions relies on the static pressure measured at Plane 01 and Plane 06 (see Section 2.4.2.3).

Based on the results previously displayed in Fig. 4.30 and Fig. 4.32, the averaged inlet and outlet isentropic Mach number as function of the cobra five-hole probe and L-shaped five-hole probe probe pitchwise position were obtained, respectively. Fig. 4.38(a) displays the deviation of the isentropic Mach number with respect to the undisturbed case. The solid line denotes the isentropic Mach number at Plane 01, while the dashed line is at Plane 06. The black line represents measurements in which the probe was near the endwall (z_{C5HP}/H=0.01), while the red line represents measurements performed with the cobra five-hole probe at

midspan. The presence of the cobra five-hole probe in the test section translates into variations of the averaged isentropic Mach number within ± 0.005. This value is considered satisfactory small.

The same type of analysis for when the L-shaped five-hole probe is measuring at Plane 06 is displayed in Fig. 4.38(b). The averaged isentropic Mach number at the inlet is impacted by the systematic deficit reported previously (see Fig. 4.32(a) and Fig. 4.32(b)). However, the fluctuations when the probe is traversed over one pitch are still within ± 0.005.

The variations at Plane 06 are non-negligible. Traversing the L-shaped five-hole probe near the endwall resulted in a variation of the mean outlet isentropic Mach number of ± 0.05. The difference was significantly lower when the probe was traversed at midspan (± 0.01). However, large fluctuations are still overall compared to the inlet values.

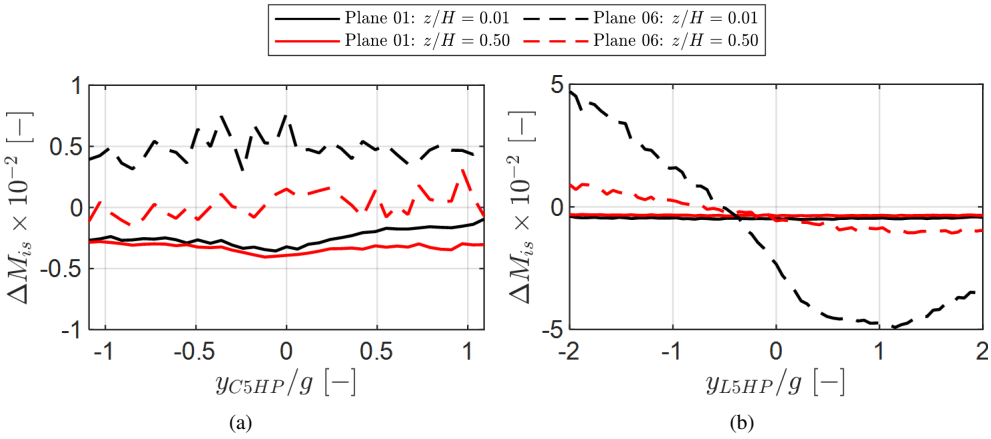

Figure 4.38: Impact of measuring probes on inlet and outlet isentropic Mach number: Cobra five-hole probe (a) and L-shaped five-hole probe (b).

Attempting to reduce the probe impact on the outlet Mach number by reducing the number of averaging taps is not a viable way of ensuring the stability of the monitored flow conditions. Fig. 4.39 displays the time history of the isentropic Mach number during a traverse performed with the L-shaped five-hole probe (2D mapping in span and pitch). The colored lines denote the number of taps used to obtain the averaged outlet isentropic Mach number. The number of taps increases from negative towards positive pitches, as highlighted in the sketch in Fig. 4.39(a).

Periodic oscillations due to the probe movement are present regardless of the number of taps used in the averaging procedure. At a given spanwise location, z_i, the probe is traversed in the pitchwise direction. If the probe is moved towards negative pitches, the averaged outlet Mach number increases (black shaded region in Fig. 4.39(b)) and vice-versa. Typically, after the probe reaches the far most position in the measurement grid, it is moved in the spanwise direction before being traversed in the opposite pitchwise direction (red shaded region in Fig. 4.39(b)).

The cascade far exit pressure tap (see Section 2.4.2.4) was used to monitor an isentropic Mach number computed with the cascade inlet total pressure and the local static pressure to circumvent this issue. The far exit tap computed quantity is independent of the probe location,

as highlighted by the solid black line in Fig. 4.39(b).

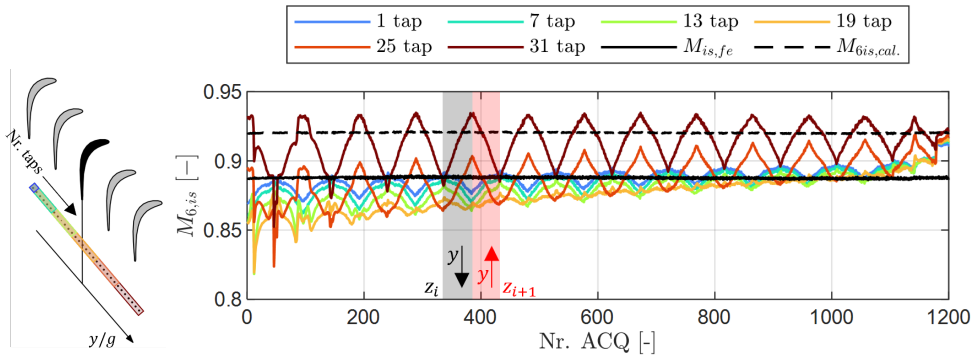

(a) (b)

Figure 4.39: Variation of outlet isentropic Mach number during L-shaped five-hole probe traverse: taps used for averaging (a) and time-history of averaged outlet Mach number (b).

A correlation based on measurements performed in the absence of the probes inside the test section was built to estimate the Mach number at the cascade outlet during probe measurements. The polynomial was selected to be a function of the far exit isentropic Mach number (2^{nd} order) and Reynolds number (1^{st} order):

$$M_{6,cal}\left(M_{fe}, Re_{fe}\right) = C_1 M_{fe}^2 + C_2 M_{fe} + C_3 Re_{fe} + C_4 M_{fe} Re_{fe} + C_5 \tag{4.7}$$

The fitted coefficients and goodness of correlation parameters are reported in Table 4.6. Even though the isentropic Reynolds number at the far exit was used as a variable, the outlet Mach number is poorly correlated to this quantity, as highlighted by coefficients C_3 and C_4. Nonetheless, the correlation is considered under-constrained (49 degrees of freedom), and the dependency was kept.

Table 4.6: Calibration coefficients, goodness of fitting, and standard error of far exit flow correlation.

C_1 [−]	C_2 [−]	C_3 [−]	C_4 [−]	C_5 [−]	R^2	$S_{\mathbb{M}}$ [−]
-0.709	2.09	-8.955e-08	1.348e-07	-0.3698	0.999945	1.096e-4

Using the above correlation, one can retrieve and monitor the outlet Mach number in the test section (dashed line in Fig. 4.39(b)). The retrieved quantity is also independent of the probe location.

4.5 Conclusions

The rig has been commissioned regarding stability, periodicity, and probe interference. Throughout the test campaign, the rig was found to be stable. A variation in Mach and

Reynolds numbers within $\pm 0.22\%$ and $\pm 0.40\%$ from the nominal operating point, respectively. The Strouhal number was found to be within $\pm 0.27\%$ from the nominal value, and the purge massflow ratio to be within $\pm 0.46\%$.

The inlet boundary layer was highly periodic to steady inlet flow cases (variation of displacement thickness within $\pm 0.5\%$ of the chord). Introducing the wake generator resulted in a variation of the periodicity at Plane 02 due to the rotating motion of the wake generator. In particular, the near-endwall quantities suffered the most. Variations in incidence exceeding $\pm 2.00^\circ$ were observed. The variation near the endwall reached $\pm 1.25\%$ of the inlet total pressure. At Plane 03, the purge-induced flow non-periodicity was found to be negligible in terms of normalized total pressure and incidence (within $\pm 0.37\%$ of the inlet total pressure and $\pm 0.60^\circ$, respectively). The introduction of the wake generator impacted the flow periodicity at the outlet. In the absence of unsteady wakes, the maximum pitch-to-pitch variation of the kinetic energy loss coefficient was within $\pm 0.5\%$ of the main value in the secondary flow region. Due to the thicker inlet boundary layer towards negative pitchwise locations, the secondary flow strength and loss increased by 0.014 in the maximum. The introduction of purge flow significantly reduced the non-periodicity at the outlet.

Interference from the intrusive probes at the inlet and outlet was highlighted in the scope of measurements performed in transonic flowfields. Inlet flow measurements do not significantly disturb the flowfield at the inlet or outlet. A redistribution of the massflow at the inlet takes place. The mean value varies within ± 0.005 as a result. Probe measurements at the outlet are critical. It was found that the presence of the probe at Plane 06 causes massflow redistribution, which can be seen as far as Plane 01. The probe strongly impacts the Plane 06 taps, and the measured static pressure is unreliable enough to monitor the rig outlet Mach number. The variations of the mean Mach number can reach ± 0.05 when the probe is near the endwall. The stem-derived massflow redistribution impacts the blade loadings in the passages blocked by the stem. A partial compensation was achieved by increasing the overall massflow through the cascade.

References

[1] H. Schlichting and K. Gersten. *Boundary-layer theory*. springer, 2016.

[2] J.A. Walsh and D.G. Gregory-Smith. *Inlet Skew and the Growth of Secondary Losses and Vorticity in a Turbine Cascade*. Journal of Turbomachinery, 112(4):633–642, 10 1990.

[3] F Truckenmüller and H Stetter. *Measurement errors with pneumatic probes behind guide vanes in transonic flow-fields*. In 13th Symposium on Measuring Techniques for Transonic and Supersonic Flow in Cascades and Turbomachines. Zürich, Switzerland, 1996.

[4] J. Aschenbruck, T. Hauptmann, and J.R. Seume. *Influence of a multi-hole pressure probe on the flow field in axial-turbines*. In 11 th European Conference on Turbomachinery Fluid dynamics & Thermodynamics. EUROPEAN TURBOMACHINERY SOCIETY, 2015.

[5] C. Sanders, M. Terstegen, M. Holle, P. Jeschke, H. Schonenborn, and T. Frobel. *Numerical Studies on the Intrusive Influence of a Five-Hole Pressure Probe in a High-Speed Axial Compressor*. volume Volume 2A: Turbomachinery of *Turbo Expo: Power for Land, Sea, and Air*, page V02AT39A009, 06 2017.

[6] M. Boerner, M. Bitter, and R. Niehuis. *On the challenge of five-hole-probe measurements at high subsonic Mach numbers in the wake of transonic turbine cascades*. Journal of the Global Power and Propulsion Society, 2:453–464, 2018.

[7] A.F.M. Torre, M. Patinios, G. Lopes, L. Simonassi, and S. Lavagnoli. *Vane–Probe Interactions in Transonic Flows*. Journal of Turbomachinery, 145(6):061010, 01 2023.

[8] M. Okada, L. Simonassi, G. Lopes, and S. Lavagnoli. *Particle Image Velocimetry Measurements in a High-Speed Low-Reynolds Low-Pressure Turbine Cascade*. Journal of Turbomachinery, 146(3):031010, 12 2023.

[9] S. Lavagnoli, M. Okada, and G. Lopes. *SPLEEN - High Speed Turbine Cascade – Test Case Database - PIV Measurements*, 2023.

[10] V. Chernoray and J. Hjarne. *Improving the Accuracy of Multihole Probe Measurements in Velocity Gradients*. volume Volume 2: Controls, Diagnostics and Instrumentation; Cycle Innovations; Electric Power of *Turbo Expo: Power for Land, Sea, and Air*, pages 125–134, 06 2008.

[11] H.T. Hoenen, R. Kunte, P. Waniczek, and P. Jeschke. *Measuring Failures and Correction Methods for Pneumatic Multi-Hole Probes*. volume Volume 1: Aircraft Engine; Ceramics; Coal, Biomass and Alternative Fuels; Controls, Diagnostics and Instrumentation of *Turbo Expo: Power for Land, Sea, and Air*, pages 721–729, 06 2012.

[12] P.M. Ligrani, L.R. Baun, and B.A. Singer. *Spatial resolution and downwash velocity corrections for multiple-hole pressure probes in complex flows*. Experiments in Fluids, 7(6):424–426, 1989.

5 Profile Aerodynamics

This chapter addresses the profile aerodynamics at on- and off-design flow conditions. The inlet boundary conditions with and without unsteady wakes are provided. The steady-state aerodynamics are compared against numerical schemes. The impact of unsteadiness on the blade loading is depicted. The blade surface boundary layer is described thoroughly for steady and unsteady inlet flowfields. The profile loss is reported as well. The phase-averaged flowfield is investigated. The inlet bar wake is characterized by pressure loss and turbulence signature. Wake-boundary layer interaction at off-design conditions is reported to gather transition mechanisms. Finally, the outlet flowfield is scrutinized in terms of its unsteadiness.

5.1 Flow Conditions

The profile aerodynamics are investigated at on- and off-design Mach and Reynolds numbers. The Mach and Reynolds numbers range from 0.70 to 0.95 and 65k to 120k, respectively. The blade is designed to operate at an outlet Mach number of 0.90 and outlet Reynolds number of 70k. Tests with unsteady incoming flow are performed with the same bar peripheral speed. The resultant bar reduced frequency from varying the outlet Mach number while keeping the wake generator RPM constant is contained in Table 5.1.

Table 5.1: Variation of the Strouhal number with the outlet Mach number.

M	f^+
0.70	1.16
0.80	1.05
0.90	**0.95**
0.95	0.91

5.2 Time-Averaged Results

5.2.1 Cascade Inlet

5.2.1.1 Cascade Inlet with Steady Flow

The inlet flowfield to the cascade was investigated at on- and off-design flow conditions without a wake generator. Pitchwise traverses at midspan performed with the C5HP at Plane 02 enabled the characterization of the inlet flow in terms of incidence, cascade pitch angle, and velocity profile.

Fig. 5.1(a) displays the pitchwise distribution of the inlet incidence angle. The line color denotes the cascade outlet Mach number. The type of marker denotes the cascade Reynolds number based on outlet flow conditions. A monotonic decrease in incidence occurs in the pitchwise direction. The pitch-to-pitch variation for a given flow condition is within $\pm 1.00°$. For a given pitch, the incidence variation is within $\pm 0.24°$ for all investigated flow conditions. A mean incidence of -1.00° is present for all cases.

The cascade pitch angle (see Fig. 5.1(b)) was considered Reynolds dependent. The pitch angle for a given pitchwise location was lower for the highest Reynolds number case. The curves display good agreement with varying Mach number for a fixed Reynolds number. The pitch-to-pitch variation is practically negligible, and so is the mean value. The mean value close to zero ensures that the midspan flow is 2D.

Lastly, the inlet Mach number profiles measured with the C5HP are displayed in Fig. 5.1(c). The quantity is normalized by the value at y/g=0.00. The velocity distribution was found to be independent of the flow condition.

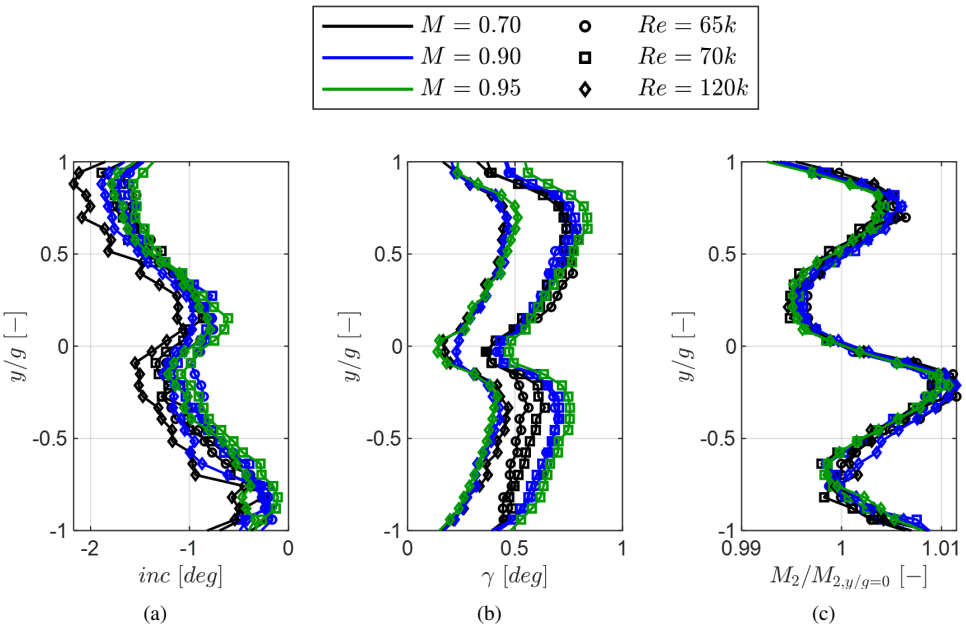

Figure 5.1: Characterization of midspan inlet flowfield at Plane 02 in the absence of wake generator: inlet flow incidence (a), cascade pitch angle (b), and normalized Mach number (c).

5.2.1.2 Cascade Inlet with Unsteady Wakes

The introduction of the wake generator required a re-assessment of the inlet flowfield to the cascade. Similar traverses to the first testing phase were performed (see Fig. 5.3). The flow conditions were extended to include M=0.80 and Re=100k.

Fig. 5.3(a) displays the pitchwise distribution of incidence. The incidence is Mach number dependent. The decrease in incidence with Mach number stems from the wake generator rotational velocity being kept constant during the off-design tests. As a result, the Strouhal number and flow coefficient were modified with respect to the nominal operating point. Fig. 5.2 displays a sketch of the velocity triangles upstream and downstream of the wake generator bar. The absolute inlet flow angle, α_1, is maintained despite the Mach number variation. The lower inlet (and outlet) Mach number cases are characterized by higher relative flow angle at the inlet, β_1, due to the lower axial velocity component and same wake generator speed. Simoni et al. [1] applied the momentum integral equation to a 2D control volume and formulated the following relation between the inlet and outlet absolute flow angles:

$$\tan\alpha_2 = \tan\alpha_1 - \frac{1}{2}\frac{C_D d}{g_{bar}}\frac{1}{\cos\beta_1}\tan\beta_1 \tag{5.1}$$

C_D is the wake generator bar drag coefficient, d is the bar diameter, and g_{bar} is the bar pitch. All of the above parameters are fixed throughout the current experimental campaign. The equation links the decreasing outlet flow angle, α_2, with the increasing inlet relative flow angle, β_1.

The Reynolds number does not significantly impact the wake convection and, therefore, has a low impact on the incidence.

The mean incidence was found to vary from -2.50° to -1.75° as the outlet Mach number was increased from the minimum to the nominal one. Attempts were made to align the blade inlet angle with the incoming flow. However, the rotation of the cascade was also accompanied by a deflection of the inlet flow. To this date, the cause of such an effect is unknown. For the range of incidence found for the final configuration, the variation was not expected to significantly alter the blade aerodynamics, except for a slight reduction of the suction side loading from the leading edge up to the velocity peak.

Both the pitch angle (see Fig. 5.3(b)) and the normalized Mach number (see Fig. 5.3(c)) were found to be flow independent. The pitch angle was near 0°, contributing to the two-dimensionality of the flow at midspan.

The wake generator-induced flow deflection in the rig was estimated. No instrumentation was available upstream of the wake generator during the measurements with the latter. The incidence measured experimentally in the absence of the wake generator (see Section 5.2.1.1) was assumed to be conserved during tests performed with wake generator ($\alpha_{in} \approx 32.87°$). The angle downstream of the wake generator is the one displayed in Fig. 5.3(a). The experimental flow turning is contained in the fourth column of Table 5.2. The deflection estimated with the model of Simoni et al. [1] is added for completeness. A bar drag coefficient C_D=1.2 was used due to the transonic regime experienced by the bars. The experimentally estimated deflection is significantly overestimated. However, the cascade angle concerning the wind tunnel was adjusted from the tests performed without and with the wake generator (40.73°

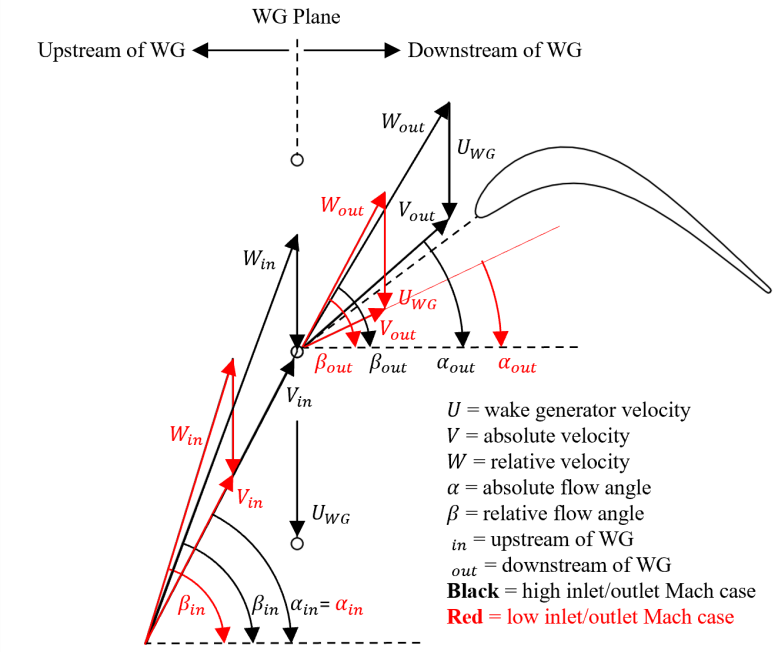

Figure 5.2: Velocity triangles resultant from the variation of flow incidence with outlet Mach number.

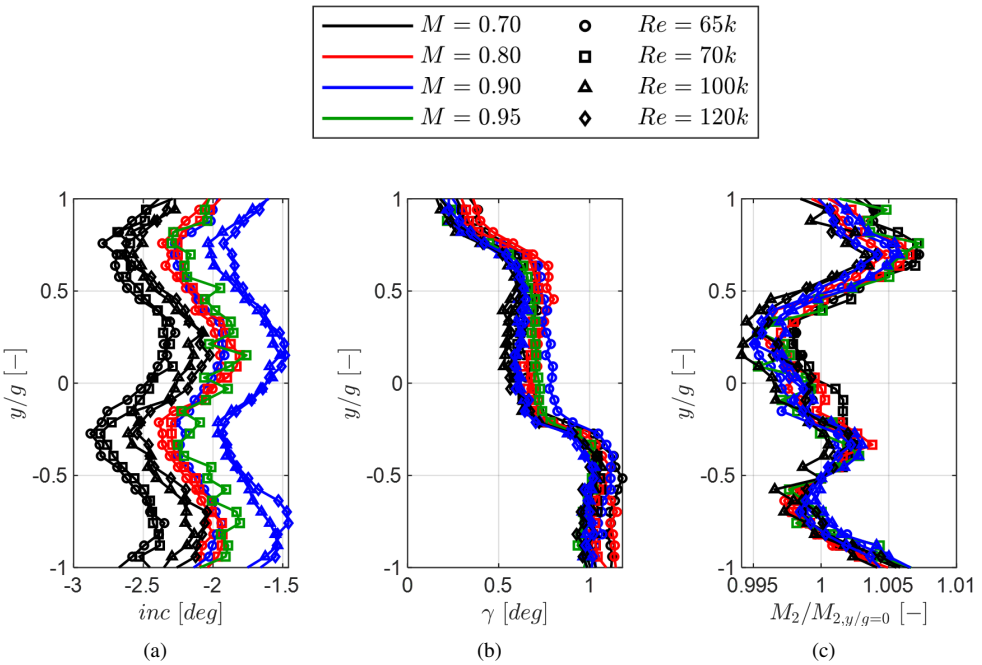

Figure 5.3: Characterization of midspan inlet flowfield at Plane 02 in the presence of wake generator: inlet flow incidence (a), cascade pitch angle (b), and normalized Mach number (c).

vs. 46.90°). Without measurements performed upstream of the wake generator, the difference between the model and experiments can be due to an erroneous value of the inlet flow angle upstream of the wake generator. The latter statement is supported by the wake generator characterization performed by Clinckemaillie and Arts [2], who found that the flow deflection and loss of the current wake generator are satisfactorily represented by the model in [1].

Typical values of the absolute and relative Mach number are also included for completeness.

Table 5.2: Wake generator-induced flow turning computed with the model and estimated experimentally, and absolute and relative Mach number.

		$\Delta\alpha$ [°]			
M	Re	Simoni et al. [1]	Exp.	M_{abs}	M_{rel}
0.70	65k	4.49	7.74	0.400	0.811
0.80		4.18	7.31	0.424	0.834
0.90		4.04	7.25	0.436	0.846
0.70	70k	4.45	7.67	0.402	0.814
0.80		4.11	7.24	0.429	0.839
0.95		3.95	7.20	0.444	0.853
0.70	100k	4.33	7.51	0.413	0.825
0.90		3.88	6.92	0.450	0.856
0.70	120k	4.27	7.46	0.416	0.827
0.90		3.82	6.86	0.457	0.864

5.2.1.3 Turbulent Quantities

Fig. 5.4(a) displays the pitchwise distribution of turbulence intensity measured throughout the experimental campaign. The decay computed with the correlation of Roach [3] is added for completeness. The hot-wire technique in low-density and transonic flows has been developed over four years (since 2020). The "XW1" measurements were obtained in 2023 [4]. The latter data obtained was the one used to set up boundary conditions for the numerical simulations reported in this work (see Section 3.2).

The turbulence decays towards negative pitchwise locations due to increased axial distance to the turbulence grid. The correlation of Roach closely describes all the data. The "XW1" data was obtained under the isotropic assumption. Recent developments (early 2024) in the methodology allowed us to get the streamwise and crosswise components of turbulence ("XW2-ANISO"). The profile computed under the isotropic flow assumption during the latest measurements is also included for completeness ("XW2-ISO"). The profiles calculated with the isotropic flow assumption display good agreement and decay. Even though the decay is similar, the turbulence computed with multiple components is 0.27% lower.

The similar decay of the profiles is supported by the pitchwise distribution of the integral length scale displayed in Fig. 5.4(b). The length scale is relatively constant in the range of pitchwise locations investigated. This is supported by the similar slope of the turbulence intensity decay in the same range. The length scale was obtained by integrating the spectrum of the streamwise velocity in the 20–100 Hz range. An integral length scale of $\sim$12 mm was

found. The latter value was not used in the numerical setup as the computed decay was better represented by a different length scale (see Section 3.2).

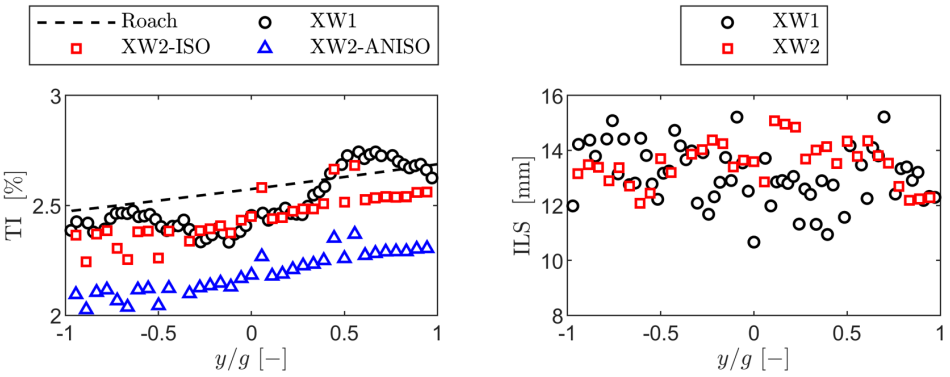

Figure 5.4: Pitchwise distribution of turbulent quantities in the absence of wake generator: turbulence intensity (a), and integral length scale (b).

The power law described by Roach [3] was used to fit the turbulence data:

$$TI = A\left(\frac{x}{d}\right)^{B} \tag{5.2}$$

x represents the axial distance to the turbulence grid, and d represents the turbulence grid bar diameter. The fitted coefficients, compared against the ones in [3] for turbulence grids made of an array of cylindrical parallel rods, are contained in Table 5.3.

Table 5.3: Power law coefficients fitted to HW data.

	A	B
Roach [3]	0.800	-0.714
XW1	0.771	-1.178
XW2-ISO	0.804	-1.112
XW2-ANISO	0.677	-1.173

5.2.2 Blade Loading and Boundary Layer

5.2.2.1 Steady Inlet Flow

A similar flow topology for various flow conditions characterizes the SPLEEN C1 blade. Fig. 5.5 highlights zoomed regions of the PS near the leading edge (top row). A detailed view of the SS near the trailing edge is also provided (bottom row). The contour of turbulent kinetic energy obtained with the transitional RANS simulations is highlighted. Streamlines are included to highlight the flow features.

A laminar separation bubble is formed on the pressure side regardless of the flow condition investigated. The extent of the separation is flow-dependent. As a result of the turbulent

mixing occurring in the shear layer, a sudden increase in the turbulent kinetic energy occurs over the separation bubble.

On the suction side, a laminar separation bubble is formed due to the adverse pressure gradient experienced by the flow. The separation location shifts upstream or downstream depending on the Mach and Reynolds numbers. The flow condition also impacts the separation bubble extent. Like the pressure side, turbulent kinetic energy increases in the shear layer over the separation bubble. The latter is equally attributed to turbulent mixing processes.

Fig. 5.5 provides a brief overview of the type of flow that will be characterized in the following sections. The influence of the flow condition of the laminar separation bubble extent, particularly on the suction side, will be detailed.

The blade loadings defined in terms of surface isentropic Mach number in the absence of unsteady wakes are displayed in Fig. 5.6. The loadings are displayed at four different Reynolds numbers: 65k in Fig. 5.6(a), 70k in Fig. 5.6(b), 100k in Fig. 5.6(c) and 120k in Fig. 5.6(d); and Mach numbers in the range of 0.70 to 0.95. For each sub-figure, the color of the line-marker arrangement denotes the Mach number. The markers refer to experimental data, the solid line to the CFD results obtained with the $\gamma - Re_{\theta t}$ model, and the dashed line to the MISES results coupled with the AGS transition model.

The overall loadings obtained with MISES and RANS show good agreement with the experimental data on the suction and pressure sides. For all cases, the suction side has an underprediction of the Mach number, which is more pronounced with increasing Mach number.

A zoomed-in region highlighting the suction side aerodynamics is displayed in Fig. 5.7. The reader is referred to the legend of Fig. 5.6. Even though they agree, the numerical results struggle to capture the experimental suction side loading for M$>$0.90, regardless of the Reynolds number. This has been observed in other numerical studies concerning the SPLEEN test case [5].

For the lowest Mach number, a closed laminar separation bubble occurs on the suction side for the Re=100k and higher (see Fig. 5.7(c) and Fig. 5.7(d)). The reattachment point is relatively far from the trailing edge. The CFD and MISES remarkably capture the topology and extent of the laminar separation bubble. This is also applicable to the M=0.80 cases. The robustness of the MISES and RANS in capturing the laminar separation bubble comes from a careful adjustment of the turbulence models in both solvers (see Section 3.1.4 and Section 3.2.4).

At Re=65k (see Fig. 5.7(a)) and Re=70k (see Fig. 5.7(b)) cases, the laminar separation bubble is shifted downstream. The reattachment occurs near the trailing edge. For these cases, the CFD struggles to capture the blade loading at the lowest Mach number. On the other hand, the turbulence intensity imposed in MISES was tailored to match the loading. The loading and blade boundary layer are well retrieved.

Fig. 5.8 displays a zoomed-in region of the pressure side blade loading in a region characterized by a laminar separation bubble. The reader is referred to the legend of Fig. 5.6. The CFD, MISES, and experiments agree well. The computations retrieve the separation-induced "plateau" in the loading. The highest disagreement occurs for the higher Mach numbers at Re=100k.

The skin friction is used to characterize the laminar separation bubble occurring on the suction and pressure sides and better understand the pressure and suction side boundary layer. Fig. 5.9 displays the skin friction coefficient distribution along the pressure and suction side

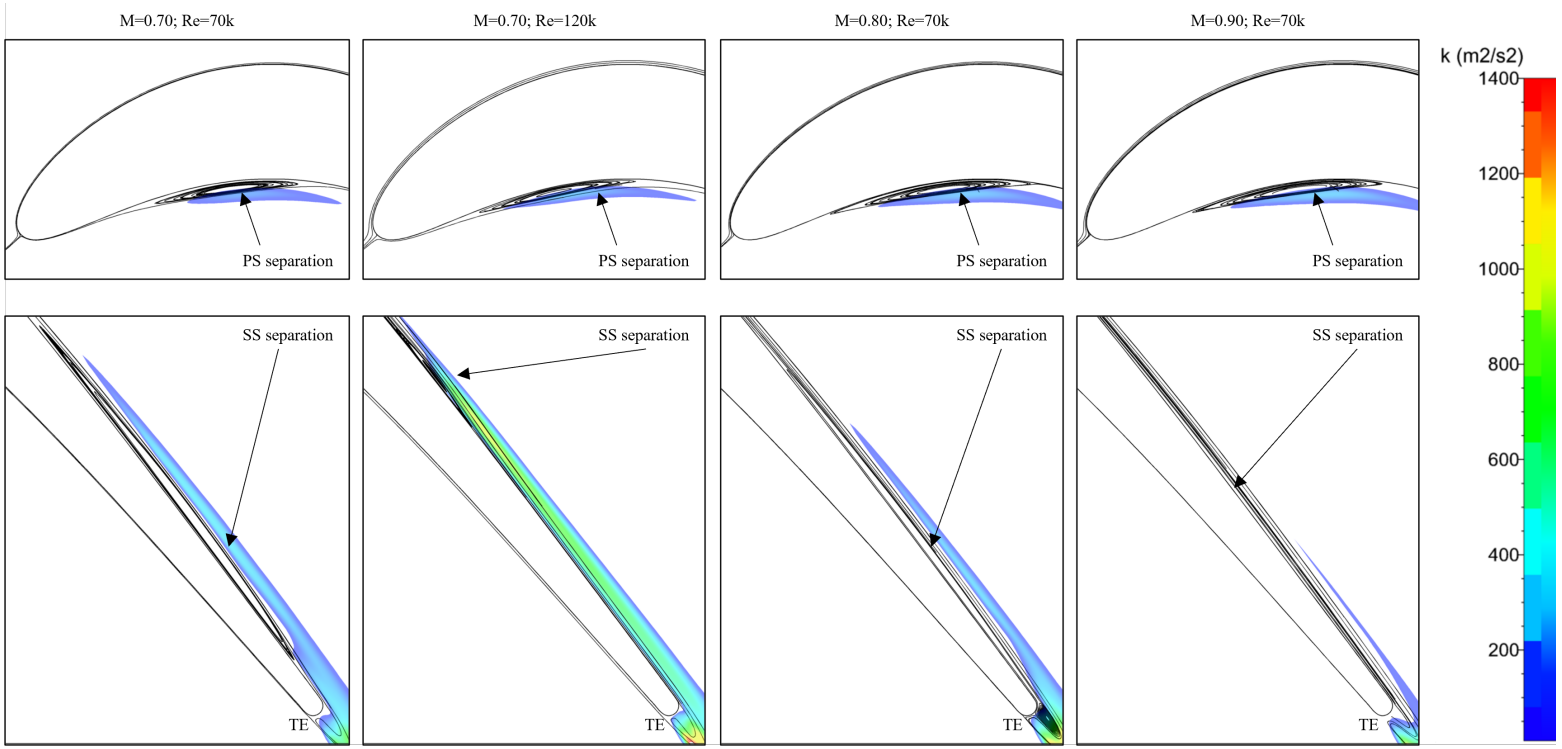

Figure 5.5: Suction side and pressure side flow topology for several flow conditions.

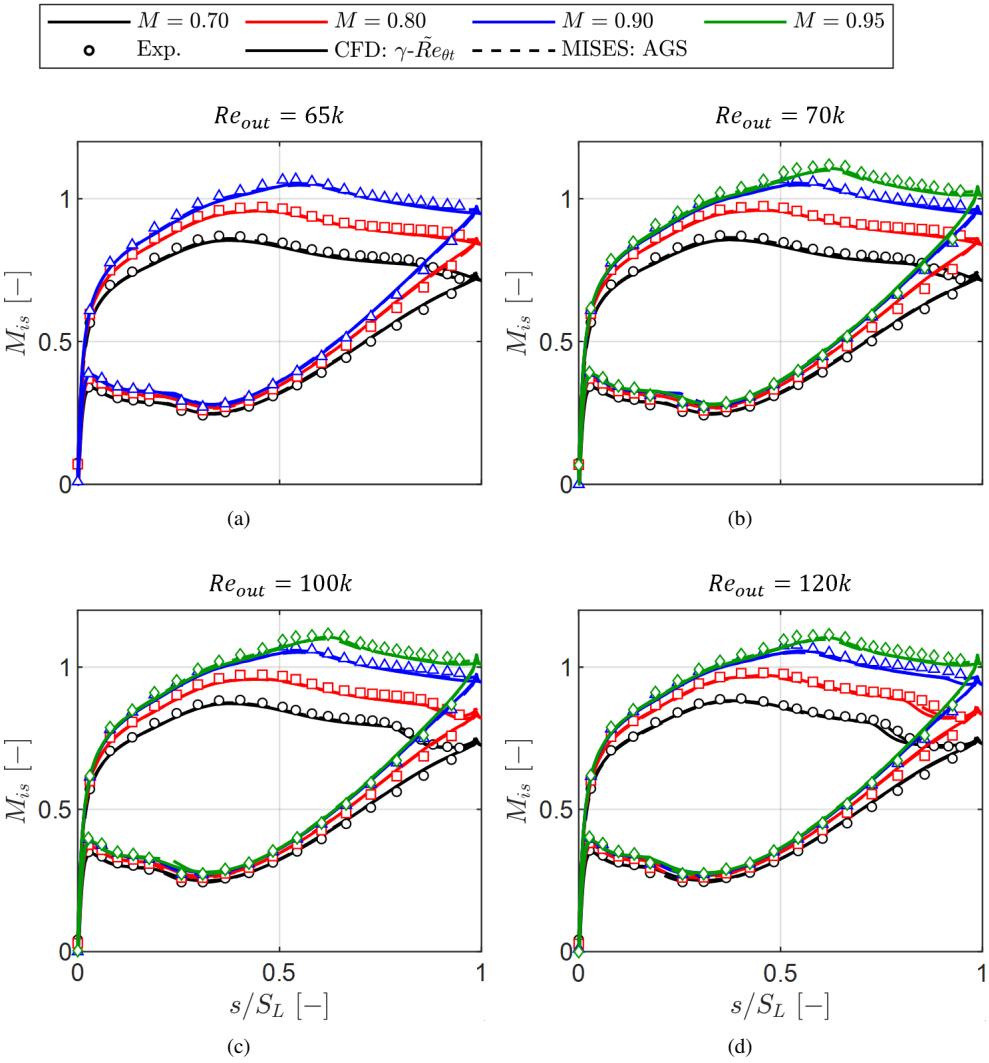

Figure 5.6: Blade loading: experimental (markers), CFD γ-$\tilde{Re}_{\theta t}$ (solid line) and MISES AGS (dashed line); Re=65k (a), Re=70k (b), Re=100k (c) and Re=120k (d).

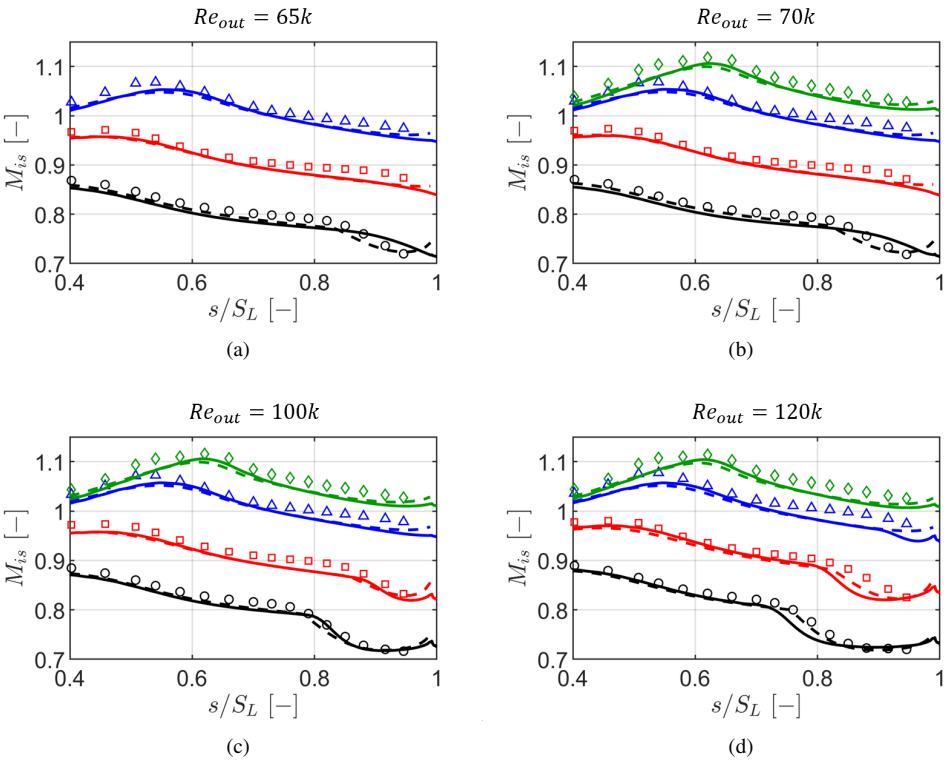

Figure 5.7: Blade loading zoomed-in SS region: experimental (markers), CFD γ-$\tilde{Re}_{\theta t}$ (solid line) and MISES AGS (dashed line); Re=65k (a), Re=70k (b), Re=100k (c) and Re=120k (d).

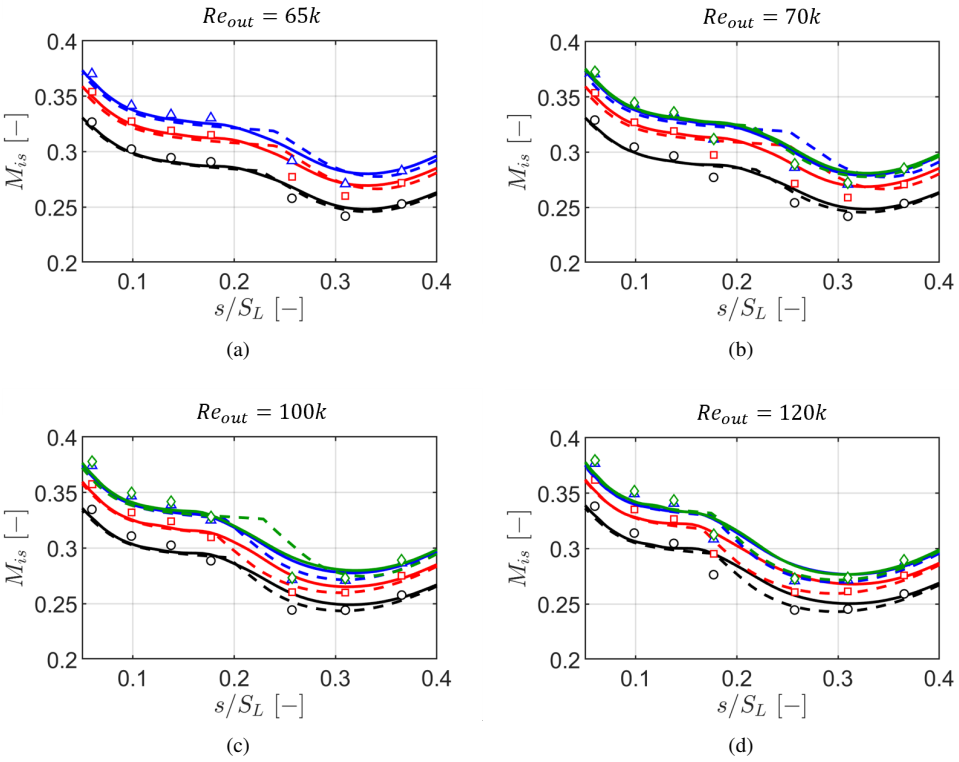

Figure 5.8: Blade loading zoomed-in PS region: experimental (markers), CFD γ-$\tilde{Re}_{\theta t}$ (solid line) and MISES AGS (dashed line); Re=65k (a), Re=70k (b), Re=100k (c) and Re=120k (d).

surface lengths. The pressure side is represented by the negative s/S_L coordinate and vice-versa for the suction side. The figure contains only flow cases for which experimental data is available. However, these address the range/type of separation for the SPLEEN C1. Markers represent the experimental data, the CFD γ-$\tilde{Re}_{\theta t}$ by a solid line, and the MISES AGS by a dashed line. The numerical skin friction coefficient was normalized by the global maximum. The experimental skin friction was obtained by multiplying the quasi-wall shear stress measured with surface-mounted hot-films by a constant to find the best agreement with the numerical data. The methodology employed for the hot-film measurements cannot provide quantitative results.

From a computational point of view, the CFD and MISES globally agree. The pressure side separation bubble extent and associated skin friction are lower for the MISES computations for all flow conditions. The magnitude of the skin friction is also lower on the trailing edge. On the other hand, the shape and magnitude of the skin friction on the suction side agree well.

The experimental data is characterized by significant scattering due to the limitations of the hot-film application in the VKI S-1/C. Nonetheless, the experiments capture increased skin friction along the pressure side. The same can be said about the suction side, particularly at the rear portion of the suction side. The M=0.70; Re=70k flow case is well captured.

Surface-mounted hot-film measurements were not performed for other flow conditions. The laminar separation bubble was characterized based on the blade loading. Pinpointing the separation location was of interest to address different methodologies in the loss breakdown Section 7.1.2.1 and to investigate the transition mechanisms present in the current test case. It is not uncommon to do such based on visual inspection of the loading [6]. In the scope of this work, a methodology based on the acceleration parameter was developed.

The acceleration parameter is defined as [7, 8]:

$$K_s = \frac{\nu}{V_{is}^2} \frac{\partial V_{is}}{\partial s} \tag{5.3}$$

V_{is} is the local isentropic velocity (see Eq. 2.20) computed on the blade surface, ν is the kinematic viscosity, and S is the position along the surface length.

Fig. 5.10(a) displays the suction side loading along the normalized surface length with a black line for the M=0.70; Re=120k flow case. The acceleration parameter for the corresponding blade loading is plotted on the right y-axis with a red line. The derivative of the acceleration parameter is scaled and plotted on the right y-axis with a blue line. All of the quantities were obtained from experimental data. The acceleration parameter and its derivative were fitted with a Cubic spline.

The velocity peak can be identified by the point where the flow has no acceleration. The new method assumes that the separation location ("S") sits near a local minimum of the acceleration parameter. No point in the acceleration parameter represents the reattachment location. However, the laminar separation bubble produces a sinusoidal-like profile in the acceleration parameter. An inflection point, detected with the derivative of the acceleration parameter, is representative of the reattachment location ("R").

For all the flow conditions with M$\leq$0.90, the acceleration parameter displays similar characteristics that allow identifying the separation and reattachment whenever occurring. For the

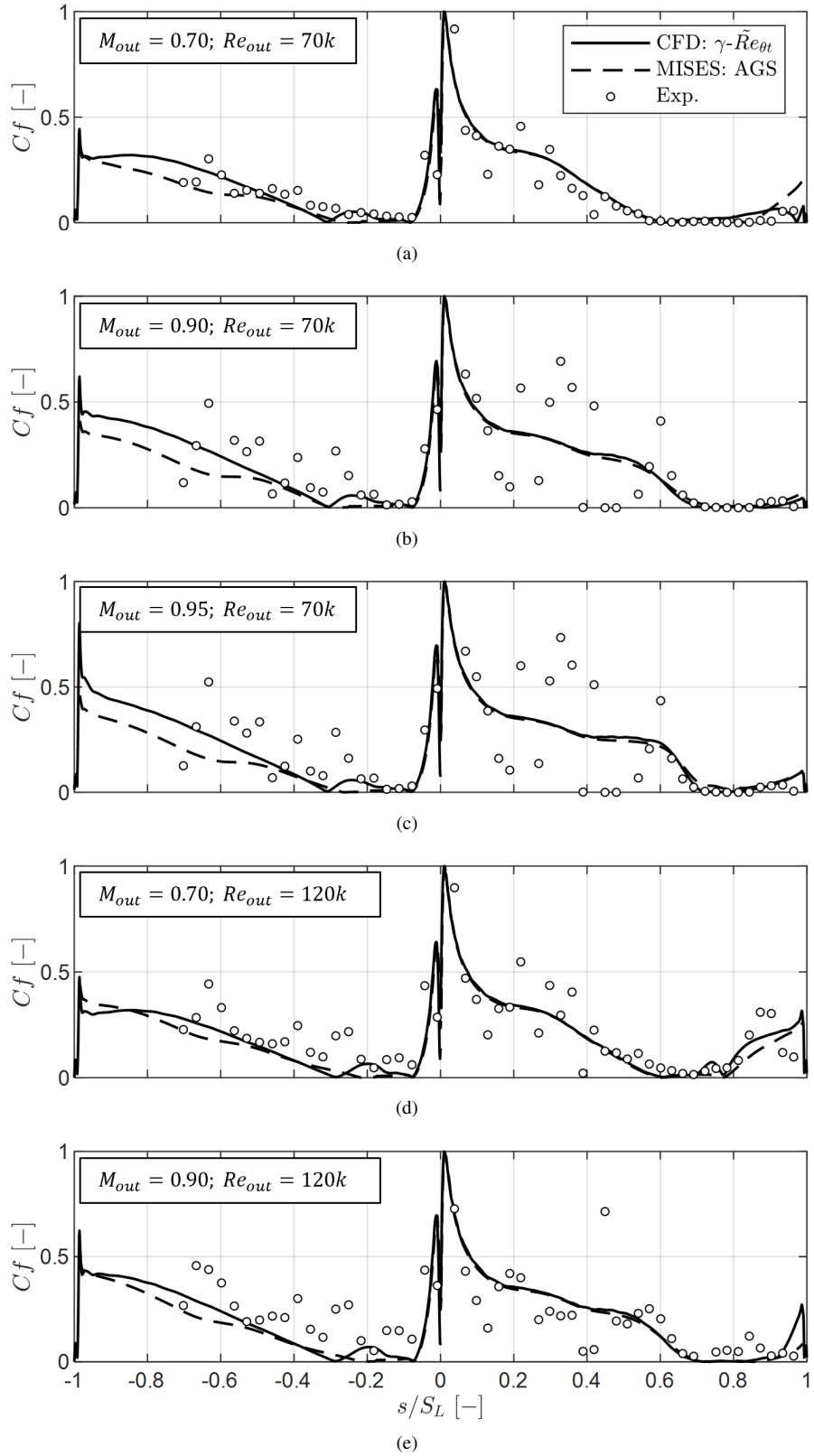

Figure 5.9: Blade skin friction: experimental (markers), CFD γ-$\tilde{Re}_{\theta t}$ (solid line) and MISES AGS (dashed line); M=0.70; Re=65k (a), M=0.90; Re=70k (b), M=0.95; Re=70k (c), M=0.70; Re=120k (d) and M=0.90; Re=120k (e).

highest investigated Mach number (see Fig. 5.10(b)), the experimental loading displays an almost flat curve in the rear portion of the suction side.

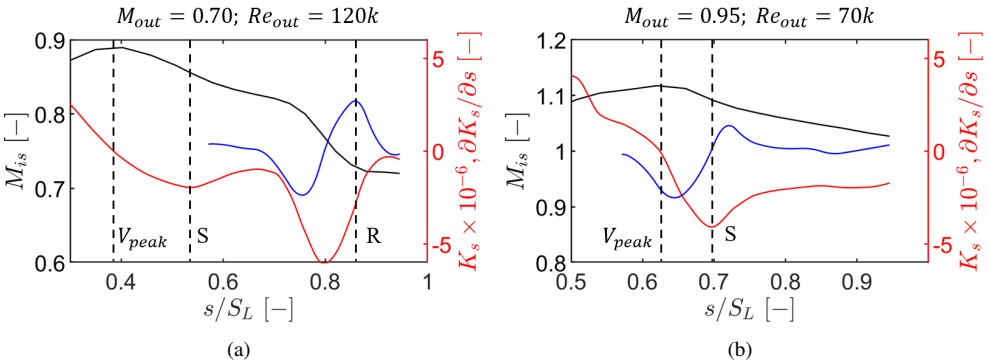

Figure 5.10: Blade isentropic Mach number along SS surface plotted on the left y-axis (solid black line), acceleration parameter plotted on the right y-axis (solid red line) and scaled local derivative of acceleration parameter plotted on the right y-axis (solid blue line): M=0.70; Re=120k (a) and M=0.95; Re=70k (b).

The above methodology was calibrated with the CFD and MISES data. The separation location was retrieved for each flow condition using the skin friction coefficient and the acceleration parameter methodology highlighted above.

Fig. 5.11 compares the separation location retrieved with both methods. The axes display the surface length at which separation occurs, normalized by the surface length. Black markers represent the CFD data, while red markers represent the MISES data. The y=x curve is added to show the "lag" between both methods. The shaded area denotes a deviation from the y=x of ±15%.

A linear curve was fitted to the data to relate the lag between both methodologies. The data obtained at M=0.95 was not included since, as detailed later, the separation is driven by a shock at this Mach number.

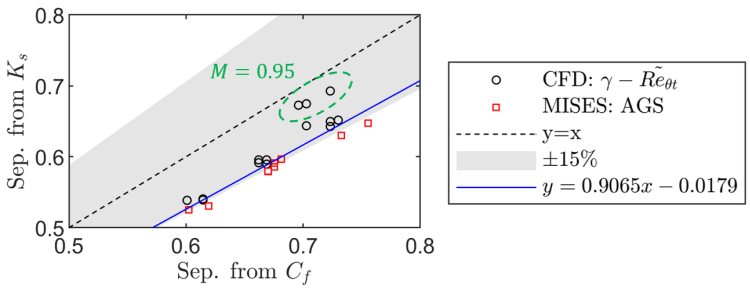

Figure 5.11: Relation between separation location computed with skin friction and with the acceleration parameter methodology.

The fitting was used to recompute the separation location based on the one obtained from the experimental acceleration parameter according to Eq. 5.4.

$$s_{C_f} = 1.1031 s_{K_s} + 0.0197 \tag{5.4}$$

Fig. 5.12(a) displays the acceleration parameter at the separation location as a function of the surface length Reynolds number. The markers represent the experimental data points without applying the correction above. The solid line defines the correlation of Hatman and Wang [8]. The correlation of Michalek et al. [9] is also added for completeness and is represented by the dashed line.

$$Re_{S,Hatman} = 5750 - \frac{215000}{K_s \cdot 10^6} - \frac{45500}{(K_s \cdot 10^6)^2} - \frac{5750}{(K_s \cdot 10^6)^3} - \frac{250}{(K_s \cdot 10^6)^4} \tag{5.5}$$

$$Re_{S,Michalek} = 6860 - \frac{255190}{K_s \cdot 10^6} - \frac{94770}{(K_s \cdot 10^6)^2} \tag{5.6}$$

The data is scattered mainly due to the incorrect location of the corrected separation. The correction significantly improves the agreement between the experimental data and the correlation of Hatman and Wang (see Fig. 5.12(b)). The latter was built with low-subsonic flat plat and cascade measurements under a turbulence intensity of $\sim$0.60%.

Upon application of the correction, Hatman's correlation describes the boundary layer behavior for Mach numbers up to 0.90 well. The agreement is particularly good for Re>100k. Even though the M=0.95 cases follow the same type of fitting as the remaining cases, separation location is significantly underpredicted with respect to the correlations. The final fitted correlation is the following:

$$Re_{S,corrected} = -4974 - \frac{240100}{K_s \cdot 10^6} - \frac{45410}{(K_s \cdot 10^6)^2} \tag{5.7}$$

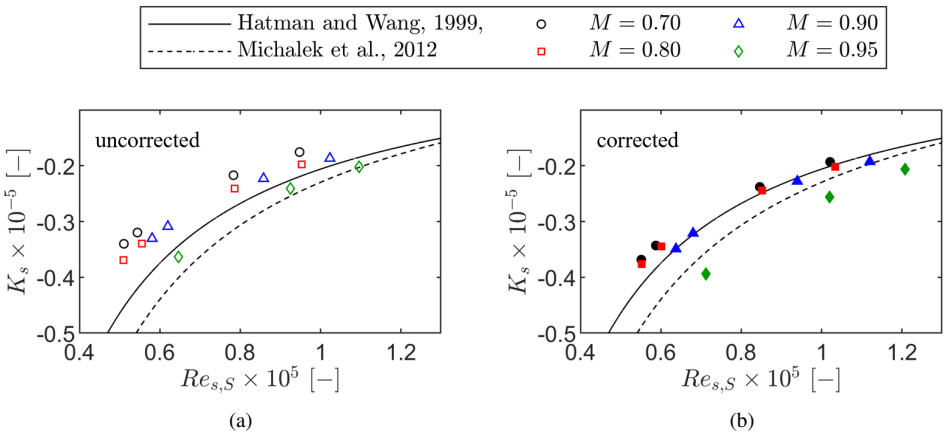

Figure 5.12: Acceleration parameter versus surface length based Reynolds number at the separation location for experimentally investigated cases: without (a) and with (b) correcting the separation location obtained from the acceleration parameter methodology.

Fig. 5.13 displays the surface Reynolds number at the separation location versus the one at the reattachment location. The Reynolds number at the separation location is the corrected one. The correlations of Hatman and Wang (solid line), Michalek et al. (dashed line), and Houtermans [10] (dotted-dashed line) are added as well.

$$Re_{R,Hatman} = 1.0608 Re_{S,Hatman} + 34890 \tag{5.8}$$

$$Re_{R,Michalek} = 1.0660 Re_{S,Michalek} + 24733 \tag{5.9}$$

$$Re_{R,Houtermans} = 1.0074 Re_{S,Houtermans} + 17996 \tag{5.10}$$

The experimental results are nearly linear. The lowest Mach number cases superimpose the correlation of Hatman and Wang. As the Mach number is decreased, the correlation of Houtermans describes the data better. Nonetheless, the experimental data is within the existing correlations. The correlation fitted to the experimental data takes the form:

$$Re_{R,current} = 1.256 Re_{S,corrected} + 9706 \tag{5.11}$$

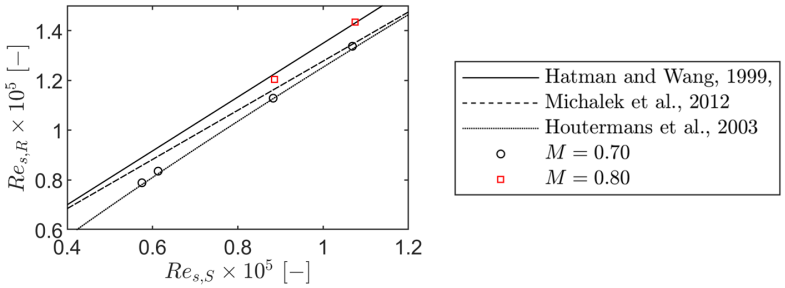

Figure 5.13: Surface length-based Reynolds number at reattachment versus at the separation location.

The significant variation in the separation location calculated by the highest Mach number compared to the low-order models is thought to be linked to compressibility effects. To comprehend the factors affecting the cases at M=0.95, numerical Schlieren emphasized shock-boundary layer interactions.

Fig. 5.14 displays the normalized density gradient in the passage at Re=120k. The findings are similar for lower Reynolds numbers. The two figures concern the M=0.90 case, in Fig. 5.14(a), and M=0.95 case, in Fig. 5.14(b). The isolines of M=1.00 are highlighted in red.

The density gradient highlights the formation of a shock in the throat region for the highest Mach number. Upstream of the shock, a lighter region is visible ("A"). An oblique darker line ("B") can also be identified downstream of the shock.

The shock topology is in line with the one reported in [11] and displayed in Fig. 5.15. Upstream of the main shock, a fan of compression waves is formed. The pressure rise across the fan of compression waves causes a sudden increase of the boundary layer thickness and the separation of the boundary layer if the pressure gradient is sufficient [12–14]. At the foot

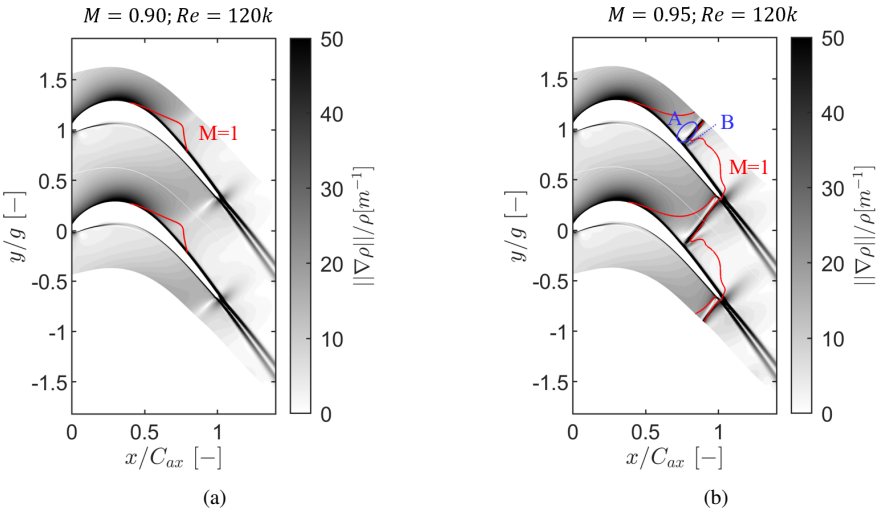

Figure 5.14: Normalized density gradient inside passage: M=0.90; Re=120k (a) and M=0.95; Re=120k (b).

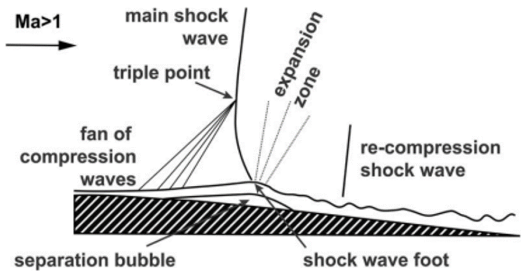

Figure 5.15: Sketch of shock-boundary layer interaction after Boerner and Niehuis [11]

of the shock, a series of expansion waves promote flow, turning towards the blade surface. If the pressure gradient is not large enough, this will promote flow reattachment.

In the work of Boerner and Niehuis, the flow reattached further downstream. The authors do not consider the blade loading since the study targeted the characterization of shock-boundary layer interaction under low-pressure turbine engine-representative conditions. However, the incapability of the flow to reattach can be exploited by employing CFD and increasing the pitch-to-chord ratio of the SPLEEN C1 blade.

Fig. 5.16(a) displays the density gradient for the SPLEEN pitch-to-chord ratio (g/C=0.63). Fig. 5.16(b) displays the same quantity for an increased pitch-to-chord ratio for g/C=0.78. The isolines of M=1.00 are highlighted in red. The shock structure changes significantly. Even though a shock system is still present at the throat of the cascade, a more pronounced shock occurs near the trailing edge on the suction side.

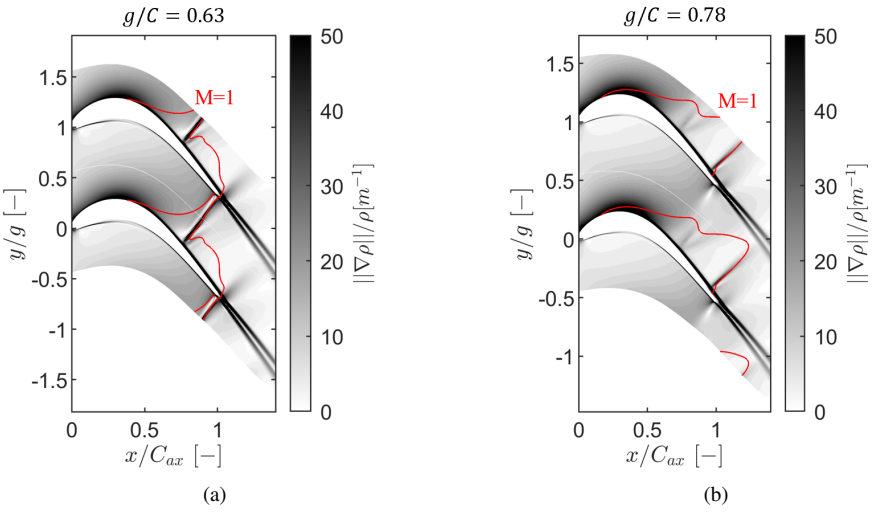

Figure 5.16: Normalized density gradient inside passage at M=0.95; Re=120k: g/C=0.63 (a) and g/C=0.78 (b).

The different shock topology significantly impacts the suction side boundary layer development. Fig. 5.17 displays the isentropic Mach number, skin friction coefficient, and boundary layer integral parameters along the normalized suction side surface length for the low (left column) and high (right column) pitch-to-chord-ratio. The position of the separation ("S") and reattachment ("R") locations obtained from the CFD are included as solid lines. The rough location of the shock impingement on the suction side ("S*") is highlighted by a dashed line. The skin friction is normalized with the maximum value. The boundary layer displacement and momentum thickness are plotted on the same y-axis and not labeled as the figure serves to qualify the impact of the shock on the boundary layer. Nonetheless, the scale for both pitch-to-chord ratios is the same.

By increasing the pitch-to-chord ratio, there is an increase in the blade loading for the same outlet dynamic head (see Fig. 5.17(a) and Fig. 5.17(b)). The first shock at s/S_L≈0.65 triggers the separation of the boundary layer. The separation occurs upstream of the shock

due to the compression fans mentioned above. The consequent adverse pressure gradient is strong enough to prevent the first shock system from promoting the reattachment of the shear layer, causing a separation bubble to form.

The skin friction coefficient (see Fig. 5.17(c) and Fig. 5.17(d)) supports the findings. For the smallest pitch-to-chord ratio, the separation bubble has a small extent due to being contained by the shock system. A large separated region is perceived concerning the largest pitch-to-chord ratio. Before the reattachment, a local peak ("T") in the skin friction coincides with the location of the second shock system. It is likely that the shock accelerates transition and promotes reattachment [15].

The boundary layer parameters support the rapid increase in the displacement thickness (black solid line) upstream of the shock. Due to the stability of the momentum thickness, the shape factor increases as a consequence. Due to the quick reattachment for the lower pitch-to-chord ratio (see Figure5.17(e)), the displacement thickness is reduced immediately. The rapid growth of the boundary layer thickness can also be observed for the higher pitch-to-chord ratio (see Fig. 5.17(f)). However, the displacement thickness keeps increasing due to the increase of the shear layer thickness. The momentum thickness remains relatively similar, and therefore, the shape factor also increases. Before the second shock, the separation bubble thickness starts decreasing. The displacement thickness decreases as a consequence. The shape factor suffers a rapid decrease towards the trailing edge.

The flow features for the higher pitch-to-chord ratio are remarkably similar to the work of Boerner and Niehuis [11]. The intermediate conclusion of this exercise is that at M=0.95, the boundary layer development is dictated by shock-boundary layer interactions. Due to the low pitch-to-chord ratio encountered in the SPLEEN C1 test case, the shock intensity is enough to promote reattachment near the main shock foot. The exercise also proves why the separation location does not fit the model of Hatman and Wang [8] that concerns separated induced transition through inflectional instabilities.

For the remaining cases characterized by $M \leq 0.90$, separated flow transition under a long bubble is expected [7, 8]. The transition onset occurs downstream of the separation point by inflectional instabilities, typically Kelvin-Helmholtz. It is typical to have a combined effect of viscous and inflectional instabilities. McAuliffe and Yaras [16] have detected the growth of Tollmien-Schlichting instabilities downstream of the separation of a flat plate under a pressure gradient. These instabilities led to the formation of Kelvin-Helmholtz roll-ups.

The surface-mounted hot-films are used to gain further insight into the transition process. Similar findings were observed for the cases characterized by separated flow transition ($M<0.90$). Only the case with the most developed boundary layer is presented (M=0.70; Re=120k). The case with the shock is also presented. The remaining cases are in Appendix E for completeness.

Fig. 5.18(a) displays the isentropic Mach number for the M=0.70; Re=120k case. A well-defined laminar separation bubble characterizes the flow. The separation ("S") and reattachment ("R") locations measured experimentally are represented by the dashed lines. Fig. 5.18(c) displays the standard deviation of the bridge voltage measured by the surface-mounted hot-films. After the velocity peak, the quantity slowly grows to a local maximum near the separation location. A similar behavior is reported in [17, 18]. The peak is associated with the separation location unsteadiness. The separation location coincides with increased signal skewness (see Fig. 5.18(e)), supporting the onset of transition. The kurtosis increases

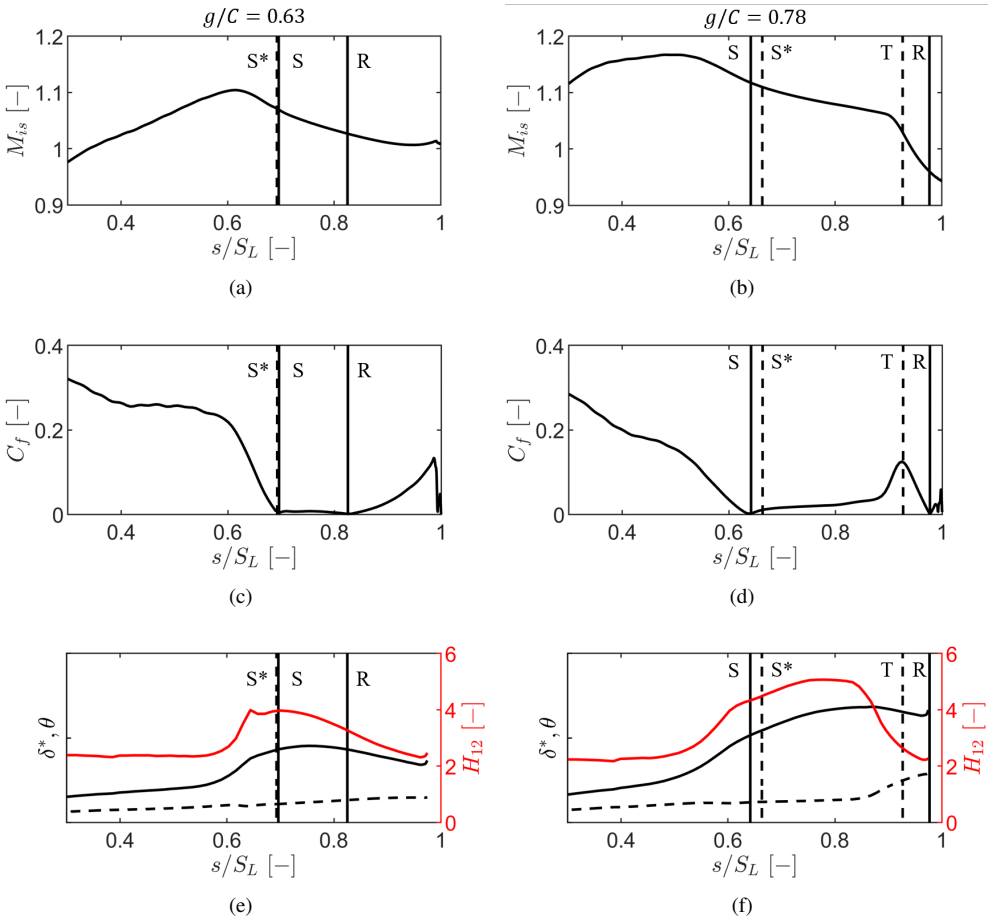

Figure 5.17: Blade SS isentropic Mach number for g/C=0.63 (a) and g/C=0.78 (b), skin friction coefficient for g/C=0.63 (c) and g/C=0.78 (d), and boundary layer integral parameters for g/C=0.63 (e) and g/C=0.78 (f). Displacement thickness (−) and momentum thickness (−−) are plotted on the left y-axis in black, and the shape factor is plotted on the right y-axis in red.

in the separated flow region (see Fig. 5.18(g)).

The laminar separation bubble keeps developing, and the standard deviation increases to a global maximum, highlighted as the transition location ("T"), represented by the dotted line. The boundary layer has equal laminar and turbulent portions. The resultant signal has zero skewness. At this point, the laminar separation bubble thickness decreases, and the flow eventually reattaches. The standard deviation signal did not reach a "plateau". In addition, the skewness did not return to zero. It can be concluded that the transition process is not finished by the blade trailing edge. The same occurs for all the M<0.90 cases. The kurtosis decreases by the reattachment location. Similar to the skewness, it does not reach a plateau. Since the kurtosis is likely related to the status of the boundary layer. A lower kurtosis is expected in the turbulent portion with respect to the laminar one. The kurtosis reinforces that the boundary layer is transitional by the last sensor.

Similar features occur at M=0.95, for which the loading is displayed in Fig. 5.18(b). The dashed line highlights the shock location. Compared to the previous case, a steeper increase in the voltage fluctuations occurs upstream of the shock impingement location. Nonetheless, the standard deviation (see Fig. 5.18(d)) and skewness (see Fig. 5.18(f)) display similar features to the one presented for the lower speed. A possible peak in the std(E_b) accompanied by zero skewness would occur near or after the location of the last sensor. For this reason, it is not clear if the transition point is within the surface covered by the surface-mounted hot-film sensors. However, the potential zero crossing of the skewness indicates that for high Mach number cases, the transition is not over by the location of the last sensor.

The probability density function (PDF) of typical signals measured over the blade surface at M=0.70; Re=120k is reported for completeness in Fig. 5.19. The probability density function is reported in the laminar region (black line), in the transitional region before the transition point (red line), near the transition point (blue line), and in the region of the most developed boundary layer (green curve). The laminar region signal is characterized by low standard deviation and zero skewness. Once transition begins, the standard deviation and skewness increase. The signal displays a significant standard deviation and practically zero skewness at the transition point. Downstream of the transition point, still within the transitional regime, high standard deviation and non-zero skewness characterize the signal.

The transition location obtained with the surface-mounted hot-film sensors is compared against the correlation of Hatman and Wang [8] in Fig. 5.20.

$$Re_{T,Hatman} = 1.0816 Re_{S,Hatman} + 26805 \tag{5.12}$$

The experimental data follows the correlation trend. The error is always within $\pm 10\%$. For the two Points at Re=120k, the error is within 5%. This result suggests that the transition observed in the current test case is within existing correlations dealing with separated flow transition in flat plates. Based on the three available data points, the following linear correlation can be fitted to the data:

$$Re_{T,current} = 1.062 Re_{S,corrected} + 18200 \tag{5.13}$$

Table 5.4 contains the separation locations obtained experimentally and numerically. The experimental ones are given using the K_s methodology and the quasi-wall shear stress values. The local maximum in the root-mean-square level of the bridge voltage is used to identify the

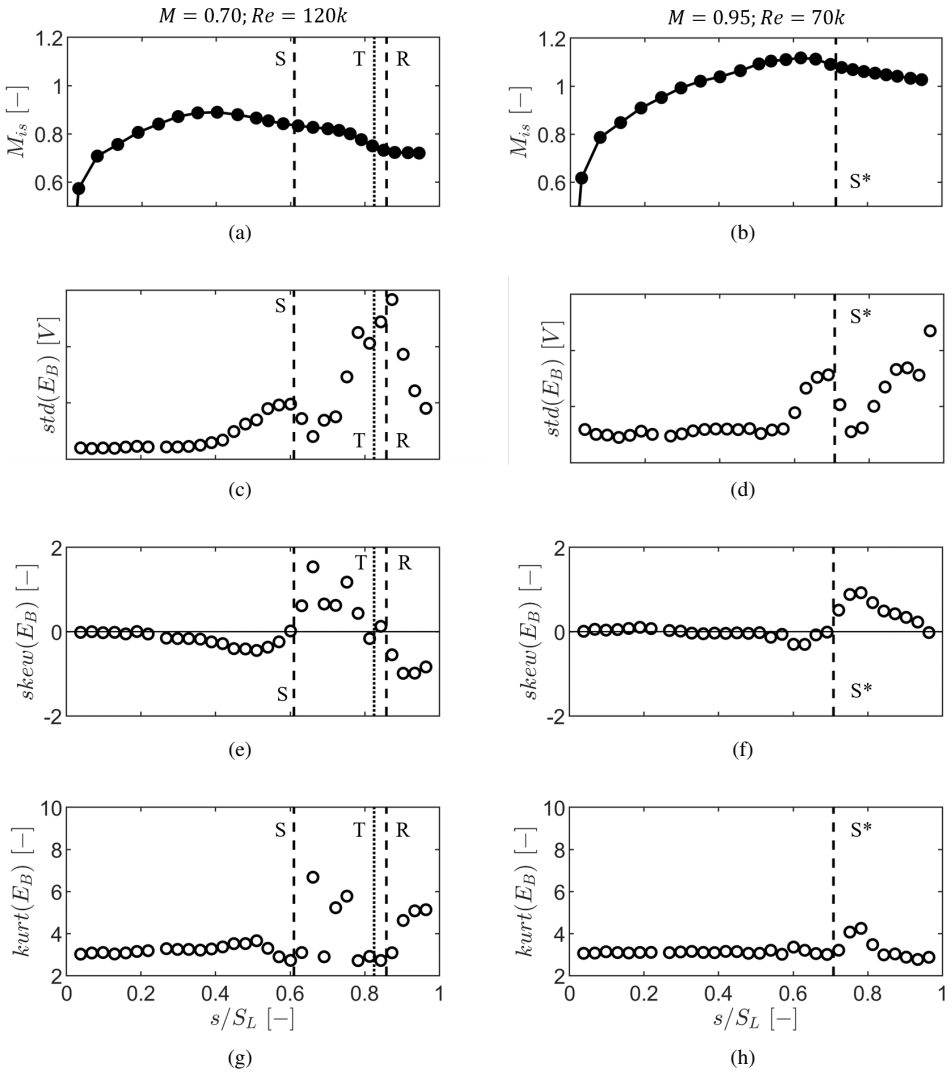

Figure 5.18: Blade isentropic Mach number for M=0.70; Re=120k (a) and M=0.95; Re=70k (b), standard deviation of HF bridge voltage for M=0.70; Re=120k (c) and M=0.95; Re=70k (d), skewness of HF bridge voltage for M=0.70; Re=120k (e) and M=0.95; Re=70k (f), and kurtosis of HF bridge voltage for M=0.70; Re=120k (g) and M=0.95; Re=70k (h).

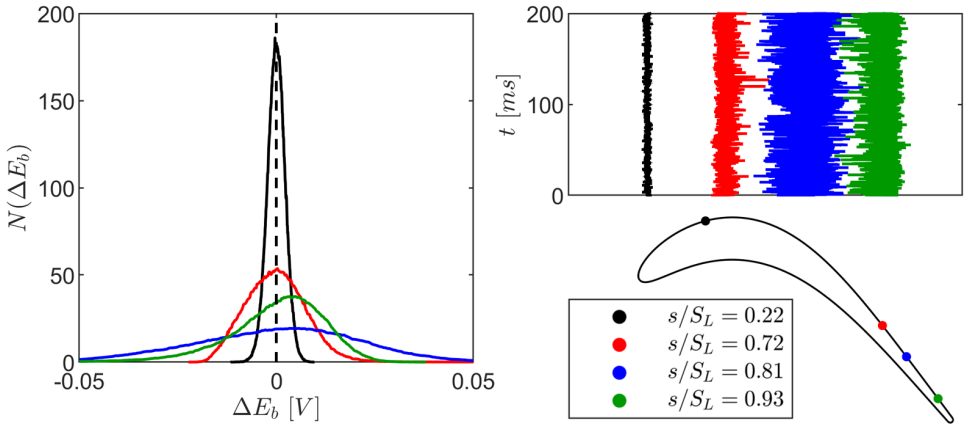

Figure 5.19: PDF of hot-film bridge voltage for M=0.70; Re=120k: in the laminar region at s/S_L=0.22, in the early transitional region at s/S_L=0.72, near the transition location at s/S_L=0.81, and in a late transitional region at s/S_L=0.93.

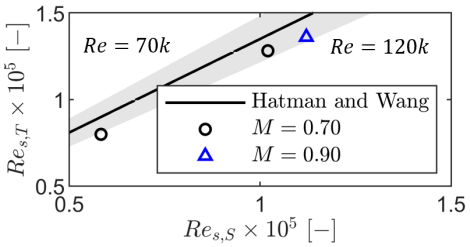

Figure 5.20: Comparison of transition point between model of Hatman and Wang [8] and current experimental data.

separation location. The error, ϵ, to the experimental one obtained with the K_s method is provided as a distance between the locations normalized by the surface length. Negative values denote that the separation occurs prematurely with respect to the reference method (K_s methodology) and vice-versa.

Table 5.4: Separation location, s_{sep}/S, obtained experimentally, with CFD and MISES under steady inlet flow.

		Exp.						
		from K_s	from τ_q	ϵ [%]	CFD	ϵ [%]	MISES	ϵ [%]
65,000	0.70	0.612	-	-	0.614	0.21	0.619	0.68
	0.80	0.637	-	-	0.669	3.17	0.681	4.41
	0.90	0.747	-	-	0.730	-1.67	-	-
70,000	0.70	0.610	0.601	-1.53	0.614	0.42	0.619	0.89
	0.80	0.637			0.662	2.49	0.676	3.84
	0.90	0.741	0.752	1.55	0.723	-1.73	-	-
	0.95	0.788	0.752	-4.57	0.723	-6.49	-	-
100,000	0.70	0.612	-	-	0.601	-1.15	0.602	-1.00
	0.80	0.635	-	-	0.669	3.37	0.676	4.04
	0.90	0.716	-	-	0.703	-1.29	0.756	3.99
	0.95	0.784	-	-	0.703	-8.11	-	-
120,000	0.70	0.610	0.601	-1.53	0.614	0.42	0.602	-0.79
	0.80	0.637	-	-	0.662	2.49	0.670	3.27
	0.90	0.712	0.691	-2.89	0.723	1.16	0.733	2.10
	0.95	0.780	-	-	0.696	-8.38	-	-

Concerning the K_s methodology, the separation location obtained with τ_q is prematurely predicted by $\sim$1.5% of the surface length for the lower Mach number. On the other hand, an underprediction of the separation location by $\sim$2.90% occurs at M=0.90; Re=120k.

The maximum difference between the CFD and the experiments in the separation location occurred for the higher Mach number (M=0.95) cases (up to $\sim$8%). However, for the remaining flow conditions, where the separation is expected to be driven by the same mechanism, delayed separation was often found in the CFD results. The maximum difference to the experiments was found to be $\sim$3.37%. MISES typically predicted the separation to occur downstream of the experimentally measured one. The maximum difference was found to be $\sim$4.00%. Two exceptions occurred at M=0.70, where the MISES predicted earlier separation (ϵ=1.00%).

Table 5.5 depicts the predicted reattachment locations. The CFD computations predicted a late reattachment with a difference of up to $\sim$5.50% at Re=65k and 70k. The opposite occurred for the highest Reynolds, where premature reattachment was found compared to the experiments (i.e., a shorter laminar separation bubble). The MISES computations underpredict the reattachment location by $\sim$9% regardless of the flow condition.

A detailed analysis of the status of the boundary layer on the blade pressure side was not attempted. Fig. 5.21 displays the acceleration parameter along the pressure side at different Mach and Reynolds numbers. The surface length is denoted by a negative coordinate where the origin is the leading edge, and s/S_L=-1 denotes the trailing edge. The critical value required for relaminarization ($K_{s,crit}$=3.5$\times 10^6$) is highlighted with a dashed line. Even though

Table 5.5: Reattachment location, s_{reatt}/S, obtained experimentally, with CFD and MISES.

		Exp.						
		from K_s	from τ_q	ϵ [%]	CFD	ϵ [%]	MISES	ϵ [%]
65,000	0.70	0.931	-	-	0.985	5.46	0.848	-8.23
70,000	0.70	0.921	-	-	0.972	5.12	0.837	-8.45
	0.95		-	-	0.778	-	-	-
100,000	0.70	0.871	-	-	0.852	-1.84	0.802	-6.86
	0.80	0.932	-	-	0.915	-1.75	0.854	-7.86
	0.95	-	-	-	0.812	-	-	-
120,000	0.70	0.858	0.873	1.800	0.771	-8.68	0.773	-8.44
	0.80	0.921	-	-	0.845	-7.58	0.831	-9.05
	0.95	-	-	-	0.825	-	-	-

a pressure side separation bubble characterizes all cases, the boundary layer goes above the critical value. It is, therefore, believed that it relaminarizes as the flow is accelerated in the rear portion of the pressure side.

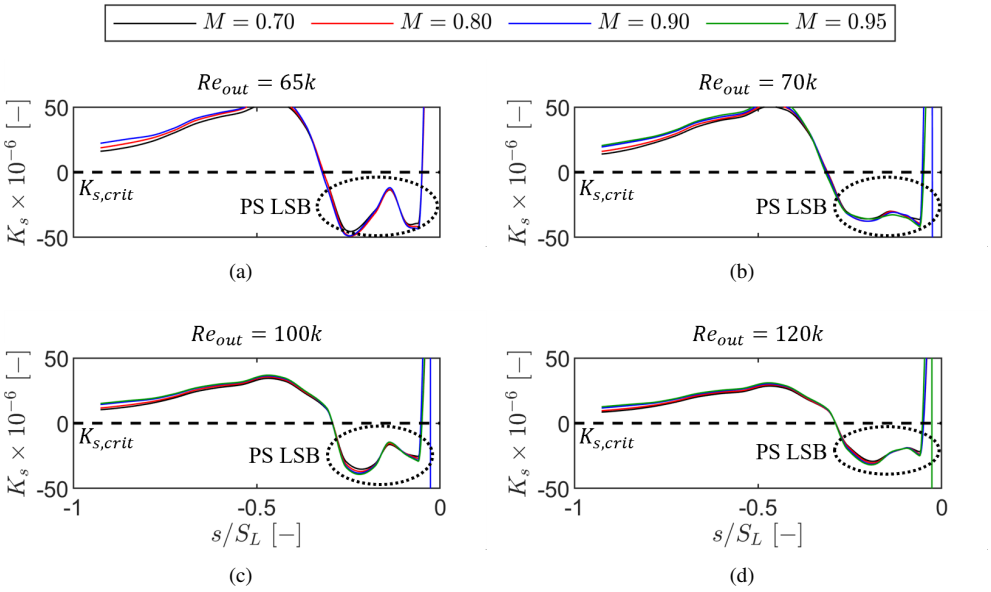

Figure 5.21: Acceleration parameter on the pressure side: Re=65k (a), Re=70k (b), Re=100k (c) and Re=120k (d).

Crossing the acceleration parameter with the critical value occurs near the reattachment of the boundary layer obtained with the transitional RANS simulations. Table 5.6 contains the location of the reattachment of the boundary layer obtained with the transitional RANS CFD and the relaminarization obtained experimentally. The relaminarization location is insensitive to the Mach number and shifts upstream with increasing Reynolds number. Similar findings are obtained for the reattachment location of the laminar separation bubble formed on the pressure side.

Table 5.6: PS laminar separation bubble reattachment location against relaminarization location.

M	Re	$s/S_{L,Reatt}$	$s/S_{L,Relam}$
0.70	65,000	-0.310	-0.318
0.80	65,000	-0.310	
0.90	65,000	-0.310	
0.70	70,000	-0.310	-0.313
0.80	70,000	-0.310	
0.90	70,000	-0.310	
0.95	70,000	-0.310	
0.70	100,000	-0.295	-0.293
0.80	100,000	-0.288	
0.90	100,000	-0.295	
0.95	100,000	-0.295	
0.70	120,000	-0.288	-0.289
0.80	120,000	-0.288	
0.90	120,000	-0.288	
0.95	120,000	-0.280	

5.2.2.2 Impact of Unsteady Wakes

Fig. 5.22 displays the surface isentropic Mach number distribution along the blade pressure side and suction side surfaces during tests performed with the wake generator at on- and off-design flow conditions. A dashed line and hollow markers represent the loadings for the case with the wake generator. The latter is compared against the loadings obtained in the absence of the wake generator (solid lines and filled markers). The color of the marker-line arrangement represents the Mach number.

A significant effect of incidence can be observed for all cases. The incidence measured for the unsteady cases is double the one measured under steady inlet flow (see Section 5.2.1.1 and Section 5.2.1.2). Consequently, the suction side loading from the leading edge to the velocity peak is reduced.

The pressure side distribution is generally not significantly impacted by the introduction of unsteady wakes. However, a significant increase of the pressure side loading occurs for one distinct case: M=0.70; Re=100k in Fig. 5.22(c). Even though with a lower extent, something similar happens for the M=0.90; Re=65k case. The opposite trend is observed for the two Mach numbers investigated for the highest Reynolds number (see Fig. 5.22(d)).

Even though negative incidences can promote or enhance the extent of the pressure side separation, this only occurs for large angles [1]. Furthermore, the same effect would have been observed for all flow cases since the incidence is similar.

The significant impact of the unsteady wakes occurs in the rear portion of the suction side as a result of the wake-boundary layer interaction playing a role in the wake-induced transition [19–23]. Fig. 5.23 displays a zoomed region highlighting the rear suction side aerodynamics.

Laminar separation occurs for all the steady flow cases. An exception is made for the highest Mach number case, in which the transition mechanism is shock-driven. For cases

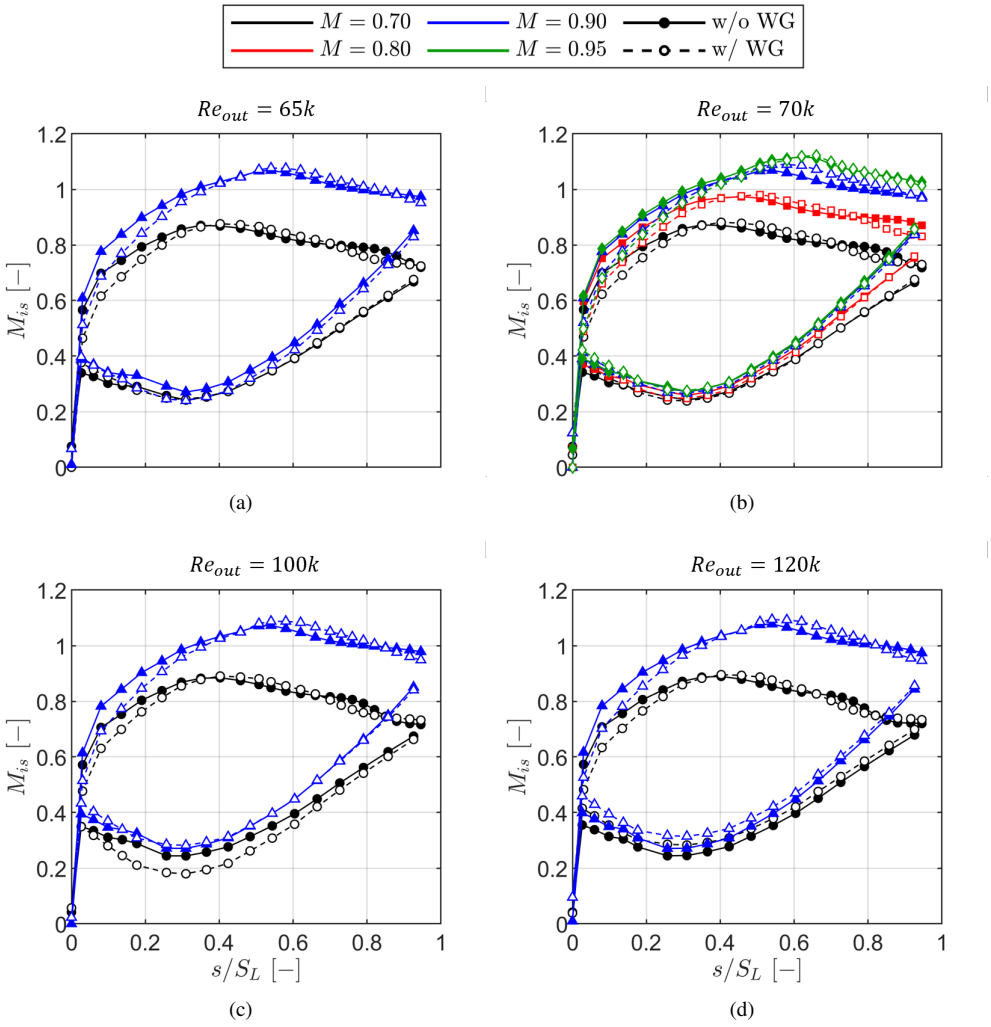

Figure 5.22: Impact of introducing unsteady wakes on the overall surface isentropic Mach number distribution: Re=65k (a), Re=70k (b), Re=100k (c), and Re=120k (d).

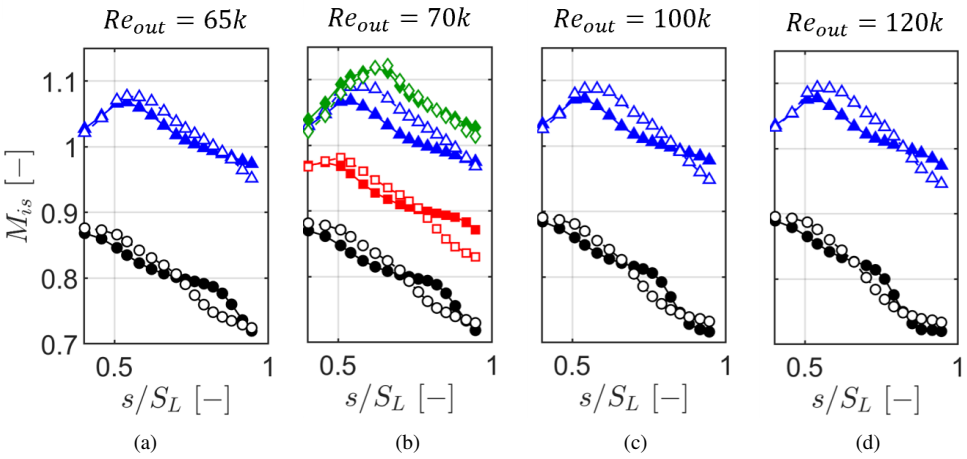

Figure 5.23: Impact of introducing unsteady wakes on the laminar separation bubble region: Re=65k (a), Re=70k (b), Re=100k (c) and Re=120k (d).

where reattachment was captured experimentally, the unsteady wakes reduce the extent of the separation bubble. The latter is evident at M=0.70, regardless of the Reynolds number. The reduction of the bubble extent can also be perceived by an increase in the blade loading from the velocity peak to the trailing edge (the separation bubble has a lower impact on the overall potential flowfield in the passage).

Surface-mounted hot-film retrieved quantities are used to understand better the status of the boundary layer on the blade suction side. Fig. 5.24 compares the blade loadings, and surface-mounted hot-film mean and statistical quantities for a case with separated flow transition (left column) and with a shock in the passage (right column). Black lines/markers denote the steady flow case, while the red ones denote the unsteady flow case. The analysis concerns the time-averaged aerodynamics. The phase-averaged quantities are reported in Section 5.3.2.

The blade loading, in Fig. 5.24(a), for the lower Mach number case evidences the shorter extent of the laminar separation bubble for the case with unsteady wakes. The quasi-wall shear stress, in Fig. 5.24(c), decreases for both cases up to the separation. The quicker reattachment for the unsteady flow case promotes a faster increase of the shear stress quantity that is low for the steady flow case. A slight increase of the shear stress for the steady case near the reattachment location is visible for the steady flow case.

As a result of the wake-induced unsteadiness, the std(E_B) is higher for the unsteady flow case from the leading edge (see Fig. 5.24(e)). Like the steady flow case, the std(E_B) rapidly increases after the separation, suggesting the transition onset occurs in the shear layer. The latter effect is backed up by increased skewness displayed in Fig. 5.24(g).

The main difference between the steady and unsteady cases is that the shorter laminar separation bubble is associated with a faster transition. This is highlighted by the premature location of the global maximum in the std(E_B) for the unsteady flow case concerning the steady one. As a result, the crossing of the skewness at zero is also premature since it

highlights the location of the transition point.

Even though the unsteady wakes accelerate the transition process, the std(E_B) does not reach a "plateau" nor does the skewness. In the time-averaged frame, the boundary layer is still undergoing transition before the trailing edge. The kurtosis increases after the separation location for the cases with and without wakes (see Fig. 5.24(i)). It then decreases up to the reattachment location. A further developed boundary layer characterizes the unsteady case. However, the fact that the kurtosis does not reach a plateau supports the skewness measurements.

The passage shock is the main flow feature driving transition at higher Mach numbers. The blade loadings, in Fig. 5.24(b), are similar after the shock impingement location (S^*). The separation occurs in the vicinity of the shock impingement. In Fig. 5.24(d), the quasi-wall shear stress decreases towards the shock location. Downstream of this location, the quantity is similar for the steady and unsteady flow cases (discrepancies can be attributed to scaling).

Similar to the lower Mach number case, the std(E_B) displayed in Fig. 5.24(f) is higher for the unsteady case due to the deterministic noise introduced by the wakes. Following a local maximum upstream of the shock, the std(E_B) increases rapidly, suggesting transition onset. The local maximum is associated with the upstream separation unsteadiness [11]. The increase of the skewness (see Fig. 5.24(h)) past the shock location supports the onset of the transition hypothesis.

The main difference between the steady flow case and the transition is that the transition is delayed (delayed reduction in the skewness with respect to the steady case). For the steady case, a transition point can be seen before the trailing edge (zero crossing of the skewness). Nonetheless, the transition process is incomplete at this flow condition for either case.

Similar trends concerning the blade loading and surface-mounted hot-film retrieved quantities can be observed for other flow conditions reported in Appendix E for completeness.

Table 5.7 compares the separation location obtained through the K_s and τ_q methodologies. An underprediction of the separation location using τ_q, displaying a maximum error of $\sim$8% at M=0.90 and $\sim$3% at M=0.70, is highlighted. The increase of the error with respect to the steady flow case is thought to be due to the correlation found to correct the K_s methodology may not apply to the unsteady flow case and/or the dependency of the separation and reattachment locations with the spatial resolution of the surface-mounted hot-film sensors. The lack of surface-mounted hot-film measurements at off-design conditions required using the K_s methodology to determine the separation location.

The comparison between both methods in retrieving the reattachment location is contained in Table 5.8. The maximum error between both methods was within $\sim$2.42% at M=0.70.

Table 5.9 contains the separation and reattachment location for the steady and unsteady flow cases obtained with the K_s methodology. The effect of the wakes in reducing the laminar separation extent results from delaying the separation location and shifting the reattachment location upstream.

An open separation is suppressed by introducing wakes in the flow domain at M=0.80; Re=70k (see Fig. 5.23(c)). Using the acceleration parameter methodology highlighted previously, the wakes impact the separation up to M=0.90.

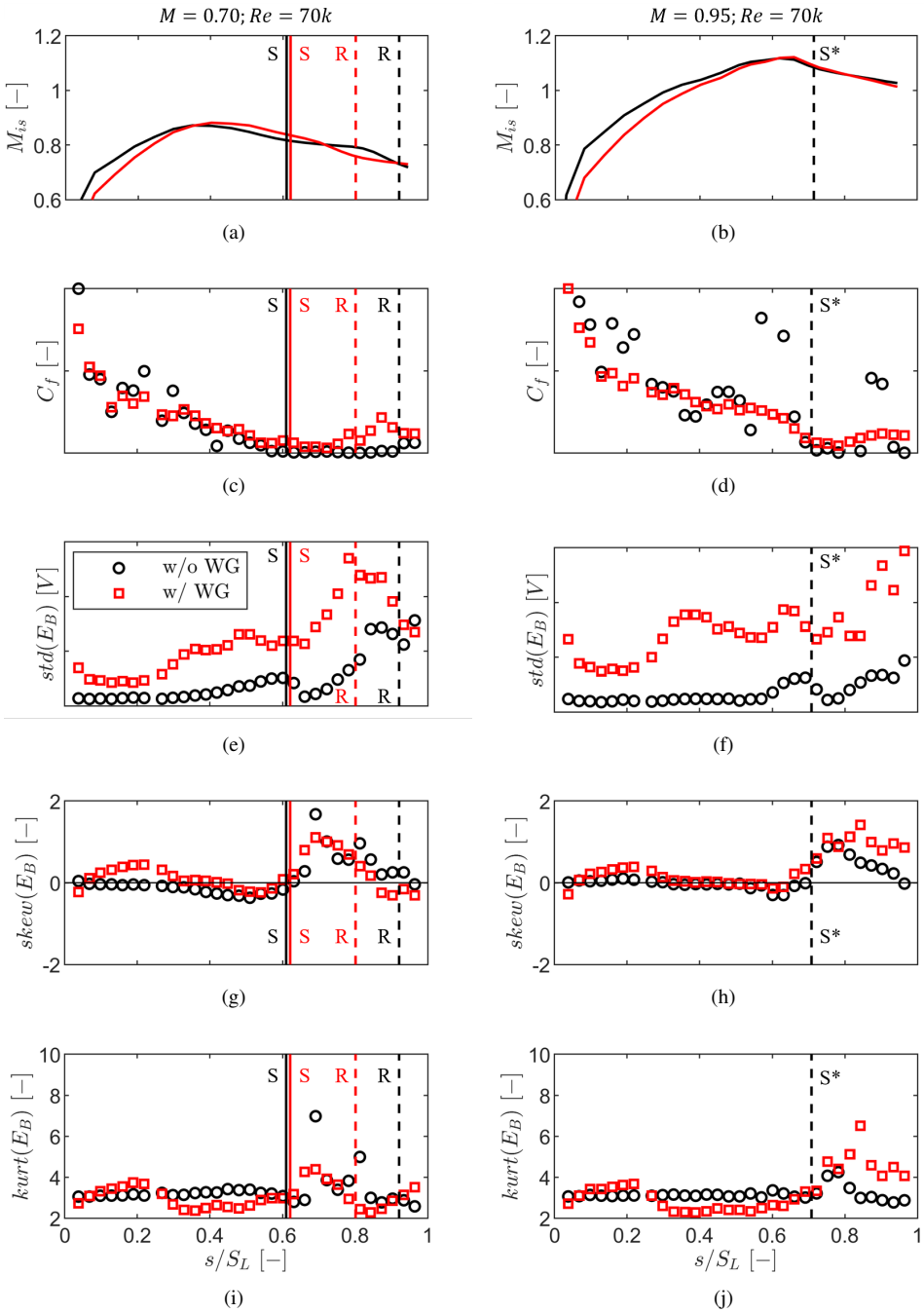

Figure 5.24: Blade isentropic Mach number for M=0.70; Re=120k (a) and M=0.95; Re=70k (b), pseudo skin friction coefficient for M=0.70; Re=120k (c) and M=0.95; Re=70k (d), standard deviation of HF bridge voltage for M=0.70; Re=120k (e) and M=0.95; Re=70k (f), skewness of HF bridge voltage for M=0.70; Re=120k (g) and M=0.95; Re=70k (h), and kurtosis of HF bridge voltage for M=0.70; Re=120k (i) and M=0.95; Re=70k (j).

Table 5.7: Separation location, s_{sep}/S, obtained experimentally under unsteady inlet flow.

		Exp.: from K_s	Exp.: from τ_q	ϵ [%]
65,000	0.70	0.623	–	–
	0.90	0.767	–	–
70,000	0.70	0.621	0.601	-3.16
	0.80	0.658	–	–
	0.90	0.774	0.722	-6.67
	0.95	0.790	0.722	-8.62
100,000	0.70	0.635	–	–
	0.90	0.761	–	–
120,000	0.70	0.647	–	–
	0.90	0.753	0.691	-8.22

Table 5.8: Reattachment location, s_{sep}/S, obtained experimentally under unsteady inlet flow.

		Exp.: from K_s	Exp.: from τ_q	ϵ [%]
65,000	0.70	0.811	–	–
	0.90	–	–	–
70,000	0.70	0.801	0.782	-2.42
	0.80	0.867	–	–
	0.90	–	–	–
	0.95	–	–	–
100,000	0.70	0.871	–	–
	0.90	0.899	–	–
120,000	0.70	0.858	–	–
	0.90	0.886	0.873	-1.43

Table 5.9: Separation, s_{sep}/S, and reattachment location, s_{reatt}/S, obtained experimentally for the inlet steady and unsteady flow cases.

		$s_{sep}/S\ [-]$		$s_{reatt}/S\ [-]$	
$Re_{out}\ [-]$	$M_{out}\ [-]$	Steady	Unsteady	Steady	Unsteady
65,000	0.70	0.612	0.623	0.931	0.811
	0.90	0.747	0.767	–	–
70,000	0.70	0.610	0.621	0.921	0.801
	0.80	0.637	0.658	–	0.867
	0.90	0.741	0.774	–	–
	0.95	0.788	0.790	–	–
100,000	0.70	0.612	0.635	0.871	0.871
	0.90	0.716	0.761	0.932	0.899
120,000	0.70	0.610	0.647	0.858	0.858
	0.90	0.712	0.753	0.921	0.886

5.2.3 Profile wake and Loss

5.2.3.1 Steady Inlet Flow

The blade wake is investigated in terms of the pitchwise profile of the kinetic energy loss coefficient. The inlet freestream total pressure was used to define the inlet kinetic energy. The static pressure at the endwall from the Plane 06 taps was used to define the outlet kinetic energy. Fig. 5.25 displays the blade wakes measured at Plane 06 employing the L5HP with markers for Re=70k (see Fig. 5.25(a)) and Re=120k (see Fig. 5.25(b)). Solid lines represent the CFD predictions. The color of the marker line represents the Mach number.

The CFD struggles to capture the wake depth measured experimentally for the lowest Reynolds number. There is negligible variation in the wake width and depth predicted with CFD. The widest wake occurs at M=0.80. This case is characterized by an open separation, which increases the thickness of the blade suction side boundary layer. The experimental data reflects the differences observed in the blade loading. A late reattachment characterizes the lowest Mach number. A larger thickness defines the developed boundary layer. As the Mach number increases, the boundary layer becomes thinner near the trailing edge.

Nonetheless, the surface length at which the boundary layer develops over the separated flow is smaller since the separation location shifts downstream as the Mach number increases. This results in a thinning of the wake with increasing Mach number. The CFD wake depth for the highest Mach number cases is similar to the one measured experimentally.

At the highest Reynolds number, the CFD predicts the flow to reattach for both Mach number cases. As a result, the boundary layer is thinner at M=0.90, and so is the wake. The same does not occur for the experimental results. The flow is reattached at the lowest Mach number. An open separation occurs for the remaining cases. However, since the Mach number is higher, the resulting profile still displays similar width and depth.

The loss coefficient has been averaged over one cascade pitch. The results are presented in terms of mass-averaged quantities. Fig. 5.26 displays the mass-averaged profile loss for the investigated cases. Solid lines identify experimental data. Dashed lines represent CFD predictions.

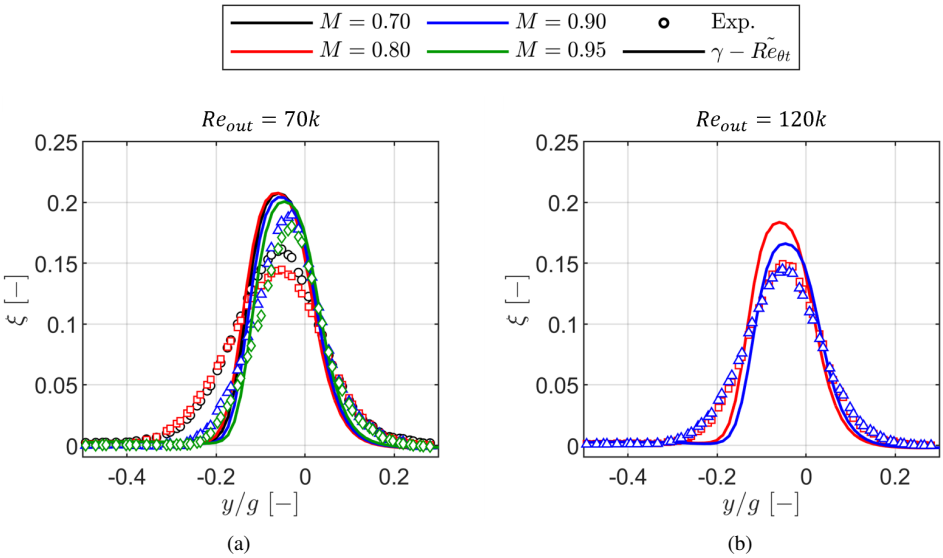

(a) (b)

Figure 5.25: Pitchwise distribution of kinetic energy loss coefficient during the first phase of testing: Re=70k (a) and Re=120k (b).

The loss decreased monotonically with the Mach number for the low Reynolds number cases for experiments and computations. A decrease in the experimental loss by ∼23% was recorded (vs. ∼9% from computations). The CFD consistently underpredicts the loss except for M=0.95.

A drop in the loss coefficient occurs with increasing Reynolds number. The suppression of the open separation for the Mach number of 0.80 reduces the loss by ∼19%. The loss coefficient was independent of the Mach number for the highest Reynolds number measured experimentally. The CFD predicted a decrease in the loss with Mach number.

The dependency of the Mach number on the profile loss contradicts previous findings reported by Vera et al. [24] and Vazquez et al. [25]. The first study was performed in a linear cascade configuration characterized by Re=190k. The second study was conducted in an annular cascade configuration. The impact of the Reynolds number is in line with the studies mentioned above. A loss breakdown (see Section 7.1) was performed to justify the current loss trends.

5.2.3.2 Impact of Unsteady Wakes

Fig. 5.27 displays the pitchwise distribution of the kinetic energy loss coefficient obtained at Plane 06 when tests were performed with the wake generator (dashed lines). The distributions obtained without the wake generator are added for the same flow conditions (solid lines). The marker-line color represents the Mach number.

The modification of the blade suction side boundary layer and the status of the separation are reflected in the wake width and depth. The loss in the suction side boundary layer in the presence of a laminar separation bubble can be broken down into three main contributors [26]:

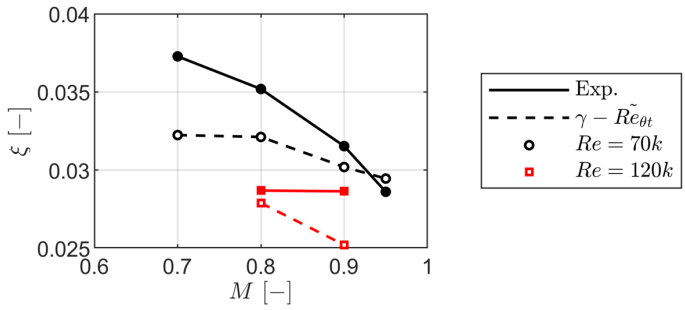

Figure 5.26: Mass-averaged profile loss in terms of kinetic energy loss coefficient obtained during the first testing phase.

the contribution of the turbulent boundary layer, the contribution of the separation bubble, and the contribution of unsteady interaction.

Fig. 5.27(a) highlights a significant increase in the wake width and depth for the M=0.70 case. A closed laminar separation bubble in steady flow conditions characterizes this flow condition. The unsteady wakes reduce the extent of the bubble (see Fig. 5.23(b)). The boundary layer thickness is increased with respect to the steady flow case, leading to a wider wake. In particular, the increase in the wake width occurs towards the suction side (y/g$<$0), consistent with the findings.

For the lowest Reynolds number (see Fig. 5.27(a)), the introduction of unsteady wakes in the flow domain reduces the wake depth. These cases are characterized by a late separation due to the increased Mach number. However, transporting the wake fluid from the pressure side to the suction side creates a stronger mixing [22] and turbulent kinetic energy [27, 28] near the suction side—-the combination of both results in a more considerable wake depth with respect to the steady cases.

For the highest Reynolds number (see Fig. 5.27(b)), the suppression of the open separation enhances the wake width and depth as at M=0.70; Re=70k (see Fig. 5.27(a)).

Fig. 5.28 displays the mass-averaged kinetic energy loss coefficient at on- and off-design flow conditions. A dashed line and steady cases by a solid line represent unsteady inlet flow conditions. The color of the curve denotes the Reynolds number: black for Re=70k and red for Re=120k.

Introducing wakes into the flow domain promotes an increase in the mass-averaged loss. This is consistent with the increased turbulent kinetic energy and mixing promoted by the wakes. Similar findings were reported by Vera et al. [24].

For both Reynolds numbers, the loss decreases monotonically with the Mach number. An increase of the profile loss by $\sim$40% occurs at M=0.70; Re=70k case due to increasing the turbulent wetted area and boundary layer thickness on the suction side. For the highest Mach number case, the impact of the unsteady wakes resulted in a loss increase of 32%.

Even though the wakes aid at suppressing open separations for the highest Reynolds number, an increase in the loss is still perceived (21% at M=0.90).

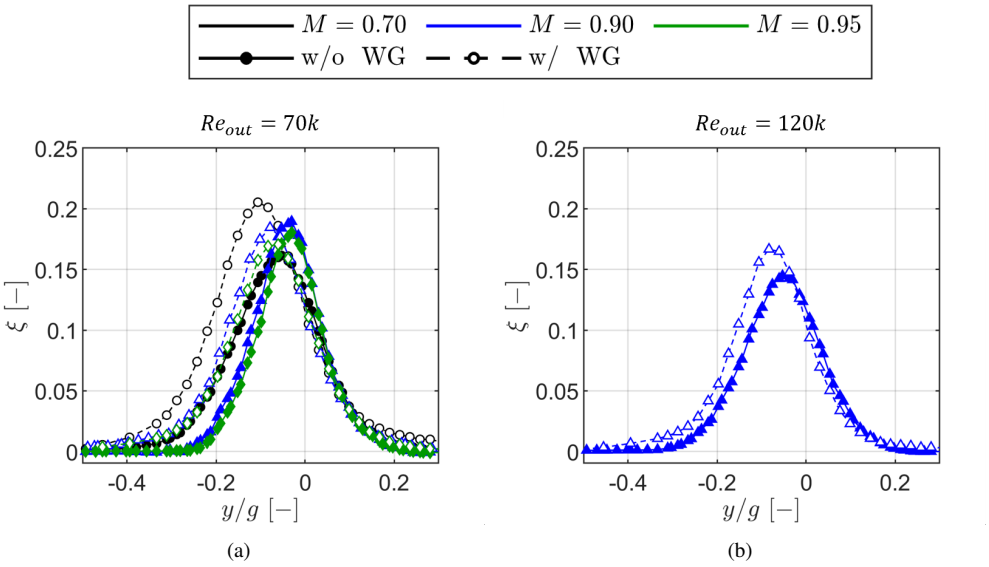

Figure 5.27: Comparison of pitchwise distributions of kinetic energy loss coefficient with and without wakes: Re=70k (a) and Re=120k (b).

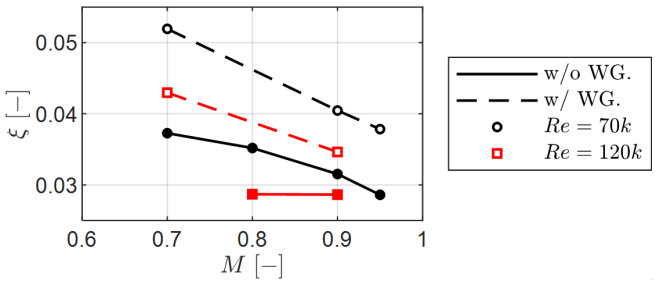

Figure 5.28: Comparison of mass-averaged profile loss in terms of kinetic energy loss coefficient with and without wakes.

5.3 Time-Resolved Measurements

5.3.1 Bar Wake Characterization

The inlet unsteady wakes have been measured experimentally at on- and off-design flow conditions utilizing the FRV4HP. The pitchwise variation of the velocity triangles due to the wake generator's rotating motion in relation to the cascade was assessed.

Fig. 5.29 displays the phase-resolved total pressure fluctuations, $\Delta P_{02}/P_{01,fs}$, at different pitchwise locations. The signals are scaled for visualization purposes. Three flow conditions with varying Reynolds numbers and fixed M=0.70 are displayed to address the Reynolds number effect. The wake trajectory along the pitch is marked with the line "A". For y/g≥0, all the curves collapse as the Reynolds number does not greatly impact the bar wake Strouhal number. A slight discrepancy is visible for negative pitches ($\Delta t \approx 0.01$ ms), specifically at Re=100k. The difference is considered negligible. The wake profile at y/g=0.00 can be used to inform and provide boundary conditions for CFD frameworks.

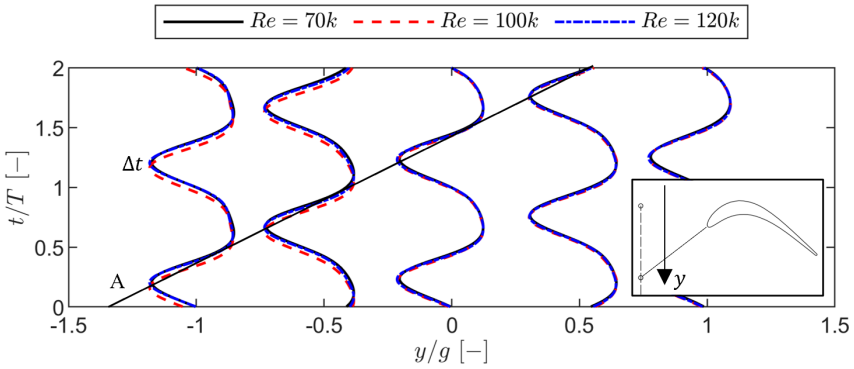

Figure 5.29: Pitch-to-pitch phase-resolved normalized total pressure fluctuations as a function of the Reynolds number at M=0.70 measured experimentally.

Fig. 5.30 addresses the periodicity with varying Mach number at Re=70k. The modification of the Mach number results in different Strouhal numbers. The main variation occurs as the Mach number increases from 0.70 to 0.95. Two wake trajectories are distinct: "A" for the lower Mach number and "B" for the two highest Mach numbers.

A different interpretation of the Reynolds number dependence on the wake in terms of normalized total pressure fluctuations and angular fluctuations is performed in Fig. 5.31. For a typical inlet total pressure in the rig, there are ±200 Pa fluctuations in the bar wake (see Fig. 5.31(a)). The Reynolds number dependence is negligible as the wakes are practically superimposed. Similar findings are reported for the angular fluctuations displayed in Fig. 5.31(b). The angular fluctuations in the wake are contained within ±5°. The angular fluctuations can be interpreted as fluctuations around the incidence as well. The figure highlights that at t/T≈1.2, the incidence can reach up to -6°. The Reynolds number effect on the angular fluctuations is negligible.

Phase lag and variation of the fluctuation amplitude are observed if the Mach number is varied at a fixed Reynolds number (see Fig. 5.32). At a higher outlet Mach number, the wake

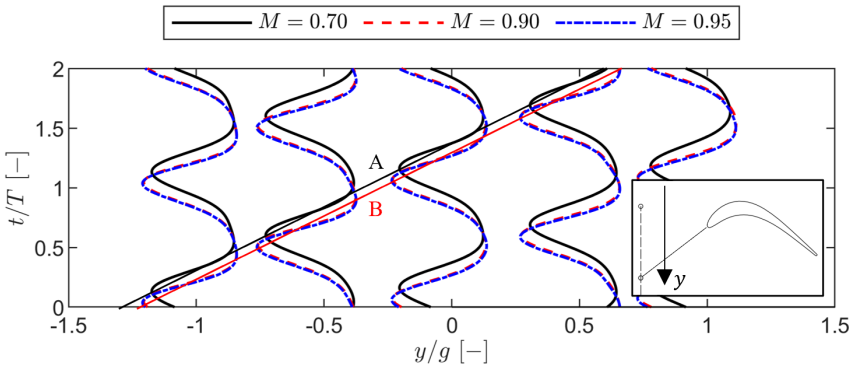

Figure 5.30: Pitch-to-pitch phase-resolved normalized total pressure fluctuations as a function of the Mach number at Re=70k measured experimentally.

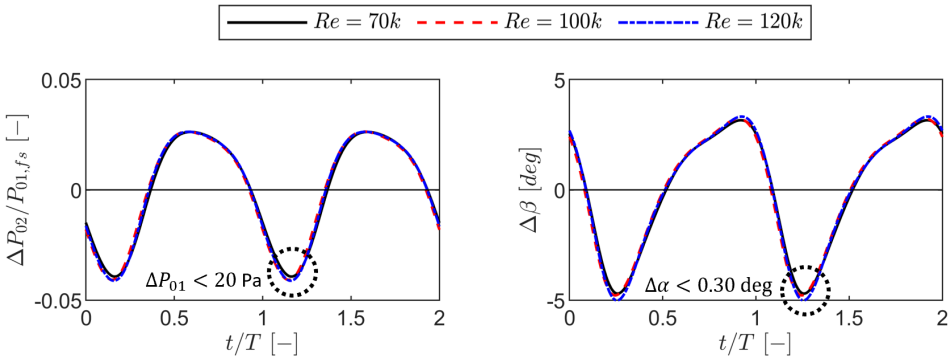

Figure 5.31: Experimental wakes measured at y/g=0.00 for M=0.70: normalized total pressure fluctuations (a) and angular fluctuations (b).

arrives faster at the measurement location (Δt≈0.02 ms). The peak magnitude of the normalized total pressure is not significantly modified, as displayed in Fig. 5.32(a). On the other hand, an increase of 60 Pa is observed in the wake center as the Mach number increases from M=0.70 to 0.90. Increasing the Mach number results in a decrease in angular fluctuations by 0.30° near the wake center (see Fig. 5.32(b)).

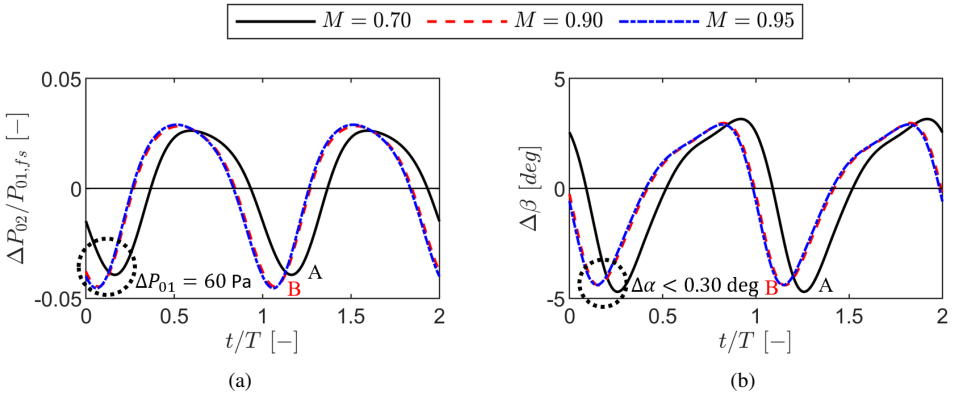

Figure 5.32: Experimental phase-averaged wakes measured at y/g=0.00 with varying Mach number at Re=70k: normalized total pressure fluctuations (a) and angular fluctuations (b).

Fig. 5.33 displays the phase-resolved turbulence intensity in the central pitchwise location. Fig. 5.33(a) addresses the impact of the Reynolds number. The undisturbed level in the absence of the wake generator wake measured with a cross-wire (XW) and reported in [4] is included for reference. The dotted line represents the phase-resolved turbulence measured at M=0.90; Re=70k with the cross-wire.

The FRV4HP estimated turbulence displays a similar shape to the XW profile. The latter probe relies on local measurements obtained with a different probe to compute the phase-resolved turbulence. The FRV4HP relies solely on quantifies retrieved with itself. The profiles of turbulence measured with the FRV4HP nearly reach the freestream value in the absence of wakes in between passing wakes (marker "A" at t/T≈0.80). An increase of the turbulence intensity at this phase by 0.40% occurs with increasing Reynolds number. Two local maximum of turbulence, "B" and "C", can be observed for all profiles. These result from the turbulence generated in the counter-rotating vortices derived from the bar shedding [29–31]. This type of wake has been measured experimentally for bar and airfoil wakes in low-pressure turbine testing [32]. In region "B", the turbulence intensity increases by 0.20% with increasing Reynolds number.

Similar trends are observed for the normalized pressure and angular fluctuations with varying Mach numbers. Fig. 5.33(b) displays the phase-resolved turbulence intensity obtained at fixed Re=70k with varying Mach number. The peak in turbulence arrives prematurely at the highest Mach number (about the same as for the profiles reported in Fig. 5.32). Nonetheless, the magnitude of the trough "D" between two wake passing events is independent of the Mach number. The amplitude of the more prominent peak "E" decreases by 0.30% with increasing Mach number.

As highlighted in Fig. 5.34(a), the bar wake causes a local reduction of the flow incidence.

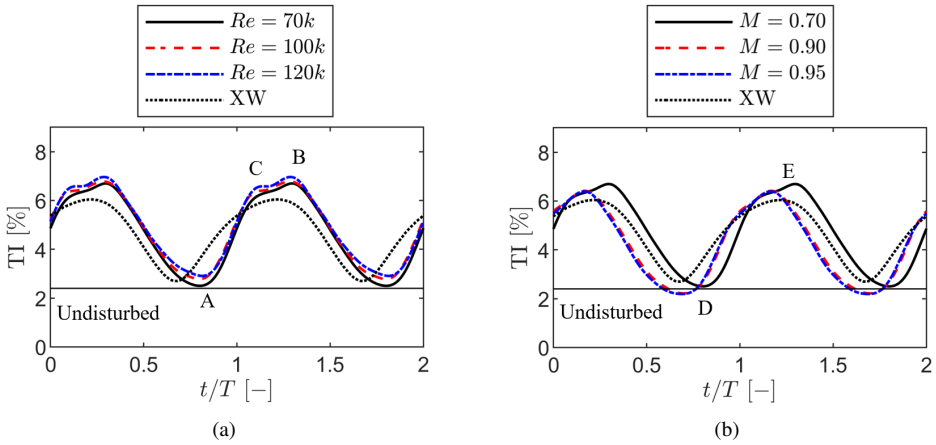

Figure 5.33: Experimental phase-averaged wakes measured at y/g=0.00 characterized in terms of turbulence intensity: at M=0.70 (a) and Re=70k (b).

The lower incidence reduces from the reduction of the wake relative angle due to the negative jet effect [33]. On the other hand, the peak turbulence intensity is observed in the center of the wake (see Fig. 5.34(b)). The turbulence intensity is centered so that the reported peaks associated with the shed vorticity are symmetric around the maximum wake deficit. Even though dependent on the upstream article: bar, blade, etc., the turbulence fluctuations found experimentally are in line with ones found in the wake of an axial turbine [34] and downstream of translating wake generators [35].

It is worth noticing that for all of the above quantities, "flat" regions are never observed between wakes. The latter is attributed to the high Strouhal number and wake relative angle. The decrease between the center of adjacent wakes decreases, which allows adjacent wakes to mix before the measurement location. The latter effect is evident in previous works performed in the same rig with the same wake generator [2].

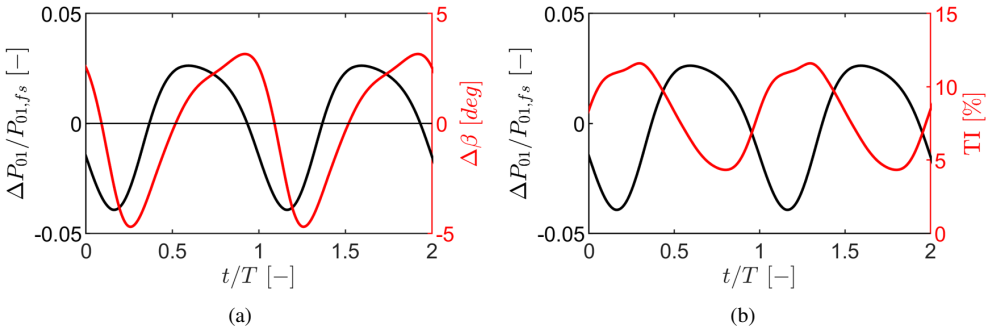

Figure 5.34: Wake relative position of pressure deficit in relation to angular fluctuations (a) and turbulence intensity (b).

5.3.2 Wake-Boundary Layer Interaction

The unsteady wakes result in deterministic wake-boundary layer interactions that were investigated using surface-mounted hot-film sensors and fast-response pressure transducers. Fig. 5.35 aims to characterize the boundary layer flow features.

Fig. 5.35(a) displays the space-time diagram of the quasi-wall shear stress during two bar passing periods at M=0.70; Re=70k. The time-averaged separation ("S") and reattachment ("R") locations are highlighted by the red-dashed lines. The quasi-wall shear stress is normalized by the maximum at each surface location to highlight the modulation of the boundary layer features in the transition region. The approach is similar to Howell et al. [36]. The wake trajectory is highlighted.

The wake impingement point on the blade surface was tracked as a local static pressure maximum during one bar passing period. This was measured with the fast-response pressure sensor installed on the leading edge (see Section 2.4.10). The trajectory was obtained by assuming the wake portion near the blade surface travels at the local freestream velocity (isentropic velocity). The static pressure taps (see Section 2.4.8) were used to compute the convection time, knowing the distance between sensors. The various lines representing the speed of the transition-related features originate from the same point because of the limited experimental resolution in the hot-film measurements. As measured by the sensor closest to the separation location, the minimum in the phase-averaged quasi-wall shear stress was chosen as the origin.

Before the separation, deterministic fluctuations of the shear stress are caused by the wake velocity deficit. In this region, the boundary layer is laminar, and the fluctuations are not attributed to transition-related phenomena. Transition-related features such as Klebanoff streaks and Kelvin-Helmholtz instabilities result in a wedge-shaped configuration due to the varied propagation velocities of turbulent flow features triggered by the wake. Four propagating velocity lines can be identified due to the persistence of the wake after it has passed. The wake passing triggers the formation of turbulent spots propagating slower than the wake itself. The leading edge of the turbulent spots sits at 0.88U while the trailing edge of the spots can be seen at 0.50U [37] for a zero-pressure gradient. This region of the transitional/turbulent boundary layer is pink-shaded. In fact, for wake-induced transition in separated flow, this region is better described by the propagation of broken-down Kelvin-Helmholtz roll-ups that form as the inflectional boundary layer is disturbed by the incoming wake [19, 38].

The 0.50U line also corresponds to the leading edge of the becalmed region (green-shaded) that persists while the laminar separation bubble grows to its original undisturbed extent. Even though not explicitly displayed in Fig. 5.35, the wake passing causes an increase in quasi-wall shear stress. The magnitude of the quasi-wall shear stress decreases in the becalmed region up to the lowest value as the laminar separation bubble regains shape. A last line is identified with 0.70U. The latter corresponds to the propagating velocity of Klebanoff streaks that can develop near the leading edge and propagate along the suction side surface [33].

The triggering/formation of turbulent spots in the shear layer results in high levels of turbulent mixing. The std(E_B) suffers a significant increase as a result (see Fig. 5.35(b)). An increase near the reattachment location is also present. The becalmed and separated regions are characterized by low values of std(E_B).

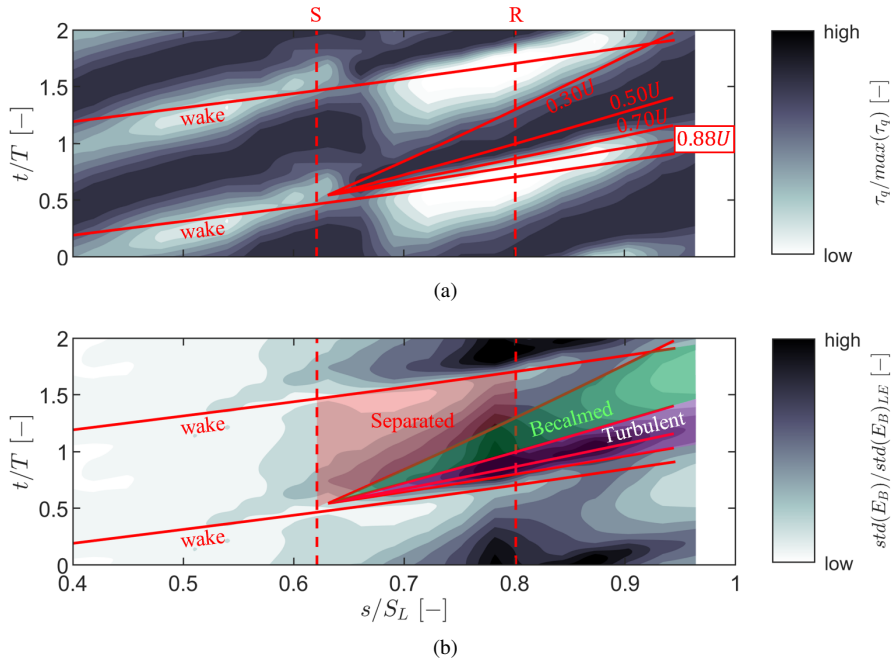

Figure 5.35: Schematic space-time diagrams for M=0.70; Re=70k case: quasi-wall shear stress normalized by a local maximum at which surface coordinate (a) and standard deviation of bridge voltage normalized by leading edge time-averaged value (b).

The normalized quasi-wall shear stress (see Fig. 5.36(a)), standard deviation of the bridge voltage (see Fig. 5.36(c)) and skewness of the bridge voltage (see Fig. 5.36(e)) at M=0.70; Re=70k are displayed in the left column of Fig. 5.36. The same quantities for the increased Mach number of 0.95 are shown in the right column of Fig. 5.36. For the lower Mach number case, the wake trajectory ("W"), separation ("S"), and reattachment ("R") are displayed. For the highest Mach number, the shock impingement location ("S*") is used instead.

Besides the flow features described in Fig. 5.35, the skewness provides additional insight into the status of the boundary layer. The turbulent and calmed regions limit a region of negative skewness after the flow reattaches. The latter suggests that the flow is characterized by a late transitional state after reattachment. Near the location of the last sensor and inside the becalmed region, there is a region ("A") of zero skewness after the negative portion. In this region, the flow has become fully turbulent. The statement is backed up by the low std(E_B) values in the same region. Once the becalmed region effect has passed and the bubble regains its original extent, the flow returns to an early stage of transition (region "B") characterized by positive skewness.

The wedge shape and turbulence flow features are less evident for the highest Mach number. This is partly because the separation/transition features are shifted downstream with increasing Mach number. The quasi-wall shear stress displayed in Fig. 5.36(b) displays large fluctuations in the laminar region. The shock location represents a sudden modification of the oscillation patterns with an opposite slope in relation to the wake trajectory. The maximum shear stress variation occurs after the becalmed region, while the minimum shear stress occurs between the 0.88U and 0.50U trajectories (transitional/turbulent region).

The maximum fluctuations also occur in the becalmed region after s/S_L≈0.90 as displayed in Fig. 5.36(d). After the wake calming effect, there is a further increase in fluctuations at s/S_L≈0.80. The boundary layer also suffers significant variations in this region, as highlighted by the skewness (see Fig. 5.36(f)). These boundary layer fluctuations are attributed to the unsteady reattachment downstream of the shock impingement. However, it is suggested that the wake-boundary layer interaction and transition mechanism for the case with a shock in the flow domain is not well described by existing literature on separated flow wake-induced transition.

In unsteady low-speed flows over blades, the boundary transition relaxes towards a laminar state after the wake passage. However, at the start of this relaxation, the velocity profile remains close to the turbulent one, while turbulence decays very rapidly. This is observed at M=0.70; Re=70k. The wake-induced transition is significantly different at M=0.95. It seems that the incoming wake slightly perturbs the shock wave (S), but this does not cause an immediate transition under the wake impact, unlike what is observed in low-speed turbine flows. The near-wall turbulence is generated downstream at s/S_L>0.9, as shown in Fig. 5.36(d). It is likely that in this case, the wake turbulence cannot immediately trigger the transition, and it only influences the boundary layer flow further downstream when the turbulence diffuses towards the blade surface. A different effect is observed in the next Fig. 5.37 (M=0.90; Re=120k) in which the absence of the shock wave (see also Fig. 5.14) results in a more direct impact of the wake turbulence on the transition in the separated boundary layer.

The previous conclusions are backed up by the wake-boundary layer interaction mechanisms that can be observed at M=0.90 for low Reynolds number (left column of Fig. 5.37) and high Reynolds number (right column of Fig. 5.37).

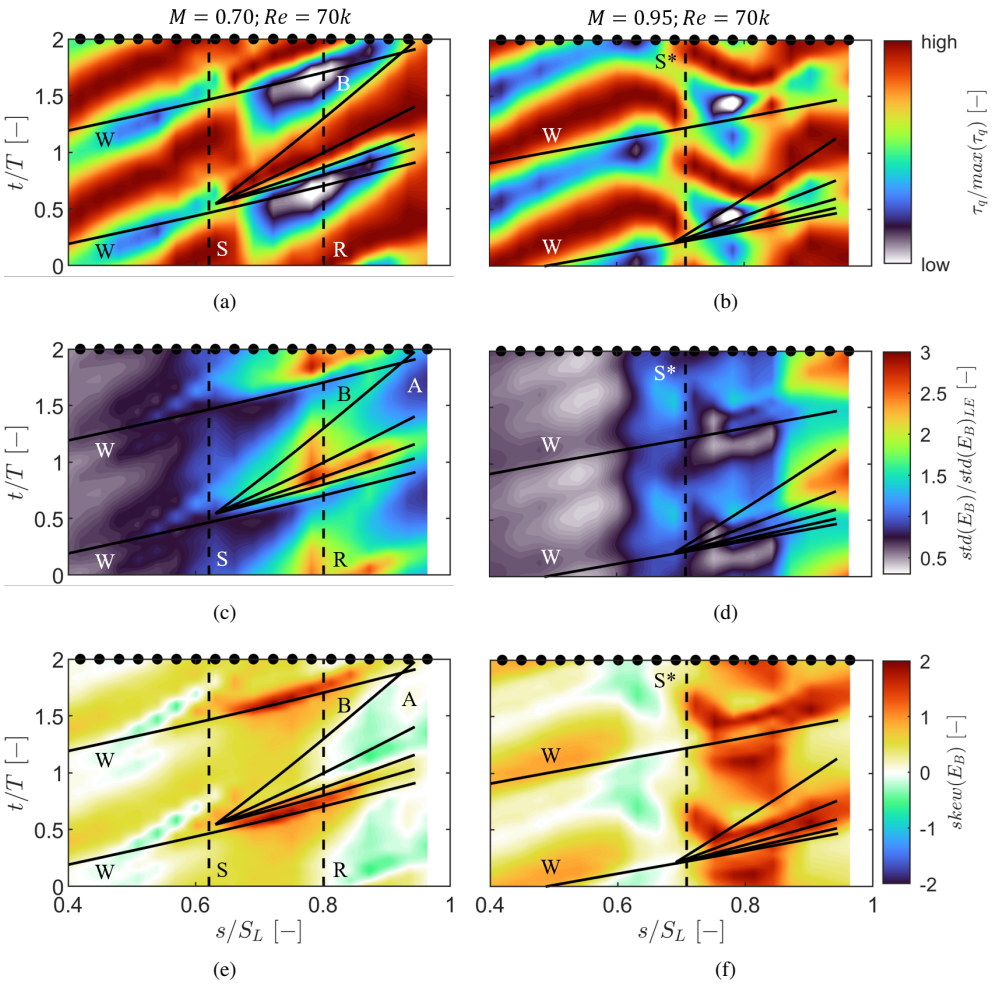

Figure 5.36: Quasi-wall shear stress (a, b), standard deviation of bridge voltage (c, d), and skewness of bridge voltage (e, f) for M=0.70 and M=0.90 at Re=70k.

At Re=70k (see Fig. 5.37(a)), the flow does not reattach in the time-averaged frame of reference. The quasi-wall shear stress increases in the separated shear layer after the wake passes. The level remains high in the transitional/turbulent region $\in [0.30U, 0.50U]$. A reduction occurs as the becalmed region takes over the blade surface. The successive wake passing promotes an increase in the shear stress.

The same is observed for the highest Reynolds number (see Fig. 5.37(b)) except that reattachment occurs. The latter case highly resembles the M=0.70; Re=70k case. The high shear stress delimited region is particularly evident in cases with reattachment.

The STD is found to be higher in the turbulent and becalmed regions for both cases. Due to the reattachment that occurs for the highest Reynolds number case, there are large regions of exceptionally high std(E_B) compared to cases without predicted reattachment.

Lastly, Fig. 5.37(e) displays the space-time diagram of skewness for the lowest Reynolds number. The skewness by the location of the last sensor is positive, suggesting an early-stage transitional boundary layer. On the other hand, regions ("A") of advanced transitional status occur for the highest Reynolds number (see Fig. 5.37(f)). Opposite to the M=0.70; Re=70k case where reattachment occurs further upstream, the skewness never returns to zero. Therefore, there are no regions on the blade surface where the transition is complete before the location of the last sensor.

The phase-averaged pressure fluctuations can be used to infer the nature of the transition mechanism for the present test case. Fig. 5.38(a) displayed the phase-averaged pressure fluctuations along the blade suction side surface with varying Reynolds number for a fixed M=0.70. The inlet total pressure normalizes the pressure fluctuations. The wake trajectories for each case are also in the figure for completeness. The vertical lines highlight the separation and reattachment locations for the shortest and longest laminar separation bubbles. The color of the line arrangement represents the Reynolds number.

The separation location for these cases occurs at s/S_L≈0.62. The pressure traces describe a topology similar to the last sensor before separation. A decrease in the phased pressure peak occurs with increasing Reynolds number. After the separation, fluctuations characterized by over/undershoots can be observed. These appear right after the wake has passed. Their topology is resembling of Kelvin-Helmholtz roll-ups [38]. The Kelvin-Helmholtz roll-ups are deterministic since they are triggered by the periodic negative jet effect [39]. The fluctuations for the lower Reynolds number are more pronounced. The latter observation is particularly evident for the signals captured by the last sensor at s/S_L≈0.90.

The perturbations can also be observed at M=0.90 as displayed in Fig. 5.40. The signals measured by the second-to-last sensor (s/S_L≈0.753) are similar to the ones measured by the previous sensor (s/S_L≈0.637) for the lower Mach number. The latter effect results from shifting the wake-boundary layer interaction characteristics downstream with the Mach number.

The current results suggest that up to M=0.90, the transition mechanism is driven by the breakdown of Kelvin-Helmholtz structures as the wake interacts with the separation bubble.

Fig. 5.39(a) displays the phase-averaged traces of normalized static pressure (solid line) and standard deviation of the static pressure (dashed lines). The standard deviation is normalized by the inlet total pressure as well. The separation ("S") and reattachment ("R") locations are highlighted with blue lines. The disturbance's celerity taken from the surface-mounted hot-film measurements are superimposed.

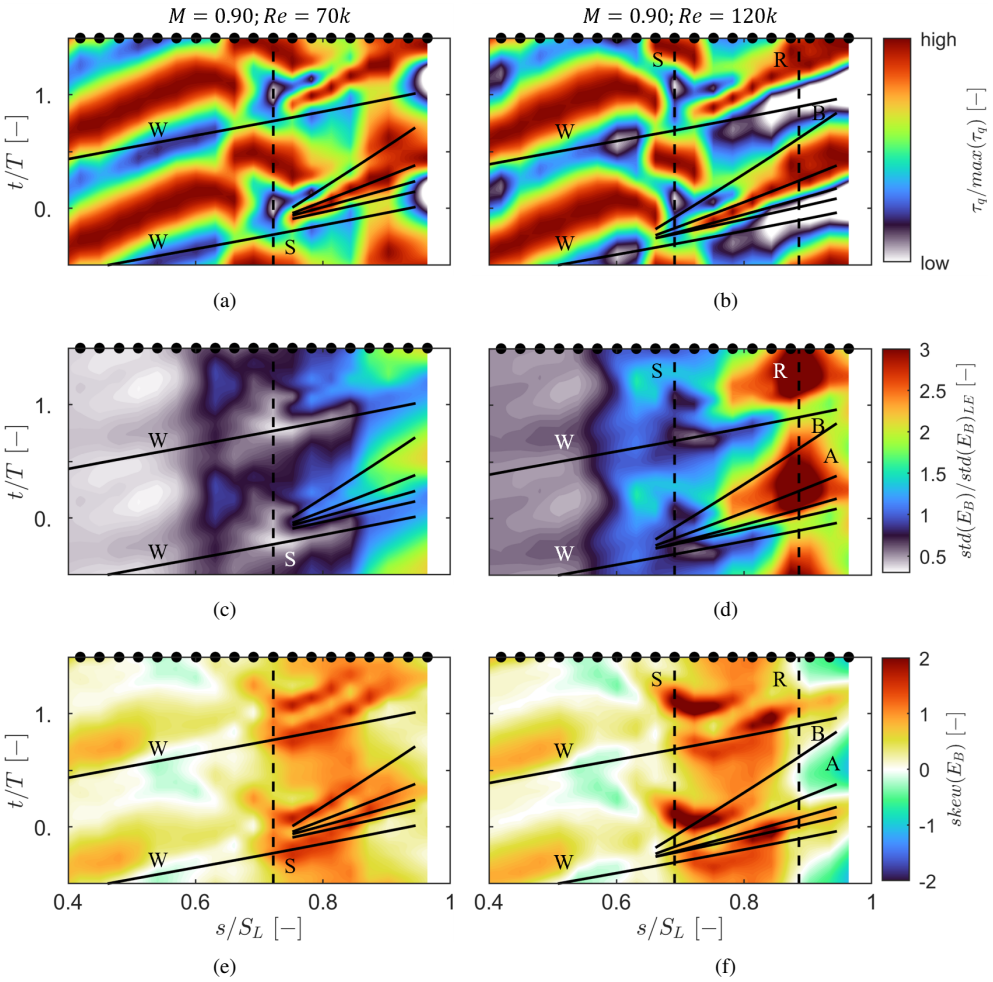

Figure 5.37: Quasi-wall shear stress (a, b), standard deviation of bridge voltage (c, d), and skewness of bridge voltage (e, f) for Re=70k and Re=120k at M=0.90.

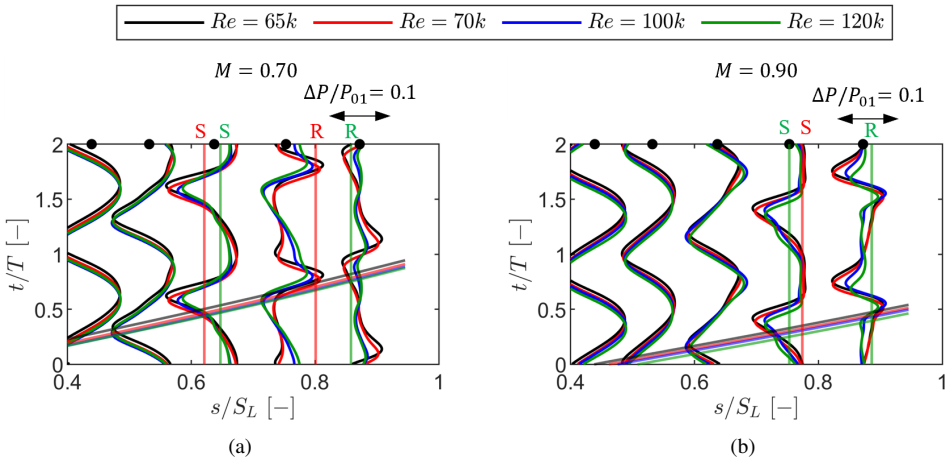

Figure 5.38: Phase-averaged normalized pressure traces along the blade SS with varying Reynolds number: M=0.70 (a) and M=0.90 (b).

Before the separation, the pressure oscillations display a sinusoidal behavior. Fluctuations of $\pm 0.05 P_{01}$ are observed. These persist up to the sensor near the separation. Peaks in the standard deviation occur near the pressure deficit. After separation, over/undershoots in the pressure signal related to the roll-up of spanwise Kelvin-Helmholtz instabilities are formed. These propagate at $\sim$0.50U, which is consistent with the findings of Stieger et al. [38]. The magnitude of the pressure fluctuations is reduced by half in the last sensor. The signal upstream of the reattachment location displays the largest stochastic pressure fluctuations of $\pm 0.04 P_{01}$.

At M=0.95 (see Fig. 5.39(b)), the pressure fluctuations are similar, but the standard deviation decreases significantly ($<0.01 P_{01}$). Before the shock location (S*), there was a considerable reduction in pressure fluctuations. After the shock impingement point, the sensor records the most significant fluctuations. However, the over/undershoot signature is not developed by the location of the last sensor, even though the pressure fluctuations are more than double the ones at the lower Mach number. Likely, the transition does not occur due to the formation of Kelvin-Helmholtz structures as opposed to the lower Mach number cases.

At M=0.90, the findings concerning the development of the pressure signature up to the separation location are similar to those reported at M=0.70. Before the separation, the STD of the pressure has a minimum that coincides with the local pressure minimum in terms of phase. Up to the separation location, the amplitude and phase of the pressure fluctuations and its RMS are similar between Re=70k (a) and Re=120k (b).

For both Mach numbers, the Kelvin-Helmholtz structures propagating at 0.50U are visible, especially at the location of the last sensor. A peak in the pressure STD occurs in the inflection of Kelvin-Helmholtz structures' location in the pressure signals. The STD fluctuations are higher than for the M=0.90; Re=70k, for which there is no time-averaged reattachment.

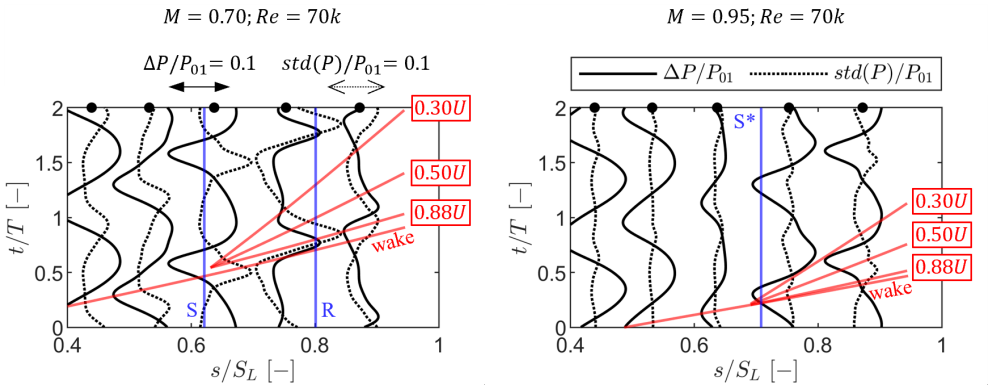

Figure 5.39: Phase-averaged normalized pressure traces (solid line) and standard deviation (dashed line) along the blade SS with varying Mach number: M=0.70; Re=70k (a) and M=0.95; Re=70k (b).

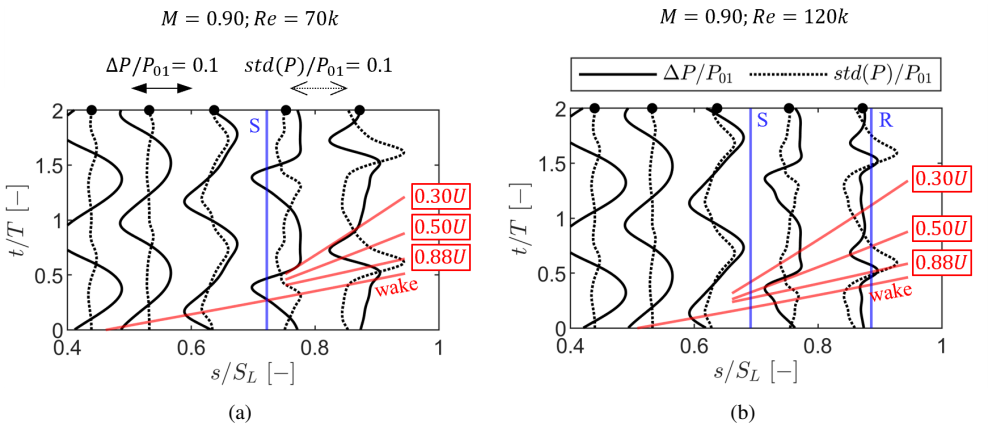

Figure 5.40: Phase-averaged normalized pressure traces (solid line) and standard deviation (dashed line) along the blade SS with varying Reynolds number: M=0.90; Re=70k (a) and M=0.90; Re=120k (b).

5.3.3 Blade Wake Aerodynamics

The unsteady wakes produce a varying outlet flowfield. The topology of the outlet flowfield is similar for all the investigated conditions. Fig. 5.41 displays the space-time diagrams of the kinetic energy loss coefficient measured at Plane 06 with the FRV4HP. The pitchwise location is represented in the x-axis. The bar phase is defined in the y-axis. The suction side and pressure side in the vicinity of the trailing edge are highlighted.

The Reynolds number does not change the overall contour topology. Three main regions are highlighted for the lowest Mach number (see Fig. 5.41(a)). Near the trailing edge on the suction side, a region of modulated loss coefficient is visible ("A"). This peak occurs when the wake convecting along the suction side arrives at Plane 06. Due to the lower freestream velocity on the pressure side, the wake propagation time is higher. The delayed arrival of this wake portion at Plane 06 is highlighted by a region modulated with the wake passing ("B"). The wake modulation in the freestream region ("C") is less severe as it does not contain blade boundary layer loss.

The same flow topology is observed for the highest Mach number (see Fig. 5.41(b)). The main difference is a phase shift between the flow structures. The latter results from the different Strouhal numbers from the fixed wake generator rotational velocity. For the same bar speed, the wake conveys faster for the highest Mach number.

In region "C", the kinetic energy loss coefficient takes negative values ($P_{06} > P_{02}$). The phenomena through which the outlet fluctuations are amplified with respect to the inlet wake is denominated "energy separation" [40].

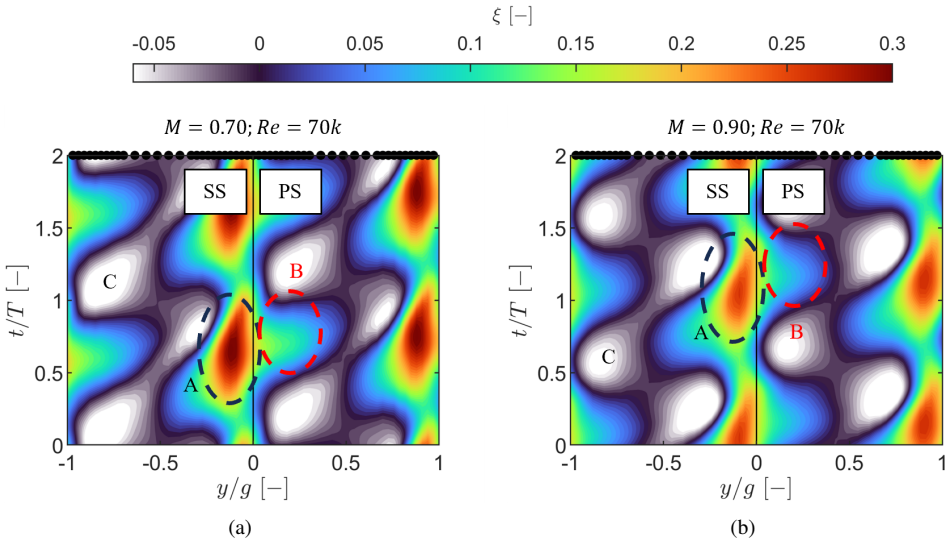

Figure 5.41: Space-time diagram of kinetic energy loss coefficient at Re=70k: M=0.70 (a) and M=0.90 (b).

The phase-averaged signals at specific pitchwise locations highlight the dependence of the Mach and Reynolds numbers on the outlet kinetic energy loss coefficient. The signals were

extracted in the freestream region (y/g=-0.58), near the suction side surface (y/g=-0.18), and near the pressure side (y/g=+0.03).

Fig. 5.42 displays the kinetic energy at the specified locations. The curve's color denotes the Mach number, and the line type indicates the Reynolds number. The freestream fluctuations are much lower than the ones near the blade, as displayed in Fig. 5.42(a). For a fixed Mach number, the curves display insensitivity to the Reynolds number. The fluctuations for the lower Mach number are almost two times larger than for the increased cases. A change in the blade loading due to modifying the Mach number modifies the cross-passage pressure gradient. As a result, the wake redistribution towards the suction side is also impacted. Even though not critically noticeable, the more considerable extent of the loss region "B" towards the suction side is visible for the lowest Mach number in Fig. 5.41(a).

Near the suction side (see Fig. 5.42(b)), the loss is composed of the wake generator wake low-momentum fluid in addition to the separated shear layer loss that is impacted by the wake itself. The phase shift by half a bar period with increasing Mach number is noticeable. Similar loss fluctuations occur for the lowest Mach number. A delay in the loss peak by less than 10% of the bar phase is visible. The same happens at M=0.90. For the lowest Mach number, the wake-induced loss at t/T≈1.50 increases by 0.25 with respect to the "freestream" value at t/T≈1.00. At M=0.90, the most noticeable feature is the substantial increase in the "energy separation" phenomenon with increasing Reynolds number at t/T≈1.30. The fluctuations' amplitude is of the same order as the lowest Mach number, and so is the shape of the signal.

Fig. 5.42(c) displays the energy loss coefficient fluctuations in the pressure side portion of the wake. For the lowest Mach number, the phase shift described for the suction side wake portion also applies at this location. The fluctuations are similar as well. The significant difference is the shape of the signal. A "fuller" loss profile characterizes the higher Mach number cases. The latter is attributed to the more substantial amount of wake fluid near the pressure side for the higher Mach number due to the lower blade loading.

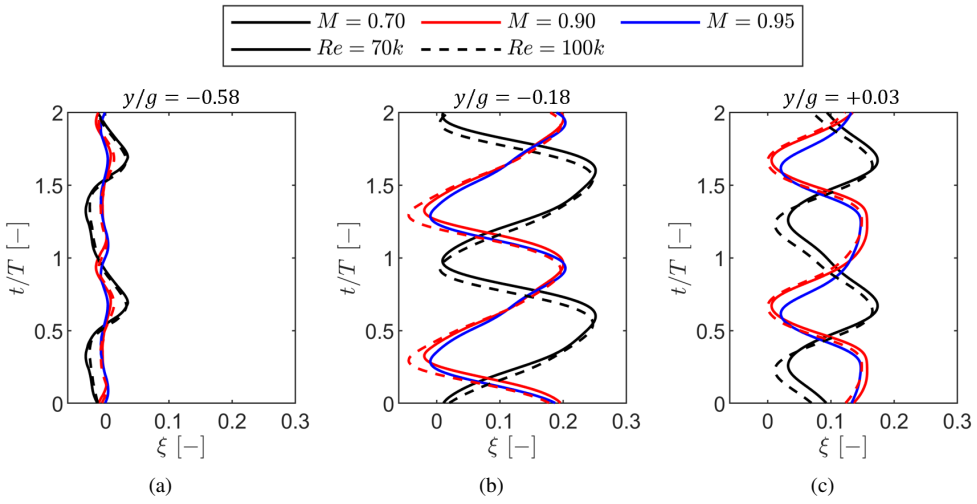

Figure 5.42: Phase-averaged kinetic energy loss coefficient at on- and off-design flow conditions: y/g=-0.58 (a), y/g=-0.18 (a), and y/g=+0.03 (c).

Fig. 5.43 displays the experimental phase-resolved mass-averaged kinetic energy loss coefficient over one blade pitch. The color of the line denotes the Mach number, and the type of the line denotes the Reynolds number.

In agreement with the previous findings, the Reynolds number does not significantly modify the signal phase. The loss peak occurs earlier as the Mach number is increased. At M=0.70, the loss profiles are nearly Reynolds number-independent. At M=0.90, the peak loss magnitude is similar. However, in the freestream region between t/T=0.25 and 0.50, the loss is 34% higher for the lowest Reynolds number. This is associated with the larger separation bubble for the lowest Reynolds number. For the steady flow case, increasing the Reynolds number from 70k to 100k considerably modifies the extent of the separation bubble [41]. It is likely that between bar passing events, the losses associated with the separation bubble being reestablished are higher for the lower Reynolds number.

As the Mach number increases, both the peak and mean levels increase. While the signal resembles a sine wave for the lowest Mach number, the signals at higher Mach number display a "plateau" between adjacent peaks. For the lowest Mach number, the wake passing causes a trough-to-peak loss increase of 676%. The variation is lower at higher Mach number (267% at M=0.95).

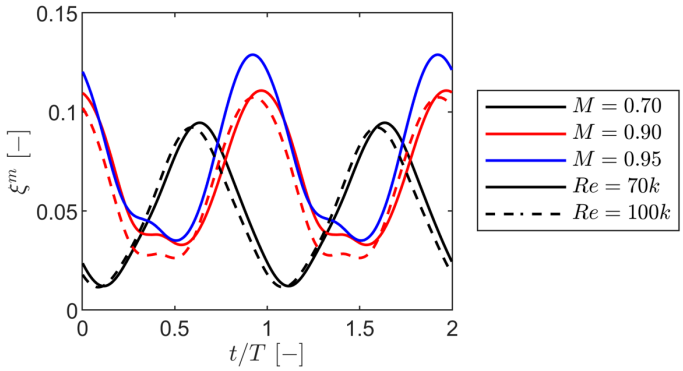

Figure 5.43: Phase-resolved kinetic energy loss coefficient mass-averaged over one blade pitch.

The outlet flow angle also characterizes the modulation of the outlet flowfield. Fig. 5.44 displays the space-time diagrams of the angular fluctuations around the outlet flow angle. The topology is similar for all cases, with a phase shift apparent with varying Mach numbers. The contours are superimposed with the isolines extracted from the kinetic energy loss coefficient. The regions previously highlighted, freestream, vicinity of suction side, and vicinity of pressure side, are displayed for completeness. The wake-induced loss peaks ("A", "B") are associated with flow angles lower than the time-averaged outlet flow angle. In the freestream, the flow angle is larger than the outlet flow angle.

Similar to the loss, the angular fluctuations are addressed at specific pitchwise locations. In the freestream (see Fig. 5.45(a)), the fluctuations are the largest compared to the remaining measured flowfield. The amplitude is insensitive to the Mach and Reynolds numbers. As previously reported, a significant phase shift occurs when the Mach number is increased. The increase of the Reynolds number for a fixed Mach number results in a premature arrival of

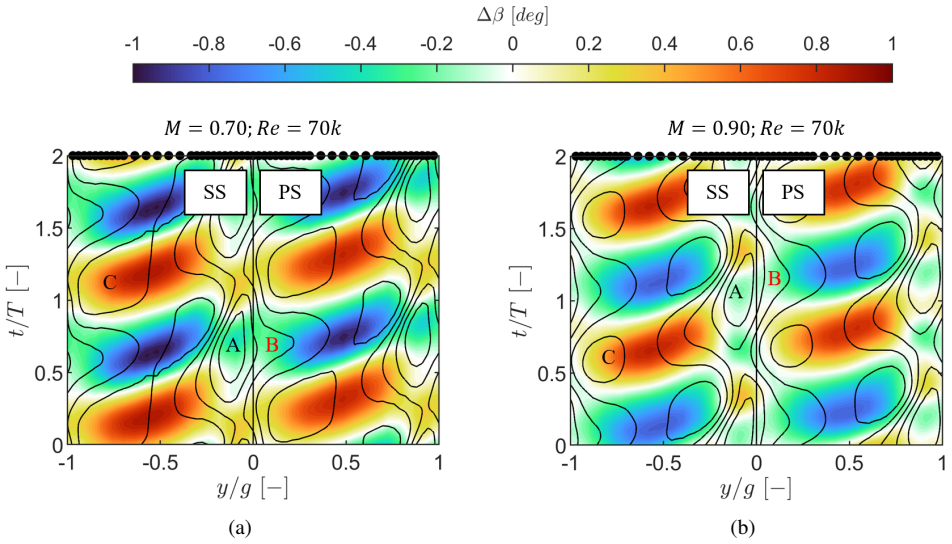

Figure 5.44: Space-time diagram of angular fluctuations at Re=70k: M=0.70 (a) and M=0.90 (b).

the wake by t/T≈0.03.

The amplitude and phase dependence near the blade suction side, in Fig. 5.45(b), and the pressure side, in Fig. 5.45(c), are similar. The amplitude fluctuations are the highest for M=0.70. Near the blade, the effect of the Reynolds number in shifting the phase is analogous to what happens in the freestream. Interestingly, the amplitude of the angular fluctuations at M=0.95 is higher and shifted with respect to M=0.90. The shift is more pronounced than the previously investigated loss coefficient (see Fig. 5.42). The effect is noticeable for the near suction side and pressure side signals.

The fluctuations of primary flow direction induced by the blade trailing edge are one order of magnitude lower than the ones measured downstream of the wake generator bar (see Fig. 5.3.1).

As a result of having higher amplitude fluctuations at freestream, the mass-averaged outlet flow angle deviation displays low variation. Fig. 5.46 displays the phase-averaged deviation from the primary flow direction mass-averaged over one blade pitch. The phase shift with the Mach number number is dominant. The mass-averaged fluctuations are contained within $\pm 0.60°$. Variations in the magnitude of the fluctuations occur for a varying Reynolds number and fixed Mach number. However, the fluctuations are within $0.05°$ and are therefore negligible.

Lastly, considerations are performed on the fluctuating nature of the turbulence intensity at the cascade outlet under the effect of unsteady wakes. Similar to the loss and angular fluctuations, the space-time diagrams of turbulence intensity are identical for all flow conditions. The space-time diagrams of turbulence intensity for two cases are displayed in Fig. 5.47. For the lowest Mach number (see Fig. 5.47(a)), the contour is superimposed with the isolines of the loss coefficient to highlight possible trends in the turbulence intensity with respect to the loss cores.

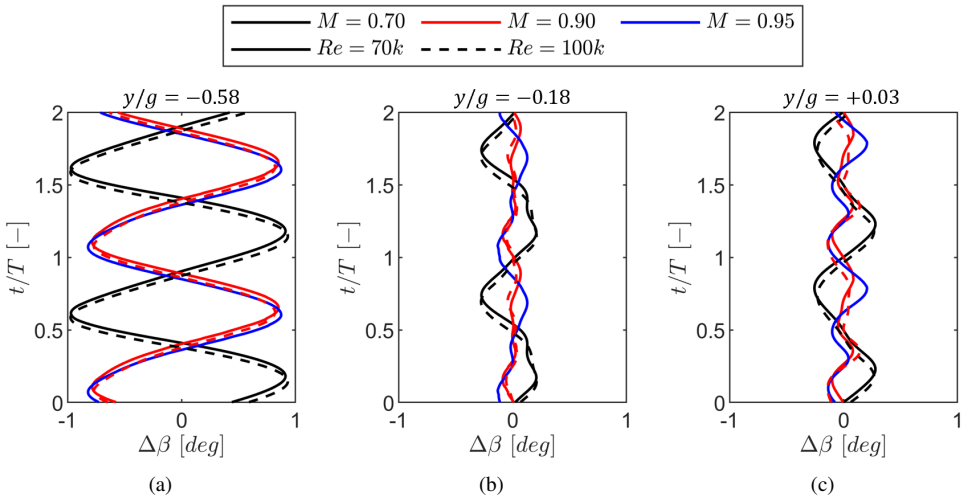

Figure 5.45: Phase-averaged angular fluctuations at on- and off-design flow conditions: y/g=-0.58 (a), y/g=-0.18 (a) and y/g=+0.03 (c).

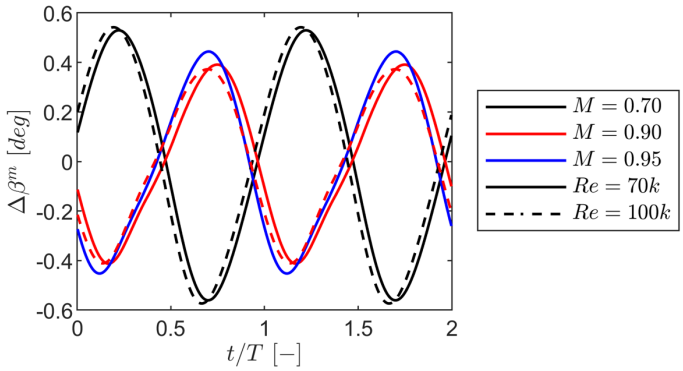

Figure 5.46: Phase-resolved deviation from primary flow direction mass-averaged over one blade pitch.

On both the suction side and pressure side, two peaks of turbulence intensity are out of phase. The peaks are better evidenced in the contour for the highest Mach number where no isolines are superimposed (see Fig. 5.47(b)). The pressure side peak is delayed by t/T≈0.20 with respect to the one on the suction side. Common to both peaks is that the trailing edge delimiting region of the turbulence intensity peak coincides with the leading edge of the loss peak. The turbulent structures are likely the result of the interaction of the bar wake with the blade boundary layer and/or the trailing edge shed vorticity and propagate slower than the wake itself. At M=0.70, the suction side-related peak is higher in magnitude than the pressure side. The latter statement strengthens the possibility that the peak in turbulence results from the wake-boundary layer interaction-generated turbulence that propagates at half the freestream velocity on the blade surface.

Even though not exploited to the same extent, Volino [32] displays results that support the current ones while testing a very high lift low-pressure turbine cascade tested at low speed.

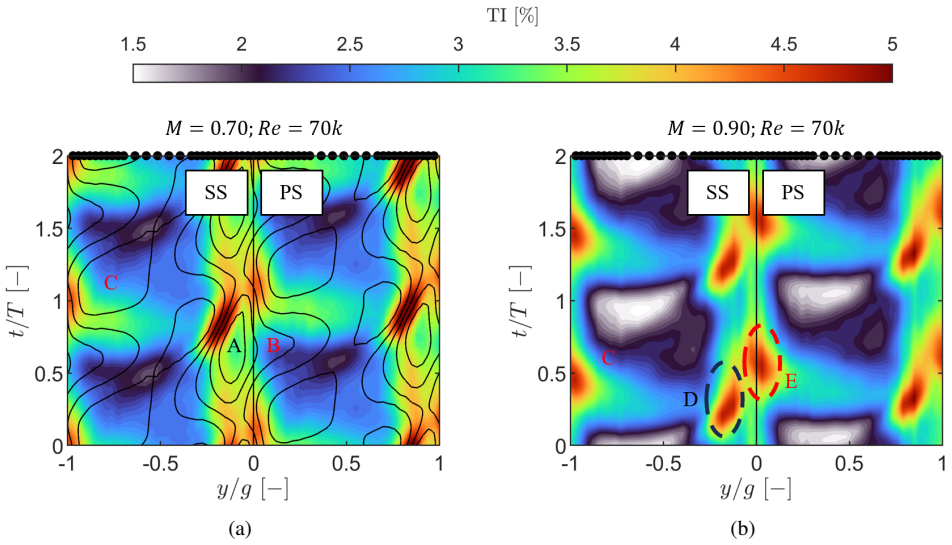

Figure 5.47: Space-time diagram of turbulence intensity at Re=70k: M=0.70 (a) and M=0.90 (b).

The effect of the two turbulence intensity lobes can be better appreciated in the time-averaged frame. The time-averaged pitchwise distributions of turbulence intensity measured at Plane 06 are displayed in Fig. 5.49. A horizontal line highlights the wake topology in relation to the blade trailing edge. The pressure side portion of the wake sits at positive pitchwise values. The opposite is true for the suction side. The profiles have a shared topology. Two peaks on each side of the trailing edge result from the vortex shedding similarity between round trailing edges and cylindrical bars [31]. In addition, wake-boundary layer interactions occurring on the suction side and responsible for Kelvin-Helmholtz (KH) roll-ups contribute to this peak. A similar topology was observed by Volino [42].

Fig. 5.48(a) highlights the turbulence intensity wake for increasing Reynolds number and fixed M=0.70. Both cases are characterized by a similar topology, especially near the trailing edge. The turbulence intensity in the freestream region increases with Reynolds number. The

suction side peak is related to the early reattachment for this Mach number.

As the Mach number increases to 0.90 (see Fig. 5.48(b)), the independence of the freestream to the Reynolds number becomes more pronounced. The profiles practically overlap in the trailing edge region.

The dependence of the topology to the Mach number for a fixed Reynolds number is more pronounced. Fig. 5.48(c) displays the turbulence intensity profiles obtained at Re=70k with increasing Mach number. The first noticeable feature is the considerable decrease in freestream turbulence with increasing Mach number. Nonetheless, the pressure side-related peak of turbulence remains practically unaltered. The latter suggests that the wake-pressure side boundary layer interaction is independent of what is occurring on the suction side.

The Mach number significantly impacts the wake-boundary layer interaction on the suction side adverse pressure gradient. At low Mach number, the separation/reattachment occurs prematurely with respect to the increased Mach number cases. This allows a longer distance for mixing the wake-induced Kelvin-Helmholtz roll-ups with the more turbulent boundary layer-—the increased mixing results in a more prominent peak. As the Mach number is increased, the separation/reattachment occurs later, and the suction side peak turbulence intensity is significantly reduced.

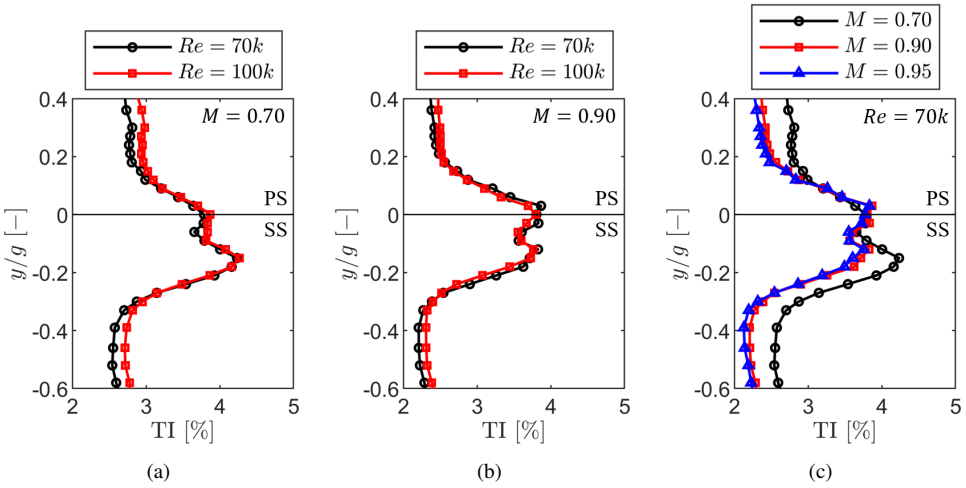

Figure 5.48: Pitchwise profiles of turbulence intensity measured experimentally downstream of the cascade at fixed: M=0.70 (a), M=0.90 (b), and Re=70k (c).

The phase-resolved traces are extracted in the freestream region, in Fig. 5.49(a), in the region of higher suction side loss, in Fig. 5.49(b), and in the region of higher pressure side loss, in Fig. 5.49(c). The solid lines denote the Mach number, while the line type denotes the Reynolds number.

In the freestream region (see Fig. 5.49(a)), the signal shape is nearly insensitive to the flow condition. The Reynolds number does not play a significant dependence on the fluctuations. The phase of the signal is highly dependent on the outlet Mach number. The signals at M=0.70 arrive at the same location roughly half a bar period later. The magnitude of the fluctuations is similar for all cases.

The mean level and amplitude fluctuations change significantly in the highest energy loss region on the suction side (see Fig. 5.49(b)). Even though the mean level for the higher Mach number cases is lower, the amplitude fluctuations increase. The Reynolds number has little impact on the signals. At lower Mach numbers, a periodic increase in turbulence intensity by $\sim$1.5% is registered. At M=0.9, the turbulence intensity peak increase is higher ($\sim$2%). At the lowest Mach number, the turbulence intensity reaches a "plateau" following the turbulence intensity peak. The turbulence intensity remains high up to the periodic repetition of the turbulence intensity peak at t/T$\approx$ 1.80. At M=0.90; the turbulence intensity decreases following the peak. There is a "bump" at t/T$\approx$0.70. The bump also occurs in the case with the lowest Mach number. As reported in Section 5.3.2, a conventional transitional mechanism occurs up to M=0.90. For the highest Mach number, at which no Kelvin-Helmholtz roll-ups were detected, the turbulence intensity decreases continuously until the next turbulence intensity peak. The turbulence intensity time traces are believed to be impacted by the status of the suction side boundary layer.

Lastly, the amplitude of the turbulence intensity fluctuations in the vicinity of the pressure side highest loss decreases with respect to the ones on the suction side as displayed in Fig. 5.49(c). The Reynolds number plays a minor effect on the mean level even though the amplitude of the fluctuations is the same. The signals are shifted by half a bar passing period as the Mach number increases from 0.70 to the highest. Even though the mean level is lower with the Mach number, the amplitude of the fluctuations is similar. Besides a slight phase change for the highest Mach number, no significant differences are observed with respect to the M=0.90 case.

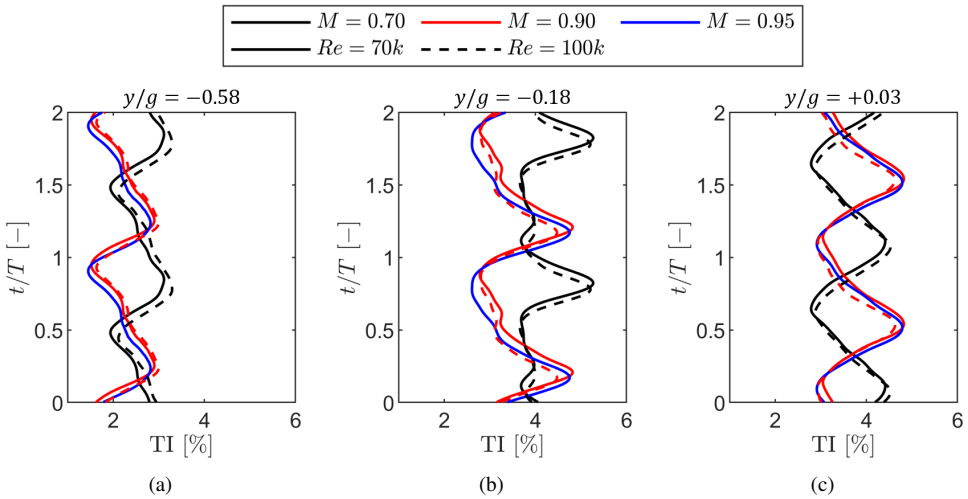

Figure 5.49: Phase-averaged turbulence intensity fluctuations at on- and off-design flow conditions: $y/g = -0.58$ (a), $y/g = -0.18$ (a) and $y/g = +0.03$ (c).

5.4 Spectral Analysis

The fast-response instrumentation bandwidth was used to identify possible deterministic frequencies related to the bar passing, instabilities, and passage shock. The frequency content in the rig was first characterized. The frequency study was done using power spectral density (PSD). For all cases, a 50% overlap was used. A window of 75,000 samples was used, resulting in a frequency resolution of ∼10 Hz.

5.4.1 Rig Characteristic Frequencies

Cross-wire measurements at Plane 02 were used to identify rig-related frequencies. The power spectral density (PSD) of the measured voltage of the thinnest wire was used for the effect. Fig. 5.50 displays the PSD of the voltage signal obtained at y/g=0.00 at M=0.70; Re=70k with and without turbulence grid.

Without the turbulence grid, the turbulence nearly follows the -5/3 decay slope characteristic of the inertial sub-range. A frequency "F1" is identified at ∼180 Hz. In addition, a characteristic peak at ∼9,300 Hz. The peak is, therefore, linked to the turbulence grid.

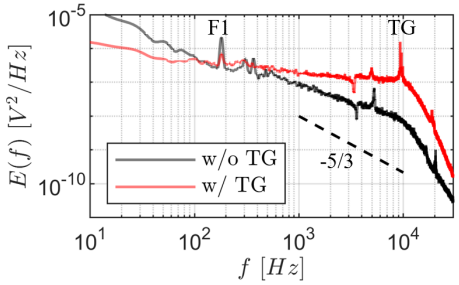

Figure 5.50: Power spectral density of cross-wire voltage with and without grid at M=0.70; Re-70k.

The impact of the Mach and the Reynolds numbers is highlighted in Fig. 5.51. Fig. 5.51(a) displays the PSD for increasing Mach number at Re=120k. Since the measurements are performed at Plane 02, this peak is not expected to be related to any cascade flow physics. The turbulence grid peak shifts downstream with increasing Mach number. This feature is better highlighted in the zoomed region in Fig. 5.51(c). The lowest to highest peak frequency ratio is ∼0.92. The value is consistent with the ratio of inlet velocities for both cases. Therefore, the "turbulence grid" peak results from the shedding frequency since the bar Strouhal number and characteristic dimension remain constant between cases.

Fig. 5.51(b) displays the PSD for increasing Reynolds number at M=0.90. The "turbulence grid" peak frequency remains unaltered since the inlet velocity is nearly insensitive to the Reynolds number. Frequency content related to the cross-wire can be seen in the 3000–6000 Hz range. The features are better highlighted in Fig. 5.51(d). These frequencies have been previously observed in similar measurements in the VKI S-1/C [4]. They are related to the probe since they do not occur for the remaining instrumentation.

The PSD content at different pitchwise locations upstream and downstream of the cascade was investigated employing the FRV4HP. The locations at Plane 02 and Plane 06 are highlighted in Fig. 5.52.

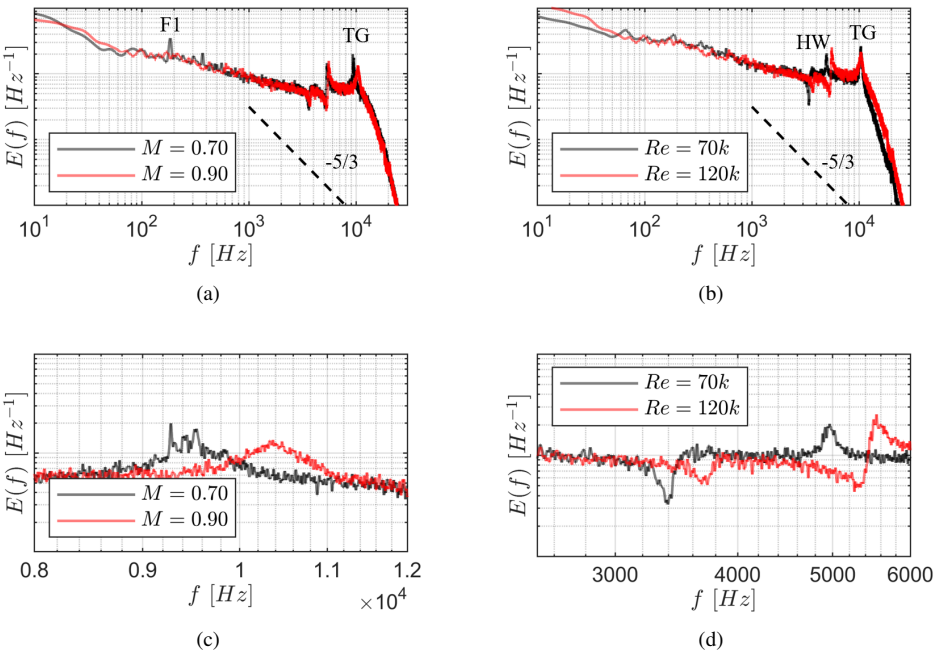

Figure 5.51: Power spectral density of cross-wire voltage with turbulence grid: sensitivity to Mach number (a) and zoomed detail (c), sensitivity to Reynolds number (b), and zoomed detail (d).

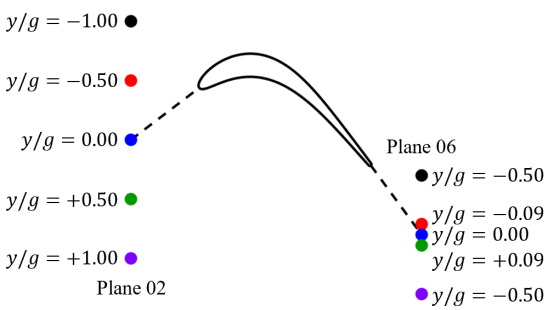

Figure 5.52: Location of inlet and outlet fast-response probe measurement locations.

Fig. 5.53(a) displays the PSD at Plane 02 without the wake generator at M=0.90; Re=70k. The square of the freestream inlet total pressure normalizes the PSD of the local pressure fluctuations. The spectra are insensitive to the pitchwise location. The turbulence-related frequency is still observable. The shedding frequency at M=0.90 is ∼10,200 Hz. Due to the larger bandwidth of the FRV4HP in comparison to the XW, the first harmonic of the turbulence grid ("TG2") can also be detected at ∼20,370 Hz.

Introducing wakes in the flow domain significantly increases the spectra energy in the low-frequency range. High-frequency content can be observed up to the bar passing frequency (BPF) at ∼5280 Hz. The first ("H1") and second ("H2") harmonic of the bar passing frequency are also visible. The spectra remain insensitive to the pitchwise location. The turbulence grid shedding frequency and the first harmonic are "masked" by the wake generator characteristic frequencies.

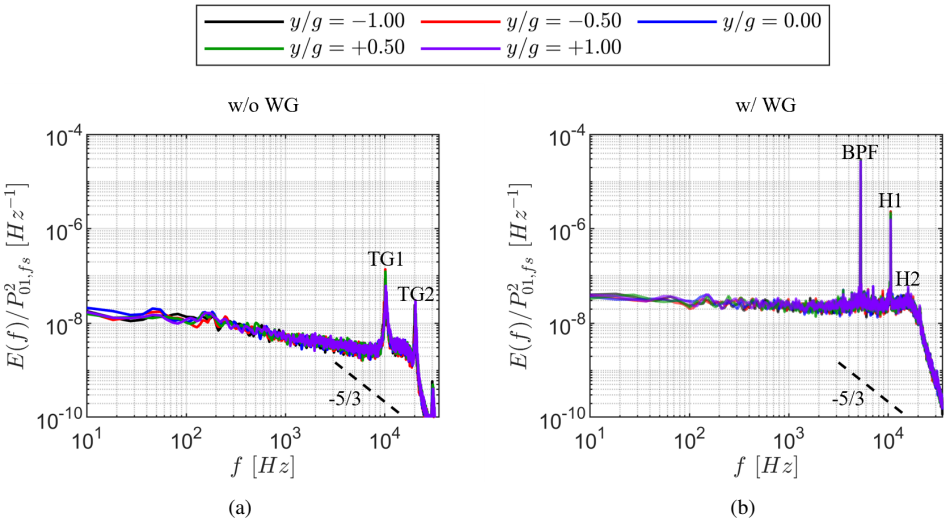

Figure 5.53: Sensitivity of power spectral density at Plane 02: without wake generator (a) and with wake generator (b).

Fig. 5.54 displays the PSD obtained at Plane 06 during measurements performed at M=0.90; Re=70k. The spectra are shown in the freestream of adjacent passages and the wake region of the central blade. In the absence of unsteady wakes (see Fig. 5.54(a)), the freestream-related spectra display the highest energy content. In the blade wake, the total pressure deficit causes an overall reduction of the frequency content. Regardless of the pitchwise location, the turbulence grid-related frequency is observable at Plane 06. In the freestream region, the first harmonic is also present.

The case with unsteady wakes is displayed in Fig. 5.54(b)—-the spectral energy increases from low frequencies up to the bar passing frequency. The bar passing frequency, first, and second harmonic are visible despite the pitchwise location.

In sum, the rig's main prevalent frequencies are turbulence grid and wake generator related when unsteady wakes are present. The turbulence grid shedding frequency is similar to the first harmonic of the bar passing frequency. Both frequencies can be seen in Plane

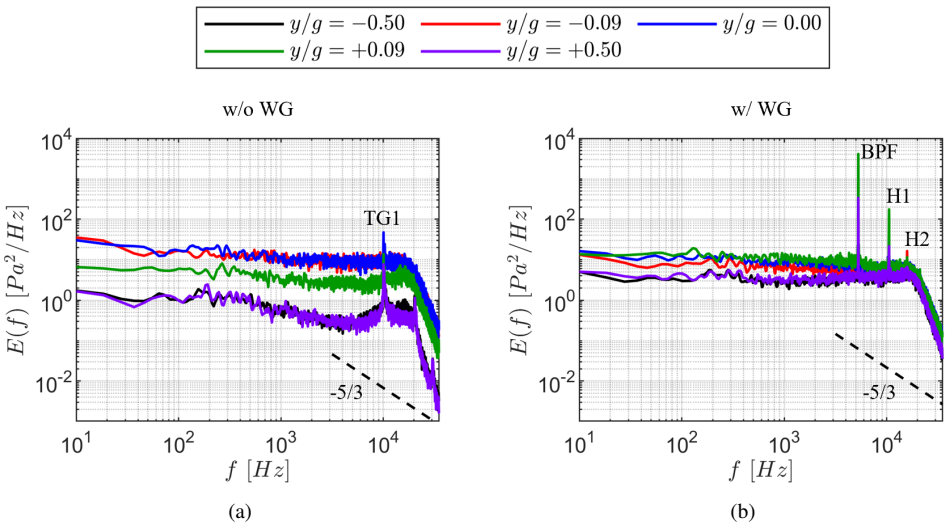

Figure 5.54: Sensitivity of power spectral density at Plane 06: without wake generator (a) and with wake generator (b).

06, including in the blade wake region. An additional peak was found for the M=0.70 cases. Table 5.10 summarizes the main rig-related frequencies.

Table 5.10: Rig characteristic frequencies in Hz.

		$M = 0.70$	$M = 0.90$
turbulence grid	Shedding	9,330	10,390
	First harmonic	18,660	20,785
wake generator	BPF	5,280	
	First harmonic	10,563	
	Second harmonic	15,844	

5.4.2 Blade Surface Frequencies

The blade fast-response pressure sensor spectra were used to survey the frequency content on the blade suction side. The main frequencies associated with possible instabilities on the blade surface concern Tollmien-Schlichting (Tollmien-Schlichting) instabilities, Kelvin-Helmholtz instabilities, and shock instabilities.

According to Walker [43], the dominant frequency associated with the growth of Tollmien-Schlichting waves can be computed as:

$$f_{TS} = \frac{3.2U^2_{fs,sep}}{2\pi\nu Re^3_{\delta^*}/2} \tag{5.14}$$

The Reynolds number based on the local displacement thickness at the separation location was obtained from the MISES computations. The characteristic frequencies of possible

Tollmien-Schlichting instabilities are contained in Table 5.11.

Table 5.11: Dominant frequency in Hz associated with the growth of Tollmien-Schlichting waves on blade suction side.

		M			
		0.70	0.80	0.90	0.95
Re	$65k$	10,138	12,478	10,711	–
	$70k$	10,403	12,654	10,955	11,632
	$100k$	10,733	13,552	12,356	12,082
	$120k$	11,316	14,040	12,610	12,244

The frequency associated with Kelvin-Helmholtz instabilities is usually defined using a Strouhal number. Based on the work of Pauley et al. [44]:

$$f_{KH} = \frac{St \cdot U_{fs,sep}}{\theta_{sep}} \tag{5.15}$$

Several experimental and numerical works have made use of this definition to find St $\in [0.005, 0.013]$ [16, 44–50]. A bulk of the works were performed in low-speed cascades or flat plates. To reduce the searching range for the present test case, the recent numerical work of Marty [45] on the T106 geometry at conditions relevant to this thesis was considered (St $\in [0.0065, 0.0072]$). The range of expected frequencies for possible Kelvin-Helmholtz instabilities, based on the range of Strouhal numbers reported by Marty, are reported in Table 5.12.

Table 5.12: Frequency range in Hz associated with Kelvin-Helmholtz instability related to suction side separation bubble.

		M			
		0.70	0.80	0.90	0.95
Re	$65k$	14,380–15,929	15,034–16,653	16,084–17,816	–
	$70k$	14,936–16,544	15,867–17,576	16,662–18,457	17,113–18,956
	$100k$	18,545–20,542	18,730–20,747	19,542–21,646	20,387–22,582
	$120k$	20,540–22,752	21,024–23,288	21,980–24,347	22,117–24,499

Lastly, flow cases at M=0.95 are characterized by a passage shock. The shock dynamics typically produce two dominant frequencies [51]. A low frequency is associated with the shock large-scale oscillation due to the modulation of the separation bubble near the shock foot. The second frequency is related to small scales occurring due to the interaction of turbulent fluctuations with the separated shear layer. Boerner and Niehuis [11] investigated the dynamics of shock waves in a transonic low-pressure turbine cascade configuration at engine-relevant Mach and Reynolds numbers. They found low-frequency oscillations in the 691–717 Hz range and high-frequency oscillations in the 1781–1889 Hz range. They used the definition of Sartor et al. [52] to derive a Strouhal number based on the separation bubble length: $St = f_{shock} \cdot L_{sep}/U_{fs,sep}$. In the scope of this work, there was no reliable method to

estimate the separation length experimentally. The length was obtained from the RANS simulations. The frequencies were calculated with the St provided in [11]. Table 5.13 contains the separation bubble length and associated frequencies.

Table 5.13: Estimated shock-related frequencies in Hz on blade suction side.

$Re\ [-]$	$L_{sep}\ [mm]$	$St_{low}\ [-]$	$f_{low}\ [Hz]$	$St_{high}\ [-]$	$f_{high}\ [Hz]$
70k	3.59	0.07	6,402	0.18	16,463
100k	7.19	0.07	3,193	0.18	8,209
120k	8.53	0.07	2,682	0.18	6,898

Fig. 5.55 displays the location of the fast-response pressure sensors on the blade.

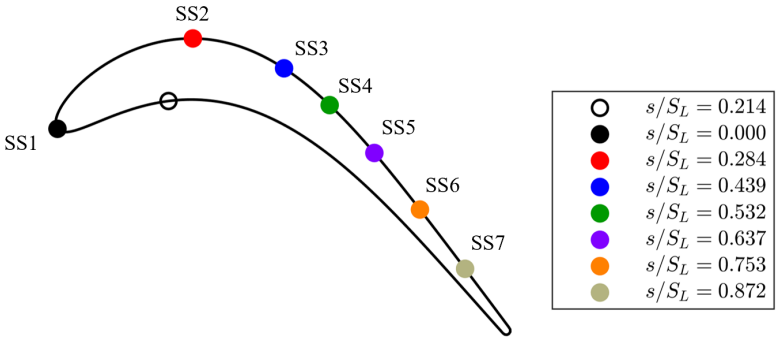

Figure 5.55: Location of blade fast-response pressure sensors on the blade surface.

The sensitivity of the PSD to Mach and Reynolds numbers was investigated at specific sensor locations: the pressure side, the suction side before the separation, and the last sensor on the suction side. Fig. 5.56(a) displays the spectra on the pressure side with increasing Reynolds number for M=0.90. The PSD enables the turbulence grid shedding frequency to be distinguished, as well as its first and second harmonics. The frequency is not sensitive to the Reynolds number. As the Reynolds number increases, the frequency content increases in 10,000–35,000 Hz. The more significant energy content is particularly evident after the first harmonic. From ongoing numerical works on the SPLEEN C1 profile, the shedding in the pressure side separation bubble depends on the Reynolds number. The higher energy content is likely related to Kelvin-Helmholtz roll-ups on the separated shear layer.

Fig. 5.56(b) displays the spectra at Re=100k with increasing Mach number. The frequency peaks related to the turbulence grid and harmonics increase with the Mach number. The pressure sensors experience this effect and are not associated with flow physics occurring on the blade surface. Overall, the energy content is similar for all cases for the displayed range. The peak at $\sim$180 Hz is also shown on the blade for the lowest Mach numbers. A second peak "F2" is present. The peak frequency is in line with the first harmonic of "F1". Low-frequency peaks in the range of "F1" and "F2" were observed with other instrumentation and the inlet and outlet, even in the absence of flow through the cascade. For this reason, the nature of these peaks is not clear.

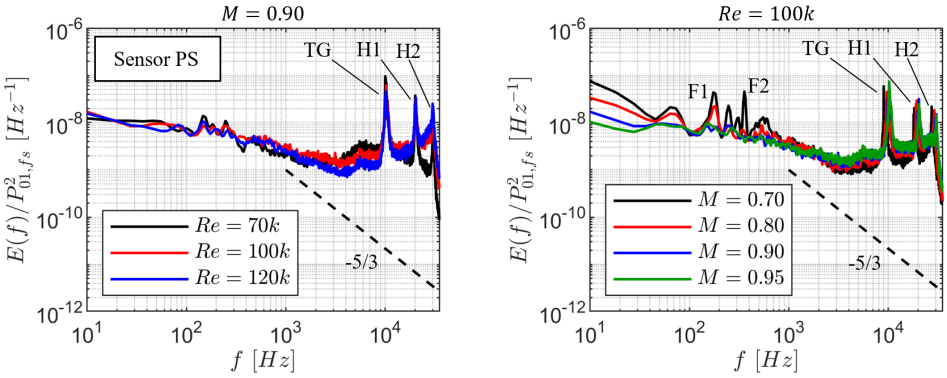

Figure 5.56: Power spectral density on blade pressure side sensor at s/S_L=0.214: sensitivity to Reynolds number (a) and sensitivity to Mach number (b).

Fig. 5.57 displays the spectra upstream of the separation location measured for all cases. Similar frequencies characterize the spectra. The turbulent grid-related frequencies and harmonics are still present. The low frequencies identified for the low Mach number case are also present. At this location, the PSD agrees with the sub-inertial turbulence decay. As displayed in Fig. 5.57(a), the spectra are reasonably insensitive to the Reynolds number up to ∼2,000 Hz. No Tollmien-Schlichting-related frequencies (11,000–12,600 Hz) can be distinguished from the turbulence grid-related ones. Towards the end of the investigated range, the spectra remain "flat".

Fig. 5.57(b) shows that the spectra are more sensitive to the Mach number variation. This is attributed to the modification of the boundary layer and the shift of the separation downstream. As a result, the thinner boundary layer with increasing Mach number displays less frequency content up to the turbulence grid shedding frequency. Nonetheless, the spectra display a sub-inertial turbulence decay in the 500–3,000 Hz range. The turbulence grid-related frequency peaks, and its harmonics increase with the Mach number. Peaks related to potential Tollmien-Schlichting waves cannot be distinguished from the turbulence grid-related peaks.

Fig.5.58(a) displays the spectra at s/S_L=0.872. The spectra agree up to 1,000 Hz. The energy spectra are higher for the highest Reynolds number in the range up to 35,000 Hz. The spectra display sub-inertial decay in the 200–1,000 Hz range. The turbulence grid peaks and harmonics are present. There is an energy content increase from the turbulence grid shedding frequency towards 35,000. The observation is consistent with frequencies expected for Kelvin-Helmholtz instabilities (18,500–22,500 Hz). Even though no distinct peaks can be isolated, the increase in this band of frequencies is attributed to Kelvin-Helmholtz instabilities, which have more energy when increasing Reynolds number.

The sensitivity of the spectra to the Mach number is displayed in Fig.5.58(b) at Re=100k. The location of the sensor is coincident with the flow reattachment location for the Re=100k case at M=0.70 (see Section 5.2.2.1). The energy content in the investigated range increases with Mach number. The turbulence grid-related peaks are present in all cases. A significant

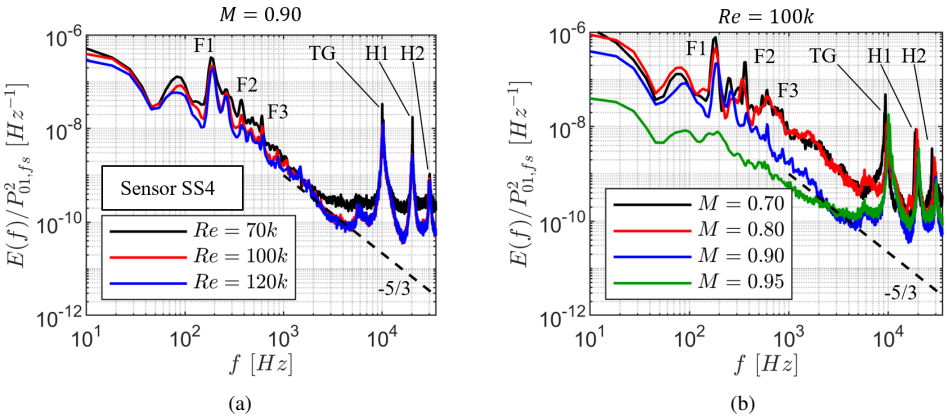

Figure 5.57: Power spectral density on blade suction side sensor at s/S_L=0.532: sensitivity to Reynolds number (a) and sensitivity to Mach number (b).

increase in the spectra energy occurs after 20,000 Hz. The frequency increases up to 35,000 Hz. Like the cases at fixed Mach number, the increase is associated with Kelvin-Helmholtz instabilities.

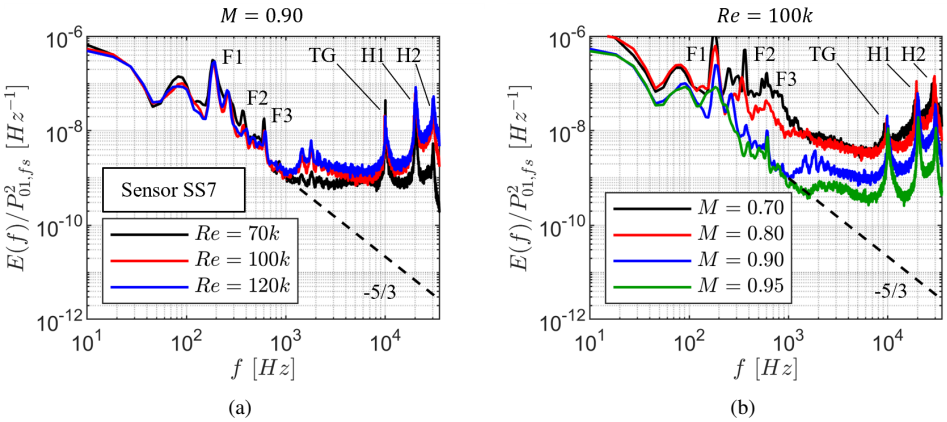

Figure 5.58: Power spectral density on blade suction side sensor at s/S_L=0.872: sensitivity to Reynolds number (a) and sensitivity to Mach number number (b).

The detection of possible shock motions was also attempted. Fig. 5.59(a) displays the PSD with increasing Mach number at s/S_L=0.637 and fixed Reynolds. The only distinct frequency for the most significant Mach number is highlighted as "S1" at 3,810 Hz. According to the estimations based on the separation length obtained from CFD, this value can be associated with the bubble's low-frequency motion. For the same Strouhal number reported in [11], this frequency would require a separation length 16% smaller. Assuming the separation length is well predicted, the frequency is associated with a Strouhal number of 0.08. The peak is absent in the spectra obtained at s/S_L=0.753, which sits near the shock foot. In ad-

dition, the peak was not observed for the Re=120k case. The measurements did not observe a frequency peak associated with the turbulent mixing (∼8,209 Hz) in the shear layer. The frequency is likely combined with the turbulence grid-related energy content.

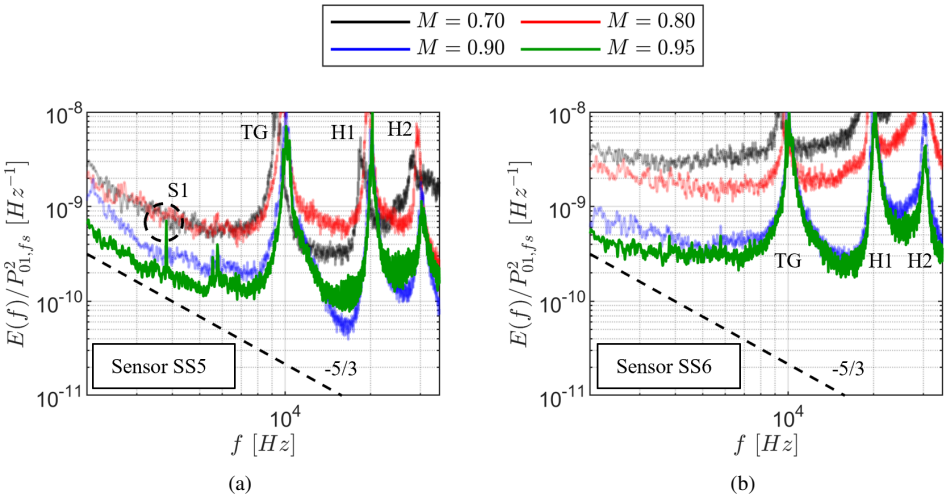

Figure 5.59: Power spectral density on blade suction side sensor at Re=100k: s/S_L=0.637 (a) and s/S_L=0.753 (b).

A separate investigation of the surface-mounted hot-films was performed to search for shock-related frequencies. Fig 5.60 displays the PSD of the surface-mounted hot-film voltage along the suction side near the shock impingement location. The PSD was multiplied by the local frequency to highlight features at higher frequencies. The contour displays higher resolution in the shock region. However, no shock-related features could be identified.

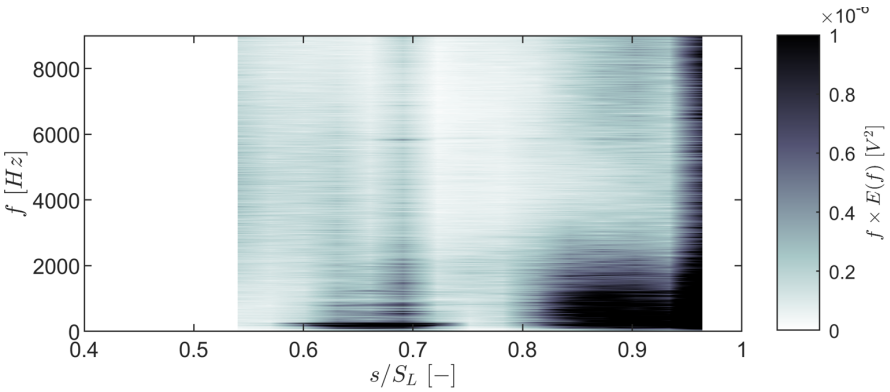

Figure 5.60: Power spectral density of hot-film voltage at M=0.95; Re=70k.

The introduction of unsteady wakes in the flow domain gives rise to the bar-related frequencies. The sensitivity of the spectra energy to the Mach and Reynolds numbers is similar to the cases without wakes. The coupling of the turbulence grid and wake generator frequencies are highlighted in Fig. 5.61 for the pressure side fast-response pressure sensor. The bar

passing frequency at 5,280 Hz is the dominant frequency in the spectrum. Deterministic sharp peaks can still be perceived for the first ("H1") and second harmonics ("H2"). The turbulence grid-related frequency band sits near the bar passing frequency while the first harmonic (red "H1") coincides with the third harmonic of the bar passing frequency. The peaks' location is insensitive to the Reynolds number (see Fig. 5.61(a)). A region of high frequency content ("F2") arises in the range of 1,500–9,00 Hz. This region was also observed for the suction side sensors up to the separation location. It is likely attributed to wake-induced content rather than local flow physics.

The sensitivity to the Mach number is displayed in Fig. 5.61(b). The turbulence grid-related peaks shift with Mach number as observed for the steady inlet flow cases. The wake generator-related peaks are insensitive to the Mach number. The wake generator and turbulence grid, alongside their harmonic, are still largely coincident.

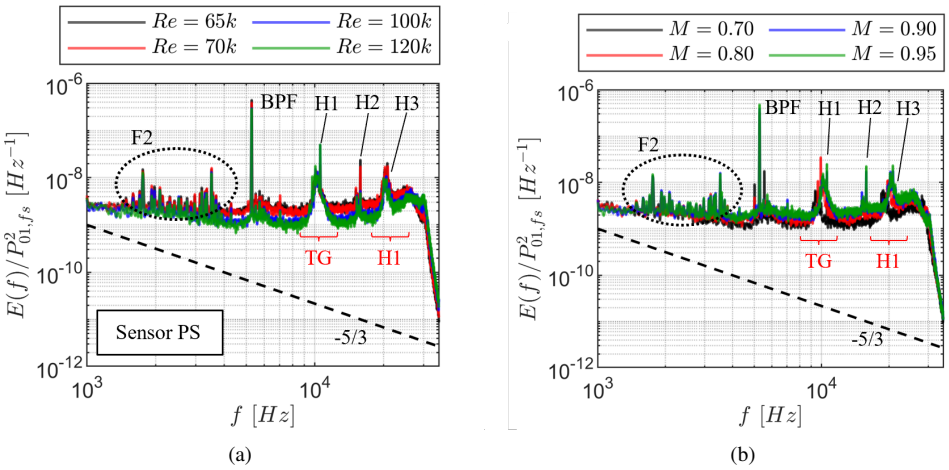

Figure 5.61: Power spectral density on blade pressure side sensor at s/S_L=0.214: sensitivity to Reynolds number number at M=0.90 (a) and sensitivity to Mach number at Re=70k (b).

The turbulence grid and wake generator-related frequencies can also be found on the suction side regardless of the flow condition. The spectra with and without wakes for the M=0.70; Re=120k in the acceleration portion of the loading (sensor at s/S_L=0.284 is displayed in Fig. 5.62(a). The frequency band "F2" is visible. The latter can be perceived up to sensor 6 (not displayed). The spectra with unsteady wakes have higher energy from 2,000 Hz to the end of the investigated range. Both spectra display good agreement with the sub-inertial turbulence decay rate. The wake generator and turbulence grid, alongside their harmonics, are found to be coincident. Similar conclusions can be drawn for a case with increased Mach and lower Reynolds numbers (see Fig. 5.62(a)).

At the location of the last sensor, the flow is reattached for the most significant Reynolds number case (see Fig. 5.62(c)). The frequency band "F2" is no longer present. The bar passing frequency and first harmonic dominate the region, with frequencies lower than the turbulence grid shedding. As speculated previously, the increase in the frequency content around 18,500–22,500 Hz is attributed to Kelvin-Helmholtz instabilities. The spectra with unsteady wakes do not display this feature. After the second harmonic of the bar passing

frequency, the spectra decay. The case with a higher Mach number (see Fig.5.62(d)) for which the Kelvin-Helmholtz related frequencies are not distinguished, the spectra with unsteady wakes contains higher frequency content.

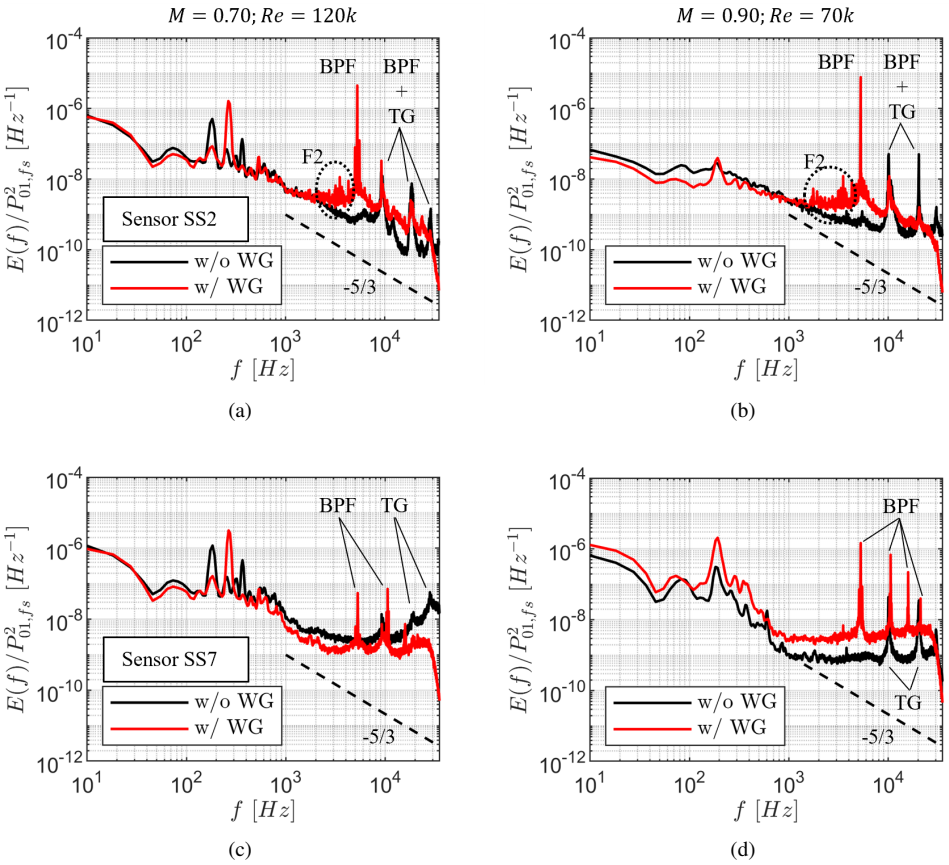

Figure 5.62: Sensitivity of power spectral density to unsteady wakes at M=0.70; Re=120k for suction side sensor 2 (a) and 7 (c), and at M=0.70; Re=120k for suction side sensor 2 (b) and 7 (d).

5.5 Conclusions

Characterizing the inlet incidence revealed that the impact of unsteady wakes reduced the incidence by $\sim$1.00°. The variation reduced the blade suction side loading near the leading edge for the unsteady inlet flow cases.

Both CFD and MISES have shown overall good agreement with the experimental data. The CFD fails to predict the blade loading at a low Reynolds number, particularly for cases with open separation or reattachment near the trailing edge. The Mach number was found to modify the blade loading. The laminar separation bubble features shifted towards the trailing edge with Mach number, promoting open separation bubbles for cases with low Reynolds and Mach numbers over 0.80. Increasing the Reynolds number promoted the shortening

of the laminar separation bubble and even the flow reattachment for M=0.80. The laminar separation location is in good agreement against correlations in literature obtained with low-speed tests of flat plates and cascades up to a Mach number of 0.90. At M=0.95, a weak shock occurs in the throat region. The shock triggers the separation of the boundary layer, which is reattached immediately due to the low blade loading of the SPLEEN C1 blade. Therefore, classical literature and models can characterize the boundary layer transition unless shocks interact with the blade boundary layer. The unsteady wakes reduced the extent of the laminar separation bubble in the time-averaged frame of reference. However, the boundary layer for all the cases investigated is still believed to be transitional by the trailing edge.

The losses were found to be poorly captured by the CFD due to their sensitivity to the mesh. The experimental data highlight a monotonic reduction of the profile loss with the Mach number. At Re=70k, the loss decreased by 24% under steady inlet flow. The profile loss is also reduced with the Reynolds number. At M=0.80, increasing the Reynolds number enabled suppressing an open separation, decreasing the loss by 19%. The introduction of unsteady wakes increases the loss for all cases. (28% at design Mach and Reynolds numbers). Nonetheless, the loss decreased with Mach (27% at Re=70k) and Reynolds (15% at M=0.90) numbers.

The unsteady nature of the wake generator bar wake has been investigated. The pressure loss, angle, and turbulence intensity agree with cases found in the literature (both bar and blade wakes). The bar phase was found to be insensitive to the Reynolds number. The bar generated fluctuations of $\sim$7.5% of the inlet total pressure and $\pm 4^{\circ}$. The turbulence intensity increased by $\sim$200% in the wake region. Due to the high bar reduced frequency, the turbulence intensity and total pressure never reached a "plateau" between bar passing events.

The wake-boundary layer interaction was investigated utilizing surface-mounted hot-films and fast-response pressure sensors. The celerities of conventional wake-induced transition mechanisms could be sensed by the surface-mounted hot-film traces up to M=0.90. The instrumentation allowed highlighting the turbulent patch propagating at half the freestream velocity and the becalmed region that follows with a trailing edge celerity of about 30% of the freestream velocity. For the M=0.95 case, the wake trajectory was still in line with the surface-mounted hot-film measured quantities, but the wake-boundary layer interaction features presented different characteristics. The use of fast-response pressure sensors allowed inferring that for cases where shocks are not present, the transition is triggered by Kelvin-Helmholtz roll-ups that arise when the wake negative jet interacts with the separated shear layer. Fluctuations of the static pressure in the order of $\pm 1\%$ of the freestream total pressure for the lower Mach number cases for which the Kelvin-Helmholtz signature is stronger. The Kelvin-Helmholtz roll-up signature was not observed at the highest Mach number.

The phase-averaged flowfield measurements revealed that the angular fluctuations from the inlet are highly dampened. Pockets of negative loss were observed, attributed to the energy separation phenomenon. Following wake passing, turbulent structures were observed near the pressure and suction sides. The Reynolds number was found to have little impact on the phase of the outlet fluctuations.

The rig characteristic frequencies are dominant with respect to potential instabilities for the steady inlet flow case. The addition of wakes further aggravates the issue since the wake generator characteristics frequencies and harmonics largely coincide with frequencies of interest. The potential non-linear combination of the frequencies makes identifying potential

Tollmien-Schlichting waves, Kelvin-Helmholtz instabilities, and shock dynamics even more challenging. These flow mechanisms should be investigated as early as during the design phase to avoid having combined interactions.

References

[1] D. Simoni, M. Berrino, M. Ubaldi, P. Zunino, and F. Bertini. *Off-Design Performance of a Highly Loaded Low Pressure Turbine Cascade Under Steady and Unsteady Incoming Flow Conditions*. Journal of Turbomachinery, 137(7):071009, 07 2015.

[2] J. Clinckemaillie and T. Arts. *Characterization of Periodic Incoming Wakes in a Low-Pressure Turbine Cascade Test Section by Means of a Fast-Response Single Sensor Virtual Three-Hole Probe*. International Journal of Turbomachinery, Propulsion and Power, 4(3), 2019.

[3] P.E. Roach. *The generation of nearly isotropic turbulence by means of grids*. International Journal of Heat and Fluid Flow, 8(2):82–92, 1987.

[4] G. Pastorino, L. Simonassi, G. Lopes, E. Boufidi, F. Fontaneto, and S. Lavagnoli. *Measurements of Turbulence in Compressible Low-Density Flows at the Inlet of a Transonic Linear Cascade With and Without Unsteady Wakes*. Journal of Turbomachinery, pages 1–26, 12 2023.

[5] N. Rosafio, G. Lopes, S. Salvadori, S. Lavagnoli, and D.A. Misul. *RANS Prediction of Losses and Transition Onset in a High-Speed Low-Pressure Turbine Cascade*. Energies, 16(21), 2023.

[6] S. Brunner, L. Fottner, and H. Schiffer. *Comparison of Two Highly Loaded Low Pressure Turbine Cascades Under the Influence of Wake-Induced Transition*. volume Volume 3: Heat Transfer; Electric Power; Industrial and Cogeneration of *Turbo Expo: Power for Land, Sea, and Air*, page V003T01A073, 05 2000.

[7] R.E. Mayle. *The 1991 IGTI Scholar Lecture: The Role of Laminar-Turbulent Transition in Gas Turbine Engines*. Journal of Turbomachinery, 113(4):509–536, 10 1991.

[8] A. Hatman and T. Wang. *A Prediction Model for Separated-Flow Transition*. Journal of Turbomachinery, 121(3):594–602, 07 1999.

[9] J. Michalek, M. Monaldi, and T. Arts. *Aerodynamic Performance of a Very High Lift Low Pressure Turbine Airfoil (T106C) at Low Reynolds and High Mach Number With Effect of Free Stream Turbulence Intensity*. Journal of Turbomachinery, 134(6):061009, 08 2012.

[10] R. Houtermans, T. Coton, and T. Arts. *Aerodynamic Performance of a Very High Lift LP Turbine Blade With Emphasis on Separation Prediction*. volume Volume 6: Turbo Expo 2003, Parts A and B of *Turbo Expo: Power for Land, Sea, and Air*, pages 339–349, 06 2003.

[11] M. Boerner and R. Niehuis. *Dynamics of Shock Waves Interacting With Laminar Separated Transonic Turbine Flow Investigated by High-Speed Schlieren and Surface Hot-Film Sensors*. Journal of Turbomachinery, 143(5):051010, 04 2021.

[12] K. Sabnis and H. Babinsky. *A review of three-dimensional shock wave–boundary-layer interactions*. Progress in Aerospace Sciences, 143:100953, 2023. SI: Ramjet/Scramjet Aerodynamics: A Progress Review.

[13] R. A. HUMBLE, F. SCARANO, and B. W. van OUDHEUSDEN. *Unsteady aspects of an incident shock wave/turbulent boundary layer interaction*. Journal of Fluid Mechanics, 635:47–74, 2009.

[14] N.T. Clemens and V. Narayanaswamy. *Low-Frequency Unsteadiness of Shock Wave/Turbulent Boundary Layer Interactions*. Annual Review of Fluid Mechanics, 46(1):469–492, 2014.

[15] N. Bonne, V. Brion, E. Garnier, R. Bur, P. Molton, D. Sipp, and L. Jacquin. *Analysis of the two-dimensional dynamics of a Mach 1.6 shock wave/transitional boundary layer interaction using a RANS based resolvent approach*. Journal of Fluid Mechanics, 862:1166–1202, 2019.

[16] B.R. McAuliffe and M.I. Yaras. *Numerical Study of Instability Mechanisms Leading to Transition in Separation Bubbles*. Journal of Turbomachinery, 130(2):021006, 02 2008.

[17] J. Hourmouziadis, F. Buckl, and P. Bergmann. *The Development of the Profile Boundary Layer in a Turbine Environment*. Journal of Turbomachinery, 109(2):286–295, 04 1987.

[18] F. Kost, W. Braunling, E. Schupferling, and R. Gohl. *Detection of separation bubbles by heated thin-film sensors in transonic turbine cascades*. In Proceedings of the 9th Symposium of Measuring Techniques for Transonic and Supersonic Flow in Cascades and Turbomachines, Oxford, volume 21, page 22, 1988.

[19] R. Stieger, D. Hollis, and H. Hodson. *Unsteady Surface Pressures Due to Wake Induced Transition in a Laminar Separation Bubble on a LP Turbine Cascade*. volume Volume 6: Turbo Expo 2003, Parts A and B of *Turbo Expo: Power for Land, Sea, and Air*, pages 927–935, 06 2003.

[20] V. Schulte and H.P. Hodson. *Unsteady Wake-Induced Boundary Layer Transition in High Lift LP Turbines*. Journal of Turbomachinery, 120(1):28–35, 01 1998.

[21] X.F. Zhang, H.P. Hodson, and N.W. Harvey. *Unsteady boundary layer studies on ultra-high-lift low-pressure turbine blades*. Proceedings of the Institution of Mechanical Engineers, Part A: Journal of Power and Energy, 219(6):451–460, 2005.

[22] A. Mahallati and S.A. Sjolander. *Aerodynamics of a Low-Pressure Turbine Airfoil at Low Reynolds Numbers—Part II: Blade-Wake Interaction*. Journal of Turbomachinery, 135(1):011011, 11 2012.

[23] N.W. Harvey, J.C. Cox, V. Schulte, R. Howell, and H.P. Hodson. *The role of research in the aerodynamic design of an advanced low-pressure turbine*. Proceedings of the Institution of Mechanical Engineers, Part A: Journal of Power and Energy, 213(4):235–242, 1999.

[24] M. Vera, H.P. Hodson, and R. Vazquez. *The Effect of Mach Number on LP Turbine Wake-Blade Interaction*. In K.C. Hall, Robert E. Kielb, and Jeffrey P. Thomas, editors, Unsteady Aerodynamics, Aeroacoustics and Aeroeslaticity of Turbomachines, pages 203–216, Dordrecht, 2006. Springer Netherlands.

[25] R. Vazquez, A. Antoranz, D. Cadrecha, and L. Armananzas. *The Influence of Reynolds Number, Mach Number and Incidence Effects on Loss Production in Low Pressure Turbine Airfoils*. volume Volume 6: Turbomachinery, Parts A and B of *Turbo Expo: Power for Land, Sea, and Air*, pages 949–960, 05 2006.

[26] J.D. Coull and H.P. Hodson. *Predicting the Profile Loss of High-Lift Low Pressure Turbines*. Journal of Turbomachinery, 134(2):021002, 06 2011.

[27] R.D. Stieger and H.P. Hodson. *The Unsteady Development of a Turbulent Wake Through a Downstream Low-Pressure Turbine Blade Passage*. Journal of Turbomachinery, 127(2):388–394, 05 2005.

[28] E. Canepa, D. Lengani, A. Nilberto, D. Petronio, D. Simoni, M. Ubaldi, and P. Zunino. *Flow Coefficient and Reduced Frequency Effects on Wake-Boundary Layer Interaction in Highly Accelerated LPT Cascade*. International Journal of Turbomachinery, Propulsion and Power, 6(3), 2021.

[29] L.S.G. Kovasznay. *Hot-wire investigation of the wake behind cylinders at low Reynolds numbers*. Proceedings of the Royal Society of London. Series A. Mathematical and Physical Sciences, 198(1053):174–190, 1949.

[30] L. Ong and J. Wallace. *The velocity field of the turbulent very near wake of a circular cylinder*. Experiments in fluids, 20(6):441–453, 1996.

[31] H. Pfeil and J. Eifler. *Measurements in the turbulent wake of the individual cylinder*. Research in Engineering A, 41:137–145, 1975.

[32] R.J. Volino. *Effect of Unsteady Wakes on Boundary Layer Separation on a Very High Lift Low Pressure Turbine Airfoil*. Journal of Turbomachinery, 134(1):011011, 05 2011.

[33] J.D. COULL and H.P. HODSON. *Unsteady boundary-layer transition in low-pressure turbines*. Journal of Fluid Mechanics, 681:370–410, 2011.

[34] H.P. Hodson. *Measurements of Wake-Generated Unsteadiness in the Rotor Passages of Axial Flow Turbines*. Journal of Engineering for Gas Turbines and Power, 107(2):467–475, 04 1985.

[35] M. Ladwig and L. Fottner. *Experimental Investigations of the Influence of Incoming Wakes on the Losses of a Linear Turbine Cascade*. volume Volume 3C: General of *Turbo Expo: Power for Land, Sea, and Air*, page V03CT17A055, 05 1993.

[36] R.J. Howell, O.N. Ramesh, H.P. Hodson, N.W. Harvey, and V. Schulte. *High Lift and Aft-Loaded Profiles for Low-Pressure Turbines* . Journal of Turbomachinery, 123(2):181–188, 02 2000.

[37] G.B. Schubauer and P.S. Klebanoff. *Contributions on the mechanics of boundary-layer transition*. Technical report, 1956.

[38] R.D. Stieger and H.P. Hodson. *The Transition Mechanism of Highly Loaded Low-Pressure Turbine Blades* . Journal of Turbomachinery, 126(4):536–543, 12 2004.

[39] H.P. Hodson and R.J. Howell. *Bladerow Interactions, Transition, and High-Lift Aerofoils in Low-Pressure Turbines*. Annual Review of Fluid Mechanics, 37(1):71–98, 2005.

[40] H.P. Hodson and W.N. Dawes. *On the Interpretation of Measured Profile Losses in Unsteady Wake–Turbine Blade Interaction Studies*. Journal of Turbomachinery, 120(2):276–284, 04 1998.

[41] G. Lopes, L. Simonassi, A.F.M. Torre, M. Patinios, and S. Lavagnoli. *An Experimental Test Case for Transonic Low-Pressure Turbines - Part 2: Cascade Aerodynamics at On- and Off-Design Reynolds and Mach Numbers*. volume Volume 10B: Turbomachinery — Axial Flow Turbine Aerodynamics; Deposition, Erosion, Fouling, and Icing; Radial Turbomachinery Aerodynamics of *Turbo Expo: Power for Land, Sea, and Air*, page V10BT30A027, 06 2022.

[42] R.J. Volino. *Separated Flow Measurements on a Highly Loaded Low-Pressure Turbine Airfoil*. Journal of Turbomachinery, 132(1):011007, 09 2009.

[43] G.J. Walker. *Transitional flow on axial turbomachine blading*. AIAA journal, 27(5):595–602, 1989.

[44] L.L. Pauley, P. Moin, and W.C. Reynolds. *The structure of two-dimensional separation*. Journal of Fluid Mechanics, 220:397–411, 1990.

[45] J. Marty. *Numerical investigations of separation-induced transition on high-lift low-pressure turbine using RANS and LES methods*. Proceedings of the Institution of Mechanical Engineers, Part A: Journal of Power and Energy, 228(8):924–952, 2014.

[46] M. Talan and J. Hourmouziadis. *Characteristic regimes of transitional separation bubbles in unsteady flow*. Flow, turbulence and combustion, 69(3):207–227, 2002.

[47] B.R. McAuliffe and M.I. Yaras. *Transition Mechanisms in Separation Bubbles Under Low- and Elevated-Freestream Turbulence*. Journal of Turbomachinery, 132(1):011004, 09 2009.

[48] J.C.M. Lin and L.L. Pauley. *Low-Reynolds-number separation on an airfoil*. AIAA Journal, 34(8):1570–1577, 1996.

[49] M.D. Ripley and L.L. Pauley. *The unsteady structure of two-dimensional steady laminar separation*. Physics of Fluids A, 5(12):3099–3106, 1992.

[50] B.R. McAuliffe and M.I. Yaras. *Separation-Bubble-Transition Measurements on a Low-Re Airfoil Using Particle Image Velocimetry*. volume Volume 3: Turbo Expo 2005, Parts A and B of *Turbo Expo: Power for Land, Sea, and Air*, pages 1029–1038, 06 2005.

[51] M.E. Erengil. *Physical causes of separation shock unsteadiness in shock wave/turbulent boundary layer interactions*. PhD thesis, University of Texas, Austin, January 1993.

[52] F. Sartor, M. Clement, D. Sipp, and R. Bur. *Dynamics of a shock-induced separation in a transonic flow: a linearized approach*. In 43rd AIAA Fluid Dynamics Conference, page 2735, 2013.

6
Secondary Flows

This chapter addresses the secondary flows in the linear cascade tests. The on- and off-design aerodynamics with steady inlet flow are addressed. Both the inlet boundary layer and outlet flowfield are exploited. The impact of introducing the wake generator on the inlet boundary layer and secondary flow signature is depicted. Lastly, the effect of replacing the flat endwall with a cavity slot and injecting purge flow is addressed on the secondary flow losses. For cases with unsteady inlet flow, the inlet and outlet flowfields are characterized by their unsteadiness: loss, angles, and turbulence intensity.

6.1 Flow Conditions

The secondary flows have been investigated in three phases. Firstly, the cascade aerodynamics are investigated under steady inlet flow at on- and off-design conditions. The flow conditions are highlighted in Table 6.1. The on-design point is underlined.

Table 6.1: Flow conditions exploited with steady inlet flow.

M	Re
0.70	$70k$
0.80	$70k$
0.90	***70k***
0.95	$70k$
0.80	$120k$
0.90	$120k$

The impact of introducing the wake generator on the inlet boundary layer development and outlet flowfield was addressed solely at the design point. A wake-reduced frequency of

0.95 was used for the case with a wake generator.

Lastly, the impact of modifying the endwall from a flat surface to a cavity-representative one was addressed. In addition, the effect of increasing the purge massflow ratio was addressed at design Mach and Reynolds numbers. The flow conditions are summarized in Table 6.2.

Table 6.2: Flow conditions exploited with wake generator and purge flow.

M	Re	f^+	PMFR [%]
0.90	$70k$	0.95	–
0.90	$70k$	0.95	0.00%
0.90	$70k$	0.95	0.50%
0.90	$70k$	0.95	0.90%

6.2 Time-Averaged Measurements

6.2.1 Inlet Boundary Layer Characterization

6.2.1.1 Steady Inlet Flow

The inlet boundary layer under steady inlet flow was surveyed at Plane 01 through a Preston tube. Fig. 6.1(a) displays the spanwise distribution of the pressure coefficient in the boundary layer at on- and off-design flow conditions. The color of the line-marker arrangement represents the Mach number. The type of marker denotes the Reynolds number. The pressure coefficient is defined as:

$$C_p = \frac{P_{BL} - P_{01,fs}}{P_{01,fs} - P_1} \tag{6.1}$$

Where P_{BL} is the Preston probe retrieved pressure, $P_{01,fs}$ is the inlet freestream total pressure, and P_1 is the endwall static pressure measured by the endwall taps at Plane 01. Good agreement between all flow cases is observed. Fig. 6.1(b) displays the average C_p along the span. The shaded area bounds the maximum and minimum variation from the mean level. The difference in the boundary layer total pressure was within $\pm$0.4$ of the inlet freestream total pressure.

The boundary layer integral parameters, displacement thickness, momentum thickness, and shape factor are displayed in Fig. 6.2. The displacement thickness (see Fig. 6.2(a)) generally decreases with the Mach number. No evident trend with the Reynolds number is observed. The maximum variation is within $\pm$0.15 mm. The momentum thickness (see Fig. 6.2(b)) also decreases with the Mach number and is insensitive to the Reynolds number. The variation is found to be within $\pm$0.08 mm. The resulting shape factor (see Fig. 6.2(c)) is not sensitive to the Mach or Reynolds numbers. The mean value of 1.38 suggests a turbulent boundary layer for all cases [1]. Based on the previous observations, it can be concluded that the inlet boundary layer is independent of the flow condition. The integral parameter values are contained in Table F.1 present in Appendix F for completeness.

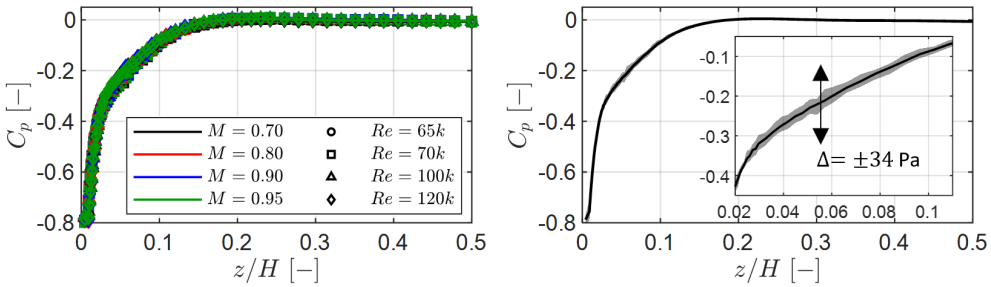

Figure 6.1: Inlet boundary layer profiles: all flow cases (a) and mean level with shaded area (b).

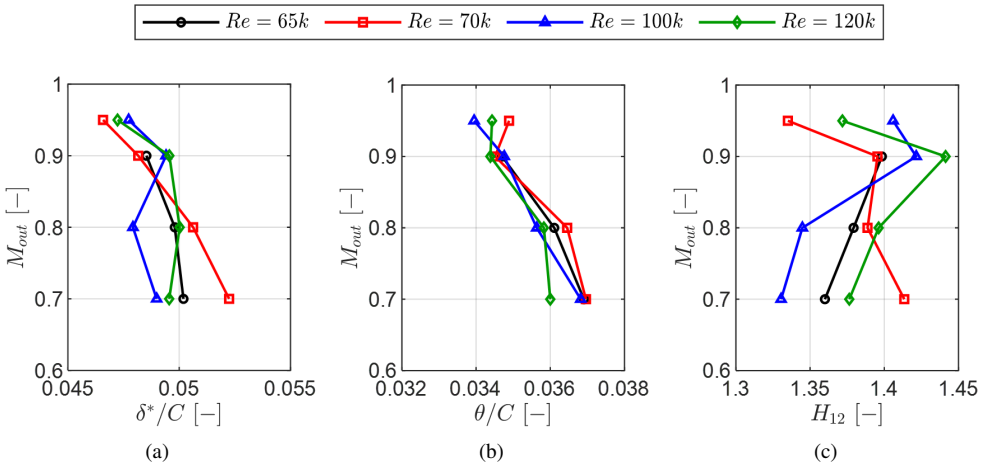

Figure 6.2: Variation of boundary layer integral parameters with Mach and Reynolds numbers: displacement thickness (a), momentum thickness (b), and shape factor (c).

6.2.1.2 Turbulent Quantities

Fig. 6.3 displays the radial profiles of turbulence intensity and integral length scale measured with the cross-wire probe at Plane 02 in the absence of incoming wakes.

The turbulence intensity (see Section 6.3(a)) reports the quantity computed under isotropic turbulence assumption (XW2-ISO) and by accounting for the streamwise and crosswise components (XW2-ANISO). For both, the turbulence is found to increase towards the endwall. For the anisotropic case, the turbulence reaches values as high as 26%. The anisotropic turbulence is higher than the isotropic along the span, being 32% higher at the endwall nearest measured point.

The radial distribution of the integral length scale is displayed in Fig. 6.3(b). The length scale was obtained by integrating the spectrum in the 20–100 Hz range. The length scale increases from ∼14 mm to ∼30 mm in the boundary layer, reaching a maximum at z/H≈0.10. The peak is followed by a decrease towards the endwall where the length scale is ∼20 mm.

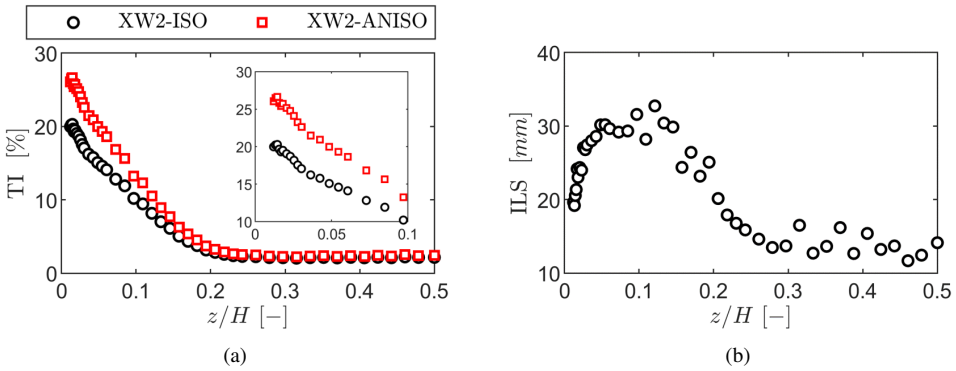

Figure 6.3: Radial profiles of turbulence: turbulence intensity (a) and integral length scale (b).

6.2.1.3 Unsteady Inlet Flow with Flat Endwall

Upon introducing the wake generator, the inlet flow field was re-characterized at Plane 02 utilizing the Cobra five-hole probe. The 2D mapping of the flow has been solely performed for the nominal operating point (M=0.90; Re=70k). Fig. 6.4 displays the contours of the inlet boundary layer kinetic energy loss coefficient based on the outlet dynamic head for the case without and with unsteady wakes. The coefficient is expressed as the ratio of outlet kinetic energy to isentropic outlet kinetic energy:

$$\xi = 1 - \frac{1 - \left(\frac{P_6}{P_02}\right)^{\frac{\gamma-1}{\gamma}}}{1 - \left(\frac{P_6}{P_{01,fs}}\right)^{\frac{\gamma-1}{\gamma}}} \tag{6.2}$$

The contours highlight the pitch-to-pitch periodicity, particularly for the case without a wake generator. In the absence of the wake generator slot, a higher loss is observed near the endwall due to the thicker boundary layer. The noticeable variation of the pitch-to-pitch

periodicity with the wake generator has been previously ascribed to the rotating motion of the wake generator (see Section 4.3.2).

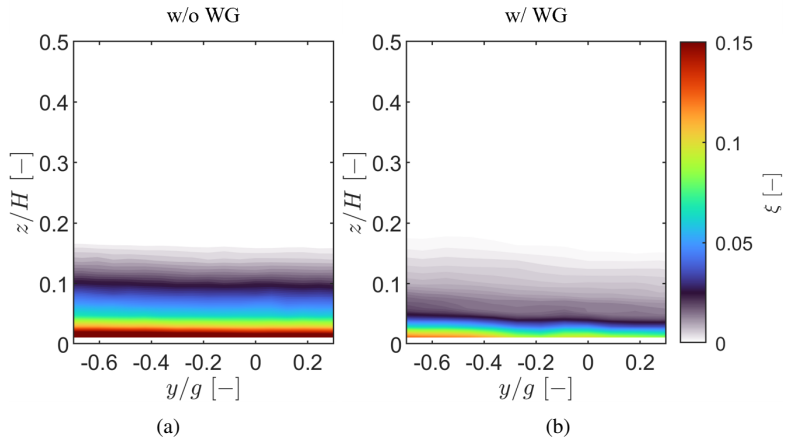

Figure 6.4: Contours of inlet kinetic energy loss coefficient: without wake generator (a) and with wake generator (b).

Fig. 6.5 displays the radial profile in terms of pressure coefficient and kinetic energy loss coefficient based on the outlet dynamic head at y/g=0.00. The solid line marker displays the case without a wake generator, while the dashed line-hollow marker arrangement represents the case with a wake generator.

The radial profiles of the pressure coefficient for the cases with steady and unsteady inlet flow are displayed in Fig. 6.5(a). The pressure coefficient has been computed with the local total pressure, P_{02}, and the local static pressure, P_2, measured by the Cobra five-hole probe. The inlet freestream total pressure normalized the static pressure at midspan. The normalized static pressure was dimensionalized by multiplying the non-dimensional quantity by the local freestream total pressure. The coefficient is computed as:

$$C_p = \frac{P_{02} - P_{01,fs}}{P_{01,fs} - P_2} \tag{6.3}$$

The profile is thicker for the case without the wake generator. The endwall slot from which the wake generator bars enter the test section possibly triggers a restart of the boundary layer. At z/H=0.05, the total pressure deficit between both cases can amount to as much as 2% of the inlet freestream total pressure.

Fig. 6.5(b) displays the radial profile of the kinetic energy loss coefficient (Eq. 6.2) for both cases. Consistent with the pressure coefficient, the profile obtained with steady inlet flow displays higher kinetic energy loss near the endwall due to the thicker inlet boundary layer.

Even though the wake generator introduces radial and tangential local velocity effects due to its rotating motion, the mass-averaged profile is not significantly impacted by the flow non-uniformity. Fig. 6.5(c) displays the difference between the mass-averaged kinetic energy

loss coefficient and the profile at y/g=0.00. Differences along the span are constrained within ± 0.004.

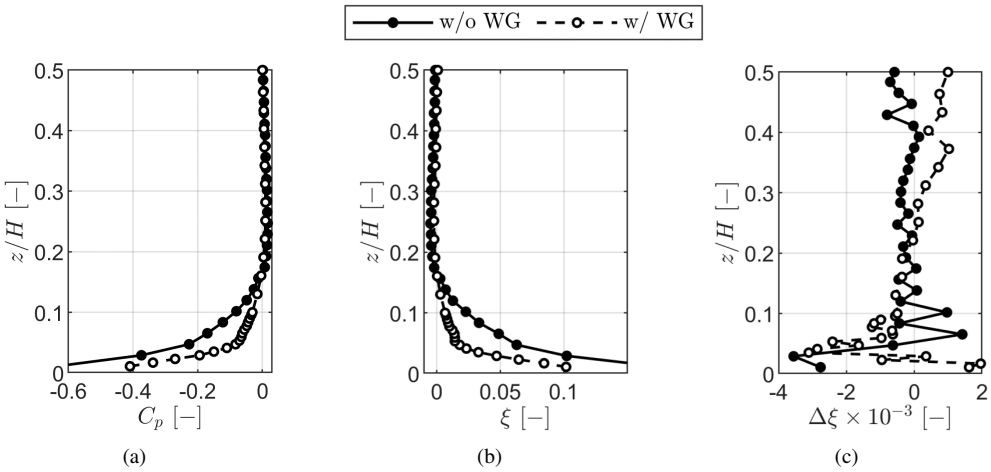

Figure 6.5: Comparison between mass-averaged radial profiles with steady and unsteady inlet flow: pressure coefficient (a) and kinetic energy loss coefficient (b), and pitch-to-pitch variation of kinetic energy loss coefficient (c).

The boundary layer integral parameters reflect the findings from the radial profiles. The inlet boundary layer parameters for both cases is displayed in Fig. 6.6. The integration region was truncated at the spanwise location where the boundary layer total pressure reached the freestream total pressure.

Fig. 6.6(a) displays the pitchwise distribution of the boundary layer displacement thickness for both cases. The quantity is normalized by the blade true chord. The displacement thickness for the unsteady inlet flow condition was 55% lower than for the steady flow case. Regardless of potential wake generator local effects, the pitch-to-pitch periodicity was comparable to the steady inlet flow case. The findings are similar concerning the momentum thickness displayed in Fig. 6.6(b).

Fig. 6.6(c) displays the resulting shape factor. As a result of the similar variation in relative terms, the shape factor of the boundary layer downstream of the wake generator slot shows low pitch-to-pitch variation. The mean value decreases to 1.20. Table F.2 in Appendix F contains the mean values of the boundary layer integral parameters.

The inlet cascade incidence reflects the flow non-uniformity produced by the wake generator. Fig. 6.7 displays the radial incidence profiles at discrete pitchwise locations for the steady and unsteady inlet flow cases.

The lower incidence at midspan for the case with unsteady wakes is present regardless of the pitchwise location. The radial profiles are not uniform. A decrease in incidence occurs towards the endwall up to z/H$\approx$0.05. For positive pitchwise locations, the incidence increases to the closest point to the endwall for the unsteady inlet flow case.

The profile obtained with steady inlet flow resembles a positively skewed one. On the other hand, the unsteady inlet flow can be regarded as having zero skew. Walsh and Gregory-Smith [2] found that negatively skewed profiles result in higher secondary loss with respect

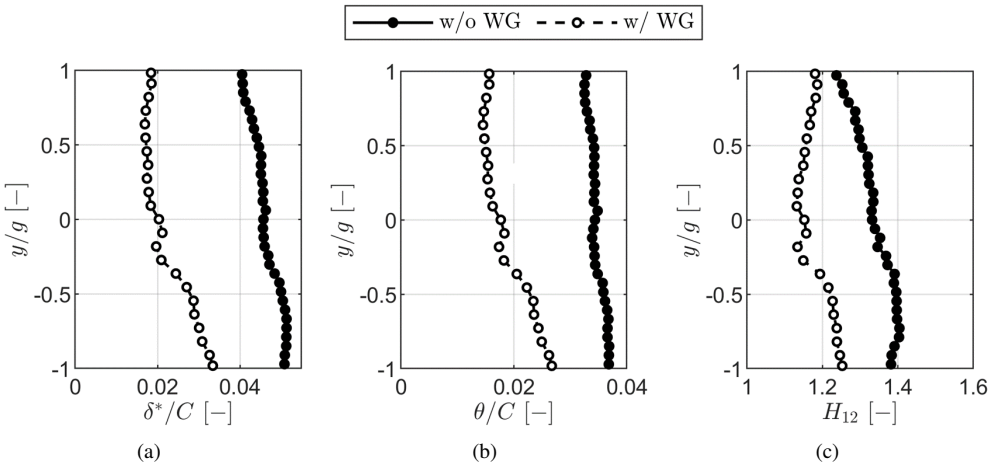

Figure 6.6: Pitchwise distribution of boundary layer integral parameters measured for steady and unsteady inlet flow cases: displacement thickness (a), momentum thickness (b), and shape factor (c).

to positively skewed ones. In their study, the boundary layer loss of the imposed profiles was higher for the negatively skewed boundary layer. These findings are supported by the boundary layer profiles measured in the scope of this work.

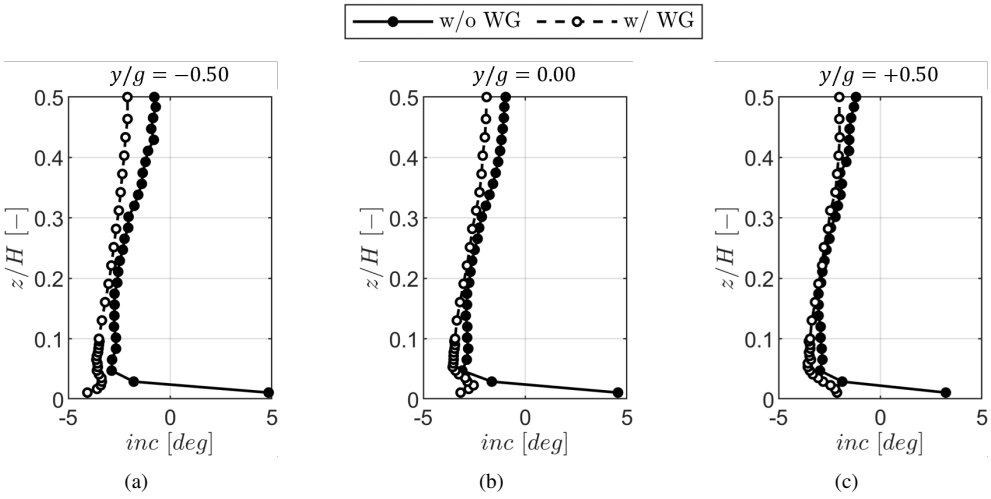

Figure 6.7: Radial profiles of cascade inlet incidence for steady and unsteady inlet flow cases: y/g=-0.50 (a), y/g=0.00 (b), and y/g=+0.50 (c).

6.2.1.4 Unsteady Inlet Flow with Cavity Slot

A re-characterization of the inlet flow field at Plane 02 is performed upon introducing the cavity slot. The measurements aimed at assessing the impact of modifying the wake generator bar geometry (see Section 2.3.2). The cavity slot is downstream of the measurement location.

The case with unsteady inlet flow and a flat endwall (NC) is compared against the cases where the cavity slot is present. Purge massflow ratios from 0.00% to 0.90% are investigated.

Fig. 6.8(a) displays the radial profiles of mass-averaged pressure coefficient computed according to Eq. 6.3. The freestream-related profile is similar for all cases. From the endwall to z/H≈0.05, the profiles for the cases in which the cavity slot is present are thinner regardless of the purge massflow ratio. For the closest point to the endwall, the difference amounts to ∼200 Pa for a typical rig dynamic pressure. The variation is attributed to the alteration of the bar support, which is likely to have modified the ingress/egress from the wake generator slot.

The previous findings are reflected in the kinetic energy loss coefficient computed according to Eq. 6.2 and displayed in Fig. 6.8(b). Higher boundary layer loss occurs in cases where the cavity slot is present. Even though the introduction of the slot generates a potential flow interaction with the probe that causes a modification of the profiles mentioned above, the inlet flow field is periodic. Fig. 6.8(c) displays the difference between the mass-averaged kinetic energy loss coefficient and the profile at y/g=0.00. The variations along the pitch are found to be within ±0.006.

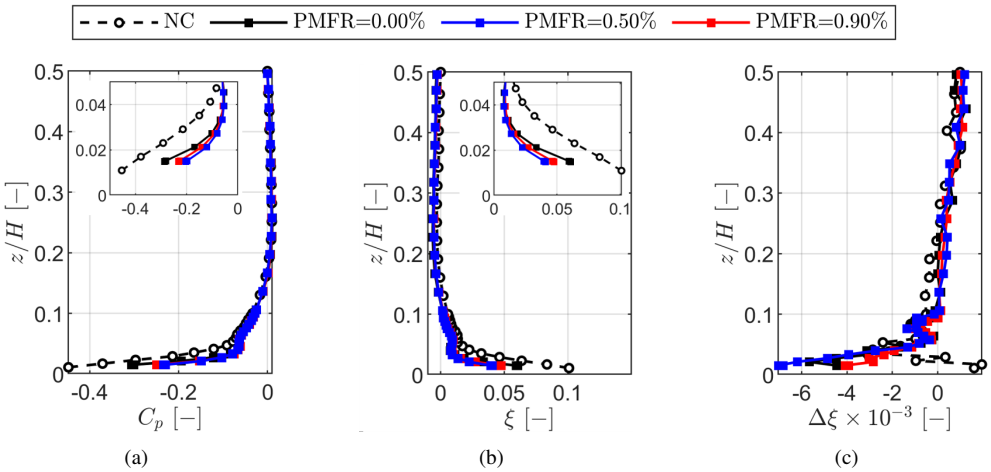

Figure 6.8: Comparison between mass-averaged radial profiles with and without cavity slot with increasing purge massflow ratio: pressure coefficient (a) and kinetic energy loss coefficient (b), and pitch-to-pitch variation of kinetic energy loss coefficient (c).

The boundary layer integral parameters have been used to quantify the thinning of the inlet boundary layer in the cases with cavity slots. Fig. 6.9(a) displays the pitchwise distribution of the displacement thickness. The pitch-to-pitch trend is kept for the cases with the cavity. A general reduction by 52% occurs. Similar findings can be drawn regarding the momentum thickness (see Fig. 6.9(b)). The resulting shape factor displays a pitch-to-pitch variation within ±0.05. The mean values are similar for the case with and without the cavity slot. Table F.2 in Appendix C contains the mean values of the boundary layer integral parameters.

Modifying the wake generator bar support also impacts the flow incidence to the cascade. Fig. 6.10 displays the radial incidence profiles at specific pitchwise locations. The incidence is negative throughout the spanwise direction for all cases. The incidence decreases from

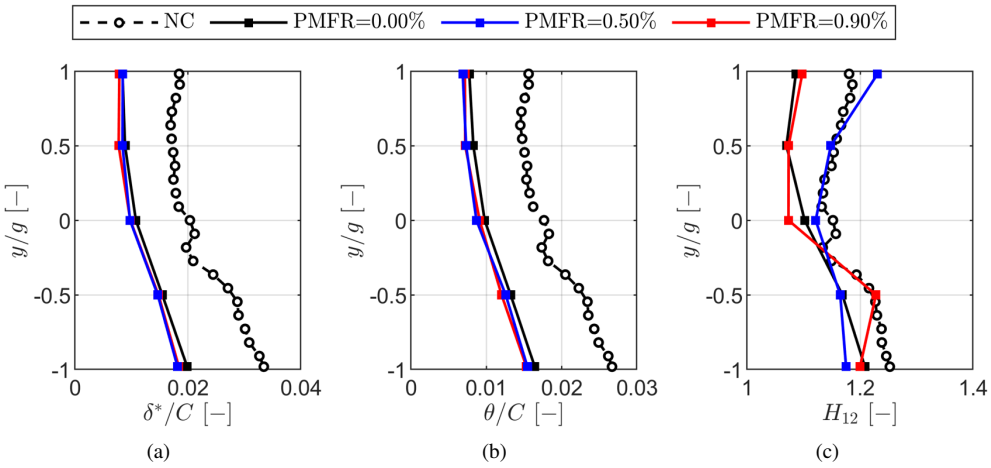

Figure 6.9: Pitchwise distribution of boundary layer integral parameters measured for cases with and without cavity slot: displacement thickness (a), momentum thickness (b), and shape factor (c).

midspan towards the endwall to a minimum at z/H≈0.05 (depending on the pitch location). A maximum pitch-to-pitch variation of ±0.10° exists at midspan for all cases. Near the endwall, the latter reaches ±0.50° when purge flow is injected, and as much as ±1.50° for the cases with flat endwall and cavity endwall without purge flow injection. For a fixed pitchwise location, the variation in the incidence between the investigated cases is higher at y/g=-0.50 (see Fig. 6.10(a)), where the variation reaches up to ±1.50° at the location of the point closest to the endwall. The difference between the cases is significantly reduced at y/g=+0.50 (see Fig. 6.10(c)). The possible wake generator slot ingress/egress impacts the pitch-to-pitch variations since the bars are dragging/pushing air into the slot because of the rotational motion (see Fig. 4.12).

The cascade pitch angle also varies, as displayed in Fig. 6.11. For a fixed pitchwise location, the cascade pitch angle was the lowest for the case with the cavity slot and without purge flow throughout the span. The cascade pitch angle increases when purge flow is injected. However, the growth is not monotonic. Between the two cases where no purge flow is injected, with a flat endwall and cavity slot, the deficit in pitch angle is as high as ∼1.5° at z/H=0.06. The difference decreases towards midspan.

The pitch-to-pitch sensitivity of the cascade pitch angle is also observed. At y/g=-0.50, the pitch angle increases from midspan towards the endwall in the presence of purge flow. The “overshoot” in cascade pitch angle decreases towards positive pitchwise locations. At the far most pitchwise location, the cascade pitch angle monotonically decreases with the spanwise coordinate for all the investigated cases.

6.2.2 Blade Aerodynamics

6.2.2.1 On- and Off-Design Impact

The on- and off-design blade loadings have been investigated employing the traversing blade. The load was found to decrease towards the endwall for all cases. Fig 6.12(a) displays

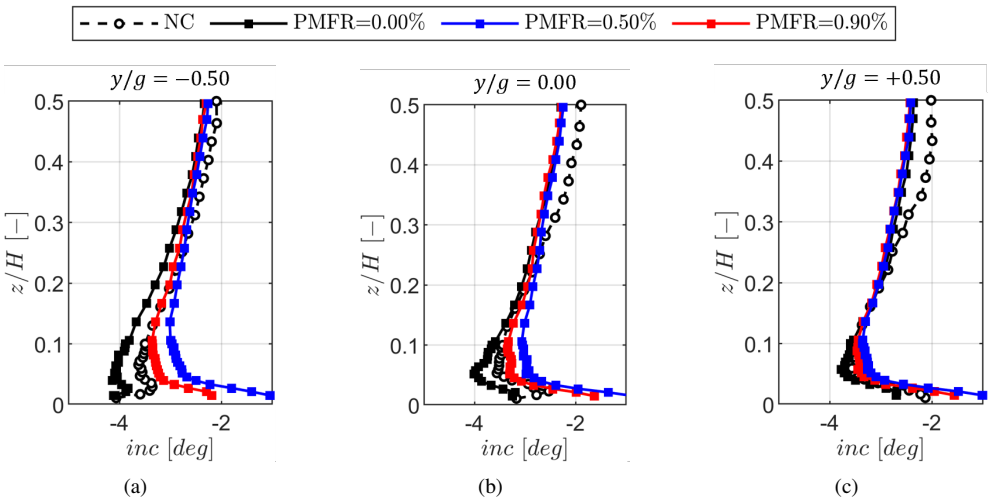

Figure 6.10: Radial profiles of cascade inlet incidence for cases with and without cavity slot and increasing purge massflow ratio: y/g=-0.50 (a), y/g=0.00 (b) and y/g=+0.50 (c).

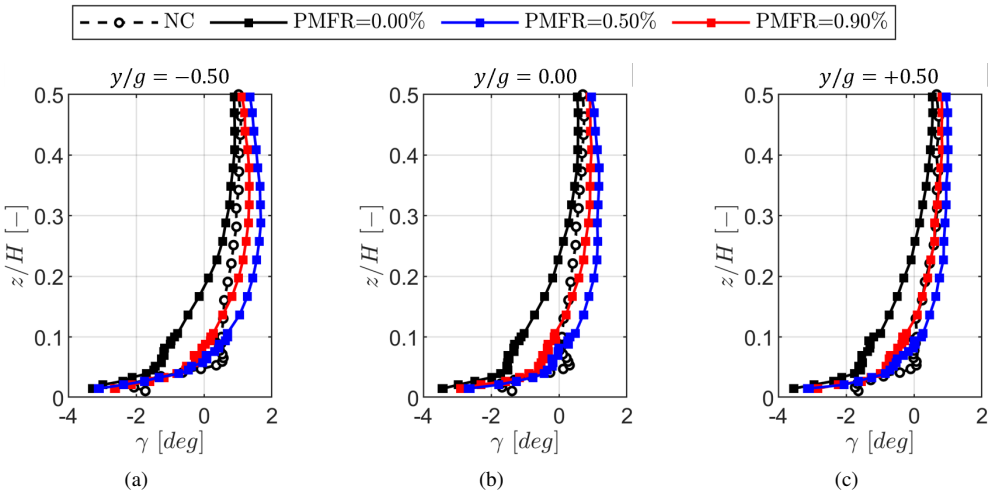

Figure 6.11: Radial profiles of cascade pitch angle for cases with and without cavity slot and increasing purge massflow ratio: y/g=-0.50 (a), y/g=0.00 (b), and y/g=+0.50 (c).

the blade loadings at decreasing spanwise coordinate. The zoomed-in portion highlights the reduction of the separation bubble extent near the endwall due to the presence of secondary flows that will be highlighted in Section 6.2.3. The reduction of the blade loading is particularly evident in the front portion of the profile. It results from lower momentum fluid in the boundary layer.

The loading changes significantly with the Mach number due to the variation of the outlet dynamic head. However, for a fixed Mach number, the loading in the region impacted by secondary flows is insensitive to the Reynolds number. The effect is displayed in Fig. 6.12(b) for the M=0.80 case.

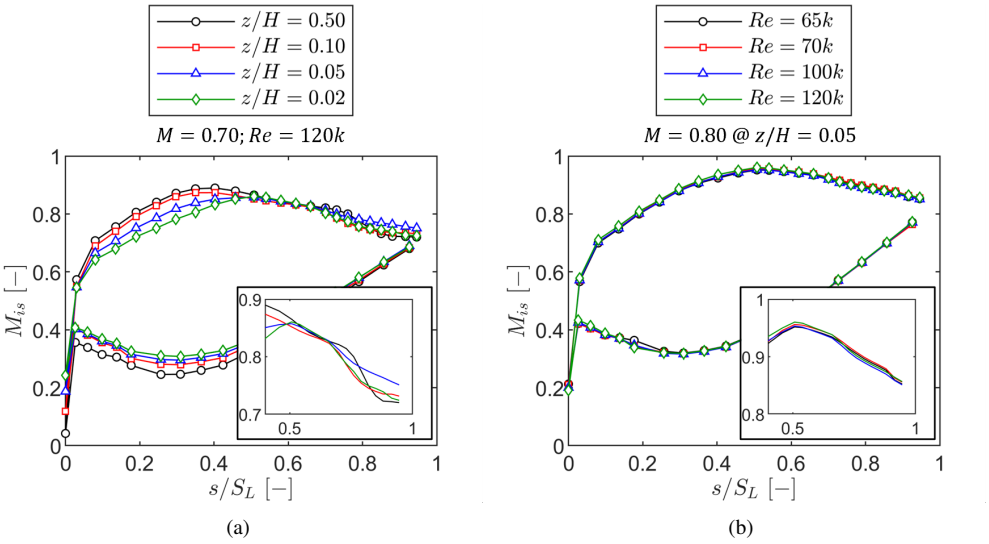

Figure 6.12: Variation of blade loading along span for M=0.70; Re=120k (a) and sensitivity of near-wall loading at z/H=0.05 to Reynolds number at M=0.80 (b).

6.2.2.2 Impact of Unsteady Wakes

The wake generator bars introduced variations in the radial profile of total pressure and incidence. The incidence with incoming wakes is lower from midspan to the endwall (see Fig. 6.7). As a result, the front portion of the suction side loading is lower. Fig 6.13 compares the blade loading for the steady and unsteady inlet flow cases. The loading is lower on the front portion of the suction side throughout the span. Near the endwall, the thinner boundary layer for the unsteady inlet flow case also results in a lower loading on the pressure side.

6.2.2.3 Impact of Purge Flow on Blade Loading

Fig. 6.14 displays the difference in the isentropic Mach number distributions computed with the static pressure taps and freestream total pressure between the case with a flat endwall and the cases with the cavity. The difference for each case with purge massflow ratio is computed as:

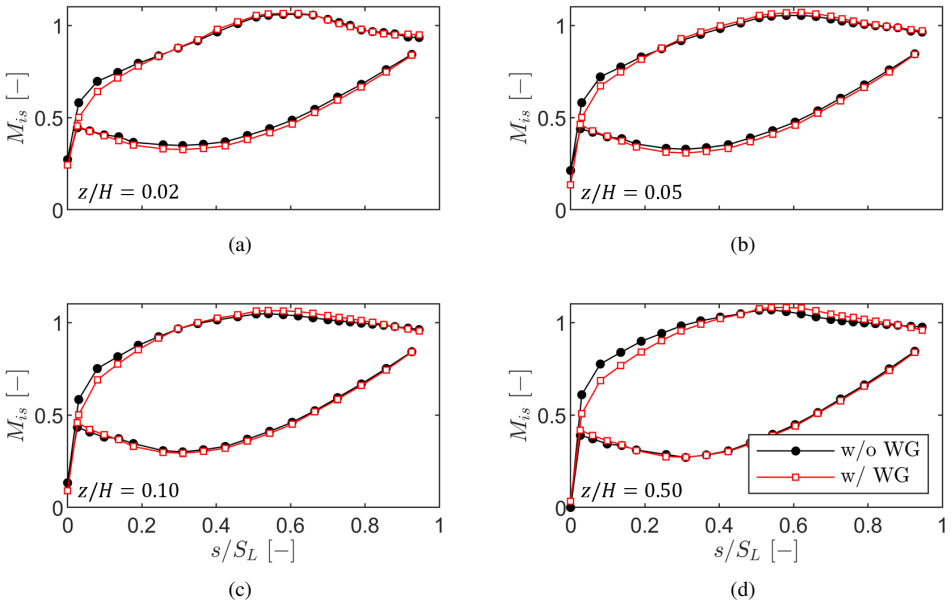

Figure 6.13: Sensitivity of unsteady wake radial profile on blade loading: z/H=0.02 (a), z/H=0.05 (b), z/H=0.10 (c), z/H=0.50 (d).

$$\Delta M_{is} = M_{is,NC} - M_{is,PMFR} \tag{6.4}$$

The quantities are plotted along the surface position on the blade pressure (negative coordinate) and the suction side (positive coordinate). The contours are displayed from the endwall to z/H=0.20, where the flow is two-dimensional. A subtle difference in the loading is observed for the case where the cavity is present, but no purge flow is injected (see Fig. 6.14(a)). The difference at z/H=0.20 is justified by the fact that the outlet Mach number achieved for the case without the endwall is slightly higher ($\approx$ 0.906 versus 0.900). The same feature can be observed for the cases of PMFR=0.50% and 0.90% in Fig. 6.14(b) and Fig. 6.14(c), respectively.

The difference in the isentropic Mach number between the cases with flat endwall and the cavity endwall without purge flow (see Fig. 6.14(a)) is the largest near the leading edge on the suction side because of the different incidence reported previously. This is further aggravated in cases with purge flow where a significant reduction of the isentropic Mach number on the suction side occurs because of the impingement of the purge flows. The blade isentropic Mach number variations can be better visualized in the plot containing the distributions for all the cases at z/H=1.52% (see Fig. 6.15(a)).

The regions on the blade suction side (s/S_L>0.30) dominated by the secondary flow structures are significantly modified in the presence of purge flow injection. At z/H=1.52%, the isentropic Mach number is reduced by as much as 0.080 and 0.084 for the cases of PMFR=0.50% and 0.90% at $s/S_L \approx$0.40, respectively (see Fig. 6.15(a) with individual blade distributions). These variations occur in the region where the suction side corner vortex is

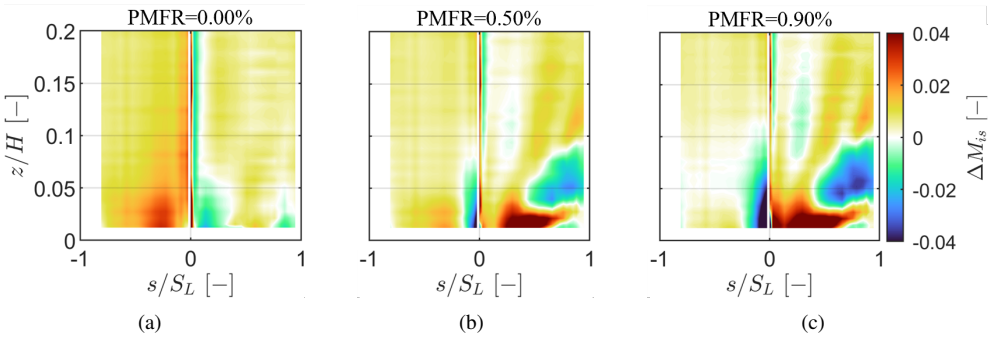

Figure 6.14: Contours of difference in surface isentropic Mach number in relation to the case without cavity slot: PMFR=0.00% (a), PMFR=0.50% (b), and PMFR=0.90% (c).

expected.

At z/H≈2.50%, the isentropic Mach number is comparable between all cases. After this location, the isentropic Mach number for the cases without purge flow becomes lower than those with purge flow injection (see Fig. 6.15(b)). The isentropic Mach number at z/H=5.15% for the case of PMFR=0.50% and 0.90% is higher than the case with the flat endwall by 0.027 and 0.036, respectively. The region where the isentropic Mach number is higher for the cases with purge flow ends at z/H=10.00%. As it will be displayed later, the passage vortex is constrained in a region with a similar spanwise extent. After z/H=20.00%, there is a little spanwise variation of the isentropic Mach number. The distributions at midspan (see Fig. 6.15(d)) are in good agreement and suggest that the extent of the impact that the purge flows have on the blade loading is constrained near the endwall.

6.2.3 Characterization of Secondary Flows

A brief characterization of the flowfield in terms of primary flow structures is provided to inform the upcoming measurements at the cascade outlet. The results of a 3D transitional RANS simulation at M=0.90; Re=70k were used to find the imprint of potential secondary flow structures on the blade surface. The simulation was performed with the inlet representative boundary conditions measured experimentally: inlet radial profiles of total pressure, incidence, turbulent properties, and outlet static pressure. The results are part of ongoing work with another research group; therefore, this manuscript will not provide details of the simulation. The results will be used qualitatively.

Fig. 6.16 displays the Q-criterion obtained at M=0.70; Re=120k. Their local vorticity colors the iso-surfaces. The passage (PV) can be easily identified as the most significant flow structure in green. Two distinct structures are highlighted. Using the Q-criterion can result in two different stream tubes due to its formulation. A double passage vortex was observed in the simulations of Gross et al. [3] and Bear et al. [4] at low Reynolds numbers. In this work, an analysis of the secondary flow structures through vorticity and secondary velocity vectors did not allow for identifying distinct secondary flow structures in the passage vortex region. A structure with opposite vorticity develops above the passage vortex. The structure remains

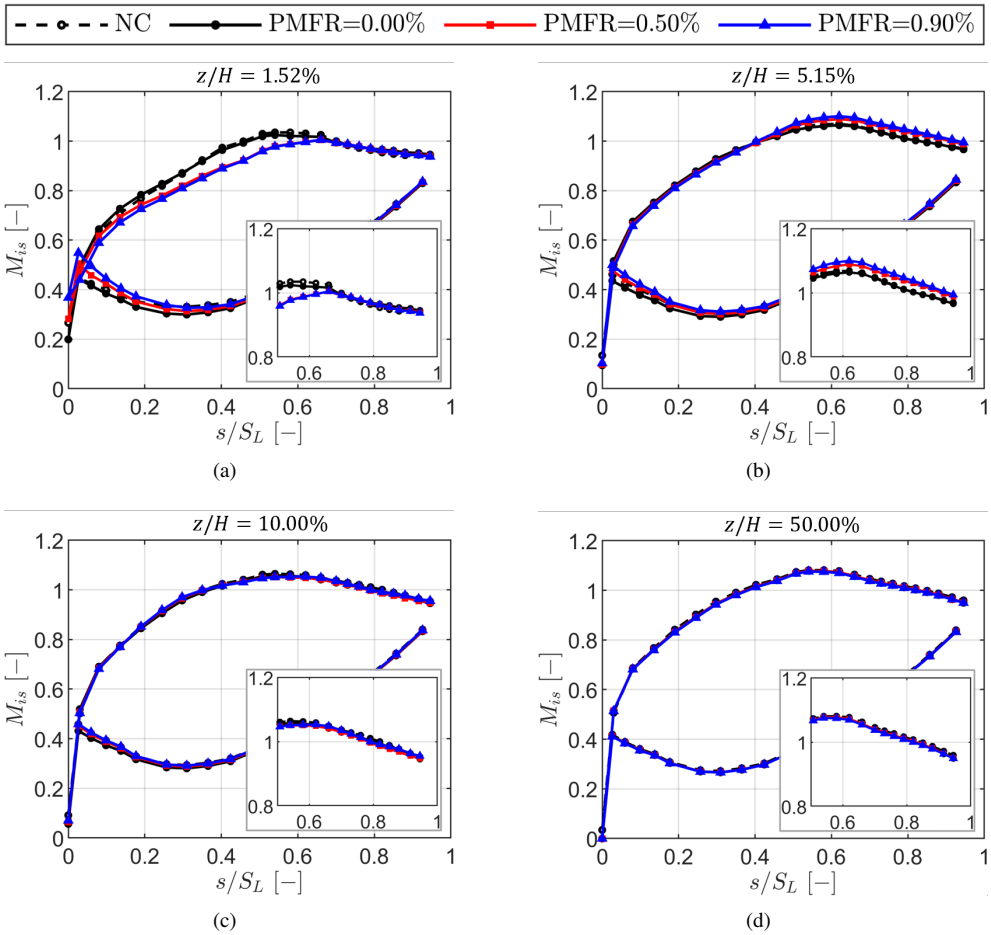

Figure 6.15: Blade surface isentropic Mach number distributions for cases with and without cavity sot and varying purge massflow ratio: z/H=1.52% (a), z/H=5.15% (b), z/H=10.00% (c) and z/H=50.00% (d).

attached to the suction side surface and is associated with a wall-induced vortex (WIV). Due to the reduction of the blade loading towards the endwall, a region of counter vorticity forms above the passage vortex. The so-called trailing shed vorticity (TSV) includes the contribution of the wall-induced vortex. In the intersection of the endwall and blade suction side, a corner vortex is formed (CV).

The structures mentioned above are the main ones that will be identified in this work. Characterization of other secondary and even tertiary vortices is outside the scope of this work.

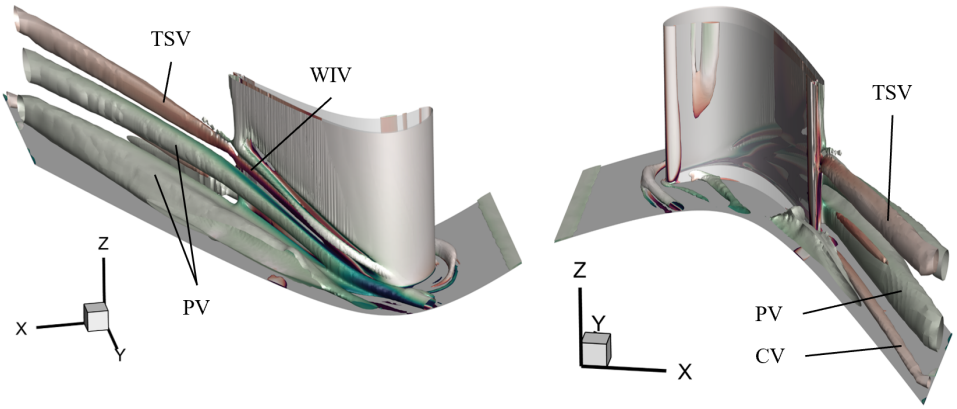

Figure 6.16: Representation of primary and secondary flow structures with Q-criterion.

6.2.3.1 Off-Design Performance under Steady Inlet Flow

The secondary flow structures at the outlet were mapped utilizing the L-shaped five-hole probe at Plane 06. The kinetic energy loss coefficient, streamwise vorticity coefficient, and secondary kinetic energy coefficient characterize the outlet flow field. The formed quantities thoroughly describe the secondary flow structures in terms of location and intensity.

Fig. 6.17 concerns the nominal flow case. However, the following description applies to the remaining flow conditions. Fig. 6.17(a) displays the kinetic energy loss coefficient contours, ξ, for one cascade pitch and half of the blade span. The loss topology is characterized by the wake loss profile at midspan and two loss cores near the endwall. The loss core "C1" sits above 10% span and is shifted from the trailing edge metal angle location ($y/g = 0.00$). The loss core "C2" sits near the endwall and follows the blade outlet metal angle.

Fig. 6.17(b) displays the streamwise vorticity coefficient, K_ω, superimposed with the kinetic energy loss coefficient. The red color denotes counter-clockwise motion, and vice-versa for the blue color. The streamwise vorticity coefficient highlights three main regions of increased vorticity. The latter regions are related to the secondary flow structures present in the flow field. The region close to the endwall displays clockwise motion and is attributed to the corner vortex (CV). Closer inspection suggests that this structure is the main contributor to the second loss core in the kinetic energy loss coefficient. Above the suction side corner vortex at around z/H=10%, another region of increased clockwise vorticity exists. This region is

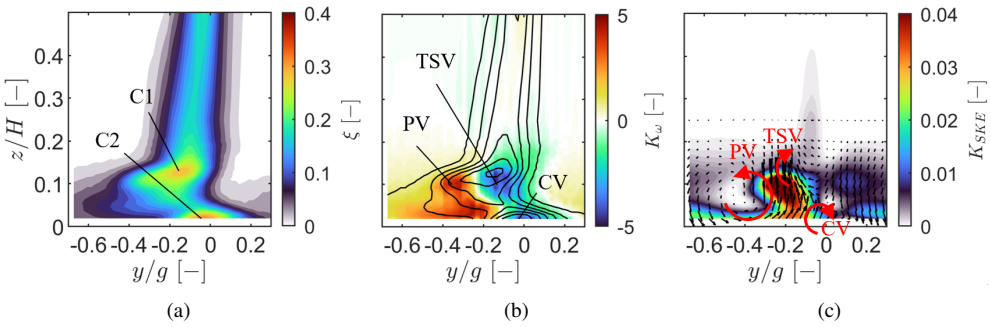

Figure 6.17: Characterization of secondary flow structures downstream for nominal flow case: kinetic energy loss coefficient (a), streamwise vorticity coefficient superimposed with isolines of kinetic energy loss coefficient (b) and secondary kinetic energy coefficient superimposed with secondary velocity vectors (c). The observer looks upstream.

mainly impacted by the trailing shed vorticity (TSV). Lastly, a region of large extent characterized by counter-clockwise vorticity exists towards the pressure side of the adjacent blade. This near-wall region is dominated by the passage vortex (PV). Even though the location of the core is better correlated with the trailing shed vorticity region, both the passage vortex and trailing shed vorticity interact and contribute to the first kinetic energy loss core.

Fig. 6.17(c) contains the secondary kinetic energy coefficient, K_{SKE}, superimposed with the secondary velocity vectors. Red arrows denote the rough location of the secondary flow structures highlighted in the previous paragraph. Regions of high K_{SKE} occur in the interface of adjacent secondary flow structures and the interface of the secondary flow structures with the endwall. The largest local K_{SKE} is located in the region of shear interaction between the passage vortex and trailing shed vorticity. The magnitude of the secondary velocity vectors is also intensified.

Fig. 6.18 displays the kinetic energy loss coefficient with increasing Mach number for Re=70k. As the Mach number is increased, the location of the loss core "C1" is shifted towards the endwall. The shift is highlighted by comparing the location for the case of M=0.70 (line "A") and M=0.90 (line "B"). The migration secondary flows towards the endwall with increasing Mach number has been previously observed in linear cascade [5, 6] and annular cascade studies [7, 8].

The increase of the Mach number also skewed the wake. For the lower Mach number, the blade wake is described by a pitchwise-invariant line up to the region impacted by secondary flows (line "C"). The wake is skewed for the highest Mach number (line "D") from midspan to near the endwall spanwise values.

The spanwise distribution of the mass-averaged secondary kinetic energy loss coefficient, ξ_{sec}, is displayed in Fig. 6.19(a). The coefficient is obtained by subtracting the profile loss from the gross loss. The presence of the two loss cores in the radial profile is perceivable. The first loss core comprises the loss generated by the passage vortex and trailing shed vorticity. The larger magnitude second loss core includes the contribution of the suction side corner vortex and endwall boundary layer fluid. The shift of "C1" towards the endwall due to the migration of the secondary flow strictures is observable in the zoomed insert. The mass-

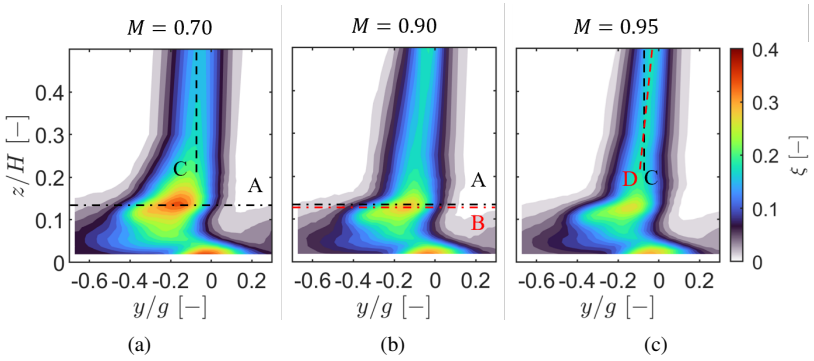

Figure 6.18: Impact of Reynolds number on kinetic energy loss coefficient at Re=70k: M=0.70 (a), M=0.90 (b) and M=0.95 (c).

averaged loss is found to decrease with the Mach number across the whole spanwise range. In particular, the "C1" peak is reduced by 25%.

As a result of the vorticity generated by the secondary flow structures, the outlet radial, angular profile is not constant. Fig. 6.19(b) displays the mass-averaged radial deviation profile from the primary flow direction. The radial profile is characterized by regions of underturning and overturning near the endwall—-the overturning near the endwall results from the portion of the passage vortex below the center of rotation. Above the center of the passage vortex, the combined interaction of the latter and the trailing shed vorticity increases the underturning up to a peak. As a result of the weaker secondary flow structures, the peak decreases by 9% with the Mach number.

The Mach number effect is also captured by the secondary kinetic energy loss coefficient displayed in Fig. 6.19(c). The radial profile is characterized by two regions of high S_{SKE}. The region near the endwall ("A") captured the loss associated with the suction side corner vortex and the endwall boundary layer flow. The region above ("B") captures the shear interaction between the passage vortex and trailing shed vorticity. The loss peak varies less with the Mach number than for the ξ_{sec}. Nonetheless, a reduction of the peak by $\sim$7% in region "B" takes place.

The variation of the Reynolds number does not significantly modify the topology of the contours displayed for a fixed Reynolds number (see Fig. 6.18). The radial profiles of secondary kinetic energy, deviation from the primary flow direction, and secondary kinetic energy coefficient for M=0.90 are displayed in Fig. 6.20(c).

The secondary kinetic energy loss coefficient is displayed in Fig. 6.20(a). The increase in Reynolds number mainly impacts the region below the first loss core. The increase in Reynolds number promoted a decrease in the magnitude of "C1" by $\sim$11%.

Even though the loss decreases with the Reynolds number, the underturning in the passage vortex region increases (see Fig. 6.20(b)). The intensification of the secondary flow structures is also backed up by the secondary kinetic energy coefficient displayed in Fig. 6.20(c). The higher loss core magnitude increased by $\sim$13%. It is worth noticing that while the kinetic energy loss coefficient decreases with the Reynolds number in the secondary flows, the secondary kinetic energy coefficient increases. The discrepancy between the ξ_{SKE} and K_{SKE}

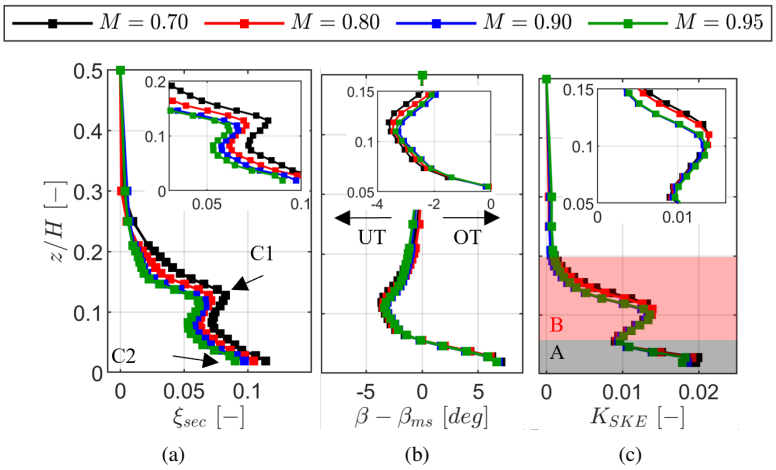

Figure 6.19: Radial profiles for Re=70k: secondary kinetic energy loss coefficient (a), deviation from primary flow direction (b), and secondary kinetic energy coefficient (c).

could come from the former coefficient not decoupled from the inlet boundary layer contribution.

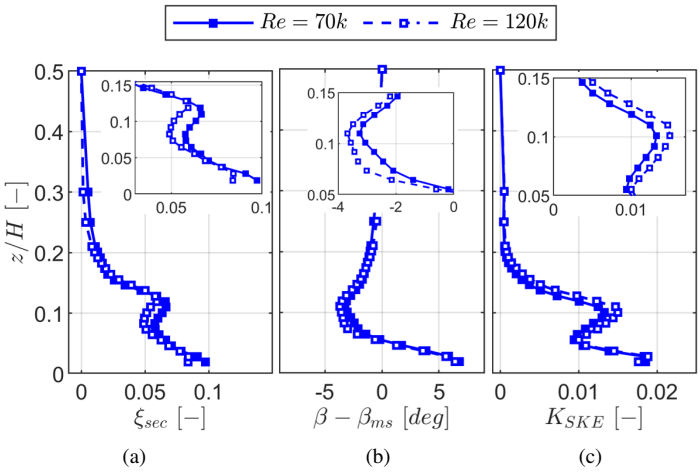

Figure 6.20: Radial profiles for M=0.90: secondary kinetic energy loss coefficient (a), deviation from primary flow direction (b), and secondary kinetic energy coefficient (c).

The kinetic energy of the inlet boundary layer measured at Plane 01 is considered to perform the loss breakdown displayed in Fig. 6.21. The planewise net loss is computed by subtracting the contribution of the profile loss (prof) and planewise inlet boundary layer (BL) loss from the planewise gross loss at Plane 06:

$$\xi_{net} = \xi_{gross} - \xi_{prof} - \xi_{BL} \tag{6.5}$$

Therefore the net loss comprises the endwall boundary layer dissipation and secondary

flow mixing [9]. The boundary layer loss is independent of the Reynolds number. The curves are practically superimposed.

The profile loss is the more significant contributor to the gross loss (more than twice the contribution of the endwall loss). The inlet boundary layer loss is found to decrease with the Mach number (kinetic energy) and is found to be independent of the Reynolds number. Therefore, the reason why the ξ_{sec} and K_{SKE} in Fig. 6.20(c) display the opposite trend cannot be explained by a potential different boundary layer contribution.

The endwall net loss was found to decrease with the Mach number generally. The loss decreased by 25% as the Mach number increased from 0.70 to 0.95 for the Re=70k case. The minimum loss for this Reynolds number was found for a Mach number of 0.80.

The endwall loss was also found to decrease with Reynolds number, regardless of the Mach number. Linear cascade tests performed by Hodson and Dominy [10] support the findings. The loss breakdown values are reported in Appendix G.

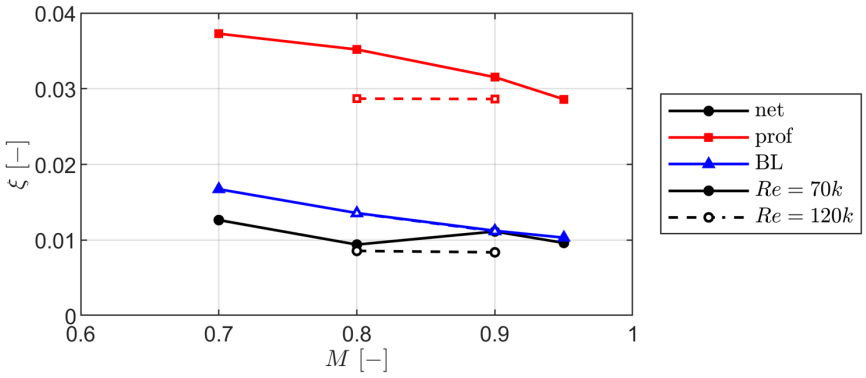

Figure 6.21: Breakdown of the planewise mass-averaged losses for the steady inlet flow cases.

6.2.3.2 Impact of Unsteady Wakes

The secondary flow field at the outlet has been mapped by the L-shaped five-hole probe at Plane 06. Fig. 6.22(a) displays the kinetic energy loss coefficient contour in the range of one cascade pitch and from the endwall to midspan. The topology is similar to the one described thoroughly for the steady inlet flow case (see Fig. 6.17(a)). The loss core "C1" resultant in the trailing shed vorticity region is still present. However, the second loss core associated with the suction side corner vortex is no longer present. The thinner inlet boundary layer impacts the secondary flow development for the unsteady flow case.

Fig. 6.22(b) displays the secondary kinetic energy coefficient contour superimposed with the secondary velocity vectors. The loss core resultant from the combined interaction of the passage vortex and trailing shed vorticity is visible. Even though there is increased loss near the suction side corner vortex location, the probe spatial resolution forbids mapping of this structure closer to the endwall in relation to the steady inlet flow case.

Fig. 6.23(a) displays the radial profiles of mass-averaged kinetic energy loss coefficient measured at Plane 06 for both cases. The loss peak associated with the trailing shed vorticity migrated towards the endwall by 1.8% of the cascade span. However, the magnitude of the

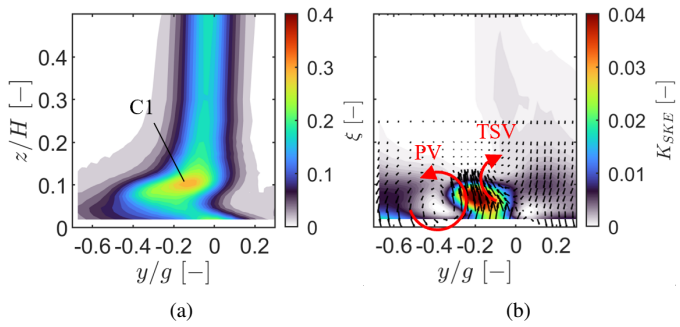

Figure 6.22: Contours obtained with unsteady inlet flow: kinetic energy loss coefficient (a) and secondary kinetic energy coefficient superimposed with secondary velocity vectors (b).

peak increased by ∼8% with the introduction of unsteady wakes. The comparison is impacted because the inlet boundary layer loss is not decoupled from ξ.

The migration of the secondary flow structures towards the endwall is supported by the radial profiles of mass-averaged deviation from the primary flow direction displayed in Fig. 6.23(b). The peak in underturning shifted by the same amount as the kinetic energy one. The underturning increased by 18% with the introduction of unsteady wakes in the flow domain.

The secondary kinetic energy coefficient displayed in Fig. 6.23(c) points out a reduction of the secondary loss for the unsteady inlet case. A reduction of the peak resulting from the interaction of the passage vortex and trailing shed vorticity by ∼11% occurs. The near wall region characterized by the weaker suction side corner vortex sees a reduction by ∼50%.

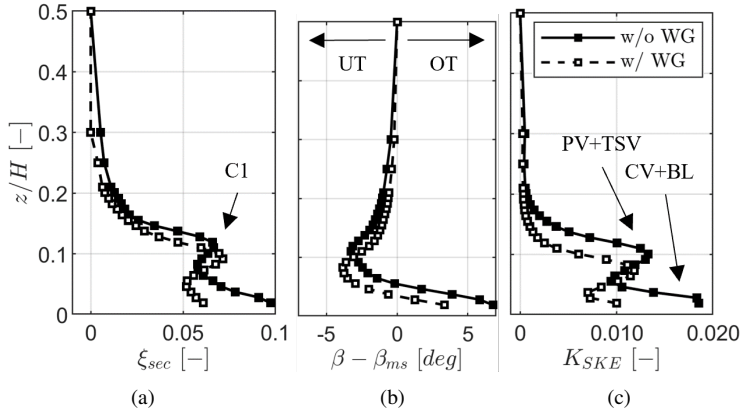

Figure 6.23: Impact of unsteady wakes on radial profiles of mass-averaged quantities: secondary kinetic energy loss coefficient (a), deviation from primary flow direction (b), and secondary kinetic energy coefficient (c).

Fig. 6.24 presents a loss breakdown for both cases. The profile loss contributes the most to the gross loss. After decoupling the profile loss and inlet boundary layer loss from the gross

planewise mass-averaged loss, the unsteady wakes promote a decrease in the net endwall loss by ∼5%. The loss breakdown values are reported in Appendix G.

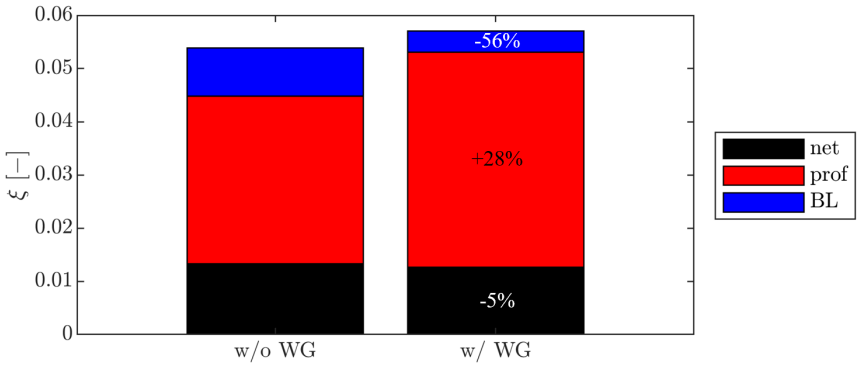

Figure 6.24: Breakdown of the planewise mass-averaged losses for steady and unsteady inlet flow cases.

6.2.3.3 Impact of Purge Flow

Figures 6.25(a)– 6.25(d) present the contour of kinetic energy loss coefficient measured at Plane 06 using the L-shaped five-hole probe. The contoured region concerns one cascade pitch and half of the blade span. A similar topology is observed for all cases: a core of higher loss exists at z/H≈0.10 ("C1"). This loss core is mainly impacted by the trailing shed vortex (TSV), as discussed before (see Section 6.2.3). In cases with the cavity, an additional loss core near the endwall occurs in the region where the suction side corner vortex is typically found ("C2").

The investigation of the impact of cavity flows on the secondary flow development as reported in Refs. [11–13]. Mass and momentum exchange between fluid that recirculates in the slot and the mainstream occurs, mainly in regions of the slot where the static pressure distribution upstream of the leading edge is lower. Typically, the cavity leakage vortex interacts with the pressure side leg of the horseshoe vortex, giving rise to a stronger passage vortex.

Comparing Figures 6.25(a) and 6.25(b), the loss magnitude and location of "C1" does not change significantly (reduction of loss coefficient below 1%) with the introduction of the cavity slot-—the extent of the region associated with the suction side corner vortex enlarged. The loss magnitude did not increase significantly. The injection of purge flow does not modify the suction side corner vortex region significantly nor the magnitude of "C2". The magnitude of "C1" increases by 14% and 22% compared to the case with cavity and without purge injection for the cases with PMFR=0.50% and 0.90%, respectively. The increase in the purge flow rate also shifts "C2" away from the endwall because of the translation of the trailing shed vorticity and passage vortex away from the endwall.

A new loss core is identified for the cases of PMFR=0.50% and 0.90% ("C3"). This loss peak is due to the more considerable extent of the passage vortex in the passage. The latter feature is better shown using the contours of streamwise vorticity coefficient and pitchwise mass-averaged distributions.

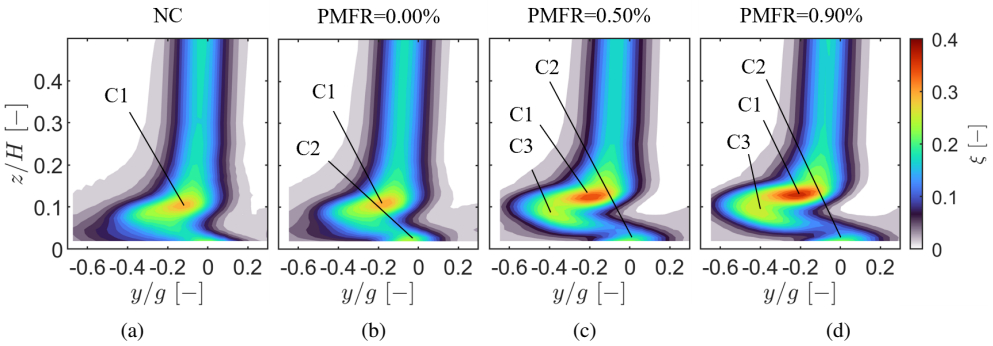

Figure 6.25: Contours of kinetic energy loss coefficient at M=0.90; Re=70k for cases with and without cavity slot and varying purge flow: no cavity slow (a), PMFR=0.00% (b), PMFR=0.50% (c) and PMFR=0.90% (d).

Figures 6.26(a)– 6.26(d) display the contours of streamwise vorticity coefficient. The isolines of the kinetic energy loss coefficient are superimposed to highlight the location of the loss cores in relation to the secondary flow structures. The passage vortex rotates counterclockwise (observer looking upstream) in the red-colored region for all the cases. The clockwise motion trailing shed vorticity can be identified by the blue region at z/H≈0.10 even though limited by the spatial resolution of the L-shaped five-hole probe, the suction side corner vortex is distinguished by its clockwise rotation near the endwall.

The streamwise vorticity coefficient in the passage vortex region increases when the cavity endwall is added, even without purge flow. On the other hand, the trailing shed vorticity remains nearly unaltered. When purge flow is injected, the extent of the passage vortex region increases compared to the cases without purge flow. The magnitude of the K_ω associated with the passage vortex decreases. The same occurs with the K_ω linked to the trailing shed vorticity. Both structures are displaced away from the endwall.

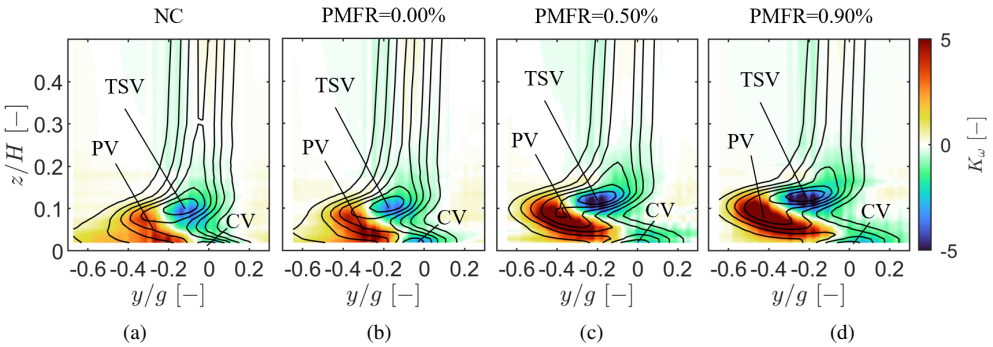

Figure 6.26: Contours of streamwise vorticity coefficient for cases with and without cavity slot and varying purge flow: no cavity slow (a), PMFR=0.00% (b), PMFR=0.50% (c) and PMFR=0.90% (d).

The contours of the secondary kinetic energy coefficient displayed in Figures 6.27(a)–

6.27(d) support the features highlighted in the kinetic energy loss coefficient and streamwise vorticity coefficient. The contours are superimposed with the secondary velocity vectors to highlight secondary flow structures.

The loss magnitude associated with the interaction of the passage vortex and trailing shed vorticity is unaltered as the cavity endwall is inserted, and no purge flow is injected—-the extent of a region near the endwall increases. MacIsaac et al. [13] found similar features and attributed them to the flow overturning near the endwall region due to the cross-passage pressure gradient.

The K_{SKE} increases when purge flow is injected. This region is shifted away from the endwall. Comparatively to the case where the cavity slot is present, and no purge flow is injected, an increase in the maximum K_{SKE} by 96% and 147% occurs for the cases of PMFR=0.50% and 0.90%, respectively. The increase in the magnitude of the secondary velocities with the purge massflow ratio supports this.

The extent of a region near the endwall is also significantly impacted as purge flow is injected. The region extends to the location of the suction side corner vortex, contributing to the K_{SKE} due to the shear interaction with the passage vortex.

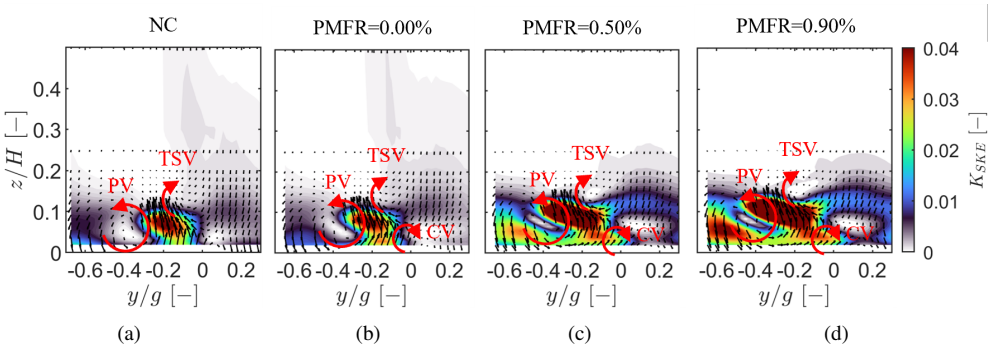

Figure 6.27: Contours of secondary kinetic energy coefficient for cases with and without cavity slot and varying purge massflow ratio: no cavity slow (a), PMFR=0.00% (b), PMFR=0.50% (c) and PMFR=0.90% (d).

Fig. 6.28(a) presents the radial profiles of mass-averaged secondary kinetic energy loss coefficient for all cases. The radial profiles contain the loss cores “C1”, “C2”, and “C3”. The losses are similar for the case with and without the cavity slot in the absence of purge flow. A shift of the loss peaks away from the endwall occurs. Higher near-endwall loss occurs with a flat endwall since the inlet boundary layer is thicker.

As purge flow is introduced, the magnitude of “C1” increases significantly. The magnitude increases by 29% and 44% for the cases of PMFR=0.50% and 0.90%, respectively. The displacement of the core away from the endwall also occurs due to the migration and strengthening of the secondary flow structures.

The mass-averaged deviation from the primary flow direction is displayed in Fig. 6.28(b). The intensification of the secondary flows results in increased under/overturning at the cascade outlet. The underturning peak associated with the passage vortex and trailing shed vorticity increases by 93%. A peak in overturning near the endwall occurs. The suction side

corner vortex causes the reduction of the overturning. In cases where the purge flow is injected, the passage vortex is displaced away from the endwall. The contribution of the suction side corner vortex is not masked for the cases where no pure flow is injected. The overturning peak increases by 148% for the maximum purge massflow ratio investigated.

The secondary kinetic energy coefficient displayed in Fig. 6.28(c) complements the previous quantities. The K_{SKE} produced by the secondary flow structures is constrained between the endwall and z/H≈0.20. Starting from the endwall, the combination of the suction side corner vortex with the near wall overturning gives rise to a first region of increase K_{SKE} ("B"). Toward midspan, K_{SKE} decreases due to the weak interaction between the secondary flow structures. A following spike above the latter occurs where the passage vortex and trailing shed vorticity interact ("A")

The K_{SKE} distributions for the NC and PMFR=0.00% cases have the same topology throughout the span. Near the endwall, the K_{SKE} associated with the endwall flow is higher up to z/H≈0.05. On the other hand, the K_{SKE} associated with the passage vortex and trailing shed vorticity displays a similar magnitude even though it is lifted off towards the center of the passage. The increase of the K_{SKE} near the endwall results from increased overturning when injecting purge flow. A distinct peak in this region occurs due to the intensified suction side corner vortex with a larger spanwise extent. As the purge massflow ratio is increased, the peak associated with the passage vortex and trailing shed vorticity is pushed away from the endwall. Comparatively to the NC case, the magnitude of the K_{SKE} associated with this region increases by 135% and 205%, for PMFR=0.50% and 0.90%, respectively.

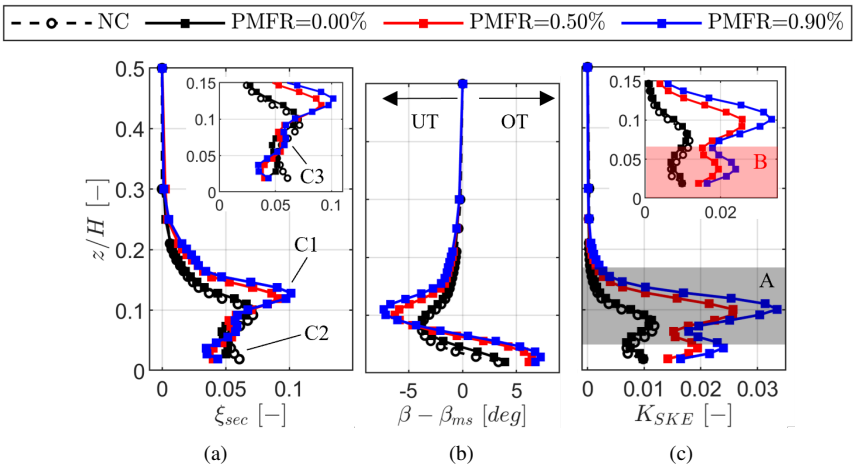

Figure 6.28: Impact of endwall geometry and purge flow on radial profiles of mass-averaged quantities: secondary kinetic energy loss coefficient (a), deviation from primary flow direction (b), and secondary kinetic energy coefficient (c).

A loss breakdown similar to the ones performed for the steady inlet flow cases (see Fig. 6.21) was performed. The purge flow contribution is considered by substituting the freestream total pressure with the mixed-out inlet total pressure. The method reported by de la Rosa Blanco et al. [11], based on a constant-area mixing calculation of the inlet total pressure, is used:

$$P_{0,mix} = \frac{\dot{m}_{main} P_{01,fs} + \dot{m}_{purge} P_{0,cav}}{\dot{m}_{main} + \dot{m}_{purge}} \tag{6.6}$$

The total pressure inside the splitter (see Fig. 2.5 and Fig. 2.6) is used instead of the $P_{0,cav}$. This limits the variation of $P_{0,mix}$ within $\pm$8 Pa for the highest purge massflow ratio. This variation is not expected to impact the conclusions of the loss breakdown.

The profile loss was found to be invariable. The purge flow effect does not extend to midspan. Accounting for the thicker inlet boundary layer for the case without cavity slot, the net endwall loss increased for the remaining cases. Introducing the cavity slot without purge flow injection increased the planewise losses by 8%. As the purge massflow ratio was increased to 0.50% and 0.90%, the loss further increased by 39% and 61% with respect to the case without a cavity slot. The loss breakdown values are reported in Appendix G.

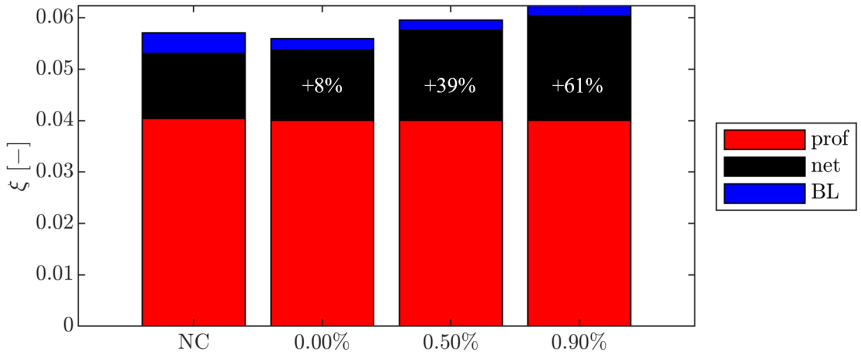

Figure 6.29: Breakdown of the planewise mass-averaged losses for cases with and without cavity slot and varying purge flow.

6.3 Time-Resolved Measurements

6.3.1 Unsteadiness of the Inlet Boundary Layer

The wake generator causes a modulation of the cascade inlet flowfield. The fast-response virtual four-hole probe characterized the unsteadiness. Fig. 6.30(a) displays the inlet normalized total pressure radial profile measured at y/g=0.00. The measurements were performed at Plane 02, which sits upstream of the cavity slot. The time-averaged quantity measured by the Cobra five-hole probe and fast-response virtual four-hole probe agree. A maximum variation of 20 Pa occurs at z/H$\approx$0.10. Similarly, the fast-response virtual four-hole probe well captures the angular profile with respect to the Cobra five-hole probe (see Fig. 6.30(b)).

The fast-response virtual four-hole probe was used to quantify the radial distributions of turbulence intensity. Fig. 6.31 displays the radial profiles of turbulence intensity measured at different pitchwise locations. The turbulence intensity increases in the boundary layer by nearly 45%. The pitch-to-pitch variation is contained within $\pm$0.15%. Volino et al. [14], and MacIsaac and Sjolander [15] have similarly reported an increase in the boundary layer in the scope of low-speed cascade testing.

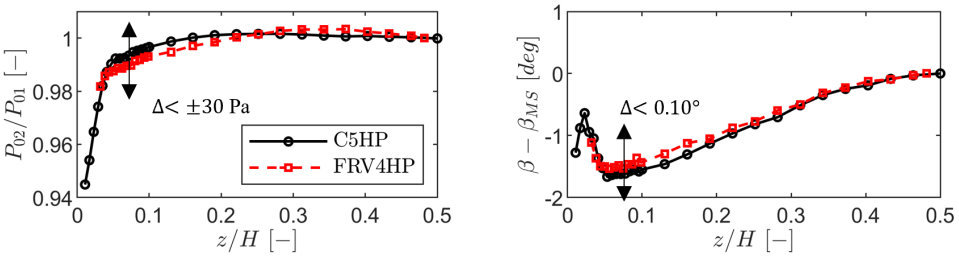

Figure 6.30: Inlet quantities measured with Cobra five-hole probe and fast-response virtual four-hole probe at Plane 02 and y/g=0.00: inlet normalized total pressure (a) and primary flow direction (b).

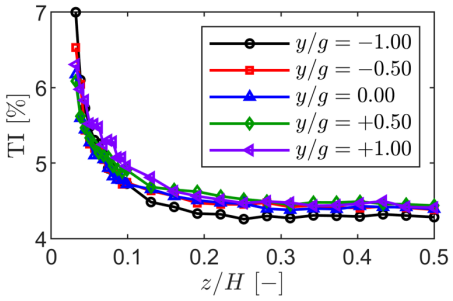

Figure 6.31: Radial profiles of turbulence intensity measured with the fast-response virtual four-hole probe at Plane 02.

Fig. 6.32 displays the mapping of different inlet aero-thermodynamic quantities for a given time instant (t/T≈0) along two cascade pitches and from the endwall up to midspan.

Fig. 6.32(a) displays the mapping of inlet fluctuations of total pressure normalized by the inlet freestream total pressure. The wake deficit is represented by low values of $\Delta P_{02}/P_{01,fs}$. Two adjacent wakes are highlighted as "B" and "C". The wakes are skewed due to the rotating motion of the wake generator that imposes radial velocity when the bar is not aligned with the leading edge. In addition, as the velocity decreases in the boundary layer region, the wake takes more time to convect and reach the same pitchwise coordinate. Due to the spatial resolution of the fast-response virtual four-hole probe, the first measured point near the endwall does not allow drawing considerations in the boundary layer. The wake displays a relatively two-dimensional nature from the midspan to the nearest point to the endwall.

The total pressure deficit isolines are superimposed with the angular fluctuations in Fig. 6.32(b). The bar profile regarding angular fluctuations is also conserved along the span. The same conclusions can be drawn for the turbulence intensity displayed in Fig. 6.32(c). The flow only starts to be influenced by boundary layer effects below z/H≈0.10. This is evidenced by the correlation coefficient (see Eq. 2.54) map in Fig. 6.32(d). The coefficient quantifies how well the phase-averaged pressure measured by the FRV4HP is correlated with the wake generator bar passing event. The correlation coefficient displays a rapid decrease near the endwall as the boundary layer flow is less correlated with the bar passing events. The correlation coefficient drops by nearly 50% between z/H=0.10 and 0.05. Lastly, it is found that the 2D flow correlates differently with the wake passing. Line "A" denotes a valley in R-squared. This line is periodic in pitch and front of the blade leading edge.

The fast-response virtual four-hole probe was used to quantify the unsteadiness of the inlet conditions. Fig. 6.33 displays the phase-resolved fluctuations of total pressure, primary flow direction, and turbulence intensity along different spanwise locations.

The amplitude of the total pressure fluctuations is found to be conserved up to z/H=0.06. A phase shift by nearly 20% of the bar phase occurs between measurements at midspan and z/H=0.10. Near the endwall, point "A" denotes a decrease in the wake deficit by 27% from z/H=0.10 to the point near the endwall. The phase shift is also observable in the freestream region denoted with "B".

The previous findings are analogous to the angular fluctuations in Fig. 6.33(b). In the wake deficit region denoted by "A", the angular fluctuations decrease by 23% from midspan to near the endwall.

The turbulence intensity phase-resolved traces are displayed in Fig. 6.33(c). The undisturbed level line is also shown for completeness. Up to z/H=0.10, the freestream value ("B") is comparable to the undisturbed one. In addition to the increase of the mean level towards the endwall, the amplitude of the fluctuations also increases by 8% at the nearest point to the endwall with respect to the midspan.

Lastly, the inlet cascade boundary layer strongly influences the secondary loss development. The steady-state boundary layer is reported in Section 6.2.1.1. The fast-response virtual four-hole probe was used to estimate the phase-resolved variation of the boundary layer thickness at Plane 02. Since the probe measures up to z/H≈0.05, the endwall quantities have been calculated assuming a no-slip condition. Nonetheless, the quantity magnitude provides a good order of magnitude for boundary layer fluctuations. The phase-resolved displacement thickness normalized by the true chord is displayed in Fig. 6.34. The traces are shown for

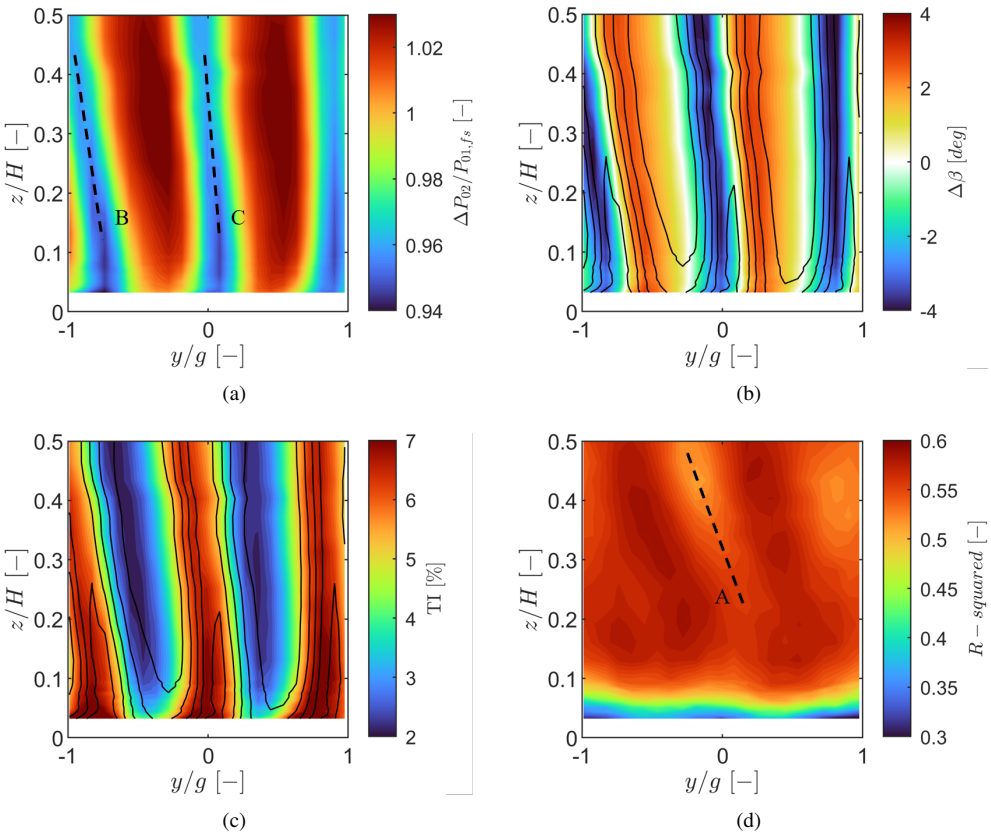

Figure 6.32: Inlet mapping at t/T=0: normalized total pressure fluctuations (a), angular fluctuations (b), turbulent intensity (c), and correlation coefficient (d).

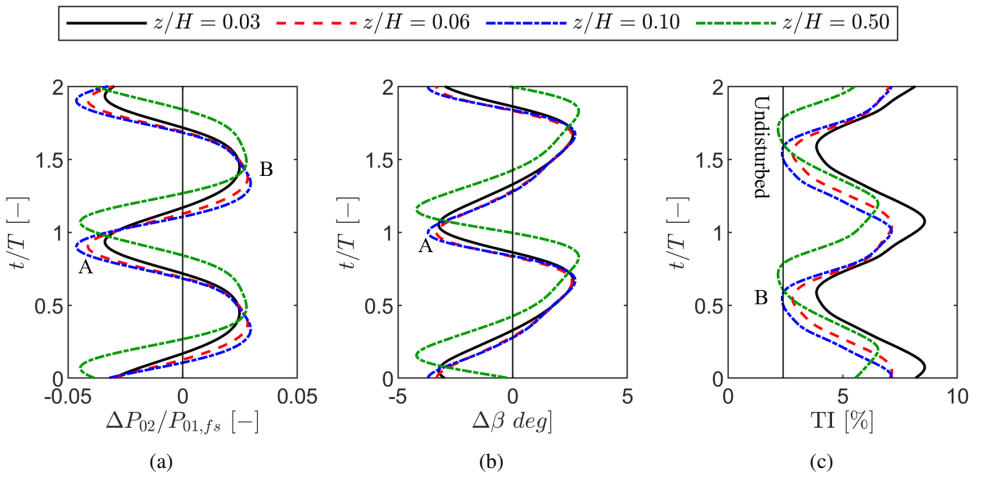

Figure 6.33: Phase-resolved inlet quantities with varying spanwise location: normalized total pressure fluctuations (a), angular fluctuations (b), and turbulent intensity (c).

three pitchwise locations: y/g$\in \{-0.50, 0.00, +0.50\}$.

Three distinct profiles occur for each pitchwise location due to the wake generator layout. Even though the mean thickness is larger at negative pitchwise locations, the fluctuations are around two times lower than at y/g=0.00 and positive pitchwise locations. This aligns with the steady results reported in Fig. 6.6. The mean level is higher than the one measured by the Cobra five-hole probe due to the lack of points near the endwall and the no-slip condition.

The traces at y/g=0.00 and +0.50 display a similar mean level and amplitude signature. A phase shift by nearly 50% of a bar passing period is visible. At y/g=0.00, the displacement thickness is varying by $\pm$0.35 mm. Literature concerning the unsteadiness of the inlet boundary layer is scarce. Studies dealing with the impact of unsteady wakes often report periodic modulation and reduction of the secondary loss [14, 16]. However, the variation of the inlet boundary layer thickness is not often reported, even though it is likely to be modulated since the introduction of wake generator bars into the flow field is made through endwall slots. The variation of the inlet boundary layer thickness reported in this work is likely one of the reasons impacting the secondary flow modulation at the outlet (see Section 6.3.4).

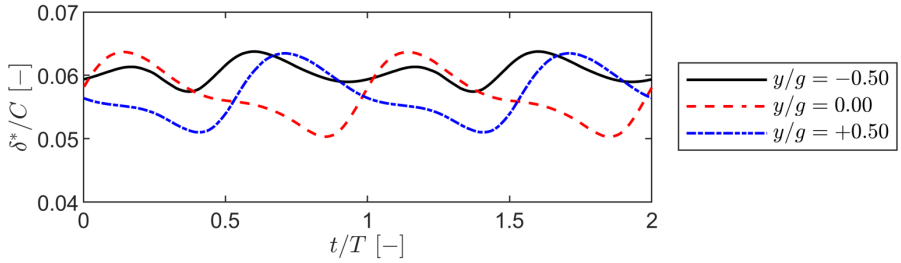

Figure 6.34: Phase-resolved boundary layer thickness at Plane 02.

6.3.2 Unsteadiness of the Inlet Purge Flow

The fast-response virtual four-hole probe addressed the potential unsteadiness of the inlet purge flow at Plane 03. A time-averaged analysis was performed to confirm the validity of the measurements with respect to the pneumatic virtual four-hole probe. Fig. 6.35(a) displays the radial profile of normalized total pressure at Plane 03 measured for two purge massflow ratios.

Between the two purge massflow ratios, the profiles are superimposed for each probe. A discrepancy between both probes is present near the endwall. The variation at z/H=0.10 is within $\pm$30 Pa, within the instrument uncertainty.

The results of deviation from the primary flow direction displayed in Fig. 6.35(b) highlight similar trends. The angle variation is within $\pm 0.20^\circ$ and is considered small considering that the probe is measuring at the leading edge plane.

The turbulent quantities are also insensitive to the purge massflow ratio. The turbulence intensity relies on the local freestream velocity. Since the measurements are performed at Plane 03, the retrieved velocity may be impacted by the potential flowfield of the cascade. Therefore, the turbulent kinetic energy was also used to assess the impact of the purge massflow ratio on the inlet turbulent quantities.

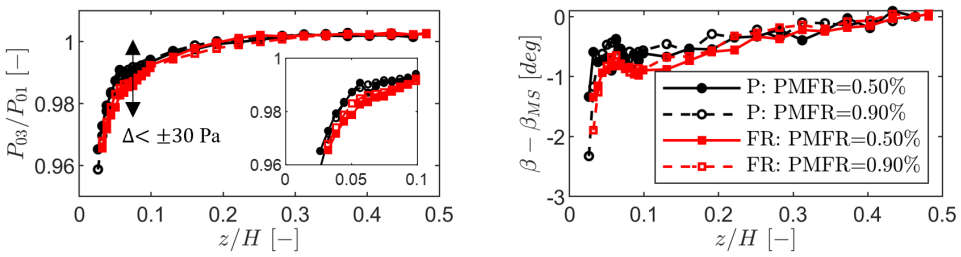

Figure 6.35: Comparison between inlet quantities measured with PV4HP and fast-response virtual four-hole probe at Plane 03 and y/g=-0.83: inlet normalized total pressure (a) and deviation from primary flow direction (b).

Fig. 6.36(a) displays the radial profiles of turbulent kinetic energy measured at Plane 03. The one measured at Plane 02 is reported for completeness. Turbulence decay from Plane 02 to 03 causes the turbulent kinetic energy to drop. In addition, the freestream value at Plane 02 was subtracted from the profile, and the latter was superimposed with the profiles at Plane 03. The profiles are all superimposed, suggesting that the same decay of turbulent kinetic energy occurs along the span and that the purge flow does not impact the flow fluctuations at the cascade inlet.

Similar findings concerning the turbulence intensity were found (see Fig. 6.36(b)). The turbulence intensity decays from Plane 02 to Plane 03. By subtracting the turbulence intensity measured at midspan from the radial profile measured at Plane 02, the profiles collapse up to z/H≈0.10. After this, the turbulence intensity increases faster for the Plane 02 measurements. Nonetheless, the difference to the Plane 02 measurements is around 0.20%.

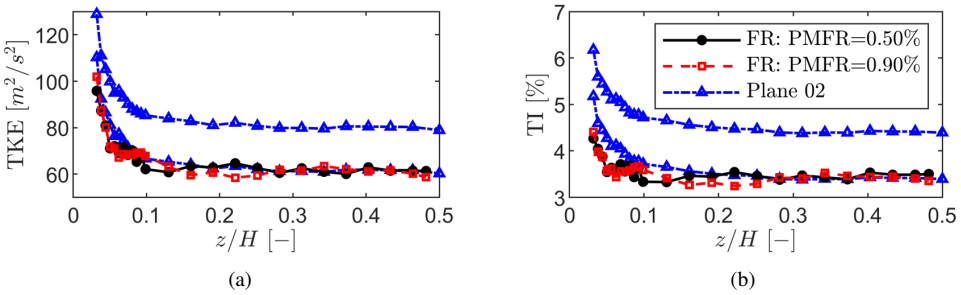

Figure 6.36: Inlet radial profiles of turbulent quantities at y/g=-0.83: turbulent kinetic energy (a) and turbulence intensity (b). The blue data points with lower magnitude represent the profile at Plane 02 normalized to match the midspan value at Plane 03.

The unsteadiness of the flow downstream of the slot was investigated in terms of total pressure, angular fluctuations around the mean value, and turbulence intensity. The investigation was performed at several spanwise locations for the two purge massflow ratios investigated. Fig. 6.37 displays the time traces of the different quantities at z/H=0.03, 0.06, 0.10,

and 0.50. It was found that the purge flow has little impact on the magnitude of the pressure and angular fluctuations. The pressure fluctuations displayed in Fig. 6.37(a) decrease by 16% with purge massflow ratio (equivalent to $\sim$50 Pa). Near the endwall, there is a phase shift of the quantities with varying purge flow (Δt/T=0.06). The variation of the turbulence intensity (see Fig. 6.37(c)) is significant. Due to the fuller profile for the PMFR=0.90% case, a variation in the turbulence intensity past the peak can reach up to 0.50% in absolute terms.

Towards higher spanwise locations, the phase shift between both cases is reduced, and so is the impact of the purge flow. The turbulence intensity profiles at z/H=0.10 are worth pointing out. The amplitude and topology of the fluctuations are similar for both cases. However, there is a shift in the mean. The dependence of the local velocity on the turbulence intensity cannot justify the latter. The mean turbulent kinetic energy follows the same trend displayed in Fig. 6.36(a). The difference is likely attributed to the scattering of the mean turbulent kinetic energy measured with the fast-response virtual four-hole probe at Plane 03.

At midspan, both the pressure and angular fluctuations are in phase. The turbulence intensity behaves similarly to that of the location above. Nonetheless, the amplitude of the fluctuations and phase are similar.

6.3.3 Unsteadiness on Blade Surface

Identifying the secondary flow structures on the blade surface was achieved through the 3D CFD results described in Section 6.2.3.

Fig. 6.38(a) displays the viscous stress streamlines superimposed to the contour of normalized shear stress. The signature of the passage vortex, suction side corner vortex, and wall-induced vortex is traceable through the streamlines. The stagnation lines were superimposed to the skin friction coefficient in Fig. 6.38(b). The stagnation lines can be divided into separation (S_{PV}) or reattachment (R_{WIV}, R_{CV}) depending on the vorticity of the secondary flow structure. These lines follow paths of low skin friction. On the other hand, they are the boundaries of increased shear stress. The paths of increased shear stress qualitatively describe the trajectory (T_{PV}, T_{WIV}) of the secondary flow structures.

The hot-film data has been used to draw considerations on the location of the secondary flow structures for the cases with unsteady inlet flow. The analysis included the statistical moments that can be investigated due to the bandwidth of the instrumentation. Fig. 6.39(a)– 6.39(c) displays the quasi-wall shear stress on the blade suction side for the case without cavity slot and cases with increasing purge massflow ratio. The quasi-wall shear stress is normalized by the one at midspan at each location along the surface. Fig. 6.39(d)– 6.39(f) displays the standard deviation of the bridge voltage. Fig. 6.39(g)– 6.39(i) displays the skewness of the bridge voltage.

The contours allow the identification of a region of increased shear stress in the region impacted by the passage vortex. The separation line follows a path of decreased shear. In addition, the separation line is a limit of high standard deviation in the region characterized by the wall-induced vortex. Lastly, the S_{PV} also follows a path of increased skewness. In the passage vortex region, the trajectory has been identified by low std(E) and as the separation line between two regions of negative skewness.

The wall-induced vortex region was characterized by high shear stress and std(E). The upper bound of the region was identified from the sharp reduction of shear stress and std(E).

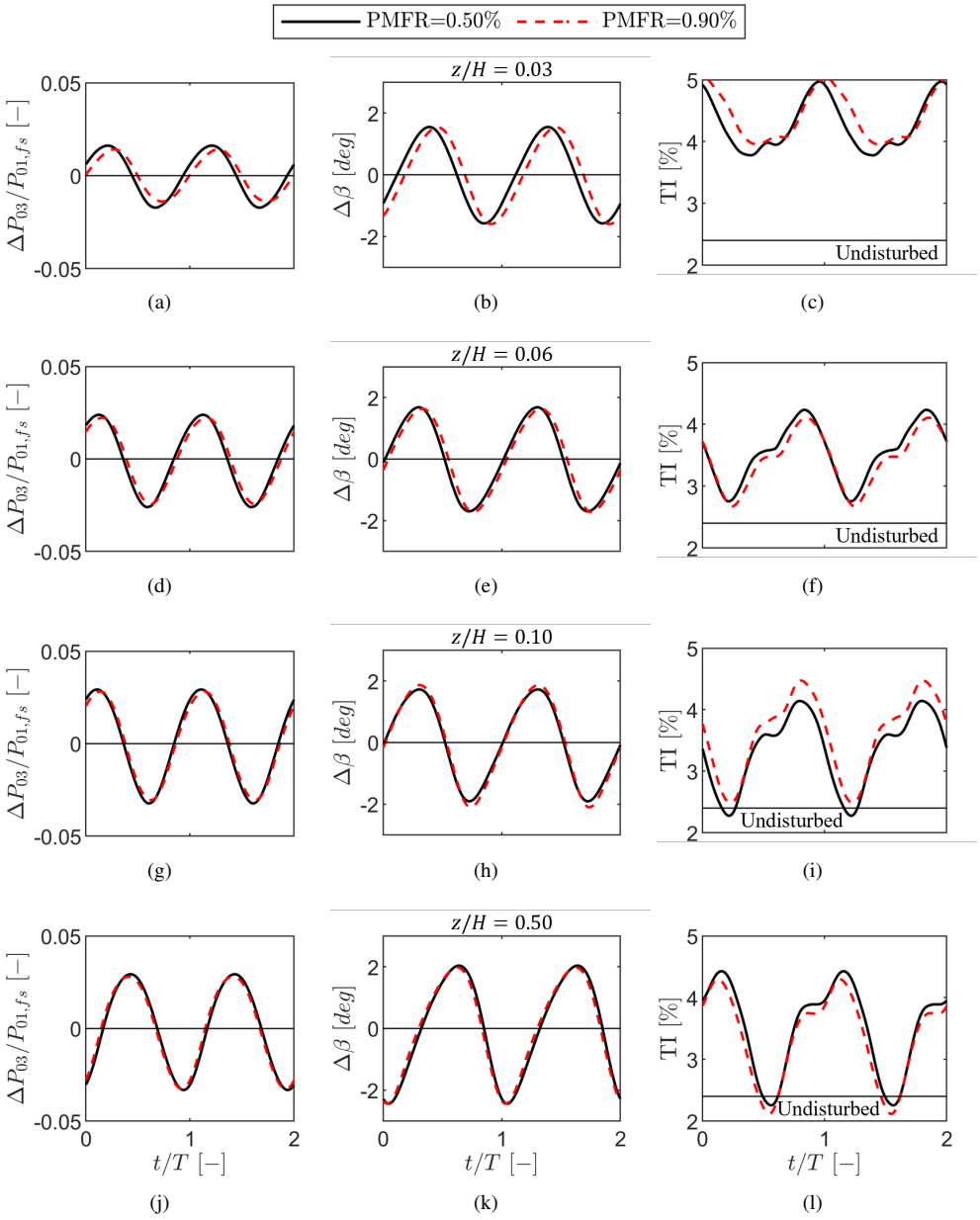

Figure 6.37: Phase-averaged traces of normalized total pressure fluctuatiIdentifyingions, and turbulence intensity at Plane 03, y/g=-0.83: z/H=0.03 (a–c), z/H=0.06 (d–f), z/H=0.10 (g–i) and z/H=0.50 (j–l).

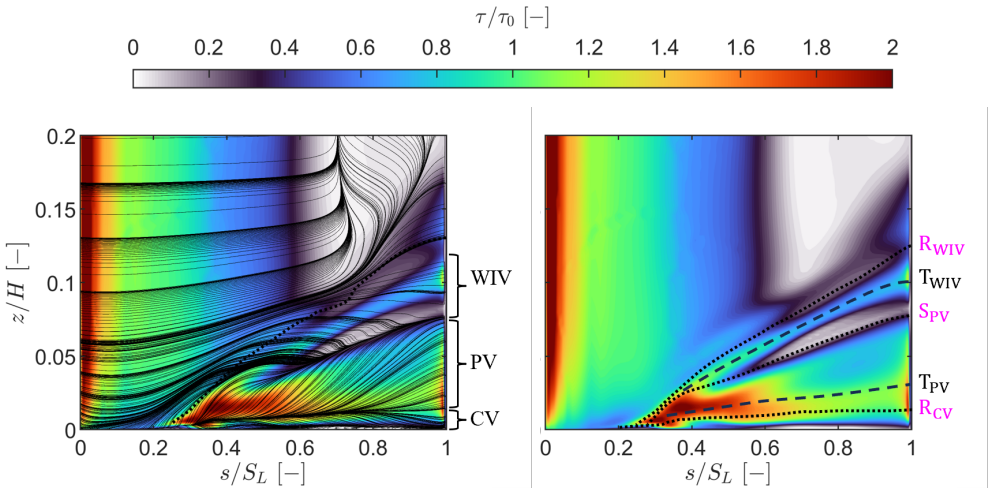

Figure 6.38: Contour of skin friction coefficient superimposed with viscous stress streamlines (a) and identification of stagnation lines of secondary flow structures (b).

Similar to the passage vortex, the stagnation line also follows a path of increased skewness. The trajectory of the wall-induced vortex follows the maximum shear stress and splits the region of high std(E) into two regions.

The contours provide a qualitative interpretation of the displacement of the secondary flow structures away from the endwall as purge flow is injected in the passage. The bridge voltage and bar passing frequency correlation coefficient is displayed in Fig. 6.39(j)– 6.39(l). The contours highlight that wake-boundary interaction mechanisms mainly impact the low correlation of the blade surface fluctuations of voltage in the secondary flows compared to the 2D portion of the blade. The bar passing frequency does not significantly modulate the location of the secondary flow structures on the blade surface. The extent of the region increases with the purge massflow ratio.

Based on the identified secondary flow topology on the blade suction side, the FR pressure sensors were used to characterize the secondary flows regarding pressure fluctuations. Fig. 6.40(a)– 6.40(c). The fluctuations in the secondary flow region are considerably lower than in the 2D region.

Low-pressure fluctuations are observed in the stagnation lines (T_{WIV}, T_{PV}). In the reattachment line of the wall-induced vortex, the last sensor measures fluctuations of $\pm$20 Pa for a typical inlet freestream total pressure of $\sim$10,000 Pa. The fluctuations in the separation line of the passage vortex are significantly higher. They can reach up to $\pm$70 Pa at the location of the last sensor.

The pressure fluctuations in the passage vortex and wall-induced vortex regions are higher. In the passage vortex region, $\pm$100 Pa fluctuations were measured for the NC case. The fluctuations associated with the passage vortex increase with the purge massflow ratio. At PMFR= 0.90%, the fluctuations reached $\pm$110 Pa. The fluctuations caused by the wall-induced vortex are similar in magnitude to the ones caused by the passage vortex.

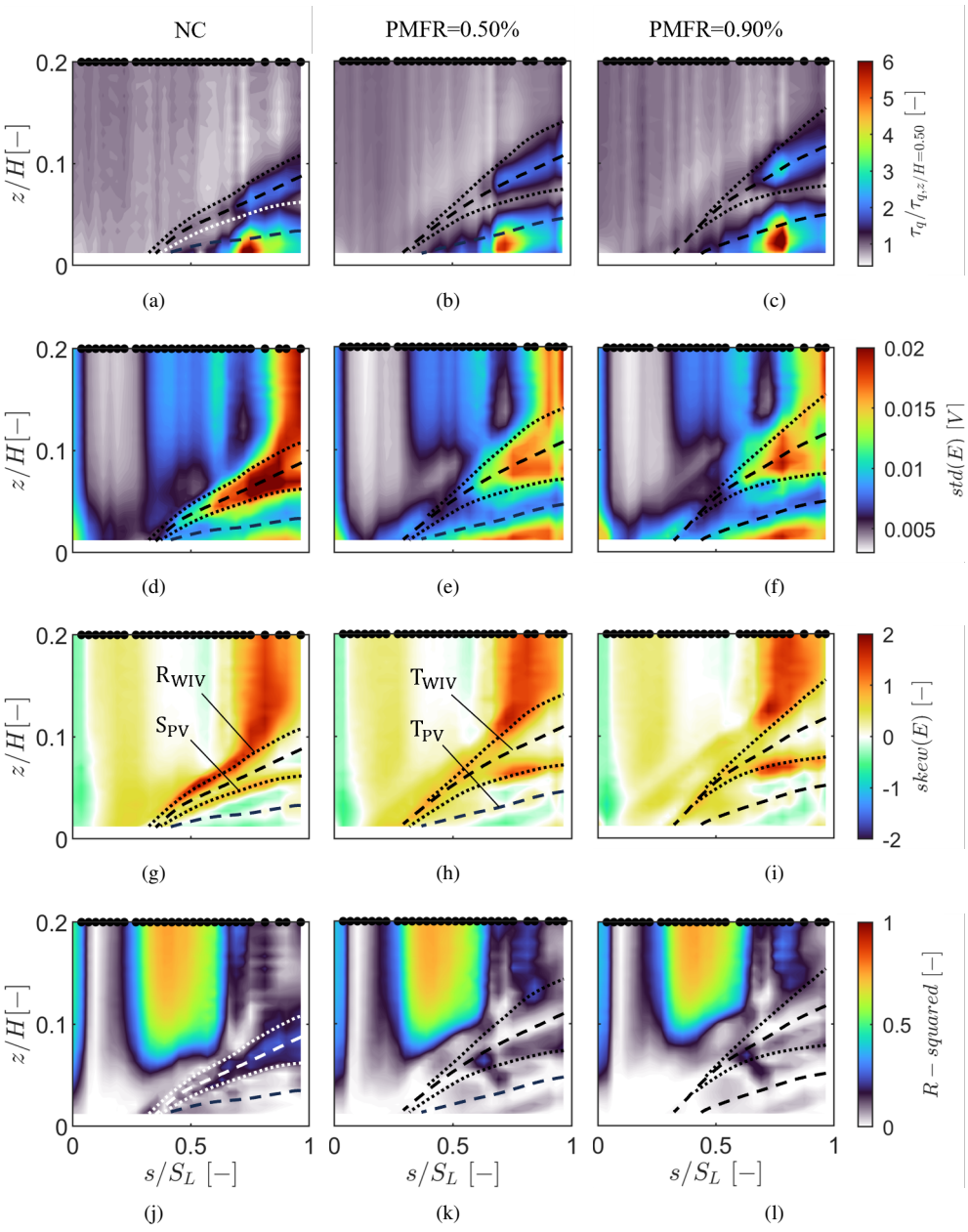

Figure 6.39: Contours for cases with unsteady inlet flow, without and with cavity and purge flow: normalized quasi-wall shear stress (a–c), standard deviation of bridge voltage (d–f), skewness of bridge voltage (g–i), and correlation coefficient (j–l).

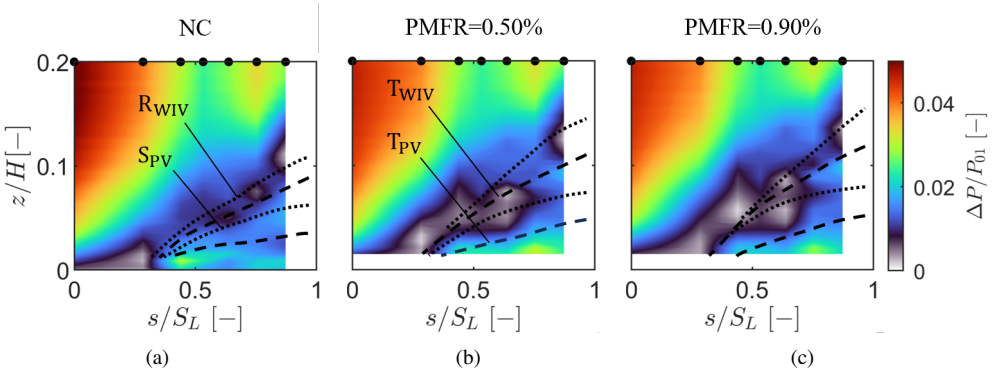

Figure 6.40: Contour of normalized surface pressure fluctuations: no cavity (a), PMFR=0.50% (b), and PMFR=0.90% (c).

6.3.4 Secondary Flows

Before investigating the unsteadiness in the secondary flows downstream of the cascade, the fast-response virtual four-hole probe time-averaged quantities were compared against the L-shaped five-hole probe. Fig. 6.41 displays the contours of kinetic energy loss coefficient (see Fig. 6.41(a)), streamwise vorticity coefficient (see Fig. 6.41(b)) and secondary kinetic energy (see Fig. 6.41(c)) obtained from the fast-response virtual four-hole probe for the PMFR=0.90% case. The contours are superimposed with the isolines from the contours obtained with the L-shaped five-hole probe (see Fig. 6.25(d), Fig. 6.26(d), Fig. 6.27(d)). The color bar limits are also taken from the L-shaped five-hole probe measurements.

The topology agrees with the L-shaped five-hole probe measurements, particularly the kinetic energy loss coefficient displayed in Fig. 6.41(a). The loss peak migrates closer to the endwall due to the shift of the secondary flow structures. The streamwise vorticity coefficient displayed in Fig. 6.41(b) highlights a more substantial magnitude in the core of the secondary flow structures. The wake of the blade is characterized by negative streamwise vorticity. The secondary kinetic energy (see Fig. 6.41(c)) also displays a higher level in the passage vortex and trailing shed vorticity interacting region. The magnitude is overpredicted with respect to the L-shaped five-hole probe measurements. Similar to the streamwise vorticity, the wake is characterized by non-zero values.

Compared to the kinetic energy loss coefficient, the higher discrepancy between both probes for the streamwise vorticity and secondary kinetic energy loss coefficient is attributed to the more significant fast-response virtual four-hole probe interference. The probe is inserted and measured at Plane 06, whereas the L-shaped five-hole probe is inserted further downstream. The most impacted quantities are the retrieved flow angles utilized to compute the secondary velocity components used in K_ω and K_{SKE}.

The probe interference can be better appreciated in the pitchwise distribution of deviation from primary flow direction, cascade pitch angle, and kinetic energy loss coefficient at midspan displayed in Fig. 6.42. As Torre et al. [17] highlight, introducing a probe downstream generates a sinusoidal-like angular distribution. The probe interference is mainly related to the effect of the probe stem. Fig. 6.42(a) highlights the same topology for both

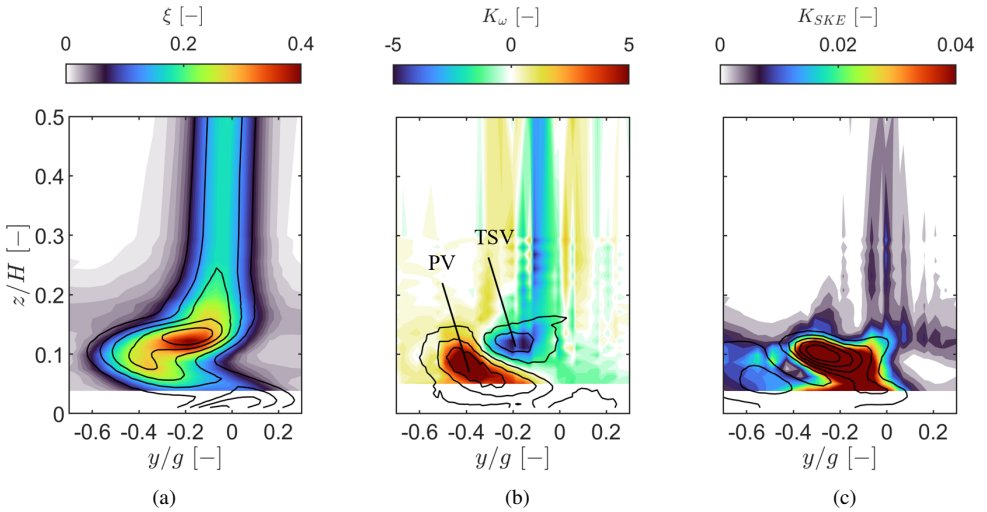

Figure 6.41: Contours obtained with FRV4HP superimposed with isolines of L5HP for PMFR=0.90% case: kinetic energy loss coefficient (a), streamwise vorticity coefficient (b) and secondary kinetic energy (c).

probes. The under/overshoots related to the probe interference increase by 70% when the fast-response virtual four-hole probe is considered.

Nonetheless, the mean value is not impacted. The impact of the probe on the cascade pitch angle is more significant for the fast-response virtual four-hole probe. The quantity overshoots by more than 2° at y/g≈-0.16. The cascade pitch fluctuations around the mean are responsible for the non-zero values of streamwise vorticity coefficient and secondary kinetic energy in the blade wake.

The kinetic energy loss coefficient relies solely on the total pressure measured by the probe and endwall static pressure. Even though the total pressure is retrieved from the aerodynamic coefficients and is a function of the yaw and pitch angle in the probe reference system, the quantity is remarkably insensitive to them in the range of angles measured in this work. As a result, the L-shaped five-hole probe and fast-response virtual four-hole probe retrieved kinetic energy loss coefficient displayed in Fig. 6.42(c) are in good agreement. In addition, the loss is insensitive to the purge massflow ratio at midspan.

The discrepancies between both probes in the secondary flows' region are addressed with the pitchwise mass- and time-averaged radial profiles. The deviation from the primary flow direction is displayed in Fig. 6.43(a). The radial profiles measured with both probes follow similar trends. The underturning peak location and magnitude are identical for the case without purge flow. The peak value is higher by 11% if the L-shaped five-hole probe is considered. For the cases with purge flow, the underturning peaks are shifted towards the endwall by as much as 1.35 mm. The peak underturning is 13% higher when measured with the L-shaped five-hole probe.

The cascade pitch angle displayed in Fig. 6.43(b) shows higher discrepancy between both probes. The agreement between both probes is good from midspan up to z/H≈0.10, after

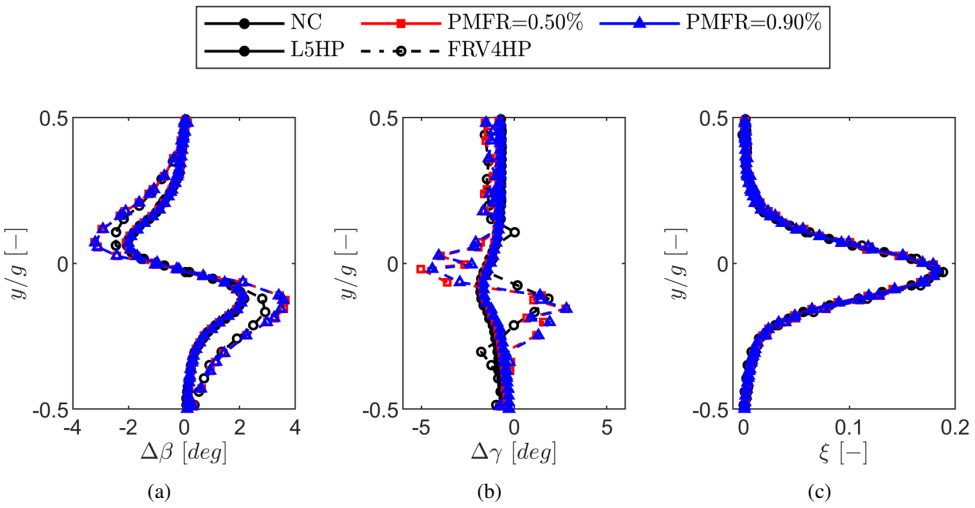

Figure 6.42: Pitchwise distribution measured with L5HP and FRV4HP: deviation from primary flow direction (a), cascade pitch angle (b), and kinetic energy loss coefficient (c).

which the fast-response virtual four-hole probe measured angle increases to the closest measured point to the endwall. At z/H≈0.05, the angle measured by the fast-response virtual four-hole probe is 4° larger than the one calculated for the L-shaped five-hole probe. The cascade pitch angle is impacted mainly by probe interference, especially as the probe gets closer to the endwall. The larger magnitude of the streamwise vorticity coefficient and secondary kinetic energy measured by the fast-response virtual four-hole probe compared to the L-shaped five-hole probe is attributed to the cascade pitch angle.

The kinetic energy loss coefficient reflects similar trends (see Fig. 6.43(c)). The higher peak loss (PV+TSV) migrates toward the endwall when measuring with the fast-response virtual four-hole probe. The magnitude of the peak is higher when measuring with the fast-response probe. The most considerable discrepancy occurs when no purge flow is injected, for which the loss peak is underpredicted by 24%.

Lastly, the secondary kinetic energy depends on the probe used to measure it. The K_{SKE} is found to be higher for the L-shaped five-hole probe measurements, even though the absolute local magnitude is higher for the other probe. The most significant variation occurs for the highest purge massflow ratio investigated (+29%).

Despite the variations induced by probe interference effects, the quantities are within the same order of magnitude, particularly the primary flow direction and kinetic energy loss coefficient.

The fast-response virtual four-hole probe computed turbulence intensity contours are presented in Fig. 6.44. The kinetic energy loss coefficient isolines are superimposed to relate the turbulence intensity topology to the existing secondary flow structures. The freestream turbulence value is around 2.20%. Even though at steady inlet flow conditions, Okada et al. [18] also found a decay of turbulence along the passage. The secondary flow region is characterized by turbulence intensity values exceeding 6% for the highest purge massflow ratio investigated. In particular, two distinct peaks of turbulence intensity can be distinguished

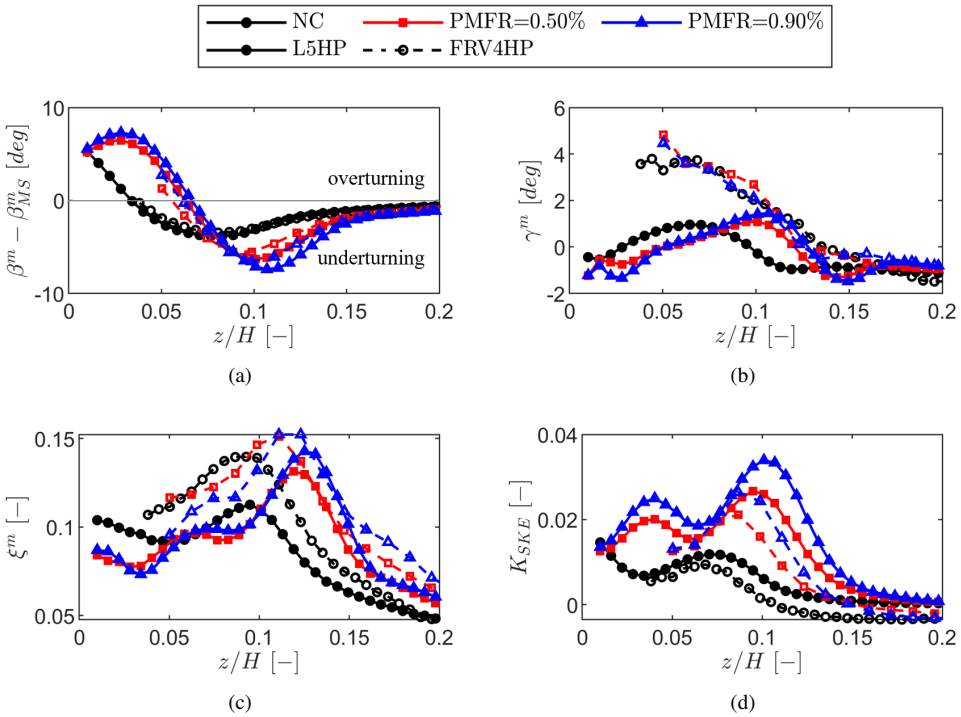

Figure 6.43: Mass-averaged quantities measured with L5HP and FRV4HP: deviation from primary flow direction (a), cascade pitch angle (b), kinetic energy loss coefficient (c), and secondary kinetic energy (d).

for the cases impacted by purge flow. Both individual peaks sit at the location of the trailing shed vorticity and passage vortex. The passage vortex-related turbulence intensity is higher in the core of the passage vortex with respect to the trailing shed vorticity. The findings are supported by linear cascade testing [19, 20].

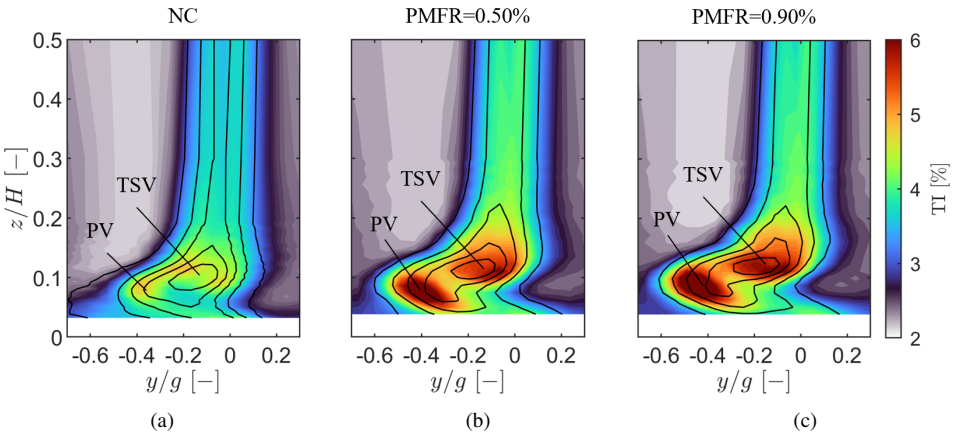

Figure 6.44: Contours of turbulence intensity superimposed with the kinetic energy loss coefficient isolines: NC (a), PMFR=0.50% (b) and PMFR=0.90% (c).

Fig. 6.45(a) displays the phase-averaged pitchwise averaged profiles of kinetic energy loss for the case without cavity, while Fig. 6.45(b) and Fig. 6.45(c) display the same for the case with PMFR=0.50% and 0.90%, respectively.

Two instants denominated as “Min.” and “Max.” are highlighted. The maximum corresponds to the phase instant at which the loss in the core resultant from the passage vortex and trailing shed vorticity reaches its maximum. The minimum corresponds to the phase instant at which the loss at the same spanwise location reaches the minimum. The phase instants at which the maxima and minima were extracted are reported in Table 6.3 for completeness.

Table 6.3: Phase instants at which the minimum and maximum of the loss core are observed for the case without cavity slot and with increasing purge massflow ratio.

	Min.	Max.
NC	0.227	1.015
PMFR=0.50%	0.544	1.095
PMFR=0.90%	0.430	0.980

Due to increasing wake relative velocity with spanwise location, the highest loss occurs at a position where the wake is passing Plane 06 at midspan. However, the wake has passed Plane 06 near the endwall. The maximum secondary flow loss occurs just after the wake has passed Plane 06. The interaction of the purge flow with the secondary flow development does not significantly impact the phase of the maximum. The phase of the minimum increases by injecting purge flow and is relatively insensitive to the purge massflow ratio. The extent in the

spanwise direction also increases with the purge massflow ratio, as highlighted by the marker "B".

The angular fluctuations centered around the midspan time-averaged deviation from the primary flow direction are displayed in Fig. 6.45(d), Fig. 6.45(e) and Fig. 6.45(f). The maximum loss peak coincides with a local minimum of underturning ("C") that results from the interaction of the passage vortex and trailing shed vorticity. The underturning peak is the highest for the highest purge massflow ratio. The minimum loss sits near the region with the lowest underturning when the secondary flow strength is the lowest. For the case without the cavity slot, there is an instant at which the underturning region is nearly suppressed. For cases with purge flow, the underturning decreases between two adjacent bar wakes. However, the local underturning never gets higher than -4°.

The phase-averaged mass-averaged turbulence intensity radial profiles are displayed in Fig. 6.45(g), Fig. 6.45(h) and Fig. 6.45(i). The maximum loss is not coincident with the peak turbulence intensity at midspan, as discussed in the Section dealing with the phase-averaged aerodynamics at midspan (see Section 5.3.3). The maximum turbulence intensity peak ("D") in the secondary flows' region occurs just after the maximum loss. The turbulence intensity signature develops in two regions of high turbulence intensity along the span. The first one sits at z/H≈0.05 and is likely associated with the passage vortex. The second sits at the span height of the loss core and is mainly the result of the trailing shed vorticity.

A better interpretation of what happens at each phase can be provided using phase-averaged contours. Fig. 6.46 displays the kinetic energy loss coefficient contours for each case investigated. The top row contains the contours at the phase instant corresponding to the minimum loss, while the bottom row contains the ones associated with the maximum loss. The contours are superimposed with the local secondary velocity vectors.

For the minimum loss, the contours concerning the cases with purge flow highlight the blade wake in the absence of the bar wake passing at Plane 06. For the case without cavity, the signature of the unsteady wake is still visible towards positive pitches. The phase-averaged mass-averaged diagram (see Fig. 6.45(a)) displays the intersection of the "Min." line with the wake at midspan. A loss core in the secondary flow region is observable for all cases.

The contour at the phase instant for which the highest secondary loss presents similar features for all the cases since the phase instant is identical. The blade wake is indistinguishable and mixed with the bar wake passing at Plane 06. Increased loss cores near the endwall are observable when compared against the minimum loss phase contours.

The contour for the minimum secondary loss for the case without cavity slot (see Fig. 6.46(a)) highlights the low underturning observed in Fig. 6.45(d). The increasing concentration of secondary velocity vectors near the loss core highlights the trailing shed vorticity in "A". However, the passage vortex is unidentifiable at this time instant. When the loss and underturning are maximum (see Fig. 6.46(d)), the trailing shed vorticity remains. In addition, the passage vortex ("B") can be identified from the secondary velocity vectors. The passage vortex is periodically weakened during consecutive bar-passing events. The statement is supported by the periodic decrease of the inlet boundary layer thickness (see Fig. 6.34).

For the cases impacted by purge flows, both the passage vortex and trailing shed vorticity are identifiable at the lower and higher loss instants. A concentration of secondary velocity vectors occurs in the interface of the passage vortex and trailing shed vorticity for the minimum loss. Increasing the purge massflow ratio does not significantly impact the mag-

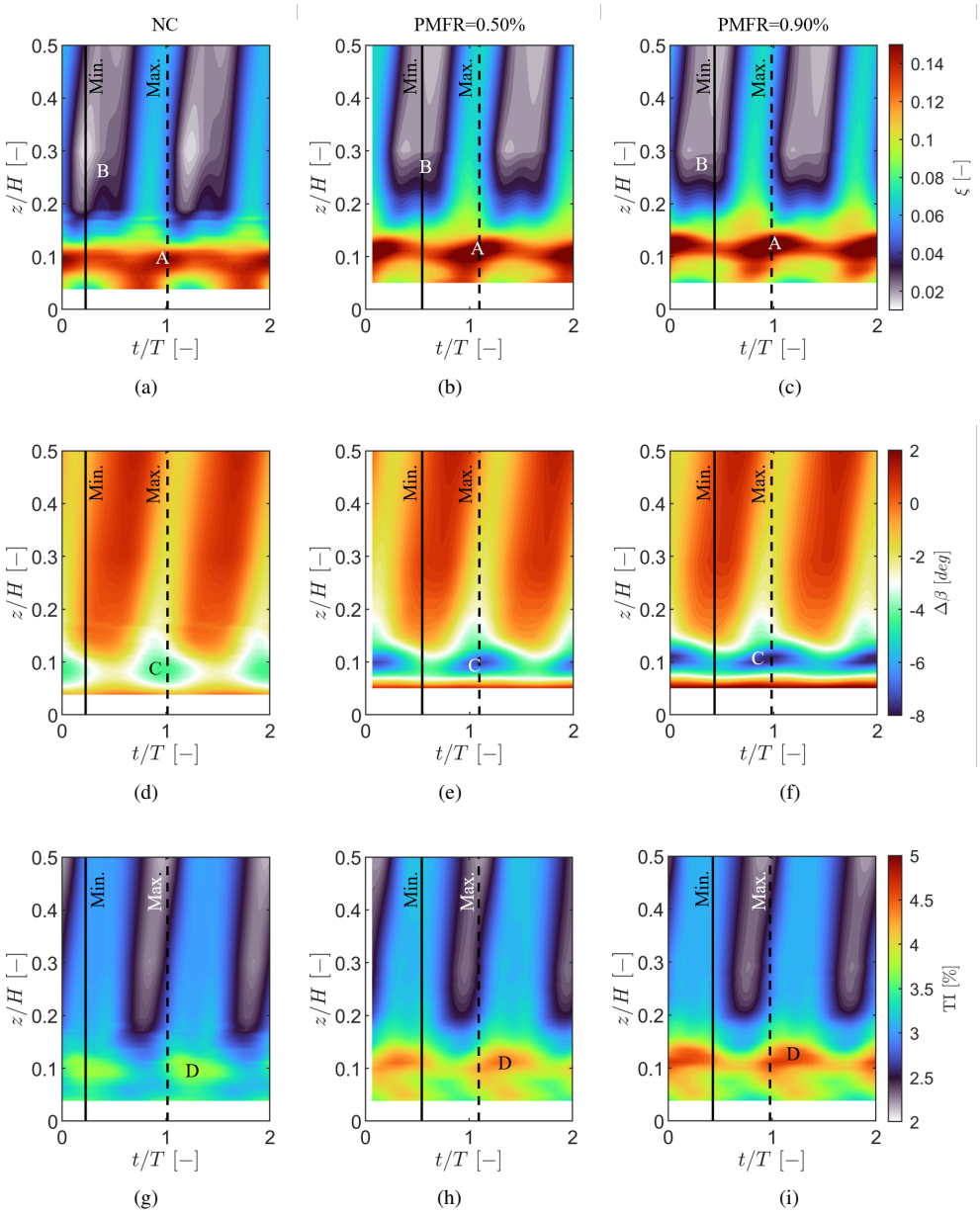

Figure 6.45: Phase-averaged pitchwise mass-averaged kinetic energy loss coefficient (a–c), deviation from primary flow direction (d–f), and turbulence intensity (g–i) for the case without the cavity, and cases with increasing PMFR.

nitude of the loss cores associated with both structures. The existence of a defined passage vortex between consecutive wake-passing events for the cases with purge reveals that the purge flow may have a more substantial effect than increasing the loss magnitude alone. The inlet boundary layer is still modulated, but the steady-state purge stream provides enough low-momentum fluid to be rolled up into the passage vortex.

At the maximum loss instants, the loss is found to increase significantly in the passage vortex ("B") and trailing shed vorticity ("A") regions. The stronger secondary flow structures cause the density of the secondary velocity vectors to increase.

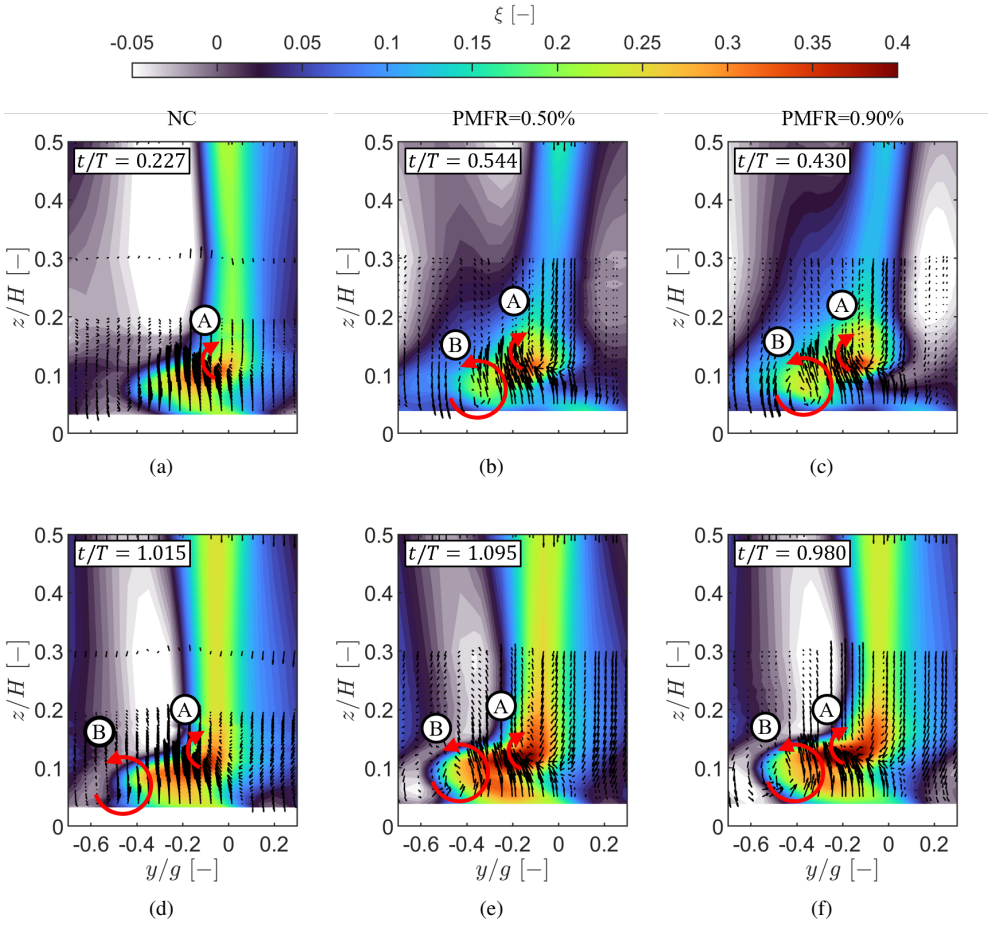

Figure 6.46: Instantaneous contours of kinetic energy loss coefficient at time instants of minimum (top row) and maximum (bottom row) secondary loss.

The same contours for the turbulence intensity are displayed in Fig. 6.47. Rather than using the secondary velocity vectors, the isolines of the kinetic energy loss coefficient are used to highlight the relative position between the loss cores and highly turbulent regions. Arrows extracted from the secondary velocity vectors are added to locate the secondary flow structures roughly.

For the case without the cavity slot, the turbulence intensity distribution at Plane 06 is

similar at the instants of minimum and maximum loss. A "strip" of high turbulence intensity sits at the boundary of the passage vortex. The region extends from the location of the trailing shed vorticity ("A") to the center of the passage vortex. The magnitude is not strongly impacted either.

When purge flow is injected, the contours at the instants of minimum and maximum loss are significantly different than the case without cavity slot but are similar in topology and magnitude. At the time of the lowest secondary loss, a strong core of turbulence intensity matches the location of the loss core, which is mainly impacted by the trailing shed vorticity. At this time instant, the passage vortex is at its weakest during one bar passing period. Even though there is a noticeable concentration of high turbulence intensity in the core of the passage vortex, the magnitude is 15% lower than in the trailing shed vorticity.

At the instant of maximum secondary loss, the turbulence intensity near the trailing shed vorticity is still larger than 6% and shifted towards the center of the passage. The turbulence intensity in the passage vortex core is 34% higher than in the trailing shed vorticity. The significant increase is likely associated with high levels of mixing in the passage vortex as it reestablishes its undisturbed state. Increasing the purge massflow ratio has little impact on the turbulence intensity in the passage vortex region (variation of $\sim$1%) and trailing shed vorticity.

The instantaneous contours reveal that the unsteady wake significantly modulates the outlet flowfield. The correlation coefficient between the FRV4HP center tap pressure and the wake generator bar passing frequency highlights which flow features are impacted by the unsteady wakes. Fig. 6.48(a), Fig. 6.48(b) and Fig. 6.48(c) displays the correlation coefficient for the cases without cavity slot and cases with purge flow. The contours are superimposed with the time-averaged isolines of kinetic energy loss coefficient to highlight the location of the bar wake and secondary flow structures. Schematic arrows are added to highlight the passage vortex and trailing shed vorticity.

The freestream region, especially at midspan, is the most correlated with the wake-passing events. The passage vortex region also correlates with the wake passing in the secondary flow structures. On the other hand, the trailing shed vorticity displays considerable insensitivity to the flow unsteadiness. As purge flow is injected into the flowfield, the secondary flow structure is lifted off the endwall. For the cases with purge, the low correlated region in the trailing shed vorticity region does not extend to the endwall. The overall topology and magnitude of the R-squared do not change significantly with the purge massflow ratio.

Fig. 6.48(d), Fig. 6.48(e) and Fig. 6.48(f) display the contours of maximum to minimum local fluctuations. Following the findings from the correlation coefficient, the loss fluctuations near the loss core are low. Three main regions of high fluctuations due to the unsteady wakes can be highlighted. The first one "A" is located in the freestream near the blade suction side. This results in low-momentum wake fluid accumulating near the blade suction side due to the cross-passage pressure gradient. The second one "B," sits at the location of the passage vortex, which was seen to be heavily modulated during one bar passing event. Lastly, "C" sits at the interface of the blade 2D flow with the secondary flow region near the trailing shed vorticity.

The kinetic energy loss coefficient fluctuations are quantified in the form of the bar chart displayed in Fig. 6.49. The near suction side fluctuations at "A" are seen to be independent of the case since the purge flow has little impact on the midspan flow. These are the lowest in

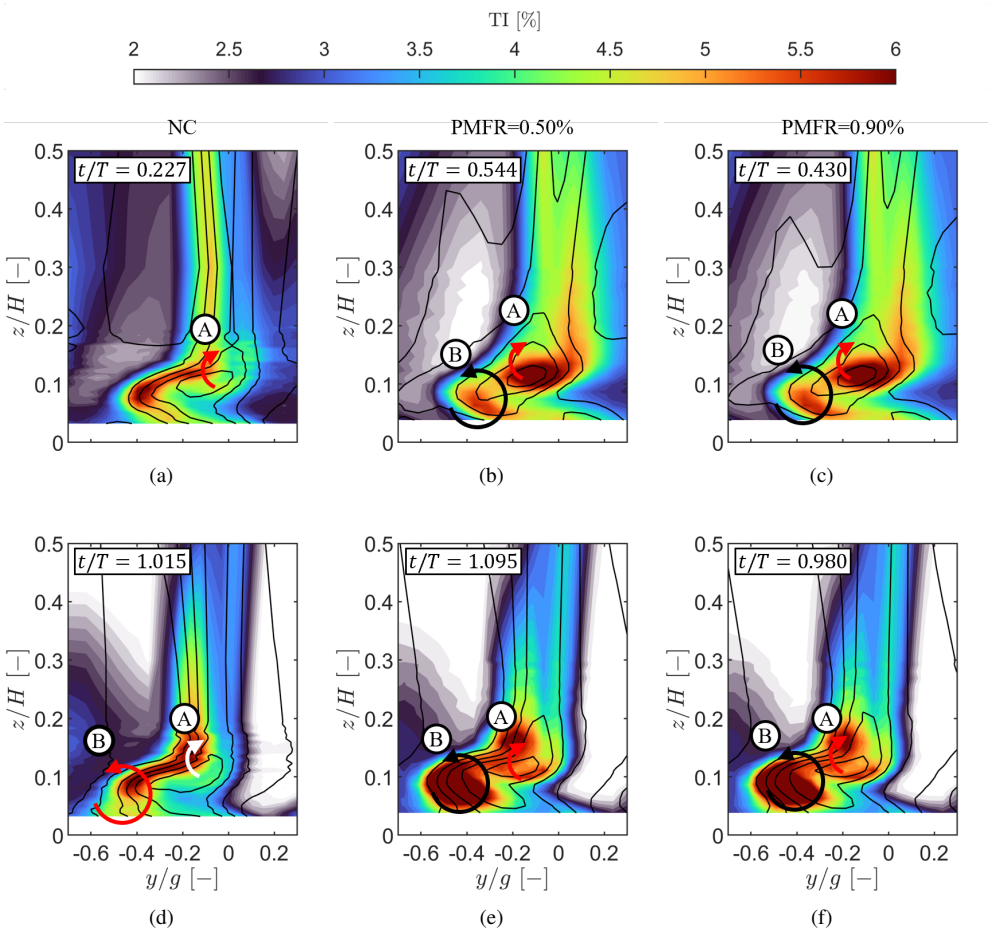

Figure 6.47: Instantaneous contours of turbulence intensity at time instants of minimum (top row) and maximum (bottom row) secondary loss.

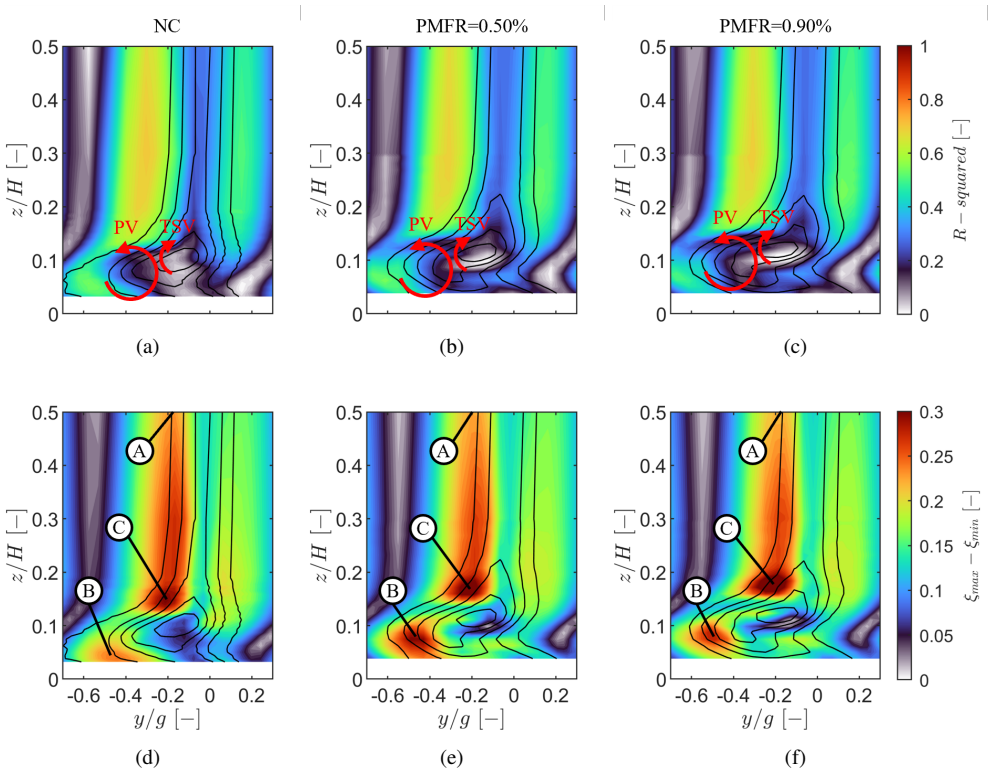

Figure 6.48: Correlation coefficient of center tap pressure (top-row) and kinetic energy fluctuations (bottom-row).

comparison to the remaining cases. The fluctuations in the passage vortex region are found to increase by 24% when purge flow is injected. The fluctuations were reduced by 7% with increasing purge massflow ratio. The latter is likely attributed to the higher contribution of the steadiness of the purge flow for a higher purge massflow ratio that is less susceptible to being modulated. The correlation coefficient agrees with the previous statement. Even though subtle, there is a decrease in the R-squared as the purge massflow ratio is increased.

The loss fluctuations in the trailing shed vorticity vicinity increase by introducing purge and increasing the purge massflow ratio. Likely, the latter region is mainly impacted by the higher time-averaged secondary flow strength with increasing purge flow (see Section 6.2.3.3). In region "C", the fluctuations increase by 3% from the case without cavity to the lowest purge massflow ratio. The fluctuations further increase by 7% with increasing purge massflow ratio.

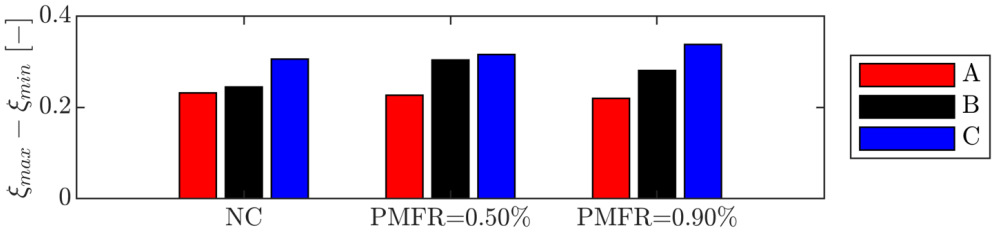

Figure 6.49: Breakdown of kinetic energy loss coefficient fluctuations. A corresponds to the freestream region near the blade SS, B corresponds to the core of the PV, and C corresponds to the interface of the TSV and near-SS wake.

6.4 Spectral Analysis

6.4.1 Blade Surface

The spectra have been extracted at the stagnation lines of the wall-induced vortex and passage vortex. In addition, two extra locations near the trajectory of the secondary flow structures have been investigated. The spectra in the secondary flow region have been studied at the location of the last sensor (s/S_L=0.872). The latter location was chosen since it represents where secondary flows have the most significant impact. However, the findings are analogous to upstream sensors. The location of the points of interest in relation to the secondary flow lines at the location of the last FR sensor for the PMFR=0.90% case is highlighted in Fig. 6.50 for completeness.

Fig. 6.51 highlights that a high-frequency band around 180 Hz occurs for all cases. The frequency has also been observed on the blade pressure measurements performed at midspan (see Section 5.4.2), in particular at M=0.90 in the sensors near the trailing edge for which the decay of power spectral density is sharper.

Fig. 6.51(a) displays the spectra in the stagnation line of the wall-induced vortex for three flow cases: without the cavity, with the cavity, and with increasing purge massflow ratio. The spectra are highly insensitive to the endwall geometry and purge flow. Similar findings were observed concerning the stagnation line of the passage vortex displayed in Fig. 6.51(c).

On the other hand, the regions characterized by the wall-induced vortex and passage

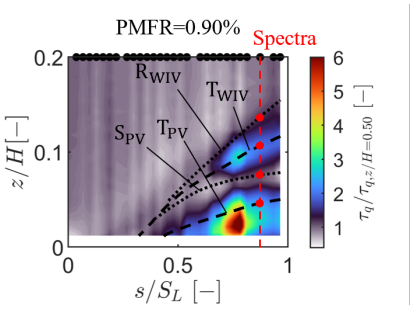

Figure 6.50: Locations of investigated spectra in relation to secondary flow structures at PMFR=0.90%.

vortex are sensitive to the endwall and the purge flow injection. Fig. 6.51(b) displays the spectra on the trajectory of the wall-induced vortex. Up to ∼1,000 Hz, the spectra for all cases are in good agreement. The purge flow introduces a band of increased frequency content that extends up to the second harmonic of the wake generator. The energy content increases with the purge massflow ratio. The amplitude of the bar passing frequency and the first harmonic are not impacted. The "bump" induced by the secondary flows sits at ∼2,000 Hz. A similar but further critical amplification of the spectra occurs in the passage vortex trajectory.

6.4.2 Secondary flows

The investigation of spectra in the downstream flow region was performed at locations with the maximum loss amplitude as discussed in Section 6.3.4. The mapping at PMFR= 0.90% is recalled in Fig. 6.52. The spectra have been investigated in the 2D flow region, in a region impacted by the blade suction side boundary layer ("A"), in the core of the passage vortex ("B"), in the interface of the trailing shed vorticity and 2D blade wake ("C"). An additional location at which the pressure fluctuations are the lowest ("D") within the secondary flow structures was targeted.

The spectra at the specified locations are displayed in Fig. 6.53. In the 2D wake region (see Fig. 6.53(a)), the spectra are not impacted by the endwall geometry nor purge massflow ratio. The spectra are superimposed. The bar passing frequency and harmonics up to the third one are the dominant frequencies, and their amplitude is also insensitive to the case. In the interfacing region between the 2D blade wake, and the trailing shed vorticity (see Fig. 6.53(c)), the spectra are also mainly driven by the wake generator-related frequencies.

The injection of purge flow impacts the spectra in the core of the secondary flow structures. The spectra in the core of the passage vortex are displaced in Fig. 6.53(b). The energy in the 400–12,000 Hz range is significantly increased for the cases with purge flow. The spectra also display insensitivity to the purge massflow ratio. These findings are supported by the similar turbulence intensity found in the core of the secondary flow structures (see Fig. 6.44). The amplitude of the bar passing frequency and its first harmonic remain unaltered. Similar findings are reported for the trailing shed vorticity region ("D") as displayed in Fig. 6.53(d). The main difference with respect to the passage vortex is that the amplitude of the bar passing frequency significantly decreases for the purge flow cases. The finding is consistent with

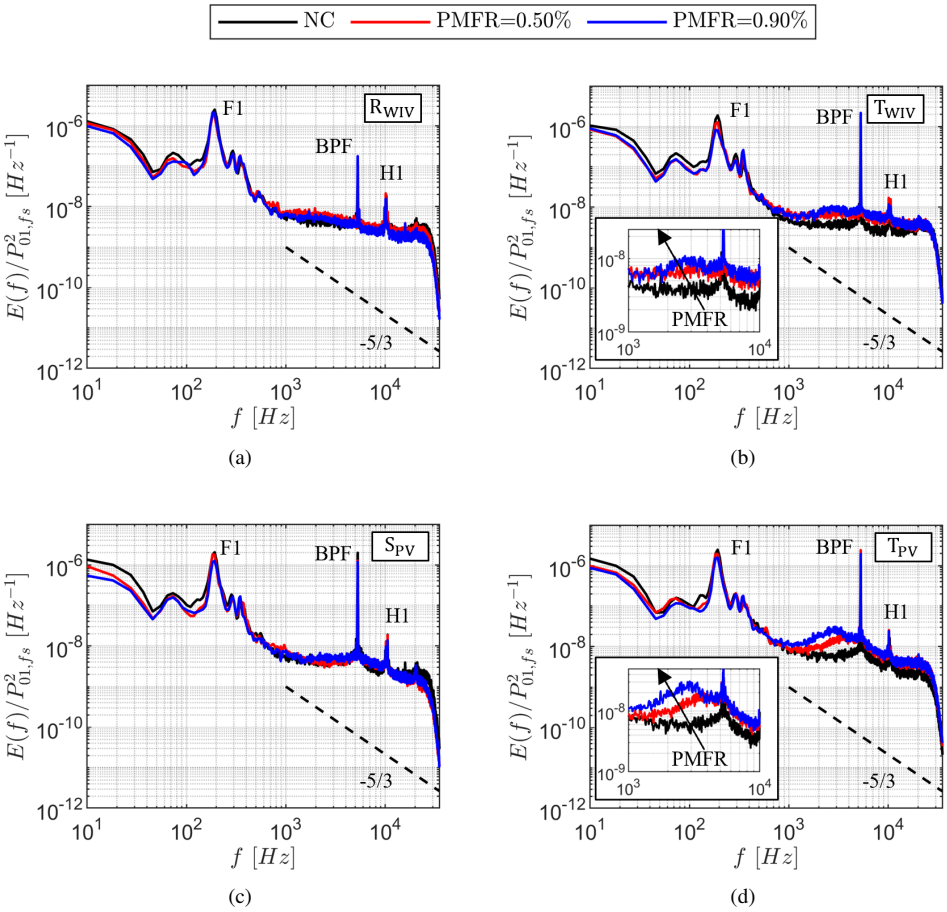

Figure 6.51: Power spectral density of blade static pressure fluctuations: in reattachment line of wall induced vortex (a), in the trajectory of wall induced vortex (b), in separation line of passage vortex (c), and trajectory of passage vortex (d).

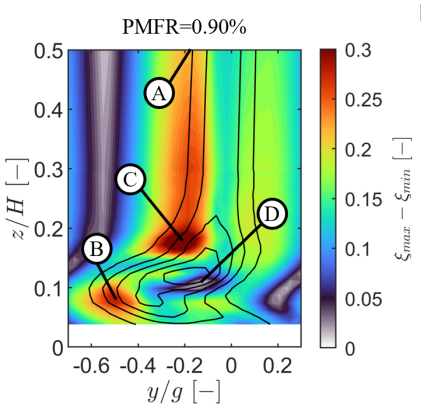

Figure 6.52: Regions of interest for investigation of spectra.

the increase of the extension of the low fluctuating loss region (see Fig. 6.48). This finding suggests that the purge flow impacts the modulation of the trailing shed vorticity. Increasing the purge massflow ratio reduces the correlation of the trailing shed vorticity with the wake passing.

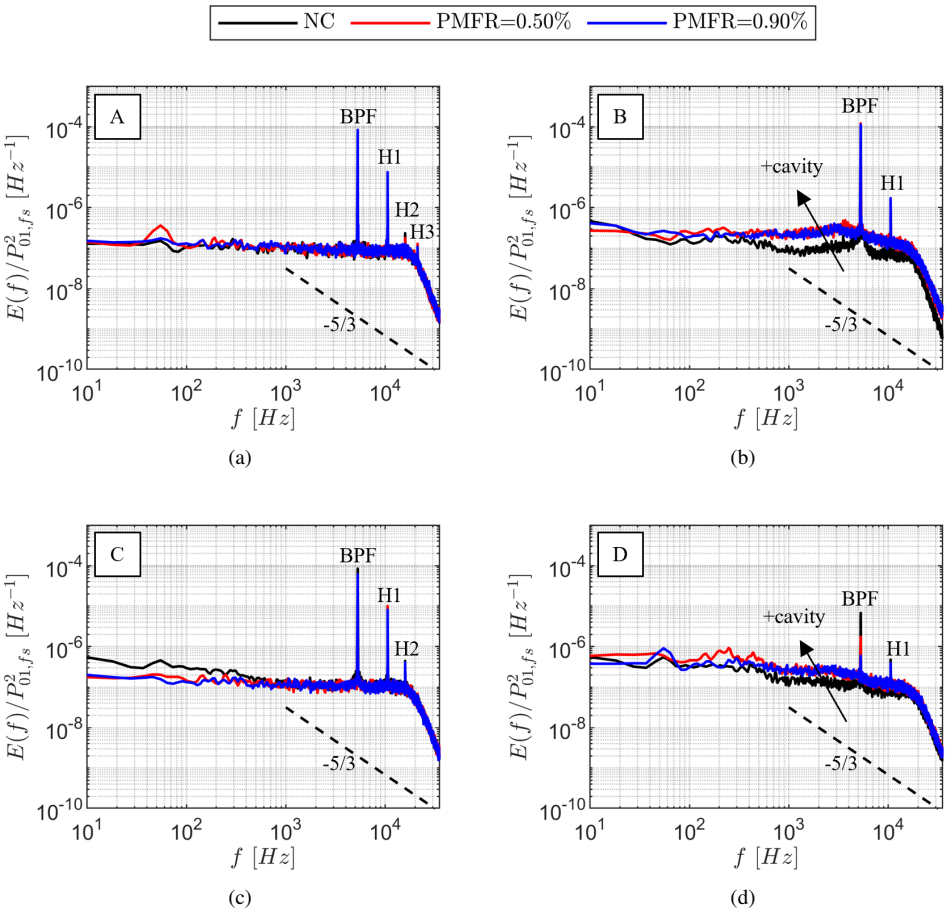

Figure 6.53: Power spectral density of flow total pressure fluctuations: in the 2D flow region near the SS (a), in the passage vortex core (b), in the interface between SS wake and trailing shed vorticity region (c), and the trailing shed vorticity region (d).

6.5 Conclusions

The SPLEEN C1 cascade secondary flow aerodynamics and loss were investigated at on- and off-design conditions. Variation of the Mach and Reynolds numbers has been performed under steady inlet flow conditions. The turbulent inlet boundary layer was found to be flow-independent. Similar secondary flow signatures were observed for all conditions. The passage vortex, trailing shed vorticity, and corner vortex characterize the outlet flow.

The secondary loss was found to be one-third of the profile loss. As a consequence of reducing the blade loading, the secondary flows were found to be weakened with increasing Mach number. The secondary loss decreased by 24% with increasing Mach number at Re=70k. The loss was also found to decrease with the Reynolds number (25% at Re=70k).

Introducing the wake generator caused the inlet boundary layer to restart due to the wake generator slot. The incidence of radial distributions was also found to suffer from the introduction of the wake generator slot. The significant skewness associated with the steady inlet flow was significantly reduced. The secondary flows were weakened and migrated toward the endwall. The loss was reduced by 5% as a consequence.

Modifying the flat endwall to the cavity endwall without injecting purge flows increased the secondary loss by 8%, despite the thinner inlet boundary layer for the case with the cavity slot. The increase in loss has been reported in the literature and is justified by generating a leakage vortex that forms in the cavity slot. The secondary flows were displaced towards the center of the passage with an increasing purge massflow ratio, resulting in a higher secondary loss. For the highest purge massflow ratio, a loss increase of 61% is recorded in relation to the baseline case without the cavity slot. Despite the variations in loss and secondary flow extent, the topology of the outlet flowfield in terms of existing secondary flow structures remained similar throughout the experiments.

The unsteady investigation of the development of the wakes at the inlet revealed the skewed nature of the wakes due to the rotating motion of the wake generator. The inlet boundary layer thickness was found to vary significantly during a bar passing event. The periodic modulation of the boundary layer thickness is responsible for the periodic modulation of the secondary flow strength. For the flat endwall case, at the instant of minimum secondary loss, the signature of the passage vortex is barely visible from the secondary velocity vector field. The flowfield for cases with purge flow is characterized by the typical flow structure (passage vortex and trailing shed vorticity), even though their intensity varies throughout a bar period.

Hot-film sensors allowed for identifying primary and secondary flow structures on the blade suction side. The passage vortex and wall-induced vortex were found to have an imprint on the wall shear stress and its statistical moments. Even though the surface quantities in the secondary flow region were found to be poorly correlated with the wake passing, wall fluctuations over ± 100 Pa were still detected in the trajectory of the secondary flow structures.

Three main regions with significantly increased fluctuations were observed: in the 2D flow region, near the blade suction side, in the passage vortex core, and the wake-trailing shed vorticity interacting region. Whereas the near 2D fluctuations are insensitive to the purge flow, the loss fluctuations in the passage vortex and trailing shed vorticity regions increase with the purge massflow ratio.

Spectral analysis of the blade suction side pressure traces revealed that the unsteady wakes still modulate the measured quantities. The bar passing frequency was found at all locations investigated. In the stagnation lines of the secondary flow structures (interface of passage vortex and wall-induced vortex), the spectra were insensitive to the purge massflow ratio. In the trajectory region, the spectra were impacted by the injection of purge flow. A band of frequencies associated with the purge flow was found in the 1000–10,000 Hz range at both the passage vortex and wall-induced vortex regions.

The spectra downstream of the cascade were also investigated at particular locations: 2D

blade wake, core of passage vortex, interfacing region of trailing shed vorticity and blade wake, and core of trailing shed vorticity. The BFP and harmonics were observed at all locations. The 2D flow region is insensitive to purge flow injection and endwall geometry. The interfacing region of the trailing shed vorticity and blade wake also revealed insensitivity across the different cases. The spectra in the core of the secondary flow structures displayed an increase in the spectral energy for the purge flow cases. No difference between both cases was observed with varying purge massflow ratios. The finding is supported by similar turbulence intensity in the core of the secondary flow structures. The correlation of the passage vortex modulation by the wake was case insensitive. On the other hand, the trailing shed vorticity decreased the bar passing frequency amplitude with the introduction of purge flow. The latter suggests that the purge suppresses the wake-induced unsteadiness and that the trailing shed vorticity is strongly driven by the blade geometry and operating point rather than the inlet boundary layer.

References

[1] H. Schlichting and K. Gersten. *Boundary-layer theory*. springer, 2016.

[2] J.A. Walsh and D.G. Gregory-Smith. *Inlet Skew and the Growth of Secondary Losses and Vorticity in a Turbine Cascade*. Journal of Turbomachinery, 112(4):633–642, 10 1990.

[3] Andreas Gross, Christopher R. Marks, Rolf Sondergaard, Philip S. Bear, and J. Mitch Wolff. *Experimental and Numerical Characterization of Flow Through Highly Loaded Low-Pressure Turbine Cascade*. Journal of Propulsion and Power, 34(1):27–39, 2018.

[4] Philip Bear, Mitch Wolff, Andreas Gross, Christopher R. Marks, and Rolf Sondergaard. *Experimental Investigation of Total Pressure Loss Development in a Highly Loaded Low-Pressure Turbine Cascade*. Journal of Turbomachinery, 140(3):031003, 12 2017.

[5] A. Perdichizzi. *Mach Number Effects on Secondary Flow Development Downstream of a Turbine Cascade*. Journal of Turbomachinery, 112(4):643–651, 10 1990.

[6] H.M. Abo El Ella, S.A. Sjolander, and T.J. Praisner. *Effects of an Upstream Cavity on the Secondary Flow in a Transonic Turbine Cascade*. Journal of Turbomachinery, 134(5):051009, 05 2012.

[7] R. Vazquez, A. Antoranz, D. Cadrecha, and L. Armananzas. *The Influence of Reynolds Number, Mach Number and Incidence Effects on Loss Production in Low Pressure Turbine Airfoils*. volume Volume 6: Turbomachinery, Parts A and B of *Turbo Expo: Power for Land, Sea, and Air*, pages 949–960, 05 2006.

[8] R. Vazquez and D. Torre. *The Effect of Mach Number on the Loss Generation of LP Turbines*. volume Volume 8: Turbomachinery, Parts A, B, and C of *Turbo Expo: Power for Land, Sea, and Air*, pages 1131–1142, 06 2012.

[9] J.D. Coull. *Endwall Loss in Turbine Cascades*. Journal of Turbomachinery, 139(8):081004, 03 2017.

[10] H.P. Hodson and R.G. Dominy. *The Off-Design Performance of a Low-Pressure Turbine Cascade*. Journal of Turbomachinery, 109(2):201–209, 04 1987.

[11] E. de la Rosa Blanco, H.P. Hodson, and R. Vazquez. *Effect of the Leakage Flows and the Upstream Platform Geometry on the Endwall Flows of a Turbine Cascade*. Journal of Turbomachinery, 131(1):011004, 10 2008.

[12] I. Popovic and H.P. Hodson. *The Effects of a Parametric Variation of the Rim Seal Geometry on the Interaction Between Hub Leakage and Mainstream Flows in High Pressure Turbines*. Journal of Engineering for Gas Turbines and Power, 135(11):112501, 09 2013.

[13] G.D. MacIsaac, S.A. Sjolander, T.J. Praisner, E.A. Grover, and R. Jurek. *Effects of Simplified Platform Overlap and Cavity Geometry on the Endwall Flow: Measurements and Computations in a Low-Speed Linear Turbine Cascade*. volume Volume 6A: Turbomachinery of *Turbo Expo: Power for Land, Sea, and Air*, page V06AT36A035, 06 2013.

[14] R.J. Volino, C.D. Galvin, and M.B. Ibrahim. *Effects of Periodic Unsteadiness on Secondary Flows in High Pressure Turbine Passages*. volume Volume 6C: Turbomachinery of *Turbo Expo: Power for Land, Sea, and Air*, page V06CT42A042, 06 2013.

[15] G.D. MacIsaac and S.A. Sjolander. *Anisotropic Eddy Viscosity in the Secondary Flow of a Low-Speed Linear Turbine Cascade*. volume Volume 7: Turbomachinery, Parts A, B, and C of *Turbo Expo: Power for Land, Sea, and Air*, pages 653–665, 06 2011.

[16] D. Infantino, F. Satta, D. Simoni, M. Ubaldi, P. Zunino, and F. Bertini. *Phase-Locked Investigation of Secondary Flows Perturbed by Passing Wakes in a High-Lift LPT Turbine Cascade*. volume Volume 2C: Turbomachinery of *Turbo Expo: Power for Land, Sea, and Air*, page V02CT44A008, 06 2015.

[17] A.F.M. Torre, M. Patinios, G. Lopes, L. Simonassi, and S. Lavagnoli. *Vane–Probe Interactions in Transonic Flows*. Journal of Turbomachinery, 145(6):061010, 01 2023.

[18] M. Okada, L. Simonassi, G. Lopes, and S. Lavagnoli. *Particle Image Velocimetry Measurements in a High-Speed Low-Reynolds Low-Pressure Turbine Cascade*. Journal of Turbomachinery, 146(3):031010, 12 2023.

[19] A. Perdichizzi, M. Ubaldi, and P. Zunino. *Reynolds stress distribution downstream of a turbine cascade*. Experimental thermal and fluid science, 5(3):338–350, 1992.

[20] L. Porreca, M. Hollenstein, A.I. Kalfas, and R.S. Abhari. *Turbulence Measurements and Analysis in a Multistage Axial Turbine*. Journal of Propulsion and Power, 23(1):227–234, 2007.

7 Loss Modeling

In this chapter, the time-averaged loss data depicted in the previous chapters are compared against loss correlations available in the literature. Based on the experimental and numerical data obtained in the scope of this work, the underlying assumptions of the most advanced loss models are challenged. Both profile and secondary loss are broken down to explain the trends observed experimentally.

7.1 Profile Loss

7.1.1 Past models

An estimation of the profile loss was performed with two categories of models:

- Model of Ainley and Mathieson (AM) [1] and derivatives based on latter formulation such as the model of Dunham and Came (DC) [2], Kacker and Okapuu (KO) [3], Zhu and Sjolander (ZS) [4], Benner et al. (BSM) [5, 6],

- Model of Craig and Cox [7].

The latter models, particularly the one of Ainley & Mathieson, are still arguably among the most used due to their simplicity. It is worth mentioning the model of Traupel that was not used in the scope of this work [8].

Fig. 7.1(a) displays the comparison between the models mentioned above and the profile loss for the steady flow cases measured experimentally at Plane 06 (see Table G.2). The experimental loss is represented on the x-axis, and the predicted one on the y-axis. A black solid line denotes a perfect match between the experimental values and the predicted ones (ζ_{pred}=ζ_{exp}). A shaded region remarks an error of $\pm$10% with respect to the solid line.

Newer methods improved the agreement between the models and the current data. Models, especially in the early 2000s, started including high-lift low-pressure turbine geometries within which the SPLEEN C1 geometry falls.

Fig. 7.1(b) presents the same type of plot for the unsteady flow cases. The models do not account for the contribution of unsteady wakes and are therefore unsuitable as they underpredict the profile loss.

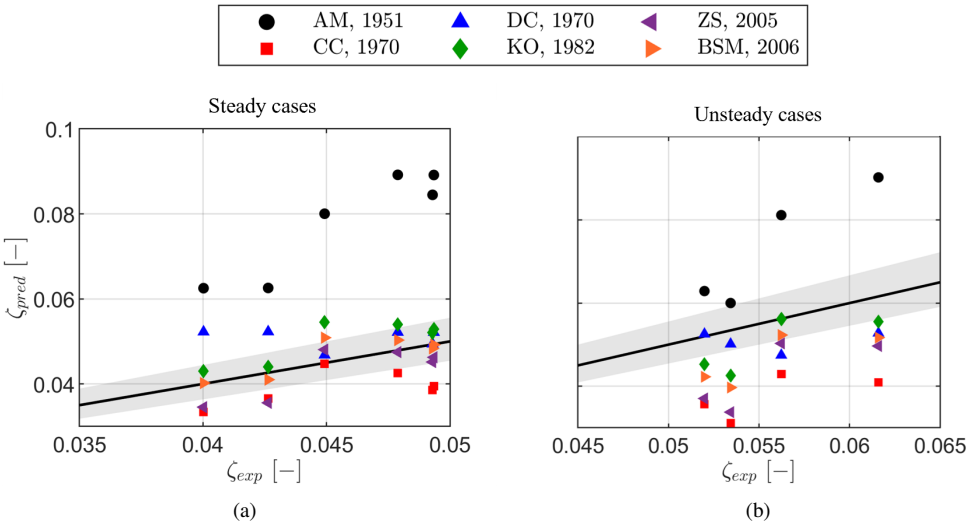

Figure 7.1: Comparison between experimental and predicted profile loss using different models: steady flow cases (a) and unsteady flow cases (b).

Fig. 7.2 compares the profile loss measured experimentally and the model of Benner et al. [5, 6]. The latter is arguably the most advanced Ainley & Mathieson model derivative at the time of writing of this manuscript. The model overpredicts the loss for all cases. The reduction of loss with increasing Reynolds number is well captured. The model predicts increasing loss with the Mach number, which is inconsistent with the experimental findings. In addition, the model does not enable the breakdown of terms contributing to the loss.

7.1.2 Model of Coull & Hodson

The model proposed by Coull & Hodson (CH) [9] was exploited to characterize the terms contributing to the loss thoroughly. The model requires the blade loading as input. The authors suggest tripping the boundary layer at the velocity peak location, specifically in the scope of numerical predictions. However, for high Mach number cases, it was found that the tripping is insufficient to trigger boundary layer transition.

Fig. 7.3(a) displays the blade loadings obtained with MISES for a fixed Re=120k and varying Mach number. The profiles represented by a solid line have been obtained by tripping the boundary layer at the separation location. The dashed lines represent profiles with a tripped boundary layer near the leading edge. A discrepancy on the suction side near the velocity peak for the two highest Mach numbers can be observed. The latter is better highlighted in the zoomed Fig. 7.3(b).

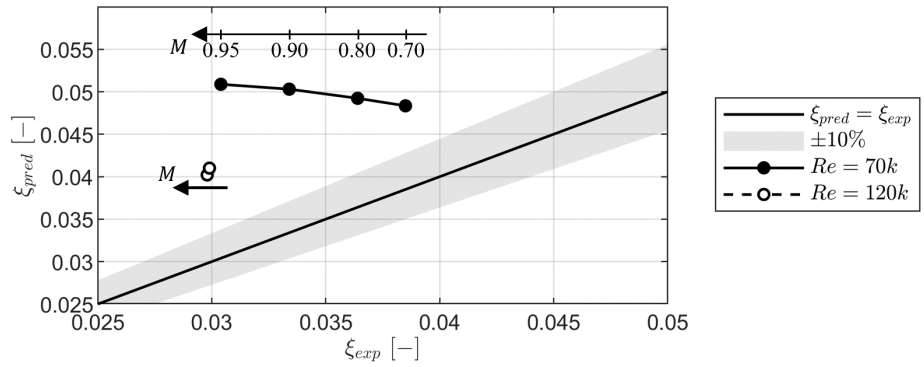

Figure 7.2: Comparison between experimental and predicted profile loss using the model of Benner et al. [5, 6].

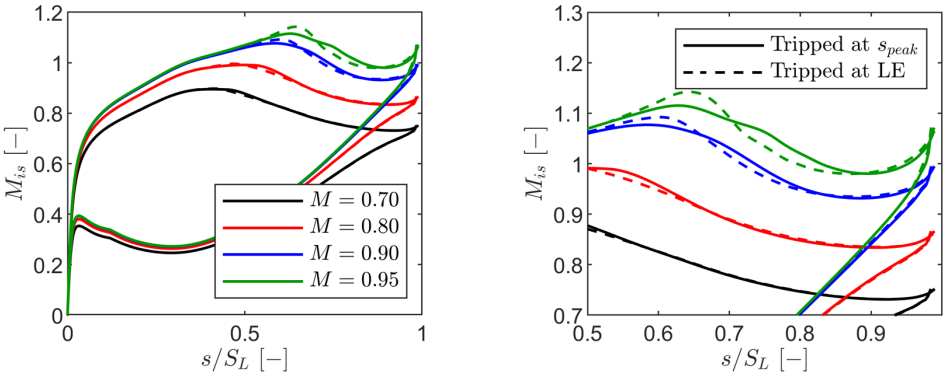

(a) (b)

Figure 7.3: Impact of boundary layer tripping location on blade loading obtained with MISES: pressure side and suction side (a) and zoomed-in region of SS (b).

The early tripped MISES computations match fully turbulent RANS computations regardless of the flow condition. Fig. 7.4(a) and Fig. 7.4(b) display the comparison between MISES tripped near the leading edge and fully turbulent RANS computations for the cases mentioned above at Re=120k for which the late tripping did not allow to retrieve the fully turbulent loading.

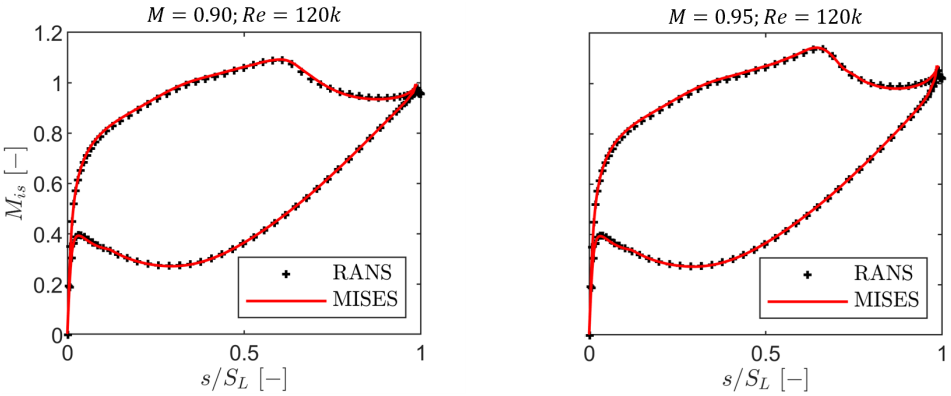

Figure 7.4: Comparison between MISES computations tripped near the leading edge and fully turbulent RANS: M=0.90; Re=120k (a) and M=0.95; Re=120k (b).

By applying the loss model of Coull & Hodson without any further considerations, the loss obtained with the CFD and MISES loadings is well matched as displayed in Fig. 7.5. Therefore, the MISES computations used in the scope of the following sections were conducted by tripping the boundary layer near the leading edge.

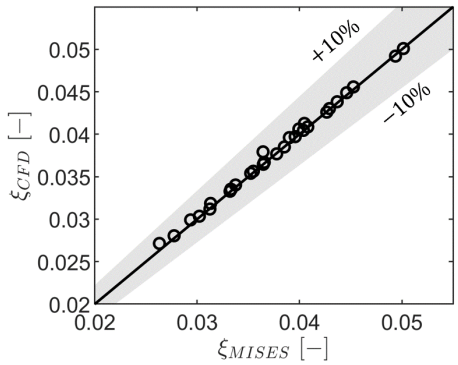

Figure 7.5: Relationship between loss computed using model of Coull & Hodson [9] for fully turbulent MISES and RANS loadings.

7.1.2.1 Estimation of Separation Location

Coull & Hodson reviewed different methods of estimating the separation location. The methods are divided into two families: based on the Thwaites parameter [10–14] and based on the work of Stratford [15]. The Thwaites method takes the form of:

$$[\lambda_\theta]_{sep} = \left[\frac{\theta^2}{\nu}\frac{dU}{dS}\right]_{sep} \approx const. \tag{7.1}$$

Where the constant is variable between the suggested methods, the constant for each sub-method is reported in Table 7.1 for completeness.

Table 7.1: Constants for each of the methods based on the Thwaites parameter.

Model	Const.
Pohlhausen [10]	-0.1567
Timman [11]	-0.0871
Walz [12]	-0.0682
Thwaites [13]	-0.0820
Curle and Skan [14]	-0.0900

The Stratford method takes the form of:

$$\left[C_p^*\left((S-S_B)\frac{dC_p^*}{dS}\right)\right]_{sep} \approx const. \tag{7.2}$$

Where the constant depends on an m coefficient used to describe the boundary layer inner layer and S_B is used for velocity profiles that are not constant up to the velocity peak of a blade loading:

$$S_B = S_{peak} - \int_0^{S_{peak}} \left(\frac{V}{V_{peak}}\right)^5 dS \tag{7.3}$$

The latter term is called a leading edge correction and equals zero, where no correction is applied. The constant for each of the sub-methods is reported in Table 7.2 for completeness.

Table 7.2: Constants for each of the methods based on the Stratford parameter.

Model	Const.
Stratford [15], $m = 3$	0.0108
Stratford [15], $m = 4$	6.48×10^{-3}

Coull & Hodson found an approximate method of Stratford with m=4, and without applying the leading edge correction, to provide the best agreement between their model and existing experimental data from the literature in addition to their own. The prediction of the separation location was challenged in the scope of this work. The methods highlighted in [9] were compared against the experimental predictions for the steady flow cases (see Table 5.4).

Fig. 7.6 displays the experimental predicted separation location, s_{sep}/S_L, against the one predicted using the Thwaites family of methods. The method of Pohlhausen [10] was found to give the best overall agreement with respect to experiments. For all flow conditions, the error with respect to the experiments fell within $\pm 10\%$.

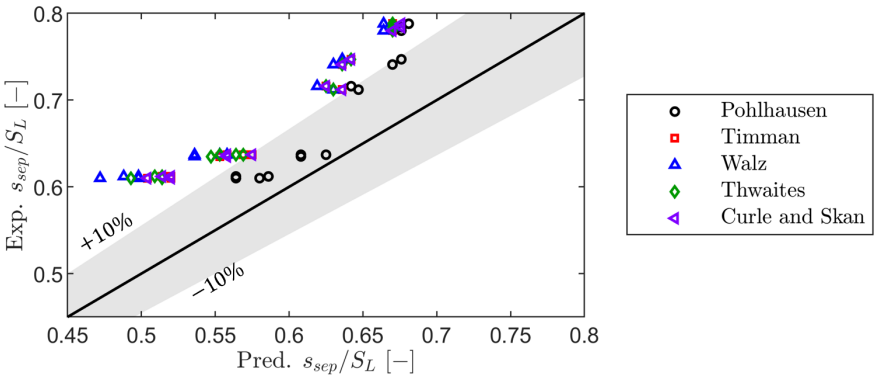

Figure 7.6: Comparison of experimentally obtained separation locations against those estimated with different Thwaites-derived methods.

Fig. 7.7 displays the experimentally predicted separation location, s_{sep}/S_L, against the one predicted using the MISES loading as an input and the Stratford-related methods. The coefficient m was varied between three and four. The application of the leading edge was considered. The minimum error for the experiments was found for the case where the leading edge correction was applied and m=3 (red markers).

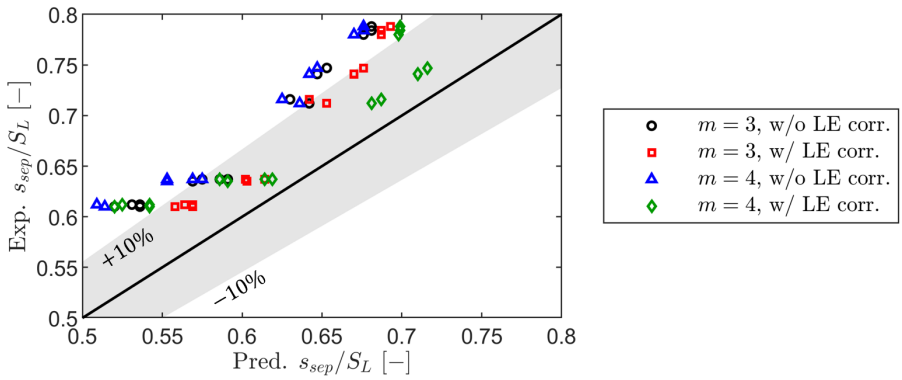

Figure 7.7: Comparison of experimentally obtained separation locations against those estimated with different Stratford-derived methods.

As pointed out in [9], cases characterized by moderate deceleration (U_{sep}/U_{peak} >0.935) are better represented by m=3. All the SPLEEN steady and unsteady cases fall within this range. Table 7.3 contains the blade loading parameters.

Table 7.4 contains the mean error in estimating the separation location with respect to experiments. All methods underpredict the separation location. The minimum mean error in

Table 7.3: Summary of blade loading parameters.

M $[-]$	Re $[-]$	U_{sep}/U_{peak} $[-]$	DF $[\%]$	$\Delta U^*/\Delta S$ $[-]$	Zw $[-]$
0.70	65,000	0.95	25	0.35	0.82
0.80	65,000	0.95	20	0.33	0.78
0.90	65,000	0.95	18	0.35	0.73
0.70	70,000	0.94	25	0.35	0.82
0.80	70,000	0.95	21	0.34	0.78
0.90	70,000	0.97	18	0.37	0.73
0.95	70,000	0.98	16	0.39	0.71
0.70	100,000	0.95	24	0.34	0.81
0.80	100,000	0.97	20	0.35	0.77
0.90	100,000	0.99	16	0.36	0.73
0.95	100,000	0.98	17	0.40	0.71
0.70	120,000	0.95	24	0.35	0.81
0.80	120,000	0.97	21	0.36	0.77
0.90	120,000	0.98	17	0.36	0.73
0.95	120,000	0.98	16	0.38	0.70

determining the separation location with respect to the experimental data is found to be 7.8% for the Pohlhausen method within the family of Thwaites parameter methods and 8.1% for the Stratford method, taking m=3 and applying the leading edge correction. In Appendix H, the reader can find a table with a breakdown of the error for each flow condition.

Table 7.4: Mean error in estimating separation location for each method.

Model	Mean error $[\%]$
Pohlhausen [10]	-7.8
Timman [11]	-13.6
Walz [12]	-15.8
Thwaites [13]	-14.2
Curle and Skan [14]	-13.4
Stratford [15], $m = 3$, w/o LE corr.	-11.7
Stratford [15], $m = 4$, w/o LE corr.	-13.8
Stratford [15], $m = 3$, w/ LE corr.	-8.1
Stratford [15], $m = 4$, w/ LE corr.	-8.2

Despite the lower mean error from the Polhausen method, the Stratford method presents advantages for specific cases. Fig. 7.8 plots the experimentally determined separation location against the one predicted. The shaded area corresponds to the interval constraining the error within $\pm 10\%$ of the expected value. The type of marker denotes the method. The color of the marker indicates the Mach number.

The method of Pohlhausen displays a worse agreement to the experiments for the high Mach number cases with respect to the Stratford method. The mean error for each set of Mach numbers is contained in Table 7.5 for completeness. The Stratford method with m=3 and the application of the leading edge correction was used in the scope of this work.

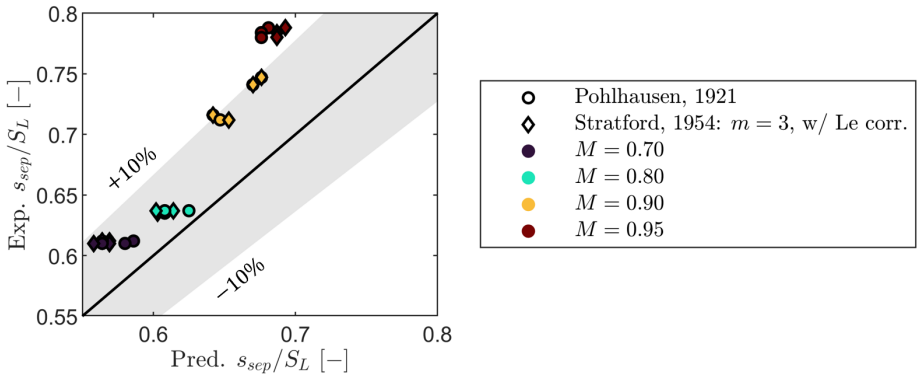

Figure 7.8: Comparison of experimentally obtained separation location against the one estimated with the best method of the Thwaites and Stratford type methods.

Table 7.5: Mean error in estimating separation location for each Mach number for the methods of Pohlhausen and Stratford

M [−]	Pohlhausen	Stratford, $m = 3$, w/ LE corr.
0.70	-6.2	-7.5
0.80	-3.1	-4.5
0.90	-9.7	-9.5
0.95	-13.6	-12.1

7.1.2.2 Comparison of Model with Calibrated MISES

MISES uses a trailing edge model to account for the loss in the blade wake. The model is calibrated against data from an RAE 2822 airfoil and a transonic compressor cascade. The model disregards trailing edge shedding and assumes constant pressure across the dead air region.

Fig. 7.9 compares the mixed-out kinetic energy loss coefficient measured experimentally against the one obtained with transitional MISES. The figure highlights the $\pm 10\%$ error bands using the shaded area. The MISES provides excellent agreement for all cases. The only case outside the 10% error band occurs at M=0.80; Re=70k, for which the flow is characterized by an open separation bubble (see Section 5.2.2.1). For the latter, MISES underpredicts the loss by 11%. MISES correctly predicts the dependence of the Mach number on the loss at Re=70k. The trend is not captured for the highest Reynolds number even though the error to experiments is within the $\pm 10\%$ range. MISES underperdicts the loss by 7% at M=0.90; Re=120k as well. The latter case is also characterized by an open separation suppressed at M=0.80 for the same Reynolds number. The root-mean-square error of the MISES predictions with respect to the available experimental cases amounts to $\sim$6%.

The accuracy of MISES with respect to RANS, in addition to the computational cost, highlights the power of the tool to develop low-order models and inform the design of new blading [16]. Despite loss models being built on fully turbulent loadings, the previous exer-

cise highlighted the capability of MISES to provide satisfactory predictions for transitional cases. Nonetheless, the comparison quality relies on the correct calibration of the turbulence intensity to match the experimental loadings that may not be known before testing. Furthermore, the calibration of the transition model is complicated by the ambiguity in defining the turbulence intensity (see Section 3.1).

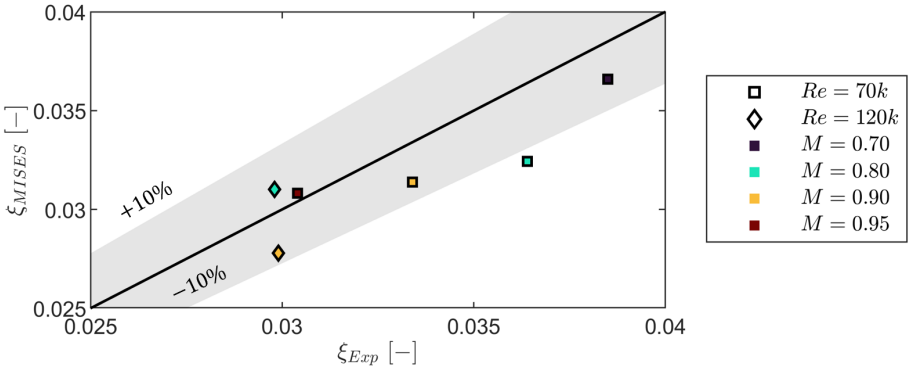

Figure 7.9: Comparison of profile loss obtained experimentally and one obtained from transitional MISES.

The quantities obtained from the model of Coull & Hodson were compared against the ones obtained from the MISES transitional results calibrated to match the experimental blade loadings to challenge the applicability of the model. The boundary layer on the blade pressure side is assumed to be attached throughout the surface length, even though a laminar separation bubble was captured with RANS and MISES. The momentum thickness was computed using the method of Thwaites as suggested in [9]:

$$\theta^2_{PS,TE} \approx \frac{0.45\nu}{V^6} \int_0^s V^5 ds \tag{7.4}$$

The shape factor can be estimated using the correlation of White [17].

$$H \approx 2.0 + 4.14z - 83.5z^2 + 854z^3 - 3337z^4 + 4576z^5 \tag{7.5}$$

Where $z = (0.25 - \lambda_\theta)$, and $\lambda_\theta = \frac{\theta^2}{\nu}\frac{dV}{ds}$. The displacement thickness, $\delta^*_{PS,TE}$, can be obtained once the momentum thickness and shape factor are known.

Fig. 7.10 displays the boundary layer parameters on the blade pressure side near the trailing edge-—the displacement thickness data collapse on a single curve as shown in Fig. 7.10(a). The slope of the curve does not agree with the one where the predictions would match the computations ($\delta^*_{PS,CH}$=$\delta^*_{PS,MISES}$). This is likely due to the laminar separation bubble in the MISES and RANS computations. There is no apparent impact from the Mach or Reynolds number. The MISES computations overpredict the δ^*_{PS} with respect to the modeled values at Re=100k and 120k. The error is within the $\pm 10\%$ margin for lower Reynolds numbers.

Fig. 7.10(b) displays a similar plot for the momentum thickness. Opposite from the displacement thickness, the MISES computations underpredict the θ_{PS}, especially at low Reynolds number (error can reach up to $\sim$25%). At Re=100k, the error with respect to the

computations is within $\pm 10\%$, while for the highest Reynolds number is slightly higher (up to $\sim 13\%$).

The Coull and Hodson model inaccurately captures the boundary layer parameters of the blade PS, which is characterized by a laminar separation bubble. This results in a considerable error in the displacement and momentum thickness. However, as will be demonstrated, this inaccuracy does not significantly impact the loss since the suction side boundary layer is the largest contributor.

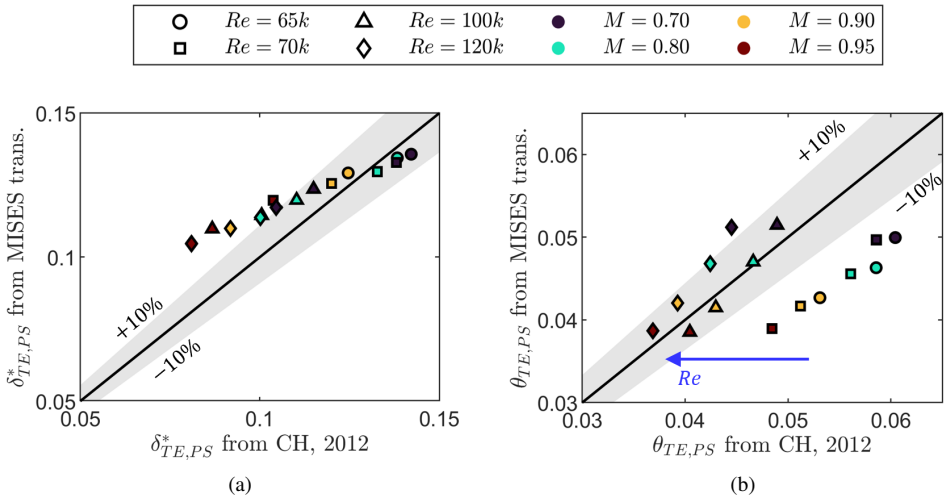

Figure 7.10: Comparison between pressure side boundary lower obtained with transitional MISES and model of Coull & Hodson: displacement thickness (a) and momentum thickness (b).

Fig. 7.11 displays the momentum thickness at the separation location predicted by the MISES transitional computations against the one predicted with the method in [9]. The latter work suggests integrating the Thwaites formulation from the leading edge to the separation location (see Eq. 7.6). The displacement thickness can be obtained once the shape factor is computed with Eq. 7.5.

$$\theta^2_{SS,sep} \approx \frac{0.45\nu}{V^6_{sep}} \int_0^{s_{sep}} V^5 ds \tag{7.6}$$

Two datasets were investigated: the black markers refer to the quantities computed based on the separation location estimated using the Stratford method. The red markers refer to data from the separation location measured experimentally (see Section 5.2.2.1).

Using the separation location obtained with the method of Stratford results in a consistent underprediction of the momentum thickness at the separation location by as much as $\sim 24\%$, depending on the flow case, with respect to the MISES computations. The overall agreement increases using the experimentally derived separation location (which is within 4% of the one predicted by MISES as displayed in Table 5.4). An underprediction by $\sim 9\%$ still occurs for the higher Mach numbers. However, the θ_{sep} is perfectly modeled for the lower Mach number investigated, regardless of the Reynolds number. As seen in Fig. 7.8, the separation

location at M=0.70 estimated with Stratford's method is underpredicted with respect to the experiments.

Fig. 7.11(b) contains the data for the Stratford method only. The marker color and type represent the flow condition. Cases for M=0.95 are not presented since separation was not predicted with MISES. The underprediction of the quantity by the Coull & Hodson method with respect to the transitional MISES increases with the Mach number. The methods of Thwaites and Stratford were built with low-speed data. Fig. 7.11 challenges the applicability of the methods mentioned above to cases where compressibility impacts the boundary layer separation.

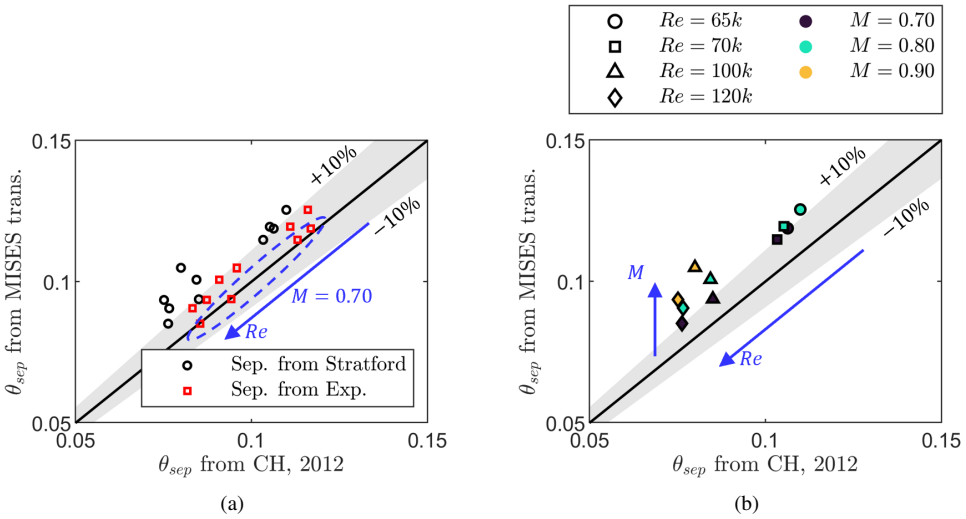

Figure 7.11: Comparison between momentum thickness at the separation location for transitional MISES and CH model: impact of separation location (a) and dependence from flow condition using the method of Stratford (b).

The correlations of Coull & Hodson [9] estimate the boundary layer growth after the laminar separation. The boundary layer growth is split into the contributions of the bubble, turbulent wetted area, and wake:

$$[\theta_{SS,TE}]_{bubble} = \theta_{SS,sep}\left(6.69 \times 10^{6}\right)\left(Re_{\theta,sep}\right)^{(-4.28+2.05(\Delta U^*/\Delta S^*)-0.16St)} \tag{7.7}$$

$$[\theta_{SS,TE}]_{turb} = \theta_{SS,sep}\left(Re_{\theta\,sep}\right)^{0.322}\left(\frac{1-s_{sep}}{S_L}\right)\left(0.166+3.13\left(\frac{\Delta U^*}{\Delta S^*}\right)\right) \tag{7.8}$$

$$[\theta_{SS,TE}]_{wake} = S_L\left(7.06 \times 10^{-4}\right)(St) \tag{7.9}$$

The total momentum thickness is computed as the sum of the contributions:

$$[\theta_{SS,TE}] = [\theta_{SS,TE}]_{bubble} + [\theta_{SS,TE}]_{turb} + [\theta_{SS,TE}]_{wake} \tag{7.10}$$

Coull & Hodson also provided a correlation for the shape factor (see Eq. 7.10). The displacement thickness, $\delta^*_{SS,TE}$, can be computed with the momentum thickness and shape factor.

$$H_{SS,TE} = 1.545 + \left(2.57 \times 10^9\right) \left(Re_{S_L}\right)^{(-1.93DF + 0.619(\Delta U^*/\Delta S^*) - 0.085St - 1.77)} \quad (7.11)$$

Fig. 7.12 displays the boundary layer integral parameters on the suction side near the trailing edge computed with the model of Coull and Hodson and by estimating the separation location with the method of Stratford with m=3. Regardless of the flow condition, the model overpredicts the boundary layer displacement thickness (see Fig. 7.12(a)) with respect to the MISES. No apparent trend is observed with Mach or Reynolds numbers. The error is lower and within $\pm 10\%$ for low Reynolds number and M=0.80. A maximum error of $\sim 52\%$ is observed at M=0.95; Re=70k.

Fig. 7.12(b) displays the same plot for the momentum thickness. The model is found to overpredict the $\theta_{TE,SS}$ with respect to MISES. The error is independent of the Mach and Reynolds numbers. The lowest and highest mean errors are $\sim 48\%$ at M=0.70 and $\sim 65\%$ at M=0.95, respectively.

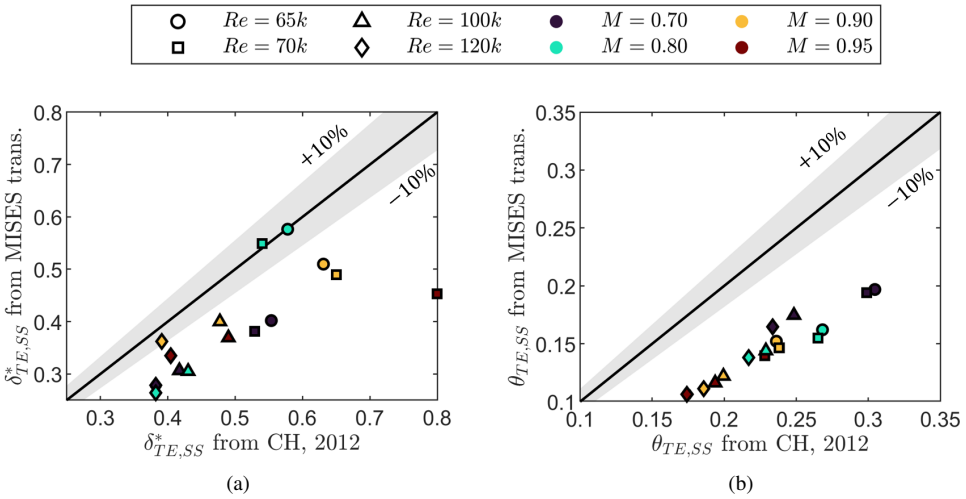

Figure 7.12: Comparison between SS boundary layer obtained with transitional MISES and model of Coull & Hodson, estimating the separation location with the method of Stratford with m=3: displacement thickness (a) and momentum thickness (b).

The boundary layer integral parameters at the trailing edge were used to estimate the profile loss according to Denton's loss breakdown [18] (see Eq. 7.12) with the velocity ratio corrective term proposed in [9]. The base pressure term was neglected from the analysis as in [9].

$$\xi_{Denton} \approx \left(\frac{V_{TE,SS}}{V_{out}}\right)^2 \left[\left(\frac{2\sum \theta_{TE}}{g\cos\alpha_{out}}\right) + \left(\frac{\sum \delta^*_{TE} + t_{TE}}{g\cos\alpha_{out}}\right)^2 - \frac{C_{pb}t_{TE}}{g\cos\alpha_{out}}\right] \quad (7.12)$$

Fig. 7.13 compares the experimentally measured profile loss and the one computed with the model of Coull & Hodson. Black markers denote that the loss has accounted for the boundary layer integral parameters estimated with the model of Coull & Hodson. Red markers denote that the loss was predicted with the boundary layer parameters retrieved from the transitional MISES. The loss is expressed as the kinetic energy loss coefficient.

The underprediction of the boundary layer integral parameters with the transitional MISES with respect to the model of Coull & Hodson results in an underprediction of the modeled loss with respect to experiments. The reader is recalled for the fact that the loss directly obtained from MISES provided a much better agreement (see Fig. 7.9). The overprediction of the boundary layer quantities employing the correlations of Coull & Hodson significantly improves the agreement between the modeled and experimental loss.

A preliminary conclusion of this exercise is that the model of Coull & Hodson [9] is a robust tool to predict the profile loss of new blading. The model is more advantageous than transitional MISES since it uses the fully turbulent profile and does not rely on the calibration of a transitional model.

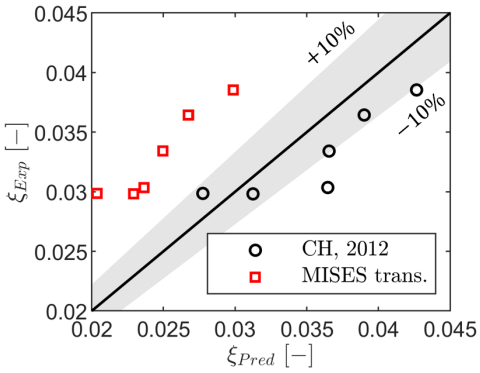

Figure 7.13: Comparison of profile loss obtained experimentally and predicted by incorporating boundary layer parameters from MISES computations and estimated with the model of Coull & Hodson [9], in the breakdown scheme of Denton [18].

7.1.2.3 Comparison of Loss Breakdown Schemes

Typically, the overall profile loss is computed with the mixed-out breakdown of Denton (see Eq. 7.12). The breakdown scheme of Senior & Miller [16] accounts for the trailing edge wedge angle, α_w, a term that is not present in Denton's loss breakdown:

$$\xi = \frac{2\sum\theta}{g\cos\alpha_{out}}\left(\frac{V_{TE,SS}}{V_{out}}\right)^2 + \left(\frac{t_{TE}+\sum\delta^*_{TE}}{g\cos\alpha_{out}}\right)\frac{V_{TE,SS}}{V_{out}}\left(\frac{V_{TE,SS}}{V_{out}}\cos\frac{\alpha_w}{2} - 1\right)$$
$$+ \left(\frac{t_{TE}+\sum\delta^*}{g\cos\alpha_{out}}\right)\left(\frac{V_{TE,SS}}{V_{out}}\right)^2\sin\frac{\alpha_w}{2} - C^*_{pb}\left(\frac{t_{TE}+\sum\delta^*_{TE}}{g\cos\alpha_{out}}\right)\left(\frac{V_{TE,SS}}{V_{out}}\right)^2 \quad (7.13)$$

Where the base pressure coefficient, C^*_{pb}, is defined as:

$$C_{pb}^{*} = \frac{P_{base} - P_{TE,SS}}{\frac{1}{2}\rho V_{TE,SS}^{2}} \tag{7.14}$$

The model also considers the recent findings from Melzer and Pullan [19] and Rossiter et al. [20] concerning trailing edge loss. Based on the boundary layer parameters in the trailing edge vicinity obtained with the model of Coull, the ratio of trailing edge thickness to the sum of pressure side and suction side momentum thickness was computed. A maximum $t_{TE}/\sum\theta$=4.4 was found for all the flow conditions investigated. The data of Melzer and Pullan [19] suggest a detached vortex shedding regime for round trailing edge geometries operating at transonic Mach number for the given $t_{TE}/\sum\theta_{TE}$.

Coull & Hodson [9] pointed out that in high-lift low-pressure turbine geometries, the local freestream velocity near the trailing edge tends to decrease as the blade loading increases. Based on the data from previous investigations, they built a correlation for the ratio $V_{TE,SS}/V_{out}$:

$$\frac{V_{TE,SS}}{V_{out}} = 1 - \frac{0.0006}{0.73 - g/S_L} \tag{7.15}$$

The left-hand term of Eq. 7.15 is below unity. The correlation of Senior & Miller [16] does not account for this effect. In fact, for a velocity ratio below unity, the second loss term (blockage term) in Eq. 7.13 decreases the overall loss.

MISES has been used to investigate the latter effect for the SPLEEN C1 geometry. The pitch-to-chord ratio was increased for fixed outlet Mach and Reynolds numbers. The computation was performed at M=0.70; Re=120k while keeping the turbulence intensity constant at 0.4%. Fig. 7.14(a) displays the blade loadings with increasing pitch-to-chord ratio. The near trailing edge Mach number is never found to go below the freestream value.

Fig. 7.14(b) displays the $V_{TE,SS}/V_{out}$ ratio as a function of the normalized cascade pitch. The suction side surface length normalizes the pitch to enable the comparison with Eq. 7.15, represented by the dashed line. The velocity ratio obtained for the SPLEEN blade tends to unity at the theoretical limit of Eq. 7.15 (0.73).

A similar pitchwise effect in the passage was observed for all flow conditions investigated with MISES (i.e., ratio above unity). Fig. 7.15 displays the pitchwise distribution of the velocity ratio just upstream of the trailing edge (x/C_{ax}=0.985). The profiles are characterized by an overshoot near the suction side and an undershoot near the pressure side. All the profiles investigated display a velocity ratio above unity near the trailing edge on the suction side. For a fixed Reynolds number, the overshoot typically decreases with the Mach number due to the reduction of the blade loading.

The impact from the velocity ratio for each loss breakdown scheme is compared in Fig. 7.16. The boundary layer integral quantities estimated with the model of Coull & Hodson [9] were used.

The black markers represent Denton's loss breakdown scheme (see Eq. 7.12). Red markers represent the correlation of Senior & Miller (SM). Full markers identify the loss obtained using the velocity ratio from Eq. 7.15. Hollow markers identify the loss obtained by using the $V_{TE,SS}$ from the MISES computation (also contained in Fig. 7.15).

The results for the steady flow cases are displayed in Fig. 7.16(a). The predicted loss increases with respect to experiments when the velocity ratio is inferior to unity. The recent

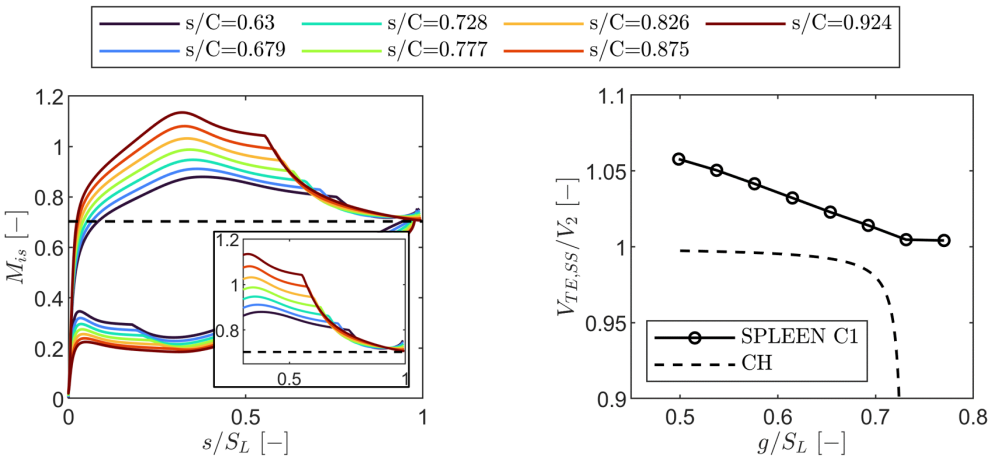

Figure 7.14: Impact of increasing the blade loading on the $V_{TE,SS}/V_{out}$ ratio (a) and ratio as a function of normalized cascade pitch (b).

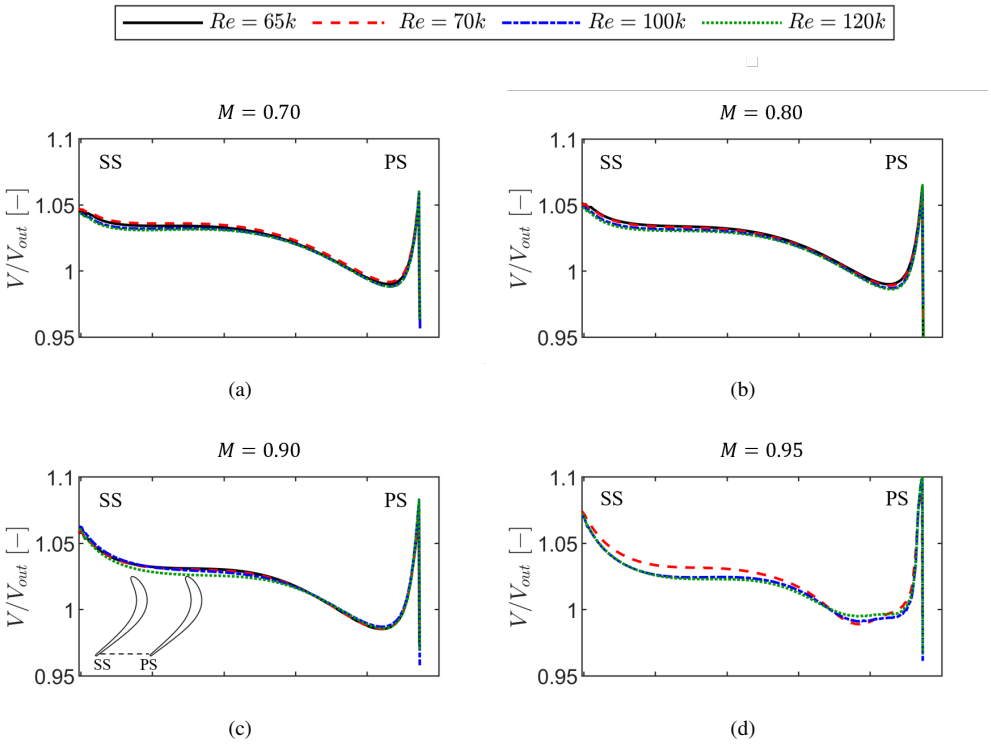

Figure 7.15: Pitchwise distribution of velocity ratio inside the passage in the vicinity of the TE obtained with MISES: M=0.70 (a), M=0.80 (b), M=0.90 (c), and M=0.95 (d).

model of Senior & Miller [16] best represents the experimental data. The root-mean-square error (RMSE) is ∼4.9% for the latter case (solid red markers), compared to an error of 11% for the loss breakdown of Denton coupled with the methodology of Coull & Hodson.

An analogous plot concerning the unsteady flow cases is presented in Fig. 7.16(b). The loss breakdown of Senior & Miller is found to provide the closest match of the experimental data (RMSE of ∼4.6%). A RMSE of ∼5.9% characterizes the model of Coull & Hodson.

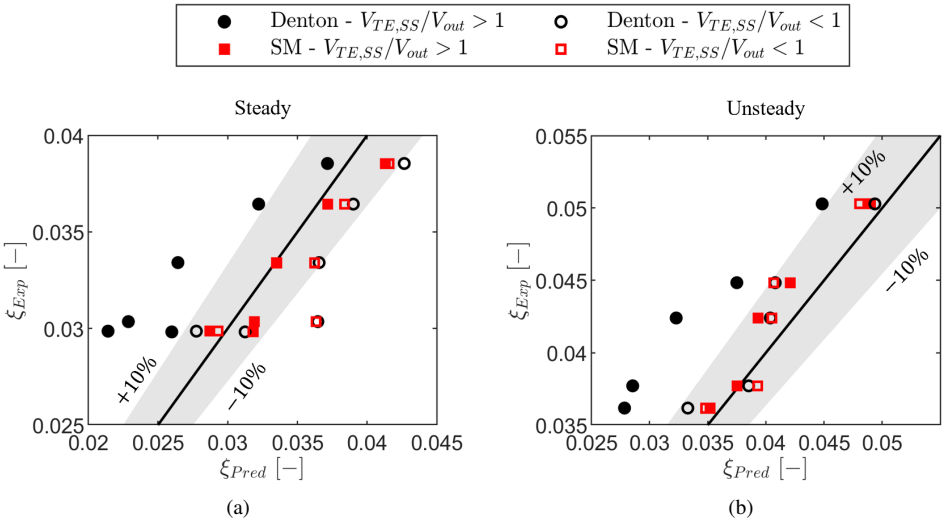

Figure 7.16: Impact of $V_{TE,SS}/V_{out}$ and loss breakdown scheme on profile loss prediction against experimental data: steady flow cases (a) and unsteady flow cases (b).

If both the steady and unsteady cases are considered, the model of Senior & Miller provides the best agreement to experiments with an RMSE of ∼4.7%. The model of Coull & Hodson resulted in an RMSE of ∼9.1%.

Table 7.6 summarizes the error for each flow condition and scheme coupling with the velocity ratio assumption.

Table 7.6: RMSE in estimating profile loss with breakdown of Denton [18], and Senior & Miller [16] with varying velocity ratio.

			Denton + CH		SM	
M $[-]$	Re $[-]$	St $[-]$	$\frac{V_{TE,SS}}{V_{out}} < 1$	$\frac{V_{TE,SS}}{V_{out}} > 1$	$\frac{V_{TE,SS}}{V_{out}} < 1$	$\frac{V_{TE,SS}}{V_{out}} > 1$
0.70	70,000	0.00	10.69	-3.60	7.83	7.18
0.80	70,000	0.00	7.05	-11.58	5.29	2.04
0.90	70,000	0.00	9.42	-20.90	8.46	0.24
0.95	70,000	0.00	20.13	-24.64	19.68	5.17
0.80	120,000	0.00	4.79	-12.85	6.67	6.76
0.90	120,000	0.00	-7.06	-28.28	-1.86	-3.85
0.70	70,000	1.19	-1.82	-10.83	-4.46	-2.67
0.90	70,000	0.95	-4.76	-23.85	-4.46	-7.26
0.95	70,000	0.91	2.14	-24.30	4.16	-0.52
0.70	120,000	1.19	-9.00	-16.36	-9.25	-6.11
0.90	120,000	0.95	-7.98	-23.03	-3.80	-2.65
		RMSE [%]	9.08	19.61	8.28	4.74

The exercise highlights the applicability of the model of Senior & Miller to model the profile loss of low-pressure turbine blading operating at low-Reynolds number in the presence of laminar separation bubbles and unsteady wakes. The model accounts for a trailing edge wedge angle term that is not present in the model of Coull & Hodson. In addition, the base pressure coefficient-related loss is also considered.

To capture the effect of the separation bubble and unsteady wakes, it is suggested that the model of Coull & Hodson is first used to estimate the boundary layer parameters based on the provided correlations. The terms should then be fed into the model of Senior & Miller to assess the loss contributions in terms of boundary layer mixing, blockage, trailing edge wedge angle, and base pressure coefficient.

7.1.2.4 Loss Breakdown

The model of Coull & Hodson was used to estimate the contributions of the turbulent wetted area, the separation bubble, and the wake to the boundary layer momentum thickness on the suction side in the vicinity of the trailing edge. The terms were then used to compute the loss contributions according to the loss breakdown scheme of Senior & Miller.

Fig. 7.17(a) displays the experimental versus predicted loss for the steady flow cases. The model captures the decrease of profile loss with Mach number. The model also correctly captures the reduction of the loss with Reynolds number. The maximum loss overprediction occurs at M=0.70; Re=65k, with an error of $\sim$7% to the experimental data.

Table I.1 and Table I.2 in Appendix I contain the boundary layer parameters computed with the Coull & Hodson model for the steady and unsteady flow cases. The pressure side displacement thickness is, at most, $\sim$40% of the suction side one ($\delta^*_{PS,TE} < 0.30\delta^*_{SS,TE}$). Similarly, the momentum thickness on the pressure side is also significantly lower than the one on the suction side ($\theta_{SS,TE}/\theta_{PS,TE}$ $\approx$50% at M=0.90 for steady flow cases and lower for unsteady ones). The contribution of the pressure side boundary layer increases with the Mach

number since the laminar separation bubble is shifted downstream, resulting in a thinner boundary layer by the trailing edge. At M=0.70, the pressure side contribution decreases to ∼30%.

Following the model of Coull & Hodson [9], a breakdown of the $\theta_{SS,TE}$ is performed. Fig. 7.17(b) displays the contribution of each term to the suction side momentum thickness as a function of the Mach number. The color of the curve highlights the Reynolds number. A different combination of line markers represents each term.

The total $\theta_{SS,TE}$ follows the trend of the profile loss and total momentum thickness. The increase of the momentum thickness due to the turbulent growth of the boundary layer is found to amount to as much as ∼99% of the total quantity. The bubble associate term decreases with Mach and Reynolds numbers.

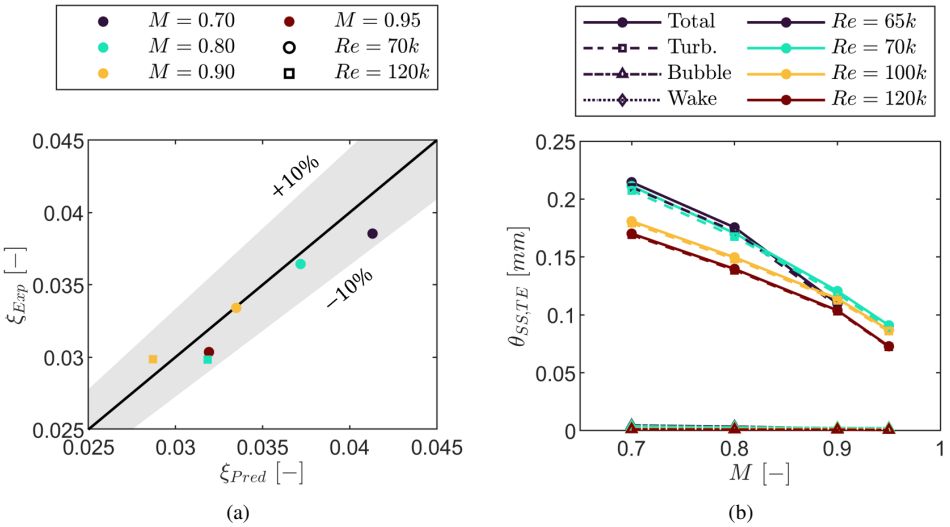

(a) (b)

Figure 7.17: Loss breakdown by flow condition (a), and contributions of BL on SS (b) for steady inlet flow cases.

Fig. 7.18(a) compares the experimentally measured profile loss with the modeled one for the unsteady cases. Overall, the modeled loss is underpredicted with respect to experiments. The largest underprediction occurs at M=0.90; Re=70k, for which the loss is underpredicted by ∼7% with respect to experiments. The model correctly captures the effect of the Mach and Reynolds numbers on the profile loss (i.e., decrease of the profile loss with Mach and Reynolds numbers).

A similar breakdown was performed for the steady case. Fig. 7.18(b) displays the breakdown of boundary layer contributions for the unsteady flow cases. The wake term is present in the contributions. The total quantity is found to be mainly impacted by the turbulent term. The contribution of the turbulent term amounts to as much as ∼75% of the overall $\theta_{SS,TE}$. The contribution of the bubble is smaller than for the steady cases and is more significant at M=0.95 (up to 0.6% of overall momentum thickness).

The wake contribution is found to be independent of the Reynolds number. This is likely associated with the fact that the Strouhal number remains unaltered with varying Reynolds

number. An increase in the Mach number results in a decrease in the reduced frequency. The contribution of the wake on the overall momentum thickness also decreases with the Mach number. The wake can amount to as much as 40% of the overall momentum thickness for the highest Mach number cases due to the reduction of the turbulent term. At M=0.70, the wake contribution ranges from 24%–28%.

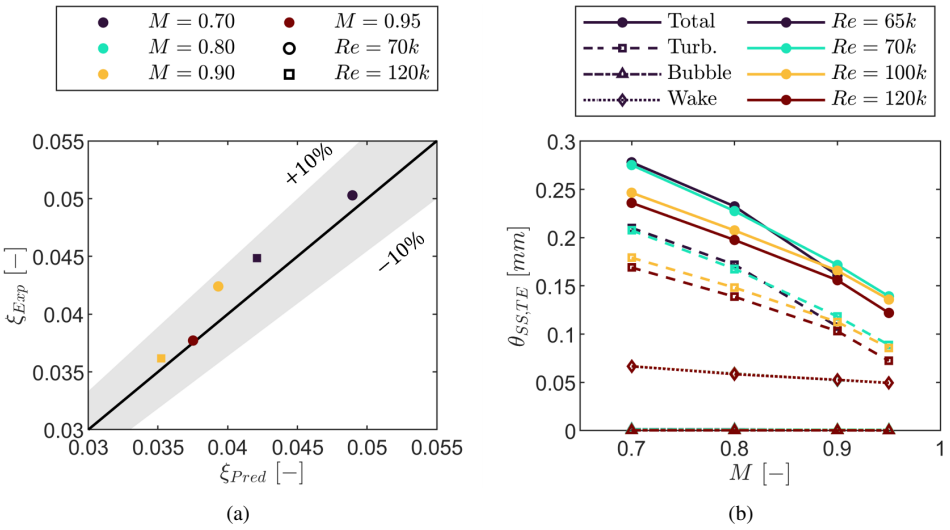

Figure 7.18: Loss breakdown by flow condition (a), and contributions of BL on SS (b) for unsteady inlet flow cases.

Recalling the model of Senior & Miller, the loss can be broken down into boundary layer mixing loss, blockage-induced loss, trailing edge wedge angle loss, and base pressure coefficient loss.

$$\xi_{mixing} = \frac{2\sum\theta}{g\cos\alpha_{out}}\left(\frac{V_{TE,SS}}{V_{out}}\right)^2 \tag{7.16}$$

$$\xi_{blockage} = \left(\frac{t_{TE}+\sum\delta^*_{TE}}{g\cos\alpha_{out}}\right)\frac{V_{TE,SS}}{V_{out}}\left(\frac{V_{TE,SS}}{V_{out}}\cos\frac{\alpha_w}{2}-1\right) \tag{7.17}$$

$$\xi_{wedge} = \left(\frac{t_{TE}+\sum\delta^*}{g\cos\alpha_{out}}\right)\left(\frac{V_{TE,SS}}{V_{out}}\right)^2\sin\frac{\alpha_w}{2} \tag{7.18}$$

$$\xi_{base} = C^*_{pb}\left(\frac{t_{TE}+\sum\delta^*_{TE}}{g\cos\alpha_{out}}\right)\left(\frac{V_{TE,SS}}{V_{out}}\right)^2 \tag{7.19}$$

C^*_{pb} is the base pressure coefficient computed as:

$$C^*_{pb} = \frac{P_{base}-P_{TE,SS}}{\frac{1}{2}\rho V^2_{TE,SS}} \tag{7.20}$$

P_{base} was taken at the last available data point on the blade pressure and suction surfaces, which is the same due the treatment that MISES employs to model the blunt trailing edge as

a viscous layer (see Section 3.1) , and $P_{TE,SS}$ was taken to be the freestream static pressure near the trailing edge on the SS.

Fig. 7.19 highlights the loss breakdown for the steady and unsteady inlet flow cases. The left column contains the loss terms for the steady flow cases, while the right column contains the loss for the unsteady terms. The profile loss is represented as a function of the Mach number for each Reynolds number highlighted by the color of the marker–line arrangement. Overall, the trends found for the steady and unsteady cases are similar.

The mixing loss (see Fig. 7.19(a) and Fig. 7.19(b)) resemble the overall shape of the loss trends described previously. The profile loss decreases with Mach and Reynolds numbers. The trend results from reducing the boundary layer momentum thickness with Mach and Reynolds numbers in Eq. 7.16. The trends are similar for the steady and unsteady cases. However, the mixing loss is higher for the unsteady inlet flow cases.

The blockage loss (see Fig. 7.19(c) and Fig. 7.19(d)) is found to increase with Mach number. Even though the boundary layer displacement thickness plays a role in the loss term, the term is strongly driven by the velocity ratio term, $V_{TE,SS}/V_{out}$, that increases with Mach number (i.e., decreases with loading). The term accounts for 90% of the overall blockage loss. The blockage term displays insensitivity to the unsteady wakes.

Fig. 7.19(e) and Fig. 7.19(f) displayed the trailing wedge-related loss for the steady and unsteady flow cases, respectively. The loss component remains nearly unaltered with the Mach number. The negligible reduction is due to a decrease of the first term in Eq. 7.18 attributed to the reduction of the displacement thickness with Mach number. The maximum variation amounts to $\Delta\xi_{wedge}\approx$0.01% for the steady case at M=0.95. This result was expected since Eq. 7.18 is mainly driven by the wedge angle rather than the flow parameters. Reducing the trailing edge wedge angle loss term with Reynolds number is also visible—-the latter results from lowering the first and second terms in Eq. 7.18. The overall level is conserved between the steady and unsteady inlet flow cases.

Lastly, the loss term related to the trailing edge base pressure is displayed in Fig. 7.19(g) and Fig. 7.19(h) for the steady and unsteady flow cases, respectively. Even though the term increases with the Reynolds number, the Mach number displays a more substantial effect. Even though the displacement thickness decreases with the Reynolds number, the base pressure coefficient and velocity (first and third terms in Eq. 7.19) ratio increase enough to promote an enhancement of this loss term. Since the velocity ratio and base pressure coefficient terms dominate the loss term, the steady and unsteady loss are similar.

The previous results highlight trends in the loss terms without providing a relative weight of each term to the overall loss. Fig. 7.20 displays the breakdown of loss components normalized by the total loss for the steady and unsteady flow cases. The color of the marker–line arrangement represents the Reynolds number.

The boundary layer mixing loss is the most significant contributor to the overall profile loss and can account for as much as 75% at M=0.70. The relative contribution increases for the unsteady inlet flow cases, for which the relative contribution is nearly 80%. The mixing loss contribution decreases with Mach and Reynolds numbers. The decrease in the contribution of the mixing loss to the overall loss is less severe for the unsteady flow cases, with respect to the steady ones ($\Delta\xi/\xi_{mixing}\approx$0.17 vs. 0.22).

The second largest contributor to the loss comes from the boundary layer blockage. The contribution to the overall loss doubles as the Mach number increases from 0.70 to 0.95.

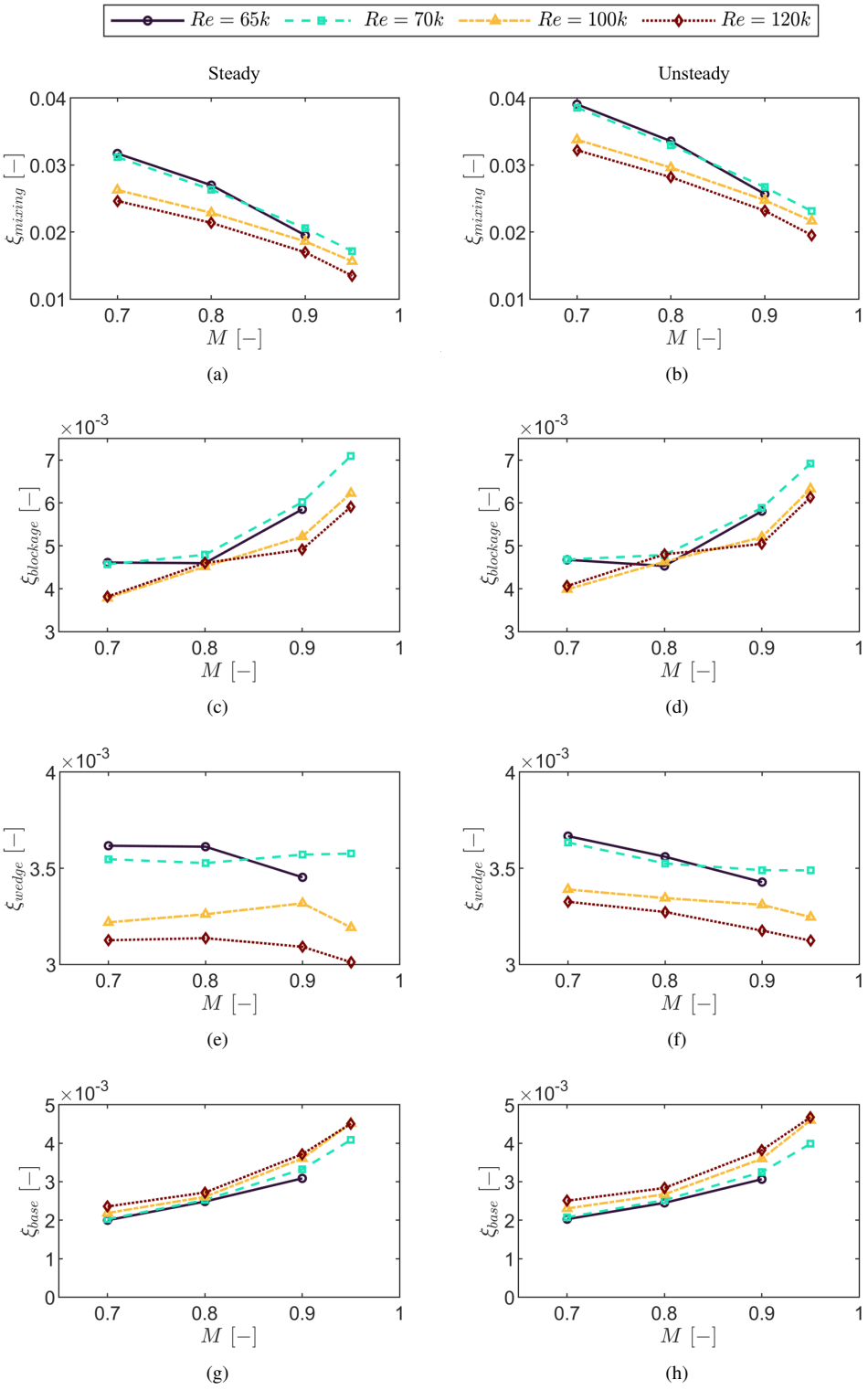

Figure 7.19: Breakdown of loss contributions of profile loss for steady and unsteady inlet flow from Eq. 7.16–Eq. 7.19: mixing loss (a, b), blockage loss (c, d), trailing edge wedge angle loss (e, f), and base pressure loss (g, h).

The term is negligibly independent of the Reynolds number. The contribution of the term decreases for the unsteady inlet flow cases even though the absolute magnitude is similar (see Fig. 7.19(c) and Fig. 7.19(d)). The latter is attributed to the weaker reduction of the mixing contribution for the unsteady inlet flow cases with respect to the steady ones.

The wedge loss term amounts to $\sim$10% of the overall loss. The term is independent of the Reynolds number. The contribution to the overall loss increases by $\sim$20% with the Mach number for both steady and unsteady cases. Due to the more substantial contribution of the mixing loss for the unsteady cases, the wedge term is characterized by a lower contribution for the unsteady flow cases.

The base pressure loss term has a weaker contribution than the wedge term up to M=0.80. The increase in the magnitude of base pressure coefficient a and velocity ratio with Mach number increases the contribution towards higher Mach numbers (lower blade loading). The loss contribution increases with the Reynolds number as well. The contribution to the loss decreases for the unsteady flow cases.

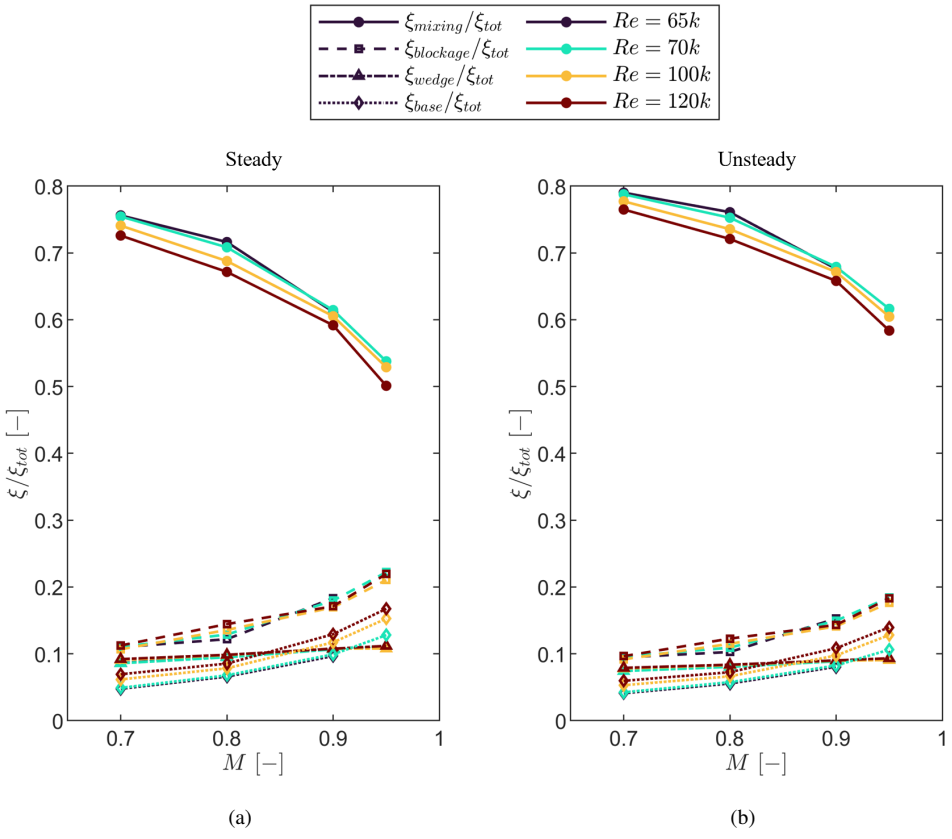

Figure 7.20: Loss breakdown relative to total loss for each flow case.

7.2 Secondary Loss

Both families of Ainley and Mathieson [1–3, 5–7], and Craig and Cox [7] models also provide correlations for the estimation of the secondary loss. Fig. 7.21(a) compares the predicted and experimentally measured secondary loss with the surveyed models. Similar to the profile loss model, the agreement with the correct experimental data improved for recent models. The model of Ainley & Mathieson overpredicts the loss by as much as 360%. The improved model of Dunhan and Came [2] still underpredicts the loss by more than 200%. The Ainley & Mathieson models and variants assume that the secondary flow loss is exclusively a function of the blade geometry. Not accounting for the loading variation with Mach number nor inlet boundary layer properties is translated into a constant loss value regardless of the flow condition. Even though the model of Benner et al. [5, 6] accounts for the inlet boundary layer thickness, blade aspect ratio, and geometrical parameters, the loss is still insensitive to the Mach number and greatly overpredicted.

Fig. 7.21(a) compares the predicted and experimentally measured secondary loss with the Craig & Cox model and the model proposed by Coull [21].

The model of Craig and Cox [7] provides good agreement with the experiments (the model was published around the same time as the DC model). The better agreement from the Craig & Cox model is justified by accounting for the inlet-to-outlet velocity ratio and the blade geometry as a lifting parameter. The aspect ratio is also considered. The model captures the impact of the Mach number.

The model of Coull estimates values near the ones measured experimentally and predicts decreasing secondary loss with Mach number.

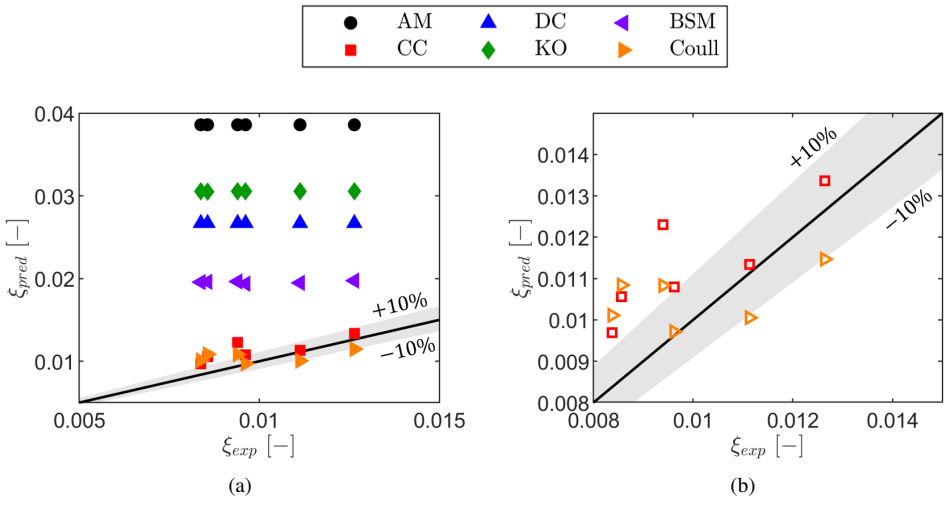

Figure 7.21: Comparison between experimentally measured and predicted secondary loss with different models (a) and the highlight of most accurate models in the family of models of Ainley and Mathieson models, Craig and Cox model, and Coull. Only the steady cases without purge are included.

7.2.1 Model of Coull, 2017

The Craig & Cox model is incredibly reliable in estimating the secondary loss compared to its simplicity. It is also among the most reliable for profile loss. The latter was also pointed out in [9]. However, the shortcoming of the Ainley & Mathieson model derivatives and Craig & Cox model is that they do not allow a qualitative interpretation of the factors driving the loss. The model of Coull, on the other hand, allows a decoupling of loss contributors: passage vortex, trailing shed vorticity, and corner vortex. The endwall loss due to the boundary layer dissipation is approximated by:

$$\xi_{CD} \approx 2C_D \left(\frac{A_{end}}{Hg\cos\alpha_{out}}\right) \int \left(\frac{T_{out}}{T_{end}}\right) \left(\frac{\rho_{end}}{\rho_{out}}\right) \left(\frac{V_{end}}{V_{out}}\right)^3 d\left(\frac{A}{A_{end}}\right) \tag{7.21}$$

The dissipation coefficient in the boundary layer, $C_D \approx 0.02$, is assumed to be constant [18]. A_{end} is the endwall area used to integrate the loss, H is the cascade span, g is the cascade pitch, α is the flow angle, T is the static temperature, ρ is the density, and V is the local isentropic flow velocity. The subscripts denote whether the quantity is local at the endwall surface or the cascade outlet.

The work of Coull [21] suggests two methods to estimate the above loss term. The recommended one is to use actual endwall data from a CFD computation. Without this data, this work uses the flowfield at midspan from fully turbulent MISES computations. A comparison of the quantities from the MISES and endwall experimental data is performed to quantify the impact.

The visual comparison is performed regarding the isentropic Mach number along streamlines following the passage. Fig. 7.22(a) displays the five streamlines along which data is compared. The isentropic Mach number along the normalized axial distance is shown in Fig. 7.22(b). Filled markers denote the experimental points, while the lines represent the MISES computations. The Mach number was found to be overpredicted by the MISES near the pressure side (black line). The opposite applies near the suction side (purple line). The "symmetry" of the variation contributes to reducing the difference between the integral computed with the endwall quantities versus the one using MISES data.

Eq. 7.21 has been solved in the endwall area constrained by the existing experimental data points. Fig. 7.23 compares the endwall integrated loss in the experimental delimited area using the experimental quantities (y-axis) and MISES (x-axis). The experimental data underpredicts the loss with respect to MISES by $\sim$27%. Nonetheless, this amounts to $\sim$0.01% in absolute terms (5% of expected endwall loss). The MISES approach is deemed satisfactory in the scope of this work. Rather than just using the endwall area delimited by the available experimental taps, the whole flow domain from Plan 01 to 06 was considered (i.e., $x/C_{ax} \in [-1.12C_{ax}, 1.50C_{ax}]$).

The endwall dissipation loss is summed to the secondary flow-induced loss estimated based on the vorticity amplification factor described as:

$$\xi_{sec} \approx 0.0021 \times 2M^* \left(\frac{V_{in}}{V_{out}}\right)^2 \left[\frac{\Delta T^*}{g\cos\alpha_{out}} + \frac{|\frac{V_{out}}{V_{in}}\sin\alpha_{in} - \sin\alpha_{out}|}{\cos\alpha_{out}}\right] \tag{7.22}$$

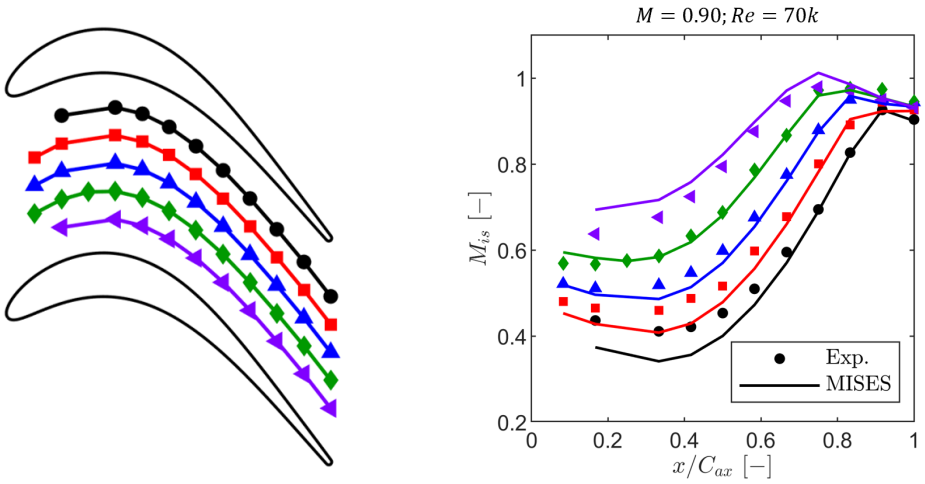

Figure 7.22: Streamlines along the passage used to compare endwall experimental quantities against ones retrieved from MISES (a) and isentropic Mach number distribution along the normalized axial direction (b).

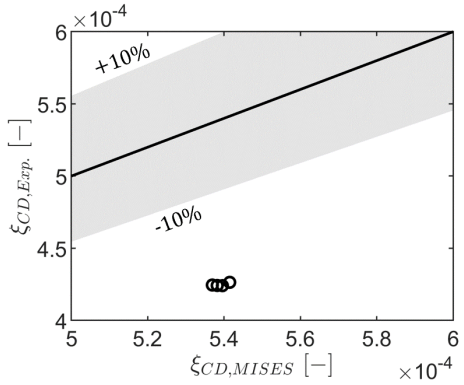

Figure 7.23: Endwall loss computed with experimental data against one compute with MISES results. Loss integral is solved in an experimentally delimited area.

M^* is the compressibility factor, V is the velocity, ΔT^* is the non-dimensional transit time between the blade pressure and suction side flow, g is the cascade pitch, and α is the flow angle. The reader is referred to [21] for a detailed description of the terms in Eq. 7.21 and Eq. 7.22.

The model of Coull was compared against experimental data in Fig. 7.24(a). The experimental endwall loss under steady inlet flow is computed by subtracting the profile loss and inlet boundary layer loss from the gross loss. Solid markers highlight cases where the inlet boundary layer kinetic energy is calculated at Plane 01 using the data measured with the Preston tube. The boundary layer at Plane 02 under steady flow conditions has been solely measured for the nominal flow case (black hollow marker). For cases where the wake generator was present (with and without cavity), the boundary layer has only been characterized at Plane 02. The red marker denotes the case with the wake generator and flat endwall. The blue markers concern the cases with cavity endwall and increasing purge massflow ratio.

The endwall loss computed by accounting for the kinetic loss coefficient at Plane 01 displays good agreement with the Coull model. For steady inlet flow, accounting for the kinetic energy deficit at Plane 02 significantly increases the experimental endwall loss. An error of $\sim$30% with respect to the predictions is observed.

The model does not represent the case well with the wake generator. An underprediction of the loss by $\sim$26% is observed for the case with the flat endwall. Introducing the cavity endwall worsens the underprediction, which becomes more critical with increasing the purge massflow ratio. For the highest purge massflow ratio, the model underpredicts the loss by more than 100%. The former results highlight the sensitivity of the experimental loss, which is strongly influenced by the measuring environment. Coull [21] pointed out inconsistencies in the type and quality of the data used in loss correlations as a bottleneck for accurate models.

A flow condition sensitivity considering the steady inlet flow cases and accounting for the inlet kinetic energy deficit at Plane 01 is displayed in Fig. 7.24(b). The color of the marker corresponds to the flow Mach number, and the marker corresponds to the flow Reynolds number. The model captures the Mach number dependency on the loss for both Reynolds number investigated. All cases are near the $\pm$10% bound for the lowest Reynolds number except for the M=0.80 case. A higher Reynolds number results in an overprediction of the loss with respect to experiments. The latter can be attributed to the model being relatively insensitive to the Reynolds number (uses fully turbulent blade loading) and not capturing the decrease in loss observed experimentally.

The method of Coull is used to provide a characterization of the secondary flow features impacting the overall endwall loss. The model relates non-dimensional amplification factors (AF) of the passage vortex 7.23, corner vortex 7.24, and trailing shed vorticity 7.25 to the secondary flow mixing induced loss:

$$AF_{PV} = \left(\frac{V_{in}}{V_{out}}\right)^2 \left(\frac{\Delta T^* C_{ax}}{g \cos \alpha_{out}} + \frac{\left|\frac{V_{out}}{V_{in}} \sin \alpha_{in} - \sin \alpha_{out}\right|}{\cos \alpha_{out}}\right) \tag{7.23}$$

$$AF_{CV} = -\left(\frac{V_{in}}{V_{out}}\right)^2 \frac{\Delta T^* C_{ax}}{g \cos \alpha_{out}} \tag{7.24}$$

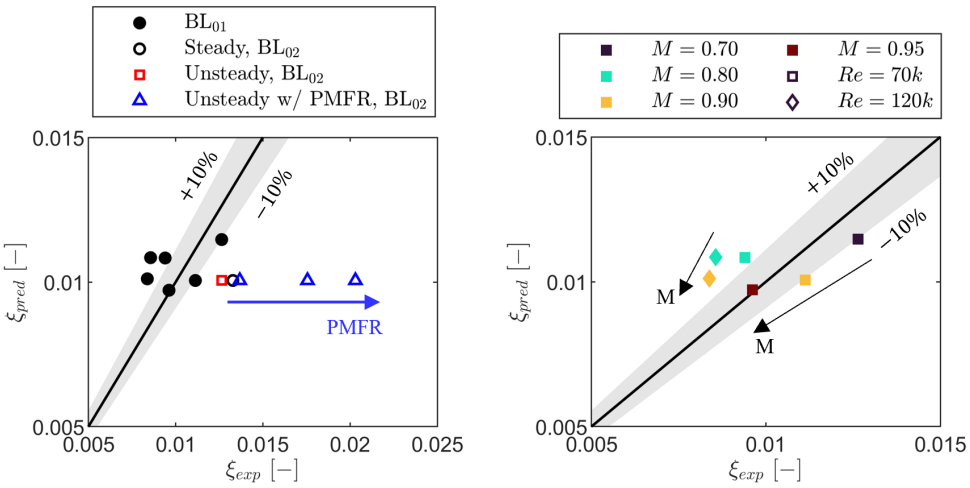

Figure 7.24: Sensitivity of experimental loss to inlet kinetic energy loss coefficient (a), and impact of Mach and Reynolds numbers if inlet kinetic energy at Plane 01 is accounted for (b).

$$AF_{TSV} = -\left(\frac{V_{in}}{V_{out}}\right)\frac{\cos\alpha_{in}}{\cos\alpha_{out}}\left|\tan\alpha_{out} - \tan\alpha_{in}\right| \tag{7.25}$$

The sum of the amplification factors is related to the secondary flow mixing loss through a constant (see Eq. 7.26). Therefore, the contribution of each term to the overall loss can be addressed independently.

$$\xi_{mix} \approx 0.0021 \sum AF \tag{7.26}$$

Fig. 7.25(a) displays the various amplification factors (AF) in the function of the Mach number. The color of the curve represents the Reynolds number. The marker-line combination is associated with the amplification factor of each flow structure and the sum of the contributions. The passage vortex is the major contributor to the mixing loss. It roughly accounts for 50% of the loss. The trailing shed vorticity is the second largest contributor to low Mach numbers. At higher Mach numbers, the contribution of the trailing shed vorticity and suction side corner vortex are similar. All contributions decrease with the Mach number and are practically insensitive to the Reynolds number.

A similar exercise is performed to decouple the contribution of the endwall boundary layer dissipation loss and mixing terms in Fig. 7.25(b). The mixing loss associated with the secondary flow structures accounts for ∼75% of the overall endwall loss. The mixing loss follows the same trend as the sum of the amplification factors. As a result, a decrease of loss with Mach number is observed. The loss is also insensitive to the Reynolds number. The endwall dissipation loss is relatively insensitive to Mach and Reynolds numbers.

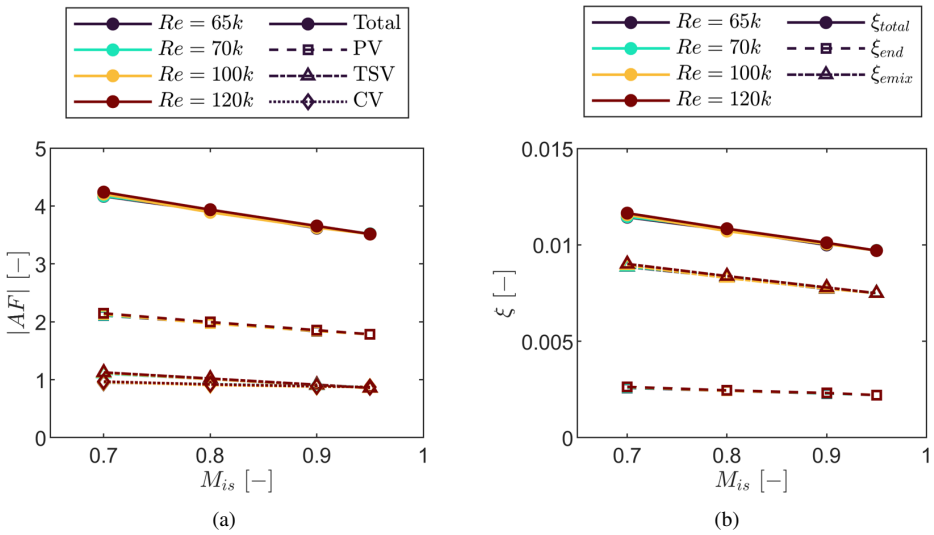

Figure 7.25: Breakdown of contribution by secondary flow structure (a) and breakdown of loss into endwall dissipation and mixing (b) for steady flow cases.

7.2.2 Model of Coull and Clark, 2022

An alternative approach to avoid relying on the characterization of the boundary layer in terms of kinetic energy is the one proposed by Coull and Clark [22]. The method takes into account the inlet boundary layer using its thickness and shape factor in the parameter:

$$\Pi_{SKE} = f\left(\frac{\delta_{98}}{g\cos\alpha_{out}}, H_{12}\right) \tag{7.27}$$

The parameter is obtained from a look-up table that requires the boundary layer parameters as inputs. A wide range of boundary layers was considered to build the coefficient typical of high-pressure, low-pressure, and linear cascades. The parameter is used in the estimation of the secondary kinetic energy loss coefficient:

$$\zeta_{SKE} \approx 2\left(\frac{g\cos\alpha_{out}}{H}\right)\left[\frac{\Gamma_{sec}}{V_{out}g\cos\alpha_{out}}\right]^2 \Pi_{SKE} \tag{7.28}$$

Where g is the cascade pitch, α is the flow angle, H is the cascade span, Γ_{sec} is the total secondary circulation, and V is the velocity. The first term in the previous equation captures the decreasing loss with aspect ratio, while the second captures the effect of the blade geometry on the secondary loss. The third term captures the impact of the boundary layer. The secondary circulation is defined as:

$$\frac{\Gamma_{sec}}{V_{out}g\cos\alpha_{out}} = V^*\frac{\Delta T^* C_{ax}}{g\cos\alpha_{out}} + \left|\frac{V_{in}}{V_{out}}\frac{\sin\alpha_{in}}{\cos\alpha_{out}} - V^*\tan\alpha_{out}\right| \tag{7.29}$$

The secondary kinetic energy coefficient computed with the model of Coull is compared against experiments in Fig. 7.26(a). Solid markers describe the cases obtained considering the

boundary layer parameters measured at Plane 01. Overall, there is a good agreement between predicted and experimental values. Using the boundary layer quantities measured at Plane 02 under steady inlet flow (hollow black marker) does not significantly modify the findings as for the kinetic energy loss coefficient displayed in Fig. 7.24(b). The wake generator promoted an overall disagreement between the experiments and predictions. For cases where the cavity is present (blue hollow markers), the disagreement results from characterizing the boundary layer upstream of the cavity slot. However, the case with the wake generator and flat endwall (red hollow marker) is still significantly overpredicted by the model with respect to experiments (by 60%). The considerable variation of the experiments with respect to the model for the cases with purge likely steers from the lack of the inlet boundary layer characterization downstream of the cavity slot. On the other hand, the discrepancy for the unsteady flow case in the absence of the cavity slot can be partially attributed to the measurement challenges in a transonic flow environment.

A flow sensitivity breakdown is performed for the steady inlet cases in Fig. 7.26. For the lowest Reynolds number, the lowest and highest Mach number cases are outside the $\pm 10\%$ bounds by as much as 23% at M=0.95. In addition, the loss is underpredicted by 17% with respect to experiments at M=0.80; Re=120k.

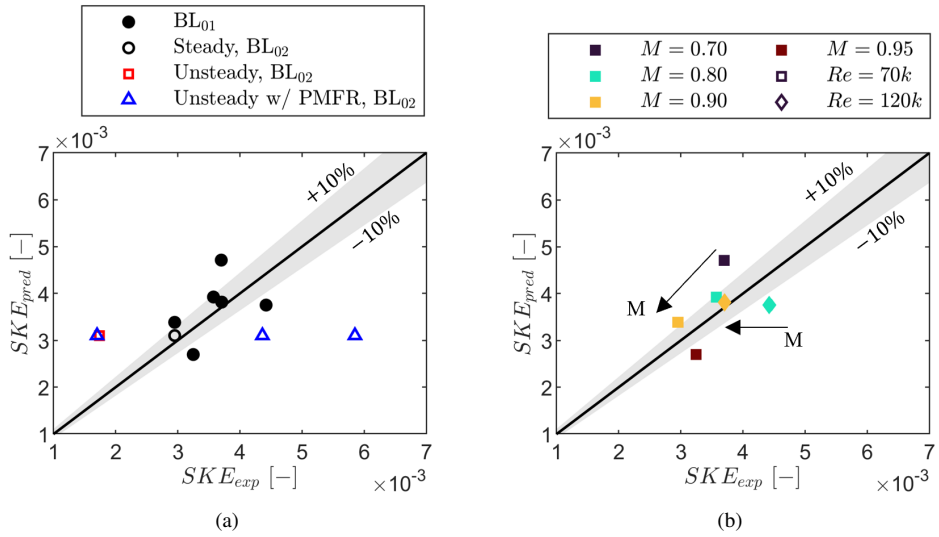

Figure 7.26: Sensitivity of experimental loss to inlet boundary layer parameters (a) and impact of Mach and Reynolds numbers if inlet boundary layer at Plane 01 is accounted for (b).

7.3 Conclusions

Different profile loss correlations from the 1950s onwards have been compared against the experimental data. The models consisted of Ainley & Mathieson variants and the model of Craig & Cox. An improvement of the agreement between the Ainley & Mathieson family of models occurred over the years due to updating the model with state-of-the-art turbine

designs. The model of Benner et al. [5, 6] provided the best agreement to the experimental data out of the Ainley & Mathieson family. The model correctly predicts a reduction of the profile loss with Reynolds number but wrongly predicts the Mach number dependence.

The model of Coull & Hodson [9] is used to provide insight into the profile loss terms. The underlying assumptions of the model were challenged and calibrated with the data of the current work. A comparison of the experimental data with the transitional MISES computations revealed the capability of the tool to predict the profile loss of turbine blading operating with open separation bubbles. Nonetheless, the latter findings were biased due to the use of the turbulence intensity that best represents the blade loading. The predicted boundary quantities were fed into the newly developed loss breakdown model of Senior & Miller [16]. A remarkable agreement, characterized by a root-mean-square error of 4.7%, was found between the experiments and predicted loss. The exercise highlighted the potential of the model in predicting the profile loss of turbine blading operating at flow conditions that can promote a laminar separation bubble in addition to the impact of unsteady wakes.

The proposed methodology correctly captured the effect of Mach and Reynolds numbers on the profile loss. Interestingly, the profile loss was well captured at M=0.95, for which shocks may impact the separation and transition of the boundary layer. A breakdown of the boundary layer momentum thickness on the suction side revealed that the suction side loss is strongly influenced by the boundary layer turbulent wetted for the SPLEEN C1 profile. The latter is attributed to the low loading, which characterizes the investigated blading and results in a thin separation bubble. As a result, the turbulent term amounts to as much as 99% of the overall quantity for the steady inlet flow cases. Upon the introduction of unsteady wakes, the contribution of the turbulent term was reduced to 75%.

The model of Senior and Miller was used to break down the contribution of loss terms: boundary layer mixing, trailing edge blockage, trailing edge wedge angle, and base pressure coefficient. Similar trends were found for the steady and unsteady inlet flow cases. The boundary layer mixing loss was found to amount to as much as 70% and 80% of the overall profile loss at M=0.70 for the steady and unsteady inlet flow cases, respectively. The mixing loss term was found to decrease with Mach and Reynolds numbers. On the other hand, the blockage-related loss contributed to as much as 20% of the overall profile loss at M=0.95. The trailing edge wedge angle associated term accounted for nearly 10% of the overall loss and remained relatively unaltered since the geometry was not varied.

Similarly, the secondary loss is overpredicted by models from the Ainley & Mathieson family. The model of Craig & Cox provides excellent agreement. This is believed to be due to the model considering the blade loading as a lifting coefficient. Nonetheless, the model cannot give a detailed breakdown of the loss terms.

The model of Coull [21] is used for such an effect. The model takes into account the blade loading. Due to the lack of 3D endwall data at the inlet and outlet of the cascade, the potential flowfield from MISES has been used to determine the endwall dissipation coefficient. A comparison with the limited experimental data revealed a mismatch near the pressure side and suction side. However, the contribution to the overall loss is satisfactory small (5% of the secondary loss).

The model displayed considerable sensitivity to the cases with purge flow. The case with the wake generator was also not exceptionally matched against the loss prediction (misprediction by 26% for the case with cavity slot without purge injection). For the steady flow cases,

the experimental secondary loss was revealed to be extremely sensitive to the inlet boundary layer kinetic energy deficit. The loss in the case of the wake generator and flat endwall was also underpredicted by the model.

The boundary layer at Plane 02 overpredicted the loss by 19%. Therefore, the probe and location of the boundary layer measurements are crucial for quantifying secondary loss.

The model somewhat represents the steady flow cases well. The cases at Re=70k generally fall within the $\pm$10% error band. The model overpredicts the loss at a higher Reynolds number with respect to the experiments.

A loss breakdown revealed that the passage vortex has the highest contribution to the secondary loss ($\sim$50% of overall secondary mixing loss). The suction side corner vortex and trailing shed vorticity have similar contributions at high Mach numbers. At M=0.70, the trailing shed vorticity represents $\sim$27%, while the suction side corner vortex accounts for $\sim$23% of the overall secondary mixing loss. The model does not predict the Reynolds number sensitivity observed during the experiments.

Lastly, the model of Coull and Clark was considered. The model accounts for inlet boundary layer features: thickness and shape factor. The cases with wake generators were still poorly described by the model. On the other hand, the secondary loss computed with the boundary layer parameters at Plane 01 (with the Preston tube) and at Plane 02 (with the C5HP) is within a $\pm$10% tolerance. The better agreement is attributed to the sensitivity of the model to the inlet boundary layer parameters. The model describes the experimental data with good agreement except for the lowest and highest Mach numbers at Re=70k, and M=0.80; Re=120k.

References

[1] D.G. Ainley and G.C.R. Mathieson. *A method of performance estimation for axial-flow turbines*. 1951.

[2] J. Dunham and P.M. Came. *Improvements to the Ainley-Mathieson Method of Turbine Performance Prediction*. Journal of Engineering for Power, 92(3):252–256, 07 1970.

[3] S.C. Kacker and U. Okapuu. *A Mean Line Prediction Method for Axial Flow Turbine Efficiency*. Journal of Engineering for Power, 104(1):111–119, 01 1982.

[4] J. Zhu and S.A. Sjolander. *Improved Profile Loss and Deviation Correlations for Axial-Turbine Blade Rows*. volume Volume 6: Turbo Expo 2005, Parts A and B of *Turbo Expo: Power for Land, Sea, and Air*, pages 783–792, 06 2005.

[5] M.W. Benner, S.A. Sjolander, and S.H. Moustapha. *An Empirical Prediction Method for Secondary Losses in Turbines—Part I: A New Loss Breakdown Scheme and Penetration Depth Correlation*. Journal of Turbomachinery, 128(2):273–280, 02 2005.

[6] M.W. Benner, S.A. Sjolander, and S.H. Moustapha. *An Empirical Prediction Method For Secondary Losses In Turbines—Part II: A New Secondary Loss Correlation*. Journal of Turbomachinery, 128(2):281–291, 02 2005.

[7] H.R.M. Craig and H.J.A. Cox. *Performance Estimation of Axial Flow Turbines*. Proceedings of the Institution of Mechanical Engineers, 185(1):407–424, 1970.

[8] W. Traupel. *Thermische Turbomaschinen: Band 1: Thermodynamisch-stromungstechnische Berechnung*. Springer-Verlag, 2019.

[9] J. Coull and H. Hodson. *Predicting the Profile Loss of High-Lift Low Pressure Turbines*. Journal of Turbomachinery, 134(2):021002, 06 2011.

[10] K. Pohlhausen. *Zur näherungsweisen Integration der Differentialgleichung der Iaminaren Grenzschicht*. ZAMM - Journal of Applied Mathematics and Mechanics / Zeitschrift für Angewandte Mathematik und Mechanik, 1(4):252–290, 1921.

[11] R. Timman. *A one parameter method for the calculation of laminar boundary layers*. National Aeronautical Research Institute, 1948.

[12] A. Walz. *Ein neuer Ansatz für das Greschwindligkeitsprofil der laminaren Reibungsschicht*. Lilienthal-Bericht, 141, 1941.

[13] B. Thwaites. *Approximate Calculation of the Laminar Boundary Layer*. Aeronautical Quarterly, 1(3):245–280, 1949.

[14] N. Curle and S.W. Skan. *Approximate Methods for Predicting Separation Properties of Laminar Boundary Layers*. Aeronautical Quarterly, 8(3):257–268, 1957.

[15] B.S. Stratford and G.E. Gadd. *Flow in the laminar boundary layer near separation*. (3002), 1954.

[16] A. Senior and R. Miller. *A Data-Centric Approach to Loss Mechanisms*. Journal of Turbomachinery, 146(4):041007, 12 2023.

[17] F.M. White and J. Majdalani. *Viscous fluid flow*, volume 3. McGraw-Hill New York, 2006.

[18] J.D. Denton. *The 1993 IGTI Scholar Lecture: Loss Mechanisms in Turbomachines*. Journal of Turbomachinery, 115(4):621–656, 10 1993.

[19] A.P. Melzer and G. Pullan. *The Role of Vortex Shedding in the Trailing Edge Loss of Transonic Turbine Blades*. Journal of Turbomachinery, 141(4):041001, 01 2019.

[20] A.D. Rossiter, G. Pullan, and A.P. Melzer. *The Influence of Boundary Layer State and Trailing Edge Wedge Angle on the Aerodynamic Performance of Transonic Turbine Blades*. Journal of Turbomachinery, 145(4):041008, 11 2022.

[21] J.D. Coull. *Endwall Loss in Turbine Cascades*. Journal of Turbomachinery, 139(8):081004, 03 2017.

[22] J.D. Coull and C.J. Clark. *The Effect of Inlet Conditions on Turbine Endwall Loss*. Journal of Turbomachinery, 144(10):101011, 06 2022.

8 Conclusions

This thesis presented a comprehensive experimental characterization of the aerodynamics of an open-access transonic low-pressure turbine cascade. The rig, alongside its constituents, has been thoroughly characterized. The setup consists of a linear cascade with 23 blades representative of the rotor hub geometry of a geared turbofan. The experiments were carried out at engine-relevant Mach and Reynolds numbers. The unsteady wakes shed from upstream stages were simulated employing cylindrical bars. The bar wake reduced frequency and flow coefficients represent the ones found in geared low-pressure turbine models. The impact of purge flows on the secondary flow development and loss was made by injecting a secondary air stream between the wake generator plane and the cascade. Ultimately, the experimental campaign generated unprecedented open-access data concerning the profile and secondary aerodynamics of turbine blading operating with loading and flow conditions relevant to geared turbofans.

The experimental investigation required adapting and commissioning a transonic linear cascade, the VKI S-1/C, to enable near-wall measurements. The test section is heavily instrumented with time-averaged and phase-averaged instrumentation. Even though the experimental techniques used in this work are considered conventional, a development of their capabilities to measure transonic low-density flows was achieved. Particular attention was paid to the development of a suitable hot-wire technique.

The revamped rig was commissioned in terms of flow stability, blade-to-blade periodicity, and probe interference in transonic flows. During the multi-year experimental campaign, the rig flow was stable (variation in Mach and Reynolds numbers within $\pm 0.22\%$ and $\pm 0.40\%$ from the nominal operating point, respectively. The Strouhal number was found to be within $\pm 0.27\%$ from the nominal value, and the purge massflow ratio to be within $\pm 0.46\%$). Characterization of potential interactions of the measuring probes with the cascade flow highlighted the challenges of measuring with probes of finite size in internal transonic flows. Measurements at the cascade outlet were particularly impacted. The probe caused a redistribution of

the massflow that could be experienced as far as one axial chord upstream of the cascade leading edge plane. Variations in the endwall static pressure at the probe axial plane were ± 0.05. The endwall static pressure used for the loss computation was, therefore, one obtained in the absence of the probe at the outlet.

The experimentally measured profile aerodynamics have been benchmarked against a boundary layer Euler code (MISES) and RANS with a state-of-the-art transitional model. The MISES transitional model was "calibrated" to match the experimental loadings. An ambiguous turbulence intensity of $\sim$0.4% (vs. 2.4% measured experimentally) was required to capture the laminar separation bubble topology. The inlet boundary conditions to the RANS computation were calibrated to match the turbulence decay profile measured experimentally. Both CFD and MISES have shown overall good agreement with the experimental data. The CFD fails to predict the blade loading at a low Reynolds number, particularly for cases with open separation or reattachment near the trailing edge.

Existing models obtained in low-speed flat plate and cascade testing could capture the separation and reattachment locations of the separation bubble up to the Mach number at which shocks impact the separation and/or transition of the boundary layer. This finding suggests that conventional tools can describe high-speed low-pressure turbines.

In the scope of wake-boundary layer interaction, the celerities of conventional wake-induced transition mechanisms could be sensed by the surface-mounted hot-film traces up to M=0.90. For the M=0.95 case, the wake trajectory was still in line with the surface-mounted hot-film measured quantities, but the wake-boundary layer interaction features presented different characteristics. Using fast-response pressure sensors allowed us to infer that for cases where shocks are not present, the transition is triggered by Kelvin-Helmholtz roll-ups that arise when the wake negative jet interacts with the separated shear layer.

The passage vortex, trailing shed vorticity, and suction side corner vortex largely dominated the outlet flowfield. Under steady inlet flow, the secondary loss was one-third of the profile loss. The inlet boundary layer was thinned due to the introduction of the wake generator slot. The thinner inlet boundary layer, characterized by lower skewness, reduced the secondary loss by 5%. It is not evident if the introduction of wakes for fixed inlet boundary layer properties would have had an impact. Modifying the endwall geometry by introducing a cavity slot resulted in a more significant secondary loss, as previously observed in the literature. The secondary flows were displaced towards the center of the passage with an increasing purge massflow ratio, resulting in a higher secondary loss.

The phase-averaged analysis highlighted that the inlet boundary layer is strongly modulated during one bar passing period. The periodic thinning of the boundary layer is believed to reduce the secondary loss. The outlet flowfield was also found to be modulated by the unsteady wakes. In particular, the passage vortex was the secondary flow structure most impacted. The trailing shed vorticity region was barely affected.

The experimental data was critically compared against profile and secondary loss correlations to challenge their applicability to the current test case and potential geared low-pressure turbine blading. In the scope of profile loss modeling, low-pressure turbines pose a multi-disciplinary challenge. A low-speed correlation was obtained to estimate the contribution of different effects: boundary layer, separation bubble, and wake on the profile loss. The modeled quantities were fed into a state-of-the-art loss breakdown scheme. Coupling the loss breakdown scheme with the quantities describing the boundary layer growth in low-pressure

turbines allowed for the experimental profile loss retrieval. The modeled loss was characterized by a root-mean-square error of 4.7% with respect to experiments.

The agreement between the experimental and modeled secondary loss was flow-dependent, with some cases falling outside the $\pm 10\%$ error band. The poor agreement is attributed to challenges posed by measuring with probes in transonic flows and inconsistencies in the location where the inlet boundary loss was measured and how it was computed. In the presence of the wake generator, the boundary layer was measured upstream of the cavity slot. Therefore, the impact of the purge flow on the inlet boundary layer thickness and shape factor could not be captured.

8.0.1 Future Work and Remarks

In light of the main challenges encountered during the experimental campaign, the author believes that this work can trigger future actions:

- Aspects concerning probe interference and measurement errors were one of the main issues throughout the experimental campaign. The multi-hole probes were only calibrated at the relevant Mach number and used in a low-Reynolds number environment. It is known that the retrieved static pressure depends on both quantities. Efforts should be made to characterize the aerodynamics of the probes at the correct Mach number, Reynolds number, and turbulence levels. In addition, errors such as wall proximity and measuring in gradients impact the retrieved quantities. Future activities developing probe corrections would significantly reduce the gap between probe quality and optical measurements. These activities could start with low-speed testing downstream of simple geometries: cylinders and prisms.

- The fast-response instrumentation, notably the fast-response virtual four-hole probe, was chosen to be equipped with low-range absolute pressure sensors to reduce the instrumentation uncertainty. The aerodynamic calibration of the probe is not possible at ambient conditions. In addition, the dynamic calibration of the line-cavity system formed by recessing the sensors from the surface cannot be evaluated in conventional shock tubes that work at over-pressure. Even though often neglected, the dynamic response of the line-cavity system also depends on the pressure level and temperature at which the dynamics are surveyed. A future improvement of the fast-response virtual four-hole probe methodology could involve developing numerical and/or experimental calibrations at test-relevant conditions. Alternatively, a bare fast-response total pressure probe can be used at the same measuring plane as the virtual probe to act as a reference.

- Even though the SPLEEN test case enabled studying the combined effect of Mach and Reynolds numbers, unsteady wakes, and purge flows, decoupling the effects is not trivial. In particular, tests without the wake generator in the presence of purge flow would have contributed to increasing the database extent and quality and decoupling effects. The fact that the boundary layer was not controlled throughout different testing phases impacts conclusions on the impact of unsteady wakes on secondary flows, for instance. In particular, controlling the skewness would be of interest since it is one of the main parameters impacting vorticity distribution in the boundary layer and, consequently, secondary loss generation.

- The blade was heavily instrumented with fast-response instrumentation to survey the status of the boundary layer. Nonetheless, hot-films and fast-response pressure sensors still suffer from spatial resolution constraints compared to optical techniques. The author believes that applying temperature-sensitive paint (or a similar technique capable of retrieving heat flux) would significantly contribute to characterizing the separated flow transition occurring on the rear portion of the suction side.

- The characterization of the profile aerodynamics highlighted that the flow mechanisms are captured by existing models as long as shocks do not impact boundary layer separation/transition. However, the flow mechanism promoting transition at M=0.95, under the effect of unsteady wakes, remains unclear from the existing data. The author believes there could be scientific relevance in launching a numerical activity, employing LES or DNS, in a low technology readiness level setup where the interaction of unsteady wakes with shock-induced separation at low Reynolds number is investigated. The hypothetical 2D channel could account for a pressure gradient.

- Time-accurate measurements highlighted the dominance of rig characteristic frequencies in relation to potential frequencies associated with boundary layer and shock instabilities. Future surveys in the rig should consider this aspect in the design of the experiments. As for the current test case, the author believes that the characterization of potential frequencies associated with boundary layer features in the absence of the turbulence grid and wake generator would be beneficial.

- Challenging the applicability of existing secondary loss models against the current experimental data was somewhat compromised by the quality of the inlet boundary loss retrieval. Future investigations in the VKI S-1/C should target consistency when measuring the inlet boundary layer. The error associated with the static pressure measurements can be circumvented by ensuring endwall taps at the probe measuring plane. In addition, the author believes that measuring the boundary layer properties downstream of the cavity slot and upstream of the cascade would be of interest to compare the experimental data with the boundary layer multiplier provided by the last secondary loss model highlighted in the results section.

A Publications

A.1 Journal Publications

- Pastorino, G., Simonassi, L., **Lopes, G.**, Boufidi, E., Fontaneto, F., and Lavagnoli, S. (February 26, 2024). "Measurements of Turbulence in Compressible Low-Density Flows at the Inlet of a Transonic Linear Cascade With and Without Unsteady Wakes." ASME. J. Turbomach. July 2024; 146(7): 071002. https://doi.org/10.1115/1.4064369
- Rosafio N., **Lopes G.**, Salvadori S., Lavagnoli S., Misul D.A. "RANS Prediction of Losses and Transition Onset in a High-Speed Low-Pressure Turbine Cascade." Energies. 2023; 16(21):7348. https://doi.org/10.3390/en16217348
- **Lopes, G.**, Simonassi, L., and Lavagnoli, S. (November 13, 2023). "Time-Averaged Aerodynamics of a High-Speed Low-Pressure Turbine Cascade With Cavity Purge and Unsteady Wakes." ASME. J. Turbomach. February 2024; 146(2): 021008. https://doi.org/10.1115/1.4063878
- Okada, M., Simonassi, L., **Lopes, G.**, and Lavagnoli, S. (December 14, 2023). "Particle Image Velocimetry Measurements in a High-Speed Low-Reynolds Low-Pressure Turbine Cascade." ASME. J. Turbomach. March 2024; 146(3): 031010. https://doi.org/10.1115/1.4063674
- **Lopes G**, Simonassi L, Lavagnoli S. "Impact of Unsteady Wakes on the Secondary Flows of a High-Speed Low-Pressure Turbine Cascade". International Journal of Turbomachinery, Propulsion and Power. 2023; 8(4):36. https://doi.org/10.3390/ijtpp8040036
- Simonassi L, **Lopes G**, Lavagnoli S. "Effects of Periodic Incoming Wakes on the Aerodynamics of a High-Speed Low-Pressure Turbine Cascade". International Journal of

Turbomachinery, Propulsion and Power. 2023; 8(3):35. https://doi.org/10.3390/ijtpp8030035

- Torre, A. F. M., Patinios, M., **Lopes, G.**, Simonassi, L., and Lavagnoli, S. (January 9, 2023). "Vane–Probe Interactions in Transonic Flows." ASME. J. Turbomach. June 2023; 145(6): 061010. https://doi.org/10.1115/1.4056578

- **G. Lopes** and L. Simonassi and A.F.M. Torre and S. Lavagnoli. "Instrumentation Interference in a Transonic Linear Cascade." Journal of Physics: Conference Series. https://doi.org/10.1088/1742-6596/2511/1/012018

A.2 Conference Proceedings

- Boudin, A., Dombard, J., Duchaine, F., Gicquel, L., Odier, N., Lavagnoli, S., **Lopes, G.**, & Simonassi, L. (2023). "Analysis of rotor/stator interactions in a high-speed low-pressure turbine cascade using Large-Eddy Simulations". In 15th European Turbomachinery Conference. https://doi.org/10.29008/ETC2023-257

- Simonassi, L, **Lopes, G**, Gendebien, S, Torre, AFM, Patinios, M, Lavagnoli, S, Zeller, N, & Pintat, L. "An Experimental Test Case for Transonic Low-Pressure Turbines – Part I: Rig Design, Instrumentation and Experimental Methodology." Proceedings of the ASME Turbo Expo 2022: Turbomachinery Technical Conference and Exposition. Volume 10B: Turbomachinery — Axial Flow Turbine Aerodynamics; Deposition, Erosion, Fouling, and Icing; Radial Turbomachinery Aerodynamics. Rotterdam, Netherlands. June 13–17, 2022. V10BT30A012. ASME. https://doi.org/10.1115/GT2022-81566

- **Lopes, G**, Simonassi, L, Torre, AFM, Patinios, M, & Lavagnoli, S. "An Experimental Test Case for Transonic Low-Pressure Turbines - Part 2: Cascade Aerodynamics at On- and Off-Design Reynolds and Mach Numbers." Proceedings of the ASME Turbo Expo 2022: Turbomachinery Technical Conference and Exposition. Volume 10B: Turbomachinery — Axial Flow Turbine Aerodynamics; Deposition, Erosion, Fouling, and Icing; Radial Turbomachinery Aerodynamics. Rotterdam, Netherlands. June 13–17, 2022. V10BT30A027. ASME. https://doi.org/10.1115/GT2022-82626

A.3 Data Sets

- Lavagnoli, S., **Lopes, G.**, Simonassi, L., & Torre, A. F. M. (2023). "SPLEEN - High Speed Turbine Cascade – Test Case Database". Zenodo. https://zenodo.org/doi/10.5281/zenodo.7264761

- Lavagnoli, S., Okada, M., & **Lopes, G.** (2023). "SPLEEN - High Speed Turbine Cascade – Test Case Database - PIV Measurements". Zenodo. https://zenodo.org/doi/10.5281/zenodo.10253212

B

Calibration of Instrumentation

B.1 Static Calibration of reference K-type Thermocouple

The thermocouple has been statically calibrated in three instances:

- Phase 1: Before the experimental campaign; used throughout measurements performed without wake generator bars nor cavity purge flow,
- Phase 2: Before tests performed with wake generator bars; used throughout the latter tests in the absence of purge flow,
- Phase 3: Before tests performed with wake generator bars and cavity purge flow; used for the latter conditions.

The calibration data was fitted with a first-order polynomial curve in the form of Eq. B.2.

$$T(E) = EC_1 + C_2 \tag{B.1}$$

The calibration curves obtained for each one of the phases are displayed in Fig. B.1(a). The residuals from the fitted curves are displayed in Fig. B.1(b) for completeness. Even though the residuals display a parabolic trend, suggesting that a secondary order polynomial should be used instead, the first order was preferred since a good R^2 was achieved and the range of application in terms of temperature is quite limited.

The calibration coefficients along the goodness of fitting and fitting error are contained in Table B.1.

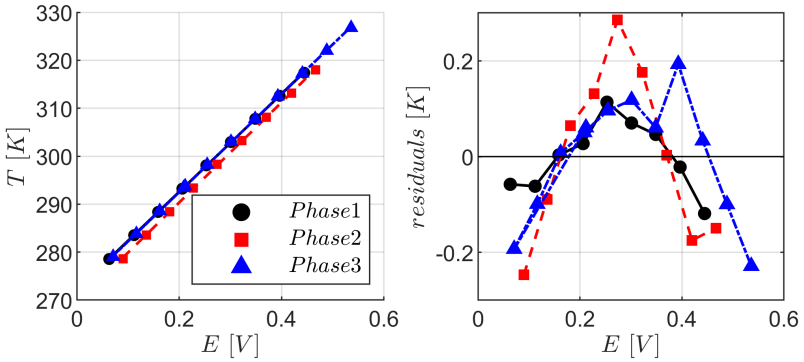

Figure B.1: Reference K-type thermocouple calibration curves for the various phases of testing (a) and residuals for the obtained calibrations (b).

Table B.1: Calibration coefficients, goodness of fitting, and standard error of calibrations performed of reference thermocouple for each phase of testing.

	C_1 $[KE^{-1}]$	C_2 $[K]$	R^2	$S_{\bar{\mathbb{M}}}$ $[K]$
Phase 1	102.082	272.158	0.999970	0.026
Phase 2	104.460	269.450	0.999824	0.063
Phase 3	102.732	271.954	0.999930	0.040

B.2 Static Calibration of Injection Circuit K-type Thermocouple

The calibration curve obtained for this thermocouple is displayed in Fig. B.2(a). The residuals from the fitted curves are displayed in Fig. B.2(b) for completeness.

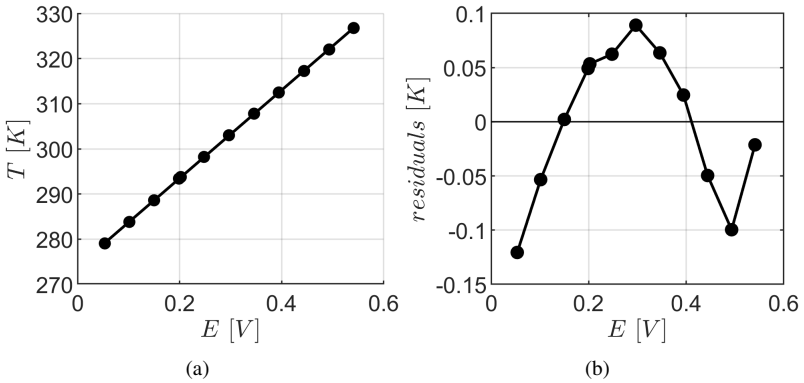

Figure B.2: Injection K-type thermocouple calibration curve (a) and residuals for the obtained calibration (b).

The calibration coefficients along the goodness of fitting and fitting error are contained in

Table B.2.

Table B.2: Calibration coefficients, goodness of fitting and standard error of calibrations performed of injection thermocouple.

	C_1 $[KE^{-1}]$	C_2 $[K]$	R^2	$S_{\bar{\mathbb{M}}}$ $[K]$
Phase 3	97.659	273.954	0.999980	0.0520

B.3 Static Calibration of Injection Circuit Validynes

Even though the sensors have a symmetric range, single-sided calibrations were performed since the larger pressure port was not altered during testing. For both of the instruments, a 1^{st} order polynomial was used to describe the relationship between the measured voltage and differential pressure:

$$\Delta P\left(E\right) = EC_1 + C_2 \tag{B.2}$$

V1 was calibrated for ΔP$\in$[0, 300] Pa. The calibration curve obtained for this Validyne is displayed in Fig. B.3(a). The residuals are displayed in Fig. B.3(b) for completeness.

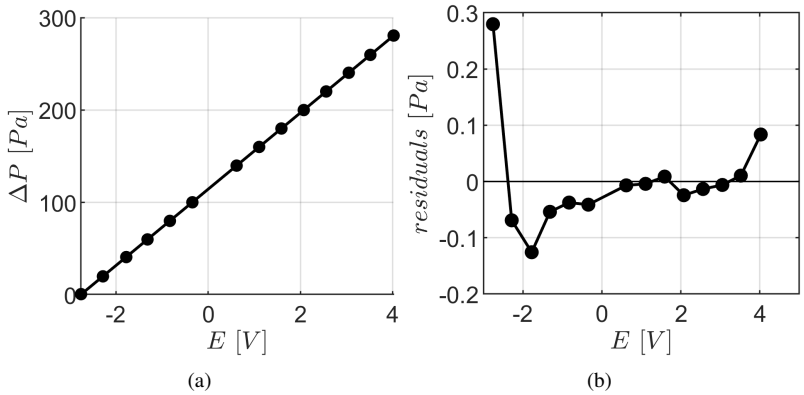

Figure B.3: Validyne 1 calibration curve (a) and residuals for the obtained calibration (b).

On the other hand, V2 was calibrated for ΔP$\in$[-500, 3500]. The calibration curve obtained from the calibration is shown in Fig. B.4(a). The residuals are also plotted in Fig. B.4(b) for completeness.

The resulting coefficients from the calibration along parameters defining the goodness of fitting (R^2 and $S_{\bar{\mathbb{M}}}$) are contained in Table B.3.

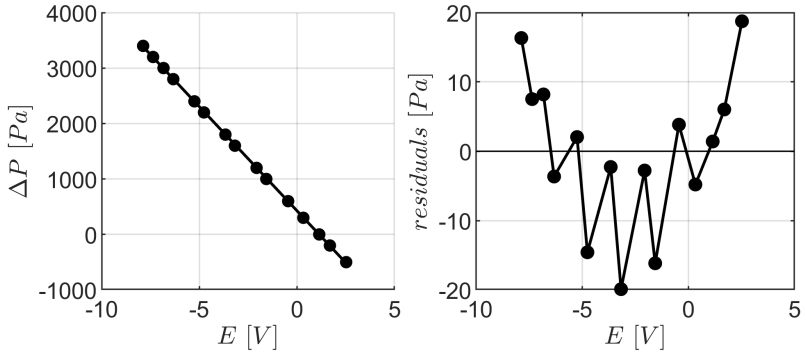

(a) (b)

Figure B.4: Validyne 2 calibration curve (a) and residuals for the obtained calibration (b).

Table B.3: Calibration coefficients, goodness of fitting and standard error of calibrations performed for Validynes.

	$C_1\ [PaE^{-1}]$	$C_2\ [Pa]$	R^2	$S_{\bar{\mathbb{M}}}\ [Pa]$
V1	41.293	114.378	0.999999	0.113
V2	-375.083	429.001	0.999927	11.492

B.4 Aerodynamic Calibration of C5HP

B.4.1 Sensitivity of the Aerodynamic Calibration Coefficients to P_{ave}

Hall and Povey [1] investigated the sensitivity of an open-access five-hole probe geometry to different denominators of the aerodynamic coefficients. This was achieved by modifying the definition of P_{ave}. They investigated the cases of:

- $P_{ave,1} = \frac{1}{2}(min(P_L, P_R) + min(P_D, P_U))$,
- $P_{ave,2} = \frac{1}{4}(P_L + P_R + P_D + P_U)$ (used in this thesis),
- $P_{ave,3} = min(P_L, P_R, P_D, P_U)$.

They found that $P_{ave,2}$ can cause the denominator of the aerodynamic coefficients to be zero for high yaw/pitch angles, creating singularity points. The benefit of using $P_{ave,2}$ lies in the fact that the sensitivity of the retrieved yaw/pitch to the measured pressures is higher, resulting in lower measurement uncertainties as well.

The sensitivity of K_α to the yaw angle, for a fixed pitch angle of 0°, is displayed in Fig. B.5(a). The same is presented for K_γ as a function of the pitch angle, for a fixed yaw angle of 0°, since this coefficient is relatively insensitive to the yaw angle (see Fig. B.5(b)). The calibration curves are plotted for a fixed Mach number of 0.40. Both figures highlight the higher sensitivity derived from using the second definition of P_{ave} through the higher slope of the calibration curves.

[1] F Hall and T Povey. The Oxford Probe: an open-access five-hole probe for aerodynamic measurements. Measurement Science and Technology, 28(3):035004, jan 2017.

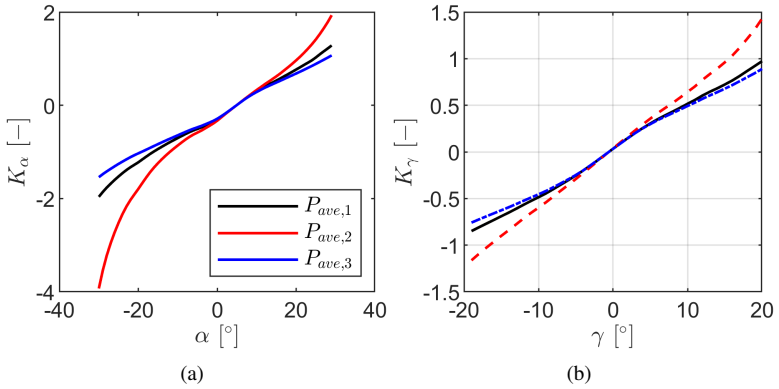

Figure B.5: Comparison of the sensitivity of the aerodynamic coefficients of the C5HP to P_{ave}: (a) K_α in function of the yaw angle and (b) K_γ in function of the pitch angle.

The orthogonality map provides a measure of the dependence between K_α and K_γ. Since K_{tot} and K_{stat} are a function of K_α and K_γ, there cannot exist more than one point with the same values of K_α and K_γ for the range of calibration angles as this would result in a non-singular solution. Fig. B.10 displays the orthogonality maps for the different definitions of P_{ave} obtained for M=0.40. The maps are shown for K_α and K_γ computed every 2° to ease up the reading of the figure. Similar conclusions can be obtained in the full range of the Mach number for which the probe was calibrated. The benefit of using $P_{ave,2}$ on the increased sensitivity can also be perceived from the larger extension of the orthogonality map for the calibration performed at M=0.40.

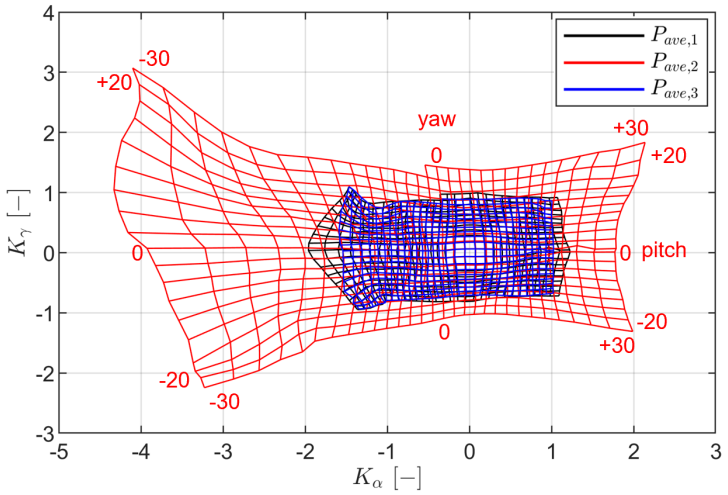

Figure B.6: Orthogonality map resultant from the calibration of the C5HP at M=0.40.

B.4.2 Aerodynamic Calibration Coefficients

The aerodynamic coefficients used to retrieve the local flowfield quantities throughout this thesis are displayed in Fig. B.7(a), Fig. B.7(c), Fig. B.7(e), Fig. B.7(g). The coefficients are plotted for angle increments of 2°. Cuts of the calibration coefficients at fixed α=0° or γ=0° are also displayed in Fig. B.7(b), Fig. B.7(d), Fig. B.7(f), Fig. B.7(h).

B.4.3 Orthogonality Map

The orthogonality maps for the Cobra five-hole probe's final aerodynamic coefficients are displayed in Fig. B.8.

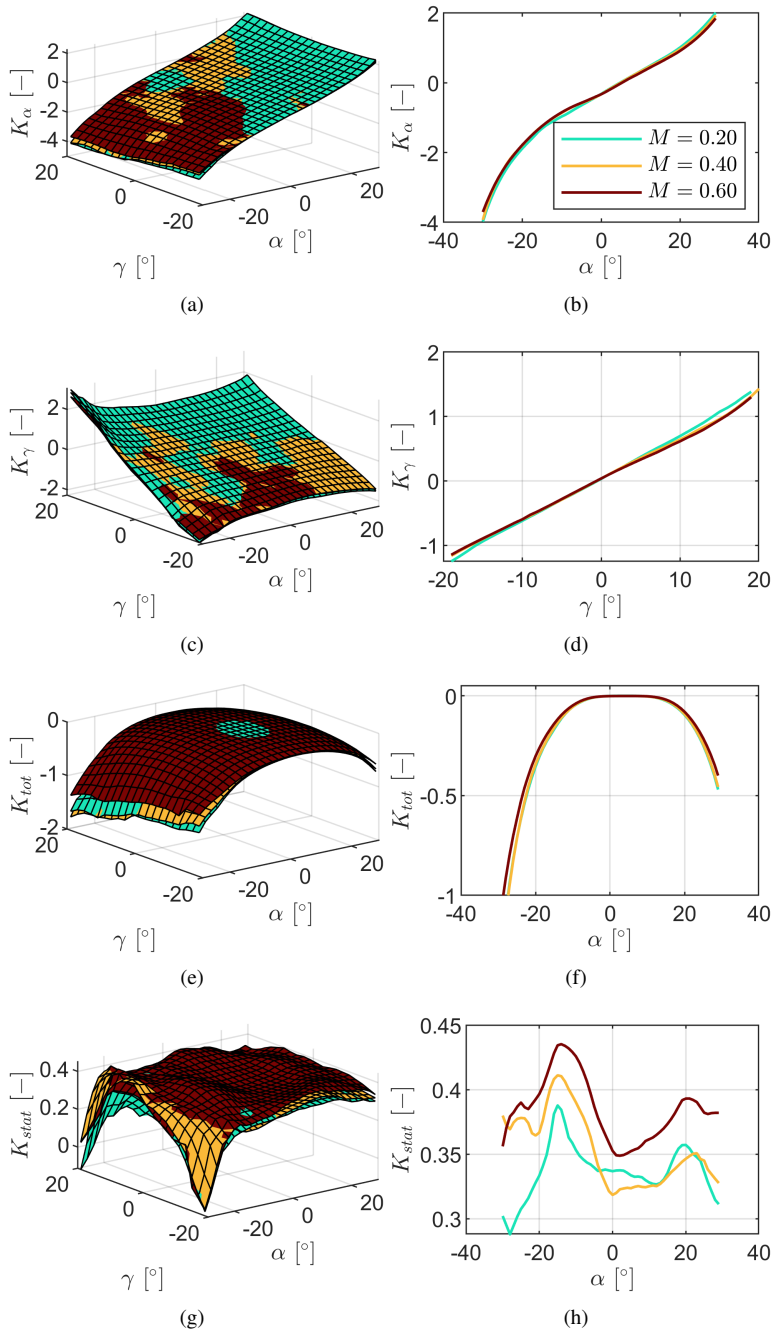

Figure B.7: Aerodynamic calibration coefficients of C5HP for the calibrated Mach numbers: (a) K_α as function of α and γ, (c) K_γ as function of α and γ, (e) K_{tot} as function of α and γ and (g) K_{stat} as function of α and γ; and cuts of the surfaces at fixed α or γ for (b) K_α, (d) K_γ, (f) K_{tot} and (h) K_{stat}.

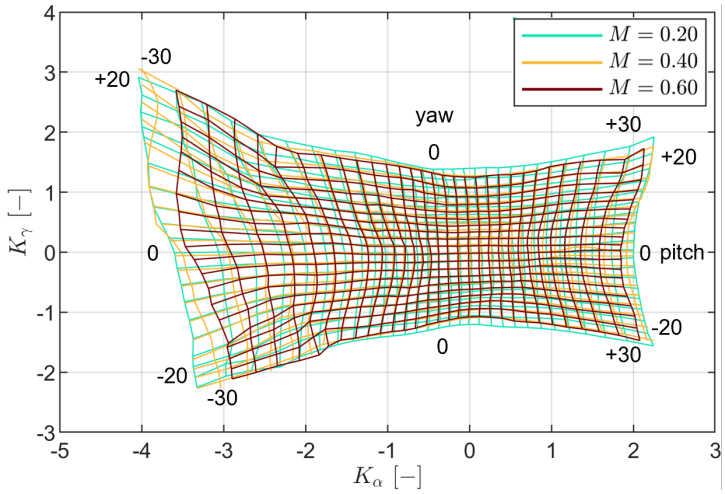

Figure B.8: Orthogonality maps for the range of M for which the C5HP was calibrated.

B.5 Aerodynamic Calibration of L5HP

B.5.1 Sensitivity of the Aerodynamic Calibration Coefficients to P_{ave}

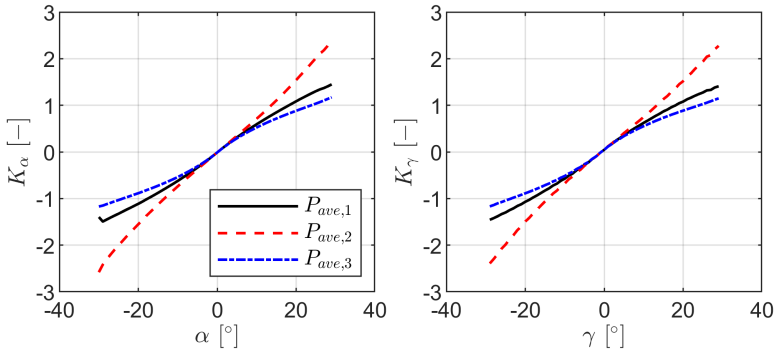

(a) (b)

Figure B.9: Comparison of the sensitivity of the aerodynamic coefficients of the L5HP to P_{ave}: (a) K_α in function of the yaw angle and (b) K_γ in function of the pitch angle.

The increased sensitivity for the second definition of P_{ave} is also clearly highlighted in the orthogonality map of the L5HP obtained at M=0.80. This is particularly evident at the edges of the calibration range.

B.5.2 Aerodynamic Calibration Coefficients

The calibration maps obtained for the L5HP in function of the α, γ and Mach number are displayed in Fig. B.11(a), Fig. B.11(c), Fig. B.11(e), Fig. B.11(g). Cuts of the calibration

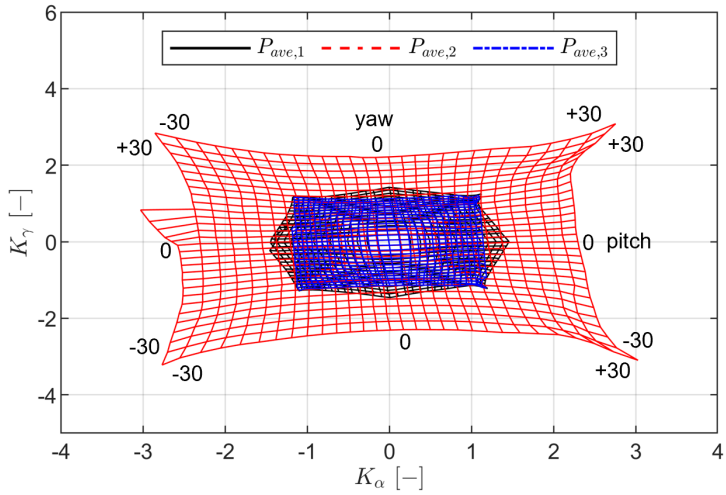

Figure B.10: Orthogonality map resultant from the calibration of the L5HP at M=0.80.

maps at fixed α=0°, for K_α, K_{tot}, K_{stat}, or γ=0°, for K_γ, are also depicted in Fig. B.11(b), Fig. B.11(d), Fig. B.11(f), Fig. B.11(h). As for the C5HP, the L5HP displays remarkable insensitivity of K_α and K_γ to γ and α, respectively (see Fig. B.11). Both α, γ and K_{tot} are fairly insensitive to Mach number for the range of angles expected in this investigation (α, γ $\in$ [-10°, +10°]).

B.5.3 Orthogonality Map

The orthogonality maps for the L5HP final aerodynamic coefficients are displayed in Fig. B.12.

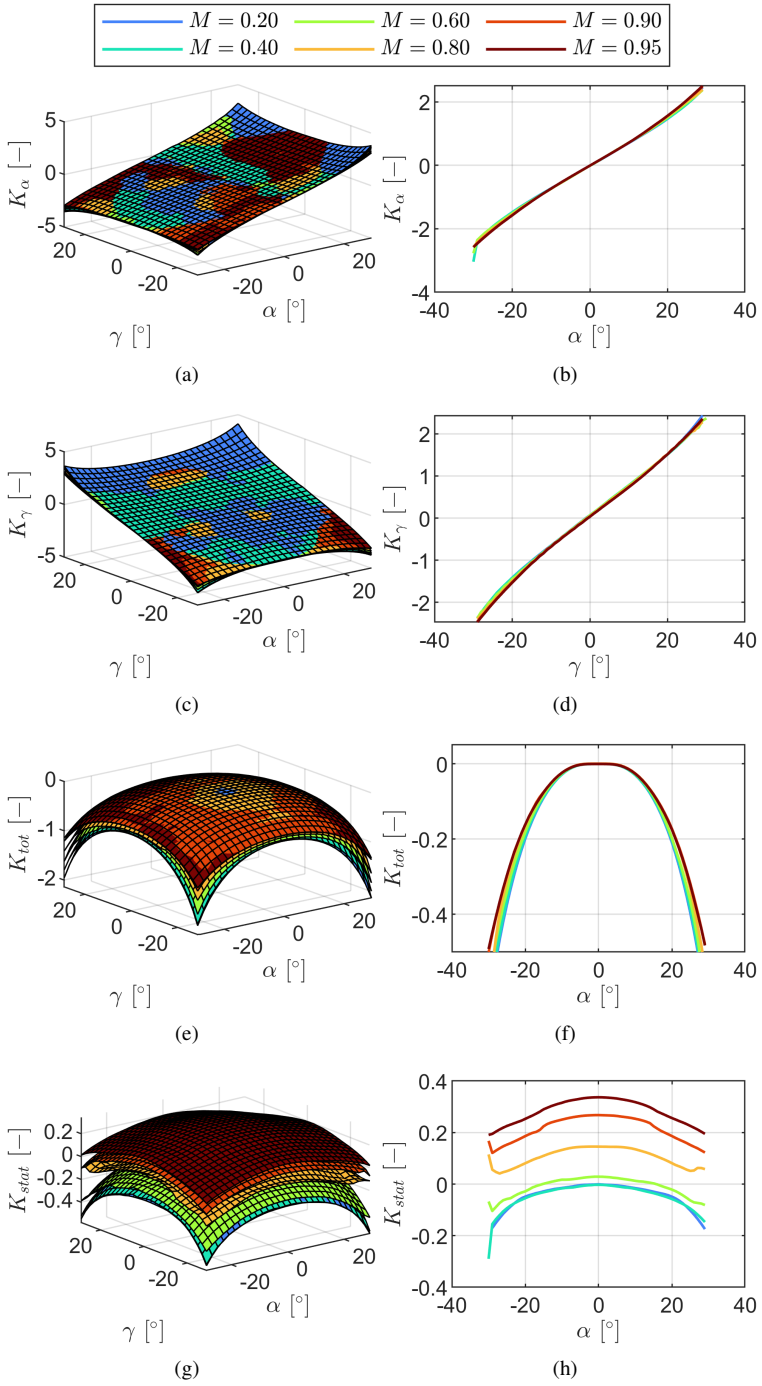

Figure B.11: Aerodynamic calibration coefficients of L5HP for the calibrated Mach numbers: (a) K_α as function of α and γ, (c) K_γ as function of α and γ, (e) K_{tot} as function of α and γ and (g) K_{stat} as function of α and γ; and cuts of the surfaces at fixed α or γ for (b) K_α, (d) K_γ, (f) K_{tot} and (h) K_{stat}.

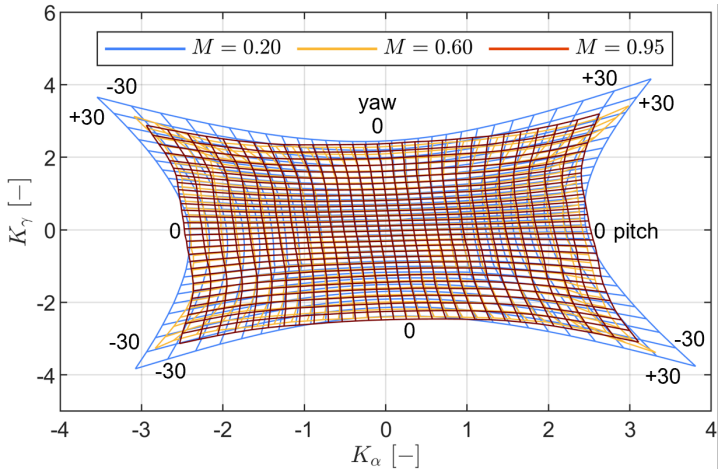

Figure B.12: Orthogonality maps for the range of M for which the L5HP was calibrated.

B.6 Aerodynamic Calibration of PV4HP

B.6.1 Aerodynamic Calibration Coefficients

The calibration maps obtained for the pneumatic V4HP as function of α, γ and M are displayed in Fig. B.13(a), Fig. B.13(c), Fig. B.13(e), Fig. B.13(g). Cuts of the calibration maps at fixed α=0°, for K_α, K_{tot}, K_{stat}, or γ=0°, for K_γ , are also depicted in Fig. B.13(b), Fig. B.13(d), Fig. B.13(f), Fig. B.13(h). Naturally, the maps display a symmetric behavior around $\alpha = 0°$ since the probe is rotated around its axisymmetric axis.

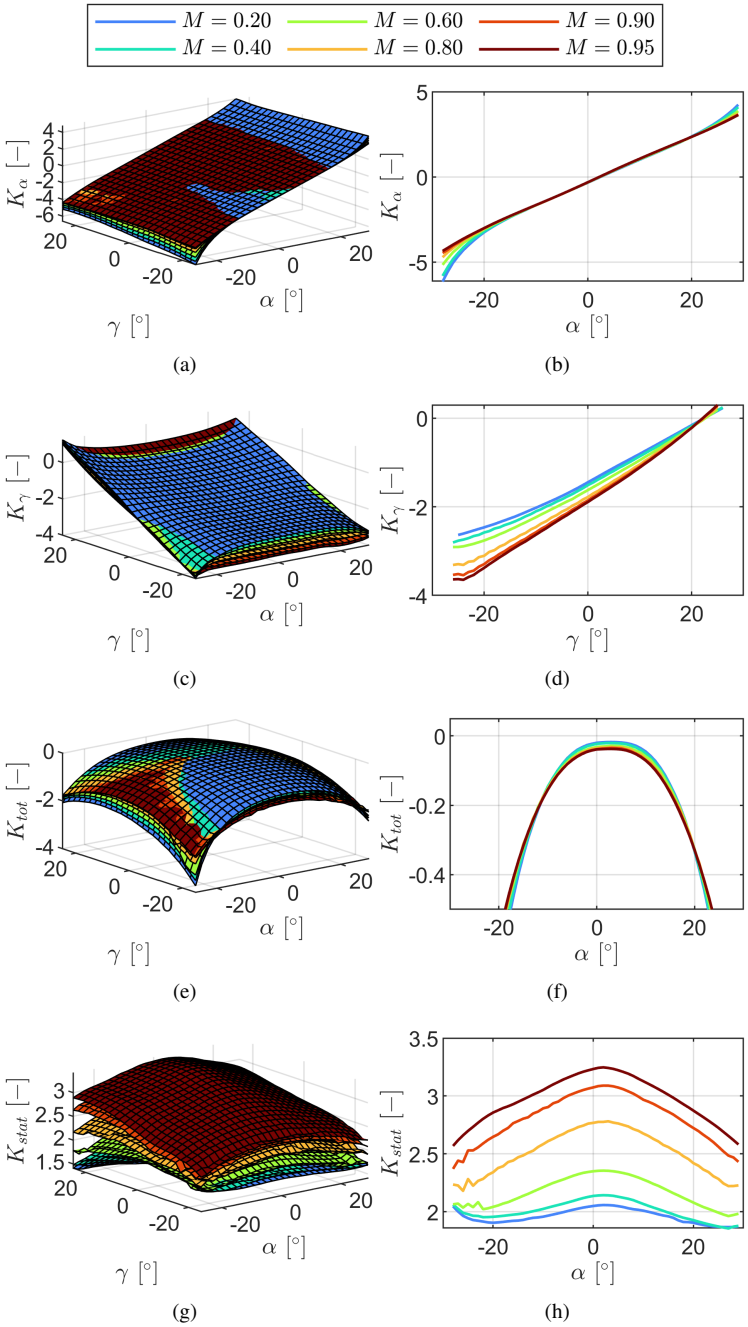

Figure B.13: Aerodynamic calibration coefficients of Pneumatic V4HP for the calibrated Mach numbers: (a) K_α as function of α and γ, (c) K_γ as function of α and γ, (e) K_{tot} as function of α and γ and (g) K_{stat} as function of α and γ; and cuts of the surfaces at fixed α or γ for (b) K_α, (d) K_γ, (f) K_{tot} and (h) K_{stat}.

B.7 Static Calibration of FRV4HP Sensors

B.7.1 Pressure

Table B.4: Calibration coefficients, goodness of fitting, and standard error of pressure calibrations performed for V4HP FR sensors throughout different phases of testing.

$P = f(V_P, V_S)$	Loc.	Sensor	C_1	C_2	C_3	C_4	C_5	R^2	$S_{\bar{\mathbb{M}}}$ $[Pa]$
Phase 1	Inlet	1	7452.1	3368.0	-1379.8	0.0	0.0	0.99969	42.7
		2	-5293.2	3870.6	3045.2	0.0	0.0	0.99972	40.3
	Outlet	1	2300.4	6885.6	1878.0	199.7	1104.7	0.99975	139.8
		2	3876.4	7930.0	1343.5	-63.1	2811.4	0.99970	155.1
Phase 2	Inlet	1	13000.9	683.5	3280.8	0.0	0.0	0.99999	15.3
		2	10920.5	784.6	2673.8	0.0	0.0	0.99998	16.6
	Outlet	1	11251.9	683.1	3263.5	0.0	0.0	0.99995	26.2
		2	10357.6	785.3	2641.3	0.0	0.0	0.99994	28.5
Phase 3	Inlet	1	8776.0	680.6	3264.0	0.0	0.0	0.99989	20.8
		2	7600.7	782.5	2631.9	0.0	0.0	0.99987	22.7
	Outlet	1	8740.3	678.9	2984.1	0.0	0.0	0.99987	25.6
		2	7608.7	780.3	2373.3	0.0	0.0	0.99990	21.9

B.7.2 Temperature

Table B.5: Calibration coefficients, goodness of fitting, and standard error of temperature calibrations performed for V4HP FR sensors throughout different phases of testing.

$T = f(V_P, V_S)$	Loc.	Sensor	C_1	C_2	C_3	C_4	C_5	R^2	$S_{\bar{\mathbb{M}}}$ $[K]$
Phase 1	Inlet	1	495.0	0.2	-58.8	0.0	0.0	0.80883	0.5
		2	292.2	0.1	87.1	0.0	0.0	0.73933	0.5
	Outlet	1	291.9	-0.1	88.8	0.1	8.1	0.99998	0.1
		2	291.7	-0.1	86.3	0.0	5.8	0.99998	0.1
Phase 2	Inlet	1	291.6	0.0	56.8	0.00	0.00	0.99066	0.4
		2	291.0	0.0	55.0	0.00	0.00	0.99365	0.3
	Outlet	1	290.9	0.0	58.8	0.00	0.00	0.99476	0.3
		2	291.0	0.0	55.2	0.00	0.00	0.99544	0.3
Phase 3	Inlet	1	295.4	-0.1	59.1	0.0	0.0	0.99662	0.2
		2	295.2	-0.1	56.0	0.0	0.0	0.99704	0.2
	Outlet	1	292.9	-0.1	66.9	0.0	0.0	0.99811	0.2
		2	292.7	-0.0	69.0	0.0	0.0	0.99587	0.2

B.8 Static Calibration of Blade FR Pressure Sensors

B.8.1 Pressure

Table B.6: Calibration coefficients, goodness of fitting, and standard error of pressure calibrations performed for Blade FR sensors throughout different phases of testing.

$P = f(V_P, V_S)$	Blade	Sensor	C_1	C_2	C_3	R^2	$S_{\mathbb{M}}$ $[Pa]$
Phase 1	SS	1	-3852.79	4693.67	2906.75	0.99999	18.66
		2	1574.51	5041.69	1819.74	0.99993	33.57
		3	-4143.75	4124.89	2626.55	0.99999	13.04
		4	1282.64	4939.55	2377.76	0.99998	16.34
		5	-10444.62	4085.46	3013.10	0.99999	13.08
		6	-5487.88	3570.35	2677.20	0.99999	15.17
		7	-1924.99	4929.45	2248.01	0.99999	13.53
	PS	1	-25.01	4468.73	2145.25	0.99989	35.56
Phase 2	SS	1	18207.58	949.50	3411.22	0.99999	17.67
		2	12741.87	1006.89	2136.67	0.99999	13.27
		3	7933.13	834.65	2717.54	0.99999	10.90
		4	10283.64	1000.25	2229.02	0.99999	11.10
		5	5520.29	824.44	2688.87	0.99998	12.99
		6	7222.54	720.25	2711.78	0.99997	12.91
		7	9580.16	991.47	2120.09	0.99999	8.78
	PS	1	7550.55	8964.37	2220.40	0.99989	35.56
Phase 3	SS	1	20824.77	941.47	6211.53	0.99974	35.15
		2	22922.30	1010.71	5508.51	0.99941	52.60
		3	12689.79	833.65	5215.17	0.99984	27.55
		4	13319.26	991.92	3327.94	0.99994	17.27
		5	6452.13	819.19	4119.91	0.99995	15.36
		6	8572.11	715.14	3276.13	0.99999	7.04
		7	12625.45	989.69	2532.57	0.99995	15.43
	PS	1	7641.45	900.27	2314.08	0.99989	35.56

B.8.2 Temperature

Table B.7: Calibration coefficients, goodness of fitting, and standard error of temperature calibrations performed for Blade FR sensors throughout different phases of testing.

$T = f(V_P, V_S)$	Blade	Sensor	C_1	C_2	C_3	R^2	$S_{\bar{\mathbb{M}}}$ $[K]$
Phase 1	SS	1	181.89	-0.67	51.55	0.99214	0.31
		2	266.90	-0.53	35.46	0.99618	0.22
		3	152.78	-0.61	54.43	0.99272	0.30
		4	205.01	-0.70	49.71	0.99217	0.31
		5	19.05	-0.59	70.47	0.99129	0.33
		6	94.76	-0.53	61.76	0.99309	0.29
		7	180.15	-0.69	51.41	0.99295	0.30
	PS	1	166.76	-0.47	62.48	0.99827	0.16
Phase 2	SS	1	354.06	0.01	47.40	0.99789	0.17
		2	392.39	0.00	40.16	0.99893	0.12
		3	320.13	0.00	48.27	0.99785	0.17
		4	367.26	0.01	44.48	0.99817	0.16
		5	267.67	0.00	58.29	0.99783	0.17
		6	305.41	0.00	52.29	0.99784	0.18
		7	351.30	0.00	46.52	0.99783	0.17
	PS	1	348.20	0.17	38.65	0.958243	0.70
Phase 3	SS	1	355.24	-0.07	51.00	0.988468	0.19
		2	391.45	-0.08	40.77	0.989190	0.19
		3	338.33	-0.06	52.75	0.986941	0.20
		4	357.51	-0.08	47.17	0.989177	0.19
		5	265.05	-0.06	62.94	0.989670	0.18
		6	306.61	-0.06	57.68	0.988815	0.19
		7	356.47	-0.08	50.33	0.988380	0.19
	PS	1	360.33	0.00	44.82	0.997394	0.12

C

Location of instrumentation

C.1 Blade SS: pneumatic taps

Table C.1: Location of pneumatic static pressure taps on Blade SS.

Sensor #	x/C_{ax} $[-]$	s/S_L $[-]$	Sensor #	x/C_{ax} $[-]$	s/S_L $[-]$
1	0.000	0.000	13	0.649	0.580
2	0.003	0.030	14	0.687	0.620
3	0.045	0.080	15	0.723	0.660
4	0.105	0.135	16	0.758	0.700
5	0.173	0.190	17	0.784	0.730
6	0.247	0.245	18	0.809	0.760
7	0.319	0.298	19	0.835	0.790
8	0.391	0.350	20	0.860	0.820
9	0.458	0.403	21	0.885	0.850
10	0.523	0.458	22	0.910	0.880
11	0.577	0.508	23	0.940	0.916
12	0.611	0.540	24	0.965	0.946

C.2 Blade PS: pneumatic taps

Table C.2: Location of pneumatic static pressure taps on Blade PS.

Sensor #	x/C_{ax} $[-]$	s/S_L $[-]$	Sensor #	x/C_{ax} $[-]$	s/S_L $[-]$
1	0.030	0.026	10	0.554	0.483
2	0.068	0.060	11	0.613	0.543
3	0.112	0.098	12	0.669	0.604
4	0.156	0.138	13	0.722	0.665
5	0.202	0.177	14	0.774	0.726
6	0.298	0.257	15	0.827	0.790
7	0.362	0.310	16	0.881	0.857
8	0.427	0.365	17	0.937	0.926
9	0.492	0.424			

C.3 Endwall Insert 1: pneumatic taps

Table C.3: Location of pneumatic static pressure taps on Endwall Insert 1.

Sensor #	x/C_{ax} $[-]$	y $[mm]$	Sensor #	x/C_{ax} $[-]$	y $[mm]$
1	0.000	0.000	13	0.649	0.580
2	0.003	0.030	14	0.687	0.620
3	0.045	0.080	15	0.723	0.660
4	0.105	0.135	16	0.758	0.700
5	0.173	0.190	17	0.784	0.730
6	0.247	0.245	18	0.809	0.760
7	0.319	0.298	19	0.835	0.790
8	0.391	0.350	20	0.860	0.820
9	0.458	0.403	21	0.885	0.850
10	0.523	0.458	22	0.910	0.880
11	0.577	0.508	23	0.940	0.916
12	0.611	0.540	24	0.965	0.946

C.4 Endwall Insert 2: pneumatic taps

Table C.4: Location of pneumatic static pressure taps on Endwall Insert 2.

Sensor #	x/C_{ax} $[-]$	y $[mm]$	Sensor #	x/C_{ax} $[-]$	y $[mm]$
1	0.083	9.390	19	0.583	15.956
2	0.083	13.509	20	0.583	24.193
3	0.083	17.628	21	0.667	15.413
4	0.167	7.325	22	0.667	19.532
5	0.167	11.444	23	0.667	23.650
6	0.167	15.563	24	0.667	27.769
7	0.167	19.682	25	0.750	23.669
8	0.250	10.342	26	0.750	31.907
9	0.333	6.133	27	0.833	24.078
10	0.333	10.252	28	0.833	28.197
11	0.333	14.371	29	0.833	32.315
12	0.333	18.490	30	0.833	36.434
13	0.417	11.191	31	0.917	33.006
14	0.417	19.429	32	0.917	41.243
15	0.500	9.006	33	1.000	33.956
16	0.500	13.125	34	1.000	38.075
17	0.500	17.244	35	1.000	42.193
18	0.500	21.363	36	1.000	46.312

C.5 Blade SS: fast-response taps

Table C.5: Location of fast-response static pressure taps on Blade SS.

Sensor #	x/C_{ax} $[-]$	s/S_L $[-]$	Sensor #	x/C_{ax} $[-]$	s/S_L $[-]$
1	0.000	0.000	5	0.702	0.637
2	0.300	0.284	6	0.803	0.753
3	0.502	0.439	7	0.903	0.872
4	0.603	0.532			

C.6 Blade PS: fast-response taps

Table C.6: Location of fast-response static pressure taps on Blade PS.

Sensor #	x/C_{ax} $[-]$	s/S_L $[-]$
1	0.246	0.214

C.7 Endwall Insert 1: fast-response taps

Table C.7: Location of fast-response static pressure taps on Endwall insert 1.

Sensor #	x/C_{ax} $[-]$	y $[mm]$	Sensor #	x/C_{ax} $[-]$	y $[mm]$
1	0.083	-24.713	4	0.250	-16.475
2	0.083	-16.475	5	0.583	-16.475
3	0.250	-24.713	6	0.917	-16.475

C.8 Endwall Insert 2: fast-response taps

Table C.8: Location of fast-response static pressure taps on Endwall insert 2.

Sensor #	x/C_{ax} $[-]$	y $[mm]$
1	0.083	24.713
2	0.250	24.713

C.9 Blade SS: surface mounted hot-films

Table C.9: Location of surface mounted hot-films on Blade SS.

Sensor #	x/C_{ax} $[-]$	S/S_L $[-]$	Sensor #	x/C_{ax} $[-]$	S/S_L $[-]$
1	0.013	0.009	17	0.609	0.535
2	0.038	0.03	18	0.638	0.566
3	0.068	0.056	19	0.667	0.598
4	0.101	0.086	20	0.695	0.628
5	0.137	0.117	21	0.721	0.659
6	0.176	0.151	22	0.747	0.689
7	0.215	0.184	23	0.774	0.721
8	0.279	0.238	24	0.8	0.752
9	0.32	0.272	25	0.825	0.782
10	0.361	0.306	26	0.851	0.814
11	0.402	0.341	27	0.876	0.845
12	0.441	0.374	28	0.901	0.876
13	0.478	0.407	29	0.926	0.907
14	0.513	0.439	30	0.951	0.938
15	0.547	0.472	31	0.976	0.969
16	0.579	0.504			

C.10 Blade PS: surface mounted hot-films

Table C.10: Location of surface mounted hot-films on Blade PS.

Sensor #	x/C_{ax} $[-]$	S/S_L $[-]$	Sensor #	x/C_{ax} $[-]$	S/S_L $[-]$
1	0.013	0.009	12	0.456	0.387
2	0.054	0.044	13	0.494	0.422
3	0.092	0.077	14	0.53	0.456
4	0.131	0.112	15	0.565	0.49
5	0.171	0.147	16	0.599	0.524
6	0.211	0.181	17	0.632	0.559
7	0.252	0.215	18	0.662	0.592
8	0.294	0.25	19	0.693	0.627
9	0.335	0.284	20	0.724	0.662
10	0.377	0.319	21	0.752	0.695
11	0.417	0.353			

D

Detailed Breakdown of Uncertainty Estimation

D.1 Loss Correlation for Turbulence Grid and Wake Generator

Estimating the inlet total pressure through a correlation rather than direct measurement generates an extra source of uncertainty in this quantity. The computation of the turbulence grid(+ wake generator) is done using:

$$Y = \frac{P_{0,ref} - P_{01/02}}{P_{0,ref}} \tag{D.1}$$

The propagation of the error yields:

$$UY_{TG} = \sqrt{\left(\frac{P_{01/02}}{{P_{0,ref}}^2} UP_{0,ref}\right)^2 + \left(-\frac{1}{P_{0,ref}} UP_{01/02}\right)^2} \tag{D.2}$$

Once the correlation has been built (see Section 4.2.1), the total pressure at the inlet can be estimated as $P_{01/02} = P_{0,ref}\,(1 - Y)$. The resultant uncertainty on $P_{01/02}$ is computed as:

$$UP_{01/02} = \sqrt{\left(\frac{\partial P_{01/02}}{\partial P_{0,ref}} UP_{0,ref}\right)^2 + \left(\frac{\partial P_{01/02}}{\partial Y} UY\right)^2} \tag{D.3}$$

D.2 Flow Conditions and Surface Measurements

Throughout the work, small variations of the measured quantities around the mean were taken into account. In this case, the propagation can be performed by Taylor series expansions and neglecting higher-order terms. The uncertainty for measured quantities based on this type of error propagation is detailed in the following sections.

D.2.1 Uncertainty of isentropic Mach number

The isentropic Mach number M_{is} at the inlet, outlet, or blade surface is computed as:

$$M_{is} = \sqrt{\frac{2}{\gamma - 1}\left[\left(\frac{P_{01}}{P}\right)^{\frac{\gamma}{\gamma-1}} - 1\right]} \tag{D.4}$$

Following the error propagation theory, the uncertainty can be expressed as:

$$UM_{is} = \frac{1}{\gamma P M_{is}}\left(\frac{P}{P_{01}}\right)^{\frac{1}{\gamma}}\sqrt{{UP_{01}}^2 + \left(\left(\frac{P_{01}}{P}\right)UP\right)^2} \tag{D.5}$$

D.2.2 Uncertainty of static temperature

The static temperature, T, is computed using:

$$T = \frac{T_{01}}{1 + \frac{\gamma-1}{2}M_{is}^2} \tag{D.6}$$

Following the error propagation theory, the uncertainty is:

$$UT = \frac{1}{1 + \frac{\gamma-1}{2}M_{is}^2}\sqrt{UT_{01}^2 + \left(\left(1-\gamma\right)TM_{is}UM_{is}\right)^2} \tag{D.7}$$

D.2.3 Uncertainty of isentropic velocity

The isentropic velocity is computed using:

$$V_{is} = M_{is}\sqrt{\gamma RT} \tag{D.8}$$

Following the error propagation theory, the uncertainty is:

$$UV_{is} = \sqrt{\left(\sqrt{\gamma RT}UM_{is}\right)^2 + \left(\frac{\gamma R M_{is}}{2\sqrt{\gamma RT}}UT\right)^2} \tag{D.9}$$

D.2.4 Uncertainty of density

The isentropic density is computed using:

$$\rho = \frac{P}{RT} \tag{D.10}$$

Following the error propagation theory, the uncertainty is:

$$U\rho = \sqrt{\left(\frac{1}{RT}UP\right)^2 + \left(-\frac{P}{RT^2}UT\right)^2} \tag{D.11}$$

D.2.5 Uncertainty of dynamic viscosity

The dynamic viscosity is computed with the Sutherland's relation as:

$$\mu = \mu_0 \frac{T_{01} + S}{T + S} \left(\frac{T}{T_{01}}\right)^{\frac{3}{2}} \tag{D.12}$$

Following the error propagation theory, the uncertainty is:

$$U\mu = \mu_0 \frac{T_{01} + S}{T + S} \left(\frac{3}{2} - \frac{T}{T + S}\right) \sqrt{\frac{T}{{T_{01}}^3}UT} \tag{D.13}$$

D.2.6 Uncertainty of isentropic Reynolds number

The isentropic Reynolds number is computed as:

$$Re_{is} = \frac{\rho_{is} V_{is} C}{\mu} \tag{D.14}$$

Following the error propagation theory, the uncertainty is:

$$URe_{is} = Re_{is}\sqrt{\left(\frac{1}{\rho_{is}}U\rho\right)^2 + \left(\frac{1}{V_{is}}UV_{is}\right)^2 + \left(\frac{1}{C}UC\right)^2 + \left(-\frac{1}{\mu}U\mu\right)^2} \tag{D.15}$$

D.3 Quantities Retrieved with Directional Multi-Hole Probes

The quantities retrieved with the multi-hole probes at the inlet and outlet are obtained by interpolating in a 3D calibration map (see Section B.4.2 and Section B.5.2). Making use of Taylor series expansions, the uncertainty on the measured angles and pressures can be computed.

D.3.1 Probe yaw angle

The probe yaw angle is obtained from:

$$\alpha = f\left(K_\alpha, K_\gamma, M\right) \tag{D.16}$$

The Taylor expansion of this quantity can be expressed as:

$$U\alpha = \sqrt{\left(\frac{\partial\alpha}{\partial K_\alpha}UK_\alpha\right)^2 + \left(\frac{\partial\alpha}{\partial K_\gamma}UK_\gamma\right)^2 + \left(\frac{\partial\alpha}{\partial M}UM\right)^2 + {U_{sys}\alpha_{cal}}^2 + {U_{sys}\alpha_{meas}}^2} \tag{D.17}$$

Where the terms $U_{sys}\alpha_{cal}$ is a bias and denotes the uncertainty resultant from the calibration uncertainty, and $U_{sys}\alpha_{meas}$ results from the uncertainty of mounting the probe in the test section with an angle meter.

D.3.2 Probe pitch angle

The uncertainty on the pitch angle measured in the probe reference system is computed similarly to the yaw angle. The pitch angle is computed as:

$$\gamma = f\left(K_\alpha, K_\gamma, M\right) \tag{D.18}$$

The Taylor expansion of this quantity can be expressed as:

$$U\gamma = \sqrt{\left(\frac{\partial\gamma}{\partial K_\alpha}UK_\alpha\right)^2 + \left(\frac{\partial\gamma}{\partial K_\gamma}UK_\gamma\right)^2 + \left(\frac{\partial\gamma}{\partial M}UM\right)^2 + {U_{sys}\alpha_{cal}}^2} \tag{D.19}$$

In the previous equation, the term $U_{sys}\gamma_{meas}$ is removed since the probe can only be rotated around the axisymmetric axis of the stem, which impacts only the yaw angle.

D.3.3 Total pressure

The total pressure is computed from K_{tot} as:

$$P_{tot} = P_C - K_{tot}\left(P_C - P_{ave}\right) \tag{D.20}$$

Following a Taylor series expansion:

$$UP_{tot} = \sqrt{\left(\frac{\partial P_{tot}}{\partial P_C}UP_C\right)^2 + \left(\frac{\partial P_{tot}}{\partial P_{ave}}UP_{ave}\right)^2 + \left(\frac{\partial P_{tot}}{\partial K_{tot}}UK_{tot}\right)^2} \tag{D.21}$$

Where $K_{tot} = f\left(K_\alpha,\ K_\gamma, M\right)$. Therefore, it can be expanded as:

$$UK_{tot} = \sqrt{\left(\frac{\partial K_{tot}}{\partial K_\alpha}UK_\alpha\right)^2 + \left(\frac{\partial K_{tot}}{\partial K_\gamma}UK_\gamma\right)^2 + \left(\frac{\partial K_{tot}}{\partial M}UM\right)^2 + {U_{sys}K_{tot}}^2} \tag{D.22}$$

Where $U_{sys}K_{tot}$ is the systematic uncertainty on K_{tot} from the ex-situ probe calibration. This term can be computed as:

$$K_{tot} = \frac{P_C - P_{tot}}{P_C - P_{ave}} \tag{D.23}$$

Therefore, depends on the instrumentation used to measure these quantities. The uncertainties on these measured quantities during the calibration phase are in Table D.1.

Table D.1: Uncertainty of sources used to build map of K_{tot}.

UP_{tot}	29.16	$[Pa]$
UP_C	34.47	$[Pa]$
UP_{ave}	17.24	$[Pa]$

D.3.4 Static pressure

Similar to the previous section, the static pressure retrieved with the L5HP and C5HP is computed from:

$$P_{stat} = P_{ave} - K_{stat}\left(P_C - P_{ave}\right) \tag{D.24}$$

A slightly different coefficient is used for the FRV4HP:

$$P_{stat} = P_C - K_{stat}\left(P_C - P_{ave}\right) \tag{D.25}$$

Following a Taylor series expansion that can be applied for Equation D.24 and Equation D.25:

$$UP_{stat} = \sqrt{\left(\frac{\partial P_{stat}}{\partial P_C} UP_C\right)^2 + \left(\frac{\partial P_{stat}}{\partial P_{ave}} UP_{ave}\right)^2 + \left(\frac{\partial P_{stat}}{\partial K_{stat}} UK_{stat}\right)^2} \tag{D.26}$$

Where $K_{stat} = f\left(K_\alpha,\ K_\gamma, M\right)$. Therefore, it can be expanded as:

$$UK_{stat} = \sqrt{\left(\frac{\partial K_{stat}}{\partial K_\alpha} UK_\alpha\right)^2 + \left(\frac{\partial K_{stat}}{\partial K_\gamma} UK_\gamma\right)^2 + \left(\frac{\partial K_{stat}}{\partial M} UM\right)^2 + {U_{sys}K_{stat}}^2} \tag{D.27}$$

Where $\mathrm{U}_{sys}K_{stat}$ is the systematic uncertainty on K_{stat} from the ex-situ probe calibration. For the L5HP and C5HP, this term can be computed as:

$$K_{stat} = \frac{P_{ave} - P_{stat}}{P_C - P_{ave}} \tag{D.28}$$

For the FRV4HP, the term is computed as:

$$K_{stat} = \frac{P_C - P_{stat}}{P_C - P_{ave}} \tag{D.29}$$

The equations for both probes depend on the instrumentation used to measure these quantities. The uncertainties on these measured quantities during the calibration phase are in Table D.2.

Table D.2: Uncertainty of sources used to build map of K_{stat}.

UP_{stat}	25.00	$[Pa]$
UP_C	34.47	$[Pa]$
UP_{ave}	17.24	$[Pa]$

D.3.5 Mach number

The Mach number retrieved with the probes is obtained by using the isentropic equation and the retrieved P_{tot} and P_{stat}:

$$M\left(P_{tot}, P_{stat}\right) = \sqrt{\frac{2}{\gamma - 1}\left[\left(\frac{P_{stat}}{P_{tot}}\right)^{-\frac{\gamma-1}{\gamma}} - 1\right]} \tag{D.30}$$

Therefore, an extra equation can be derived:

$$UM = \sqrt{\left(\frac{\partial M}{\partial P_{tot}} UP_{tot}\right)^2 + \left(\frac{\partial M}{\partial P_{stat}} UP_{stat}\right)^2} \tag{D.31}$$

D.3.6 System of equations to retrieve unknown uncertainties

From the equations established in the previous Sections, one can notice that the computation of the uncertainties depends on unknown terms (e.g., the uncertainty of K_{tot} depends on the uncertainty of M).

The uncertainty of K_α, K_γ, and P_{ave} can be computed since it solely relies on measured quantities. The uncertainty of K_{tot}, K_{stat}, P_{tot}, P_{stat} and M can be obtained simultaneously by using a system of Equations: Equation D.21, Equation D.22, Equation D.26, Equation D.27 and Equation D.30. The resulting system of equations for the L5HP and C5HP can be represented in matrix form as follows:

$$\begin{bmatrix} 1 & 0 & 0 & 0 & -\left(\frac{\partial K_{tot}}{\partial M}\right)^2 \\ 0 & 1 & 0 & 0 & -\left(\frac{\partial K_{stat}}{\partial M}\right)^2 \\ -\left(P_{ave} - P_{center}\right)^2 & 0 & 1 & 0 & 0 \\ -\left(P_{ave} - P_{center}\right)^2 & 0 & 0 & 1 & 0 \\ 0 & 0 & -\left(\frac{\partial M}{\partial P_{tot}}\right)^2 & -\left(\frac{\partial M}{\partial P_{stat}}\right)^2 & 1 \end{bmatrix} \begin{bmatrix} {UK_{tot}}^2 \\ {UK_{stat}}^2 \\ {UP_{tot}}^2 \\ {UP_{stat}}^2 \\ UM^2 \end{bmatrix}$$

$$= \begin{bmatrix} \left(\frac{\partial K_{tot}}{\partial K_\alpha} UK_\alpha\right)^2 + \left(\frac{\partial K_{tot}}{\partial K_\gamma} UK_\gamma\right)^2 + U_{sys}{K_{tot}}^2 \\ \left(\frac{\partial K_{stat}}{\partial K_\alpha} UK_\alpha\right)^2 + \left(\frac{\partial K_{stat}}{\partial K_\gamma} UK_\gamma\right)^2 + U_{sys}{K_{stat}}^2 \\ \left(\left(1 - K_{tot}\right) UP_{center}\right)^2 + \left(K_{tot} UP_{ave}\right)^2 \\ \left(\left(1 + K_{stat}\right) UP_{ave}\right)^2 + \left(-K_{stat} UP_{center}\right)^2 \\ 0 \end{bmatrix} \tag{D.32}$$

In the former system, the right-hand-side terms represent the known quantities. The Uα and Uγ can be obtained using Equation D.17 and Equation D.19 once the remaining terms have been computed.

A different, but similar, system can be obtained for the FRV4HP due to the different static pressure coefficient definition (the fourth line is modified):

$$\begin{bmatrix} 1 & 0 & 0 & 0 & -\left(\frac{\partial K_{tot}}{\partial M}\right)^2 \\ 0 & 1 & 0 & 0 & -\left(\frac{\partial K_{stat}}{\partial M}\right)^2 \\ -\left(P_{ave}-P_{center}\right)^2 & 0 & 1 & 0 & 0 \\ -\left(P_{ave}-P_{center}\right)^2 & 0 & 0 & 1 & 0 \\ 0 & 0 & -\left(\frac{\partial M}{\partial P_{tot}}\right)^2 & -\left(\frac{\partial M}{\partial P_{stat}}\right)^2 & 1 \end{bmatrix} \begin{bmatrix} {UK_{tot}}^2 \\ {UK_{stat}}^2 \\ \\ {UP_{tot}}^2 \\ {UP_{stat}}^2 \\ {UM}^2 \end{bmatrix}$$

$$= \begin{bmatrix} \left(\frac{\partial K_{tot}}{\partial K_\alpha} UK_\alpha\right)^2 + \left(\frac{\partial K_{tot}}{\partial K_\gamma} UK_\gamma\right)^2 + {U_{sys}K_{tot}}^2 \\ \left(\frac{\partial K_{stat}}{\partial K_\alpha} UK_\alpha\right)^2 + \left(\frac{\partial K_{stat}}{\partial K_\gamma} UK_\gamma\right)^2 + {U_{sys}K_{stat}}^2 \\ \left(\left(1-K_{tot}\right)UP_{center}\right)^2 + \left(K_{tot}UP_{ave}\right)^2 \\ \left(K_{stat}UP_{ave}\right)^2 + \left(\left(1-K_{stat}\right)UP_{center}\right)^2 \\ 0 \end{bmatrix} \tag{D.33}$$

D.4 Quantities Describing Cascade Performance

In addition to the previous quantities, the losses and flow deviation are derived from additional data reduction.

D.4.1 Primary flow direction

The primary flow direction is computed as:

$$\beta = arctan\left(\frac{V_{tan}}{V_{ax}}\right) \tag{D.34}$$

The propagated errors yield:

$$U\beta = \sqrt{\left(\frac{V_{ax}}{V_{tan}^2+V_{ax}^2}UV_{tan}\right)^2 + \left(\frac{-V_{tan}}{V_{tan}^2+V_{ax}^2}UV_{ax}\right)^2} \tag{D.35}$$

D.4.2 Cascade pitch angle

The cascade pitch angle is computed as:

$$\gamma = arctan\left(\frac{V_{rad}}{V_{ax}}\right) \tag{D.36}$$

The propagated errors yield:

$$U\gamma = \sqrt{\left(\frac{V_{ax}}{V_{rad}^2+V_{ax}^2}UV_{rad}\right)^2 + \left(\frac{-V_{rad}}{V_{rad}^2+V_{ax}^2}UV_{ax}\right)^2} \tag{D.37}$$

D.4.3 Normalized static pressure

The normalized static pressure is computed as P/P_{01}. By propagating the error, one gets the following equation:

$$U\left(\frac{P}{P_{01}}\right) = \sqrt{\left(\frac{1}{P_{01}}UP\right)^2 + \left(\frac{-P}{P_{01}^2}UP_{01}\right)^2} \tag{D.38}$$

D.4.4 Normalized total pressure

The normalized total pressure is computed as P_{06}/P_{01}. By propagating the error, one gets the following equation:

$$U\left(\frac{P_{06}}{P_{01}}\right) = \sqrt{\left(\frac{1}{P_{01}}UP_{06}\right)^2 + \left(\frac{-P_{06}}{P_{01}^2}UP_{01}\right)^2} \tag{D.39}$$

D.4.5 Total pressure loss coefficient without static pressure

The total pressure loss coefficient is computed as:

$$Y = \frac{P_{01} - P_{06}}{P_{01}} \tag{D.40}$$

The propagation of error yields:

$$UY = \sqrt{\left(\frac{P_{06}}{P_{01}^2}UP_{01}\right)^2 + \left(-\frac{1}{P_{01}}UP_{06}\right)^2} \tag{D.41}$$

D.4.6 Total pressure loss coefficient with static pressure

The total pressure loss coefficient is computed as:

$$\zeta = \frac{P_{01} - P_{06}}{P_{01} - P} \tag{D.42}$$

The propagation of error yields:

$$U\zeta = \sqrt{\left(-\frac{P - P_{06}}{(P_{01} - P)^2}UP_{01}\right)^2 + \left(\frac{1}{P - P_{01}}UP_{06}\right)^2 + \left(\frac{P_{01} - P_{06}}{(P_{01} - P)^2}UP\right)^2} \tag{D.43}$$

D.4.7 Kinetic energy loss coefficient

The kinetic energy loss coefficient is computed as:

$$\xi = 1 - \frac{1 - \left(\frac{P_6}{P_{06}}\right)^{\frac{\gamma-1}{\gamma}}}{1 - \left(\frac{P_6}{P_{01}}\right)^{\frac{\gamma-1}{\gamma}}} \tag{D.44}$$

Following the error propagation theory, the uncertainty is:

$$U\xi = \sqrt{\left(\left(AUP_6\right)^2 + \left(BUP_{06}\right)^2 + \left(CUP_{01}\right)^2\right)} \tag{D.45}$$

Where:

$$A = -\frac{dP_6^d P_{01}^{d-1}\left(-\left(\frac{P_6}{P_{06}}\right)^d + 1\right)}{\left(P_{01}^d - P_6^d\right)^2} \tag{D.46}$$

$$B = -\frac{dP_6^d}{P_{06}^{d+1}\left(-\left(\frac{P_6}{P_{01}}\right)^d + 1\right)} \tag{D.47}$$

$$C = -\frac{P_{01}^{2d}\left(\frac{dP_6^{d-1}\left(-\left(\frac{P_6}{P_{06}}\right)^d+1\right)}{P_{01^d}} - \frac{dP_6^{d-1}\left(-\left(\frac{P_6}{P_{01}}\right)^d+1\right)}{P_{06^d}}\right)}{\left(P_{01}^d - P_6^d\right)^2} \tag{D.48}$$

$$d = \frac{\gamma - 1}{\gamma} \tag{D.49}$$

E

Comparison of Blade Loading and Hot-Film Measurements for Steady and Unsteady Inlet Flow

E.1 Steady Inlet Flow

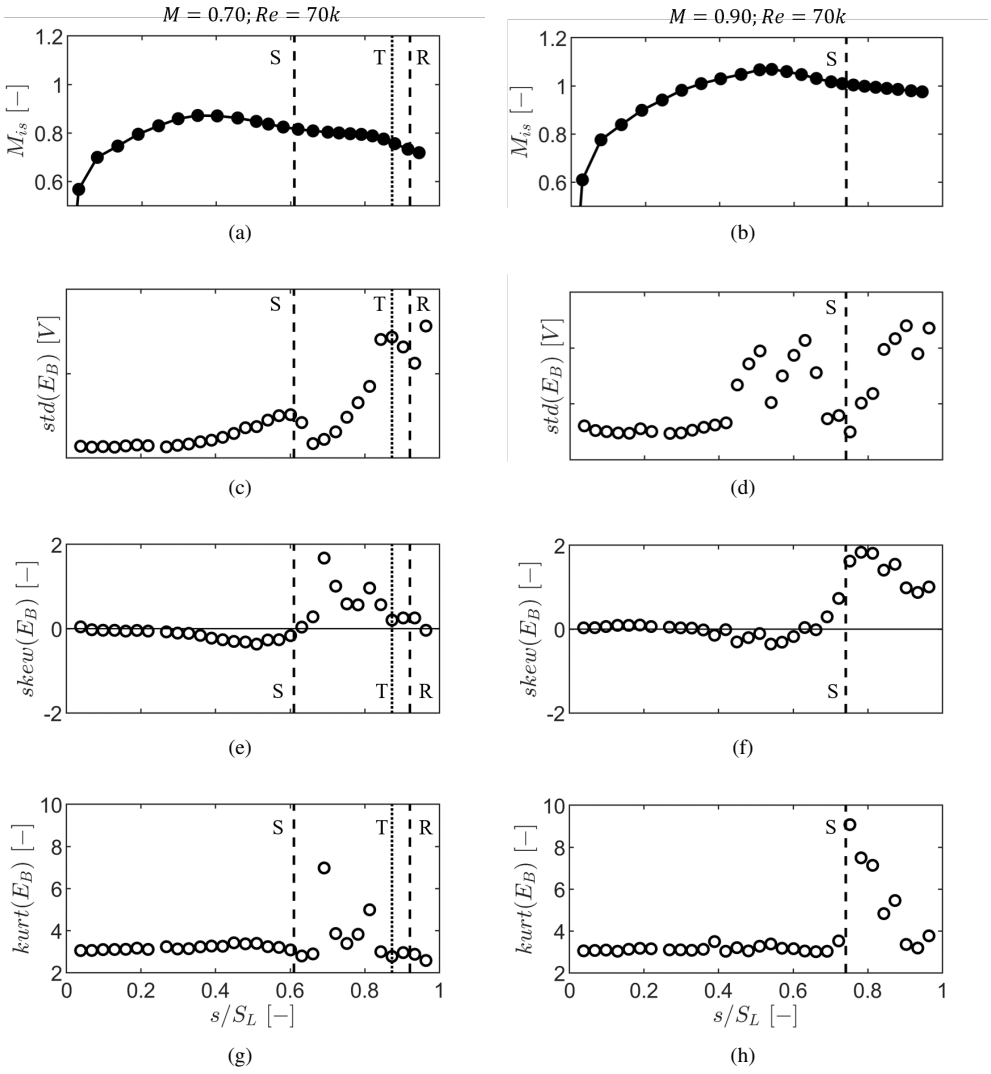

Figure E.1: Blade isentropic Mach number for M=0.70; Re=70k (a) and M=0.90; Re=70k (b), standard deviation of HF bridge voltage for M=0.70; Re=70k (c) and M=0.90; Re=70k (d), skewness of HF bridge voltage for M=0.70; Re=70k (e) and M=0.90; Re=70k (f), and kurtosis of HF bridge voltage for M=0.70; Re=70k (g) and M=0.90; Re=70k (h).

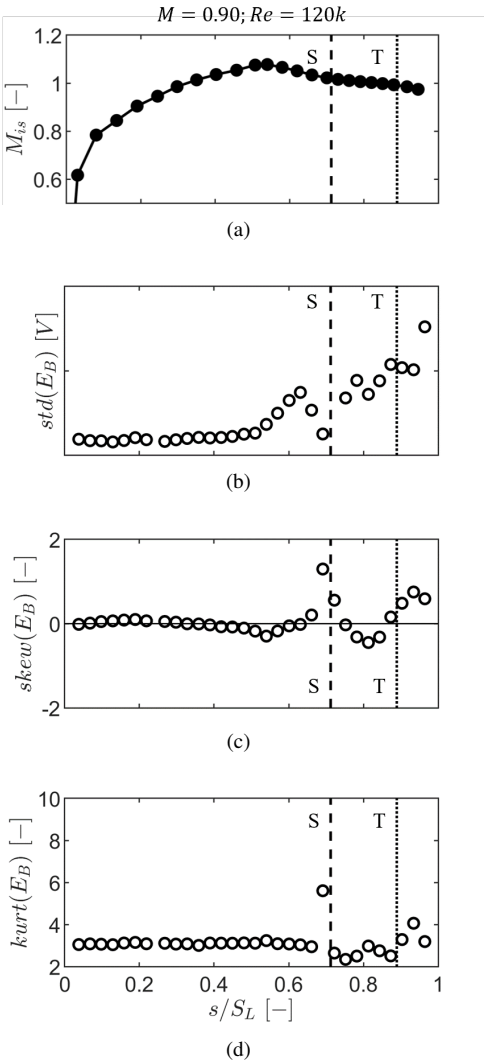

Figure E.2: Quantities for M=0.90; Re=120k: Blade isentropic Mach number(a), standard deviation of HF bridge voltage (b), skewness of HF bridge voltage (c), and kurtosis of HF bridge voltage (d).

E.2 Unsteady Inlet Flow

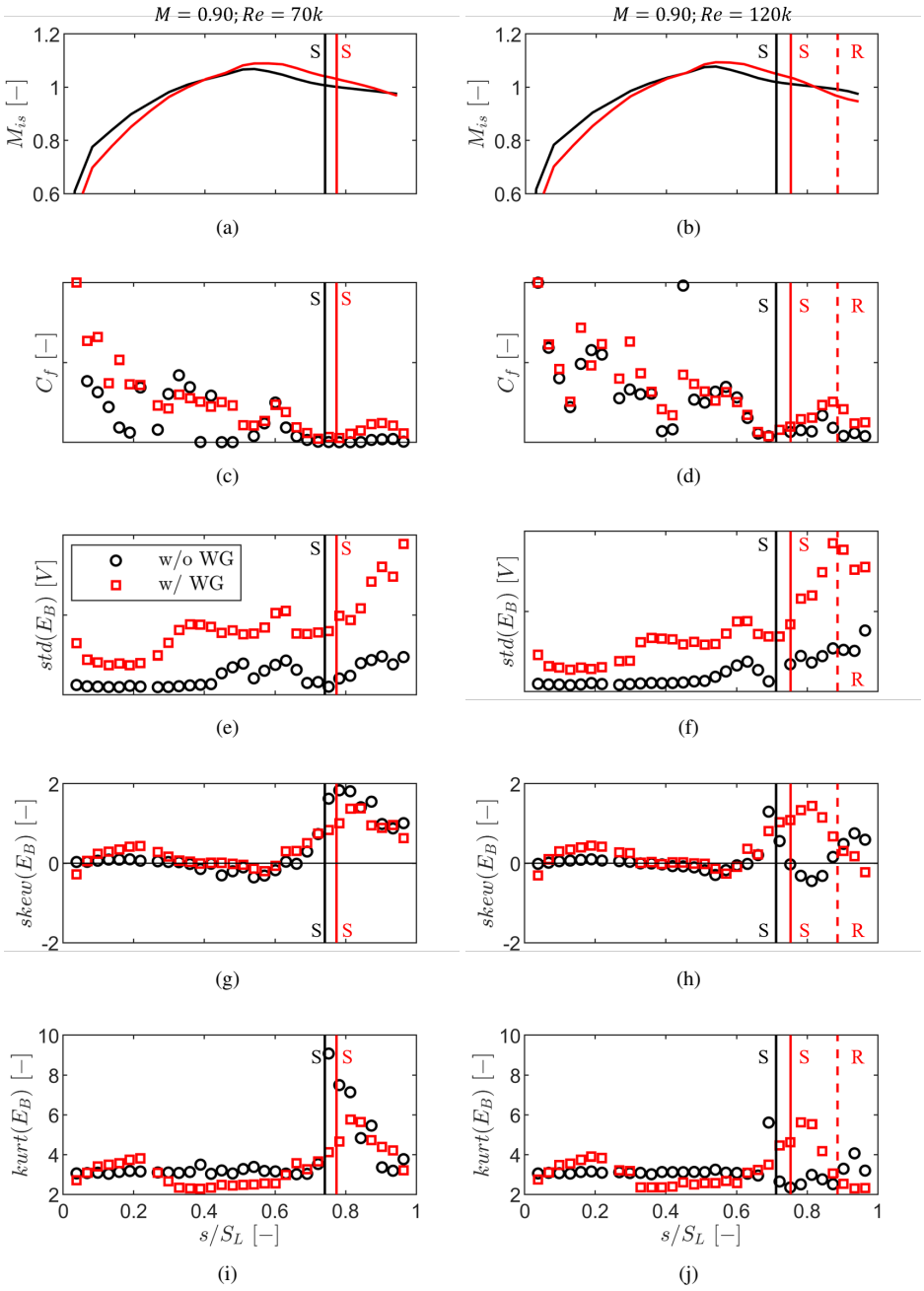

Figure E.3: Blade isentropic Mach number for M=0.90; Re=70k (a) and M=0.90; Re=120k (b), pseudo skin friction coefficient for M=0.90; Re=70k (c) and M=0.90; Re=120k (d), standard deviation of HF bridge voltage for M=0.90; Re=70k (e) and M=0.90; Re=120k (f), skewness of HF bridge voltage for M=0.90; Re=70k (g) and M=0.90; Re=120k (h), and kurtosis of HF bridge voltage for M=0.90; Re=70k (i) and M=0.90; Re=120k (j).

F

Boundary layer parameters

F.1 Plane 01

Table F.1: Boundary layer integral parameters measured at Plane 01.

M_{out} [−]	Re_{out} [−]	δ_{98}/C [−]	δ_{99}/C [−]	δ^*/C [−]	θ/C [−]	H_{12} [−]
0.70	65000	0.419	0.457	0.0502	0.0369	1.36
0.80		0.419	0.457	0.0498	0.0361	1.38
0.90		0.419	0.457	0.0485	0.0347	1.40
0.70	70000	0.419	0.495	0.0522	0.0370	1.41
0.80		0.419	0.457	0.0506	0.0365	1.39
0.90		0.419	0.457	0.0482	0.0345	1.40
0.95		0.419	0.457	0.0466	0.0349	1.34
0.70	100000	0.419	0.495	0.0490	0.0368	1.33
0.80		0.419	0.457	0.0479	0.0356	1.35
0.90		0.419	0.457	0.0494	0.0348	1.42
0.95		0.381	0.457	0.0477	0.0339	1.41
0.70	120000	0.381	0.457	0.0496	0.0360	1.37
0.80		0.419	0.457	0.0500	0.0358	1.37
0.90		0.381	0.457	0.0496	0.0344	1.44
0.95		0.381	0.457	0.0472	0.0344	1.37

F.2 Plane 02

Table F.2: Boundary layer integral parameters measured at Plane 02.

M_{out} $[-]$	Re_{out} $[-]$	St $[-]$	PMFR [%]	δ_{98}/C $[-]$	δ_{99}/C $[-]$	δ^*/C $[-]$	θ/C $[-]$	H_{12} $[-]$
0.70	70000	/	/					
0.80		/	/					
0.90		/	/	0.256	0.348	0.0463	0.0346	1.34
0.95		/	/					
0.90		0.95	/	0.111	0.169	0.0223	0.0187	1.18
0.90		0.95	0.00	0.078	0.126	0.0131	0.0114	1.13
0.90		0.95	0.50	0.069	0.115	0.0122	0.0105	1.15
0.90		0.95	0.90	0.069	0.116	0.0123	0.0106	1.17
0.80	120000	/	/					
0.90		/	/					

G

Experimental Loss Breakdown

G.1 Mass-Averaged

Table G.1: Experimental loss breakdown in terms of mass-averaged quantities.

M $[-]$	Re $[-]$	St $[-]$	PMFR $[-]$	$\xi_{BL,Preston}$	$\xi_{BL,C5HP}$	ξ_{prof}	$\xi_{net,Preston}$	$\xi_{net,C5HP}$
0.70	70k	0.00	/	0.0167	/	0.0373	0.0126	/
0.80	70k	0.00	/	0.0136	/	0.0352	0.0094	/
0.90	70k	0.00	/	0.0112	0.0091	0.0315	0.0111	0.0133
0.95	70k	0.00	/	0.0103	/	0.0286	0.0096	/
0.80	120k	0.00	/	0.0135	/	0.0287	0.0086	/
0.90	120k	0.00	/	0.0112	/	0.0286	0.0084	/
0.90	70k	0.95	/	/	0.0040	0.0405	/	0.0126
0.90	70k	0.95	0.00	/	0.0022	0.0401	/	0.0137
0.90	70k	0.95	0.50	/	0.0020	0.0400	/	0.0176
0.90	70k	0.95	0.90	/	0.0020	0.0401	/	0.0203

G.2 Mixed-Out-Averaged

Table G.2: Experimental loss breakdown in terms of mixed-out-averaged quantities.

M $[-]$	Re $[-]$	St $[-]$	PMFR $[-]$	$\xi_{BL,Preston}$	$\xi_{BL,C5HP}$	ξ_{prof}	$\xi_{net,C5HP}$
0.70	70k	0.00	/	0.0167	/	0.0385	/
0.80	70k	0.00	/	0.0136	/	0.0364	/
0.90	70k	0.00	/	0.0112	0.0103	0.0334	0.0186
0.95	70k	0.00	/	0.0103	/	0.0304	/
0.80	120k	0.00	/	0.0135	/	0.0298	/
0.90	120k	0.00	/	0.0112	/	0.0299	/
0.90	70k	0.95	/	/	0.0046	0.0424	0.0159
0.90	70k	0.95	0.00	/	0.0024	0.0420	0.0177
0.90	70k	0.95	0.50	/	0.0022	0.0420	0.0257
0.90	70k	0.95	0.90	/	0.0022	0.0421	0.0290

H

Error from Different Methods of Estimating the Separation Location

Table H.1: Error from the family of Thwaites parameter methods in estimating the separation location with respect to experimental prediction.

M $[-]$	Re $[-]$	Pohlhausen	Timman	Walz	Thwaites	Curle and Skan
0.7	65k	-4.3	-15.1	-18.6	-15.9	-15.1
0.8	65k	-1.9	-9.8	-12.4	-10.7	-9.8
0.9	65k	-9.5	-14.1	-14.8	-14.1	-14.1
0.7	70k	-4.9	-14.8	-18.3	-15.7	-14.8
0.8	70k	-1.9	-10.7	-13.3	-11.5	-9.8
0.9	70k	-9.6	-14.2	-14.9	-14.2	-14.2
0.95	70k	-13.5	-15.0	-15.7	-15.0	-14.2
0.7	100k	-7.9	-15.9	-20.3	-16.8	-15.9
0.8	100k	-4.2	-13.0	-15.6	-13.9	-12.1
0.9	100k	-10.4	-12.7	-13.5	-12.7	-12.7
0.95	100k	-13.8	-14.5	-14.5	-14.5	-13.8
0.7	120k	-7.6	-17.4	-22.7	-19.2	-17.4
0.8	120k	-4.5	-12.4	-15.8	-13.3	-12.4
0.9	120k	-9.1	-10.7	-11.5	-11.5	-10.7
0.95	120k	-13.4	-14.1	-14.8	-14.1	-14.1
Mean error [%]		-7.8	-13.6	-15.8	-14.2	-13.4

Table H.2: Error from the family of Stratford methods in estimating the separation location with respect to experimental prediction.

M $[-]$	Re $[-]$	$m = 3$ w/o LE	$m = 4$ w/o LE	$m = 3$ w/ LE	$m = 4$ w/ LE
0.7	65k	-12.4	-16.8	-7.0	-11.5
0.8	65k	-7.2	-9.8	-3.7	-2.8
0.9	65k	-12.6	-13.3	-9.5	-4.2
0.7	70k	-12.1	-15.7	-6.7	-11.2
0.8	70k	-8.0	-10.7	-3.7	-3.7
0.9	70k	-12.6	-13.4	-9.6	-4.2
0.95	70k	-13.5	-14.2	-12.1	-11.4
0.7	100k	-13.3	-16.8	-7.9	-14.2
0.8	100k	-10.4	-13.0	-5.1	-6.9
0.9	100k	-11.9	-12.7	-10.4	-4.0
0.95	100k	-13.1	-13.8	-12.4	-10.9
0.7	120k	-14.8	-18.3	-8.5	-14.8
0.8	120k	-9.8	-13.3	-5.4	-8.0
0.9	120k	-9.9	-10.7	-8.3	-4.3
0.95	120k	-13.4	-14.1	-11.9	-10.4
Mean error [%]		-11.7	-13.8	-8.1	-8.2

I

Boundary Layer Integral Parameters at Blade Trailing Edge

Table I.1: Boundary layer integral parameters on the pressure side near the trailing edge from the model of Coull.

$M\ [-]$	$Re\ [-]$	$St\ [-]$	$\delta^*_{PS,TE}\ [mm]$	$\theta_{PS,TE}\ [mm]$
0.70	65000	0.00	0.142	0.060
0.80	65000	0.00	0.138	0.059
0.90	65000	0.00	0.125	0.053
0.70	70000	0.00	0.138	0.059
0.80	70000	0.00	0.133	0.056
0.90	70000	0.00	0.120	0.051
0.95	70000	0.00	0.104	0.048
0.70	100000	0.00	0.115	0.049
0.80	100000	0.00	0.110	0.047
0.90	100000	0.00	0.101	0.043
0.95	100000	0.00	0.087	0.040
0.70	120000	0.00	0.105	0.045
0.80	120000	0.00	0.100	0.042
0.90	120000	0.00	0.092	0.039
0.95	120000	0.00	0.081	0.037
0.70	65000	1.19	0.142	0.060
0.80	65000	1.06	0.138	0.059
0.90	65000	0.95	0.125	0.053
0.70	70000	1.19	0.138	0.059
0.80	70000	1.06	0.133	0.056
0.90	70000	0.95	0.120	0.051
0.95	70000	0.91	0.104	0.048
0.70	100000	1.19	0.115	0.049
0.80	100000	1.06	0.110	0.047
0.90	100000	0.95	0.101	0.043
0.95	100000	0.91	0.087	0.040
0.70	120000	1.19	0.105	0.045
0.80	120000	1.06	0.100	0.042
0.90	120000	0.95	0.092	0.039
0.95	120000	0.91	0.081	0.037

Table I.2: Boundary layer integral parameters on the suction side near the trailing edge from the model of Coull.

M $[-]$	Re $[-]$	St $[-]$	$\delta^*_{SS,TE}$ $[mm]$	$\theta_{SS,turb}$ $[mm]$	$\theta_{SS,bubble}$ $[mm]$	$\theta_{SS,wake}$ $[mm]$	$\theta_{SS,TE}$ $[mm]$
0.70	65000	0.00	0.448	0.210	0.004	0.000	0.215
0.80	65000	0.00	0.450	0.172	0.003	0.000	0.176
0.90	65000	0.00	0.347	0.108	0.002	0.000	0.110
0.70	70000	0.00	0.422	0.208	0.004	0.000	0.211
0.80	70000	0.00	0.410	0.168	0.003	0.000	0.171
0.90	70000	0.00	0.398	0.118	0.002	0.000	0.121
0.95	70000	0.00	0.378	0.089	0.002	0.000	0.091
0.70	100000	0.00	0.327	0.179	0.002	0.000	0.181
0.80	100000	0.00	0.324	0.148	0.001	0.000	0.150
0.90	100000	0.00	0.334	0.113	0.001	0.000	0.114
0.95	100000	0.00	0.255	0.086	0.001	0.000	0.087
0.70	120000	0.00	0.294	0.169	0.001	0.000	0.170
0.80	120000	0.00	0.275	0.139	0.001	0.000	0.140
0.90	120000	0.00	0.252	0.103	0.001	0.000	0.104
0.95	120000	0.00	0.191	0.072	0.001	0.000	0.073
0.70	65000	1.19	0.468	0.210	0.001	0.067	0.278
0.80	65000	1.06	0.429	0.172	0.001	0.059	0.232
0.90	65000	0.95	0.337	0.108	0.001	0.052	0.161
0.70	70000	1.19	0.457	0.208	0.001	0.067	0.275
0.80	70000	1.06	0.409	0.168	0.001	0.059	0.228
0.90	70000	0.95	0.367	0.118	0.001	0.052	0.172
0.95	70000	0.91	0.345	0.089	0.001	0.049	0.139
0.70	100000	1.19	0.396	0.179	0.000	0.067	0.247
0.80	100000	1.06	0.357	0.148	0.001	0.059	0.208
0.90	100000	0.95	0.330	0.113	0.001	0.053	0.166
0.95	100000	0.91	0.275	0.086	0.000	0.050	0.136
0.70	120000	1.19	0.375	0.169	0.000	0.067	0.236
0.80	120000	1.06	0.329	0.139	0.000	0.059	0.198
0.90	120000	0.95	0.285	0.103	0.000	0.053	0.156
0.95	120000	0.91	0.234	0.072	0.000	0.049	0.122